Materials Horizons: From Nature to Nanomaterials

M. K. Jayaraj *Editor*

Nanostructured Metal Oxides and Devices

Optical and Electrical Properties

Springer

Materials Horizons: From Nature to Nanomaterials

Series Editor

Vijay Kumar Thakur, School of Aerospace, Transport and Manufacturing, Cranfield University, Cranfield, UK

Materials are an indispensable part of human civilization since the inception of life on earth. With the passage of time, innumerable new materials have been explored as well as developed and the search for new innovative materials continues briskly. Keeping in mind the immense perspectives of various classes of materials, this series aims at providing a comprehensive collection of works across the breadth of materials research at cutting-edge interface of materials science with physics, chemistry, biology and engineering.

This series covers a galaxy of materials ranging from natural materials to nanomaterials. Some of the topics include but not limited to: biological materials, biomimetic materials, ceramics, composites, coatings, functional materials, glasses, inorganic materials, inorganic-organic hybrids, metals, membranes, magnetic materials, manufacturing of materials, nanomaterials, organic materials and pigments to name a few. The series provides most timely and comprehensive information on advanced synthesis, processing, characterization, manufacturing and applications in a broad range of interdisciplinary fields in science, engineering and technology.

This series accepts both authored and edited works, including textbooks, monographs, reference works, and professional books. The books in this series will provide a deep insight into the state-of-art of *Materials Horizons* and serve students, academic, government and industrial scientists involved in all aspects of materials research.

More information about this series at http://www.springer.com/series/16122

M. K. Jayaraj
Editor

Nanostructured Metal Oxides and Devices

Optical and Electrical Properties

Springer

Editor
M. K. Jayaraj
Department of Physics
Cochin University of Science and Technology
Kochi, India

ISSN 2524-5384 ISSN 2524-5392 (electronic)
Materials Horizons: From Nature to Nanomaterials
ISBN 978-981-15-3313-6 ISBN 978-981-15-3314-3 (eBook)
https://doi.org/10.1007/978-981-15-3314-3

This Springer imprint is published by the registered company Springer Nature Singapore Pte Ltd.
The registered company address is: 152 Beach Road, #21-01/04 Gateway East, Singapore 189721, Singapore

To My Beloved Students……

Preface

The diverse range of optical, electrical and chemical properties exhibited by metal oxides makes them potential materials for fundamental research and technological applications. The intriguing electronic structure of metal oxides has found their applications in different areas such as microelectronics, sensors, fuel cells, coatings and catalysts. Wide band gap semiconducting oxides such as SnO_2, ZnO and TiO_2 are widely being used as optical components, transparent conductors and gas sensors. Besides, millions of dollars' worth of metal oxides are employed in the chemical and petrochemical industries as catalysts. Metal oxides are also under constant use as catalysts for the removal of toxic gases for controlling environmental pollution. Many potential applications are still being explored, and novel as well as facile synthesis methods are being developed. The advent of nanotechnology has triggered the development of nanostructures or nano-arrays with special properties when compared to their bulk or single-particle counterparts. Nanostructured materials exhibit unique physical and chemical properties due to confinement effects at smaller sizes and a high density of corner or edge surface sites. The notable change in average particle size in turn alters the band gap of metal oxides which strongly influences their intrinsic electrical conductivity and chemical reactivity. The less coordinated atoms at corners/edges of metal oxide nanostructures or the presence of O vacancies create occupied electronic states just above the valence band of the corresponding bulk material, thereby enhancing the chemical activity of the nanostructures. In general, this book covers the fundamental science, synthesis, characterization, optoelectronic properties and applications of metal oxide nanomaterials. The basic aspects of synthetic procedures and fabrication technologies are discussed, and the experimental techniques are explained. The current status of nanostructured oxide materials and related devices from a technological point of view is reviewed.

In this book, the two major aspects of metal oxide nanostructures, namely their optical and electrical properties, have been dealt with in detail. Each chapter is content-wise stand-alone though it shares a conceptual concurrence with the rest of the chapters in terms of the optoelectronic properties of oxide nanomaterials. The first five chapters help in understanding the optical characteristics of materials, especially metal oxides at nanoscale. A comprehensive idea on the luminescence

observed in metal oxides and their wide-scale use in ACTFEL devices is included. The shift in research focus from sulphide-based phosphors to oxide-based light emitters is briefly outlined. Various binary and ternary oxide-based phosphor system matrices are presented in detail. In the second chapter, different upconverted luminescent nanomaterials along with the existing mechanisms of upconversion are summarized. Reviews on the applications of upconverted materials in solar cell, bioimaging and security printing are also detailed in the discussions. The colloids synthesized via liquid phase-pulsed laser ablation help in the growth of nanoparticles without any surfactants. The luminescent surfactant-free nanoparticles grown by LP-PLA technique can be used for bioimaging. The fabrication of symmetric and asymmetric quantum well structures based on ZnO with ZnMgO and $CuGaO_2$ as the barrier layer was realized by pulsed laser ablation technique. Moreover, the book edifies another interesting phenomenon, surface-enhanced Raman scattering (SERS), exhibited by specially designed metal oxides nanostructures as substrates and their application as portable devices in the areas of sensing and bioimaging.

The electrical properties of metal oxides are found to span from insulators and semiconductors to metals and even superconductors. Nanostructured metal oxides that exhibit a high optical transmittance along with high electrical conductivity, referred to as transparent conductive oxides, have also gained immense attraction in the field of solar cells, gas sensors, field emitters, light-emitting diodes (LED), photo-catalysts, piezoelectric nanogenerators and nano-optoelectronic devices. This book compiles the reach of oxide materials in the form of nanoparticles, nanorods, nanowires, nanofibers, etc. for various device applications. A brief review explains the different growth techniques developed for fabricating one-dimensional ZnO nanostructures and their applications in conventional two terminal devices like diodes, LEDs, solar cells, etc., three terminal devices like transistors and other devices like energy generators and memory devices. The chemiresistive nature of metal oxides as efficient gas sensors, the interesting change in the magnetic structure of metal oxide thin films as dilute magnetic semiconductors for spintronic applications and the role of epitaxial growth of dielectric thin films for microwave applications are the other major highlights of this book. The gas-sensing mechanism of oxide-based sensors including heterojunction sensors like p–n junction, Schottky junction, etc. is elaborated along with some interesting results of the ethanol response characteristic of p-CuO/n-ZnO junction sensor. The book also gives an insight into the correlation of various experimental results on ZnO-based dilute magnetic semiconductors with supporting theories and ab-initio calculations. In addition to a generic overview on metal oxide-based thin-film transistors, the book has also accommodated an exclusive detailed description of the calculation of trap density states in the band gap of semiconductors using temperature-dependent measurements. In short, the book is addressed focussing active researchers and academicians in the area of material science and semiconductor technology, especially nano-photonics and electronics.

Kochi, India M. K. Jayaraj

Acknowledgements

It is with great pleasure and pride that I acknowledge all those who contributed in realizing this book on *Nanostructured Metal Oxides and Devices—Optical and Electrical Properties*.

I extend my sincere thanks to all my former students Dr. Aneesh P. M., Dr. Krishnaprasad P. S., Dr. Minikrishna K., Dr. Reshmi R., Dr. Arun Aravind, Dr. Vikas L. S., Dr. Hasna K., Dr. Subha P. P., Dr. Shijeesh M. R., Dr. Anjana Radhakrishnan, Mr. Kurias K. M. and Ms. Jasna M., who did their doctoral research under my guidance at Nanophotonic and Optoelectronic Devices Laboratory, Department of Physics, Cochin University of Science and Technology. They have contributed their research results meticulously for each chapter of this book. I also take this opportunity to thank with due regards my students, Mr. Manu Shaji, Ms. Anju K. S., Mr. Midhun P. S., Mr. Subin P. S., Ms. Priya M. J., Ms. Anamika Ashok, Ms. Krishnapriya T. K. and Mr. Frenson P. Jose, for proof reading and correcting the manuscript.

My sincere thanks to Dr. Pillai Aswathy Mohan, Assistant Professor, St. Stephens College, Pathanapuram, for helping me in the compilation and submission of this book to Springer.

I record my gratitude to the Cochin University of Science and Technology for the sabbatical leave, which gave me enough opportunity to invest my time on this book.

I extend my warm regards and gratitude to my family, especially my wife Dr. Vanaja, and my children, Ms. Anooja and Ms. Anjala, for providing me all the personal and cordial support to make my academic life fruitful.

It was a pleasant experience to work with the Springer Editorial team who enabled the timely publication of the book.

Prof. M. K. Jayaraj

Contents

Editor and Contributors

About the Editor

Dr. M. K. Jayaraj is currently a Professor at the Department of Physics, Cochin University of Science and Technology (CUSAT), India. He earned his master's and Ph.D. from CUSAT, and completed his postdoctoral research at eminent institutions in India, Italy, France, Japan, and the USA. He is the founder director of the Centre of Excellence in Advanced materials, CUSAT. He is also the mentor of 'Delgado Coating & Technology Solutions Private Limited'. Dr. Jayaraj is a pioneer in the field of thin-film and nanocomposite devices, including sensors/detectors and energy converters, and transparent conductors for photovoltaics. He has more than 180 research publications, several edited books and book chapters, and patents to his credit. In addition, he was honored with the MRSI Medal 2019, conferred by the Materials Research Society of India.

Contributors

P. M. Aneesh Department of Physics, Central University of Kerala, Kasaragod, Kerala, India

R. Anjana Department of Physics, Cochin University of Science and Technology, Kochi, India

Arun Aravind Centre for Advanced Functional Materials, Department of Physics, Bishop Moore College, Mavelikkara, India

Kudilatt Hasna Government Arts and Science College, Calicut, India

M. Jasna Cochin University of Science and Technology, Kochi, India

M. K. Jayaraj Department of Physics, Cochin University of Science and Technology, Kochi, India

P. S. Krishnaprasad Government Polytechnic College, Kothamangalam, India

Kurias K. Markose Department of Physics, Cochin University of Science and Technology, Kochi, India

K. Mini Krishna Department of Physics, Vimala College, Thrissur, Kerala, India

Pillai Aswathy Mohan St. Stephen's College, Pathanapuram, India

R. Reshmi Department of Physics, Union Christian College, Aluva, Kerala, India

M. R. Shijeesh Graphene & 2D Systems Laboratory, Department of Physics, Indian Institute of Technology Madras, Chennai, India

Subha P. P Department of Physics, Cochin University of Science and Technology, Kochi, India

K. A. Vanaja Maharaja's College, Ernakulam, India

L. S. Vikas Department of Physics, Govt. Arts College, Thiruvananthapuram, Kerala, India

Abbreviations

0D	Zero dimensional
1D	One dimensional
2DEG	Two-dimensional electron gas
3D	Three dimensional
4-MBA	4-Mercaptobenzoic acid
4-Mpy	4-Mercaptopyridine
A	Activator
AA	Amino hexanoic acid
ACPEL	Alternating current powder electroluminescent display
ACTFEL	Alternating current thin-film electroluminescent display
AFM	Atomic force microscopy
AHE	Anomalous Hall effect
Al_2O_3	Aluminium oxide
ALD	Atomic layer deposition
ALE	Atomic layer epitaxy
AOS	Amorphous oxide semiconductor
APTE	Addition de photon par transfertsd'energies
ATO	Antimony-doped tin oxide
BMP	Bound magnetic polaron
BR	Bloembergen–Rowland
BST	Barium strontium titanate
BT	Benzene thiol
BZN	Bismuth zinc niobate
$C_2H_4(NH_2)_2$	Ethylenediamine
C_2H_6OS	Dimethyl sulphoxide
$C_6H_{12}N_4$	Hexamethylenetetramine
CB	Conduction band
CdO	Cadmium oxide
CE	Chemical enhancement

CF	Crystal field
$CH_3(CH_2)_{11}OSO_3Na$	Sodium dodecyl sulphate
CIE	International commission on illumination
CL	Cathodoluminescence
CMR	Colossal magnetoresistance
CR	Cross-relaxation
CRT	Cathode ray tube
c-Si	Crystalline silicon
CSU	Cooperative sensitization upconversion
CT	Charge transfer
CTAB	Cetyltrimethylammonium bromide
CTS	Charge transfer state
$CuGaO_2$	Copper gallium oxide
CVD	Chemical vapour deposition
DBR	Distributed Bragg reflector
DCEL	Direct current electroluminescent display
DME	Domain matching epitaxy
DMS	Dilute magnetic semiconductors
DMSO	Dimethyl sulphoxide
DNA	Deoxyribonucleic acid
DOS	Density of states
DRAM	Dynamic random-access memory
DSSC	Dye-sensitized solar cell
E	Excited state
E_A	Activation energy
EBE	Electron beam evaporation
EBL	Electron beam lithography
EDA	Ethylenediamine
EDTA	Ethylenediaminetetraacetic acid
EG	Ethylene glycol
EL	Electroluminescence
EM	Electromagnetic
EMU	Energy migration-mediated upconversion
EQE	External quantum efficiency
ESA	Excited state absorption
ETU	Energy transfer upconversion
FC	Field cooled
FED	Field emission display
FESEM	Field emission scanning electron microscopy
FET	Field-effect transistors
FeTFT	Ferroelectric thin-films transistors
FIB	Focused ion beam
FPD	Flat panel display
FRET	Förster resonance energy transfer or fluorescence resonance energy transfer

FT-IR	Fourier transform infrared spectroscopy
FWHM	Full width at half maximum
G	Ground state
GaN	Gallium nitride
GMR	Giant magnetoresistance
GSA	Ground state absorption
HAp	Hydroxyapatite
HMTA	Hexamethylenetetramine
HOMO	Highest occupied orbital
HRTEM	High-resolution transmission electron microscopy
HRXRD	High-resolution X-ray diffraction
HVPE	Halide vapour phase epitaxy
IC	Internal conversion
ICP-AES	Inductively coupled plasma atomic emission spectroscopy
ID	Drain current
IDC	Interdigital capacitor
IR	Infrared
ISC	Intersystem crossing
ITO	Indium tin oxide
IUPAC	International Union of Pure and Applied Chemistry
KPFM	Kelvin probe microscopy
LCD	Liquid-crystal display
LDA	Local-density approximation
LED	Light-emitting diode
LFM	Lateral force microscopy
LME	Lattice matching epitaxy
LP-PLA	Liquid phase-pulsed laser ablation
LSI	Large-scale integrated circuit
LUMO	Lowest unoccupied molecular orbital
LVCL	Low voltage cathodoluminescent
MBE	Molecular beam epitaxy
MCD	Magnetic circular dichroism
MEMS	Micro-electro-mechanical systems
MgO	Magnesium oxide
MIS	Metal–insulator–semiconductor
MISIM	Metal–insulator–semiconductor–insulator–metal
MOCVD	Metal organic chemical vapour deposition
MOS	Metal oxide semiconductor gas sensors
MOSFET	Metal oxide field-effect transistor
MOVPE	Metal organic vapour phase epitaxy
MPMS	Magnetic property measurement system
MQW	Multiple quantum well
MRAM	Magnetic random-access memory
M_S	Saturation magnetization
MTJs	Magnetic tunnel junctions

NaOH	Sodium hydroxide
Nd:YAG	Neodymium-doped yttrium aluminium garnet
NED	Nano-emissive display
NEG	Nippon Electric Glass
NH_4OH	Ammonium hydroxide
NIL	Nano-imprint lithography
NIR	Near infrared
NMR	Nuclear magnetic resonance spectroscopy
NP	Nano phosphors
NPs	Nanoparticles
OA	Oleic acid
ODE	1-octadecene
OLED	Organic light-emitting diode
OM	Oleylamine
OTFT	Organic thin-film transistor
P3HT	Poly(3-hexylthiophene-2,5-diyl)
PA	Photon avalanche
PAA	Polyacrylic acid
PB	Propagation breakdown
PCE	Photoconversion efficiency
PCVD	Plasma chemical vapour deposition
PDA	Personal digital assistant
PDP	Plasma display panel
PEDOT	Poly3,4-ethylene dioxythiophene
PEG	Polyethylene glycol
PEI	Polyethylenimine
PET	Polyethylene terephthalate
PICT	Photoinduced charge transfer
PL	Photoluminescence
PLD	Pulsed laser deposition
PMMA	Polymethyl methacrylate
PPC	Parallel plate capacitor
PTCDI-C8	N,n′-dioctyl-3,4,9,10-perylenedicarboximide
PV	Photovoltaic
PVA	Polyvinyl alcohol
PVP	Polyvinylpyrrolidone
QC	Quantum cascade
R6G	Rhodamine-6g
RE	Rare earth
RGB	Red green blue
RKKY	Ruderman–Kittel–Kasuya–Yosida
RSO	Reciprocating sample option
RTA	Rapid thermal annealing
RTFM	Room temperature ferromagnetism

S	Sensitizer
SAED	Selected area electron diffraction
SAW	Surface acoustic waves
SERS	Surface-enhanced Raman scattering
SHB	Self-healing breakdown
SHG	Second-harmonic generation
SPM	Scanning probe microscopy
SPR	Surface plasmon resonance
SQ	Shockley–Queisser
SQUID	Superconducting quantum interference device
SQW	Single quantum well
STM	Scanning tunnelling microscopy
STPA	Simultaneous two-photon absorption
TAMRA	N,n,n′,n′-tetramethyl-6-carboxyrhodamine
T_C	Curie temperature
TCNQ	7,7,8,8-tetracyanoquinodimethane
TCO	Transparent conducting oxide
TDEL	Thick-film dielectric electroluminescence
TEM	Transmission electron microscope
TFEL	Thin-film electroluminescent display
TFT	Thin-film transistor
TM	Transition metal
TMOs	Transition metal oxides
TMR	Tunnel magnetoresistance
TOPO	Tri-n-octylphosphine oxide
TSO	Transparent semiconducting oxide
TTIP	Titanium tetraisopropoxide
UC	Upconversion
UCNPs	Upconversion nano phosphors
UCQY	Upconversion quantum yield
UV	Ultraviolet
V_O	Vacancy of oxygen
VB	Valence band
VDS	Drain-source voltage
VFD	Vacuum fluorescent display
VGS	Gate-source voltage
VLS	Vapour liquid solid
VLSI	Very large-scale integrated circuit
VOCs	Volatile organic compounds
VPE	Vapour phase epitaxy
VT	Threshold voltage
XPS	X-ray photoelectron spectroscopy
ZFC	Zero field cooled
$Zn(C_5H_7O_2)_2$	Zinc acetylacetonate

$Zn(COOH)_2$	Zinc acetate
$Zn(NO_3)_2$	Zinc nitrate
Zn_i	Zinc interstitial
ZnMgO	Zinc magnesium oxide
ZnO	Zinc oxide
ZnO:TM	Transition metal-doped ZnO
$ZnSO_4$	Zinc sulphate
ZTO	Zinc tin oxide
μ_B	Bohr magneton

List of Figures

Chapter 1

Chapter 2

Chapter 3

Chapter 4

Chapter 5

Chapter 6

Chapter 7

Chapter 8

Chapter 9

Chapter 10

List of Tables

Chapter 1

Chapter 2

Chapter 3

Chapter 6

Chapter 8

Chapter 9

Chapter 1
Oxide Luminescent Materials

K. Mini Krishna and M. K. Jayaraj

1 Introduction

The emission of light has been a source of fascination, philosophical speculation and scientific investigation since time immemorial. Light emission by matter falls into the two basic categories of **incandescence and luminescence**. Bodies that emit light solely because of their temperature are defined as incandescent. Luminescence refers to light emissions deriving their excitation energy from nonthermal sources.

In 1888, Wiedemann devised the term 'luminescence' from the Latin word meaning 'weak glow' [1]. Vavilov defined 'luminescence' as the emission of light produced by a material over and above its thermal radiation. It generally befalls when an excited electronic state relaxes to a lower energy state, the lifetime of which is much larger than that of light vibrations (10^{-10} s). Luminescence, depending on the mode of excitation, is mirrored in terms such as photo-, radio-, bio-, electro-, chemi-, thermo-, sono- or triboluminescence. In practice, the excitation is most probably via X-rays, cathode rays or UV emission of a gas discharge. Hitherto, the position of the band in a spectral output is seldom dependent on the mode of excitation but on the interlevel spacing. Numerous radiationless processes, arising from interactions with the lattice or a transfer of energy between ions, always compete in reducing the luminescent radiation.

Two other terms quite often used to classify luminescent materials are **fluorescence** ($\tau < 10$ ms) and **phosphorescence** ($\tau > 0.1$ s). The decay law of luminescence is exponential in fluorescence and hyperbolic or still more complicated for phosphorescence. With the advent of quantum theory, they were defined via the emission-based

K. Mini Krishna (✉)
Department of Physics, Vimala College, Thrissur, Kerala, India
e-mail: minikrishna@gmail.com

M. K. Jayaraj
Department of Physics, Cochin University of Science and Technology, Kochi 682022, India

M. K. Jayaraj (ed.), *Nanostructured Metal Oxides and Devices*,
Materials Horizons: From Nature to Nanomaterials,
https://doi.org/10.1007/978-981-15-3314-3_1

quantum mechanical mechanism for the orbital angular momentum multiplicity of the emitted electron. Fluorescence was henceforth defined as a photoluminescent emission that arises from the singlet electronic state and phosphorescence as that originating from the triplet electronic state. The latter, being 10–10,000 times longer than fluorescence, appear to emit much beyond the removal of the excitation radiation.

Delayed fluorescence is yet another singlet state emission with a much longer lifetime than normal. In this rare phenomenon, the electron responsible for the emission crosses over from the singlet state to the triplet state, but eventually returns to the singlet state before emission.

2 Photoluminescence (PL)

The Italian alchemist, Vincenzo Cascariolo, was the first to observe the phenomenon of 'photoluminescence' from the mineral barite on exposure to sunlight. A material photoluminesces when excited by photons (most commonly in the wavelength ranges of infrared, ultraviolet or visible light) with a spectrum broad enough to overlap the ion absorption bands. The fundamental processes involved include excitation, emission together with radiationless transitions. The emission and absorption bands overlap significantly in case of a weak ion–lattice interaction, as is for the f electrons in rare earth (RE^{3+}) ions. A stronger interaction, as the one observed in transition metal ions, causes a redshift in the emission band relative to the absorption band, as explicated by Stokes law [2]. If the system is conducive to radiationless de-excitations, it exhibits an increase in temperature along with a reduced luminescent output.

The phenomenon of photoluminescence is pictorially illustrated in Fig. 1. The configuration curves [3] convey the energy versus interionic distance relation of

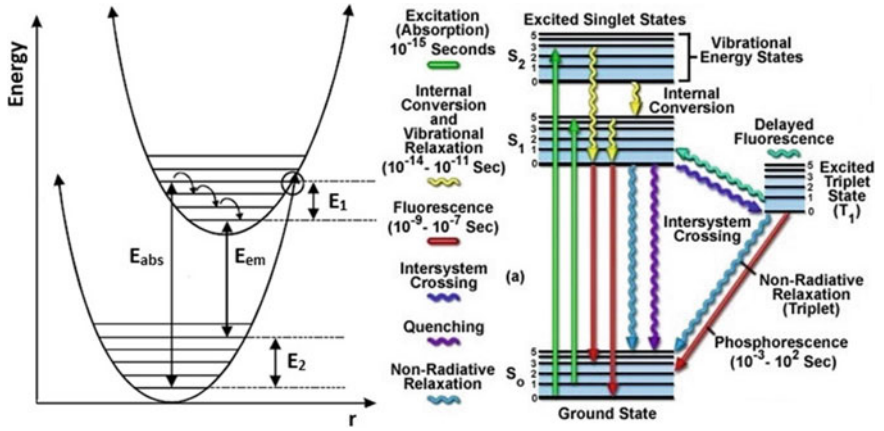

Fig. 1 Configuration coordinate diagram (left) and Jablonski diagram (right)

energy levels. The electronic states of a molecule and the transitions between them are depicted on a Jablonski diagram (named after the Polish physicist Aleksander Jabłoński). The electronic states are scaled vertically by energy and grouped horizontally by spin multiplicity. Squiggly arrows are used to indicate non-radiative transitions, and straight arrows indicate radiative transitions on the diagram. The vibrational ground states of each electronic state are depicted by thicker lines, whereas thinner lines illustrate the higher vibrational states.

In 1852, Irish physicist George G. Stokes reported the theoretical basis for the mechanism of absorption (excitation) and emission. When a system (be it a molecule or atom) absorbs a photon, it gains energy and gets excited to a higher energy state. The fluorescence lifetime of this excited state is about 10^{-8} s. Henceforth, the system, after losing a small amount of energy through vibrational relaxation, returns to its ground state emitting energy in the radiative or non-radiative form. The re-emission of lower frequency (longer wavelength) radiation by a molecule absorbing photons of higher frequency (shorter wavelength) is referred to as Stokes fluorescence. Eventually, positions of the band maxima of the absorption and emission spectra of the same electronic transition shall not coincide. This difference (in units of wavelength or frequency) is called the Stokes shift. If the emitted photon is more energetic (emitted at higher frequency or lower wavelength), the difference in energy is called an anti-Stokes shift. The excess energy in an anti-Stokes transition is extracted from the dissipation of thermal phonons in a crystal lattice, thereby cooling the crystal in the process. Such exchanges of energy radiation (absorption or emission) are unique to a molecular structure.

There are numerous mechanisms of non-radiative transitions observed in a system, as depicted in Fig. 1. When the excited state relaxes to its lowest vibrational level, we refer to it as the vibrational relaxation. This cannot occur in isolated molecules as it involves a release of energy from the molecule to its surroundings. Internal conversion (IC) is another kind of non-radiative transition where a vibrational state of an electronically excited state can couple to a vibrational state of a lower electronic state. Intersystem crossing (ISC) is yet another form where the transition involves states of a different spin multiplicity. The latter is more predominant in molecules that exhibit large spin–orbit coupling, which may subsequently give rise to phosphorescence.

2.1 Emission Kinetics

In between two energy levels, the excitation and emission processes are temporally separated by an interval, which is the lifetime of the excited state (~10^{-8} s or more). It is during this extremely short time span that the system acclimatizes itself with the excited electronic state. This encompasses shifting of the contiguous (ligand) ions to a new equilibrium state, relocating of the interionic distance and relaxation into the lowermost of the vibrational levels (~10^{-12} s) of the excited electronic level. When the system relaxes between the levels, say m and n ($m > n$), the lifetime τ_m is given by

$$\tau_m = \frac{1}{\left(\sum A_{mn} + \sum C_{mn}\right)} \tag{1.1}$$

where A_{mn} and C_{mn} refer to the probability for radiative and non-radiative transitions, respectively. The summation is pertinent to all transitions that occur over a single or several sub-adjacent levels. The fraction of emission transitions in comparison with the entire emission and radiationless transitions gives the quantum yield η:

$$\eta = \frac{\sum A_{mn}}{\left(\sum A_{mn} + \sum C_{mn}\right)} \tag{1.2}$$

If there are N_m photons in the excited state initially, the exponential law of luminescence decay states that after a time t

$$N(t) = N_m \mathrm{e}^{-t/\tau_m} \tag{1.3}$$

A direct relation exists between the emission intensity and the probability A_{mn} of emission transition given by

$$I_{em} = N_m h \nu_{mn} A_{mn} \tag{1.4}$$

Thus, if the lifetime of the excited state is shorter, more intensive shall be the glow. The greater the probability C_{mn} of radiationless transition, lesser shall be the intensity of glow and hence the quantum yield. Also, for a given transition, the greater the oscillator strength, the higher shall be the intensity of the emission, provided radiationless transitions are absent.

2.2 Intrinsic Luminescence

Photoluminescence is broadly classified into intrinsic and extrinsic type based on the nature of the electronic transition involved in generating emissive radiation.

Band-to-band luminescence, exciton and cross-luminescence are the three intrinsic varieties.

(a) **Band-to-band luminescence**:

This kind of luminescence occurs when an electron in the conduction band recombines with a hole in the valance band. It is specific to pure crystals at relatively high temperatures. Band-to-band luminescence is observed in elements like Si and Ge, IIIb-Vb compounds such as GaAs and devices such as light-emitting diodes and semiconductor lasers.

(b) **Exciton luminescence**:

An exciton translates into a crystal transmitting energy. It luminesces due to the recombination of the electron and the hole. Excitons are of two types: Wannier exciton and Frenkel exciton.

The Wannier exciton model articulates an exciton as a bound electron-hole pair in the conduction and valence band, respectively, mediated by Coulomb interaction. The span of a Wannier exciton wavefunction is much larger than the lattice constant. This is perceived in inorganic semiconductors such as IIIb-Vb and IIb-VIb compounds. Wannier excitons are stable only at relatively low temperatures where the excitonic binding energies are much above the respective thermal energy. At higher temperatures, Wannier excitons are no longer stable and band-to-band luminescence overtakes instead.

The expanse of the electron-hole wave function is lesser than the lattice constant in a Frenkel excitonic model. Typical examples are organic molecular crystals and inorganic complex salts. In such systems, the excited state of an isolated molecule or a complex ion relocates from molecule to molecule or from complex ion to ion mediated by dipole-dipole interactions. The luminescence behavior is quite similar to that of secluded molecules or complex ions.

(c) **Cross-luminescence**:

Cross-luminescence refers to the recombination between an electron in the valence band and a hole formed in the outermost core band [4]. This occurs only when the energy difference between the two bands is lesser than the bandgap energy, or else, an auger process happens selectively. Cross-luminescence is observed in a number of alkali and alkaline earth halides and double halides.

The spectral span and shape reflect the blend of molecular orbitals in the clusters comprising of cations with a hole in the core-shell and nearest neighbour halide ions. For multi-cationic crystals, the spectrum gives evidence not only about the 'active' cation carrying the core hole but also about the other cations as well. Fast decay time, of the order of nanoseconds or less, is a distinguishing feature of cross-luminescence. Henceforth, such luminescent systems are suitable for use as scintillators.

2.3 Extrinsic Luminescence

Extrinsic luminescence is caused by intentionally assimilated impurities (or activators) into a host matrix. Most of the observed types of luminescence allied with practical applications fit into this class. Extrinsic luminescence in ionic crystals and semiconductors can be categorized into two: localized and unlocalized.

(a) **Unlocalized type**:

In the unlocalized type, free electrons in the conduction band and free holes in the valence band of the host matrix participate in the luminescence process (illustrated

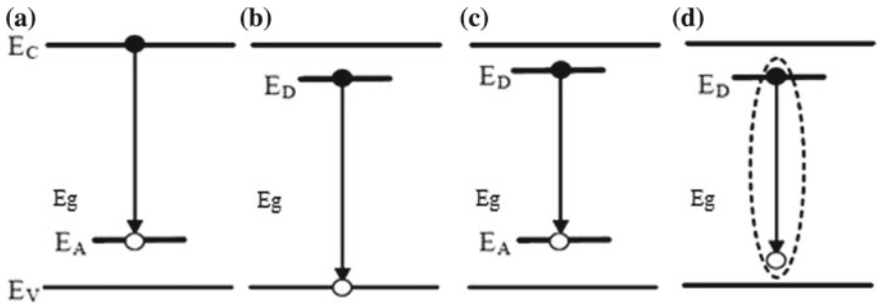

Fig. 2 Radiative recombination involving impurity levels: **a** conduction band–acceptor-state transition, **b** donor-state-valence band transition, **c** donor-acceptor recombination and **d** bound-exciton recombination

in Fig. 2). Luminescent transitions of this kind include (a) the transition of a free to a bound carrier and (b) the transition of a bound electron at a donor to a bound hole at an acceptor. These luminescent behaviours are seen in compound semiconductors such as IIIb-Vb and IIb-VIb compounds.

(b) **Localized type**:

In this kind, excitation and emission processes are narrowed to a localized luminescent center. Various metallic impurities intentionally merged into ionic crystals and semiconductors frequently act as efficient localized luminescence centers. They are further classified into allowed and forbidden transition types based on electric dipole transitions. The electric dipole transition befalls between energy levels with a parity change given by $\Delta l = \pm 1$, 'l' being the azimuthal quantum number. The incorporation of atoms and ions into a system perturbs the crystal electric field. This can occasionally modify the forbidden character of the dipole transitions transforming them into allowed kinds to a certain extent.

(i) Allowed transition type:

1. s ↔ p transition—F center ↔ (an electron trapped at an anion vacancy), Tl^0
2. s^2 ↔ sp transition—Tl^+, Pb^{2+}, Sn^{2+}, Bi^{3+}, Sb^{3+}
3. f ↔ d transition—Eu^{2+}, Ce^{3+}

The oscillator strength needed to effect such transitions lies in the range 10^{-1} to 10^{-3}. The spectral outcome presents a broad bell-shaped form.

(ii) Forbidden transition type:

1. d ↔ d transition—Ti^{3+}, Cr^{3+}, Cr^{2+}, Mn^{4+}, Mn^{2+}, Fe^{3+}, Fe^{2+}

Iron group ions luminesce in the visible to IR region due to their $3d^{n*} \leftrightarrow 3d^n$ ($n \rightarrow 2$–8) transitions. Among them, ions with $3d^3$ (Cr^{3+} and Mn^{4+}) and $3d^5$ (Mn^{2+}) configurations are vital for phosphor applications. Spectra of transition metal ions consist of either broadbands or characteristic lines.

2. f ↔ f transition—Pr^{3+}, Nd^{3+}, Sm^{3+}, Eu^{3+}, Tb^{3+}, Tm^{3+}, Dy^{3+} (and other RE^{3+} ions)

Most RE^{3+} ions luminesce in the visible to NIR region and give off an efficient line spectra (both absorption and emission spectra) due to their $4f^{n^*} \leftrightarrow 4f^n$ transitions. Amidst many of them, Eu^{3+} ion (red) and Tb^{3+} ion (green) are excellent activators. The 4f energy levels, being well secluded by the 5s5p shells, are weakly subjective to crystal field perturbations. Hence, their emission does not get much amended on varying the host lattice. These allowed transitions happen at oscillator strengths of the order of 10^{-4} to 10^{-8}.

3 Sensitization

Whenever the phosphor host matrix itself is luminescent (self-activated luminescence) or when there are two or more activators incorporated into a phosphor host lattice, an interaction happens between the luminescent centers which shall be articulated in their emission spectra. As a consequence, the absorption spectra shall be a superposition of their respective absorption spectra. The lines in the emission spectra, on the other hand, do not change position but exhibit any of the following modifications:

- The luminescent intensity of one ion can gain in strength at the expense of the diminishing intensity of the other.
- An ion, though not radiant in one system, becomes luminescent in the presence of another ion in a novel matrix.
- An ion, not luminescent as such, shall luminesce upon excitation in the absorption band of another ion, or in other words, turns luminescent in the presence of the other ion.
- An ion may also give an intensified output along with complete quenching of the other.

These varieties of luminescent expressions revealed by ions excited upon energy transfer from other ions that are excited in their absorption band are termed as **sensitized luminescence**.

There are activators in phosphor matrices, such as Mn^{2+} and RE^{3+} ions, which rarely possess suitable excitation bands. In these ions, either band-to-band excitation is feasible only at extremely high energies. or very narrow or weak absorption lines are concomitant with forbidden f-f transitions. This limitation can often be overwhelmed by incorporating a sensitizing ion into the system that is equipped with a suitable absorption band. Conversely, Cr^{3+}, RE^{2+} and other ions themselves have the ability to present broad intensive absorption bands suitable for inducing luminescence.

In sensitized luminescence, the energy absorbed in the absorption band of the sensitizer ion is released in the emission band of the activator ion. This requires a significant overlap between the absorption band of the activator ions and the emission

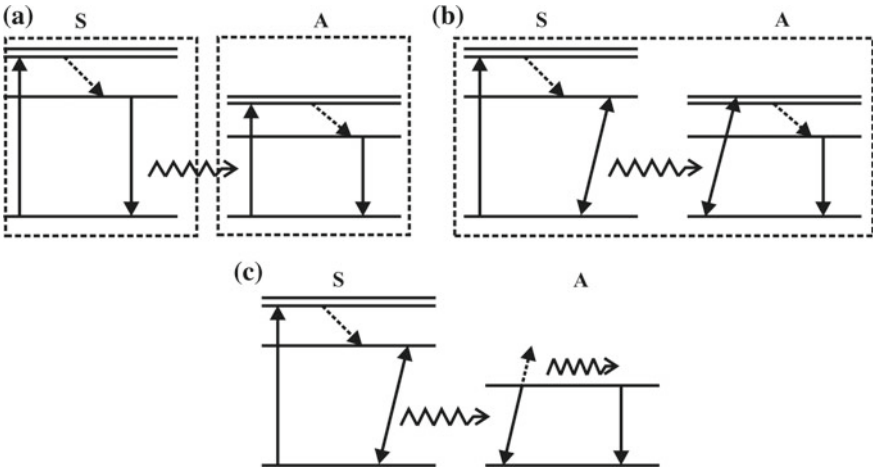

Fig. 3 Sensitized luminescence: **a** emission reabsorption, **b** resonance radiationless and **c** non-resonance radiationless

band of the sensitizer ions. Such kind of an energy transfer from the sensitizer (S) ion to the activator (A) ion is illustrated in Fig. 3 in three disparate ways [3]. Here, S is the sensitizer (energy donor), and A is the activator (energy acceptor); asterisks denote their excited states.

3.1 Emission Reabsorption

In emission reabsorption, the light emanated by the sensitizer ion (referred to as primary luminescence) is reabsorbed and later released (referred to as secondary luminescence) by the activator ion. This demands both sensitizer and activator to possess strong absorption bands and act as independent systems that can directly interact with each other. The more the proximity between the emission energy of one and the absorption energy of the other, the more probable is the chance for energy transfer. For example, the luminescence of Nd^{3+} ion is found to intensify in the presence of Sm^{3+}, Eu^{3+}, Tb^{3+} and Dy^{3+}.

3.2 Resonance Radiationless Energy Transfer

The mechanism is more frequently observed between interacting ions that together perform like a single entity. This neither requires the sensitizer to be necessarily emissive nor the activator to have strong absorption bands capable of inducing luminescence. Still, the broad absorption bands of the sensitizer and the luminescent

transitions of the activator together create a system that is capable of rendering a luminescent response. The resonant radiationless energy transfer mechanism amid an allowed transition in the sensitizer and a forbidden transition in the activator is responsible for sensitized luminescence to occur even in inorganic luminescent systems.

The process relies on dipole-dipole or dipole-quadrupole interactions among ions, the probability of the energy transfer being proportional to r^{-6} or r^{-8}, respectively, where 'r' is the mean distance between the interacting ions. Also, the lesser duration and diminished quantum yield of the sensitizer emanation are compensated by the longer extent and larger quantum yield of the activator emission. The possibility of energy transfer further improves with the decrease in the mean distance between ions, diminution of the lifetime of the sensitizer in an excited state and the larger overlap amidst activator's absorption and sensitizer's emission. The decay curve, in the place of being purely exponential, will be a summation of exponential curves.

3.3 Non-resonance Radiationless Energy Transfer

This mechanism is often observed whenever there is a substantial nonconcurrence of distances among the levels of ions transferring and receiving energy. Such a non-resonance non-radiative kind of energy transfer is seen over shorter spans and involves exchange interactions between ions. In such a scenario, sensitization is achieved through lattice modifications or by doping. The energy then gets transported to any of the acceptor levels (which may be short-lived or non-emissive) lying closer to the energy transferred by the sensitizer. By way of rapid radiationless transitions, the energy is finally transmitted to those energy levels from which the final emission takes place.

4 Concentration Quenching (Self-quenching)

In many activators, a change in luminescent intensity or quenching of luminescence is observed due to the transfer of energy from a radiating energy level to a non-emissive center. Usually, the emission intensity, with the increase in the concentration of the activator, is found to reach a maximum and then diminish. The interaction between similar activator ions profoundly influences the luminescent expressions.

- The emission reabsorption energy transfer among similar ions can lead to self-absorption, for example, as observed in Cr^{3+} ions.
- The most dominant form of concentration quenching, as found in many of the RE^{3+} ions, is the non-radiative resonance multipole energy transfer between similar ions.

- An exchange mechanism of concentration quenching is seen to occur in ions whose emissive and non-radiative levels of transitions have no profound differences in their energy (as in Eu^{3+} ions).

5 Advantages of PL Technique

Luminescent studies provide some of the most sensitive and specific analysis with the possible exception of radioactive labelling procedures. The PL technique is a nondestructive and highly sensitive procedure with a high degree of repeatability. It offers several advantages, as listed below:

High sensitivity—The sensitivity of the PL technique is approximately 10,000 times greater than absorption spectroscopy. The luminescence can be detected from concentrations as low as one part per billion to one part per trillion. In the spectrophotometric method, the absorbed radiation is measured indirectly via a comparison between the incident and transmitted lights. Thus, absorption can only be obtained by measuring a small decrease in signal within a larger one, therefore resulting in a corresponding increase in noise. But in fluorescent techniques, the sample itself is the source of emission and luminescence is measured directly. Even a small luminescent emission captured from the sample can be electronically amplified with only a minor introduction of noise.
Good selectivity—The process of luminescence is highly selective and specific. Compared to one in absorptive spectroscopy, there are two wavelengths, one excitation and the other emission, in fluorescent spectroscopy. It is a rare chance for two substances to share a common excitation and emission wavelength.
Environmental qualitative information—The longer lifetime of electronic transitions involved in the process of luminescence makes it more sensitive to the local environment than absorbance. This makes luminescence an excellent probe to the crystal field environment. This technique unveils the local polarity, viscosity, pH and temperature effects in a nondestructive and noninvasive fashion.
Large linear quantitative range—Luminescence instruments have a greater linear measurement range for quantitative analysis over spectrophotometers. The range of a typical spectrophotometer is in between 0.1 and 3 absorbance units (less than 3 orders of magnitude). Also, the absorbance errors are progressive into the extremes where they even exceed 50%. On the other hand, fluorescence instruments present a greater linear range of 6–7 orders of magnitude with a diminutive error at the extremes.
Multidimensional information—A PL spectrum gives information regarding two separate electronic transitions-excitation and emission spectra of a given substance. This provides us twice the amount of facts conveyed via absorbance spectra. The PL technique is, thereby, quite beneficial in substance identification. The retrieved information can be displayed in various formats such as excitation–emission matrix stacked plots, contour plots or synchronous scan spectra.

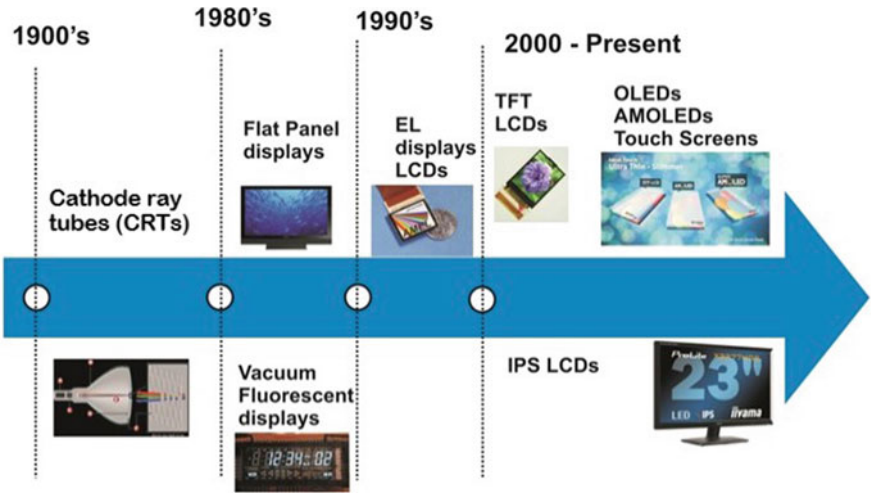

Fig. 4 Schematic representation of display evolution

6 Luminescent Displays

Displays, especially electronic, are now an indispensable part of everyday life. The revolution of the electronic display industry starts with the veteran cathode ray tubes (CRTs) advancing through vacuum fluorescent displays, liquid crystal displays (LCDs) and organic light-emitting diodes (OLEDs). Though the mature CRT technology was inexpensive and reliable, its bulkiness paved the way to the advent of thin, light portable flat panel displays (FPDs). Light-emitting diodes (LEDs), vacuum fluorescent displays (VFDs), plasma display panels (PDPs), liquid crystal displays (LCDs), thin-film electroluminescent (TFEL) displays, organic light-emitting diodes (OLEDs), field emission displays (FEDs) and nano-emissive displays (NEDs) comprise the flat panel display technologies. Among the above-mentioned FPD technologies, except LCD, all are emissive displays. However, the most dominant technologies that are competing with CRT are LCD and PDP. OLEDs will be dominating tomorrow's display industry, but the manufacturing cost is very high compared to LCD technology. A schematic representation of the display evolution is presented in Fig. 4.

7 Why TFEL?

Electroluminescent (EL) displays have developed as the most dependable emissive display technology due to its unique features, as stated below:

Solid-state nature and ruggedness: An EL device can be fully assimilated onto the substrate of the drive electronics owing to its solid-state assembly. The extreme

ruggedness of the solid-state nature makes it more resilient to shocks, vibrations and wide temperature variations. Their ability to withstand aggressive environments (heat, cold, dust, wind, sunlight, etc.) ensures the feasibility of using them in harsh environments, for military equipments and spacecrafts and for portable applications. Emission in a solid-state environment also excludes the risks adhered to the maintenance of vacuum or plasma backgrounds, as in the case of VFDs, PDPs or FEDs.

Wide viewing angle and operating temperature: The emissive TFEL displays can be operated over a wide viewing angle of more than 160°, a problem inherent with LCDs. This ability is due to the absence of optical elements in the path of the emission (excluding the glass substrate). Also, EL panels can function over a wide range of temperature, say 25–60 °C (restricted by the drive electronics). They neither freeze nor slow down at lower temperatures. These properties make EL displays suitable for critical military, medical and industrial applications.

Long life: The lifetime of TFEL display panels is over 50,000 h with less than 10% change in their luminous response.

High contrast: EL displays are 'readable' in a high ambient luminous environment, making them very effective to be used in industrial instrumentation.

Better display qualities: Reduced pixel size and subsequently high resolution are other features of TFEL displays. Their quick response to even operate at video rates makes them suitable for engineering high information content FPDs which possess the same image quality of that of the CRT.

The exceptional performance and visual features of high-performance EL displays make it an ultimate solution for the most demanding and challenging applications where other display technologies are merely inadequate. TFEL displays are suited for small area displays and displays requiring operation in harsh environments. TFEL technology is also promising owing to its wide viewing angle, high brightness, small pixel size, lightweight and addressing simplicity. These features have gained TFEL displays access to a small niche in medical and instrumentation industry. Equipment and system designers prefer EL displays to quench the mounting demand for improved image quality, longer lifetime and higher reliability. ACTFEL displays overrule LCDs in their ability to pattern much smaller pixels, performance over a wide temperature range, full-viewing angle and readability with much higher intensity background light. The acceptance of TFEL technology shall be far-reaching once the power, cost and full-colour performance limitations are overcome.

Colour TFEL technology has the potential to produce a high-performance color flat panel display without the complexity of the TFT color LCD approach. Significant progress has been made in the development of multicolor and full-colour TFEL displays. Several prototype multicolor EL panels have been fabricated. In 1993, based on an inverted, filtered thin-film EL structure, the first commercial multicolor thin-film EL panel was placed into the market. The advent of a pure blue-emitting phosphor made of rare earth thiogallates paved the way for the realization of the first prototype full-color EL panel the same year. However, the first commercial full-color EL display monitor was introduced into the market in 1994. These reports triggered interests in color thin-film EL displays. Some of the TFEL displays in use are shown in Fig. 5.

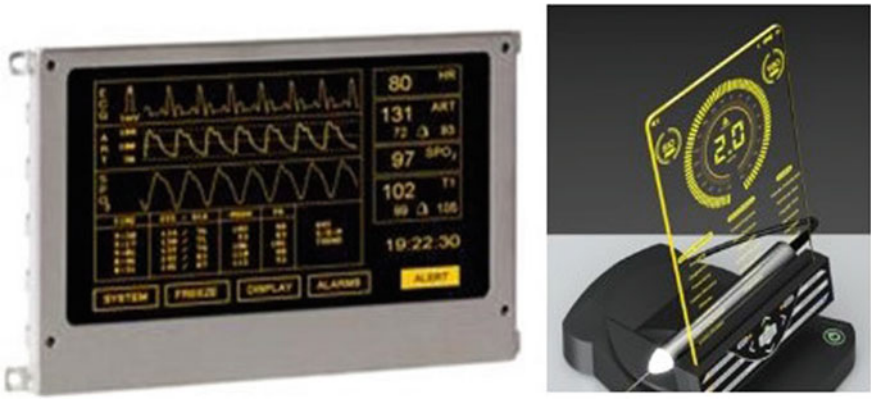

Fig. 5 TFEL displays for use in industrial, medical, transportation, military, public safety and other demanding applications (Courtesy Lumineq) (left) and transparent TFEL display (right)

In TFEL devices, the generation of light is by the impact excitation of light-emitting centers by high-energy electrons accelerated by an electric field. Even polycrystalline films could serve as the active component in high-field EL, which was a major disadvantage for thin-film EL displays. On account of the drive voltage waveform and phosphor configuration, high-field EL devices have been classified into four: alternating current-driven thin-film EL (ACTFEL), alternating current powder EL (ACPEL) and direct current thin-film/powder EL (DCEL). DCEL displays are widely used in automobiles, namely for displaying yellow fixed messages and also as backlights. The merits of alternating current electroluminescence have opened up a whole new world. Figure 1.6 outlines some comparative remarks on the four kinds of EL devices.

Personal laptops and word processors equipped with ZnS:Mn-based ACTFEL displays and liquid crystal displays supported by ACPEL backlights are today commercially available. Powder electroluminescent displays have immensely unlimited potential, such as uniform luminous emission, a skinny profile and little power

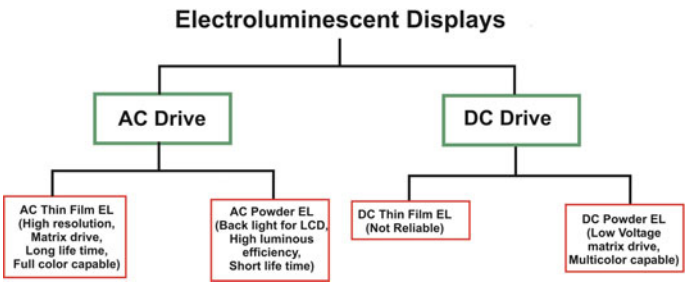

Fig. 6 Comparison between the four types of EL displays

consumption [5]. Architectural and decorative lighting, LCD backlights in cellular phones, personal digital assistants (PDAs) and palmtop computers have been equipped with powder EL lights. However, they also possess multiplexing limitations and suffer from low luminance, high operating voltage, poor contrast and significant luminance degradation over a fairly short time (~500 h). There are reports [6, 7] on flexible EL devices that can be made on paper as well as polyethylene terephthalate (PET)-coated transparent substrates.

The advances in thin-film process technology in the 1960s further triggered the research trends toward developing thin-film EL devices, which was otherwise vested on powder EL devices. Moreover, thin-film phosphors offered several benefits in comparison with the powders, such as high lateral resolution from smaller grains, superior thermal stability, reduced degassing and improved adhesion to the solid surface [8]. However, one had to compromise on brightness and efficiency while using phosphor thin films over bulk powder materials, these properties primarily being dependent on factors such as internal reflection, the small interaction volume between the incident beam and solid and absorption of generated light by substrate materials.

8 The Phenomenon of Electroluminescence (EL)

Electroluminescence is the extraction of luminous energy from a material subjecting it to a very high electric field. In 1936, G. Destriau was the first to observe this phenomenon [9] in ZnS, when a large electric field was applied to it. There are two classes of EL devices. One is the injection luminescence which is observed in light-emitting diodes (LEDs) where light is generated by electron-hole pair recombination at a p–n junction. The other is the high-field EL where light is generated by impact excitation of a luminescent center (also called activator) by high-energy electrons. Typical electric fields through which electrons are accelerated are nearly 10^6 V/cm. So, this type of luminescence is also referred to as high-field luminescence.

8.1 EL Device Structure

There are three general configurations (as illustrated in Fig. 7) for thin-film EL device structures. One is the conventional standard structure that comprises of metal–insulator–semiconductor-insulator-metal (MISIM) structure. The second one is an inverted-type structure, and in the third configuration, the insulator used is usually a thick dielectric/ceramic. In the standard MISIM structure, the active phosphor layer is sandwiched amid two insulators (or dielectrics) with an opaque top electrode (generally, Al/Au/In) and a transparent bottom electrode (normally, ITO). In contrast, the top and bottom electrodes are reversed in the case of an inverted structure and hence luminous emission occurs in the opposite direction via the substrate. The

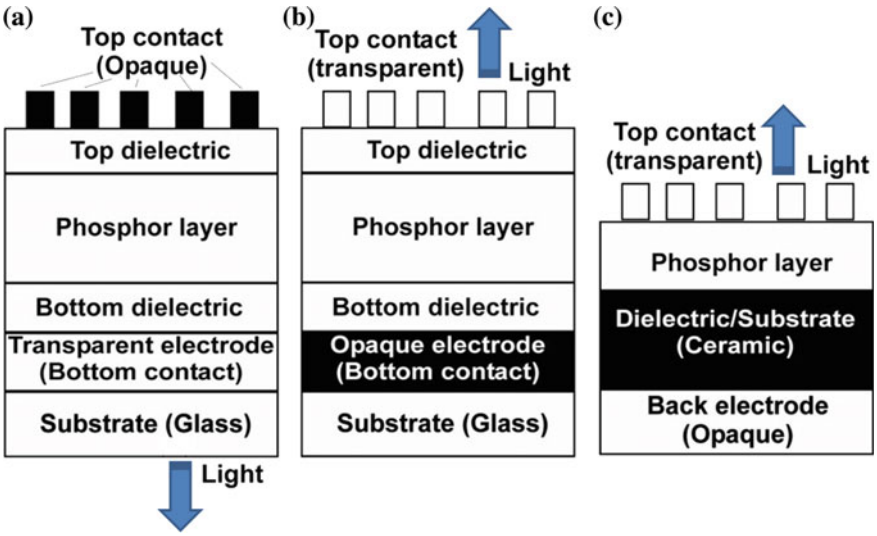

Fig. 7 Three general configurations of TFEL devices—**a** MISIM-structured, **b** inverted MISIM and **c** dielectric/ceramic substrate-based

additional advantage of the latter over the former is that opaque substrates like silicon can withstand higher temperatures as against the low processing temperatures dealt with glass substrates.

Also, some researchers adopt the structure shown in Fig. 7c where a single insulator acts as both substrate and insulator. The ceramic insulator cum substrate is 0.2 mm thick, whereas all other layers are in the nm/μm regime. The opaque electrode is deposited on the rear side of the dielectric sheet, and light extraction from the structure is through the transparent top electrode. This simple configuration also offers the additional advantage of employing high post-deposition annealing temperatures (1100 °C) that could eventually increase the crystalline quality of the active phosphor layer which cannot be accomplished with glass substrates.

8.2 Ideal ACTFEL Device

An ideal device can be demonstrated by an equivalent circuit model, as shown in Fig. 8. In this circuit, insulators are depicted by perfect capacitors. The phosphor layer is illustrated by a capacitor below the threshold and a pair of back-to-back diodes above threshold [10]. This simple circuit very well demonstrates the essential phenomenological physics of a thin-film EL device.

Below the threshold voltage V_{th}, the model portraits a TFEL device as three capacitors in series, the voltage drop across each being proportional to the thickness of the layer and the dielectric constant of its material. The two insulating layers, with

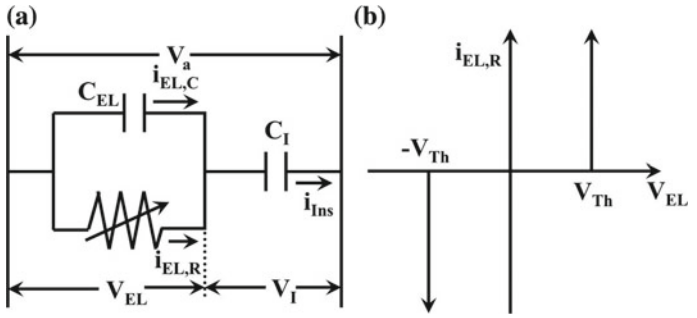

Fig. 8 **a** Equivalent circuit of an ideal ACTFEL device and **b** ideal *I*–*V* characteristics of the nonlinear resistor of the phosphor layer

capacitances per unit area C_{I1} and C_{I2}, respectively, are assimilated into one effective insulating layer. The effective capacitance per unit area C_I is, henceforth, given by

$$C_I = \frac{C_{I1} C_{I2}}{C_{I1} + C_{I2}} \tag{1.5}$$

Below V_{th}, the active phosphor layer is also treated as a capacitor characterized with a capacitance per unit area C_{EL}. Above the threshold, real (dissipative) currents flow through the active layer resulting in luminous emission. Thus, the phosphor layer is equivalent to a capacitor in parallel with a nonlinear resistor, the *I*–*V* characteristic of which is shown in Fig. 8b. Back-to-back Zener diodes simulate the nonlinear resistor in an ideal case. The model weighs the device performance based on the amounts of charge density transferred, the power dissipated and luminance output. These are, in turn, dependent on device parameters like thickness, dielectric constant and dielectric breakdown strength of each layer, luminous efficiency and threshold field.

The voltage applied, V_a, across the device is given by

$$V_a = V_I + V_{EL} \tag{1.6}$$

where V_I and V_{EL} depict the voltages across insulating and phosphor layers, respectively. When $V_a < V_{th}$, the applied voltage is capacitively divided. When $V_a > V_{th}$, current flows through the resistive branch (accompanied by luminous emission) to discharge the voltage through the phosphor capacitor back to the threshold level. The instance at which the electron injection commences in the ideal device, the entire magnitude of externally applied voltage drops across the dielectric layer(s) maintaining the voltage across the phosphor layer a constant. Now, the resistive branch delivers current to charge the insulating layer capacitor by an equivalent voltage.

8.3 The Basic Mechanism

The basic processes involved in electroluminescence [5] as in the case of the standard MISIM structure are depicted in Fig. 9.

An alternating current TFEL device is externally triggered by various waveforms such as sine, trapezoidal, triangular or square. By convention, a positive voltage is applied to the bottom opaque (Al) electrode. No free charge carriers are generated when the voltage applied is below V_{th}. Now, the entire voltage is dropped across the phosphor and dielectric layers due to their capacitive nature. When V_a reaches V_{th}, the field across the active layer increases and charges commence to flow through the device. Beyond V_{th}, the working of the device operation can be visualized using the energy band diagram shown in Fig. 9.

Due to the lattice mismatch at the insulator–phosphor boundary, numerous allowed electronic states are found within the phosphor band gap at the interface. Ideally, these are regarded as single discrete trap levels with a large carrier concentration. When the external field applied increases beyond a specific threshold value, these trapped carriers start to tunnel into the conduction band of the phosphor, as shown in the process (1) of the figure. These electrons, experiencing a large electric field in the conduction band, drift across the active phosphor layer (depicted by process 2). As electrons drift to higher energy levels in the conduction band, they gain kinetic energy from the electric field. A sufficiently energetic electron excites into a higher energy state (process 3) on colliding with a luminescent center. The rest of the electrons navigate through the phosphor field, collide randomly with the atoms of the lattice and lose energy in every bump, before regaining energy from the field.

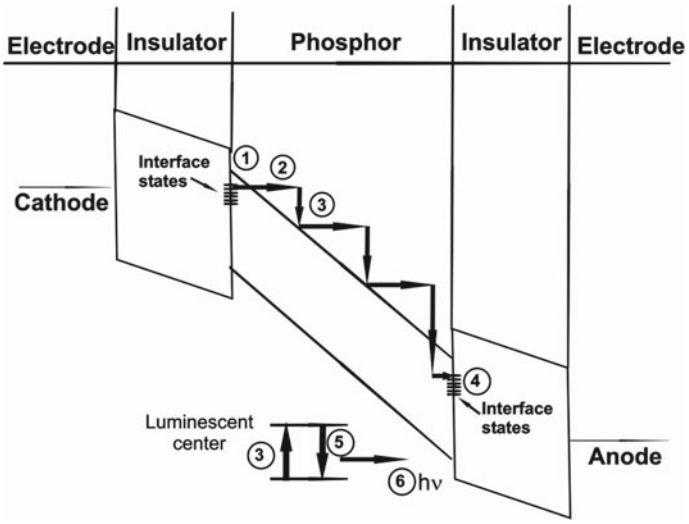

Fig. 9 Energy band diagram of ACTFEL device

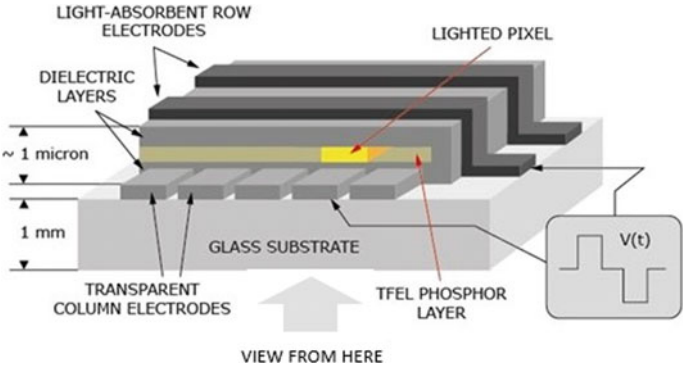

Fig. 10 The typical device structure of a TFEL device. A pixel on display is lit by applying a voltage to the row and column electrodes, thus causing the area of intersection to emit light

These electrons continue to pass through the phosphor layer under the influence of the external electric field and ultimately arrive at the conduction band discontinuity between the phosphor and dielectric layers on the anodic side of the device. Here, they thermalize and release heat energy to the lattice, move to the bottom of the conduction band and are re-trapped in a deep energy level at the phosphor–dielectric interface on the anodic side (process 4). Meanwhile, those carriers excited to a higher energy state on collision with a luminescent impurity relax back to the ground state (process 5), in due course emitting a photon, making an emissive transition. These photons are out-coupled from the device (process 6) through the transparent electrode end of the device. (Figure 10 depicts that, on applying voltage, the pixel at the area of intersection of the row and column electrodes on display gets lit.)

As the electrons drift through the active phosphor layer from the cathodic to the anodic end of the device, a net negative charge adds to the anodic interface and a net positive charge builds up at the cathodic interface, thereby introducing a polarization charge effect. This polarization field induces a negative feedback effect making the injection of more electrons from the cathode difficult. Another effect of the polarization charge is that whenever the applied voltage drops to zero, the polarization field turns prominent. It triggers the electrons trapped at the anodic end to re-emit back into the phosphor layer, and this is referred to as the leakage charge. When the subsequent negative pulse is applied to the device, the external field gets amplified by the polarization field. This makes the phosphor active at a lower external applied voltage than the threshold. The new reduced phosphor threshold is termed as turn-on voltage. Now, electrons start to tunnel at a lower external voltage; trap occupancy improves and more charge is transported across the device than during the previous one. This creates a larger polarization field, further reducing the turn-on voltage and amplifying the transferred charge. This process continues until a steady-state operating condition is achieved. In an ideal process, the steady-state operation may be attained after only a few cycles.

8.4 Space Charge in EL Devices

The generation of space charge within the phosphor layer is another cause for a major deviation from the ideal operation of an ACTFEL device. In an ACTFEL device, a positive space charge can arise in many ways. Within the phosphor, traps can get ionized by thermal or field emission or by means of electron impingement. The detached electrons are swept away by a high field applied across the phosphor layer. Now, the trap gets positively charged and forces the energy band to bend locally downward. The ionized centers can be an intentionally added impurity acting as a donor due to valency mismatch or a luminescent impurity whose excited states lie near the conduction band or a point defect or a vacancy. Band-to-band impact ionization of the lattice can also create space charge. In band-to-band impact ionization, a hole is left or formed in the valence band while an electron moves to the conduction band as a delocalized charge carrier. The holes drift toward the cathode just before getting trapped, resulting in a localized positive charge pulling the band downward.

The space charge-induced curvature of phosphor layer energy bands under device bias is shown in Fig. 11. The dotted lines denote the spatial spread of the phosphor layer energy band in the absence of space charge. The straight line indicates that in the absence of space charge, a uniform electric field subsists throughout the active phosphor layer. For an externally applied constant value of voltage, the electric field near to the cathode is higher for a phosphor layer with space charge than that without it. This is due to the fact that the tunnel emission rate of electrons is a function of the electric field.

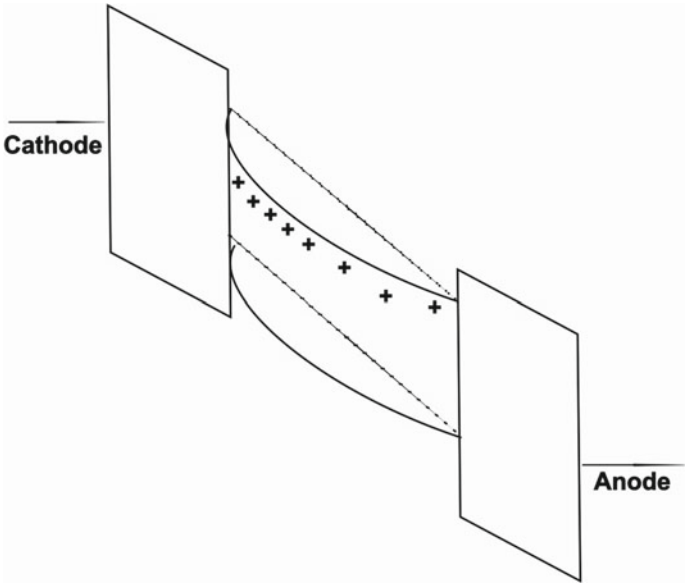

Fig. 11 Space charge-induced band bending of the phosphor layer in ACTFEL device

On the other hand, the electric field near the anode is lesser due to the reduced field experienced by the presence of space charge. The lesser density of energetic electrons in this region reduces the possibility of impact excitation but effects hot electron-induced damage in the phosphor-insulator boundary. The reduced field at the anodic edge may also lead to efficient carrier trapping that is not noticeable at the high-field cathodic region. For every phosphor system, the mechanism of space charge creation and luminous emission has apparent effects in device operation.

Based on the nature of spatio-temporal distribution, the space charge developed in ACTFEL devices may be either static or dynamic. Usually, the space charge generated gets annihilated, by either recombination of an electron with an ionized trap or the re-emission of the trapped hole, at some specific rate. If the annihilation proceeds at a slower pace than the driving waveform, the space charge progresses into a steady-state or static distribution. Dynamic space is that part of the entire space charge is not in steady-state, but both created and annihilated within one period of the drive waveform.

In a nutshell, the existence of space charge lowers the driving voltage, in turn improving reliability and efficiency. On the contrary, if the space charge is dynamic, the energy exhausted making and maintaining the space charge lowers efficiency.

9 Material Requirements for ACTFEL Devices

Substrate—The primary requisites of a substrate are surface smoothness, transparency, the capability to endure thermal treatments and cheap. The most frequently used substrate is glass. The choice of the substrate is very significant in device fabrication as the properties of the substrate often put restrictions on subsequent fabrication steps, such as high-temperature annealing and chemical cleaning. Also, the surface smoothness of the substrate impacts adhesion as well as the optical properties of the ACTFEL stack.

Electrodes—They are of two types: transparent and opaque. The transparent electrode should be necessarily conducting, transparent to the entire visible region of the electromagnetic spectrum, and must be able to withstand thermal procedures adopted for subsequent layers. A 200-nm-thick indium tin oxide (ITO) is widely used as a transparent electrode. Another material that is used as a transparent electrode in ACTFEL device is ZnO:Al. The critical requirements for an opaque electrode are that it should be highly conducting, must be well adhesive to the insulating layer and must exhibit no propagation breakdown. Aluminum (Al) is the most commonly used electrode. Aluminum is cheap and easily deposited by thermal evaporation and has a low melting point enhancing the likelihood for self-healing breakdown. Typical thickness of an opaque electrode lies in the range of 100–200 nm.

Insulators—The prime objective of an ACTFEL insulating layer is to shield the phosphor layer from catastrophic breakdown under high electric fields. The insulating material shall also possess the following requisites:

1. A high dielectric constant, $\varepsilon_0\varepsilon_r$
2. A high dielectric breakdown electric field
3. The minimum number of pinholes and defects
4. Excellent adhesion
5. Low loss factor, tanδ.

The high dielectric constant and breakdown electric field of the insulating layer ensures maximum drop of the applied voltage across the phosphor below the threshold which, in turn, maximizes ACTFEL device performance. Since the capacitance of a layer is inversely proportional to its thickness, it is also logical to reduce the layer thickness to improve the capacitance of the insulator layer instead of selecting high dielectric constant material. However, as defect and pinhole density increase on lowering the thickness, it shall not be wise to lower the layer thickness beyond a certain limit. Moreover, the breakdown field strength is inversely proportional to the thickness of a layer ($E = V/d$). It is generally observed that materials with higher dielectric constant have a small breakdown strength and vice versa. Also, an insulator must be chemically compatible with the bottom electrode and should possess excellent thermal stability as it will have to undergo the same thermal processing as the phosphor layer.

In the propagation breakdown (PB) mode, if a small part of the insulator breaks down, a short circuit is formed through the insulator that heats up and grows in size, causing catastrophic failure. In the self-healing breakdown (SHB) mode, the microscopic breakdown becomes open-circuited and hence does not grow in size. Usually, the high dielectric constant material tends to exhibit propagation breakdown. Possible ACTFEL insulating materials include Al_2O_3, SiO_2, Y_2O_3, TiO_2, TaO_5, $BaTiO_3$, $PbTiO_3$ and hybrids of these materials. Table 1 lists some of the commonly used insulators for ACTFEL displays [11].

Phosphor layer—The phosphor layer, also referred to as the 'central' or 'active' layer of an ACTFEL device, generally consists of a host lattice and an activator or luminescent center. The host matrix provides an environment to incorporate a luminescent center or activator where the absorbed energy is converted into visible light. Sulfides are commercially viable host materials used in most of the ACTFEL devices. However, oxides are widely investigated for use as hosts in ACTFEL devices owing to their distinctive advantages over sulfides. The requirements for a phosphor host are:

- The band gap of the host must be wide enough not to absorb any emanation from the luminescent center. To be capable of transmitting the entire visible range, the band gap must be at least 3.1 eV.
- The host must be insulating below the threshold to maintain a voltage drop and withstand the resulting electric field, ensuring a subthreshold capacitive nature for the phosphor.
- The host must possess high dielectric breakdown strength to permit efficient acceleration of electrons. A breakdown field of at least 1 MV/cm is generally recommended.

Table 1 Insulators commonly used for ACTFEL applications and their characteristics [11]

Material	Deposition method	ε_r	E_{BD} 10^8 V/m	$\varepsilon_o\varepsilon_r E_{BD}$ ($\mu C/cm^2$)	Breakdown mode
SiO_2	Sputtering	4	6	2	SHB
SiO_xN_y	Sputtering	6	7	4	SHB
SiO_xN_y	PCVD	6	7	4	SHB
Si_3N_4	Sputtering	8	6–8	4–6	SHB
Al_2O_3	Sputtering	8	5	3.5	SHB
Al_2O_3	ALE	8	8	6	SHB
Y_2O_3	Sputtering	12	3–5	3–5	SHB
Y_2O_3	EBE	12	3–5	3–5	SHB
$BaTiO_3$	Sputtering	14	3.3	4	SHB
Sm_2O_3	EBE	15	2–4	3–5	SHB
HfO_2	ALD	16	0.17-4	–	SHB
Ta_2O_5–TiO_2	ALE	20	7	12	SHB
$BaTa_2O_6$	Sputtering	22	3.5	7	SHB
Ta_2O_5	Sputtering	23–25	1.5	3–7	SHB
$PbNb_2O_5$	Sputtering	41	1.5	5	SHB
TiO_2	ALE	60	0.2	1	PB
$Sr(Zr,Ti)O_3$	Sputtering	100	3	26	PB
$SrTiO_3$	Sputtering	140	1.5–2	19–25	PB
$PbTiO_3$	Sputtering	150	0.5	7	PB

EBE Electron beam evaporation, *ALE* atomic layer epitaxy, *PCVD* plasma chemical vapor deposition, *ALD* atomic layer deposition

- The host must have good crystallinity and a low phonon coupling coefficient to minimize electron scattering.
- The active layer must be able to endure post-annealing procedures, if any, required.

The activator/luminescent center strongly influences the emission characteristics of a phosphor. A phosphor host lattice can also modify the colour emitted by an activator ion. This is because the crystal field environment that a host provides is specific for any activator. For example, in transition metals (Mn^{2+}, Cr^{3+}, Ag^{+}, Cu^{+}, Ti^{4+}, etc.), the impact of the crystal field environment is significant as 'd shell' electrons participate in the luminescence process. But, for rare-earth ions (Eu^{3+}, Dy^{3+}, Tm^{3+}, Tb^{3+}, Ce^{3+}), it is the 'f shell' electrons that participate and are seldom affected by crystal fields. The prerequisites of an excellent luminescent material to suit TFEL device applications include:

1. Ensure proper assimilation into host material and must emit in the visible range.
2. Must possess a large cross section for impact excitation.
3. Must be stable in the high electric field (>10^6 V/cm).

10 Inorganic Luminescent Materials

Inorganic luminescent emitters are the main prerequisite toward realizing efficient lighting and display systems. Luminescent materials, generally referred to as phosphors, are light emitters in the visible expanse of the electromagnetic spectrum under nonthermal excitation. The performance of display products very much depends upon phosphor efficiencies, their spectral distribution and long-term stability. The researches for primary colour phosphors with the best luminous efficiency and highest luminance still continue.

A phosphor may have two parts: a host material which dominates its electrical properties and a luminescent center or activator which dominates its optical properties or both. If not self-luminescent, the material chosen as the host matrix must be capable of providing a lattice for the adequate incorporation of the activator atoms. The activator concentration is of the order of one percent of the host material, which is several orders of magnitude larger than that typically used for semiconductor doping. The essential requisites of a phosphor host material are a large enough band gap to emit visible light without significant absorption and low defect density. The luminescent impurity must be stable enough to be properly incorporated into the host material and must possess a large cross-section for impact excitation.

The efficient incorporation of the activator atoms into the host lattice is ensured primarily by the crystalline quality and stoichiometry of the phosphor host matrix itself, which in turn influence the efficiency of light emission. The choice of the phosphor host lattice is very significant as each host offers its own unique local crystal field, in particular, both field symmetry and field strength. The crystal field or even a small perturbation highly contributes to the spectral output and the nature of the luminescent transition that the phosphor makes.

For instance, the 4f orbitals being chemically non-interacting, their luminescent transitions (characteristic of rare-earth ions) are comparatively unresponsive to the crystal field presented by the host lattice, and they are hence being referred to as the 'shielded' transitions. Hitherto, there are luminescent centers such as Mn^{2+} that are highly sensitive to the crystal field offered by the host lattice because in such ions, the luminescent transition arises from the outermost electronic shell. These luminescent transitions are also strongly reliant on the choice of the host lattice, permitting a possibility to amend the output color spectrum arising out of subtle changes in the crystal field.

The nature of the luminescent impurity or **activator** also determines the spectral emission from a phosphor. An excellent match between the ionic radii and valency of the activator ion and the host lattice cation that it replaces ensures effective incorporation of the activator ion into the host matrix. The larger the ionic size of the activator ion, the more challenging is the ionic diffusion into the host matrix hindering polycrystalline grain growth. On the other hand, smaller the size, these ions function as interstitial impurities and may act as non-radiative centers, thereby affecting device stability and consequently dropping the device luminance and efficiency.

Whenever a mismatch in valency occurs, compensation of charge has to be achieved either intrinsically by vacancy creation (Schottky defects) or extrinsically by co-doping with monovalent ions (like Na, K or Li) replacing divalent cationic sites. These extrinsic impurity ions utilized for compensating charge are termed co-activators. A **co-activator** performs the functions of a flux agent, a compensator or at times aid in modifying the luminescent properties of the phosphor host. They may be non-isovalent with any of the atoms of the host and hence create vacancies, which in turn help in improving the atomic diffusion and the crystallinity of the host. On using co-activators, a colour shift is perceived in the luminescence spectra. For example, blue colour-emitting Ce^{3+} and Cu^{+} serve as efficient luminescent co-activators for red-emitting Eu^{2+}, since these activator ions absorb blue light intensely. There are also constituents like Fe, which function as 'killer centers' degrading the overall performance of the phosphor host.

10.1 Phosphor Materials

There are several families of materials being explored to develop efficient EL phosphors. The entire ACTFEL technology is built around sulfide phosphors, almost exclusively due to the success of ZnS:Mn, the prototypical ACTFEL phosphor. In addition, SrS:Cu and SrS:Ce are extremely important phosphors for the realization of full-colour ACTFEL displays. ZnS:Mn with color filters in conjunction with SrS:Ce phosphors can be used to realize multicolor ACTFEL displays. The characteristics of some of the best reported ZnS:Mn and SrS:Ce ACTFEL devices are given in Table 2. The luminescence, efficiency and CIE coordinates required for primary colours so as to be used in multicoloured TFEL applications [12] are given in Table 3.

Table 2 Performance characteristics at 60 Hz of the best reported ZnS:Mn and SrS:Ce phosphors [11]

Phosphor	L_{40} (cd/m^2)	η_{40} (lm/W)	CIE$_x$	CIE$_y$
ZnS:Mn	310	2.0–3.0	0.50	0.50
SrS:Ce (greenish)	180	1.0	0.28	0.50
SrS:Ce (bluish)	155	1.0	0.20	0.38

Table 3 Target luminescence, efficiency and CIE coordinates at 60 Hz for high luminescence full-color ACTFEL display [12]

Color	L_{40} (cd/m^2)	η_{40} (lm/W)	CIE$_x$	CIE$_y$
Red	155	1.0–1.5	0.65	0.35
Green	310	2.0–3.0	0.30	0.60
Blue	52	0.3–0.5	0.15	0.10

The two properties unique to sulfide phosphors are excellent charge injection and polycrystallinity at low processing temperatures. The charge injection characteristics are due to the fortuitous combination of a high density of interface states at the proper energy for tunnel emission at readily attainable driving voltages. The melting points of binary sulfides are several hundred-degree centigrade lower than the corresponding oxides. Eventually, the possibility for sulfide compounds to exhibit polycrystallinity at normal ACTFEL processing temperatures was more probable than their oxide and nitride counterparts. Also, the deposition of sulfides is far less intricate than that of nitrides and oxides, sulfur being considerably more condensable than nitrogen and oxygen. This in turn complements the evaporation of sulfides which do not henceforth need the use of a gaseous species to compensate for the lost anionic atoms. The bulk of the binary sulfide materials are thermodynamically stable, and their thermodynamic formation energies are less than those of their corresponding oxides.

Insufficient band gap and moisture sensitivity were the core factors limiting the usage of sulfides in ACTFEL applications. Among the sulfide compounds, only CaS, SrS, BaS, ZnS and Ga_2S_3 and their ternary thiogallates exhibited properties compatible for ACTFEL applications. Although the number of sulfide phosphor hosts is quite limited, CaS, SrS and ZnS are known to be versatile phosphor hosts in terms of the number of potential activators.

In the family of selenide phosphor hosts, the alkaline earth selenides such as MgSe (5.6 eV), CaSe (3.87 eV), SrSe (3.73 eV) and BaSe (3.2 eV) are better choices as potential ACTFEL phosphors. The band gap and dielectric constant of selenides are correspondingly lower than their analogous sulfides. The main limiting factor in terms of ACTFEL application for selenides is their moisture sensitivity. Most of the binary alkaline earth compounds are moisture sensitive because of the thermodynamic stability of the alkaline earth hydroxides and carbonates. Moreover, a serious issue in the synthesis of Se compounds is the toxicity of this element and its compounds.

EL has been demonstrated in lanthanide and Mn-doped halide phosphors. Halides are attractive for ACTFEL applications because they crystallize at very low temperatures and have low dielectric constants due to their high ionic character. Also, their threshold voltage is not as abrupt as for sulfide phosphors. The main limiting factors in terms of ACTFEL application for tellurides are extremely large band gaps, relatively weak chemical bonding (affects film density as weakly bound compounds tend to nucleate poorly) and severe moisture sensitivity. An ACTFEL device with GaP:Pr active layer possesses sufficient band gap to transmit red light.

Owing to their band gap range and relatively stable nature in the presence of moisture, the III-V nitride materials—AlN, GaN, InN—are worthy choices used in fabricating bright and efficient blue-green LEDs. But the refractory nature of these binary nitrides necessitates extreme high-temperature sintering of sputter and evaporation sources, ideally in NH_3 atmosphere, and poses difficulty in achieving polycrystalline grain growth at standard ACTFEL structure processing temperatures.

11 Oxide Phosphors

Due to the inherent disadvantages of the commercially accepted sulfide phosphors such as deficiency of primary colors, vacuum instability, lesser chemical, mechanical and thermal stability, emission of corrosive gases under electron bombardment, a quest for a substitute that could satisfy the demands of the display industry was instigated. In the early 1990s, research groups shifted domain from the then commercially well-established sulfides to a much better alternative—the oxide phosphors. Several binaries, ternaries and complex oxide phosphors were proposed, and researches for new efficient oxide phosphor materials still continue. Oxide phosphors are thermodynamically stable and moisture insensitive. They are hence not sensitive to storage and handling in the open air. Compared to other species of materials that require toxic reactive gases for their synthesis, annealing and sintering processes, oxide phosphor synthesis procedures are much more easier and harmless during which reactive gases are least used.

Ternary oxides used in phosphor applications include borates, phosphates, vanadates, tungstates, molybdates, aluminates, silicates, sulfates, germinates, gallates, niobates, titanates and tantalates. More studied groups are the silicates and gallates, the phosphates and germanates to follow.

The main drawbacks of oxide phosphors are their refractory nature and non-abrupt device thresholds. Owing to their refractory nature, annealing temperature over 1000 °C is needed during fabrication of ACTFEL devices to achieve a high degree of polycrystallinity. Since deposition on glass substrates is not feasible, the inverted structure with a high-temperature tolerant substrate and a refractory insulator and bottom electrode becomes essential during fabrication of ACTFEL devices. Also, the refractory nature of oxide phosphors also restricts their deposition by thermal evaporation using a conventional resistively heated source. It is observed that this crystallinity issue may be alleviated through the addition of grain growth-promoting flux agents. The threshold of oxide ACTFEL devices is typically quite gradual compared to the abrupt threshold of sulfide ACTFEL phosphors. This is because of the large band gaps and effective masses, leading to inefficient carrier injection, which in turn causes non-abrupt device thresholds and enhances the need for larger driving voltages.

The silicate family of materials has been long known as efficient fluorescent lamp phosphors. Cd_2SiO_4, Zn_2SiO_4 (5.4 eV) and Y_2SiO_5 (>5.6 eV) are some of the most interesting phosphors of the silicate family suitable for ACTFEL applications. Zn_2SiO_4:Mn^{2+} and Y_2SiO_5:Ce^{3+} are widely investigated as low-voltage green and blue phosphors, respectively.

Table 4 gives some of the primary and white color-emitting oxide phosphors.

Table 4 Emission color of certain oxide phosphors

	Color	Reference
$ZnGa_2O_4$	Blue	[26]
$ZnGa_2O_4:Ce^{3+}$	Blue	[77]
$Y_2SiO_5:Ce^{3+}$	Blue	[153]
$Y_3Al_5O_{12}:Tm^{3+}$	Blue	[153]
$BaMgAl_{10}O_{16}:Eu^{2+}$	Blue	[153]
$TaZn_3O_8$	Blue	[154]
$Ga_2O_3:Mn^{2+}$	Green	[155]
$ZnGa_2O_4:Mn^{2+}$	Green	[77]
$ZnGa_2O_4:Tb^{3+}$	Green	[156]
$Zn_2GeO_4:Mn^{2+}$	Green	[157]
$Zn_2SiO_4:Mn$	Green	[158]
$Y_3Al_5O_{12}:Tb^{3+}$	Green	[153]
$Zn_3Ta_2O_8:Tb^{3+}$	Green	[159]
$Ca_3Sc_2Si_3O_{12}:Ce^{3+}$	Green	[160]
$CaSc_2O_4:Ce^{3+}$	Green	[161]
$TaZn_3O_8:Mn$	Green	[154]
$ZnAl_2O_4:Mn$	Green	[17]
$Y_3Al_5O_{12}:Eu^{3+}$	Red	[153]
$ZnGa_2O_4:Cr^{3+}$	Red	[162]
$Ga_2O_3:Eu^{3+}$	Red	[163]
$Y_2O_3:Eu^{3+}$	Red	[100]
$Zn_3Ta_2O_8:Eu^{3+}$	Red	[159]
$LiInO_2:Eu^{3+}$	Red	[164]
$CaIn_2O_4:Eu^{3+}$	White	[143]
$KSrPO_4:Eu^{2+}$	White	[165]
$SrIn_2O_4:Dy^{3+}$, Pr^{3+}, Tb^{3+}	White	[144]
$Sr_2SiO_4:Eu^{2+}$, Ce^{3+}	White	[139]
$CaMgSi_2O_6:Eu^{2+}$, Mn^{2+}	White	[140, 166]
$CaAl_2Si_2O_8:Eu^{2+}$, Mn^{2+}	White	[141]
$SrZn_2(PO_4)_2:Eu^{2+}$, Mn^{2+}	White	[142]
$La_{0.827}Al_{11.9}O_{19.09}:Eu^{2+}$, Mn^{2+}	White	[167]
$Ca_2P_2O_7:Eu^{2+}$, Mn^{2+}	White	[168]

12 Review on Oxide Phosphor Hosts in ACTFEL Devices

The gallate phosphor hosts suitable for ACTFEL applications are $ZnGa_2O_4$ and $CaGa_2O_4$. The ternary germanate oxide phosphor $Zn_2GeO_4:Mn^{2+}$ has been extensively studied as an efficient green phosphor. The alkaline earth phosphates are rarely

a good choice for alternating current TFEL applications since both its constituents (binary alkaline earth oxides and P_2O_5) and compounds are sensitive to moisture. They are hence better for CRT and fluorescent lamp applications because they exist in an evacuated space for these applications.

In 1990, Minami et al. first reported the fabrication of a bright electroluminescent device with an efficiency of 0.15 lm/W by sandwiching a thin film of Zn_2SiO_4:Mn^{2+} between a $BaTiO_3$ sheet and a transparent conducting electrode ZnO:Al [13]. Since then, advanced research efforts toward developing highly efficient and highly stabile oxide EL phosphors were triggered. Ouyang et al. [14] reported on the fabrication of a multilayered rf-sputtered TFEL device using Mn-activated Zn_2SiO_4 and Ce-activated Y_2SiO_5. It was observed that the processing temperature could be considerably lowered on replacing Si by Ge. Stuyven et al. [15] report on the fabrication of ACTFEL devices using the green-emitting $Zn_2Si_{0.5}Ge_{0.5}O_4$:Mn^{2+} phosphor on glass substrates (0.44 lm/W @ 60 Hz) and $BaTiO_3$ ceramic sheets.

An efficiency of 0.45 lm/W has been reported [16] for Zn_2GeO_4:Mn active ACTFEL devices fabricated on NEG/ITO/ATO substrates. Some of the other phosphors widely studied include $ZnAl_2O_4$:Mn [17], $BaAl_{12}O_{19}$:Tb [18], Mg_2SnO_4:Mn (green) [19], Sr_2CeO_4 (blue) [20] and $SrTiO_3$:Pr (red) [21, 22]. Recently, red-emitting ACTFEL devices have been realized on transparent ITO/ATO glass substrates using Ga_2O_3:Eu [23]. TFEL devices with higher luminous efficiencies of up to 10 lm/W have been reported using yellow-emitting Y_2O_3:Mn and $(Y_2O_3)_{1-x}(GeO_2)_x$:Mn as active layers [24, 25].

Some of the oxide phosphors for ACTFEL and their characteristics driven at 1 kHz sine wave are given in Table 5. Some of the potential EL phosphors investigated in the author's laboratory were $ZnGa_2O_4$:Mn^{2+}, $ZnGa_2O_4$:Dy^{3+}, Zn_2GeO_4:Mn^{2+} and Y_2O_3:Eu^{3+}. A detailed account of each of these matrix systems, along with the relevant findings, is presented here.

12.1 Zinc Gallium Oxide—$ZnGa_2O_4$

Zinc gallate is a ternary oxide phosphor widely proven as an efficient host material for EL devices. It was Itoh et al., in 1991, [26] who first reported on this new spinel phosphor system—$ZnGa_2O_4$. Zinc gallium oxide crystallizes in the normal spinel structure [space group is $Fd3m(Oh^7)$] [27]. It is a mixed oxide of ZnO and Ga_2O_3 composed of only the fourth-row cations. The n-type semiconducting [28] zinc gallate is unique, being a material with cubic symmetry and possessing a direct band gap of 4.4 eV, and renders transparency in the ultraviolet (UV) region. Itoh et al. utilized this matrix in the making of VFDs [26] as it exhibited low-voltage cathodoluminescence (LVCL), an attribute that could reduce damage to filaments in VFDs, unlike conventional sulfide phosphors. Bulk $ZnGa_2O_4$ phosphor prepared at various firing temperatures gave a bluish luminescence at 470 nm characterized by the colour coordinates $(x, y) = (0.17, 0.13)$. A 30 V dc driven VFD fabricated with zinc gallate active layer showed excellent stability and luminous efficiency of

Table 5 Oxide phosphors for ACTFEL applications and their characteristics (all devices driven with a 1 kHz sine wave)

Color	Phosphor	V_{th}	L_{max} (cd/m^2)	η_{max}	CIE$_x$	CIE$_y$
Red	Ga_2O_3:Cr	175	375	0.04	0.654	0.293
	$CaGa_2O_3$:Eu	225	215	0.026	0.687	0.331
	$ZnGa_2O_3$:Cr	250	196	0.02	0.584	0.398
	Ga_2O_3:Eu	210	152	0.02	0.587	0.385
	Y_2O_3:Eu	130	144	0.14	0.573	0.393
	$ZnGa_2O_3$:Eu	175	62	0.009	0.584	0.398
	CaO:Mn	390	55	0.016	0.603	0.391
	GeO_2:Mn	180	7	0.018	0.521	0.413
	Gd_2O_3:Eu	235	4.9	0.002	0.524	0.352
Yellow	$CaGa_2O_4$:Mn	150	2790	0.25	0.479	0.518
	$CaGa_2O_4$:Dy	215	30	0.02	0.479	0.518
Green	$Zn_2Si_{0.75}Ge_{0.25}O_4$:Mn	170	4220	0.75	0.272	0.662
	$ZnSiO_4$:Mn	160	3020	0.78	0.251	0.697
	$Zn_2Si_{0.7}Ge_{0.3}O_4$:Mn	110	1751	2.53	0.271	0.671
	Ga_2O_3:Mn	110	1018	1.7	0.116	0.676
	$ZnGa_2O_4$:Mn	135	758	1.2	0.082	0.676
	Zn_2GeO_4:Mn	55	341	0.08	0.331	0.645
	$ZnAl_2O_4$:Mn	130	21	0.006	0.150	0.708
White	SrP_2O_7:Eu	145	5.6	0.005	0.334	0.270
Blue	$ZnSiO_4$:Ti	280	15.8	0.017	0.142	0.115
	Y_2SiO_5:Ce	235	13.2	0.054	0.176	0.138
	CaO:Pb	470	5.5	0.001	0.166	0.113

0.7 lm/W [26]. Since $ZnGa_2O_4$ has a wide band gap, it has been investigated as a UV-transparent electronic conductor [28].

Pristine and doped $ZnGa_2O_4$ bulk phosphor was synthesized using various techniques like solid-state reaction [28–34], hydrothermal synthesis [35–38], microwave synthesis [39, 40], solgel route [41], citrate gel process [42], oxalate gel method [43], aerosol pyrolysis [44], multistage precipitation [45] and microencapsulation methods [46]. Omata et al. explored zinc gallate as a UV-transparent conducting oxide [28].

(a) **Crystal Structure**

$ZnGa_2O_4$, a cubic AB_2O_4 spinel, is generally a blend of zinc blende and rock salt structures. In this close-packed frame, anions occupy half of the octahedral lattice positions and cations fill one-eighth of tetrahedral positions (Fig. 12).

A normal spinel is one in which A^{2+} ions occupy tetrahedral sites and B^{3+} ions fill octahedral sites. In the inverse spinel structure, A^{2+} ions fill octahedral sites and B^{3+}

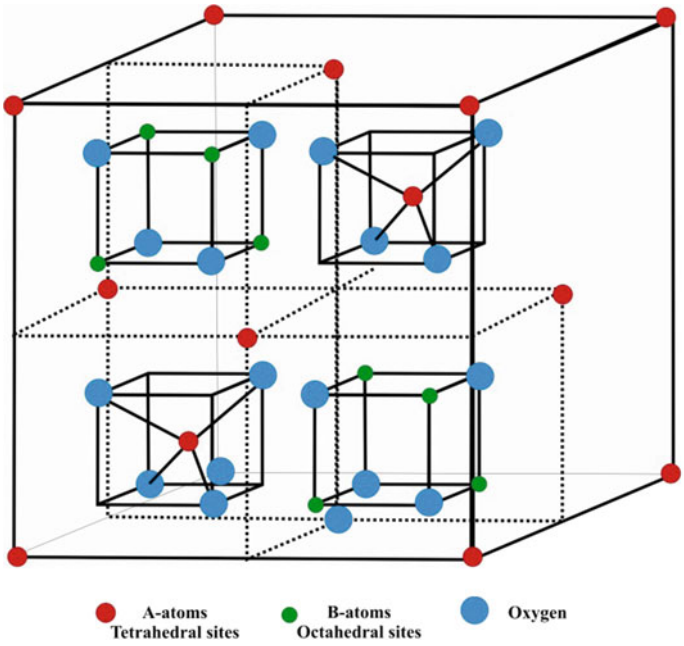

Fig. 12 Spinel structure of $ZnGa_2O_4$

ions occupy tetrahedral as well as octahedral sites in 1:1 ratio. If the cation distribution is intermediate between the two, we refer to it as the mixed spinel. $ZnGa_2O_4$ is a normal spinel with Zn^{2+} and Ga^{3+} ions aligned at tetrahedral and octahedral sites, respectively, and the lattice constant is 8.37 Å. The oxygen ions are arranged in an fcc closed packing. A single subcell of $ZnGa_2O_4$ has four atoms with tetrahedral to octahedral interstices in the 1:2 ratio. Thus, a total of twelve interstices shall be filled with one divalent and two trivalent cations. Eight such elementary cells are assembled to make a $ZnGa_2O_4$ unit cell of 32 oxygen ions, and 8 tetrahedral and 16 octahedral cations.

(b) PL Response of $ZnGa_2O_4$ matrix

Pure $ZnGa_2O_4$ gives an intense blue emission on excitation with an ultraviolet light or low-energy electrons due to transitions in a self-activated center. In $ZnGa_2O_4$ spinel, Ga^{3+} ions act as the sensitizer [33].

The wave functions associated with S, P, D… terms differ from those of their respective s, p, d… orbitals in the way they transform in a particular point group. For instance, in an octahedral environment, p orbitals transmute as T_{1u} and the P term derived from 'd' configuration transforms as T_{1g}. The interactions between orbitals of the transfigured p term with those of the six oxygen ligands lead to a shift in the energy levels of individual orbitals, lifting off the degeneracy and resulting in the 3d energy-level splitting. The influence of the strength of ligand field leads to splitting

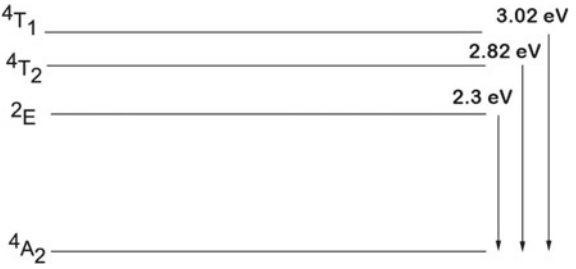

Fig. 13 Ga^{3+}-level splitting in an octahedral environment

of Ga^{3+} levels in an octahedral environment, which on tagging using spectroscopic terms $^4A_2$, $^4T_1$, $^4T_2$ and ^2E is depicted in Fig. 13.

On excitation with UV light of wavelength 260 nm, zinc gallate shows a broad fluorescence band, attributed to the self-activated Ga^{3+} ions at the octahedral site, with a peak maximum at 432 nm. Jeong et al. have studied the effect of compositional variations, $ZnGa_xO_{1+1.5x}$ with x (Ga/Zn ratio), on the luminescence of solid-state synthesized zinc gallate [33]. His group reports that the intensity of the blue broad emission band improves with Ga/Zn ratio, attributing the increase to the abundance of oxygen vacancies due to excess Ga_2O_3 in these compounds. When Ga/Zn ratio was increased much beyond 2:1, the excitation spectra, in addition to a low intense excitation peak at 260 nm, showed a shoulder peak at 246 nm. The emission spectral maximum blue-shifted to 360 nm, which may be considered to originate from β-Ga_2O_3. Since most of the spinels make a solid solution with oxides of the form B_2O_3, the solubility of Ga_2O_3 in spinel $ZnGa_2O_4$ lattice is anticipated. Finally, they established that the 432-nm emission in response to the 260-nm absorption could be accredited to the transitions in octahedral Ga–O whereas the 360-nm emission corresponding to 246 nm could be correlated with the self-activated optical centers of the tetrahedral Ga–O group.

The randomness of the spinel structure with the configuration $(A_{1-x}B_x)^{IV}(B_{2-x}A_x)^{VI}O_4$ is reported, randomness being determined by X-ray and neutron diffraction experiments. The lack of an adequate disparity amid X-ray scattering powers of Zn and Ga made this impossible. IR spectral studies of zinc gallate reveal the presence of vibration peaks at 420 and 570 cm^{-1}. But distinguishing the peak of tetrahedral Ga–O from that of octahedral Ga–O was still cumbersome. Studies also showed that there is a possibility for Ga^{3+} ions to occupy the tetrahedral sites when the zinc gallate phosphor is synthesized with β-Ga_2O_3-rich environment. It was these Ga^{3+} ions that gave an excitation band at a shorter wavelength (peaking at 246 nm) and the fluorescence band at 360 nm. Furthermore, tuning of colour has been observed in $ZnGa_2O_4$ phosphor via oxidation or reduction processes. The color oscillates between ultraviolet (360 nm) and blue (430 nm). The ultraviolet emission of reduced $ZnGa_2O_4$ always accompanied the 680-nm emission originating from single oxygen vacancies (V_O*). Also, an increase in the difference in binding energy between Ga^{3+} and O^{2+} was observed in reduced $ZnGa_2O_4$ indicative of the fact that

the configuration of octahedral sites gets distorted due to V_O* generation and it becomes more ionic shifting the emission band from 430 to 360 nm.

Dopant incorporation in $ZnGa_2O_4$ significantly affected its spectral response. When doped with Mn^{2+} or Cr^{3+}, zinc gallate luminesces in the green and red regions, respectively [45–48]. Here, the Ga–O group serves as a sensitizer that transfers the excitation energy in a non-radiative manner from the host lattice to the activator ion. Annealing in a reducing ambient improved the purity of the green emission, as this promotes the conversion of Mn^{4+}/Mn^{3+} to Mn^{2+}. Yu and Lin stated the presence of a very weak red emission at 666 nm when excited at 325 nm [29]. The green emission peaking at 508 nm is credited to the $^4T_1$–$^6A_1$ transitions of tetrahedrally coordinated Mn^{2+} ions. The excitation spectra of the phosphor examined at 508 nm revealed bands at 245 nm and 290 nm, respectively, allocated to the direct excitation of the Ga–O group and the direct excitation or the charge-transfer band of the Mn^{2+} ions. Tran et al. report that the low-temperature emission could be assigned to the presence of Mn^{2+} ions at tetrahedral Zn site or at Zn^{2+} site with distorted tetrahedron or at octahedral Ga^{3+} site [47]. Uheda et al. investigated the long-term phosphorescence in $ZnGa_2O_4$:Mn and attributed it to the formation of numerous trap states, mainly Zn vacancies, in the energy range 0.48–0.71 eV above the valence band of the host [30].

Luminescent intensity enhancement can also be accomplished in $ZnGa_2O_4$ via co-doping. For instance, co-doping with Ge and Li is found to increase the luminescent output of $ZnGa_2O_4$:Mn by 5%. An effective change in crystal field was found to red-shift the emission in Cd co-doped $ZnGa_2O_4$:Mn bulk phosphor. Choi et al. reported a tunable color emission from 350 to 520 nm in $Zn_{1-x}Cd_xGa_2O_4$ [32]. The PL and CL emission intensities were found to increase also with In_2O_3 doping [33].

(c) Review on $ZnGa_2O_4$ thin films for device applications

Pristine and doped $ZnGa_2O_4$ thin films could be grown on amorphous or single crystalline substrates using the common physical vapour deposition techniques such as pulsed laser deposition [49–61], rf magnetron sputtering [62–73], solgel process [74], solvent evaporation [75] and electrophoretic deposition [76]. Thin films were grown via PLD on various substrates such as Al_2O_3, MgO and Si. Jeong et al. demonstrated MgO as a promising substrate to grow high-quality crystalline thin films of $ZnGa_2O_4$ [53]. He also reported that Se doping could further enhance the luminescent output of $ZnGa_2O_4$:Mn phosphor thin films by a factor of 3.1 [53]. Bae et al. reported that Al_2O_3 (sapphire) is more suited for growing high-quality thin films instead of Si [54]. Yi et al. reported growth of pulsed-laser-ablated epitaxial $ZnGa_2O_4$:Mn thin films onto MgO substrates that exhibited a bluish-white luminescence for a Zn/Ga ratio of 0.4 [55].

Several groups used PLD for fabricating high-quality crystalline epitaxial thin films, whereas many others employed rf magnetron sputtering to grow polycrystalline thin films of doped and undoped $ZnGa_2O_4$. Hseih et al., who observed LVCL in rf-sputtered $ZnGa_2O_4$ thin films also investigated the effect of substrate temperature and post-deposition annealing [61].

Chung et al. studied how the use of various substrates such as ZnO:Al/glass, ZnO:Ga/glass, ZnO/ITO/glass and ITO/glass profoundly influenced the surface morphology and luminescent response of sputtered $ZnGa_2O_4$ thin films. Post-deposition annealing was found to affect the luminescent output and Zn/Ga ratio more than the surface morphology of these films [62]. Sputtered $ZnGa_2O_4$ films onto Si substrates exhibited lower grain size and better PL response than those deposited on ITO/glass substrates [64]. White light-emitting crystalline films of $ZnGa_2O_4$ could be deposited when an In_2O_3 buffer layer was employed [66]. Kim et al. demonstrated that the energetic particle bombardment dramatically affected the cross-sectional microstructure, surface morphology, degree of porosity and film density of $ZnGa_2O_4$:Mn phosphor thin films grown by rf planar magnetron sputtering [67, 68]. The films deposited at 600 °C showed a better response, and post-deposition annealing was found to better enhance the PL and CL performance of the phosphor.

$ZnGa_2O_4$ is also an excellent host material for the fabrication of multicolour-emitting ACTFEL devices. Minami et al. fabricated ACTFEL devices by sputter depositing Mn, Cr, Ce, doped $ZnGa_2O_4$ onto 0.2-mm-thick ceramic sheets of $BaTiO_3$ [77]. ZnO:Al/ITO and Al/Ag were used as transparent and opaque electrodes, respectively. Post-annealing of as-deposited devices [76–79] was found to improve their performance further. Devices were also fabricated employing dip coating [80] and chemical vapor deposition [81] techniques for growing the active layers. Flynn et al. [82] investigated the possibility of improvising the EL characteristics of $ZnGa_2O_4$:Mn-based TFEL devices on post-annealing at lower temperatures. ACPEL devices with luminescent efficiency of up to 15 lm/W were fabricated by several groups using Mn (Cr)-activated $ZnGa_2O_4$ as the active layer [83, 84].

12.2 Zinc Germanate—Zn_2GeO_4

Zinc germanate, Zn_2GeO_4, is a ternary oxide luminescent material with a band gap of 4.57 eV that crystallizes at a low temperature. The bulk material is affirmed to be an intrinsically defect phosphor [85]. On doping with Mn, Zn_2GeO_4 emits an intense green band with a peak maximum at 535 nm.

There are works on thin-film growth of Zn_2GeO_4:Mn^{2+} deposited by rf magnetron sputtering [16, 86–88] and PLD [89]. Annealing after deposition is found to improve the luminescent response of the phosphor. Thin films of Zn_2GeO_4:Mn^{2+} emit green even at moderate annealing temperatures (650–700 °C) in a furnace and at 125 °C using a hydrothermal furnace [90]. ACTFEL devices could be fabricated, making use of an rf-sputtered Zn_2GeO_4:Mn as luminescent layer [16, 87–89]. Minami et al. report that a high luminance of 1536 cd/m^2 could be observed in $Zn_2Si_{0.5}Ge_{0.5}O_4$ at a drive frequency of 60 Hz from TDEL devices designed on ceramic $BaTiO_3$ substrates [88]. The choice of substrates and various deposition parameters also was found to influence the emissive responses from laser-ablated Zn_2GeO_4:Mn profoundly, so studied by Williams et al. [89]. A green-emitting ACTFEL device was reported to be

fabricated on glass substrates by Lewis et al. using rapid thermal annealing (RTA) of the active layer at 860 °C. Baker et al. have grown EL devices on Si substrates with sputtered $Zn_2Si_{0.5}Ge_{0.5}O_4$ as the luminescent layer [90].

12.3 Yttrium Oxide—Y_2O_3

Crystals doped with a few percentage of rare-earths emit characteristic lines and not bands in the visible spectrum under irradiation with UV, X-rays or electron beams. This is because the emissive transitions in the $4f^n$ shell are well sheltered by the 5d and 6s shells.

It was Levine and Palilla who proposed the usage of YVO_4:Eu as an active material for the primary red colour in TV screens [91] and claimed enhanced colour fidelity and brightness. Other oxide materials used as red-emitting phosphors include YVO_4:Eu, Y_2O_3:Eu, Gd_2O_3:Eu and Y_2O_2S:Eu of which Y_2O_3:Eu caught much attention of researchers around the globe.

(a) Crystal structure

Yttrium oxide, an fcc C-type metal oxide, is compliant with the space group Ia3 (T_h^7). Each cation, in an ideal fluorite structure, is bounded by eight anions located at the eight corners of a cube. Yttria crystallizes into a modified fluorite structure. A quarter of the oxygen atoms are discarded to preserve charge neutrality, and the remaining one is redistributed at the cube corners. Thus, each yttrium atom is bounded by six oxygen atoms creating two kinds of distorted octahedral configurations, S_6 and C_2

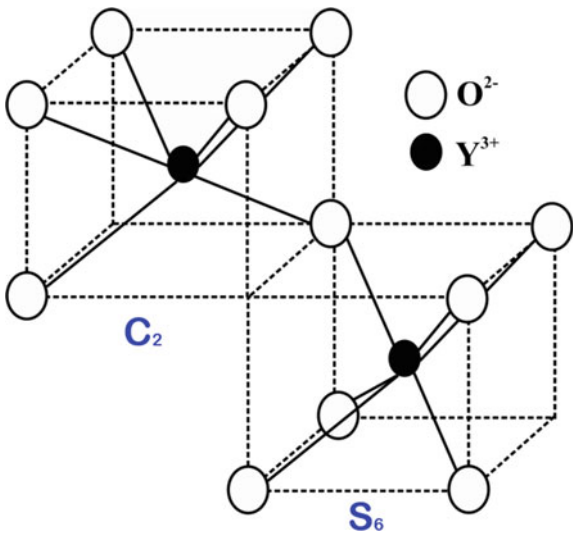

Fig. 14 Two different types of crystal structures in Y_2O_3 unit cell; C_2 (vacancies along the face diagonal) and S_6 (vacancies along the body diagonal)

sites in the unit cell (see Fig. 14), with a lattice constant of 10.60 Å. Eight yttrium atoms occupy the S_6 symmetry, and 24 atoms are in the C_2 symmetry [92].

(b) **PL Response of Y_2O_3 matrix**

In Y_2O_3:Eu^{3+}, absorption and subsequent emission mechanisms include direct excitation of the dopant ionic site, excitation via a charge-transfer state amid Eu^{3+} and neighbouring O^{2-} ions or excitation via the host lattice [93]. The photoluminescent spectra have several lines in the range 580–700 nm, assigned to $^5D_0$–^7F_J, $J = 0$, 1, 2, 3 transitions of Eu^{3+} ions, and could be further partially resolved into various m_J transitions. These emission lines correspond to inner f–f transitions and are electric dipole forbidden. From the emission spectrum, one can speak about the local crystal environment of Eu^{3+} ion, especially analyzing the relative intensity ratio of $^5D_0$–$^7F_1$ and $^5D_0$–$^7F_2$ emission lines [94]. The former transition is an electric dipole forbidden one and almost unresponsive to the local environment, whereas the latter is an electric dipole allowed transition very much sensitive to the local crystal field and symmetry [95].

Eu^{3+} ions are supposed to replace Y^{3+} ions in the host lattice, thereby creating a charge-transfer state (CTS) with neighbouring oxygen atoms. On luminescent excitation, these CT states absorb light and make a resonant transfer to Eu^{3+} ions resulting in red PL emission. The emission spectrum consists of several lines which give information about Eu^{3+} site symmetry in the lattice. The optical transitions among Eu^{3+} energy levels are more probable to happen in the C_2 site rather than in S_6 site as the former is more stable with inversion symmetry [94]. S_6 sites are more prone to magnetic dipole transitions, whereas electric dipole transitions are favoured at C_2 sites. For Eu^{3+} ion, the lines in between 538 and 585 nm $^5D_1$–$^7F_1$ are related to magnetic dipole transitions while $^5D_0$–^7F_j ($j = 0$–4) lines in the 590-715 nm span is attributed to electric dipole transitions. In the emission spectra of Y_2O_3:Eu^{3+}, the lower density of S_6 sites gives less intense magnetic dipole transitions and hence $^5D_0$–^7F_j lines with a peak maximum at 615 nm are more prominent. The PL spectra also confirm that Eu^{3+} ions are assimilated into the host lattice predominantly replacing Y^{3+} ions with C_2 symmetry.

Bulk Y_2O_3:RE can be synthesized using solid-state method [96–99], flame fusion process [100], ceramic method [101], citrate gel acid method [102], simultaneous addition method [103], combustion method [104] and self-propagating high-temperature synthesis [105].

Chang et al. report a stimulated emission from single crystals of Y_2O_3:Eu [100], and Nazarov et al. propose a UV-excited white emission from Y_2O_3:Eu, Sm for white LEDs [101]. Enhanced CL emissions have been observed from Y_2O_3:Eu on co-doping with La, Li and Zn [98, 99, 102].

Doped and pristine Y_2O_3 thin films can be grown by spray pyrolysis [106, 107], sol-gel technique [108–110], MOCVD [111], rf magnetron sputtering [112–115], electron beam evaporation [116] and pulsed laser ablation techniques [117–129]. Pulsed laser deposition is widely used to grow high-quality thin films of Y_2O_3. Suyama et al. report the fabrication of Y_2O_3:Eu active MISIM-structured ACTFEL device [130]. Due to low electron transport in Y_2O_3, EL could be observed only when

ZnS was employed as accelerating layers in a multilayered Y_2O_3:Eu/ZnS/glass/ITO-structured device. Yellow-emitting high-luminance TDEL devices with efficiencies up to 10 lm/W using Y_2O_3:Mn^{2+} and combination of $\{(Y_2O_3)_{1-x}(GeO_2)_x$:$Mn^{2+}\}$ have been reported by Minami et al. [24, 25, 131, 132].

13 White Phosphors

White light-emitting EL displays have stimulated much interest as they are primarily used to fabricate full-colour FPDs using filters as well as word processing white screen displays. In the latter, it would ease the tension on eyes, especially to a person viewing back and forth continuously on a black-on-white text and screen [133].

Two parallel possibilities are explored for realizing colour EL: (1) the growth of efficient broadband or white phosphor that can be filtered to create an RGB display or (2) the synthesis of highly efficient primary colour EL phosphors. The former maintains a simple sequence during the fabrication of a monochrome TFEL display, and RGB colours are achieved by laminating a patterned colour filter onto the EL device at the last stage. Also, compared to using three structurally dissimilar phosphors for an RGB or white display, the use of filters is much simpler.

It was Tanaka et al. (1987) who first reported on white EL phosphors based on rare-earth-doped alkaline earth sulfides for filtered color TFEL devices [134]. Since then, several white displays were fabricated using singly and doubly activated alkaline earth sulfides as the active luminescent material [135–137]. Devices were also fabricated stacking combinations of phosphor layers: SrS:Ce/CaS:Eu [133], SrS:Ce/SrS:Eu or SrS:Ce/ZnS:Mn [138]. The highest luminance of 470 nits @ 60 Hz has been reported by Planar International using atomic layer epitaxy (ALE)-deposited dual layers of SrS:Ce/ZnS:Mn.

Oxide phosphor matrices used to realize white light luminescence were $CaIn_2O_4$, Sr_2SiO_4 and $SrIn_2O_4$. The partial energy transfer from Ce^{3+} to Eu^{2+} is liable for white light generation in Sr_2SiO_4:Eu^{2+}, Ce^{3+} [139]. Eu^{2+} efficiently sensitizes and transfers energy to Mn^{2+} creating a white light emission on near-UV excitation in several phosphor host matrices [140–142]. $CaIn_2O_4$:Eu^{3+} [143] radiates white by a wise choice of the concentration of the dopant. The blend of multicolour emissions from a single active center is reported to lead to white light generation in $SrIn_2O_4$:Dy^{3+} [144].

14 Summary of Work Done in Laboratory

Luminescent studies in zinc gallate and zinc germinate oxide phosphors activated with transition and rare earth elements were extensively studied in our laboratory. Most of the works were focused on the deposition of transparent oxide phosphor thin

films at lower processing temperatures so as to promote the use of glass substrates in display applications.

Bulk $ZnGa_2O_4$ with its intrinsic blue emission and its doped variants were synthesized using the conventional high-temperature solid-state reaction technique. A singly activated single-phase white oxide phosphor—dysprosium (Dy)-doped $ZnGa_2O_4$—was identified [145]. A host to activator non-radiative resonant energy transfer was proposed to explain the simultaneous occurrence of multicolour dopant emissions in $ZnGa_2O_4$:Dy^{3+} matrix. The 2.5 atomic % Dy^{3+}-doped sample gave the best white emission with chromaticity coordinates (0.31, 0.33) matching well with that of achromatic white (0.33, 0.33). Transparent well-adhesive thin films of $ZnGa_2O_4$:Dy^{3+} were grown on quartz substrates by rf magnetron sputtering technique [146]. The as-deposited films at room temperature exhibited the spinel (311) peak, and their luminescent response could be improved by substrate heating prior to deposition. The maximum PL intensity was reported for the film deposited at 600 °C which gave white luminescence with chromaticity coordinates (0.34, 0.28). An all-oxide white-emitting alternating current-driven thin-film electroluminescent (ACTFEL) device was fabricated on a commercial glass substrate—glass/ITO/ATO/phosphor/$BaTa_2O_6$/Al—with $ZnGa_2O_4$:Dy^{3+} phosphor as the active layer [147]. The intensity of the EL emission could further be improved by inserting a highly crystallized interfacial layer of ZnO between the substrate and the phosphor layer [147] as is evident from Fig. 15.

Thin films of $ZnGa_2O_4$:Mn^{2+} were deposited on quartz substrates using rf magnetron sputtering of a 2 atomic % manganese-doped powder target [148]. It could be observed that apart from bulk phosphor behaviour, Mn incorporation and the subsequent luminescent outcome are strongly influenced by the dopant source. Green-emitting ACTFEL devices were fabricated on commercial glass substrates [149] in the conventional MISIM structure using $ZnGa_2O_4$:Mn^{2+} as the active layer, the results of which are consolidated in Fig. 16. In contrary to earlier reports, the EL emissions

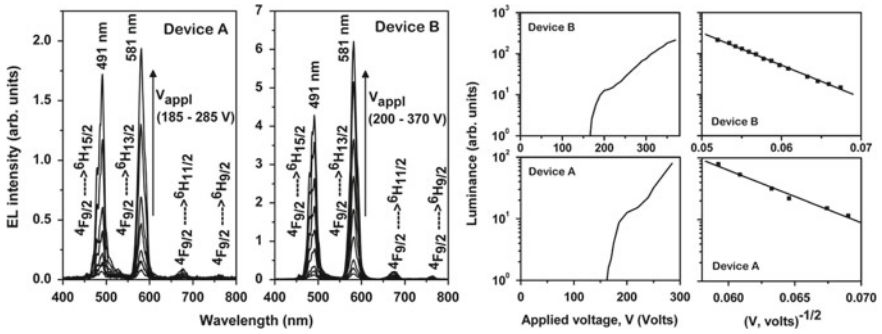

Fig. 15 EL emission spectra of NEG/ITO/ATO/$ZnGa_2O_4$:Dy^{3+}/BTO/Al (Device A) and NEG/ITO/ATO/ZnO/$ZnGa_2O_4$:Dy^{3+}/BTO/Al (Device B) at a drive frequency 1.5 kHz for various applied voltages V (left) and luminance–voltage (L–V) curve of Devices A and B along with the L versus $V^{-1/2}$ semilog plot (right)

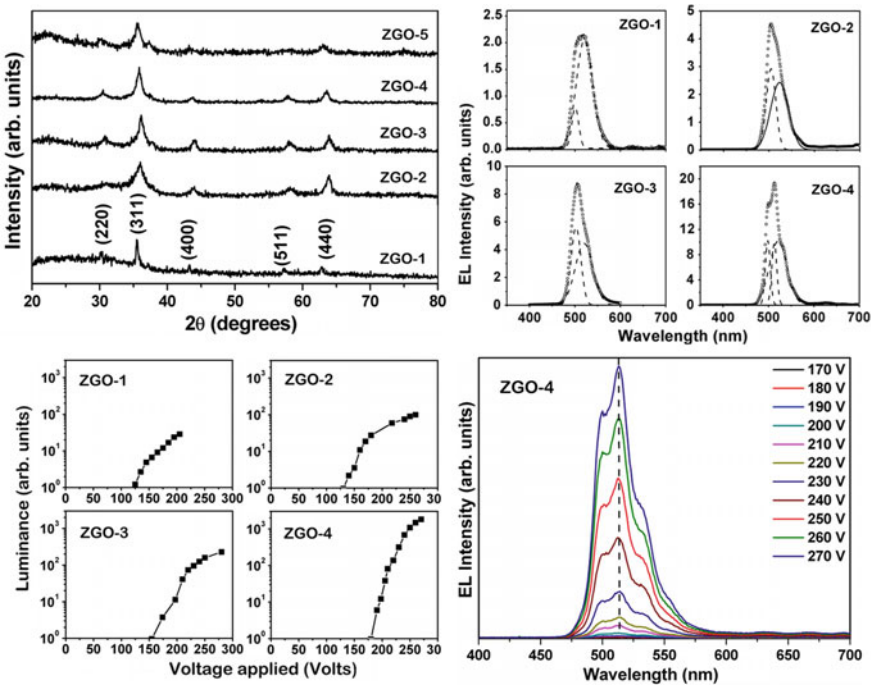

Fig. 16 XRD patterns of the active $ZnGa_2O_4:Mn^{2+}$ layer deposited at 600 °C on quartz substrates for a duration of (a) 45 min, (b) 60 min, (c) 90 min, (d) 120 min and (e) at 500 °C for 90 min (left-top) EL spectra of the $ZnGa_2O_4:Mn^{2+}$ active ACTFEL devices fabricated with different phosphor layer thicknesses (right-top) and *L*–*V* curves of the devices fabricated (left-bottom) EL spectra of ZGO-4 device recorded for various applied voltages when excited at 1 kHz (right-bottom)

could be recorded without any post-deposition treatments. The colour chromaticity diagrams are given in Fig. 17.

Mn^{2+}-activated Zn_2GeO_4 thin films were deposited on quartz substrates using the rf magnetron sputtering technique [150]. The crystallinity and green luminescent emission were found to improve on inserting a ZnO buffer layer between the substrate and the phosphor layer. Nanoparticles of bulk and Eu-doped $ZnGa_2O_4$ were hydrothermally synthesized varying the process parameters, such as the volume ratio of the cation precursor solutions, temperature and time of growth, and dopant concentration. High-resolution transmission electron microscopic images confirmed the formation of spherically shaped $ZnGa_2O_4:Eu^{3+}$ nanoparticles of particle size 8 nm [151].

Room-temperature deposition of $ZnGa_2O_4$ phosphor thin films was reported using pulsed laser deposition (PLD) technique [59]. Tin (Sn) doping was found to enhance the electrical conductivity of $ZnGa_2O_4$ spinel [58]. The conductivity of PLD-grown $ZnGa_2O_4$:Sn thin films on fused quartz substrates at room temperature could be further improved on reduction [58]. Red-emitting $Y_2O_3:Eu^{3+}$ thin films were also

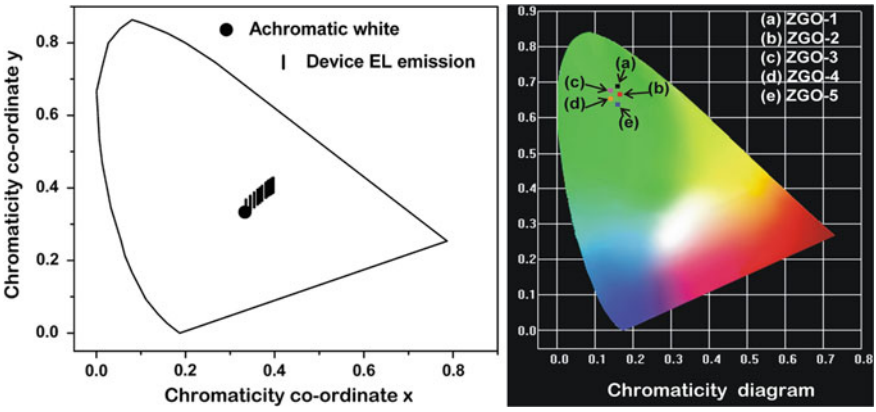

Fig. 17 Chromaticity coordinate diagram indicating the CIE coordinates of the fabricated ACTFEL devices NEG/ITO/ATO/ZnO/$ZnGa_2O_4$:Dy^{3+}/BTO/Al (left) and NEG/ITO/ATO/$ZnGa_2O_4$:Mn^{2+}/BTO/Al (right)

pulsed laser deposited onto amorphous fused silica substrates [152] which exhibited a preferred orientation along the (111) plane, irrespective of oxygen partial pressure and substrate temperature.

References

1. Wiedemann E (1888) About fluorescence and Phosphorescenz I. Treatise. Ann Phys 270(7):446–463
2. Vij DR (ed) (1998) Luminescence of solids. Plenum Press, New York, pp 95–132
3. Marfunin AS (1979) Spectroscopy, luminescence and radiation centers in minerals (trans: Schiffer VV). Springer, New York, pp 146–188
4. van Eijk CWE (1994) Cross-luminescence. In: International conference on luminescence, pp 936–941
5. Rack PD, Naman A, Holloway PH, Sun SS, Tuenge RT (1996) Materials used in electroluminescent displays. MRS Bull 21(3):49–58
6. Kim JY, Park SH, Jeong T, Bae MJ, Song S, Lee J, Han IT, Jung D, Yu S (2010) Paper as a substrate for inorganic powder electroluminescence devices. IEEE Trans Electron Devices 57(6):1470–1474
7. Kim MJ, Shin DW, Young KJ, Park SH, Han IT, Yoo JB (2009) The production of a flexible electroluminescent device on polyethylene terephthalate films using transparent conducting carbon nanotube electrode. Carbon 47(15):3461–3465
8. Hirata GA, Mckittrick J, Borja MA, Siqueiros M, Devlin D (1997) Physical properties of Y_2O_3:Eu luminescent films grown by MOCVD and laser ablation. Appl Surf Sci 113:509–514
9. Destriau G (1936) Recherches Sur Les Scintillations De Zinc Aux Rayons. J Chim Phys 33:587–625
10. Alt PM (1984) Thin-film electroluminescent displays: device characteristics and performance. Proc SID 25(2):123–145
11. Ono YA (1995) Electroluminescent displays. World Scientific Publishing Co., Singapore, pp 63–67

12. Keir PD (1999) Fabrication and characterisation of ACTFEL devices. Ph.D. thesis, Oregon State University
13. Minami T, Miyata T, Takata S, Fukuda I (1991) High-luminance green Zn_2SiO_4:Mn thin-film electroluminescent devices using an insulating $BaTiO_3$ ceramic sheet. Jpn J Appl Phys 30(1B):L117–L119
14. Ouyang X, Kitai AH, Xiao T (1996) Electroluminescence of the oxide thin film phosphors Zn_2SiO_4 and Y_2SiO_5. J Appl Phys 79(6):3229–3234
15. Stuyven G, Visschere PD, Neyts K, Kitai A (2003) Characterization of the electro-optical behavior of Zn2Si0.5Ge0.5O4:Mn thin-film electroluminescent devices. J Appl Phys 93(8):4622–4627
16. Bender JP, Wager JF, Kissick J, Clark BL, Keszler DA (2002) Zn_2GeO_4:Mn alternating-current thin-film electroluminescent devices. J Lumin 99(4):311–324
17. Lou Z, Hao J (2005) Cathodoluminescent characteristics of green-emitting $ZnAl_2O_4$:Mn thin-film phosphors. Appl Phys A 80(1):151–154
18. Lou Z, Hao J (2005) Cathodoluminescent characteristics of green-emitting $ZnAl_2O_4$:Mn thin-film phosphors. Appl Phys A Mater Sci Process 80(1):151–154
19. Xiao L, He M, Tian Y, Chen Y, Karak T, Zhang L, Wang N (2007) Structure and luminescence properties of new green-emitting phosphor $BaAl_{12}O_{19}$:Tb. Jpn J Appl Phys 46(9A):5871–5873
20. Kim KN, Jung HK, Park HD, Kim D (2002) High luminance of new green emitting phosphor, Mg_2SnO_4:Mn. J Lumin 99(3):169–173
21. Jiang YD, Zhang F, Summers CJ, Wang ZL (1999) Synthesis and properties of Sr_2CeO_4 blue emission powder phosphor for field emission displays. Appl Phys Lett 74(12):1677–1679
22. Itoh S, Toki H, Tamura K, Kataoka F (1999) A new red-emitting phosphor, $SrTiO_3:Pr^{3+}$, for low-voltage electron excitation. Jpn J Appl Phys 38(11):6387–6391
23. Wellenius P, Suresh A, Muth JF (2008) Bright, low voltage europium doped gallium oxide thin film electroluminescent devices. Appl Phys Lett 92(2):021111–021113
24. Minami T, Kobayashi Y, Shirai T, Miyata T, Suzuki S (2002) High-luminance thin film electroluminescent devices using monoclinic Y_2O_3 phosphor activated with Mn. Jpn J Appl Phys 41(4B):L478–L480
25. Minami T, Kobayashi Y, Miyata T, Suzuki S (2002) High-luminance thin-film electroluminescent devices using $((Y_2O_3)0.6\text{-}GeO_2)0.4$:Mm phosphors. Jpn J Appl Phys 41(5B):L577–L579
26. Itoh S, Toki H, Sato Y, Morimoto K, Kishino T (1991) The $ZnGa_2O_4$ phosphor for low voltage blue cathodoluminescence. J Electrochem Soc 138(5):1509–1512
27. Sickafus KE, Wills JM, Grimes NW (1999) Structure of spinel. J Am Chem Soc 82(12):3279–3292
28. Omata T, Ueda N, Ueda K, Kawazoe H (1994) New ultraviolet-transport electroconductive oxide, $ZnGa_2O_4$ spinel. Appl Phys Lett 64(9):1077–1078
29. Yu CF, Lin P (1996) Manganese-activated luminescence in $ZnGa_2O_4$. J Appl Phys 79(9):7191–7197
30. Uheda K, Maruyama T, Takizawa H, Endo T (1997) Synthesis and long-period phosphorescence of $ZnGa_2O_4:Mn^{2+}$ spinel. J Alloys Compd 262–263:60–64
31. Phani AR, Santucci S, Nardo SD, Lozzi L, Passacantando M, Picozzi P (1998) Preparation and characterization of bulk $ZnGa_2O_4$. J Mat Sci 33(15):3969–3973
32. Choi SK, Moon HS, Mho SI, Kim TW, Park HL (1998) Tunable color emission in a $Zn_{1-x}Cd_xGa_2O_4$ phosphor and solid solubility of $CdGa_2O_4$ in $ZnGa_2O_4$. Mat Res Bull 33(5):693–696
33. Jeong IK, Park HL, Mho SI (1998) Two self-activated optical centers of blue emission in zinc gallate. Solid State Commun 105(3):179–183
34. Safeera TA, Johns N, Mini Krishna K, Sreenivasan PV, Reshmi R, Anila EI (2016) Zinc gallate and its starting materials in solid state reaction route—a comparative study. Mater Chem Phys 181:21–25
35. Vasile M, Vlazan P, Avram NM (2010) Characterization and optical properties of $ZnGa_2O_4:Eu^{3+}$ nanophosphor grown by hydrothermal method. J Alloys Compd 500(2):185–189

36. Liu L, Huang J, Cao L, Jianpeng W, Fei J, Ouyang H, Yao C (2013) Influence of temperature on the morphology and photocatalytic activity of $ZnGa_2O_4$ crystallites prepared by hydrothermal method. Ceram Int 39(3):3165–3171
37. Mingjia L, Ouyan X, Songping W, Ge R, Rui X (2016) A facile hydrothermal route to self-assembled $ZnGa_2O_4$ particles and their microwave application. Appl Surf Sci 364:775–782
38. Zhang Y, Zhijian W, Geng D, Kang X, Shang M, Li X, Lian H, Cheng Z, Lin J (2018) Full color emission in $ZnGa_2O_4$:simultaneous control of the spherical morphology, luminescent and electric properties via hydrothermal approach. Adv Funct Mater 24(42):6581–6593
39. Sun M, Li D, Zhang W, Chen Z, Huang H, Li W, He Y, Xianzhi F (2012) Rapid microwave hydrothermal synthesis of $ZnGa_2O_4$ with high photocatalytic activity toward aromatic compounds in air and dyes in liquid water. J Solid State Chem 190:135–142
40. Yuan Y, Huang J, Weixia T, Huang S (2014) Synthesis of uniform $ZnGa_2O_4$ nanoparticles with high photocatalytic activity. J Alloys Compd 616:461–467
41. Hussen MK, Dejene FB (2018) Influence of annealing temperature on material properties of red emitting $ZnGa_2O_4$:Cr^{3+} nanostructures. J Sol-Gel Sci Technol 88(2):454–464
42. Duan X, Liu J, Yuanchun W, Fapeng Yu, Wang X (2014) Structure and luminescent properties of Co^{2+}/Cr^{3+} co-doped $ZnGa_2O_4$ nanoparticles. J Lumin 153:361–368
43. Park JH, Park BW, Choi NS, Jeong YT, Kim JS, Yang JS (2008) Enhancement in cathodoluminescent properties of carbon nanotube-$ZnGa_2O_4$:Mn^{2+} phosphor composites. Electrochem Solid-State Lett 11(2):J12–J14
44. Kim JS, Kim JS, Kim TW, Kim SM, Park HL (2005) Correlation between the crystalline environment and optical property of Mn^{2+} ions in $ZnGa_2O_4$:Mn^{2+} phosphor. Appl Phys Lett 86(9):091912–091914
45. Shea LE, Datta RK, Brown JJ Jr (1994) Low voltage cathodoluminescence of Mn^{2+}-activated $ZnGa_2O_4$. J Electrochem Soc 141(8):2198–2200
46. Yu M, Lin J, Zhou YH, Wang SB (2002) Citrate-gel synthesis and luminescent properties of $ZnGa_2O_4$ doped with Mn^{2+} and Eu^{3+}. Mater Lett 56(6):1007–1013
47. Tran TK, Park W, Tomm JW, Wagner BK, Jacobsen SM, Summers CJ, Yocom PN, McClelland SK (1995) Photoluminescence properties of $ZnGa_2O_4$:Mn powder phosphors. J Appl Phys 78(9):5691–5695
48. Poort SHM, Cetin D, Meijerink A, Blasse G (1997) The luminescence of Mn^{2+}-activated $ZnGa_2O_4$. J Electrochem Soc 144(6):2179–2183
49. Lee YE, Norton DP, Budai JD (1999) Enhanced photoluminescence in epitaxial $ZnGa_2O_4$:Mn thin-film phosphors using pulsed-laser deposition. Appl Phys Lett 74(21):3155–3157
50. Lee YE, Norton DP, Park C, Rouleau CM (2001) Blue photoluminescence in $ZnGa_2O_4$ Thin-film phosphors. J Appl Phys 89(3):1653–1656
51. Yi SS, Kim IW, Bae JS, Moon BK, Kim SB, Jeong JH (2002) Luminescence characteristics of $ZnGa_2O_4$ thin film phosphors grown by pulsed laser deposition. Mater Lett 57(4):904–909
52. Lee YE, Norton DP, Budai JD, Rack PD, Peterson J, Potter MD (2002) Photo- and low-voltage cathodoluminescence in lithium zinc gallate blue and green thin-film phosphors. J Appl Phys 91(5):2974–2977
53. Jeong JH, Moon BK, Seo HJ, Bae JS, Yi SS, Kim W, Park HL (2003) Enhanced green emission in $ZnGa_2O_4$:Mn thin film phosphors by Se doping. Appl Phys Lett 83(7):1346–1348
54. Bae JS, Moon BK, Choi BC, Jeong JH, Yi SS, Kim W, Lee JS (2003) Photoluminescence behaviors in $ZnGa_2O_4$ thin film phosphors deposited by a pulsed laser ablation. Thin Solid Films 424(2):291–295
55. Yi SS, Bae JS, Moon BK, Jeong JH, Kim IW, Park HL (2003) Photoluminescence behavior of pulsed laser deposited $ZnGa_2O_4$ thin-film phosphors grown on various substrates. Appl Phys A 76(3):433–437
56. Jeong JH, Bae JS, Choi BC, Yi SS, Holloway PH (2004) Luminescent characteristics of Se-doped $ZnGa_2O_4$:Mn thin film phosphors grown by pulsed laser ablation. J Vac Sci Technol A 22(4):1751–1756
57. Bae JS, Shim KS, Moon BK, Choi BC, Jeong JH, Yi SS, Kim JH (2005) Photoluminescence characteristics of $ZnGa_2O_{4-x}M_x$:Mn^{2+} (M = S, Se) thin film phosphors grown by pulsed laser ablation. Thin Solid Films 479(1–2):238–244

58. Mini Krishna K, Nisha M, Reshmi R, Manoj R, Asha AS, Jayaraj MK (2005) Electrical and optical properties of $ZnGa_2O_4$ thin films deposited by pulsed laser deposition. Mater Forum 29:243–247
59. Reshmi R, Mini Krishna K, Manoj R, Jayaraj MK (2005) Pulsed laser deposition of $ZnGa_2O_4$ phosphor films. Surf Coat Tech 198(1–3):345–349
60. Ahmad Md I, Kottaisami M, Rama N, Rao MSR, Bhattacharya SS (2006) Thin film luminescence of $ZnGa_2O_4$:Mn deposited by PLD. Scripta Mater 54(2):237–240
61. Hseih IJ, Feng MS, Kuo KT, Lin P (1994) Growth of $ZnGa_2O_4$ phosphor by radio frequency magnetron sputtering. J Electrochem Soc 141(6):1617–1621
62. Chung SM, Kim YJ (2004) Effects of substrates and heat treatment on growing behavior and luminescent characteristics of $ZnGa_2O_4$ thin film. J Vac Sci Technol A 22(1):140–145
63. Bondar V (2000) Structure and luminescence properties of individual and multi-layer thin-film systems based on oxide phosphors. Mater Sci Engg B 69–70:505–509
64. Kim YJ, Jeong YH, Kim KD, Kang SG, Lee KG, Han JI, Park YK, Cho KI (1998) Growth and luminescent characteristics of $ZnGa_2O_4$ thin film phosphor prepared by radio frequency magnetron sputtering. J Vac Sci Technol B 16(3):1239–1243
65. Yang SH, Hsueh TJ, Chang SJ (2005) Cathodoluminescence of a white $ZnGa_2O_4$/ZnO phosphor screen. J Electrochem Soc 152(11):H191–H195
66. Yang SH, Lu CY, Chang SJ (2007) Luminescence enhancement mechanism of $ZnGa_2O_4$ phosphor screen with an In_2O_3 buffer layer. J Electrochem Soc 154(8):J229–J233
67. Kim JH, Holloway PH (2004) Enhancement of cathodoluminescence of $ZnGa_2O_4$:Mn thin-film phosphor by energetic particle bombardment. Appl Phys Lett 84(12):2070–2072
68. Kim JH, Holloway PH (2006) Microstructural differences in thin film $ZnGa_2O_4$:Mn phosphor produced by differences in sputtering gas pressure. J Vac Sci Technol A 24(6):2164–2171
69. Kim YJ, Chung SM, Jeong YH, Lee YE (2001) Effects of ZnO buffer layer on the luminous properties of thin-film phosphors deposited on ZnO/ITO/glass substrates. J Vac Sci Technol A 19(4):1095–1098
70. Chung SM, Han SH, Kim YJ (2005) Characterization of compositional variation and luminescence of $ZnGa_2O_4$:Mn thin film phosphor. Mater Lett 59(7):786–789
71. Park JH, Lee SH, Kim JS, Park HW, Choi JC, Park HL, Kim GC, Yoo JH (2007) Microstructure-dependent luminescent properties of thin-film $ZnGa_2O_4$:Mn^{2+} phosphors. J Cryst Growth 299(2):369–373
72. Choi HW, Hong BJ, Lee SK, Kim KH, Park YS (2007) Cathode luminescence characteristics of $ZnGa_2O_4$ phosphor thin films with the doped activator. J Lumin 126(2):359–364
73. Yan Z, Koike M, Takei H (1996) Preparation of spinel $ZnGa_2O_4$ films on MgO substrates by the solvent evaporation epitaxy method. J Crys Growth 165(1–2):183–186
74. Yang SH (2003) Electrophoretic prepared $ZnGa_2O_4$ phosphor film for FED. J Electrochem Soc 150(10):H250–H253
75. Sei T, Nomura Y, Tsuchiya T (1997) Preparation of $ZnGa_2O_4$ thin film by sol-gel process and effect of reduction on its electric conductivity. J Non-Cryst Solids 218:135–138
76. Minami T, Takata S, Kuroi Y, Maeno T (1996) New high-luminance thin-film electroluminescent devices using $ZnGa_2O_4$ phosphor emitting layers. J Soc Inf Disp 4(2):53–58
77. Minami T, Kuroi Y, Miyata T, Yamada H, Takata S (1997) $ZnGa_2O_4$ as host material for multicolor-emitting phosphor layer of electroluminescent devices. J Lumin 72–74:997–998
78. Minami T, Maeno T, Kuroi Y, Takata S (1995) High-luminance green-emitting thin-film electroluminescent devices using $ZnGa_2O_4$:Mn phosphor. Jpn J Appl Phys 34(6A):L684–L687
79. Minami T, Toda H, Miyata T (2001) Oxide phosphor thin-film electroluminescent devices fabricated by magnetron sputtering with rapid thermal annealing. J Vac Sci Technol A 19(4):1742–1746
80. Minami T, Miyata T, Sakagami Y (1998) TFEL devices using oxide thin films without vacuum process. Surf Coat Technol 108–109:594–598
81. Minami T, Kuroi Y, Takata S (1996) Preparation of $ZnGa_2O_4$:Mn phosphor thin films as emitting layers for electroluminescent devices. J Vac Sci Technol A 14(3):1736–1740

82. Flynn M, Kitai AH (2001) $ZnGa_2O_4$:Mn phosphors for thin-film electroluminescent displays exhibiting improved brightness. J Electrochem Soc 148(10):H149–H153
83. Kim JS, Lee SG, Park HL, Park JY, Han SD (2004) Optical and electrical properties of $ZnGa_2O_4/Mn^{2+}$ powder electroluminescent device. Mater Lett 58(7–8):1354–1357
84. Qiao B, Tang ZL, Zhang ZT, Chen L (2007) Study on $ZnGa_2O_4:Cr^{3+}$ a.c. powder electroluminescent device. Mater Lett 61(2):401–404
85. Liu Z, Jing X, Wang L (2007) Luminescence of native defects in Zn_2GeO_4. J Electrochem Soc 154(6):H500–H506
86. Bondar V, Popovich S, Felter T, Wager JF (2001) Low-temperature technology and physical processes in green thin-film phosphor Zn_2GeO_4:Mn. Mater Res Symp Proc 667:G761–G766
87. Lewis JS, Holloway PH (2000) Sputter deposition and electroluminescence of Zn_2GeO_4:Mn. J Electrochem Soc 147(8):3148–3150
88. Miyata T, Mochizuki Y, Minami T (2005) High-luminance EL devices using $Zn_2Si_{1-X}Ge_XO_4$:Mn thin films prepared by combinatorial deposition by r.f. magnetron sputtering with subdivided powder targets. IEICE Trans Electron E88-C(11):2065–2069
89. Williams LC, Norton DP, Budai J, Holloway PH (2004) Cathodoluminescence from thin film Zn_2GeO_4:Mn phosphor grown by pulsed laser deposition. J Electrochem Soc 151(8):H188–H191
90. Baker CC, Heikenfeld J, Steckl AJ (2002) Photoluminescent and electroluminescent $Zn_2Si_{0.5}Ge_{0.5}O_4$:Mn thin films for integrated optic devices. IEEE J Sel Top Quantum Elec 8(6):1420–1426
91. Ozawa L, Itoh M (2003) Cathode ray tube phosphors. Chem Rev 103(10):3835–3856
92. Cho KG, Kumar D, Jones SL, Lee DG, Holloway PH, Singh RK (1998) Growth and characterization of Eu:Y_2O_3 thin-film phosphors on silicon and diamond-coated silicon substrates. J Electrochem Soc 145(10):3456–3462
93. Konrad A, Herr U, Tidecks R, Kummer F, Samwer K (2001) Luminescence of bulk and nanocrystalline cubic yttria. J Appl Phys 90(7):3516–3523
94. Jones SL, Kumar D, Singh RK, Holloway PH (1997) Luminescence of pulsed laser deposited Eu doped yttrium oxide films. Appl Phys Lett 71(3):404–406
95. Parsapour F, Kelley DF, Williams RS (1998) Spectroscopy of Eu^{3+}-doped PtS_2 nanoclusters. J Phys Chem B 102(41):7971–7977
96. Buchanan RA, Wickersheim KA, Weaver JL, Anderson EE (1968) Cathodoluminescent properties of the rare earths in yttrium oxide. J Appl Phys 39(9):4342–4347
97. Shin SH, Kang JH, Jeon DY, Choi SH, Lee SH, You YC, Zang DS (2005) Cathodoluminescence change of Y_2O_3:Eu phosphors by incorporation of Zn ions. Solid State Commun 135(1–2):30–33
98. Shin SH, Kang JH, Jeon DY, Zang DS (2005) Enhancement of cathodoluminescence intensities of Y_2O_3:Eu and Gd_2O_3:Eu phosphors by incorporation of Li ions. J Lumin 114(3–4):275–280
99. Jung MK, Park WJ, Yoon DH (2007) Photoluminescence characteristics of red phosphor Eu^{3+}, Sm^{3+} Co-doped Y_2O_3 for white light emitting diodes. Sensor Actuat B-Chem 126(1):328–331
100. Chang NC (1963) Fluorescence and stimulated emission from trivalent europium in yttrium oxide. J Appl Phys 34(12):3500–3504
101. Nazarov MV, Kang JH, Jeon DY, Popovici E-J, Muresan L, Tsukerblat BS (2005) Lattice parameter and luminescence properties of europium activated yttrium oxide. Solid State Commun 133(3):183–186
102. Sakuma S, Kominami H, Neo Y, Aoki T, Nakanishi Y, Mimura H (2005) Effect of La and Zn addition on Y_2O_3:Eu phosphors. Appl Surf Sci 244(1–4):458–460
103. Popovici EJ, Muresan L, Amalia H, Indrea E, Vasilecu M (2007) Synthesis and characterisation of europium activated yttrium oxide fine powders. J Alloys Compd 434–435:809–812
104. Rakov N, Lozano W, Maciel GS, de Araujo CB (2006) Nonlinear luminescence in Eu^{3+}-doped Y_2O_3 powders pumped at 355 nm. Chem Phys Lett 428(1–3):134–137
105. Kottaisamy M, Jeyakumar D, Jagannathan R, Mohan Rao M (1996) Yttrium oxide: Eu^{3+} red phosphor by self-propagating high temperature synthesis. Mat Res Bull 31(8):1013–1020

106. Kang YC, Roh HS, Park SB (2000) Preparation of Y_2O_3:Eu phosphor particles of filled morphology at high precursor concentrations by spray pyrolysis. Adv Mater 12(6):451–453
107. Hao J, Studenikin SA, Cocivera M (2001) Blue, green and red cathodoluminescence of Y_2O_3 phosphor films prepared by spray pyrolysis. J Lumin 93(4):313–319
108. Lee YK, Oh JR, Do YR (2007) Enhanced extraction efficiency of Y_2O_3:Eu^{3+} thin-film phosphors coated with hexagonally close-packed polystyrene nanosphere monolayers. Appl Phys Lett 91(4):041907
109. Cho JY, Huh YD, Park CR, Do YR (2007) The effect of annealing temperature on the CL properties of sol-gel derived Y_2O_3:Re (Re = Eu^{3+}, Tb^{3+}, Tm^{3+}) phosphors. J Electrochem Soc 154(9):J272–J277
110. Cho JY, Ko KY, Do YR (2007) Optical properties of sol-gel derived Y_2O_3:Eu^{3+} thin-film phosphors for display applications. Thin Solid Films 515(7–8):3373–3379
111. McKittric J, Bacalski CF, Hirata GA, Hubbard KM, Pattillo SG, Salazar KV, Trkula M (2000) Characterization of photoluminescent $(Y_{1-x}Eu_x)_2O_3$ thin films prepared by metallorganic chemical vapor deposition. J Am Ceram Soc 83(5):1241–1246
112. Jankowski AF, Schrawyer LR, Hayes JP (1993) Sputter deposition of yttrium-oxides. J Vac Sci Technol A 11(4):1548–1552
113. Evangelou EK, Wiemer C, Faniculli M, Sethu M, Cranton W (2003) Electrical and structural characteristics of yttrium oxide films deposited by rf-magnetron sputtering on n-Si. J Appl Phys 94(1):318–325
114. Ko KY, Lee YK, Do YR, Huh YD (2007) Structural effect of a two-dimensional SiO_2 photonic crystal layer on extraction efficiency in sputter-deposited Y_2O_3:Eu^{3+} thin-phosphors. J Appl Phys 102(1):013509
115. Zang DS, Ko KY, Park HK, Yoon DH, Do YR (2008) A study of the factors influencing the brightness of the photoluminescence of sputter-deposited Y_2O_3:Eu^{3+} film phosphors. J Electrochem Soc 155(5):J111–J116
116. Travlos A, Boukos N, Apostolopoulos G, Dimoulas A (2003) Oxygen vacancy ordering in epitaxial layers of yttrium oxide on Si (001). Appl Phys Lett 82(23):4053–4055
117. Korzenski MB, Lecoeur P, Mercey B, Chippaux D, Raveau B, Desfeux R (2000) PLD-grown Y_2O_3 thin films from Y metal: an advantageous alternative to films deposited from yttria. Chem Mater 12(10):3139–3150
118. Cho KG, Kumar D, Holloway PH, Singh RK (1998) Luminescence behavior of pulsed laser deposited Eu:Y_2O_3 thin films phosphors on sapphire substrates. Appl Phys Lett 73(21):3058–3060
119. Zhang S, Xiao R (1998) Yttrium oxide films prepared by pulsed laser deposition. J Appl Phys 83(7):3842–3848
120. Kumar D, Cho KG, Chen Z, Craciun V, Holloway PH, Singh RK (1999) Cathodoluminescent properties of pulsed-laser-deposited Eu-activated Y_2O_3 epitaxial films. Phys Rev B 60(19):13331–13334
121. Gao HJ, Kumar D, Cho KG, Holloway PH, Singh RK, Fan XD, Yan Y, Pennycook SJ (1999) Epitaxial growth of Y_2O_3:Eu thin films on $LaAlO_3$. Appl Phys Lett 75(15):2223–2225
122. Hones SL, Kumar D, Cho KG, Singh R, Holloway PH (1999) Pulsed laser deposition of Y_2O_3:Eu thin film phosphors. Displays 19(4):151–167
123. Craciun V, Howard J, Lambers ES, Singh RK, Craciun D, Perriere J (1999) Low-temperature growth of Y_2O_3 thin films by ultraviolet-assisted pulsed laser deposition. Appl Phys A 69(1):S535–S538
124. Kumar D, Sankar J, Cho KG, Craciun V, Singh RK (2000) Enhancement of cathodoluminescent and properties of Eu:Y_2O_3 luminescent films by vacuum cooling. Appl Phys Lett 77(16):2518–2520
125. Moll OPY, Perriere J, Millon E, Defourneau RM, Fourneau D, Vincent B, Essahloui A, Boudrioua A, Seiler W (2002) Structural and optical properties of rare-earth-doped Y_2O_3 waveguides grown by pulsed laser deposition. J Appl Phys 92(9):4885–4890
126. Bae JS, Jeong JH, Yi SS, Park JC (2003) Improved photoluminescence of pulsed-laser-ablated Y_2O_3:Eu^{3+} thin-film phosphors by Gd substitution. Appl Phys Lett 82(21):3629–3631

127. Bar S, Huber G, Gonzalo J, Perea A, Munz M (2005) Pulsed laser deposition of Eu:Y_2O_3 thin films on (0001) α-Al_2O_3. Appl Phys A 80(2):209–216
128. Yang SH, Hsueh TJ, Chang SJ (2006) Effect of ZnO buffer layer on the cathodoluminescence of $ZnGa_2O_4$:Mn/ZnO phosphor screen for FED. J. Crys. Growth 287(1):194–198
129. Yi SS, Shim KS, Yang HK, Moon BK, Choi BC, Jeong JH, Kim JH, Bae JS (2007) Improved cathodoluminescent characteristics of Y_2O_3:Eu^{3+} thin films by Li-doping. Appl Phys A 87(4):667–671
130. Suyama T, Okamoto K, Hamakawa Y (1982) New type of thin-film electroluminescent device having a multilayer structure. Appl Phys Lett 41(5):462–463
131. Minami T, Yamazaki M, Miyata T, Shirai T (2001) Mn activated Y_2O_3–GeO_2 phosphors for thin film electroluminescent devices. Jpn J Appl Phys 40(8B):L864–L866
132. Minami T, Kobayashi Y, Miyata T, Yamazaki M (2003) High-luminance thin-film electroluminescent devices using Y_2O_3:Mn phosphor. Thin Solid Films 443(1–2):91–96
133. Ono YA, Fuyama M, Onisawa K, Tamura K, Ando M (1989) White light emitting thin-film electroluminescent devices with stacked SrS:Ce/CaS: Eu active layers. J Appl Phys 66(11):5564–5571
134. Tanaka S, Yoshiyama H, Nishiura J, Ohshio S, Kawakami H, Kobayashi H (1987) Bright white-light electroluminescence based on nonradiative energy transfer in Ce- and Eu-doped SrS thin films. Appl Phys Lett 51(21):1661–1663
135. Okamoto S, Nakazawa E, Tsuchiya Y (1990) White emitting thin-film electroluminescence devices with SrS phosphor doubly activated with rare-earth ions. Jpn J Appl Phys 29(10):1987–1990
136. Tanaka S, Ohshio S, Nishiura J, Kawakami H, Yoshiyama H, Kobayashi H (1988) Bright white-light electroluminescence in SrS:Pr, K thin films. Appl Phys Lett 52(25):2102–2104
137. Kong W, Fogarty J, Solanki R, Tuenge RT (1995) White light emitting SrS: Pr electroluminescent devices fabricated via atomic layer epitaxy. Appl Phys Lett 66(4):419–421
138. Ruffner JA, Tuenge RT, Sun SS, Grandon PD, Hlava PF (1997) Sputter deposition of ZnS:Mn/SrS: Ce multilayered thin film white phosphor. Thin Solid Films 310(1–2):123–131
139. Lakshmananarasimhan N, Varadaraju UV (2005) White-light generation in Sr_2SiO_4:Eu^{2+}, Ce^{3+} under near-UV excitation. J Electrochem Soc 152(9):H152–H156
140. Lee SH, Park JH, Son SM, Kim JS, Park HL (2006) White-light emitting phosphor: $CaMgSi_2O_6$:Eu^{2+}, Mn^{2+} and its related properties with blending. Appl Phys Lett 89(22):221916
141. Yang WJ, Luo L, Chen TM, Wang NS (2005) Luminescence and energy transfer of Eu- and Mn-coactivated $CaAl_2Si_2O_8$ as a potential phosphor for white-light UVLED. Chem Mater 72(15):3883–3888
142. Yang WJ, Chen TM (2006) White-light generation and energy transfer in $SrZn_2(PO_4)_2$:Eu, Mn phosphor for ultraviolet light emitting diodes. Appl Phys Lett 88(10):101903
143. Liu X, Lin C, Lin J (2007) White-light emission from Eu^{3+} in $CaIn_2O_4$ host lattices. Appl Phys Lett 90(8):081904–081906
144. Liu X, Lin C, Luo Y, Lin J (2007) Host-sensitized luminescence of Dy^{3+}, Pr^{3+}, Tb^{3+} in polycrystalline $SrIn_2O_4$ for field emission displays. J Electrochem Soc 154(1):J21–J27
145. Mini Krishna K, Anoop G, Jayaraj MK (2007) Host-sensitized white luminescence in $ZnGa_2O_4$:Dy^{3+} phosphor. J Electrochem Soc 154(10):J310–J313
146. Mini Krishna K, Anoop G, Jayaraj MK (2007) The effect of substrate temperature on structural and luminescent characteristics of RF magnetron sputtered $ZnGa_2O_4$:Dy^{3+} thin films. J Electrochem Soc 154(11):J379–J382
147. Mini Krishna K, Anoop G, Jayaraj MK (2012) Electroluminescent characteristics of $ZnGa_2O_4$:Dy^{3+} thin film devices fabricated on glass substrates. Phys Status Solidi A 209(12):2641–2645
148. Anoop G, Mini Krishna K, Jayaraj MK (2008) Influence of dopant source on structural and optical properties of Mn doped $ZnGa_2O_4$ thin films. Appl Phys A 90(4):711–715
149. Anoop G, Mini Krishna K, Jayaraj MK (2011) Characteristics of A.C. electroluminescence in $ZnGa_2O_4$:Mn^{2+} thin film devices. J Electrochem Soc 158(8):J269–J272

150. Anoop G, Mini Krishna K, Rajeev Kumar K, Jayaraj MK (2008) Effect of ZnO buffer layer on the structural and optical properties of Zn_2GeO_4:Mn^{2+} thin films. J Electrochem Soc 155(10):J270–J273
151. Aneesh PM, Mini Krishna K, Jayaraj MK (2009) Hydrothermal synthesis and characterization of undoped and Eu doped $ZnGa_2O_4$ nanoparticles. J Electrochem Soc 156(3):K33–K36
152. Anoop G, Mini Krishna K, Jayaraj MK (2012) Structural and luminescent characteristics of pulsed laser deposited Eu^{3+} doped Y_2O_3 thin films. Philos Mag 92(14):1777–1787
153. McKittrick J, Shea LE, Bacalski CF, Bosze EJ (1999) The influence of processing parameters on luminescent oxides produced by combustion synthesis. Displays 19(4):169–172
154. Rack PD, Potter MD, Kurinec S, Park W, Penczek J, Wagner BK, Summers CJ (1998) Luminescence properties of thin film $Ta_2Zn_3O_8$ and Mn doped $Ta_2Zn_3O_8$. J Appl Phys 84(8):4466–4470
155. Minami T, Shirai T, Nakatani T, Miyata T (2000) Electroluminescent devices with Ga_2O_3:Mn thin-film emitting layer prepared by sol-gel process. Jpn J Appl Phys 39(6A):L524–L526
156. Xu Z, Li Y, Liu Z, Wang D (2005) UV and X-ray excited luminescence of Tb^{3+}-doped $ZnGa_2O_4$ phosphors. J Alloys Compd 391(1–2):202–205
157. Partlow WD, Feldman DW (1973) Trapping effects in the luminescence of Zn_2GeO_4:Mn^{2+}. J Lumin 6(1):11–20
158. Barthou C, Benoit J, Benalloul P, Morell A (1994) Mn^{2+} concentration effect on the optical properties of Zn_2SiO_4:Mn phosphors. J Electrochem Soc 141(2):524–528
159. Jiao H, Liao F, Tian S, Jing X (2003) Luminescent properties of Eu^{3+} and Tb^{3+} activated $Zn_3Ta_2O_8$. J Electrochem Soc 150(9):H220–H224
160. Shimomura Y, Kurushima T, Shigeiwa M, Kijima N (2008) Redshift of green photoluminescence of $Ca_3Sc_2Si_3O_{12}$:Ce_{3+} phosphor by charge compensatory additives. J Electrochem Soc 155(2):J45–J49
161. Shimomura Y, Kurushima T, Kijima N (2007) Photoluminescence and crystal structure of green-emitting phosphor $CaSc_2O_4$:Ce^{3+}. J Electrochem Soc 154:J234–J238
162. Kim JS, Kim JS, Kim TW, Park HL, Kim YG, Chang SK, Han SD (2004) Energy transfer among three luminescent centers in full-color emitting $ZnGa_2O_4$:Mn^{2+}, Cr^{3+} phosphors. Solid State Commun 131(8):493–497
163. Minami T, Miyata T, Shirai T, Nakatani T (2000) Electroluminescent oxide phosphor thin films prepared by a sol-gel process. Mater Res Symp Proc 621:Q431–Q436
164. Naidu SA, Varadaraju UV (2008) Electric dipole red emission in Eu^{3+}-doped low bandgap oxide $LiInO_2$. Electrochem Solid-State Lett 11(5):J40–J42
165. Tang YS, Hu SF, Lin CC, Bagkar NC, Liu RS (2007) Thermally stable luminescence of $KSrPO_4$:Eu^{2+} phosphor for white light uv light-emitting diodes. Appl Phys Lett 90(15):151108
166. Chang CK, Chen TM (2007) White-light generation under violet-blue excitation from tunable green-to-red emitting $Ca_2MgSi_2O_7$:Eu, Mn through energy transfer. Appl Phys Lett 90(16):161901
167. Won YH, Jang HS, Im WB, Jeon DY, Lee JS (2006) Tunable full-color emitting $La_{0.827}Al_{11.9}O_{19.09}$:$Eu^{2+}$, Mn^{2+} phosphor for application to warm white-light emitting diodes. Appl Phys Lett 89(23):231909
168. Hao Z, Zhang J, Zhang X, Sun X, Luo Y, Lu S, Wang XJ (2007) White light emitting diode by using α-$Ca_2P_2O_7$:Eu^{2+}, Mn^{2+} phosphor. Appl Phys Lett 90(26):261113

Chapter 2
Upconversion Nanophosphors: An Overview

Kurias K. Markose, R. Anjana and M. K. Jayaraj

1 Introduction

Luminescent materials have a wide range of potential applications in our day-to-day affair which includes the optical displays we use, biomedical applications, security printings, bioimaging, and many more [1]. Materials which glow in darkness after exposing it to light have been known as phosphors. The *Greek* word *phosphor* means light bearer. In history, there are many reports on glowing phosphors. In 1603, Vincenzo Casciarolo discovered the famous Bologian phosphor (impure barium sulfate, $BaSO_4$) [2]. Even before that, the Japanese had prepared phosphorescent paints from seashells. It is reported that Spanish botanist and physician Nicolas Mondres (the year 1565) had used the blue emission from an infusion of a wood (lignum nephriticum) for treating kidney and urinary diseases. In 1852, Sir George Gabriel Stokes described the term fluorescence (in his book "On the change of refrangibility of light") as the ability of materials like flurospar and uranium glass to convert shorter wavelength UV to long-wavelength visible emission [3], which was doubtlessly state of the art in the history of photoluminescence [1]. In 1888, Eilhard Wiedemann first introduced the term "Luminescence" for both fluorescence and phosphorescence. The word luminescence having *Latin* origin from the word "*lumen*" which means light [4]. In general, luminescence is the spontaneous emission of radiation from an electronically excited species (or from a vibrationally excited species) which is not in thermal equilibrium with its environments. Fluorescence and phosphorescence can be distinguished based on the duration of emission after the end of excitation. Fluorescence almost occurs simultaneously with excitations, and on the other hand, phosphorescence is a slow process. Nevertheless, there are materials which show long-lived fluorescence and materials which show short-lived phosphorescence. Fluorescence

K. K. Markose (✉) · R. Anjana · M. K. Jayaraj
Department of Physics, Cochin University of Science and Technology, Kochi 682022, India
e-mail: kurias.007@gmail.com

M. K. Jayaraj (ed.), *Nanostructured Metal Oxides and Devices*,
Materials Horizons: From Nature to Nanomaterials,
https://doi.org/10.1007/978-981-15-3314-3_2

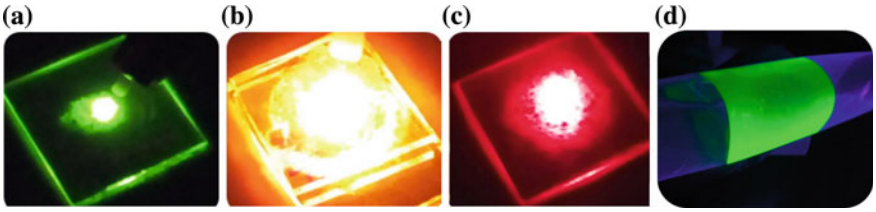

Fig. 1 Images of various **a**–**c** upconversion emissions and **d** luminescence from perovskite material

and phosphorescence can also be defined in terms of the change in the spin multiplicity. The spin multiplicity will not change in the case of fluorescence, whereas in phosphorescence, it changes from triplet to singlet or vice versa. Figure 1(a)-(c) shows the photograph of upconversion emissions when excited with 980 nm laser. Figure 1(d) shows the photograph image of luminescence observed from perovskite material under UV excitation.

For most of the luminescent materials, the energy of the exciting photon is greater than the energy of the emitted photon, and it is known as Stoke's emission. The energy difference between the emitted and excited photon is called Stoke's shift. If the emitted photon has an energy greater than the absorbed photon, it is called anti-Stoke's emission. According to the physical mechanism involved, anti-Stoke's emission can be divided into a single-photon process or multiphoton process. The single-photon process is usually observed in Raman spectroscopy (e.g., silicon crystals [5]), where higher-energy photons are radiated with the aid of phonons from the host matrix. Multiphoton conversion is a process in which light of higher energy (shorter wavelength) is emitted by absorbing low-energy (larger wavelength) light mainly by the sequential absorption of two or more low-energy photons (anti-Stoke's emission). The other two processes, which also gives anti-stokes emission, are simultaneous two-photon absorption (STPA) and second harmonic generation (SHG). Figure 2 shows the schematic diagram of all the three possible anti-Stoke's emission process.

In simultaneous two-photon absorption process, as the name indicates, two low-frequency photons are absorbed to excite the molecule to an excited state. It is a third-order nonlinear process arises from the third-order susceptibility of the material. This phenomenon was originally predicted by Maria Goeppert Mayer [6]. The first experimental confirmation of STPA processes was reported in europium-doped CaF_2 crystal by Kaiser and Garrett [7]. Second-harmonic generation is often shown by hyper polarizable materials [8], where the incident photons are effectively combined by the nonlinear property of the material to create photons with twice the energy of incident one (e.g., KH_2PO_4 crystals). In 1961, Peter Franken, A. E. Hill, C. W. Peters, and G. Weinreich were the first to demonstrate second harmonic generation [9]. Since this process requires high-energy excitation, usually it occurs under laser incidence.

STPA and SHG encompass virtual intermediate states, while in UC, real intermediate states are involved (see Fig. 2). The phenomenon of upconversion comprises of obtaining population in an excited state and consequent emission of a photon, whose

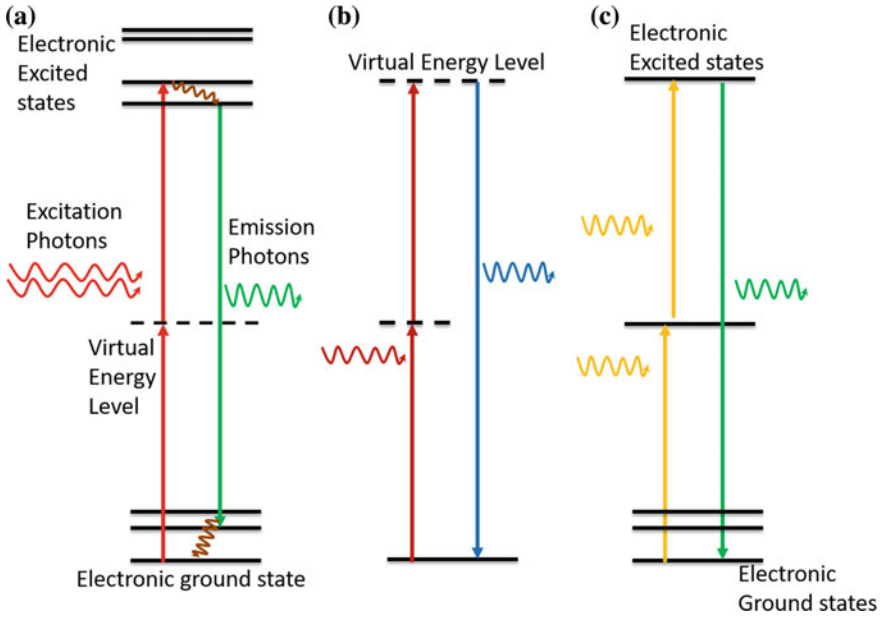

Fig. 2 Anti-Stoke's emission processes: **a** STPA, **b** SHG, and **c** UC

energy is greater than that of the pump excitation photon. UC process often relates to a nonlinear process. The materials, which show upconversion, are generally called as upconversion nanophosphors/nanoparticles (UCNP). The unique optical properties of these UC phosphors open many potential applications, predominantly in novel display technologies [10], lasers [11], solar energy harvesting [12–15], quantum cryptography [16], 3D-data storage [17], and bioimaging [18]. In the initial years of the research, the major focus was on crystalline upconversion materials. Later with the advent of nanotechnology, upconversion nanoparticles have been made, and it has a wide variety of applications in biological science in which biological imaging is the most studied one. As an emerging probe for molecular imaging in vitro and in vivo, upconversion nanophosphors (UCNPs) have many exceptional advantages over conventionally used organic dyes. It has high photostability, narrow bandwidth emission, tunable emission, a long lifetime and high resistance to photobleaching. With the excitation of near-infrared (NIR) light, the emitted light from an UCNP can be tuned from the ultraviolet (UV) to the NIR region, which can be applied for multicolour imaging. Among the various upconverted emissions, imaging using NIR-to-NIR (using NIR excited light and emitting NIR light)-based UCNPs has gained increasing attention, as both the excitation and emission NIR light can penetrate the "optical transmission window" of tissues, thus providing a powerful direct tool for visualizing the biodistribution of UCNPs in vivo.

The utilization of these materials in a solar cell for efficiency enhancement is an influential application for energy harvesting. UCNPs can convert the unabsorbed

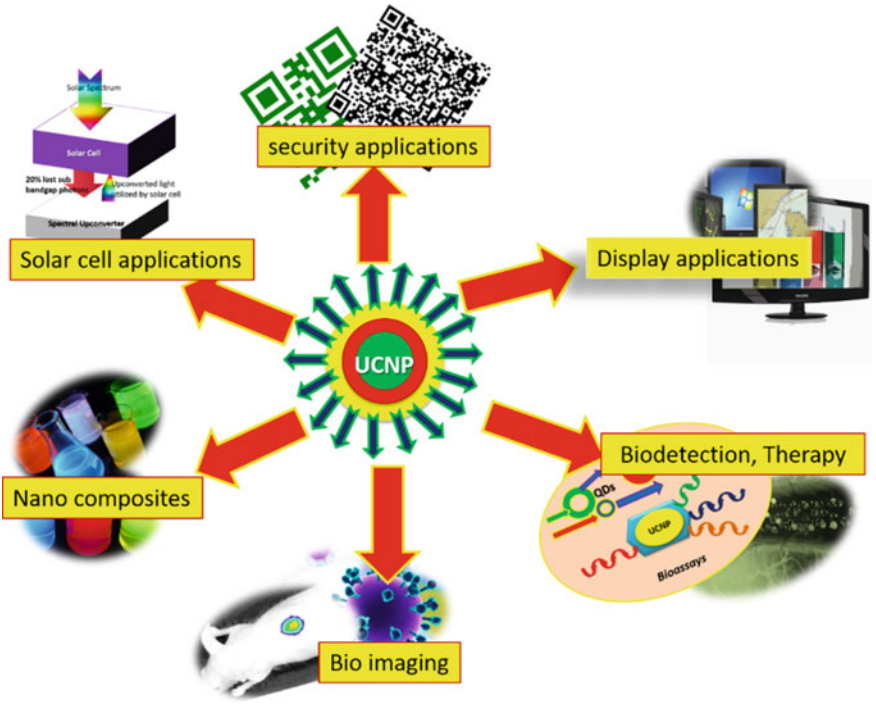

Fig. 3 Schematic diagram showing the applications of upconversion nanoparticles

infrared (IR) radiation by the solar cell to useful light radiation that can be subsequently absorbed by the solar cell [19, 20]. Another promising application of UCNPs is in security printing. Nowadays, enormous research interest in upconversion-based security inks can also be witnessed [21]. The vast and diverse applications of upconversion phosphors ground the remarkable scientific attention that the field has received in recent years. Figure 3 schematically shows the various applications of UC phosphors. This chapter deals with upconversion luminescence, the mechanisms involved in UC, synthesis of upconversion phosphors, and its various applications.

2 Mechanisms Involved in Upconversion Phosphors

The first suggestion of upconversion phenomenon was published by Bloembergen in 1959 while explaining the infrared detectors through sequential absorption of the light photon within the levels of a given ion [22]. This mechanism was later called as excited-state absorption (ESA). In reality, the upconversion process is a complicated one, and several mechanisms are involved. Different upconversion luminescence mechanisms have been recognized either alone or in combination, such

as excited-state absorption (ESA), energy transfer upconversion (ETU), cooperative upconversion, energy migration, cross-relaxation, and photon avalanche (PA) which are discussed below. Not only this, but organic molecules also show upconversion luminescence through triplet-triplet annihilation (TTA) [23] and cooperative energy pooling mechanisms (CEP) [24]. However, details on TTA and CEP are not included in this chapter since they are beyond the scope of this chapter.

2.1 Excited-State Absorption

In the ESA process, the first absorption populates a metastable intermediate reservoir level, and the successive absorption of pump photon fills the emitting level of a single ground-state ion. The diagram (Fig. 4) shows the general ESA process for a three-level system [25]. The ion 1 is excited from the ground state G1 to the intermediate level E1, and a successive pump photon promotes it to the higher energy state E2 before it decays to the lower energy state. The lifetime of the intermediate level should be about microseconds to observe an efficient ESA mechanism [26]. The upconversion emission occurs from the level E2 as shown in Fig. 4.

ESA is commonly observed in transition metal-doped crystals which are normally broadband media. ESA process is found less for rare-earth-doped crystals due to their relatively narrow bandwidth for transitions. In ions like erbium, thulium, holmium, and neodymium with ladder-like energy levels, ESA is more likely to be relevant. $Y_3Al_5O_{12}:Ce^{3+}$, $MgAl_2O_4:Mn^{2+}$, and $CaWO_4$ are some examples of materials showing ESA [27–30]. In these materials, laser action is completely quenched by excited-state absorption. The efficiency in an ESA process is independent of the dopant concentration due to its single-ion characteristics.

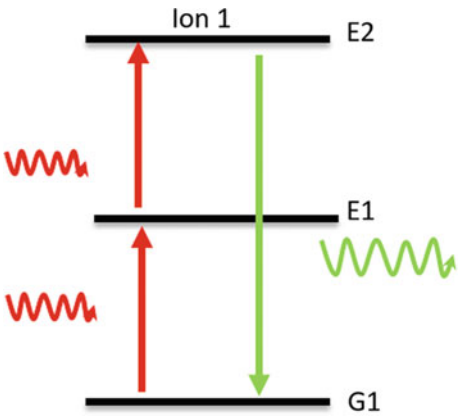

Fig. 4 Excited-state absorption. G1, E1, and E2 represent the ground level, intermediate level, and the excited state, respectively

2.2 Energy Transfer Upconversion

In 1966, Auzel [31] discovered and formulated the energy transfer upconversion (ETU) mechanism.

Energy transfer upconversion (ETU) (also known as *addition de photon par transfertsd'energies*, APTE effect [31]) involves sequential absorption of two photons to populate the metastable reservoir state as in the case of ESA (Fig. 5). The major difference between the two processes is that in ETU, two nearby lanthanide ions are involved while for ESA, it happens within a single lanthanide ion. ETU is the most efficient upconversion process. In this process, ion 1 that is excited first called usually as a sensitizer (S) and the second one, ion 2 is called as an activator (A) to which energy is transferred. In ETU, the sensitizer (S) ion absorbs pump photon and excited to the level E1, and this harvested energy is then transferred to the ground state G1 and the excited state E1 of the activator (A) ion. The electron in the E1 level of activator will excite to its upper emitting level E2. When the activator (A) and sensitizer (S) are near enough, energy can be transferred from S to A. Here, the energy is transferred through Coulombic interaction, and the probability of interaction drops off as R^{-6}, where R is the distance between the ions [31]. It is required that the concentration of ions is sufficient to allow energy migration between ions since it determines the average distance between the dopant ions. ETU mechanism also does not depend on the pump power of the laser.

For example, in $NaYF_4$:Yb^{3+}, Er^{3+} UCNP, red, blue, and green emissions were resulted through this process. The Yb^{3+} ion, with its excited state $^2F_{5/2}$, has an energy comparable to $^4I_{11/2}$ (Er^{3+}), which can act as a sensitizer for Er^{3+} and transfers its energy to Er^{3+} ion in ground state through the energy transfer process: $^2F_{5/2}$ (Yb^{3+}) + $^4I_{15/2}$ (Er^{3+}) → $^2F_{7/2}$ (Yb^{3+}) + $^4I_{11/2}$ (Er^{3+}). Further, cross-relaxation and phonon-assisted process is obtained by the $^4F_{9/2}$ {$^2F_{5/2}$ (Yb^{3+}) + $^4I_{13/2}$ (Er^{3+}) → $^2F_{7/2}$ (Yb^{3+}) + $^4F_{9/2}$ (Er^{3+})} transition resulting in red emission (~654 nm). The blue (~408 nm) and green luminescence emissions (~526 and ~533 nm) are caused by transitions from

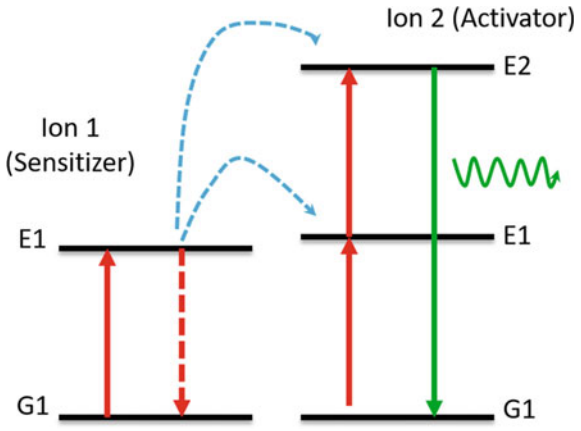

Fig. 5 Energy transfer upconversion (ETU). G1, E1, and E2 represent the ground level, intermediate level, and the excited state, respectively

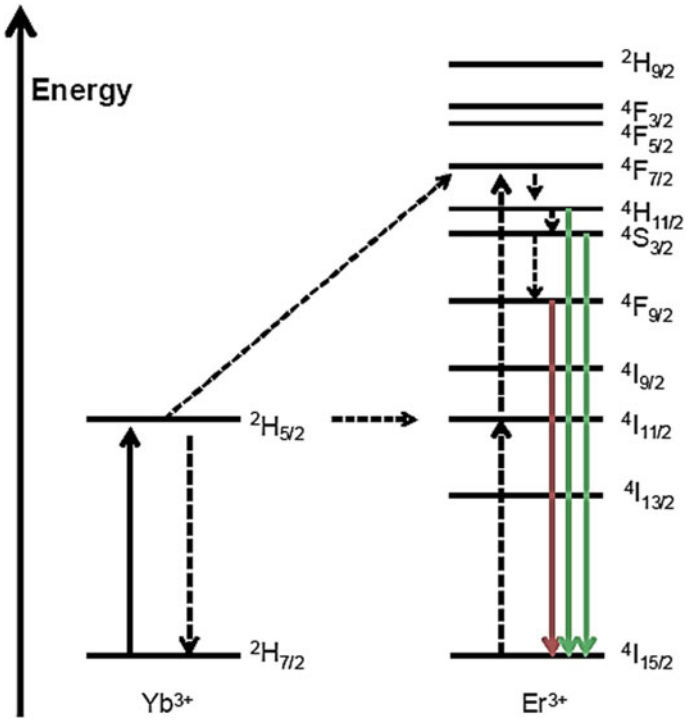

Fig. 6 Energy-level diagram of Er^{3+}/Yb^{3+} co-doped system

$^2H_{9/2}$ to $^4I_{15/2}$ and $^2H_{11/2}$–$^4I_{15/2}$ (also $^4S_{3/2}$–$^4I_{15/2}$) levels in similar ways, respectively. The schematic of the possible energy transitions in Yb^{3+}/Er^{3+} system is shown in Fig. 6.

Most of the efficient UCNPs utilize ion pairs (S/A) of Yb^{3+}/Tm^{3+}, Yb^{3+}/Er^{3+} and Yb^{3+}/Ho^{3+} for enhanced excitation at ~980 nm. Here, Yb^{3+} acts as the sensitizer. It has a sufficiently large absorption cross-section in the near-infrared region (980) nm and the majority of the works have been devoted to developing Yb^{3+}-sensitized UCNPs. In the case of single lanthanide ion-doped UCNPS like $LiYF_4:Er^{3+}$ (excited at 1490 nm) [32] and $NaGdF_4:Ho^{3+}$ (excited at 1200 nm) [33], the single lanthanide ions itself act as the sensitizer also. The sensitizers Nd^{3+}, Ho^{3+}, and Ce^{3+} were used to improve the Tm^{3+} blue emission band, Tm^{3+} NIR emission band, and Ho^{3+} red emission band, respectively [34–37].

2.3 Cooperative Sensitization Upconversion

Cooperative sensitization upconversion (CSU) involves interactions either between two ions or between a pair of ions and a third one, as shown in Fig. 7 [31]. Some

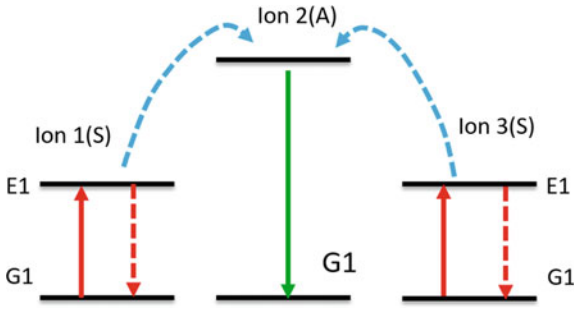

Fig. 7 Cooperative sensitization upconversion

of the theoretical predictions of upconversion by energy transfers and cooperative upconversion are analogous to each other. When a photon of sufficient pump power incident on ions 1 and 3, they will be excited to the level E1. Both the ions, ion 1 and ion 3, simultaneously interact with the activator ion 2 and excite it to the higher energy level E1. When the ion 2 undergoes radiative relaxation to the ground state, the upconverted photon is emitted. Even though ETU and CSU have some analogous nature, CSU involves quasi-virtual levels, which can be theoretically described in a higher-order perturbation. Therefore, the efficiency of CSU is of lesser magnitude than that of ESA and ETU process. For Yb^{3+}/Tb^{3+}, Yb^{3+}/Eu^{3+}, and Yb^{3+}/Pr^{3+} ion pairs, CSU mechanism has been reported [38–40]. Figure 8 shows a typical example of CSU mechanism reported in $NaYbF_4$:Tb@CaF nanophosphors [38].

In order to understand the UC mechanism involved in populating the $^5D_4$ and $^5D_3$ states of the Tb^{3+} ions, double log plot of emission intensity versus pump power had plotted (Fig. 8a, b) and the dependence was calculated. According to the equation $I_{UC} = KP^n$, the UC emission intensity depends on the power n of the excitation pump power, where n is the number of excited Yb^{3+} ions engaged in the process (see Sect. 3). For the emissions centered at 380, 414, and 435 nm, the n values were calculated as 2.94, 2.92, and 2.95, respectively (Fig. 8a). These "n" values show a cubic dependence of excitation laser power on the emission intensity. That means the transition involves three Yb^{3+} ions. Similarly, for the visible emissions centered at 487, 541, 587, and 622 nm, the n values calculated were 2.34, 2.29, 2.31, and 2.32, respectively. Figure 8c illustrates the CSU mechanism between the Yb/Tb pair. Pumped by a 980 nm excitation, Yb^{3+} ions got excited from ground level $^2F_{7/2}$ to excited level $^2F_{5/2.}$ As shown in Fig. 8c, when a couple of excited Yb^{3+} ions concurrently transmitted the energy to a Tb^{3+} ion at ground state, it was excited to the $^5D_4$ energy level. In addition, some Tb^{3+} in the excited level $^5D_4$ might still accept energy and even pumped to a higher $^5D_1$ energy level. The Tb^{3+} ion then de-excites through non-radiative transition to the $^5D_3$ energy level. Finally, radiative emission from the $^5D_3$ energy level to the $^7F_{J(j\,=\,3,\,4,\,5,\,6)}$ transitions results in various emission as depicted in Fig. 8 [38].

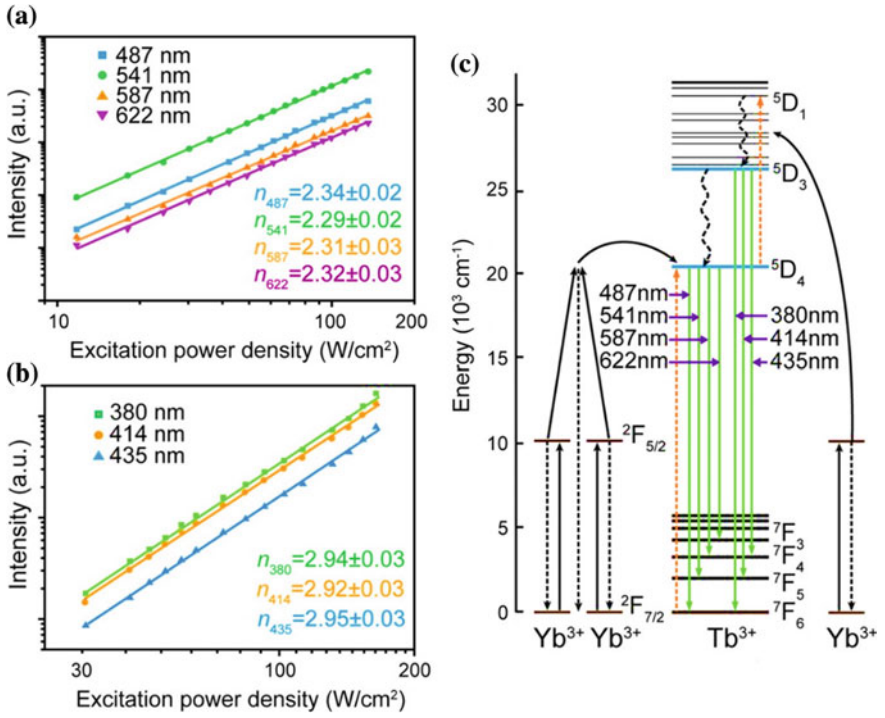

Fig. 8 **a**, **b** Double log plots of CSU emission of Tb-doped $NaYbF_4$ as a function of excitation power. **c** The schematic diagram of the CSU mechanism in $NaYbF_4$:Tb phosphor. Reprinted with permission from [38] Copyright © 2016, American Chemical Society

2.4 Cross-Relaxation

Cross-relation (CR) has more considerable significance since it is regarded as a crucial process in upconversion mechanisms. Since decades ago, people have been investigating the cross-relaxation (CR) phenomenon. It is a special case in which the ion 1 losses its energy by attaining ground level and the energy is transferred to ion 2. Ion 1 and ion 2 can either be of the same species or different. It is a reverse process of energy transfer upconversion. Typically, for upconverting phosphors, energy transfer upconversion is a wanted process while cross-relaxation is considered as a loss process. For both the ETU and CR mechanism, it is not necessary that both the ions should be identical. If the ions are same, cross-relaxation will result in "concentration quenching mechanism" which leads to the quenching of emission intensity (see Fig. 17a). Figure 9 illustrates the cross-relaxation energy transfer between Tm^{3+} ions. Even though the cross-relaxation process is considered as deleterious, researchers have used this CR mechanism to achieve pure red emissions [41]. Thus, by this mechanism of cross-relaxation, one can tune the emission colour by increasing or decreasing the dopant concentration (see Fig. 17d–h).

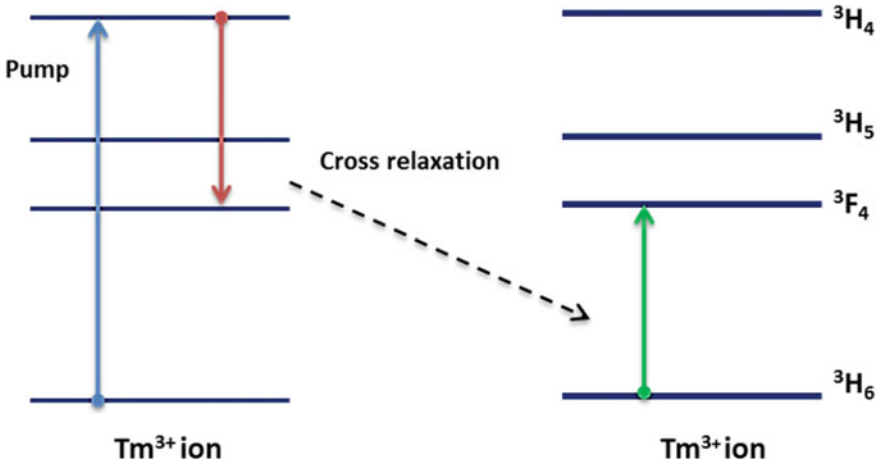

Fig. 9 Schematic of cross-relaxation energy transfer between Tm^{3+}

2.5 Photon Avalanche

Chivian et al. [42] first discovered the photon avalanche (PA) upconversion in Pr^{3+} infrared quantum counters. PA mechanism involves an ESA of the incident photon and CR process. A threshold excitation intensity is required for PA upconversion, above which upconversion luminescence is produced. Below this threshold limit, very small UC luminescence is generated, and the UCL intensity increases with excitation intensity above the threshold limit and therefore least observed UC scheme.

Figure 10 shows the simplest energy transfer scheme for the PA process. Through a non-resonant ground-state absorption (GSA), the energy level E1 of ion 2 gets populated. It should be noted that the pump wavelength is only resonant between the metastable state E1 and higher energy level E2. Then, excitation of ion 2 from E1 level to the emitting energy level (E2) occurs with ESA process. An active CR process follows between ion 1 and ion 2, which makes two ions (ion1 and ion 2) in the E1 state, as shown in Fig. 10. That is, two ion at E1 state can act as senzitizer ions and produce another four ions through this circle mechanism and the four ions will result in another eight ions. Continuing like this, the population at E1 level increases (avalanche effect) and hence the UC emission from E2. Therefore, PA process takes a long time and has a threshold intensity limit.

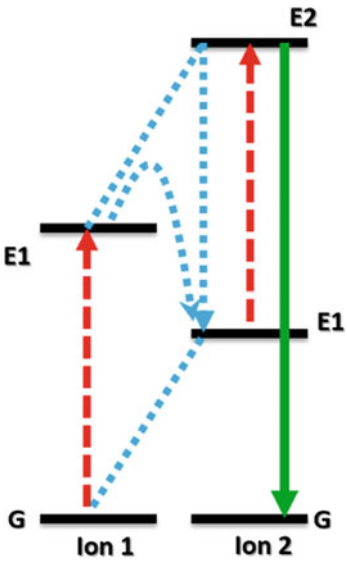

Fig. 10 Photon avalanche upconversion

2.6 *Energy Migration Upconversion*

Energy migration upconversion (EMU) is a complex process mainly observed in core-shell structures. Four ion kinds, known as a sensitizer (ion-1), accumulator (ion-2), migrator (ion-3), and activator (ion-4), are involved in this process. Figure 11

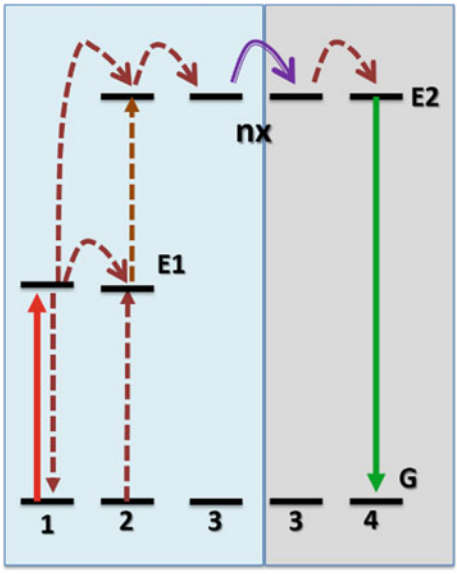

Fig. 11 EMU upconversion mechanism observed in core–shell structures (core–shell regions are shown in different colors. The "*nx*" indicates random hopping through many type-3 ions). Adapted with permission from [43], Copyright @ 2011, Springer Nature

shows the schematic of EMU mechanism. The sensitizer ion 1 gets excited when the incident photon is absorbed, and the energy is transferred to the accumulator, ion 2. Subsequently, the migrator ion 3 receives the energy from the accumulator. The excitation energy then migrates through the sublattice of migrator ion via core–shell interfaces. Finally, the activator ion 4 captures the energy that migrates and emits the upconverted radiation (see Fig. 11). Wang et al. [43] reported tunable UC emissions in $NaGdF_4:Tm^{3+}$, $Yb^{3+}/NaGdF_4:Ln^{3+}$ core–shell nanoparticles, through the energy migration via the sublattice of gadolinium for a vast range of lanthanide ions (Tb, Eu, Dy, or Sm). In their work, the sensitizer ion, activator ion, and the migrator ion were spatially confined in different layers of the core-shell structure in order to tune the energy exchange between the accumulator and the activator. This also helped to eliminate the cross-relaxation process. Besides, to bridge the energy transfer from the accumulator to activator ions, arrays of migrator ions were distributed throughout the core-shell interface. Through this, they were able to manipulate the energy transfer in UCNPs.

3 The Category of the Upconversion Materials

Upconversion phosphors mainly consist of an inorganic host material (host matrix) and emission centers, which are doped intentionally or not. Generally, the concentration of dopants should be small since more concentration will result in the quenching of luminescence emission. One can obtain new UC luminescence materials by either (a) by choosing new host materials or (b) by varying the doping concentration of the dopant ions [44]. Changes in the host materials will influence the radiative and non-radiative energy transfer mechanisms [15]. Oxide and fluoride have larger phonon energy than that of chloride, bromide, and iodide host materials (Table 2), which will accord to radiative energy transfer mechanism. However, these materials are hygroscopic, and their chemical and thermal stability is low compared to oxides and fluorides. Any specific optical or magnetic properties of the host material can also influence the luminescence emission from the dopant ions. Thus, one can interplay with host materials and dopant ions for new and unparalleled upconversion properties. Major upconversion phosphors are (a) rare earth upconverters (b) transition metal upconverters, and (c) mixed rare earth–transition metal systems.

3.1 Rare Earth Upconversion Phosphors

Today, most of the fluorescent lamps, light-emitting diodes (LEDs), and many display devices have trivalent rare-earth ions as the active component. It is primarily owing to the purity of the colour that has been emitted. Although the technology has shifted from cathode ray tube (CRT) to liquid crystal display (LCD) and LED displays, the light source still includes lanthanide ions. The luminescence emission

from the lanthanide ions extends over the spectral range, visible to the NIR, and many lanthanide ions have peculiar spectral characteristics in the visible region [45], which make them essential in many applications.

Generally, the term lanthanide (Ln) is associated with the group of elements in the periodic table (fifth period in periodic table) from lanthanum ($Z = 57$; $5\ s^2\ 5p^6\ 4f^0\ 5d^1\ 6\ s^2$) to lutetium ($Z = 71$; $5s^2\ 5p^6\ 4f^{14}\ 5d^1\ 6\ s^2$), while the term rare-earths include the group of lanthanides and the elements scandium ($Z = 21$) and yttrium ($Z = 39$). The theory of optical spectroscopy in rare-earth ions was discussed in many works, by Henderson et al. [46] and by García et al. [47]. Lanthanides can occur as doubly or triply charged ions in solids, but they more essentially exist in their most stable oxidation state as trivalent ions (Ln^{3+}). Therefore, trivalent rare-earth ions are more commonly studied. In Ln^{3+} ions, all the electrons in the $5d^1\ 6s^2$ orbits are removed. Furthermore all these trivalent lanthanides have similar electronic configurations ($[Xe]4f^N$) with the $4f$ shell unfilled ($4f^N$, $N = 1$–14) (see Table 1), exceptions are lanthanum with an empty $4f$ shell and lutetium with a completely filled $4f$ shell.

Besides other properties, these rare-earth ions feature unique optical properties due to many possible radiative transitions between the energy levels of the partially filled $4f$ shell. The $4f$ electronic shell, which is almost independent of its surrounding crystal- field due to the screening by 5 s and $5p$ electron shells, determines the optical properties of lanthanides. Because of this, there exists only weak interaction between optical centers and the crystal field, i.e., the electron-phonon coupling is weak. Weak interactions between the $4f$ electrons and the host crystal field will produce a very well resolved Stark structure of the levels, which varies slightly in one host to another. Due

Table 1 Rare earth elements

Element	RE	RE^{3+}
La	$4f^0 5d^1 6s^2$	$4f^0$
Ce	$4f^1 5d^1 6s^2$	$4f^1$
Pr	$4f^3 5d^0 6s^2$	$4f^2$
Nd	$4f^4 5d^0 6s^2$	$4f^3$
Pm	$4f^5 5d^0 6s^2$	$4f^4$
Sm	$4f^6 5d^0 6s^2$	$4f^5$
Eu	$4f^7 5d^0 6s^2$	$4f^6$
Gd	$4f^8 5d^0 6s^2$	$4f^7$
Tb	$4f^9 5d^0 6s^2$	$4f^8$
Dy	$4f^{10} 5d^0 6s^2$	$4f^9$
Ho	$4f^{11} 5d^0 6s^2$	$4f^{10}$
Er	$4f^{12} 5d^0 6s^2$	$4f^{11}$
Tm	$4f^{13} 5d^0 6s^2$	$4f^{12}$
Yb	$4f^{14} 5d^0 6s^2$	$4f^{13}$
Lu	$4f^{14} 5d^1 6s^2$	$4f^{14}$

to the same reason, trivalent rare-earth ions have very narrow electronic transitions and demonstrate very weak phonon bands.

The spectral characteristics of optical transitions of lanthanides ions in the host matrix are determined by the below-mentioned factors.

1. The number of Stark levels, which is determined by Stark splitting of the degenerated energy levels.
2. The host material, determining the magnitude of the splitting.
3. Homogeneous and inhomogeneous line broadening mechanisms.

Every lanthanide has excited states besides the ground state. Total degeneration (D) for a given electronic configuration of an element with a configuration of $4f^n$ is given by,

$$D = \frac{(4l+2)!}{(4l+2-n)!n!} = \frac{14!}{(14-n)!n!} \text{ (For } l = 3) \tag{1}$$

The electron behavior in an atom or ion can be represented by a wave function, which is a solution of the Hamiltonian (H) of the system. Then Hamiltonian for the lanthanide system is given by,

$$H = H_O + H_C + H_{\text{SO}} + H_{\text{CF}} + H_Z \tag{2.2}$$

where H_O is the kinetic energy contribution of electrons, H_C is the Coulomb interaction amoung electron–electron, H_{SO} is the contribution from spin–orbit coupling, H_{CF} is the crystal field (CF) contribution and H_Z is the contribution from the Zeeman effect. The H_O contribution is constant for all electrons, therefore not contributing in lifting the degeneracy of energy levels. Therefore, H_O can be treated as constant. When the lanthanide ion is doped into a host matrix, the Coulombic, spin–orbit, and crystal field (CF) interactions remove the degeneration of the free ion levels as shown in Fig. 12. This leads to the splitting of the free ion levels into ^{2S+1}L energy levels, which have $(2S+1)(2L+1)$ fold degeneracy.

The Coulombic interaction results in the splitting of ^{2S+1}L terms in the order of 10^4 cm^{-1}. Similarly, the spin-orbit interactions arising from the electromagnetic interaction between the electron spin and the magnetic field created by the electron's motion split each ^{2S+1}L into $(2J+1)$ states denoted by $^{2S+1}L_J$. The typical splitting of the $^{2S+1}L_J$ terms is of the order of 10^3 cm^{-1}. The crystal field effect results in symmetry-dependant splitting of energy levels. If we consider the typical value of energy splitting in a d-block element, it ranges from 15,000 to 25,000 cm^{-1}. However, in the case of lanthanide ions, the splitting is in the range of 100–500 cm^{-1} [43]. The CF interaction results in the Stark splitting of the $^{2S+1}L_J$ terms into $(2J+1)$ terms (if the number "n" of the $4f^n$ electron is even) or $(J+1/2)$ terms (if "n" is odd) represented by $^{2S+1}L_{J,\mu}$.

In 1960, Dieke et al. [48] measured the characteristic $^{2S+1}L_J$ energy levels of Ln-doped LaCl, later resulted in the elaboration of the *Dieke diagram,* which becomes the reference of the energy levels of the multiplet manifolds of trivalent lanthanide ions

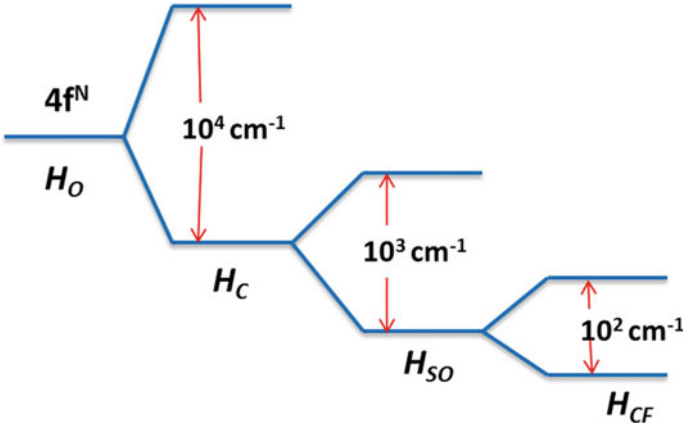

Fig. 12 Different interactions reasonable for the loss of degeneration of lanthanide 4f free ion (H_C–*Coulombic,* H_{SO}–*spin–orbit, and* H_{CF}–*crystal field interactions*)

embedded in any host. Later Orgasawara et al. [49] extended the Dieke diagram to higher energies. In Fig. 13, the width of each state designates the crystal field splitting and the center of each multiplet estimates the location of the free ion $^{2S+1}L_J$ energy level.

Concluding, f electrons in the Ln^{3+} ions display a large number of degenerate states in the absence of any interactions. Perturbations such as Coulomb interactions, spin-orbit coupling, crystal field effects, and magnetic field interaction result in the lifting of the degeneracy and the advent of several non-degenerate levels.

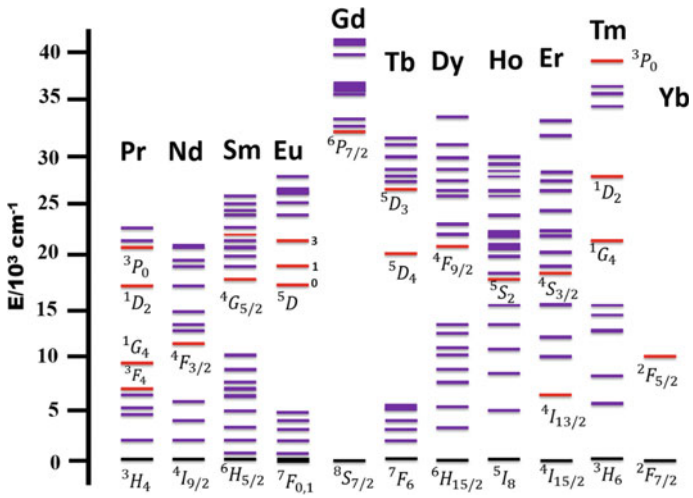

Fig. 13 Dieke diagram: partial energy diagrams for the lanthanide ions

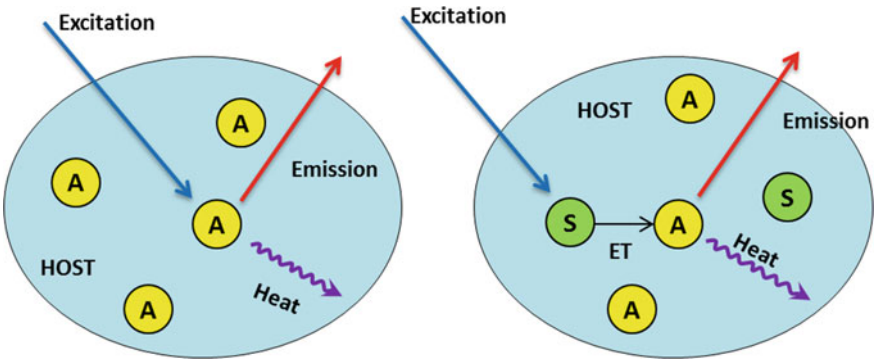

Fig. 14 Typical host lattice with activator alone and activator and sensitizer

(a) Selection of suitable dopants and host materials

An inorganic upconversion phosphor is a crystalline host material doped with low concentrations of lanthanide ion. The lanthanide dopant ion acts as the luminescent center, and the host lattice provides a matrix to bring these centers into optimal position with suitable crystal field. The distance between dopant ions and the particular arrangement of them are important. Many lanthanide-doped host materials can give upconversion emission under NIR excitation, but a highly efficient upconversion luminescence can be achieved by tuning between host lattice, dopant ions, and dopant concentration. Generally, an upconversion phosphor is consist of a host material, luminescence centre called activator. In order to increase the absorption of the incident photon, sometimes a sensitizer ion will also be doped along with the activator ion (Fig. 14).

Host lattice: Selection of appropriate host materials is essential in the synthesis of UC phosphors with high UC efficiency and controllable emission profile. An ideal host material should be chemically stable and transparent in the spectral range of interest having high optical damage threshold. The host material can affect UC efficiency through the phonon dynamics and local crystal field. Ideal host materials should also have low lattice phonon energies, which is a requirement to minimize the non-radiative loss and maximize the radiative emission. UC emissions are very sensitive to the distribution of phonon density of states in UCNPs. The cut-off phonon energy of the host lattice is a good indicator of the number of phonons required. In general, if larger, the number of phonons needed to convert the excitation energy into non-radiative transitions; the lower is the efficiency of the non-radiative process. Hence, to enhance the emission efficiency by reducing the non-radiative rate, it is desirable to have the lanthanide ions incorporated into a dielectric host of very low-frequency phonons. Oxides exhibit high chemical stability, with cut-off phonon energy larger than 500 cm^{-1} due to the stretching vibration of the host lattice. Comparing with oxides, fluorides have low phonon energy (350 cm^{-1}) thus are often used as an efficient host material for UC.

Table 2 Maximum phonon energy in the different inorganic host

Host	$\hbar\omega_{\max}$ (cm^{-1})
Iodide	160
Bromide	175–190
Chalcogenide	200–300
Fluoride	500–600
Tellurite	600–850
Germinate	800–975
Phosphate	1100
Borate	1400
$LaCl_3$	250
$NaYF_4$	370
LaF_3	350
$Y2O_3$	600
$YAlO_3$	550
YVO_4	890
Y_2BaZnO_5	966

The non-radiative relaxation rate in the phosphors can be estimated with the exponential energy gap law developed by van Dijk and Schuurmans [50, 51]

$$k_{nr} = \beta_{el} \exp[-\alpha(\Delta E - 2\hbar\omega_{\max})] \tag{3}$$

where k_{nr} is the multiphonon relaxation rate, β_{el} and α are constants for a given host lattice, ΔE is the energy difference between the energy levels considered and $\hbar\omega_{\max}$ is the maximum phonon energy. Hosts with low phonon energy may decrease the probability of non-radiative transitions, subsequently leading to high luminescence efficiency. The maximum phonon energies of different inorganic host materials are summarized in Table 2.

The crystal structure of the host materials can significantly influence the optical properties of nanocrystals. A less symmetric crystal structure is favourable for high UC efficiency [52]. In the typical case, hexagonal-phase $NaYF_4$:Yb, Er bulk materials display about an order of magnitude improvement in UC efficiency relative to their cubic phase counterparts [53].

Similarly, monoclinic ZrO_2 nanoparticles exhibit higher UC emission than their tetragonal phase [54]. The phase-dependence of optical properties of phosphors can be ascribed to the different crystal fields around trivalent lanthanide ions in matrices of different symmetries. In a low symmetry host, the crystal field contains more uneven components around the dopant ions compared to the high symmetry counterparts. In a non-centrosymmetric lattice, the parity selection rules are relaxed. The perturbation due to the odd-order terms of the crystal field will force the parity forbidden transitions to become allowed. The electronic coupling between $4f$ energy levels and higher

electronic configuration is enhanced by the uneven components, and subsequently, f–f transition probabilities of the dopant ions will increase. That is, when the symmetry at the dopant ion site is lower, the higher the transition probability. In addition, the decrease in cation size of the host will cause an increase in the crystal field strength around the dopant ions, and UC efficiency will be enhanced. Yao et al. [55] reported the enhanced emission intensity in β-$NaGdF_4$:Yb^{3+}, Er^{3+} by Bi^{3+} co-doping, and Bi^{3+} co-doping induced structural disorder which leads to the enhanced emission. Development of multifunctional luminescent materials has gained much attention. A multifunctional material that combines light emission with other intrinsic properties of the host such as ferroelectricity, magnetism, piezoelectricity will be a promising candidate for future biomedical applications.

As all trivalent rare-earth ions exhibit similar chemical properties and have comparable ionic radii, their inorganic compounds are ideal host materials for upconversion doping with lanthanide ions. Some alkaline earth ions (Ca^{2+}, Sr^{2+}, and Ba^{2+}) and transition metal ions (Zr^{4+} and Ti^{4+}) also have ionic size close to lanthanide ions. Therefore, inorganic compounds of these ions are also frequently used as host materials for UC processes. However, lanthanide doping in these nanocrystals is accompanied by the formation of crystal defects like interstitial anions and cation vacancies to maintain charge neutrality.

A single crystal host will be much efficient for UC. The dopant concentration should be stringently controlled to synthesize a single crystal host. In order to allow full visible light transmission, host materials for display and LED applications (oxide, sulfide, fluoride, etc.) must have a wide bandgap. Hence, usually, insulators are selected as hosts. As long as the luminescent excited state does not overlap with the conduction band leading to luminescence quenching, semiconductors can also be used as hosts for optically active ions. Therefore, wide bandgap semiconductors, like ZnS, GaN, and ZnO, have extensively been utilized as hosts for rare-earth doping for optical and electronic applications. However, it is still debatable whether lanthanide ions are occupying within the crystal lattice of these host materials due to a largely mismatched ionic size between the host and dopant ions. The dopant ions can be occupied at the grain boundaries of host lattice [52]. In ZnO doped with Er and Yb, the dopant ions are not replacing Zn in the crystals but occupying the grain boundaries. The host material should have excellent mechanical and chemical stability.

Figure 15 shows the upconversion luminescence from the host materials YF_3, YOF, and Y_2O_3 co-doped with Yb^{3+}/Er^{3+} ions. The oxide and oxyfluoride host were prepared by annealing the fluoride host at higher temperatures. The emission spectra of all the three host materials doped with Yb/Er showed emissions around 660 and 540 nm corresponding to the $^4F_{9/2} \rightarrow {}^4I_{15/2}$ and $^2H_{11/2}$, $^4S_{3/2} \rightarrow {}^4I_{15/2}$ transitions of the Er^{3+} ion (see Fig. 16) respectively. For the YF_3 UC phosphor host, a weak emission at (blue) 410 nm was also detected corresponding to the $^2H_{9/2} \rightarrow {}^4I_{15/2}$ transition in Er^{3+} ions (inset Fig. 15). However, these blue emission bands were absent in the case of YOF and Y_2O_3 UC phosphor host material. This is because of the high phonon energy of oxide and oxyfluoride host material [15].

As the host material is changed from fluoride to oxyfluoride and then to oxide, the red emission becomes more prominent. As the oxygen environment in the crystal

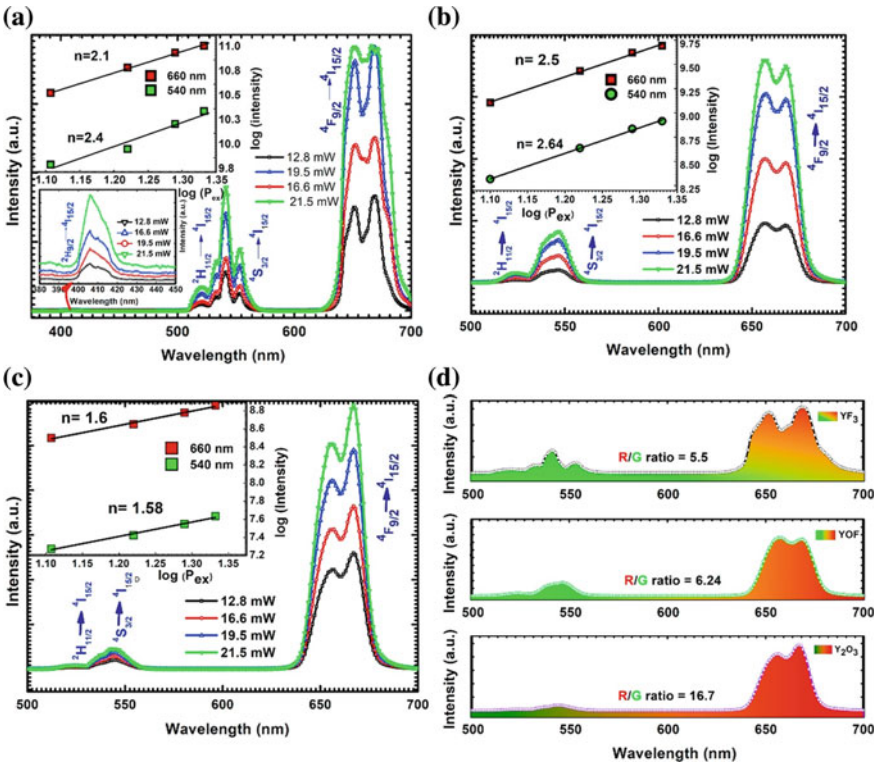

Fig. 15 UC luminescence spectra of Yb^{3+}/Er^{3+} co-doped **a** YF_3, **b** YOF and **c** Y_2O_3 under 980 nm laser illumination and **d** the intensity ratio of red and green bands are shown at a laser power of 16.6 mW. Reprinted with permission from [15] Copyright © 2018, Elsevier)

lattice had increased when the host material was changed from fluoride to oxide, the transition to $^4F_{9/2}$ energy levels was preferred, resulting in an increase in the R/G ratio. It should also be noted that the lifetimes of the intermediate levels $^4S_{2/3}$ and $^4F_{9/2}$ had a significant influence in the emission colour.

(b) **Activators**

The requirement of multiple metastable levels for UC luminescence makes the lanthanides well suited for this application. The *f–f* transitions are Laporte forbidden, and hence, intra-4*f* transition probabilities are less and the excited states are substantially long-lived (up to 0.1 s). The lanthanide ions except for La^{3+}, Ce^{3+}, Yb^{3+}, and Lu^{3+} have more than one exciting 4*f* energy level. As a consequence, UC emission can be expected in most lanthanide ions. In order to generate efficient UC emission, the energy difference between each exciting level and its lower-lying intermediate level (ground level) should be close enough to facilitate photon absorption and energy transfer mechanisms involved in UC processes. Ions like Er^{3+}, Tm^{3+}, and Ho^{3+} have ladder-like arranged energy levels and are the commonly used activators (see Fig. 13).

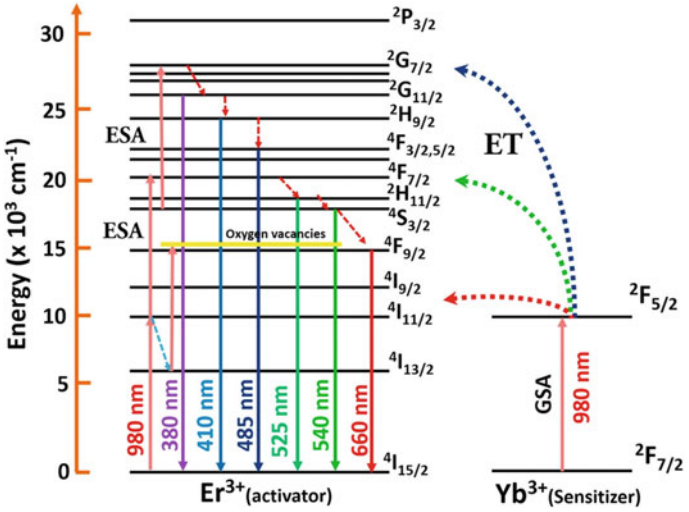

Fig. 16 Schematic diagram shows the energy transfer in Yb/Er co-doped system under 980 nm excitation. Reprinted with permission from [15] Copyright @ 2018, Elsevier

(c) **Sensitizers**

The distance between two neighbouring activator ions and the absorption cross-section of the ions are two major concerns in upconversion phosphors, which are lightly doped. On the other hand, high doping levels can lead to cross-relaxation, resulting in quenching of excitation energy. Therefore, it is important to keep the concentration of activator ions low and precisely adjusted to avoid the quenching effect. Mostly, lanthanide activator ions have low absorption cross-sections, leading to low pump efficiency. Therefore, the singly doped nanocrystals have relatively low UC efficiency. So, generally, in order to have high UC, a sensitizer ion with larger absorption cross section in the NIR region is co-doped along with the activator ion, which utilizes the efficient ETU between sensitizer and activator. For example, trivalent Yb possesses an extremely simple energy level scheme with only one excited $4f$ level of $2F^{5/2}$. The absorption band of Yb^{3+} that is located around 980 nm due to the $^2F_{7/2} \rightarrow {}^2F_{5/2}$ transition has a larger absorption cross-section than that of other lanthanide ions. Additionally, the $^2F_{7/2} \rightarrow {}^2F_{5/2}$ transition of Yb^{3+} is well resonant with many f–f transitions of typical upconverting lanthanide ions (Er^{3+}, Tm^{3+}, and Ho^{3+}), thus facilitating efficient energy transfer from Yb^{3+} to other ions. These optical characteristics make Yb^{3+} suitable for using as a UC sensitizer. The sensitizer content is normally kept high (20 mol%) in double or triple doped nanocrystals, while the activator content is relatively low (<2 mol%), minimizing cross-relaxation energy loss.

The key factors one should take care of while choosing a suitable phosphor are (1) the sensitizer should have adequate absorption cross-section in the near-infrared

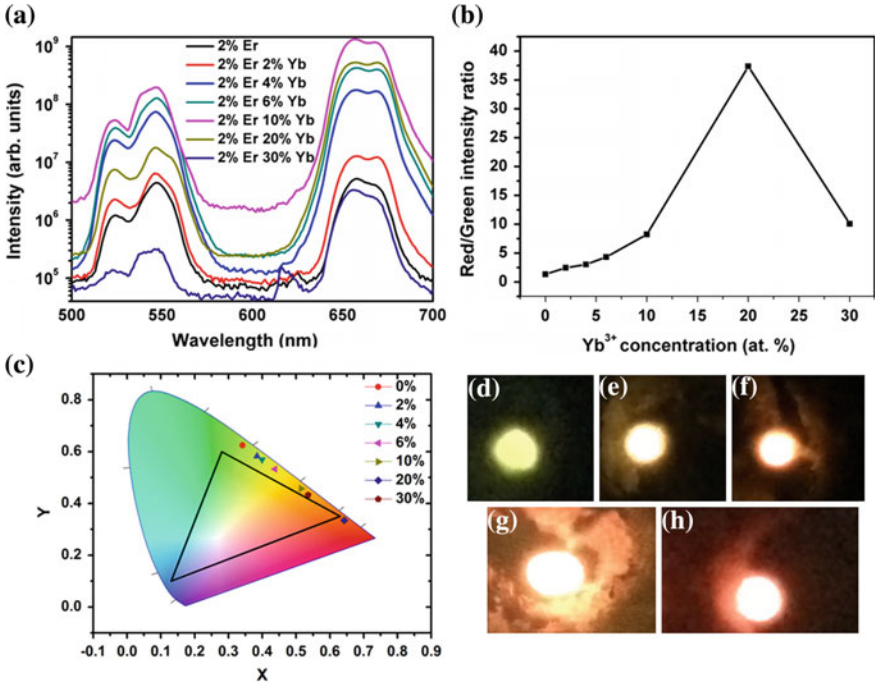

Fig. 17 Dependence of upconversion emission on sensitizer concentration. **a** Upconversion luminescence spectrum obtained from 2% Er^{3+}, x% Yb^{3+}: YF_3, **b** variation of red/green intensity ratio on Yb^{3+} concentration, and **c** CIE color coordinate diagram showing the variation of emission color with Yb^{3+} concentration, photographs of emission from 2% Er^{3+}, x% Yb^{3+}:YF_3 for x = **d** 0, **e** 2, **f** 6, **g** 10, **h** 20

region, (2) it must have characteristic overlaps with the absorption band of the activator ion, and (3) the sensitizer should not have any absorption at any region where upconversion is expected.

The variation of luminescence emission on sensitizer concentration is shown in Fig. 17. The red emission intensity was increased with Yb^{3+} concentration due to the cross-relaxation between $^4I_{11/2}$ and $^4F_{7/2}$ levels of Er populating the red-emitting level more. Also, more concentration of dopants could result in concentration quenching.

3.2 Transition Metal Upconverters

The availability of valance *d* orbitals in the transition ions makes them appealing for new novel upconverting materials. In transition metals, the valance *d* orbitals are spectroscopically sensitive to environmental perturbation than rare-earth ions. So, one can manipulate the photo-physical properties of these materials by providing external stimuli like chemical, magnetic, electric, redox, etc. The spectroscopically

active *d* orbitals are strongly affected by the crystal field effect, which in turn influence the energy level lifetime, multiphonon relaxation rates, electron-phonon interaction strengths etc. [26].

One of the first examples of an upconversion phosphor containing transition metals as active ion was discovered by Auzel [31] and his co-workers in the form of single- crystalline $MgF_2:Ni^{2+}$. This phosphor was important, because of its broadband characteristics of the *d*–*d* emission of Ni^{2+}, through ESA mechanism. $MgF_2:Ni^{2+}$ was efficient mainly at a lower temperature, for at higher temperature quenching of emission become dominant. Gamelin and Gudel et al. [56] through methodical investigation synthesize many low phonon energy halides (bromide, fluoride, and chloride) with Cr^{4+}, Ti^{4+}, Re^{4+} [57], and Os^{4+} as a doped anion. These halides are hygroscopic.

3.3 Mixed Rare Earth–Transition Metal Upconverters

The combination of trivalent rare-earth (Ln^{3+}) and transition metal (TM) ions in the same host lattice introduces new cooperative upconversion mechanisms involving both ions. Since the absorption properties of TM ions are sensitive to the environmental changes like ligand and the coordination geometry, these materials are promising for a variety of applications. Through the choice of host lattice, we can tune to some extent, the energetic positions of absorption and luminescence. This will lead to the development of upconversion materials with sharp line excitation in the near-infrared region and broadband emission in the visible spectral region and vice versa. Such materials are interesting for the development of new visible laser sources and display devices.

Two fundamentally different upconversion schemes in mixed Ln^{3+}/TM compounds are possible: lanthanide-sensitized transition metal upconversion luminescence, or transition metal-sensitized lanthanide upconversion luminescence [44]. It is possible to design a rare-earth transition metal dimer sensitizer as well to selectively enhance a particular luminescence from rare-earth ion. For example, Mo^{6+} co-doping in Er^{3+}, Yb^{3+} doped samples will enhance the green emission of Er^{3+}. The enhancement in the green emission is due to the formation of a Yb^{3+}–MoO_4^{2-} dimer sensitizer as shown in Fig. 18 [58].

The optimum doping of sensitizer and activator is essential for maximum upconversion efficiency. As the activator concentration increases, the emission intensity also increases, and however, higher doping concentration will lead to concentration quenching by cross-relaxation between adjacent ions.

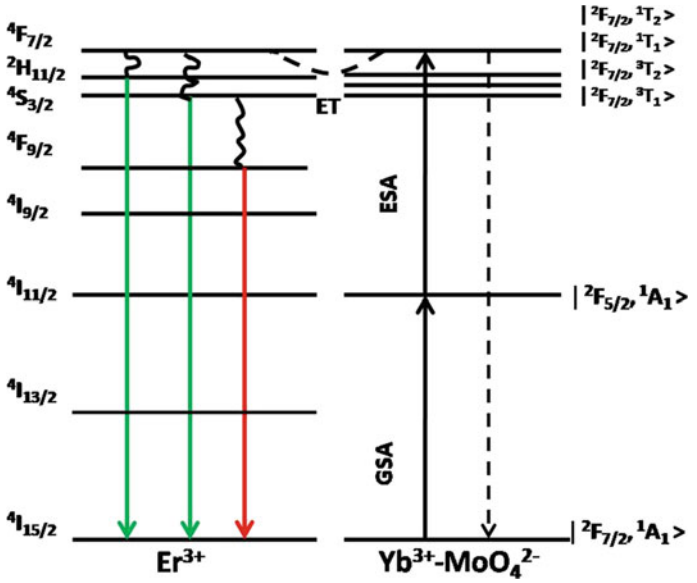

Fig. 18 Schematic energy-level diagram and energy transfer mechanism of Er, Yb, Mo co-doped system © IOP Publishing. Reproduced with permission [58]. All rights reserved

4 Upconversion Efficiency

The conversion efficiency of a phosphor, usually expressed as either quantum efficiency or energy efficiency, is an important consideration in practical applications. The quantum efficiency (or quantum yield) is the ratio of emitted photons to the input photons contributing to the desired optical process. In contrast, energy efficiency is the ratio of the output power to the input power.

$$\eta_{\mathrm{UC}} = \frac{P_{\mathrm{em}}}{P_{\mathrm{abs}}^{\mathrm{IR}}} \tag{2.4}$$

where η_{UC} is the upconversion efficiency, P_{em} is the power of the upconversion light emitted, and $P_{\mathrm{abs}}^{\mathrm{IR}}$ is the power of the fraction of incident light that is absorbed.

Generally, in a luminescence process, the excited-state decay process is a combination of both the radiative and nonradioactive processes, and the relative rate of these processes determines the quantum efficiency. In molecules, the non-radiative processes, such as vibrational relaxation and collisional quenching instead of emitting photons, can also dissipate the excited-state energy. Suppose, k_r and k_{nr} be the radiative and non-radiative decay rates, N be the population density of luminescence activators in the excited state. Then, the temporal evolution of the excited state is given by:

$$\frac{dN}{dt} = -(k_r + K_{nr})N \tag{5}$$

The luminescence decays exponentially with a time constant τ where

$$\tau = \frac{1}{k_r + k_{nr}} \tag{6}$$

The observed luminescence lifetime, τ, measures the combined rate of the radiative and non-radiative pathways. The fraction of the excitation contributing to radiative decay processes is $k_r/(k_r + k_{nr})$. Thus, the quantum efficiency (η_{PL}) can be calculated using the following formula

$$\eta_{\mathrm{PL}} = \frac{k_r}{k_r + k_{nr}} = \frac{\tau}{\tau_R} \tag{7}$$

Here, $\tau_R = \frac{1}{k_r}$ is the radiative lifetime, namely the lifetime of the excited state in the absence of non-radiative decay processes. The lifetime, τ, can be calculated from the intensity decay curve. However, the radiative lifetime, τ_{RS}, is usually estimated by the use of Judd–Ofelt theory as it is not easy to determine experimentally.

The upconversion photoluminescence has a nonlinear dependence on the excitation light intensity,

$$I_{\mathrm{UC}} = K P^n \tag{8}$$

where I_{UC} is the photoluminescence intensity, P is the pump power, K is material constant, and "n" is the number of excitation photons required to reduce for upconversion luminescence. The log-log relation of Eq. (8) gives the value of "n." However, at high-intensity excitation, the value of "n" could have calculated as a non-integral value due to the saturation effect. Therefore, while determining the UC process, saturation effect should be avoided.

Figure 19a illustrates the excitation power dependence on the intensity of UC emission bands centered at 520 and 650 nm in a Yb/Er co-doped Y_2O_3 phosphor. It can be observed that as the excitation intensity increases, the emission intensity also increases. Using Eq. 5, the nonlinear dependence of UC emission on the pump power was calculated by plotting log-log plot of intensity versus power. For the green emission band, the "n" value is calculated as 2.07, and for red emission band, the "n" value is calculated as 1.93. Since the values are greater than 1, it can be confirmed that the mechanism involved is two photons absorption.

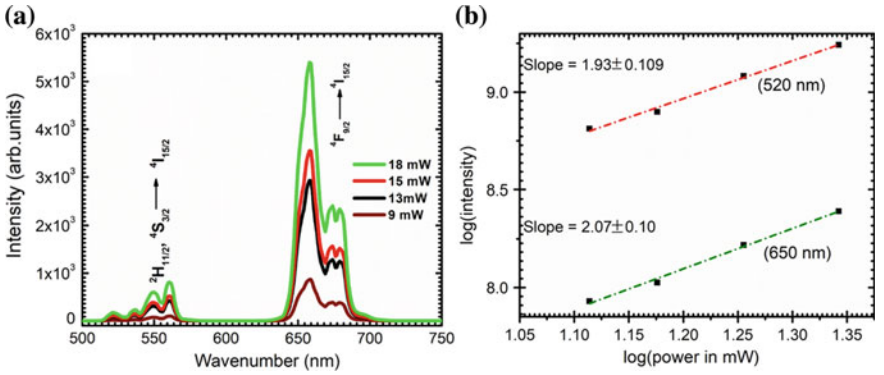

Fig. 19 **a** UC emission intensity dependence on excitation power (980 nm) in a Yb/Er co-doped Y_2O_3 phosphor and **b** log–log plot of intensities of the 650 nm (green) and 520 nm (red) emission bands versus excitation power (980 nm)

5 Synthesis Methods for Upconversion Phosphors

The upconversion luminescence properties highly depend on the structural morphologies, size, host lattice, synthesis conditions, etc. A large number of synthesis methods have been developed during the past decades. Soft chemical routes are widely used for the synthesis of nanomaterials. Since these methods provide an easy way to introduce ligands to the surface of the nanomaterials for preventing agglomeration. Also, one can easily control the size and shape of the phosphors by changing the precursor pH, temperature, and reaction time. Some of the important synthesis methods for upconversion phosphors are listed below.

5.1 Hydrothermal/Solvothermal Method

This method is widely used for the synthesis of a wide variety of nanomaterials. In the solvothermal method, the reaction is carried out in a teflon-lined autoclave under high pressure and moderate temperature. The high pressure will increase the reagent solubility and reactivity and increases the rate of reaction. The reaction temperature will be above the critical point of the solvent. This method is, therefore, more suitable and efficient for designing and synthesizing high-quality nanoparticles with different morphologies. In the synthesis of upconversion nanophosphors, most of the precursor solvents are either nitrates or chlorides. HF, NH_4F, NaF, and $NaBF_4$ are commonly used fluoride sources. The solvent mainly used are ethanol and ethylene glycol (EG). The physicochemical properties of the solvent can significantly influence the reactivity, solubility, and diffusion behaviour of the reagents and different solvents can influence and control their morphology and size. When water is used as the solvent, it is termed as hydrothermal, which has several desirable advantages like

low cost, high yield production, and non-toxic. Organic surfactants like oleic acid (OA), polyethylenimine (PEI), ethylenediaminetetraacetic acid (EDTA), and cetyl trimethyl ammonium bromide (CTAB) are used to control the size and shape of the nanomaterials. The pH of the precursor solution is also important, and it affects the crystallinity and the morphology of the phosphors.

5.2 Sol–gel Method

The sol-gel is a promising route for the synthesis of lanthanide-based UC phosphors. It involves the conversion of solutions into a colloidal sol and then the colloidal sol to a gel. Further heating at high temperatures results in the formation of pure phase nanoparticles with high crystallinity. The main steps involved in any sol-gel process are hydrolysis, condensation, gelation, ageing, drying, and densification. In this method, metal precursors such as metal nitrates, metal chlorides, and acetates are initially dissolved in aqueous solutions, after that the chelating agent such as citric acid or salicylic acid is used to form stable metal complexes. Also, polyhydroxy alcohols like polyethylene glycol (PEG) or ethylene glycol (EG) is used as a cross-linking agent for the formation of homogeneous polymeric resin at the molecular scale. This gel will reduce the segregation of particular metal ions and confirms the homogeneity of the composition. The gel is sintered at high temperatures to eliminate the organic additives and form the final product with pure phase and good crystallinity.

5.3 Co-precipitation Method

The co-precipitation method is one of the oldest and well-developed methods for the synthesis of lanthanide-based nanomaterials. The size and shape of the nanomaterials synthesized by this method can be tailored by controlling the reaction conditions. But, these nanomaterials exhibit a weak luminescence that can be enhanced by sintering at high temperatures which carbonizes the capping agent and reduces the hydrophilicity of nanoparticles. Consequently, surface modifications are needed before using these nanoparticles for security ink application. Nevertheless, the co-precipitation method has important industrial applications due to its low cost, high yield, environmental benignancy, and synthetic suitability.

Figure 20 is the SEM images of oxide (Y_2O_3), oxyfluoride (YOF), and fluoride (YF_3) host materials formed by co-precipitation method followed by annealing from a single source in our laboratory [15]. The synthesis precursors were yttrium nitrate, ytterbium nitrate, erbium nitrate, and ammonium fluoride. In deionized water, a stoichiometric amount of precursors was dissolved, and ammonium fluoride was added slowly while stirring at 90 °C. The precipitate after proper cleaning was annealed at different temperatures to form different upconversion nanomaterials. YF_3 phosphor

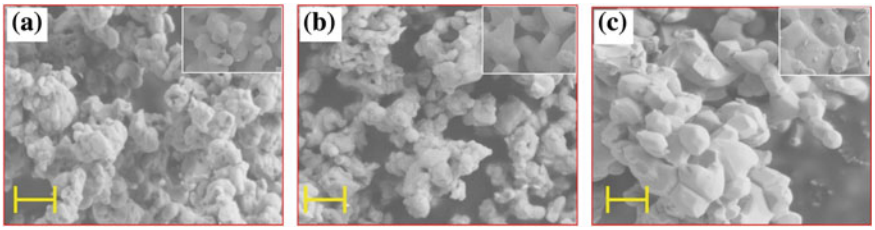

Fig. 20 SEM images of Yb^{3+}/Er^{3+} co-doped **a** YF_3, **b** YOF, and **c** Y_2O_3 UCNPs synthesized by co-precipitation method followed by annealing process (scale: 300 nm, inset is the magnified view). Reprinted with permission from [15] copyright @ 2018, Elsevier

was obtained by annealing at 500 °C while YOF and Y_2O_3 phosphors were obtained by annealing at 800 °C and 1300 °C, respectively. As observed in Fig. 16, the morphology of the phosphors had an explicit dependency on the annealing temperature. When the temperature had increased, the phase transition occurred. Orthorhombic YF_3 phosphor changed to rhombohedral YOF and cubic Y_2O_3 phosphors. The YF_3 UC phosphors shown a quasi-spherical structure, and when the temperature increased to 800 °C, the growth mechanism was influenced by the presence of oxygen. The self-assembly process resulted in the formation of YOF particles by the incorporation of oxygen in the growth process. Also, slightly larger particles were observed for the high-temperature annealed YOF and Y_2O_3 phosphors.

5.4 Thermal Decomposition Method

Thermal decomposition is a method used widely for the synthesis of luminescent nanomaterials. This method generally employs the organometallic compounds taken as precursors, which decompose at an elevated temperature in high boiling point organic solvents. Organic acid salts of rare earth such as trifluoroacetate, oleate, acetylacetonate, and acetate are the organic precursors used in thermal decomposition. Commonly used organic solvents are oleic acid (OA), oleylamine (OM), tri-n-octylphosphine oxide (TOPO), and 1-octadecene (ODE). However, ODE is most commonly used as a solvent in thermal decomposition due to its high boiling point (315 °C). More than this, surfactants are also used in the thermal decomposition method. The surfactant will act as a coating in the surface of nanoparticles preventing aggregations, and hence, the particles will be highly dispersible in organic solvents. In addition to this, the surfactant plays a vital role in controlling the growth of nanoparticles. High-quality nanomaterials with a narrow size distribution, good crystallinity, and exceptional optical properties can be synthesized by carefully varying the nature of the solvents, the concentration of metal precursors, reaction temperature, and reaction time.

6 Application of Upconversion Phosphors

The unique optical properties of upconverting nanomaterials have a great deal of attention; they are used as spectral converters in photovoltaic devices, security printing, bio-imaging applications, etc. Various applications of upconversion phosphors are discussed below.

6.1 Solar Energy Harvesting

The photovoltaic effect is a phenomenon in which voltage or electric current generated in a material upon the exposure to light. French physicist A. E. Becquerel first experimentally demonstrated the photovoltaic effect in 1839, and he built the world's first photovoltaic device [44]. The fundamental principles behind all photovoltaic cell are (a) generation of electron-hole pairs in a semiconductor material by the absorption of light and (b) the charge carriers are separated, transported, and extracted into an external circuit. In 1954, when the silicon revolution had spanned the world, scientists Darly M. Chapin, C. S. Fuller, and G. L. Pearson of Bell laboratories demonstrated the first practical silicon solar cell which has an efficiency of 6% which gave new hope of using limitless energy of the sun for mankind [59]. The main attraction of these solar cells at that time was in space application (Explorer 6, launched in 1959 by the USA had wing-shaped solar systems). The high price of the solar cell was the main challenge which mainly dominated by the semiconductor industry. Later new technological leap toward an integrated system resulted in the lowering of price.

Most of the photovoltaic cells are based on semiconductors like silicon and germanium. New approaches like dye-sensitized solar cells (DSSC), organic solar cells, quantum dot solar cells, and perovskite solar cells [60], also contributed to price deduction and better efficiency. However, silicon is the most prominent and widely used solar cell material because of its better efficiency. The heart of any solar cell is the light absorbing-material. One must have to tune these materials such that it should have characteristics that match with the solar spectrum in order to absorb it. Unfortunately, no photovoltaic cell can absorb the complete solar spectrum. Moreover, they cannot convert all the absorbed light into useful electricity due to some losses which occur during the process of photovoltaic generation. Also, losses due to reflection, recombination losses (due to interface defects/poor material quality), lattice thermalization losses (excess photon energy is transformed into heat), junction, and contact voltage losses limit the solar cell efficiency (Fig. 21).

In 1961 William Shockley and Hans Queisser calculated the maximum efficiency of the solar cell. They calculated the maximum efficiency, which can be attained for a single-junction Si solar cell as 30% and is called Shockley–Queisser (SQ) limit [61]. The energy conversion efficiency of a solar cell is defined as the percentage of the total power of sunlight converted into electricity. Later, modern SQ limit calculation

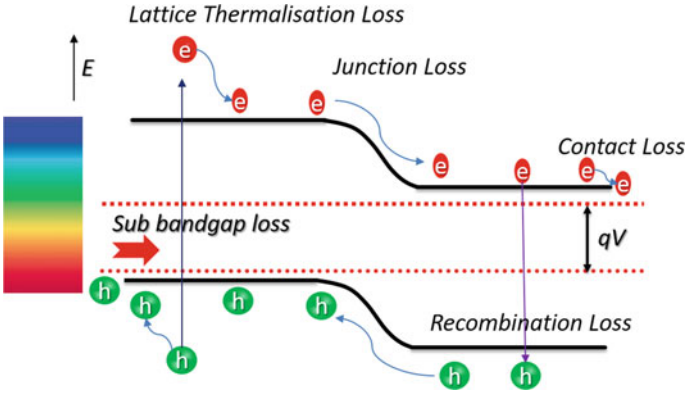

Fig. 21 Solar spectral loss due to various mechanisms in the solar cell

predicts 33% maximum efficiency for any single-junction solar cell. There have been several strategic approaches to beat the SQ limit. Some of them are (a) using more than one type of semiconductor material (multijunction photovoltaic cells/tandem solar cells), (b) concentrating sunlight (using Fresnel lens), (c) intermediate band photovoltaic, (d) hot electron capture (*thermo-photovoltaic conversion*), (e) multi-exciton generation, (f) photon upconversion, and (g) photon downconversion.

One possibility to reduce these transmission losses is the so-called impurity photovoltaic effect, i.e., the insertion of impurities with energies located in the bandgap of a solar cell material (tandem solar cells), which was proposed by Wolf in 1960 [62]. Another method to reduce the transmission losses is by upconverting the transmitted low-energy photons from the solar spectrum to higher-energy photons, which can then be utilized by the solar cell. Usually, the upconverter layer is located behind a solar cell, and it can absorb the transmitted sub-bandgap photons. The sequential absorption of photons will populate the excited state in the upconverter from which photons are emitted, which can be absorbed by the solar cell and generates electron-hole pairs. The energy conversion efficiency of this system within the radiative limit is calculated for cells of totally diverse geometries and different illumination conditions employing an elaborated balance model. It is shown that by restricting the widths of the bands in the upconverter, the conditions of photon selectivity and complete absorption of high-energy photons can be met simultaneously in this system. It is the only method that does not require any specific engineering. Upconversion material can be coupled to any type of solar cell, crystalline, amorphous, thin-film, organic solar cells, hybrid solar cells, and dye-sensitized solar cell (DSSC).

For c-Si solar cells, the transmission loss of the incident solar energy amounts to about 20%, and no conventional methods could reduce this loss. Figure 22 shows the schematic diagram of how UC phosphor based spectral upconverter works in a c-Si solar cell. Trupke et al. [63] theoretically showed that the upper limit of the energy

conversion efficiency by using UC materials as 63.2% for concentrated sunlight and 47.6% for non-concentrated sunlight.

In 1996, Gibart et al. [64] demonstrated the feasibility of this concept experimentally by stacking rare earth-doped vitro ceramic (Er^{3+}–Yb^{3+} A/S) behind a substrate-free ultrathin GaAs (1.43 eV) solar cell. The cell efficiency was 2.5% upon excitation of 256 kW/m^2 monochromatic sub-bandgap (1.391 eV) laser light (1 W on 0.039 cm^2 cell area). Many research groups then developed various upconversion-based PV system to enhance the solar cell efficiencies. Richards and Shalav [65] showed a 3.4% of external quantum efficiency (EQE) in the c-Si solar cell by using $NaYF_4$:Er^{3+} upconverter when excited at 1523 nm. Some of the works are listed in the table below. Struempel et al. [66] suggested $BaCl_2$:Er^{3+}:Dy^{3+}as a better accord for $NaYF_4$ systems due to their low phonon energy and high excitation spectrum. Yb, Er, sensitizer–activator coupled host materials are considered as the most efficient upconversion phosphors. Crystalline silicon (c-Si) has absorption in the 920–980 nm wavelength. So, Yb sensitizer cannot be used in c-Si solar cells. Er^{3+}, Ho^{3+} doped UC materials, which can absorb long-wavelength near-infrared light and emit near-infrared light is good for narrow bandgap solar cells, especially C-Si solar cell. On the other hand, for wide bandgap semiconductors, like GaAs and a-Si:H solar cells, Yb^{3+}–Ln^{3+} couples can be effectively utilized.

Later Badescu et al. [67], with a detailed model of solar cell and upconverter, confirmed the results of Trupke et al. [63]. They have taken into consideration the refractive index of the solar cell and the upconverter. An upconverter should have lower refractive index than the cell, and similar materials can improve efficiency by about 10%. Recently Atre et al. [68] endorse the above findings. In their study, radiative recombination, non-radiative relaxation, and non-ideal absorption were taken

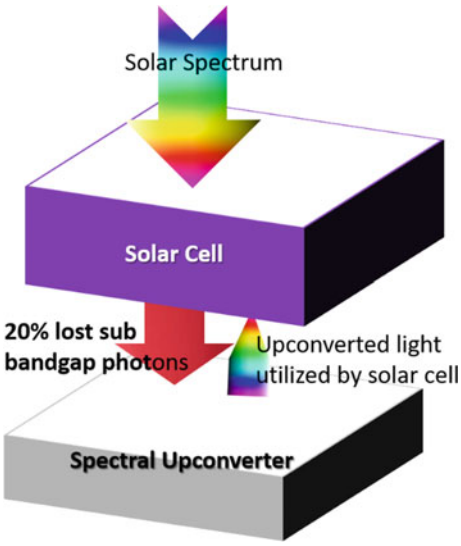

Fig. 22 Schematic diagram showing how the upconversion layer works in solar cell

into consideration. They also underline that wide bandgap solar cell would be the best nominees for upconverters.

The position of the upconverter layer in cell architecture is also important. From theoretical and experimental results, the best design is to place the upconverter on the rear side of the cell with a mirror layer. One of the major problems in these upconversion spectral converters is their narrow absorption range. Most of these UC phosphors have Yb^{3+} sensitizer, which has absorption around 980 nm. Therefore, it is necessary to broaden the absorption range of these phosphors by secondary doping or using multiple sensitizers.

(a) **Upconversion in c-Si solar cells**:

In the 800–1100 nm spectral region, the c-Si solar cells work most efficiently, but they show very low spectral response in the short-wavelength sunlight. Therefore, the most desirable upconverters for c-Si solar cells are those that are able to absorb light above 1100 nm and convert it into emission around 1000 nm. Therefore, the development of UC materials with absorption below 1100 nm and the upconverted emission in the range of ~800–1100 nm are best suitable for a c-Si photovoltaic (PV) cell. Sensitizers likeYb^{3+} or Nd^{3+} are not recommended for use in c-Si cells since they have absorption at ~980 and ~800 nm where the semiconductor silicon has high spectral responses. In principle, an upconverter for c-Si solar cells should satisfy the following requirements: (i) the excitation range longer than 1100 nm (E_g 1.12 eV); (ii) the emission range shorter than 1100 nm; (iii) good response under low-intensity excitation; and (iv) high conversion efficiency and high transparency toward the upconverted light.

Considering all these, single Er^{3+}-doped UC materials are best suitable for c-Si solar cells. Er^{3+} has absorption at 1480–1580 nm ($^4I_{15/2} \rightarrow {}^4I_{13/2}$) and shows upconversion luminescence at ~980, ~540, and 650 nm. In 2005, Shalav et al. [69] studied $NaYF_4$:20% Er^{3+} microcrystals as an upconverter in bifacial c-Si solar cells. The $NaYF_4$:20% Er^{3+} phosphors in acrylic adhesive were deposited on the rear of a bifacial c-Si solar cell. They have obtained an external quantum efficiency of 2.5% under excitation at 1523 nm (5.1 mW laser power). Later, Fischer et al. [70] also investigated bulk $NaYF_4$:20% Er^3 and obtained an external quantum efficiency of 0.34% at 1522 nm (power density: 1090 Wm^{-2}).

Lahoz et al. [71, 72] successfully demonstrated the use of single Ho^{3+} ion [absorption band in the region 1150–1225 nm ($^5I_8 \rightarrow {}^5I_6$) and UC emission at ~910 nm ($^5I_5 \rightarrow {}^5I_8$), and at ~650 nm ($^5F_5 \rightarrow {}^5I_8$)] doped upconverting oxyfluoride glass ceramics in a c-Si solar cell. In another work of theirs, Ho^{3+}–Yb^{3+} co-doped upconversion phosphors were used as spectral converters for a c-Si solar cell. They found that the Ho^{3+}–Yb^{3+} co-doped upconverter was much efficient than that of the single Ho^{3+}-doped UC phosphor. Because the Ho^{3+} ions in the excited $^5I_5$ state can sensitize Yb^{3+} ions at the ground $^2F_{7/2}$ state, resultingin both Ho^{3+} and Yb^{3+} UC luminescence. Therefore, the c-Si incorporated with Yb–Ho co-doped UCNP produced a more enhanced response in the NIR region compared to the single Ho^{3+}-doped UC phosphor. They also demonstrated a double layer design with Ho^{3+} UC layer positioned at the rear side of a bifacial C-Si cell followed by Er^{3+} UC layer and a mirror. In

2012, Chen et al. [33] proposed another design where Er^{3+} and Ho^{3+} activators were incorporated into the core and shell layer of a nanoparticle separately. This core–shell structure could extend the excitable NIR wavelength range and also minimize the luminescence quenching through cross-relaxation energy transfer between the two ions. They fabricated $NaGdF_4:Er^{3+}/NaGdF_4:Ho^{3+}/NaGdF_4$ core-shell nanoparticles and intense UC emissions from both the ions were obtained. The other major works on the upconversion layer for improving solar cell efficiency of c-Si solar cells are summarized in Table 3.

(b) **Upconversion for wide bandgap solar cells**

Compared to the traditional c-Si solar cells, wide bandgap solar cells would advantage rather more from the integration of an upconverting layer owing to the dominant transmission losses. The wide bandgap solar cells, including GaAs, amorphous Si, organic solar cells, and dye-sensitized, will work well in the visible region. However, their absorption is generally limited to a maximum wavelength of 900 nm. Figure 23 shows the bandgap of various solar cell absorbers and their efficiency comparison.

(c) **GaAs solar cells**

In 1995, Gibart et al. [64] reported the application of Yb/Er co-doped vitro ceramic UC phosphor in GaAs solar cell. They have obtained a power conversion efficiency of 2.5% under 891 nm illuminations. Lin et al. [73] used of $Y_6W_2O_{15}:Yb^{3+}$, Er^{3+} UC phosphor layer of thickness 300 μm to the rear of a GaAs solar cell and obtained a maximum output power of 0.339×10^{-6} W under 973 nm laser illumination. The Tm^{3+}–Yb^{3+}activator sensitizer couple giving a NIR-to-NIR upconversion luminescence (980 nm excitation, 800 nm emission) is likely to be more suitable for application in GaAs solar cells ($E_g = 1.43$ eV; 867 nm) compared with other activator–sensitizer couples like Er^{3+}–Yb^{3+}, due to a larger emission and absorption spectral overlap of the former.

(d) **Amorphous silicon solar cells**

Due to their low price, simple preparation and outstanding chemical stability, amorphous Si (a-Si:H) solar cells have been regarded as a promising alternative for c-Si solar cells. At approximately 1.75 eV bandgap, amorphous Si has a bigger bandgap than c-Si, which limits it to absorb light smaller than 700 nm. This means that upconverting materials with absorption above 700 nm should be appealing for uses in amorphous Si solar cells. In 2010, Zhang et al. [74] reported the use of $NaYF_4$:18% Yb^{3+}, 2% Er^{3+} nanocrystal in an amorphous Si solar cell for spectral upconversion. The material shows visible emissions at around 655 (red), 525, and 540 nm (green) under 980 nm illuminations. The incorporation of this UC layer in an a-Si:H solar cell resulted in an increase in short-circuit current density by 6.25. De Wild et al. [75] used β-$NaYF_4:Yb^{3+}/Er^{3+}$ UC phosphor to improve the power conversion efficiency of an a-Si:H solar cell. The upconverter powder was mixed with polymethyl methacrylate and a layer 300 μm thick was placed at the rear of an a-Si:H solar cell. They have obtained an external quantum efficiency of 0.02% at 980 nm. In addition, Er^{3+}-doped β-$NaYF_4$ powders were also applied to a-Si:H solar cell by Chen and co-workers

Table 3 Selected lanthanide-doped upconversion materials used for PV applications

Solar cell	Upconverter	Excitation wavelength	Remarks	References
a:Si	β-$NaYF_4$:Yb^{3+}, Er^{3+}	980 nm	28 mW/cm^2 EQE: 0.03% Yb^{3+} (18%):Er^{3+} (2%)	[94]
a:Si	β-$NaYF_4$:Yb^{3+}, Er^{3+}	980 nm	10 mW Enhancement in J_{sc}:10 μA/cm^2	[75]
a:Si	$NaYF_4$:Yb/Er/Gd–Au	980 nm	1100 mW EQE: 0.14% (core/shell nanostructured)	[77]
Bifacial Si	$NaYF_4$:Er^{3+}	1550 nm	200 mW/cm^2 EQE: 1%, EQE = 0.6%	[95]
Bifacial Si	$NaYF_4$:Er^{3+}	1523 nm	2.4 W/cm^2 EQE: 3.4%, IQE = 5.7%	[65]
Bifacial Si	$NaYF_4$:Er^{3+}	1523 nm	5.1 mW EQE: 2.5 $\pm$ 0.2%, IQE = 3.8%	[69]
Bifacial Si	$NaYF_4$:Er^{3+}	1522 nm	EQE = 0.34% (1090 W/m^2)	[70]
Bifacial Si	$NaYF_4$:Er^{3+}	1523 nm	EQE = 0.47%, 1629 W/m^2	[96]
C-Si	Gd_2O_3:Er^{3+}	1550 nm	Increase in photocurrent, 4% (p-type abs.)	[97]
Dye-Sensitized	α-$NaYF_4$:Yb^{3+}, Er^{3+}	Simulated solar light	100 mW/cm^2 Conv. Efficiency: 2.84%	[98]
Dye-Sensitized	Y_2O_3: Er^{3+}	980 nm	the light-to-electric energy conversion efficiency of 7.0 %	[99]
Dye-Sensitized	LaF_3:Yb^{3+}, Er^{3+}	980 nm	AM 1.5 sun, I_{SC} 2.4% increase	[82]

(continued)

Table 3 (continued)

Solar cell	Upconverter	Excitation wavelength	Remarks	References
Dye-Sensitized	$NaYF_4$:Yb^{3+}, Er^{3+}	980 nm	2.4 W, I_{SC} 11.2% increase Conv. Efficiency 10.6% increase	[100]
Dye-Sensitized	$NaYF_4$: Er^{3+}:Yb^{3+} + $NaYF_4$	976 nm	AM 1.5 sun, Over all Conv. Efficiency 11.9% increase (core-shell nanoparticles)	[101]
Dye-Sensitized	YF_3:Yb^{3+}, Er^{3+}	980 nm		[102]
Dye-Sensitized	YAG::Yb^{3+},Er^{3+}	980 nm	One order magnitude increase in external quantum efficiency	[103]
Dye-Sensitized	Lu_2O_3:Yb^{3+}, Tm^{3+}	980 nm	light-to-electric energy conversion efficiency increases by 11.1 %	[104]
Dye-Sensitized	YbF_3: Ho^{3+}	980 nm	23% enhancement in the overall conversion efficiency, 19% improvement in the photocurrent	[105]
Dye-Sensitized	Y_2O_3: Yb^{3+},Er^{3+}	1 sun	AM 1.5 PCE increment ratio: 12.4%	[106]
Perovskite	$LiYF_4$:Yb^{3+}, Er^{3+}	980 nm	6.2 W/cm^2 IQE: 5.72%	[107]
Organic (PCDTBT:PCBM)	Y_2BaZnO_5: Yb^{3+}, Ho^{3+}	986 nm	392 mW/cm^2 UC EQE: 0.0052%	[92]
InGaP	Gd_2O_2S, Y_2O_3, $NaYF_4$ Yb^{3+}, Er^{3+}	Broad illumination (890–1045 nm)	2.7 KW/m^2 Found increase in photocurrent	[108]
GaAs	$Y_6W_2O_{15}$: Yb^{3+}, Er^{3+}	973 nm	145.65 W/cm^2	[73]

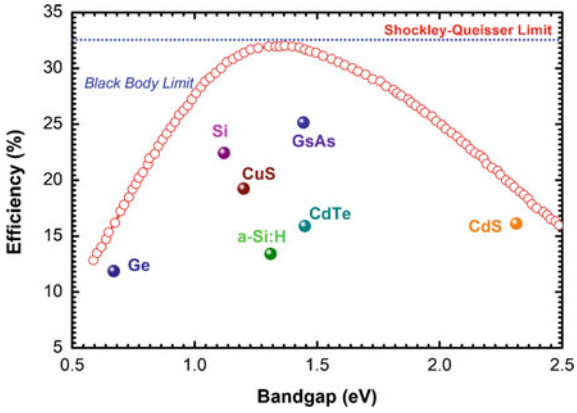

Fig. 23 Semiconductor bandgap and efficiency comparisons of different solar cell absorbers

[76]. They observed an improved current of 0.54 μA in solar cell, when illuminated with 980 and 1560 nm laser simultaneously. Recently, Li et al. [77] achieved a 72-fold enhancement in photocurrent of a a-Si:H solar cell, when $NaYF_4$:Yb^{3+}, Er^{3+}, Gd^{3+} nanorods-modified electrodes were used (980 nm excitation). Recently, our group had incorporated oxide, oxyfluoride, and fluoride UC phosphors of yttrium in a-Si:H solar cell and obtained a maximum enhancement of 7.5% in the short-circuit current density for fluoride host material [15].

The J-V characteristic curve of the solar cells with different UC phosphors based on incident intensity is shown in Fig. 24a–c. It can be seen that as the incident intensity had increased the short-circuit current density also increased. When YF_3 UC phosphor layer was incorporated in the a-Si:H solar cell, the short-circuit current density improved to 0.35 mA/cm^2 from 0.175 mA/cm^2 as the IR power increased from 17.3 to 24.8 mW. Similarly, for YOF UC layer, the J_{SC} improved to 0.235 mA/cm^2, and for Y_2O_3 UC layer, J_{SC} increased to 0.207 mA/cm^2 for the same change in the incident power Fig. 24d shown the comparison of J-V characteristics of a-Si:H solar cell with UC phosphors incorporated measured under AM1.5 G alongside with NIR illumination. Also, undoped Y_2O_3 incorporated a-Si:H solar cell was also measured under the same conditions. It was observed that the YF_3 incorporated solar cell showed an improvement of nearly 1 mA/cm^2 in short-circuit current compared to the reference cell. The superior performance of the a-Si:H with YF_3 spectral converter was attributed to high UC efficiency for the YF_3 host compared to YOF and Y_2O_3 hosts [15]. It should also be noted that solar cells with UC phosphors could larger influence in countries with direct Sun's irradiation. In addition, a holding factor of UC phosphors for solar cell application could be the nonlinear response of UC phosphors to incident intensity. However, the application of plasmonic and photonic architectures with UC phosphors can further improve the in solar cell performance.

(e) **Dye-sensitized solar cells**

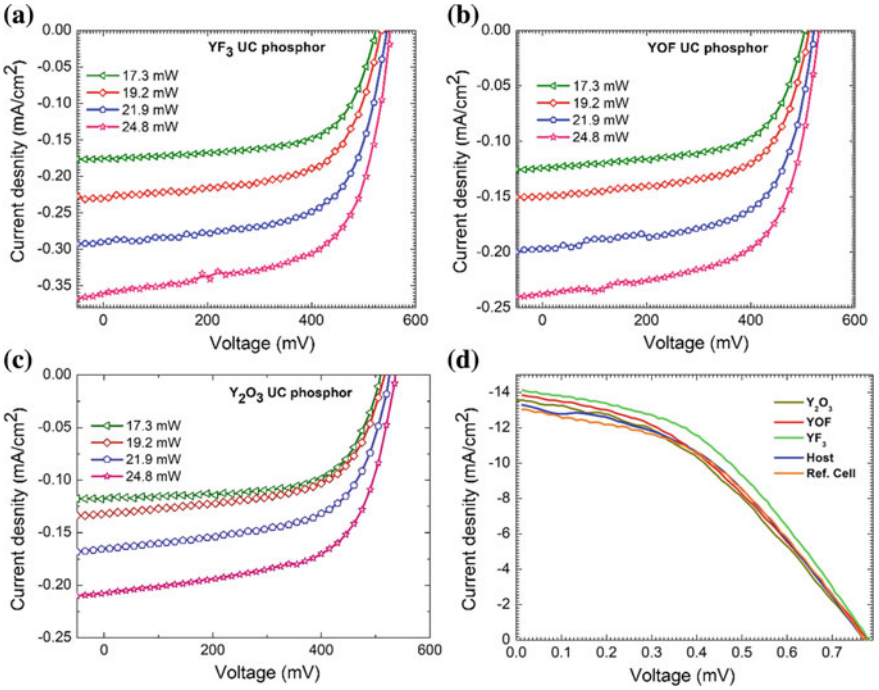

Fig. 24 J-V characteristics of a-Si:H solar cell with **a** YF_3 UC phosphor, **b** YOF UC phosphor, and **c** Y_2O_3 UC phosphor with 980 nm IR illumination. **d** J-V characteristics of a-Si:H solar cell with the three Yb^{3+}/Er^{3+} doped phosphors, undoped host material under AM 1.5 M illumination along with 980 nm NIR radiation. Reprinted with permission from [15] copyright @ 2018, Elsevier

Dye-sensitized solar cells (DSSCs) or Grätzel cell were first reported by Grätzel [78] in 1991. Because of its appealing characteristics such as low cost, ease of manufacture, eco-friendliness, semi-transparent, and flexible design, the DSSC offers an alternative idea that is technically and economically viable to today's photovoltaic intersection. A typical DSSC is composed of a porous layer of titanium dioxide nanoparticles, concealed with a molecular dye that absorbs the sunlight. However, improving the conversion efficiency of a DSSC is always a difficult job owing to the limited absorption spectrum of dyes used [79–81]. The most commonly used dyes in DSSC are ruthenium-based ones, such as N3 ($[Ru(dcbpyH_2)_2\text{-}(NCS)_2]$, $dcbpyH_2$ = 2,2′-bipyridyl-4,4′-dicarboxylic acid), N719 ($[(C_4H_9)_4N]_2[Ru(dcbpyH)_2(NCS)_2]$), and N749 ($[(C_4H_9)_4N]_3\text{-}[Ru(tcterpy)(NCS)_3]$. $3H_2O$, tcterpy = 4,4′,4″-tricarboxy-2,2′:6′,2″-terpyridine), etc., has bandgap (HOMO and LUMO) usually higher than 1.8 eV. Therefore, photons with wavelengths of less than 700 nm can only be absorbed by these cells. Most of the solar energy in the IR region is, therefore, unabsorbed. Efforts to produce panchromatic sensitizers for DSSCs have been hampered by bad injection effectiveness, and competing recombination of charges when the sensitizer's absorption spectrum is stretched to the IR region.

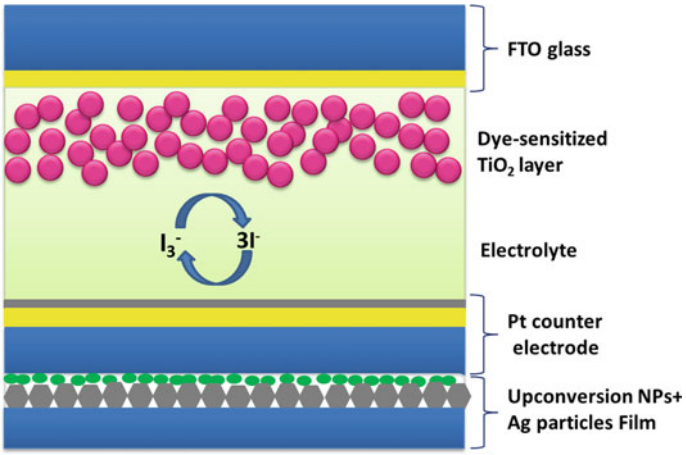

Fig. 25 A typical schematic configuration of a DSSC equipped with upconverters

Photon upconversion is an alternative approach by absorbing IR radiation and emitting high-energy photons, which in turn absorbed by the sensitizing dyes. A typical structure of a DSSC cell with upconversion phosphor is illustrated in Fig. 25.

Demopoulos et al. [82] first reported a DSSC device incorporated with lanthanide-doped UC material. They have used Yb^{3+}, Er^{3+}co-doped LaF_3-TiO_2 nanocomposites to develop the electrode structure. Under IR illumination, the upconverted phosphor incorporated DSSC device shows some response. They also deposited micro-sized β-$NaYF_4$:Yb^{3+}, Er^{3+} UC phosphors on the rear side of a counter electrode [83]. This device architecture provides a double benefit of both light reflection and NIR light harvesting. In 2012, Yuan et al. [84] used colloidal β-$NaYF_4$:2%Er^{3+}/20% Yb^{3+} nanoparticles in DSSC. The synthesized nanocolloidal particles had size less than 20 nm. Because of this, the nanoparticles could diffuse through the mesoporous TiO_2 and can effectively interact with the dyes. Later, Yang and co-workers [85] used YF_3:Yb^{3+}, Er^{3+} particles for spectral upconversion, and the power conversion efficiency was increased from 5.18 to 6.76%.

Zhang et al. [86] used core shell core-shell $NaYF_4$:Er^{3+}, Yb^{3+}/TiO_2 nanocomposite as the photo-anode. Zhao et al. [87] grown an SiO_2 layer between TiO_2 and the UCNP to prevent the recombination loss. They have obtained an improvement of 29.4% in efficiency. Demopoulos et al. [88] investigated β-$NaYF_4$:Yb^{3+}, Er^{3+}/TiO_2 submicron UC and the optimized layered DSSC structure shown a 16% relative enhancement in power conversion efficiency. Important results of UC phosphor incorporated DSSC device are summarized in Table 3.

(f) **Organic solar cells**

Because of its low price, lightweight, flexibility, and easy manufacturing methods for large-scale manufacturing, organic solar cells are regarded as one of the most

promising applicants in new generation solar cells [89, 90]. One of the major challenges of organic solar cells is the spectral mismatch of the donor organic molecule. Bulk heterojunction (BHJ) solar cells with a large HOMO-LUMO difference are able to absorb only the visible sunlight. Recently, low-bandgap polymer materials such as PCPDTBT (poly-[*N*-9′-heptadecanyl-2,7-carbazole-alt-5,5(4′,7′-di-2-thienyl-2′,1′,3′-benzothiadia-zole]) and its derivatives are utilized to enhance the spectral response of the solar cell in NIR region.

On the other hand, upconversion phosphors are more dedicated to further extending more the NIR spectral response. Wang et al. [91] demonstrated the feasibility of LaF_3:Yb^{3+}, Er^{3+}UC phosphors to improve the NIR response of P3HT:PCBM organic solar cells. Following excitation at 975 nm, an upconverted photocurrent density of ~16.5 μA/cm^2 was observed. In 2012, Wu et al. [73] applied $NaYF_4$:Yb^{3+}, Er^{3+} nanoparticles on the rear of a P3HT:PCBM organic solar cell. An increase in the short-circuit current by 0.5 μA was observed when illuminated by 980 nm laser.

Adikaari et al. [92] utilized multinary Y_2BaZnO_5:Yb^{3+}, Ho^{3+} UC phosphors in PCDTBT:PCBM organic solar cells. Under 986 nm laser illumination with an excitation density of ~390 mW/cm^2, photocurrent density of 16 μA/cm^2 was obtained. Guo et al. [93] also used a similar technique to enhance the NIR repose of polymer BHJ solar cells. They have mixed UC $NaYF_4$:Yb^{3+}, Er^{3+}phosphor along with PCDTBT:PCBM. Table 3 summarizes the major work in the application of upconversion in different types of solar cell.

6.2 Biological Applications

The extensive potential applications in the biomedical field are one of the main reasons for the exponential increase in research based on luminescent materials [109]. Recently, upconversion luminescent materials gained much attention toward biological applications because of some advantages compared to conventional luminescence materials. The main appeal toward the biological application of upconversion materials is large anti-Stoke's shift which helps to differentiate between excitation and emission wavelength, high resistance toward photobleaching, low background auto-fluorescence since biomolecules have no fluorescence with IR excitation, low toxicity to a biological system and high penetration depth. With all such advantages, upconversion luminescent nanoparticles have emerged as a new generation bio probe [110, 111]. The main challenge in the implementation of these materials as bioprobes is the lack of a general method to make water-dispersible, biocompatible, and surface-functionalized nanoparticles [109].

Currently, most of the synthesize methods of upconversion nanoparticles (UCNPs) make use of organic materials as medium and hence, the prepared particles will be capped with hydrophobic organic ligands. Suitable surface modification is necessary to obtain biocompatible UCNPs for potential biomedical applications. The particle can be made hydrophilic by coating the surface with silica, but further surface modification is required to attach functional groups on the silica surface. In most of

the cases, the surface is modified using –NH_2, –SH, and –COOH functional groups for effective bioconjugation [109]. Hydrophilic molecules like poly vinylpyrrolidone (PVP) [112, 113], polyacrylic acid (PAA) [114–116], polyethylenimine (PEI) [117], aminohexanoic acid (AA) [118, 119], and polyol [120, 121] are the common choice for surface modification since they control the growth of particle and provide the functional group for further bioconjugation. Ligand exchange [113, 122, 123], ligand attraction [124], ligand oxidation [125], layer-by-layer assembly [126], and silanization [127–129] are the commonly used methods to convert the hydrophobic nanoparticles to the hydrophilic ones. Along with such method, one can go for photosynthesis ligand oxidation with ozone [130] or ligand-free treatments [131] for surface treatment and bioconjugation [109].

In the ligand exchange method, the hydrophobic ligands on the surface of prepared nanoparticles are displaced by other polymeric molecules, which could provide a hydrophilic surface [132]. The new ligand molecules should have an affinity as strong as possible to the nanoparticle in order to quickly and effectively replace the hydrophobic original surfactant molecules [44].

Direct ligand oxidation method is the oxidation of the unsaturated carbon-carbon double bonds of the capping hydrophobic organic ligands into carboxylic acid groups to generate water-soluble UCNPs [44]. Li and co-workers [125] first demonstrated this technique by converting oleic acid capped $NaYF_4$:Yb^{3+}, Er^{3+} NPs into water-soluble ones using the Lemieux-von Rudloff reagent. The Lemieux-von Rudloff reagent would selectively oxidize a carbon-carbon double bond (R–CH = CH–R′) to carboxylic acids. The ligand oxidation method is turned very simple and easily handled for surface modification of hydrophobic nanophosphors (NPs) [130]. However, it was applicable only to ligands which contained unsaturated carbon–carbon double bond [44].

In the ligand attraction approach, the nanoparticle with a hydrophobic ligand is allowed to interact with an amphiphilic polymer. This method works based on hydrophobic–hydrophobic van der Waals interactions between the chosen amphiphilic polymers and original hydrophobic ligand, which realize the conversion of hydrophobic UCNPs to water-soluble ones.

In layer-by-layer assembly, the electrostatic attraction between oppositely charged species is used to achieve successful surface modification. Surface silanization is a powerful technique for covalent surface modification of nanoparticles. Silanization can be achieved either by treating the particle with a silane reagent to have a silane-modified surface or by treating the particle with tetraethyl orthosilicate to have a layer of silica on the surface of the particle. The resulting UCNPs were of low toxicity and can be well dispersed in aqueous solution. The silica layer will protect the UCNPs from undesired external effects such as quenching or penetrating [44].

There are many non-targeted applications of UCNPs in biological systems. Still, the biocompatible UCNPs will not have that specific functional group or biomolecules in the surfaced that can selectively recognize the analyte molecule, which limits their extensive applications as an imaging probe. Therefore, to improve selective targeting, the UCNPs are conjugated with bioactive ligand moieties, having a strong affinity to specific molecular targets in living systems. Thus, ligand-modified

UCNPs will be specifically trapped at the targeting region, and hence target-specific imaging will be possible; on the other hand, unmodified UCNPs will not have an affinity toward the target and will not accumulate during circulation. The most commonly used ligand moieties are small organic molecules, peptides, proteins, antibodies or their fragments [19].

Mader et al. [133] had tried to correlate the different possibilities of surface modification of NPs for biomedical applications and imaging. In their view, it is possible to adsorb the biomolecule on the surface of NP physically. However, the covalent linkage is preferred since desorption is not possible in this case, and hence the number and orientation of the immobilized reporter molecules can be well controlled. There is no universal method which can be adopted in any of the many applications of bioconjugated UCNP. In a covalent surface modification, carboxy, thiol, or amino groups are introduced on the surface of nanoparticles. The carboxy-modified NPs can make a carbodiimide bond with biomolecules like proteins or oligomers containing amino groups. Thiol-functionalized NPs can make a disulfide bridge with disulfide-modified oligonucleotides. Amino-modified NPs can be attached to a large variety of amino-reactive entities by forming succinimidyl esters. A schematic diagram showing a surface modification of amine-functionalized upconversion nanoparticles using different biomolecules is shown in Fig. 26 [134].

Zijlmans et al. [135] were the first to use upconversion nanoparticles for imaging applications. They imaged human prostate tissue using submicron-sized $Y_2O_2S{:}Yb^{3+}$, Tm^{3+} particles. Upon exciting with 980 nm laser, they observed low auto-fluorescence and no photobleaching even after continuous exposure. The first report on in vivo imaging applications of $NaYF_4$ UCNPs was by Chatterjee et al. [136]. They injected polyethylenimine (PEI)-functionalized UCNPs into the abdominal skin and thigh muscles of rat, and the back skin of the rat showed visible emission

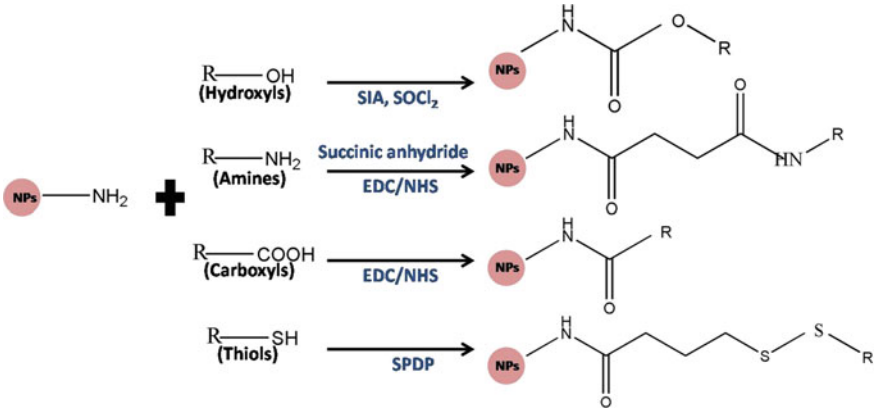

Fig. 26 Surface modification of amine-functionalized upconversion nanoparticles using different biomolecules. Reagents: succinimidyl iodoacetate (SIA), 1-ethyl-3-(3-dimethylaminopropyl) carbodiimide hydrochloride (EDC), succinimidyl ester (NHS), and N-succinimidyl 3-(2-pyridyldithio) propionate (SPDP) [134]

on 980 nm excitation. Later, Nyk et al. [137] reported the high contrast whole-body imaging using UCNPs, which was the foundation for the development in advanced whole-body imaging.

The main issue to be addressed while using rare earth-based materials for biomedical applications is the cytotoxicity. These particles can be implemented for biomedical applications only after testing the toxicity and biocompatibility. Assays like MTT (methyl thiazolyl tetrazolium) and MTS ((3-(4,5-dime-thylthiazol-2-yl)-5-(3-carboxymethoxyphenyl)-2-(4-sulfophenyl)-2H-tetrazolium, sodium salts)) can be used to test cytotoxicity of UCNPs. The studies show that within a limited incubation time, UCNPs are not cytotoxic. The in vivo cytotoxicity of UCNPs was also studied for its advanced biomedical applications. Zhao et al. [138] evaluated in vivo toxic effects and found that the survival rate of mice after thirty days was 100% for Gd/Mn-doped UCNPs. It is also possible to develop luminescent nanoparticles of biocompatible host material for future biomedical applications. Hydroxyapatite and fluorapatite are excellent biomaterials with good biocompatibility [139].

Nyk et al. [137] used $NaYF_4$:Tm^{3+}, Yb^{3+} for in vitro and in vivo bioimaging using 975 nm excitation source. The emission they used for imaging was at 800 nm since both the emission and excitation wavelengths are in the NIR range, and they obtained remarkably high optical contrast because of the absence of auto-fluorescence and decreased light scattering. Cellular imaging was done using human pancreatic cells, for which cells were cultured in essential media and UCNPs were introduced to it. The UCNPs were also used for whole-body imaging of mice, and the signal was readily detectable through the skin. The in vivo and in vitro images obtained by Nyk et al. [137] using UCNP are shown in Fig. 27.

In 2011, cancer cell imaging and therapy using UCNPs were reported by Wang et al. PEGylated (poly (ethylene glycol)) UCNPs were synthesized and loaded

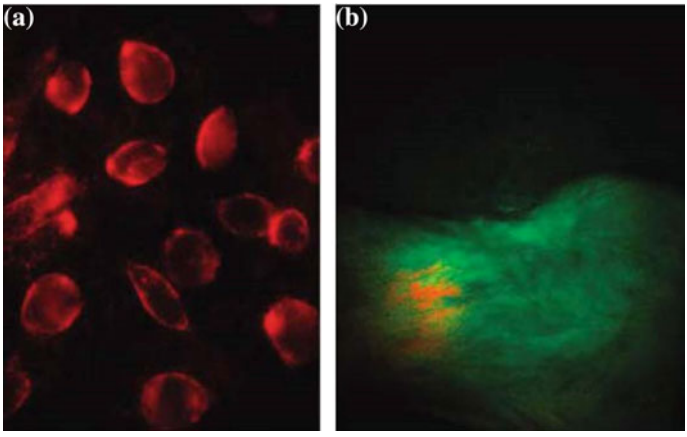

Fig. 27 **a** In vitro cell imaging and **b** in vivo imaging of mouse using UCNPs where red color indicates emission from UCNPs. Reprinted (adapted) with permission from [137] Copyright @ 2008, American Chemical Society

with a chemotherapy molecule, doxorubicin (DOX). The drug released is based on pH-dependent mechanism. Folic acid-modified UCNP was used for targeted drug delivery [140].

Cheng and others [141] synthesized multifunctional Gd^{3+} doped $NaYF_4$ UCNPs, which can be used for imaging and photo thermal therapy. The UCNPs is having ultra-small superparamagnetic Fe_2O_3 on its surface, a thin layer of gold on top and further functionalized with PEG. The surface plasmon resonance absorption and the consequent heat produced by gold shell have been utilized for photothermal ablation of cancer cells. Dual modal imaging, which contains luminescence imaging and magnetic resonance imaging with the particle, was further demonstrated with in vivo animal imaging experiments. Such UCNPs can be effectively used for multimodality imaging. Gd^{3+}-doped UCNPs can be extensively used for magnetic resonance imaging (MRI), photoinduced emission tomography (PET), and computed tomography (CT) imaging.

Hollow mesoporous luminescence materials are attractive due to its multifunctional capabilities like imaging, targeted diagnosis, and drug delivery. In 2013, Yang et al. [142] synthesized hollow $NaYF_4$:Er^{3+}, Yb^{3+}nanospheres and used for carrying the anti-cancer drug doxorubicin. Folic acid-modified UCNP could be selectively uptaken by cancer cell through receptor-mediated endocytosis and release the drug inside the cell (Fig. 28). There are several reports based on porous upconversion nanoparticles [143, 144]. A novel aptamer-guided nano drug carrier based on the mesoporous metal-organic framework shell and upconversion luminescent $NaYF_4$:Yb^{3+}/Er^{3+} core was reported by Deng et al. [145] in 2015. Such organic-inorganic hybrid materials can be effectively used for targeted imaging and drug delivery. There are different varieties of core-shell

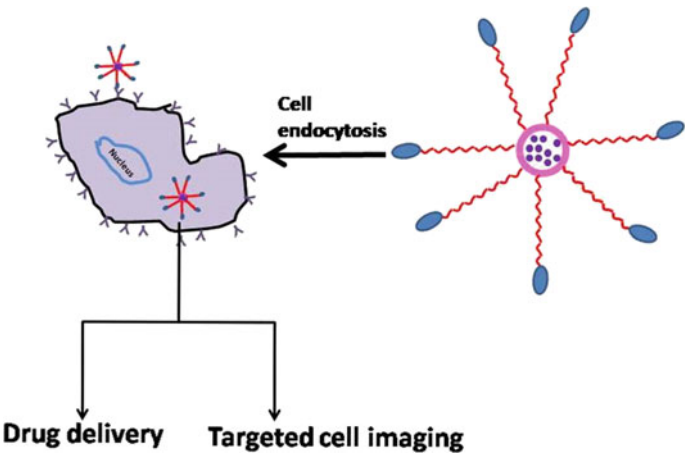

Fig. 28 Schematic diagram of showing multifunctionality of porous UCNP in the diseased cell [142]

nanoparticles designed and studied for imaging applications. For example, core-shell structure $NaYF_4:Yb^{3+}:Er^{3+}/NaYF_4:Yb^{3+}/NaNdF_4:Yb^{3+}/NaYF_4/NaGdF_4$ with $NaYF_4:Yb^{3+}:Er^{3+}$ core and four outer shells can be designed for multimodal imaging, and the shell structure will help to avoid back energy transfer between the Er^{3+} and Yb^{3+}centers. Furthermore, the undoped outer shell could reduce the quenching due to surface states [146].

Förster resonance energy transfer or fluorescence resonance energy transfer (FRET) is a non-radiative process in which electron excitation energy from a chromophore is transferred to a nearby acceptor material like metal nanoparticles through long-range dipole-dipole interaction. FRET-based biodetection has gained much attention in the previous years. A UCNPs-based FRET system can be developed for avidin detection in which amino-functionalized $NaYF_4:Er^{3+}$, Yb^{3+} conjugated with biotin as a donor and biotin-modified gold nanoparticles as acceptor. The specific binding between avidin and biotin is used for detection. The luminescence intensity of UCNP will decrease with increasing avidin concentration, and hence, the concentration of avidin can be found out from the linear relationship between fluorescence intensity and avidin concentration [126]. Schematic diagram of analyte detection using FRET sensor is shown in Fig. 29.

Chen and co-workers [125] used water-soluble and carboxylic acid-functionalized UCNPs for DNA detection. The carboxyl functionalized the particles with were further modified with streptavidin, carboxyl group on UCNPs form of amide bonds with streptavidin. In the sensor, they had used two small oligonucleotides to detect a longer target oligonucleotide. One of the short oligonucleotides, DNA 1, is linked to biotin and the other DNA 2 to TAMRA (*N*,*N*,*N*′,*N*′-tetramethyl-6-carboxyrhodamine) whose excitation spectrum overlaps with the green emission of UCNPs. TAMRA can absorb the emission from UCNPs when they are in close proximity. In the absence of a target, DNA 1 and DNA 2 are far apart and UCNPs emission can observe because non-radiative energy transfer from UCNP to TAMRA is negligible. By the addition

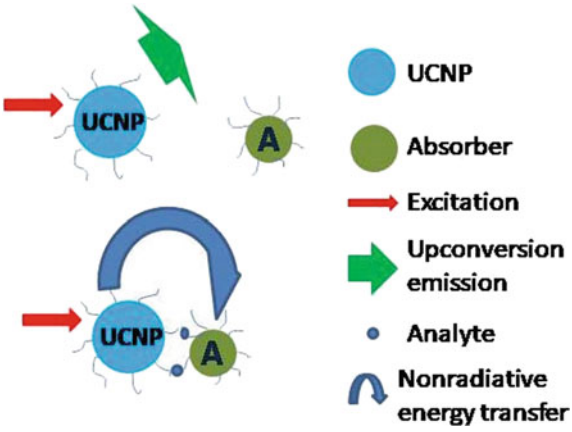

Fig. 29 Analyte detection using FRET-based energy transfer

of target DNA, the UNCP and TAMRA will be in close proximity, and hence, the emission will be quenched.

Even though the biological applications of these particles are widely studied and highly progressed, there exist much more challenges yet to be addressed. Since the f–f transitions are forbidden in RE^{3+} ions, the absorption cross-section of UCNPs will be very less, and lasers are usually required to have intense emission. Improvement in UC emission behaviour is always required. During the preparation of smaller particle, the defects will be higher, which will decrease luminescence. More defect-free methods are required for the production of better particles with good emission. The surface modification will further reduce the emission. Hence, synthesis methods have to be developed in which surface modification is less required [147].

The main challenge in biological application of these particles is the narrow excitation wavelength tunability. 980 nm excitation used most commonly is highly absorbed by water in the tissue, which will cause tissue heating. New strategies have to be developed to overcome such difficulties for better imaging using UCNPs [148, 149].

6.3 Upconversion in Security Applications

Security printing is a major concern in today's world, where it is significant for corporate, federal, and state organizations [150]. It is widely used for document authentication, counterfeit applications, labels for products, etc. Within the security printing sector, a plethora of technical techniques implemented, including watermarks, intaglio printing, microprinting, and fluorescent ink printing [151]. Most of the photoluminescent products presently used in security applications are based on luminescence downconversion for which excitation of short wavelength generates emission of long wavelengths. UV excitations are used to read these downconversion printings. UCNP inks are considered as the next-generation luminescent security inks. Fabrication of luminescence inks with stability, good dispersion of nanomaterials in the ink medium, high UC luminescence intensity, the convenience of printing, adhesiveness to various surfaces, and low cost are important for its commercial application. The appropriate choice of ink medium is an important aspect for the fabrication of luminescent inks in which the luminescent nanomaterials can be dispersed homogeneously and consequently form colloidal suspensions without forming any cluster or settling down at the bottom. Some of the reports on UC inks are reviewed below.

Photolithographic patterns of α-$NaYF_4$:Yb^{3+}, Er^{3+} (green) and α-$NaYF_4$:Yb^{3+}, Tm^{3+} (blue) upconversion nanophosphors have been produced by Anh and et al. [21]. Later, Blumenthal et al. [152] demonstrated that covert, monochrome luminescent upconversion patterns could be generated with high resolution in a one-step printing process using inks activated with β-$NaYF_4$:17% Yb^{3+}, 3% Er^{3+} nanocrystals. The UC ink has toluene as the ink medium and 2 wt% of upconversion nanoparticles, oleic acid as a capping agent, and polymethyl methacrylate (PMMA) as a binding

agent along with enough methyl benzoate. They had printed these upconversion ink using both direct-write printing and screen printing technique. These printed features are invisible in normal light, but they can be easily seen by the naked eye when these printed objects are excited under the light of 980 nm wavelength. Meruga et al. [153] created RGB additive-color printing system that produces extremely resolved pre-defined patterns that are invisible beneath close lighting, however that is seeable as light multicolor pictures beneath NIR excitation. The patterns are generated by freelance deposition of the primary colours (red, green, and blue) upconversion inks exploiting an Optomec Aerosol Jet® direct writing printer. The red, green, and blue inks are activated with β-$NaYF_4$:10% Er^{3+}, 2% Tm^{3+}, β-$NaYF_4$:17% Yb^{3+}, 3% Er^{3+} and β-$NaYF_4$:25% Yb^{3+}, 0.3% Tm^{3+} nanocrystals, respectively. The primary colour inks are written as isolated and overlapping options to supply pictures that at the same time emit red, green, blue, cyan, magenta, yellow, and white upconversion luminescence once excited employing a single NIR supply. The ink was made by dissolving UCNP in PMMA solution (Fig. 30).

Meruga et al. [154] used inks comprised of Yb^{3+}/Er^{3+}- and $Yb^{3+/}Tm^{3+}$-doped $NaYF_4$ nanoparticles capped with oleic acid in toluene and methyl benzoate with poly(methyl methacrylate) (PMMA) as the binding agent was used to print quick response (QR) codes. Wang et al. [155] demonstrated the detection of fingerprints over various surfaces which are stained with $NaYF_4$:Yb^{3+}, Er^{3+} UC phosphor. Zhang et al. [156] reported the use of multicolour emitting UC β-NaF_4 micro-rods for anti-counterfeiting application. Later, You et al. [157] demonstrated the use of both

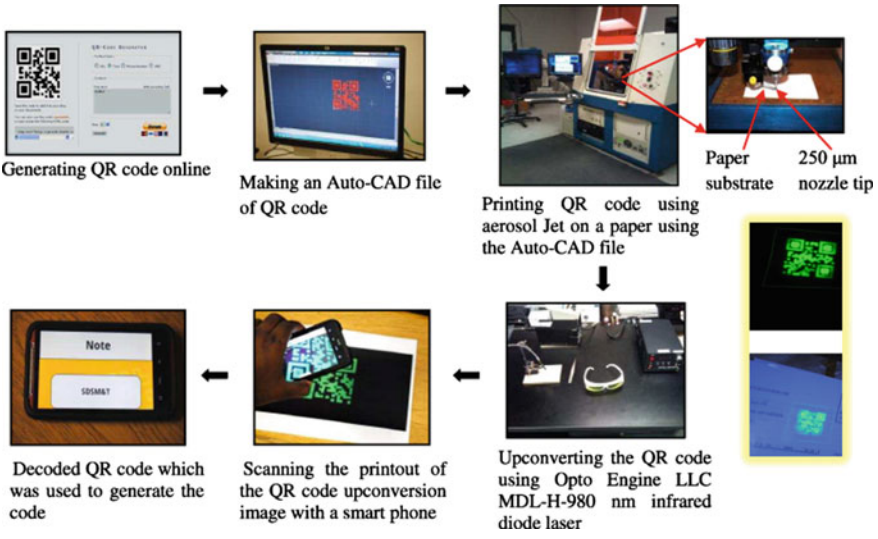

Fig. 30 Photographs of different step involving in the printing of UC security ink QR code and the printed QR code prototype. Reprinted with permission from [154] Copyright © IOP Publishing, 2012. All rights reserved

hydrophobic and hydrophilic UC phosphors for anti-counterfeiting and produce patterns with simple inkjet printing. Sangeetha et al. [158] presented three-dimensional (3D) QR codes which were formed using upconversion nanophosphors by atomic force microscopy (AFM) nanoxerography. In another interesting study, Ramos et al. [159] suggested 3D security ink stamps or fluorescent labels for visual identification of orthodontic adhesives, which exhibit visible luminescence upon infrared light. Another interesting result was reported by Barideet al. [150], and they fabricated NIR-to-NIR upconversion security inks based on Yb^{3+}/Tm^{3+}-doped β-$NaYF_4$ nanophosphors. The printed QR codes were invisible under ambient conditions, and the NIR luminescent images (800 nm) of QR codes could be easily captured by using a CCD camera. Yao et al. [160] synthesized core-triple-shell Ln^{3+} ions doped $NaYF_4$ and developed colloidal suspension for screen printing. The screen-printed patterns show multicolour display under 980 and 808 nm excitations. One of the main questions that needs to be addressed is the readability of these UC inks. Generally, high-power laser is used to demonstrate UC ink-printed images or counterfeit applications. Development of high-efficiency UC inks and UC ink based on water is necessary for commercial applications. Nowadays, many works are going on to develop stable ink with upconversion nanophosphors with water as the dispersion medium and can use in inkjet printers [161]. Recently, Liu et al. [162] reported high-resolution images printed using luminescence ink. They have incorporated the upconversion phosphors in plasmonic nanoresonators for tunable color emission. The outstanding optical properties of upconversion nanophosphors over pigments and dyes, like high photo- and thermal stability, less toxicity and chemical stability make them a possible replacement for the conventional security inks. These upconversion inks were demonstrated printing on various substrates also.

7 Conclusions

In this review, fundamentals for upconversion luminescent materials as spectral converters are presented. These materials have promising applications in solar cells, disease diagnosis, and security printing. The challenge in designing solar cell devices is to minimize energy losses due to the spectral mismatch between the absorption spectrum of solar cell and incident solar spectrum. To make use of the complete solar spectrum, upconversion, quantum cutting, and downshifting luminescent materials have to be used. Even though these methods are in the infancy stage, these materials will be useful as spectral converters to reduce the spectral mismatch losses and, consequently, boost the efficiency of solar cells. Using upconversion phosphors can harvest the sub-bandgap sunlight. Proof-of-concept experiments have been widely performed for Er^{3+}-doped upconverters (for c-Si solar cells) and Ln^{3+}–Yb^{3+} (Ln = Er, Tm, and Ho) co-doped upconverters (for wide bandgap solar cells). However, there are two major drawbacks associated with this approach that currently limit the practical application of upconverters for solar cells. First, the efficiency of current Ln^{3+}-doped upconverters investigated for solar cells is generally low (less than 3%).

The upconversion efficiency may be enhanced by using plasmonic resonance or photonic crystals. High excitation density can lead to high upconversion efficiency, but it will require concentrated sunlight. The challenge in biomedical applications of UCNP is the proper surface modification. Even though the IR excitation has high tissue penetration, the absorption of IR by water has to be addressed. These materials have to be explored more in the security printing aspect as well.

References

1. Kumar P, Singh S, Gupta BK (2016) Future prospects of luminescent nanomaterial based security inks: from synthesis to anti-counterfeiting applications. Nanoscale 8:14297–14340. https://doi.org/10.1039/C5NR06965C
2. Armaroli N, Bolink HJ (2016) Luminescence: the never-ending story. Top Curr Chem 374:44. https://doi.org/10.1007/s41061-016-0044-0
3. Stokes GG (1852) On the change of refrangibility of light. Philos Trans R Soc London 142:463–562. https://doi.org/10.1098/rstl.1852.0022
4. Valeur B, Berberan-Santos MN (2011) A brief history of fluorescence and phosphorescence before the emergence of quantum theory. J Chem Educ 88:731–738. https://doi.org/10.1021/ed100182h
5. Grosse RL (2002) Handbook of Raman spectroscopy: from the research laboratory to the process line. J Am Chem Soc 124:5601–5602. https://doi.org/10.1021/ja015342z
6. Göppert-Mayer M (1931) Über elementarakte mit zwei quantensprüngen. Ann Phys 401:273–294. https://doi.org/10.1002/andp.19314010303
7. Kaiser W, Garrett CGB (1961) Two-photon excitation in CaF_2:Eu^{2+}. Phys Rev Lett 7:229–231. https://doi.org/10.1103/physrevlett.7.229
8. Shen YR (2003) Surface second harmonic generation: a new technique for surface studies. Annu Rev Mater Sci 16:69–86. https://doi.org/10.1146/annurev.ms.16.080186.000441
9. Franken PA, Hill AE, Peters CW, Weinreich G (1961) Generation of optical harmonics. Phys Rev Lett 7:118–119. https://doi.org/10.1103/PhysRevLett.7.118
10. Downing E, Hesselink L, Ralston J, Macfarlane R (1996) A three-color, solid-state, three-dimensional display. Science 273:1185–1189. https://doi.org/10.1126/science.273.5279.1185
11. Scheps R (1996) Upconversion laser processes. Prog Quantum Electron 20:271–358. https://doi.org/10.1016/0079-6727(95)00007-0
12. Schulze TF, Czolk J, Cheng Y, Fückel B, MacQueen RW, Khoury T, Crossley MJ, Stannowski B, Lips K, Lemmer U, Colsmann A, Schmidt TW (2012) Efficiency enhancement of organic and thin-film silicon solar cells with photochemical upconversion. J Phys Chem C 116:22794–22801. https://doi.org/10.1021/jp309636m
13. Xie G, Lin J, Wu J, Lan Z, Li Q, Xiao Y, Yue G, Yue H, Huang M (2011) Application of upconversion luminescence in dye-sensitized solar cells. Chinese Sci Bull 56:96–101. https://doi.org/10.1007/s11434-010-4115-2
14. van Sark WG, de Wild J, Rath JK, Meijerink A, Schropp RE (2013) Upconversion in solar cells. Nanoscale Res Lett 8:81. https://doi.org/10.1186/1556-276X-8-81
15. Markose KK, Anjana R, Antony A, Jayaraj MK (2018) Synthesis of Yb^{3+}/Er^{3+} co-doped Y_2O_3, YOF and YF_3 UC phosphors and their application in solar cell for sub-bandgap photon harvesting. J Lumin 204:448–456. https://doi.org/10.1016/j.jlumin.2018.08.005
16. Pelc JS, Zhang Q, Phillips CR, Yu L, Yamamoto Y, Fejer MM (2012) Cascaded frequency upconversion for high-speed single-photon detection at 1550 nm. Opt Lett 37:476. https://doi.org/10.1364/OL.37.000476
17. Strickler JH, Webb WW (1991) Three-dimensional optical data storage in refractive media by two-photon point excitation. Opt Lett 16:1780. https://doi.org/10.1364/OL.16.001780

18. Cohen BE (2010) Beyond fluorescence. Nature 467:407–408. https://doi.org/10.1038/467407a
19. Min Y, Li J, Liu F, Padmanabhan P, Yeow E, Xing B (2014) Recent advance of biological molecular imaging based on lanthanide-doped upconversion-luminescent nanomaterials. Nanomaterials 4:129–154. https://doi.org/10.3390/nano4010129
20. van der Ende BM, Aarts L, Meijerink A (2009) Lanthanide ions as spectral converters for solar cells. Phys Chem Chem Phys 11:11081–11095. https://doi.org/10.1039/b913877c
21. Anh TK, Loc DX, Huong TT, Vu N, Minh LQ (2011) Luminescent nanomaterials containing rare earth ions for security printing. Int J Nanotechnol 8:335. https://doi.org/10.1504/IJNT.2011.038210
22. Bloembergen N (1959) Solid state infrared quantum counters. Phys Rev Lett 2:84–85. https://doi.org/10.1103/PhysRevLett.2.84
23. Singh-Rachford TN, Castellano FN (2010) Photon upconversion based on sensitized triplet–triplet annihilation. Coord Chem Rev 254:2560–2573. https://doi.org/10.1016/j.ccr.2010.01.003
24. Weingarten DH, LaCount MD, van de Lagemaat J, Rumbles G, Lusk MT, Shaheen SE (2017) Experimental demonstration of photon upconversion via cooperative energy pooling. Nat Commun 8:14808. https://doi.org/10.1038/ncomms14808
25. Chan EM (2015) Combinatorial approaches for developing upconverting nanomaterials: high-throughput screening, modeling, and applications. Chem Soc Rev 44:1653–1679. https://doi.org/10.1039/C4CS00205A
26. Suijver JF (2007) Upconversion phosphors. In: Ronda C (ed) Luminescence. Wiley-VCH Verlag GmbH & Co. KGaA, Weinheim, Germany, pp 133–177
27. Jacobs RR, Krupke WF, Weber MJ (1978) Measurement of excited-state-absorption loss for Ce^{3+} in $Y_3Al_5O_{12}$ and implications for tunable $5d \rightarrow 4f$ rare-earth lasers. Appl Phys Lett 33:410–412. https://doi.org/10.1063/1.90395
28. Koepke C, Wojtowicz AJ, Lempicki A (1993) Excited-state absorption in excimer-pumped $CaWO_4$ crystals. J Lumin 54:345–355. https://doi.org/10.1016/0022-2313(93)90003-6
29. Kuleshov NV, Shcherbitsky VG, Mikhailov VP, Kück S, Koetke J, Petermann K, Huber G (1997) Spectroscopy and excited-state absorption of Ni^{2+}-doped $MgAl_2O_4$. J Lumin 71:265–268. https://doi.org/10.1016/S0022-2313(96)00284-0
30. Petermann K, Clausen R, Heumann E, Ledig M (1989) Time-resolved excited-state absorption of Mn^{2+}:$MgAl_2O_4$. In: Advanced solid state lasers. OSA, Washington, DC, p FF6
31. Auzel FF (2004) Upconversion and anti-stokes processes with f and d ions in solids. Chem Rev 104:139–173. https://doi.org/10.1021/cr020357g
32. Chen G, Ohulchanskyy TY, Kachynski A, Ågren H, Prasad PN (2011) Intense visible and near-infrared upconversion photoluminescence in colloidal $LiYF_4$:Er^{3+} nanocrystals under excitation at 1490 nm. ACS Nano 5:4981–4986. https://doi.org/10.1021/nn201083j
33. Chen D, Lei L, Yang A, Wang Z, Wang Y (2012) Ultra-broadband near-infrared excitable upconversion core/shell nanocrystals. Chem Commun 48:5898. https://doi.org/10.1039/c2cc32102e
34. Chen G, Ohulchanskyy TY, Liu S, Law W-C, Wu F, Swihart MT, Ågren H, Prasad PN (2012) Core/Shell $NaGdF_4$: Nd^{3+}/$NaGdF_4$ nanocrystals with efficient near-infrared to near-infrared downconversion photoluminescence for bioimaging applications. ACS Nano 6:2969–2977. https://doi.org/10.1021/nn2042362
35. Rakov N, Maciel GS, Sundheimer ML, de S. Menezes L, Gomes ASL, Messaddeq Y, Cassanjes FC, Poirier G, Ribeiro SJL (2002) Blue upconversion enhancement by a factor of 200 in Tm^{3+}-doped tellurite glass by codoping with Nd^{3+} ions. J Appl Phys 92:6337–6339. https://doi.org/10.1063/1.1515376
36. Wang L, Qin W, Liu Z, Zhao D, Qin G, Di W, He C (2012) Improved 800 nm emission of Tm^{3+} sensitized by Yb^{3+} and Ho^{3+} in β-$NaYF_4$ nanocrystals under 980 nm excitation. Opt Express 20:7602. https://doi.org/10.1364/OE.20.007602
37. Chen D, Liu L, Huang P, Ding M, Zhong J, Ji Z (2015) Nd^{3+}-sensitized Ho^{3+} single-band red upconversion luminescence in core-shell nanoarchitecture. J Phys Chem Lett 6:2833–2840. https://doi.org/10.1021/acs.jpclett.5b01180

38. Xue M, Zhu X, Qiu X, Gu Y, Feng W, Li F (2016) Highly enhanced cooperative upconversion luminescence through energy transfer optimization and quenching protection. ACS Appl Mater Interfaces 8:17894–17901. https://doi.org/10.1021/acsami.6b05609
39. Xiang G, Ma Y, Liu W, Wang J, Gu Z, Jin Y, Jiang S, Luo X, Li L, Zhou X, Luo Y, Zhang J (2017) Enhancement of Eu^{3+} red upconversion in Lu_2O_3:Yb^{3+}/Eu^{3+} Powders under the assistance of bridging function originated from Ho^{3+} Tridoping. Inorg Chem 56:13955–13961. https://doi.org/10.1021/acs.inorgchem.7b02086
40. Zhang QY, Yang GF, Jiang ZH (2007) Cooperative downconversion in $GdAl_3(BO_3)_4$:RE^{3+}, Yb^{3+}(RE = Pr, Tb, and Tm). Appl Phys Lett 91:51903. https://doi.org/10.1063/1.2757595
41. Wei W, Zhang Y, Chen R, Goggi J, Ren N, Huang L, Bhakoo KK, Sun H, Tan TTY (2014) Cross relaxation induced pure red upconversion in activator- and sensitizer-rich lanthanide nanoparticles. Chem Mater 26:5183–5186. https://doi.org/10.1021/cm5022382
42. Joubert M-F (1999) Photon avalanche upconversion in rare earth laser materials. Opt Mater (Amst) 11:181–203. https://doi.org/10.1016/S0925-3467(98)00043-3
43. Wang F, Deng R, Wang J, Wang Q, Han Y, Zhu H, Chen X, Liu X (2011) Tuning upconversion through energy migration in core–shell nanoparticles. Nat Mater 10:968–973. https://doi.org/10.1038/nmat3149
44. Zhang F (2015) General introduction to upconversion luminescence materials. In: Zhang F (ed) Photon upconversion nanomaterials. Springer, Berlin, pp 1–20
45. Atwood DA, Hanusa TP, Lukehart CM, Messerschmidt A, Scott RA (2012) The rare earth elements: fundamentals and applications
46. Henderson B, Imbusch GF (2006) Optical spectroscopy of inorganic solids. Oxford University Press, Oxford
47. Garcia D, Faucher M (1995) Chapter 144: Crystal field in non-metallic (rare earth) compounds. In: Handbook on the physics and chemistry of rare earths. Elsevier, Amsterdam, pp 263–304
48. Dieke GH (1970) Spectra and energy levels of rare earth ions in crystals. Am J Phys 38:399–400. https://doi.org/10.1119/1.1976350
49. Ogasawara K, Watanabe S, Sakai Y, Toyoshima H, Ishii T, Brik MG, Tanaka I (2004) Calculations of complete $4f^n$ and $4f^{n-1}$ $5d^1$ energy level schemes of free trivalent rare-earth ions. Jpn J Appl Phys 43:L611–L613. https://doi.org/10.1143/JJAP.43.L611
50. Schuurmans MFH, van Dijk JMF (1984) On radiative and non-radiative decay times in the weak coupling limit. Phys B + C 123:131–155. https://doi.org/10.1016/0378-4363(84)90117-7
51. van Dijk JMF, Schuurmans MFH (1983) On the nonradiative and radiative decay rates and a modified exponential energy gap law for $4f$–$4f$ transitions in rare-earth ions. J Chem Phys 78:5317–5323. https://doi.org/10.1063/1.445485
52. Anjana R, Jayaraj MK, Yadav AK, Jha SN, Bhattacharyya D (2018) Investigating the evolution of local structure around Er and Yb in ZnO:Er and ZnO:Er, Yb on annealing using X-ray absorption spectroscopy. J Appl Phys 123:153102. https://doi.org/10.1063/1.5022638
53. Heer S, Kömpe K, Güdel H-U, Haase M (2004) Highly efficient multicolour upconversion emission in transparent colloids of lanthanide-doped $NaYF_4$ nanocrystals. Adv Mater 16:2102–2105. https://doi.org/10.1002/adma.200400772
54. Patra A, Friend CS, Kapoor R, Prasad PN (2002) Upconversion in Er^{3+}:ZrO_2 nanocrystals. J Phys Chem B 106:1909–1912. https://doi.org/10.1021/jp013576z
55. Yao L, Li Y, Xu D, Lin H, Peng Y, Yang S, Zhang Y (2019) Simultaneous enhancement of upconversion luminescence and thermometric property of upconversion nanoparticles by tuning crystal field. J Lumin 211:144–149. https://doi.org/10.1016/j.jlumin.2019.03.030
56. Gamelin DR, Güdel HU (2000) Design of luminescent inorganic materials: new photophysical processes studied by optical spectroscopy. Acc Chem Res 33:235–242. https://doi.org/10.1021/ar990102y
57. Gamelin DR, Gudel HU (1999) Spectroscopy and dynamics of Re^{4+} near-IR-to-visible luminescence upconversion. Inorg Chem 38:5154–5164. https://doi.org/10.1021/ic990556r
58. Anjana R, Subha PP, Kurias MK, Jayaraj MK (2018) Enhanced green upconversion luminescence in ZnO:Er^{3+}, Yb^{3+} on Mo^{6+} co-doping for temperature sensor application. Methods Appl Fluoresc 6:1–8. https://doi.org/10.1088/2050-6120/aa9c13

59. Chapin DM, Fuller CS, Pearson GL (1954) A new silicon p-n junction photocell for converting solar radiation into electrical power. J Appl Phys 25:676–677. https://doi.org/10.1063/1.1721711
60. Song T, Chen Q, Zhou H, Jiang C, Wang H, Yang M, Liu Y (2015) Perovskite solar cells: film formation and properties. J Mater Chem A Mater Energy Sustain 3:1–19. https://doi.org/10.1039/c4ta05246c
61. Shockley W, Queisser HJ (1961) Detailed balance limit of efficiency of p-n junction solar cells. J Appl Phys 32:510. https://doi.org/10.1063/1.1736034
62. Wolf M (1960) Limitations and possibilities for improvement of photovoltaic solar energy converters: Part I: considerations for earth's surface operation. Proc IRE 48:1246–1263. https://doi.org/10.1109/JRPROC.1960.287647
63. Trupke T, Green MA, Würfel P (2002) Improving solar cell efficiencies by up-conversion of sub-band-gap light. J Appl Phys 92:4117. https://doi.org/10.1063/1.1505677
64. Gibart P, Auzel F, Guillaume JC, Zahraman K (1996) Below band-gap IR response of substrate-free GaAs solar cells using two-photon up-conversion. Jpn J Appl Phys Part 1 Regul Pap Short Notes Rev Pap 35:4401–4402. https://doi.org/10.1143/jjap.35.4401
65. Richards BS, Shalav A (2007) Enhancing the near-infrared spectral response of silicon optoelectronic devices via up-conversion. IEEE Trans Electron Devices 54:2679–2684. https://doi.org/10.1109/TED.2007.903197
66. Struempel C, McCann M, Cañizo C, Tobias I, Fath P (2005) Erbium-doped up-converters of silicon solar cells: assessment of the potential. In: Proceedings of the 20th European photovoltaic solar energy conference, pp 43–46
67. Badescu V, Badescu AM (2009) Improved model for solar cells with up-conversion of low-energy photons. Renew Energy 34:1538–1544. https://doi.org/10.1016/j.renene.2008.11.006
68. Atre AC, Dionne JA (2011) Realistic upconverter-enhanced solar cells with non-ideal absorption and recombination efficiencies. J Appl Phys 110:034505. https://doi.org/10.1063/1.3610522
69. Shalav A, Richards BS, Trupke T, Krämer KW, Güdel HU (2005) Application of $NaYF_4:Er^{3+}$ up-converting phosphors for enhanced near-infrared silicon solar cell response. Appl Phys Lett 86:013505. https://doi.org/10.1063/1.1844592
70. Fischer S, Goldschmidt JC, Löper P, Bauer GH, Brüggemann R, Krämer K, Biner D, Hermle M, Glunz SW (2010) Enhancement of silicon solar cell efficiency by upconversion: optical and electrical characterization. J Appl Phys 108:044912. https://doi.org/10.1063/1.3478742
71. Lahoz F (2008) Ho^{3+}-doped nanophase glass ceramics for efficiency enhancement in silicon solar cells. Opt Lett 33:2982–2984. https://doi.org/10.1364/OL.33.002982
72. Lahoz F, Pérez-Rodríguez C, Hernández S, Martín I, Lavín V, Rodríguez-Mendoza UR (2011) Upconversion mechanisms in rare-earth doped glasses to improve the efficiency of silicon solar cells. Sol Energy Mater Sol Cells 95:1671–1677. https://doi.org/10.1016/j.solmat.2011.01.027
73. Lin H-Y, Chen H-N, Wu T-H, Wu C-S, Su Y-K, Chu S-Y (2012) Investigation of green up-conversion behavior in $Y_6W_2O_{15}:Yb^{3+}$, Er^{3+} phosphor and its verification in 973 nm laser-driven GaAs solar cell. J Am Ceram Soc 95:3172–3179. https://doi.org/10.1111/j.1551-2916.2012.05281.x
74. Zhang H, Xu D, Huang Y, Duan X (2011) Highly spectral dependent enhancement of upconversion emission with sputtered gold island films. Chem Commun 47:979–981. https://doi.org/10.1039/C0CC03566A
75. De Wild J, Meijerink A, Rath JK, Van Sark WGJHM, Schropp REI (2010) Towards upconversion for amorphous silicon solar cells. Sol Energy Mater Sol Cells 94:1919–1922. https://doi.org/10.1016/j.solmat.2010.06.006
76. Chen Y, He W, Jiao Y, Wang H, Hao X, Lu J, Yang S (2012) β-$NaYF_4:Er^{3+}$ (10%) microprisms for the enhancement of a-Si: H solar cell near-infrared responses. J Lumin 132:2247–2250. https://doi.org/10.1016/j.jlumin.2012.04.011

77. Li ZQ, Li XD, Liu QQ, Chen XH, Sun Z, Liu C, Ye XJ, Huang SM (2012) Core/shell structured $NaYF_4:Yb^{3+}/Er^{3+}/Gd^{+3}$ nanorods with Au nanoparticles or shells for flexible amorphous silicon solar cells. Nanotechnology 23:025402. https://doi.org/10.1088/0957-4484/23/2/025402
78. O'Regan B, Grätzel M (1991) A low-cost, high-efficiency solar cell based on dye-sensitized colloidal TiO_2 films. Nature 353:737–740. https://doi.org/10.1038/353737a0
79. Bisquert J (2011) Dilemmas of dye-sensitized solar cells. Chem Phys Chem 12:1633–1636. https://doi.org/10.1002/cphc.201100248
80. Grätzel M (2003) Dye-sensitized solar cells. J Photo chem Photobiol C Photochem Rev 4:145–153. https://doi.org/10.1016/S1389-5567(03)00026-1
81. Chen C-Y, Wang M, Li J-Y, Pootrakulchote N, Alibabaei L, Ngoc-le C, Decoppet J-D, Tsai J-H, Grätzel C, Wu C-G, Zakeeruddin SM, Grätzel M (2009) Highly efficient light-harvesting ruthenium sensitizer for thin-film dye-sensitized solar cells. ACS Nano 3:3103–3109. https://doi.org/10.1021/nn900756s
82. Shan GB, Demopoulos GP (2010) Near-infrared sunlight harvesting in dye-sensitized solar cells via the insertion of an upconverter-TiO_2 nanocomposite layer. Adv Mater 22:4373–4377. https://doi.org/10.1002/adma.201001816
83. Shan G-B, Assaaoudi H, Demopoulos GP (2011) Enhanced performance of dye-sensitized solar cells by utilization of an external, bifunctional layer consisting of uniform β-$NaYF_4:Er^{3+}/Yb^{3+}$ Nanoplatelets. ACS Appl Mater Interfaces 3:3239–3243. https://doi.org/10.1021/am200537e
84. Yuan C, Chen G, Prasad PN, Ohulchanskyy TY, Ning Z, Tian H, Sun L, Ågren H (2012) Use of colloidal upconversion nanocrystals for energy relay solar cell light harvesting in the near-infrared region. J Mater Chem 22:16709. https://doi.org/10.1039/c2jm16127c
85. Li L, Yang Y, Fan R, Jiang Y, Wei L, Shi Y, Yu J, Chen S, Wang P, Yang B, Cao W (2014) A simple modification of near-infrared photon-to-electron response with fluorescence resonance energy transfer for dye-sensitized solar cells. J Power Sources 264:254–261. https://doi.org/10.1016/j.jpowsour.2014.04.100
86. Zhang J, Shen H, Guo W, Wang S, Zhu C, Xue F, Hou J, Su H, Yuan Z (2013) An upconversion $NaYF_4:Yb^{3+}$, Er^{3+}/TiO_2 core–shell nanoparticle photoelectrode for improved efficiencies of dye-sensitized solar cells. J Power Sources 226:47–53. https://doi.org/10.1016/j.jpowsour.2012.10.073
87. Liang L, Liu Y, Zhao X-Z (2013) Double-shell β-$NaYF_4:Yb^{3+}$, $Er^{3+}/SiO_2/TiO_2$ submicroplates as a scattering and upconverting layer for efficient dye-sensitized solar cells. Chem Commun 49:3958. https://doi.org/10.1039/c3cc41252k
88. Dyck NC, Demopoulos GP (2014) Integration of upconverting β-$NaYF_4$: Yb^{3+}, Er^{3+}@TiO_2 composites as light harvesting layers in dye-sensitized solar cells. RSC Adv 4:52694–52701. https://doi.org/10.1039/C4RA08775E
89. Boudreault Pierre-Luc T, Najari A, Leclerc M (2011) Processable low-bandgap polymers for photovoltaic applications. Chem Mater 23:456–469. https://doi.org/10.1021/cm1021855
90. Chen H-Y, Hou J, Zhang S, Liang Y, Yang G, Yang Y, Yu L, Wu Y, Li G (2009) Polymer solar cells with enhanced open-circuit voltage and efficiency. Nat Photonics 3:649–653. https://doi.org/10.1038/nphoton.2009.192
91. Wang H-Q, Batentschuk M, Osvet A, Pinna L, Brabec CJ (2011) Rare-earth ion doped upconversion materials for photovoltaic applications. Adv Mater 23:2675–2680. https://doi.org/10.1002/adma.201100511
92. Adikaari AAD, Etchart I, Guéring P, Bérard M, Silva SRP, Cheetham AK, Curry RJ (2012) Near infrared up-conversion in organic photovoltaic devices using an efficient Yb^{3+}:Ho^{3+} co-doped Ln_2BaZnO_5 (Ln = Y, Gd) phosphor. J Appl Phys 111:094502. https://doi.org/10.1063/1.4704687
93. Guo W, Zheng K, Xie W, Sun L, Shen L, Liu C, He Y, Zhang Z (2014) Efficiency enhancement of inverted polymer solar cells by doping $NaYF_4:Yb^{3+}$, Er^{3+} nanocomposites in PCDTBT:PCBM active layer. Sol Energy Mater Sol Cells 124:126–132. https://doi.org/10.1016/j.solmat.2014.01.038

94. de Wild J, Rath JK, Meijerink A, Van Sark WGJHM, Schropp REI (2010) Enhanced near-infrared response of a-Si:H solar cells with beta-$NaYF_4$:Yb^{3+} (18%), Er^{3+} (2%) upconversion phosphors. Sol Energy Mater Sol Cells 94:2395–2398. https://doi.org/10.1016/j.solmat.2010.08.024
95. Trupke T, Shalav A, Richards BS, Würfel P, Green MA (2006) Efficiency enhancement of solar cells by luminescent up-conversion of sunlight. Sol Energy Mater Sol Cells 90:3327–3338. https://doi.org/10.1016/j.solmat.2005.09.021
96. Goldschmidt JC, Fischer S, Löper P, Krämer KW, Biner D, Hermle M, Glunz SW (2011) Experimental analysis of upconversion with both coherent monochromatic irradiation and broad spectrum illumination. Sol Energy Mater Sol Cells 95:1960–1963. https://doi.org/10.1016/j.solmat.2011.01.019
97. Sewell RH, Clark A, Smith R, Semans S, Jamora A, Vosters G (2009) Epitaxial rare-earth oxide layers for enhancement of silicon based solar cells. In: IEEE photovoltaic specialist conference, pp 326–331
98. Li Y, Wang G, Pan K, Jiang B, Tian C, Zhou W, Fu H (2012) $NaYF_4$:Er^{3+}/Yb^{3+}-graphene composites: preparation, upconversion luminescence, and application in dye-sensitized solar cells. J Mater Chem 22:20381. https://doi.org/10.1039/c2jm34113a
99. Wang J, Wu J, Lin J, Huang M, Huang Y, Lan Z, Xiao Y, Yue G, Yin S, Sato T (2012) Application of Y_2O_3:Er^{3+} Nanorods in dye-sensitized solar cells. Chem Sus Chem 5:1307–1312. https://doi.org/10.1002/cssc.201100596
100. Shan GB, Assaaoudi H, Demopoulos GP (2011) Enhanced performance of dye-sensitized solar cells by utilization of an external, bifunctional layer consisting of uniform β-$NaYF_4$:Er^{3+}/Yb^{3+} nanoplatelets. ACS Appl Mater Interfaces 3:3239–3243. https://doi.org/10.1021/am200537e
101. Khan AF, Yadav R, Mukhopadhya PK, Singh S, Dwivedi C, Dutta V, Chawla S (2011) Core-shell nanophosphor with enhanced NIR-visible upconversion as spectrum modifier for enhancement of solar cell efficiency. J Nanoparticle Res 13:6837–6846. https://doi.org/10.1007/s11051-011-0591-9
102. Wu J, Wang J, Lin J, Lan Z, Tang Q, Huang M, Huang Y, Fan L, Li Q, Tang Z (2012) Enhancement of the photovoltaic performance of dye-sensitized solar cells by doping $Y_{0.78}Yb_{0.20}Er_{0.02}F_3$ in the photoanode. Adv Energy Mater 2:78–81. https://doi.org/10.1002/aenm.201100531
103. Liu M, Lu Y, Xie ZB, Chow GM (2011) Enhancing near-infrared solar cell response using upconverting transparentceramics. Sol Energy Mater Sol Cells 95:800–803. https://doi.org/10.1016/j.solmat.2010.09.018
104. Li Q, Lin J, Wu J, Lan Z, Wang Y, Peng F, Huang M (2011) Enhancing photovoltaic performance of dye-sensitized solar cell by rare-earth doped oxide of Lu_2O_3:(Tm^{3+}, Yb^{3+}). Electrochim Acta 56:4980–4984. https://doi.org/10.1016/j.electacta.2011.03.125
105. Yu J, Yang Y, Fan R, Wang P, Dong Y (2016) Enhanced photovoltaic performance of dye-sensitized solar cells using a new photoelectrode material: upconversion YbF_3-Ho/TiO_2 nanoheterostructures. Nanoscale 8:4173–4180. https://doi.org/10.1039/C5NR08319B
106. Du P, Lim JH, Leem JW, Cha SM, Yu JS (2015) Enhanced photovoltaic performance of dye-sensitized solar cells by efficient near-infrared sunlight harvesting using upconverting Y_2O_3:Er^{3+}/Yb^{3+} phosphor nanoparticles. Nanoscale Res Lett 10:321. https://doi.org/10.1186/s11671-015-1030-0
107. Chen X, Xu W, Song H, Chen C, Xia H, Zhu Y, Zhou D, Cui S, Dai Q, Zhang J (2016) Highly efficient $LiYF_4$: Yb^{3+} , Er^{3+} upconversion single crystal under solar cell spectrum excitation and photovoltaic application. ACS Appl Mater Interfaces 8:9071–9079. https://doi.org/10.1021/acsami.5b12528
108. Feenstra J, Six IF, Asselbergs MAH, Van Leest RH, de Wild J, Meijerink A, Schropp REI, Rowan AE, Schermer JJ (2015) Er^{3+}/Yb^{3+} upconverters for InGaP solar cells under concentrated broadband illumination. Phys Chem Chem Phys 17:11234–11243. https://doi.org/10.1039/c4cp03752a

109. Li L, Zhang R, Yin L, Zheng K, Qin W, Selvin PR, Lu Y (2012) Biomimetic surface engineering of lanthanide-doped upconversion nanoparticles as versatile bioprobes. Angewandte 124:6121–6125. https://doi.org/10.1002/anie.201109156
110. Zheng W, Huang P, Tu D, Ma E, Chen X (2014) Lanthanide-doped upconversion nanobioprobes: electronic structures, optical properties, and biodetection. Chem Soc Rev 44:1379–1415. https://doi.org/10.1039/C4CS00178H
111. Wang M, Abbineni G, Clevenger A, Mao C, Xu S (2011) Upconversion nanoparticles: synthesis, surface modification and biological applications. Nanomedicine Nanotechnology Biol Med 7:710–729. https://doi.org/10.1016/j.nano.2011.02.013
112. Zhang F, Zhang C, Peng H, Cong H (2016) Near-infrared photocatalytic upconversion nanoparticles/TiO_2 nanofibers assembled in large scale by electrospinning. Part Part Syst Charact 33:248–253. https://doi.org/10.1002/ppsc.201600010
113. Johnson NJJ, Sangeetha NM, Boyer J, van Veggel FCJM (2010) Facile ligand-exchange with polyvinylpyrrolidone and subsequent silica coating of hydrophobic upconverting β-$NaYF_4$:Yb^{3+}/Er^{3+} nanoparticles. Nanoscale 2:771. https://doi.org/10.1039/b9nr00379g
114. Yang T, Sun Y, Liu Q, Feng W, Yang P, Li F (2012) Biomaterials cubic sub-20 nm $NaLuF_4$-based upconversion nanophosphors for high-contrast bioimaging in different animal species. Biomaterials 33:3733–3742. https://doi.org/10.1016/j.biomaterials.2012.01.063
115. Liu C, Wang Z, Jia H, Li Z (2011) Efficient fluorescence resonance energy transfer between upconversion nanophosphors and graphene oxide: a highly sensitive biosensing platform. Chem Commun 47:4661. https://doi.org/10.1039/c1cc10597c
116. Xiong L, Yang T, Yang Y, Xu C, Li F (2010) Long-term in vivo biodistribution imaging and toxicity of polyacrylic acid-coated upconversion nanophosphors. Biomaterials 31:7078–7085. https://doi.org/10.1016/j.biomaterials.2010.05.065
117. Zhao L, Kutikov A, Shen J, Duan C, Song J, Han G (2013) Stem cell labeling using polyethylenimine conjugated (α-$NaYbF_4$:Tm^{3+})/CaF_2 upconversion nanoparticles. Theranostics 3:249–257. https://doi.org/10.7150/thno.5432
118. Cao T, Yang Y, Gao Y, Zhou J, Li Z, Li F (2011) High-quality water-soluble and surface-functionalized upconversion nanocrystals as luminescent probes for bioimaging. Biomaterials 32:2959–2968. https://doi.org/10.1016/j.biomaterials.2010.12.050
119. Xiong L, Chen Z, Yu M, Li F, Liu C, Huang C (2009) Synthesis, characterization, and in vivo targeted imaging of amine-functionalized rare-earth up-converting nanophosphors. Biomaterials 30:5592–5600. https://doi.org/10.1016/j.biomaterials.2009.06.015
120. Chen H, Xu J, Yuan F, Wu Y, Zhang Y, Wang L (2013) A "turn-off" luminescence resonance energy transfer aptamer sensor based on near-infrared upconverting $NaYF_4$:Yb^{3+}, Tm^{3+} nanoparticles as donors and gold nanorods as acceptors. Chinese Chem Lett 24:79–81. https://doi.org/10.1016/j.cclet.2012.12.008
121. Gong N, Wang H, Li S, Deng Y, Chen X, Ye L, Gu W (2014) Microwave-assisted polyol synthesis of gadolinium-doped green luminescent carbon dots as a bimodal nanoprobe. Langmuir 30:10933–10939. https://doi.org/10.1021/la502705g
122. Zhang Q, Song K, Zhao J, Kong X, Sun Y, Liu X, Zhang Y, Zeng Q, Zhang H (2009) Journal of colloid and interface science hexanedioic acid mediated surface—ligand-exchange process for transferring $NaYF_4$:Yb/Er (or Yb/Tm) up-converting nanoparticles from hydrophobic to hydrophilic. J Colloid Interface Sci 336:171–175. https://doi.org/10.1016/j.jcis.2009.04.024
123. Ye X, Gordon T, Murray CB, Kikkawa JM, Chen J, Dong A, Kang Y (2010) A generalized ligand-exchange strategy enabling sequential surface functionalization of colloidal nanocrystals. J Am Chem Soc 133:998–1006. https://doi.org/10.1021/ja108948z
124. Das GK, Stark DT, Kennedy IM (2014) Potential toxicity of up-converting nanoparticles encapsulated with a bilayer formed by ligand attraction. Langmuir 30:8167–8176. https://doi.org/10.1021/la501595f
125. Chen Z, Chen H, Hu H, Yu M, Li F, Zhang Q, Zhou Z, Yi T, Huang C (2008) Versatile synthesis strategy for carboxylic acid−functionalized upconverting nanophosphors as biological labels. J Am Chem Soc 130:3023–3029. https://doi.org/10.1021/ja076151k

126. Wang L, Yan R, Huo Z, Wang L, Zeng J, Bao J, Wang X, Peng Q, Li Y (2005) Fluorescence resonant energy transfer biosensor based on upconversion-luminescent nanoparticles. Angew Chemie Int Ed 44:6054–6057. https://doi.org/10.1002/anie.200501907
127. Hu H, Xiong L, Zhou J, Li F, Cao T, Huang C (2009) Multimodal-luminescence core-shell nanocomposites for targeted imaging of tumor cells. Chem A Eur J 15:3577–3584. https://doi.org/10.1002/chem.200802261
128. Liu Z, Yi G, Zhang H, Ding J, Zhang Y, Xue J (2008) Monodisperse silica nanoparticles encapsulating upconversion fluorescent and superparamagnetic nanocrystals. Chem Commun 1:694–696. https://doi.org/10.1039/B715402J
129. Wang M, Hou W, Mi C, Wang W, Xu Z, Teng H, Mao C, Xu S (2009) Immunoassay of goat antihuman immunoglobulin G antibody based on luminescence resonance energy transfer between near-infrared responsive $NaYF_4$:Yb. Er Upconversion Fluoresc Nanoparticles Gold Nanoparticles 81:8783–8789
130. Zhou BH, Xu C, Sun W, Yan C (2009) Clean and flexible modification strategy for carboxyl/aldehyde-functionalized upconversion nanoparticles and their optical applications. Adv Funct Mater 24:3892–3900. https://doi.org/10.1002/adfm.200901458
131. Bogdan N, Vetrone F, Ozin GA, Capobianco JA (2011) Synthesis of ligand-free colloidally stable water dispersible brightly luminescent lanthanide-doped upconverting nanoparticles. Nano Lett 11:835–840. https://doi.org/10.1021/nl1041929
132. Yang Y (2014) Upconversion nanophosphors for use in bioimaging, therapy, drug delivery and bioassays. Microchim Acta 181:263–294. https://doi.org/10.1007/s00604-013-1139-8
133. Mader HS, Kele P, Saleh SM, Wolfbeis OS (2010) Upconverting luminescent nanoparticles for use in bioconjugation and bioimaging. Curr Opin Chem Biol 14:582–596. https://doi.org/10.1016/j.cbpa.2010.08.014
134. Naccache R, Rodríguez EM, Bogdan N, Sanz-Rodríguez F, Cruz MDCID, Fuente Á, Juarranz S, Vetrone F, Jaque D, Solé JG, Capobianco JA High resolution fluorescence imaging of cancers using lanthanide ion-doped upconverting nanocrystals. Cancers (Basel) 4:1067–1105. https://doi.org/10.3390/cancers4041067
135. Zijlmans HJ, Bonnet J, Burton J, Kardos K, Vail T, Niedbala RS, Tanke HJ (1999) Detection of cell and tissue surface antigens using up-converting phosphors: a new reporter technology. Anal Biochem 267:30–36. https://doi.org/10.1006/abio.1998.2965
136. Chatterjee DK, Rufaihah AJ, Zhang Y (2008) Upconversion fluorescence imaging of cells and small animals using lanthanide doped nanocrystals. Biomaterials 29:937–943. https://doi.org/10.1016/j.biomaterials.2007.10.051
137. Nyk M, Kumar R, Ohulchanskyy TY, Bergey EJ, Prasad PN (2008) High contrast in vitro and in vivo photoluminescence bioimaging using near infrared to near infrared up-conversion in Tm^{3+} and Yb^{3+} doped fluoride nanophosphors. Nano Lett 8:3834–3838. https://doi.org/10.1021/nl802223f
138. Zhou L, Gu Z, Liu X, Yin W, Tian G, Yan L, Jin S, Ren W, Xing G, Li W, Chang X, Huc Z, Zhao Y (2012) Size-tunable synthesis of lanthanide-doped Gd_2O_3 nanoparticles and their applications for optical and magnetic resonance imaging. J Mater Chem 22:966–974. https://doi.org/10.1039/c1jm13758a
139. Anjana R, Kurias KM, Jayaraj MK (2017) Biocompatible Er, Yb co-doped fluoroapatite upconversion nanoparticles for imaging applications. In: Cabrini S, Lérondel G, Schwartzberg AM, Mokari T (eds) Nanophotonic Materials, vol XIV. SPIE, Washington, p 33
140. Wang C, Cheng L, Liu Z (2011) Drug delivery with upconversion nanoparticles for multi-functional targeted cancer cell imaging and therapy. Biomaterials 32:1110–1120. https://doi.org/10.1016/j.biomaterials.2010.09.069
141. Cheng L, Yang K, Li Y, Chen J, Wang C, Shao M, Lee S, Liu Z (2011) Facile preparation of multifunctional upconversion nanoprobes for multimodal imaging and dual-targeted photothermal therapy. Angew Chem Int Ed 50:7523–7528. https://doi.org/10.1002/ange.201101447
142. Yang D, Kang X, Ma P, Dai Y, Hou Z, Cheng Z, Li C, Lin J (2013) Hollow structured upconversion luminescent $NaYF_4$:Yb^{3+} , Er^{3+} nanospheres for cell imaging and targeted

anti-cancer drug delivery. Biomaterials 34:1601–1612. https://doi.org/10.1016/j.biomaterials.2012.11.004
143. Li C, Hou Z, Dai Y, Yang D, Cheng Z, Ma P, Lin J (2013) A facile fabrication of upconversion luminescent and mesoporous core–shell structured β-$NaYF_4$:Yb^{3+} , Er^{3+} @$mSiO_2$ nanocomposite spheres for anti-cancer drug delivery and cell imaging. Biomater Sci 1:213–223. https://doi.org/10.1039/C2BM00087C
144. Ge X, Sun L, Dang S, Liu J, Xu Y, Wei Z, Shi L, Zhang H (2015) Mesoporous upconversion nanoparticles modified with a Tb(III) complex to display both green upconversion and down-conversion luminescence for in vitro bioimaging and sensing of temperature. Microchim Acta 182:1653–1660. https://doi.org/10.1007/s00604-015-1481-0
145. Deng K, Hou Z, Li X, Li C, Zhang Y, Deng X, Cheng Z, Lin J (2015) Aptamer-mediated up-conversion core/MOF shell nanocomposites for targeted drug delivery and cell imaging. Sci Rep 5:1–7. https://doi.org/10.1038/srep07851
146. Liu Y, Kang N, Lv J, Zhou Z, Zhao Q, Ma L, Chen Z, Ren L, Nie L (2016) Deep photoacoustic/luminescence/magnetic resonance multimodal imaging in living subjects using high-efficiency upconversion nanocomposites. Adv Mater 28:6411–6419. https://doi.org/10.1002/adma.201506460
147. Anjana R, Kurias KM, Jayaraj MK (2017) Clean synthesis of YOF:Er^{3+}, Yb^{3+} upconversion colloidal nanoparticles in water through liquid phase pulsed laser ablation for imaging applications. Opt Mater (Amst) 72:730–736. https://doi.org/10.1016/j.optmat.2017.07.021
148. Chen G, Ågren H, Ohulchanskyy TY, Prasad PN (2015) Light upconverting core-shell nanostructures: nanophotonic control for emerging applications. Chem Soc Rev 44(6):1680–713
149. Sun L, Wang Y, Yan C (2014) Paradigms and challenges for bioapplication of rare earth upconversion luminescent nanoparticles: small size and tunable emission/excitation spectra. Acc Chem Res 47:1001–1009. https://doi.org/10.1021/ar400218t
150. Baride A, Meruga JM, Douma C, Langerman D, Crawford G, Kellar JJ (2015) A NIR-to-NIR upconversion luminescence system for security printing applications. RSC Adv 5:101338–101346. https://doi.org/10.1039/C5RA20785A
151. Meruga JM, Baride A, Cross W, Kellar J, May PS (2014) Red-green-blue printing using luminescence-upconversion inks. J Mater Chem C 2:2221–2227. https://doi.org/10.1039/c3tc32233e
152. Meruga JM, Cross WM, May PS, Blumenthal T, Meruga J, May PS, Kellar J (2012) Patterned direct-write and screen-printing of NIR-to-visible upconverting inks for security applications. https://doi.org/10.1088/0957-4484/23/18/185305
153. Amorim H (2003) Red–green–blue upconversion emission and energy-transfer between Tm^{3+} and Er^{3+} ions in tellurite glasses excited at 1.064 μm. J Solid State Chem 171:278–281. https://doi.org/10.1016/s0022-4596(02)00176-7
154. Meruga JM, Cross WM, Stanley May P, Luu Q, Crawford GA, Kellar JJ (2012) Security printing of covert quick response codes using upconverting nanoparticle inks. Nanotechnology 23:395201. https://doi.org/10.1088/0957-4484/23/39/395201
155. Wang M, Li M, Yang M, Zhang X, Yu A, Zhu Y, Qiu P, Mao C (2015) NIR-induced highly sensitive detection of latent fingermarks by $NaYF_4$:Yb, Er upconversion nanoparticles in a dry powder state. Nano Res 8:1800–1810. https://doi.org/10.1007/s12274-014-0686-6
156. Zhang Y, Zhang L, Deng R, Tian J, Zong Y, Jin D, Liu X (2014) Multicolor barcoding in a single upconversion crystal. J Am Chem Soc 136:4893–4896. https://doi.org/10.1021/ja5013646
157. You M, Zhong J, Hong Y, Duan Z, Lin M, Xu F (2015) Inkjet printing of upconversion nanoparticles for anti-counterfeit applications. Nanoscale 7:4423–4431. https://doi.org/10.1039/C4NR06944G
158. Sangeetha NM, Moutet P, Lagarde D, Sallen G, Urbaszek B, Marie X, Viau G, Ressier L (2013) 3D assembly of upconverting $NaYF_4$ nanocrystals by AFM nanoxerography: creation of anti-counterfeiting microtags. Nanoscale 5:9587–9592. https://doi.org/10.1039/C3NR02734A
159. Mendez Ramos J, Ruiz Morales JC, Acosta Mora P, Khaidukov NM (2016) Infrared-light induced curing of photosensitive resins through photon up-conversion for novel cost-effective

luminescent 3D-printing technology. J Mater Chem C 4:801–806. https://doi.org/10.1039/C5TC03315B
160. Yao W, Tian Q, Tian B, Li M, Wang H, Zeng P, Liu L, Zheng H, Wu W (2019) Dual upconversion nanophotoswitch for security encoding. Sci China Mater 62:368–378. https://doi.org/10.1007/s40843-018-9341-8
161. Meruga JM, Cross WM, Petersen JB, May PS, Baride A, Cessac K, Kellar JJ (2018) Stable inks containing upconverting nanoparticles based on an oil-in-water nanoemulsion. Langmuir 34:1535–1541. https://doi.org/10.1021/acs.langmuir.7b03415
162. Liu H, Xu J, Wang H, Liu Y, Ruan Q, Wu Y, Liu X, Yang JKW (2019) Tunable resonator-upconverted emission (TRUE) color printing and applications in optical security. Adv Mater 31:1807900. https://doi.org/10.1002/adma.201807900

Chapter 3
Optical Properties of Metal, Semiconductor and Ceramic Nanostructures Grown by Liquid Phase-Pulsed Laser Ablation

P. M. Aneesh and M. K. Jayaraj

1 Introduction

Nanostructured materials have gained extensive research interest in the last few decades owing to its exceptional chemical, optical, electronic and magnetic properties different from their bulk counterparts. In last few decades, extensive researches were carried out in the synthesis of colloidal nanoparticles because of their versatile properties promising for application in various fields like drug delivery [1, 2], imaging [3–6], diagnostics [7–10] and for the growth of nanocomposites with peculiar optical, mechanical or bioactive properties [11–14]. Pulsed laser ablation (PLA) was first developed as technique for the growth of thin films in the 1960s, shortly after the invention of the pulsed ruby laser. Since then, the growth of thin films by laser ablation in vacuum and in various gases ambient has been studied by many researchers. Wide variety of thin films of high-temperature superconductors [15, 16], metals, semiconductors, oxides, diamond-like carbon [17, 18] and other ceramics [19, 20] can be deposited using different target materials and gaseous atmosphere, and varying parameters such as the laser fluence, laser wavelength and pulse duration.

Pulsed laser ablation is considered as the promising and most flexible technique because almost all kinds of materials can be ablated at ultra-high-energy density. The process parameters like irradiation time, energy density, wavelength, etc. during the growth process can be controlled very easily [21, 22]. Patil and co-workers in 1987 first reported the pulsed laser ablation on solid–liquid interface by ablating a pure iron target in water to form iron oxides with metastable phases using pulsed laser

P. M. Aneesh (✉)
Department of Physics, Central University of Kerala, Tejaswini Hills, Periye, Kasaragod, Kerala 671320, India
e-mail: aneeshpm@cukerala.ac.in

M. K. Jayaraj
Department of Physics, Cochin University of Science and Technology, Kochi 682022, India

M. K. Jayaraj (ed.), *Nanostructured Metal Oxides and Devices*,
Materials Horizons: From Nature to Nanomaterials,
https://doi.org/10.1007/978-981-15-3314-3_3

beam [23]. This method is known as liquid phase-pulsed laser ablation (LP-PLA), and the laser beam is focused on the solid target surface through the liquid. This pioneering work based on PLA of solids in various liquids opened new routes for the synthesis of materials and LP-PLA method has been used to produce a wide variety of novel materials, such as metallic nanocrystals, nanodiamond and related nanocrystals, nanocrystal alloys and metal oxides with peculiar properties.

LP-PLA techniques have become a promising and versatile growth technique for nanostructures that allows one to choose suitable solid targets and confining liquids. LP-PLA technique has many advantages over the other conventional physical methods such as pulsed laser ablation in vacuum, sputtering and evaporation and chemical methods such as sol–gel and co-precipitation. It is a chemically simple and clean synthesis process. One of the advantages of LP-PLA technique is that since the final product is usually obtained without any by-products and hence further purification is not required. The other advantage of this technique is that it requires only inexpensive equipment for controlling the ablation atmosphere, and the parameters can be controlled very easily. Also, the amount of chemical quantity required for synthesis is minimum as compared to the other conventional chemical process. The extreme confined conditions, induced high temperature and pressure region during the processes, favor the formation of metastable phases. Thus, nanostructures of metals and semiconductors can be easily synthesized by this technique.

Commercially available colloids are usually synthesized by sol–gel or salt precipitation processes, and in these processes precursor, additive and surfactant systems need to be designed for each type of nanoparticles. Metal acetates and carbonates are the commonly used chemical precursors for every synthesis process in nanochemistry. Oxidation of metal and hydroxylations of ceramic samples are the other drawbacks of these kinds of synthesis techniques. The unreacted precursors and substituents get agglomerated and remain as sediments in the final colloidal product [24]. These days, large endeavors are being made for an efficient and systematic purification and removal of these contaminants [25].

Regardless of the advancement in the field of wet chemistry, the potential of sol–gel chemistry, particularly product diversity, have not been utilized adequately [26]. Furthermore, the products are often constricted to thermodynamically stable crystal structures, as a result of which the fabrication of hard ceramics like alpha aluminum oxide and tetragonal zirconium dioxide becomes complicated. Also, as the required forces increase exponentially with smaller particle size, it is not possible to form nanoparticles from these hard materials by mechanical milling. Likewise, milling processes may introduce contaminants from grinding media [27]. But the development and growth of new nanomaterials with LP-PLA technique require comparably little effort. The limitations of LP-PLA technique are the low yield that is mostly restricted to about (0.01–0.1) μg/min [28], and there are knowledge deficits on the physical and chemical processes involved.

LP-PLA technique involves focusing a high-power laser beam onto the surface of a solid target, which is submerged in a liquid. During this process, the interaction of laser beam with the surface of target leads to vaporization of surface and generates an ablation plume, which contains many species such as atoms, clusters and ions, rushing

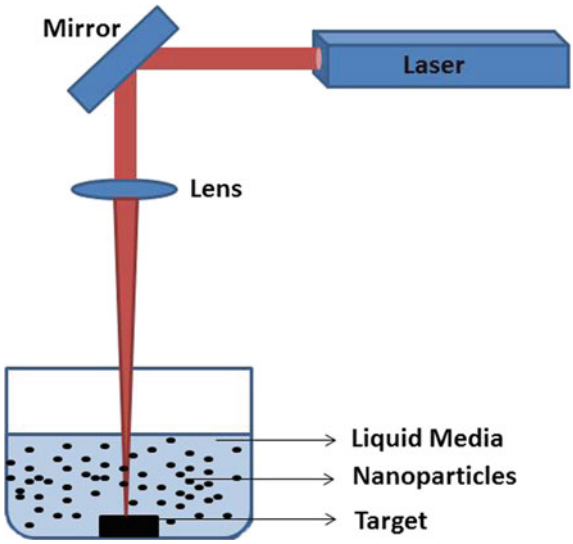

Fig. 1 Experimental setup for the LP-PLA technique

out with high kinetic energy. These intermediate species in the plume collide and react with molecules of the surrounding liquid, thus resulting in the formation of new compounds containing atoms from both the target and the liquid. Focusing of a high-power laser beam in nanosecond time scales results in the instantaneous increase in temperatures and pressures (many thousands of K at tens of GPa) within the reaction volume. LP-PLA technique which creates high-temperature, high-pressure and high-density conditions in a localized area thus leads to the formation of novel materials impossible by other conventional techniques. The experimental arrangement for the synthesis of nanostructures by LP-PLA techniques is shown in Fig. 1. The necessary condition for the formation of nanoparticles under ablation in liquid environment is the melting of the solids which occur at adequately high laser fluence relying upon the absorption efficiency of the material at the laser wavelength.

During the past decades, extensive research studies were performed in the formation of nanoparticles (NPs) employing laser ablation of solids, either in gas or in vacuum. This process of pulsed laser ablation can be controlled by understanding the mechanisms of cluster formations, and this technique is now being widely used for the growth of a large variety of compounds. LP-PLA can be considered as the extension of this concept. In both laser ablations in vacuum and at the solid–liquid interface, the interaction of laser beam with the target material is the same. Also, plasma will be produced in both types of laser ablation process and during the ablation; a strong confinement of ejected particles will be created as a result of electron–ion recombination. But the difference is that, for normal PLA the expansion of plasma occurs freely in vacuum, whereas in LP-PLA process, the plasma is confined by a liquid layer. Additionally, the presence of liquid layer delays the expansion of plasma, creating a high plasma pressure and temperature leading to the formation of novel materials. Another favorable aspect of LP-PLA process is that

the final product may contain the atoms of the solid target material and the liquid, as both are vaporized during the LP-PLA process. LP-PLA is a flexible and versatile technique for the synthesis of various novel nanoparticles and can be considered as a substitute to the well-known chemical vapor deposition (CVD) method. Besides, the generation of NPs through laser ablation of solid targets in liquid environment avoids surface functionalization and formation of counter-ions or surface-active substances [29, 30]. Thus, this LP-PLA offers the advantages of both pulsed laser deposition (PLD) and other chemical routes. The colloidal dispersion of nanoparticles obtained during LP-PLA process is found to more stable than that prepared by other chemical methods. In addition, the materials with complex stoichiometries can be grown by ablation process very easily. Moreover, materials which can only be synthesized at high pressure can also be grown by pulsed laser ablation in a liquid medium. Briefly, the material will be ejected and evaporated upon irradiating the target with high power over 0.1 GW/cm^2. A maximum pressure of several GPa generated by shock waves will be obtained with a laser power density of several GW/cm^2 [31]. But processes involved in the nucleation and transition of nanosystems in the LP-PLA technique are not clear. Some of the nucleation thermodynamics, the phase transition and the growth kinetics of nanocrystals by laser ablation of liquids are given by Yang [32].

Generally, LP-PLA is regarded as a quick and far-from-equilibrium process. In this process, the final product may contain all stable and metastable phases formed during the different stages of bulk to nanoparticle transition, especially for any metastable intermediate phases [32, 33]. Specifically, in LP-PLA process, the quenching time is very short so that the metastable intermediate phases which form during the transition from bulk to nanoparticle conversion can be frozen in, and final products will be formed. Berthe and co-workers [34] have mentioned that species ejected from the solid target surface have a large initial kinetic energy during the very initial stage of interaction of the high-energy laser with the solid–liquid interface. Due to the covering effect in the vicinity of the solid–liquid interface, the ejected species will form a dense region. This stage is similar to that of laser-generated plasma plume in vacuum or low-pressure gas. The plasma expands adiabatically at supersonic velocity leads to a shock wave in front of it as the plasma created in LP-PLA process is confined in the liquid. The shock wave thus generated will induce an extra, instantaneous pressure as it passes through the liquid. This laser-induced pressure will result in the increase in temperature in the plasma [35, 36]. Therefore, the plasma formed in LP-PLA is at higher pressure and higher density than that produced in PLA in gas or vacuum. The localized high temperature will also result in the vaporization of small amount of the surrounding liquid to form bubbles within the liquid. The bubbles will expand when more material is vaporized until at a certain combination of temperature and pressure, and finally, they will collapse. During the collapse of bubbles, the nearby species are subjected to temperatures of thousands of kelvin (K) and pressures of several gigapascal (GPa), and these extreme conditions result in the formation of novel materials [37].

LP-PLA has been used to produce nanoparticles (NPs) of many different metal elements including silicon [38, 39], titanium [40, 41], zinc [42, 43], cobalt [44, 45], silver [46, 47], copper [48, 49] and gold [50, 51]. This technique can also be used

to prepare NPs of compound materials such as TiC [52, 53], TiO_2 [54, 55] and CoO [44] in water and ZnSe and CdS in various solvents, including water [56–58]. The use of this method opens up the possibility of studying new materials at the nanoscale range for various new applications. LP-PLA has gained much attention recently for its ability to form more complex, higher-dimensional nanostructures, and a lot of research is going on the study of dynamical processes among laser–solid–liquid interactions. A summary of the nanostructures grown by LP-PLA technique is listed in Table 1.

The synthesis of various metal, semiconducting and ceramic nanostructures by LP-PLA techniques and their optical properties is discussed in the following sections.

Table 1 Summary of nanostructures grown by LP-PLA technique

Target	Medium	Laser source	Products	References
Ag	Water	Nd:YAG laser (532 nm)	Ag nanoparticles	[46]
Ag	Ethanol	Cu vapor laser (510.5 nm)	Ag nanoparticles	[52]
Au	Water	Nd:YAG laser (532 nm)	Au nanoparticles	[46]
Au	Alkane liquid	Nd:YAG laser (532 nm)	Au nanoparticles	[59]
Co	Water	Nd:YAG laser (355 nm)	Co_3O_4 nanoparticles	[44]
Hexagonal BN	Acetone	Nd:YAG laser (532 nm)	Cubic-BN nanoparticles	[60]
Graphite	Water	Nd:YAG laser (532 nm)	Diamond nanoparticles	[61]
Pt/TiO_2	Water	Nd:YAG laser (355 nm)	Pt/TiO_2 nanoparticles	[62]
Sn	Water + SDS	Nd:YAG laser (355 nm)	SnO_2 nanoparticles	[63]
Ti	Water + SDS	Nd:YAG laser (355 nm)	TiO_2 nanoparticles	[64]
Zn	Water + SDS	Nd:YAG laser (1064 nm)	ZnO nanoparticles	[65]
ZnO	Water	Nd:YAG laser (355 nm)	ZnO nanoparticles	[66]
ZnS	Water	Nd:YAG laser (266 nm)	ZnS nanoparticles	[67]

2 Metal Nanoparticles by LP-PLA Technique

The synthesis of noble metal nanoparticles such as silver, gold and copper by LP-PLA is widely studied, and the colloidal nanoparticles of these noble metals exhibit a very intense color, which is absent in the corresponding bulk counterpart as well as in the individual atoms. This coloration is due to the surface plasmon resonances (SPRs), and it is the collective oscillation of the free conduction electrons induced by the interacting electromagnetic fields [68]. This makes metal nanoparticles a prominent material for a wide range of applications, including nonlinear optical devices, biosensors, telecommunication and data storage [69, 70]. The size and shape of the nanoparticles play a key role in tuning its optical and electrical properties [71]. Several methods are available for controlling the size and shape of nanostructures and which include chemical reduction, ultrasonic reduction, and photolysis of salts [72, 73]. But these chemical reduction methods result in by-products that contaminate and affect the stability of the nanostructures. In this context, methods like laser ablation of solid target in liquid media have got considerable attention because of its safety and simplicity [74].

Mafune et al. explained the mechanism of nanoparticle growth during liquid phase-pulsed laser ablation [75], and according to this model, an electrical bilayer is formed around the nanoparticles, while the plume expands in the media like water [76]. In these media, the OH group on the nanoparticles generates surface charge and thus results in an electrical bilayer. The electrostatic repulsion between the charged nanoparticles prevents further growth and results in stable nanoparticles.

The nanoparticles of gold and silver with high quality can be synthesized by focusing second harmonics of a neodymium-doped yttrium aluminum garnet (Nd:YAG) laser (532 nm) operating at a repetition rate of 10 Hz onto a high-purity gold and silver target immersed in 15 mL of deionized water. The laser fluence dependence on the formation of these nanoparticles was studied by varying the fluences from 1.2 to 3.8 J/cm^2 with an ablation time of 1 h. The dependence of duration of laser ablation on the formation of nanoparticles has been investigated at particular laser fluence (1.2 J/cm^2), and concentrations of nanoparticles can be measured by inductively coupled plasma atomic emission spectroscopy (ICP-AES) analysis.

The UV-Vis absorption spectra will give information about the position of surface plasmon resonance in metal nanoparticles, and it can be monitored using JASCO V570 spectrophotometer in the wavelength region 200–1000 nm. Figure 2 shows the SPR peaks of gold and silver nanoparticles colloids prepared at 1.2 J/cm^2 which are in the visible region of the electromagnetic spectrum: 520 nm and 404 nm for gold and silver, respectively. According to Mie theory, a single SPR peak in the lower wavelength region for Au nanocrystals indicates the presence of spherically shaped Au nanocrystals which can be confirmed by TEM images. It is also found that the absorbance of the gold colloidal nanoparticles at a particular experimental condition is found to be smaller than silver nanoparticle colloids, and it indicates the increased concentration of the silver nanoparticles than the gold nanoparticles in water. This is due to the fact that ablation threshold is different for different materials since it

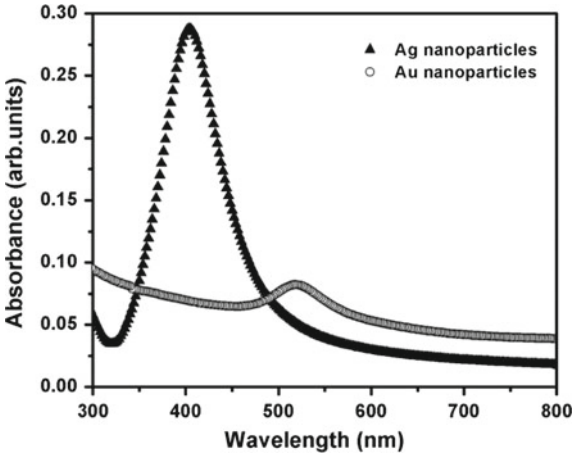

Fig. 2 The UV-Vis absorption spectra of silver and gold nanoparticles grown by LP-PLA technique at a laser fluence of 1.2 J/cm^2 for 1 h

depends upon the work function of the material. Work function may be defined as the minimum energy required for an electron to escape from the solid surface. For dragging an ion, out of the target electron requires an additional energy larger than or equal to the ion binding energy. Thus, the ablation threshold for metals is defined as the electron energy in the surface layer that must equal to the sum of atomic binding energy and work function. Assuming that during the laser–matter interaction process, the number density of the conducting electrons is unchanged and the condition to reach the ablation threshold is obtained as [77],

$$F_{\text{th}}^{\text{m}} \approx \frac{3}{8}(E_{\text{b}} + E_{\text{esc}})\frac{\lambda n_{\text{e}}}{2\pi} \tag{1}$$

where F_{th}^{m} is the threshold laser fluence for ablation of metal, E_{b} is the ion binding energy, E_{esc} is the work function, λ is the laser wavelength and n_{e} is the number density of the conduction electrons in the metal.

The work function of silver and gold is 3.7 eV and 4.7 eV, respectively, that results in higher ablation rate for silver than gold at particular laser fluence. ICP-AES analysis shows that the concentration of the silver and gold nanoparticles for a particular laser fluence is 3.8 ppm and 2.75 ppm, respectively, and it confirms the dependence of work function on the ablation rate of the metal targets.

Figure 3 shows the UV-Vis absorption spectra of gold nanoparticles prepared at different laser fluences varying from 1.2 to 3.8 J/cm^2. All the samples show a strong surface plasmon peaks only in the visible region (518–530 nm), and according to Mie theory, it is a property shown by spherical Au nanoparticles and it corresponds to the transverse mode of oscillation of the free electron cloud. Non-spherical particles, such as nanorods, exhibit an additional plasmon mode at higher wavelength (800 nm) and which correspond to the longitudinal mode of oscillation [78]. The absorption maxima of gold nanoparticles prepared at different laser fluencies show a redshift from 518 to 530 nm, and it indicates an increase in particle size [79]. For

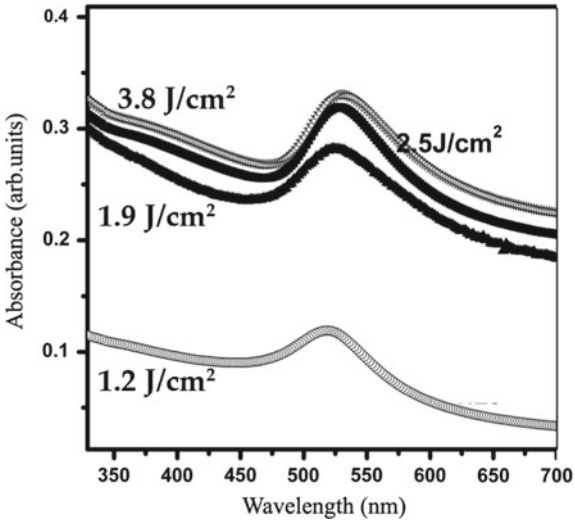

Fig. 3 UV-Vis absorption spectra of colloidal Au nanoparticles prepared at different laser fluences

larger particles, light cannot polarize the nanoparticles homogenously as the localization of the d band electrons in larger clusters increases the screening of the ions by surface electrons, thereby reducing the polarizability near the surface, and the retardation effect led to the excitation of higher-order modes [78]. This was regarded as an extrinsic size effect that results in redshift of SPR peak with an increase in nanoparticle size.

The amplitude of the SPR peak is found to increase with an increase in the ablation power, which can be attributed to the increased concentration of gold nanoparticles in water. The broadening in the SPR absorption band with decreasing particle size corresponds to the increased damping known as Landau damping [70]. There is no contribution to the observed broadening when the particles are apart, but when the volume fraction of the Au nanoparticles increased, an inter-particle interaction came into play.

Figure 4 shows the UV-Vis absorption spectra of silver nanoparticles grown at different laser fluences. The SPR bands peaking at 400 nm in the absorption spectra confirm the presence of nanosized silver particles. The plasmon band around 400 nm is attributed to the longitudinal surface plasmon resonance of the free electrons in the silver nanoparticles. A small shift from 403 to 406 nm is observed in the absorption peak with an increase in the ablation laser fluence, indicating only a small increase in the particle size which can be confirmed by TEM analysis (Fig. 6).

Transmission electron microscope (TEM) will tell about the size and shape of the synthesized metal nanoparticles and was performed with JEOL, TEM working at an accelerating voltage of 200 kV. For TEM measurements, the sample was prepared by drop-casting a drop of the colloidal nanoparticle solution onto a regular carbon-coated copper grid. Figure 5 shows the TEM, high-resolution transmission electron microscopy (HRTEM), selected area electron diffraction (SAED) patterns and size

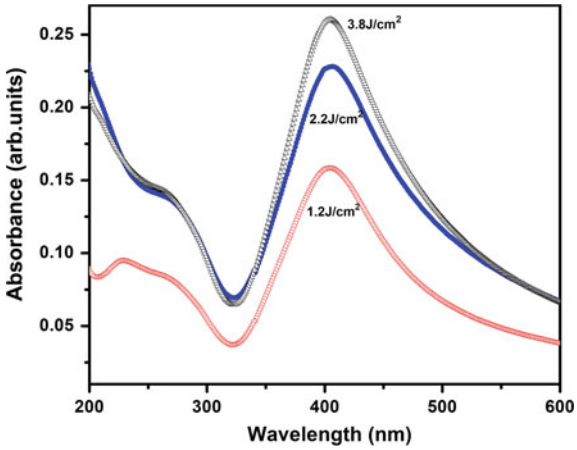

Fig. 4 UV-Vis absorption spectra of silver nanoparticles prepared at different laser fluences

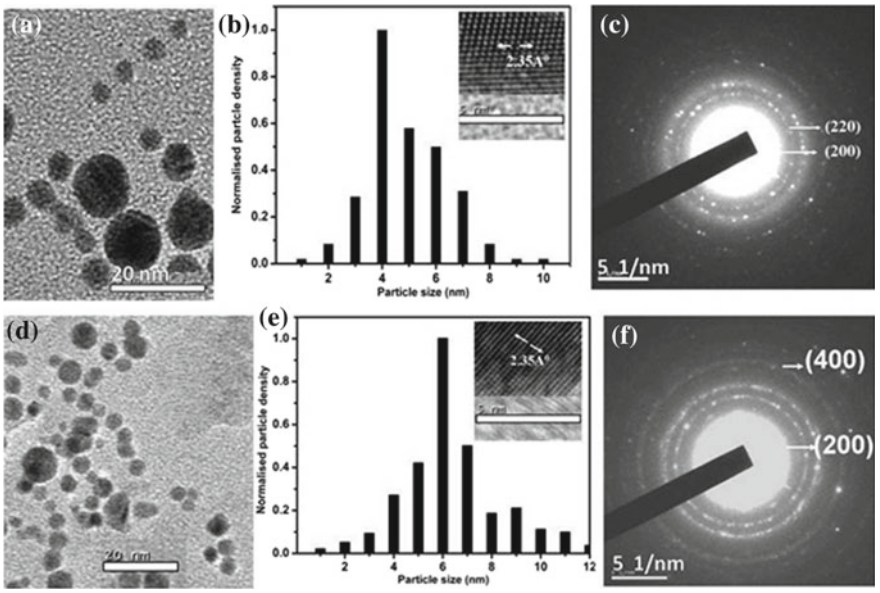

Fig. 5 **a** and **d** TEM, **b** and **e** size histograms, inset of **b** and **e** HRTEM, **c** and **f** SAED patterns of Au nanoparticles prepared at 1.2 (top row) and 3.8 J/cm^2 (bottom row)

histograms of gold nanoparticles grown at 1.2 and 3.8 J/cm^2. TEM image confirms the formation of uniformly distributed spherical gold nanoparticles in the aqueous media, as observed in the UV-Vis absorption spectra. The average particle sizes of the Au nanoparticles are 4 and 6 nm for 1.2 and 3.8 J/cm^2, respectively. The *d*-spacing values obtained from the SAED pattern are well-indexed and matches with

the (220), (200) and (400) planes of gold. The HRTEM displays the atomic planes corresponding to the (111) plane of gold with *d*-spacing of 2.35 Å.

Figure 6a and b shows the HRTEM image and SAED pattern of Ag nanoparticles grown at 1.2 J/cm^2. Similarly, Fig. 6c and d shows the HRTEM image and SAED pattern of silver nanoparticles grown at 3.8 J/cm^2. Inset of (b) and (d) shows high-resolution image showing parallel lines of atoms of silver. The *d*-values from high-resolution images and corresponding SAED pattern match with various planes of Ag. The nanoparticles grown at fluences 1.2 J/cm^2 and 3.8 J/cm^2 have an average size of about 4 nm and 7 nm, respectively.

The ICP-AES analysis shows that the concentration of the Au in the colloidal solution increases with an increase in the duration of laser ablation. Au nanoparticles of different concentrations such as 3.45, 4.25 and 7.65 ppm were synthesized at laser ablation durations of 1, 2 and 3 h, respectively. Presence of Au-NPs was confirmed

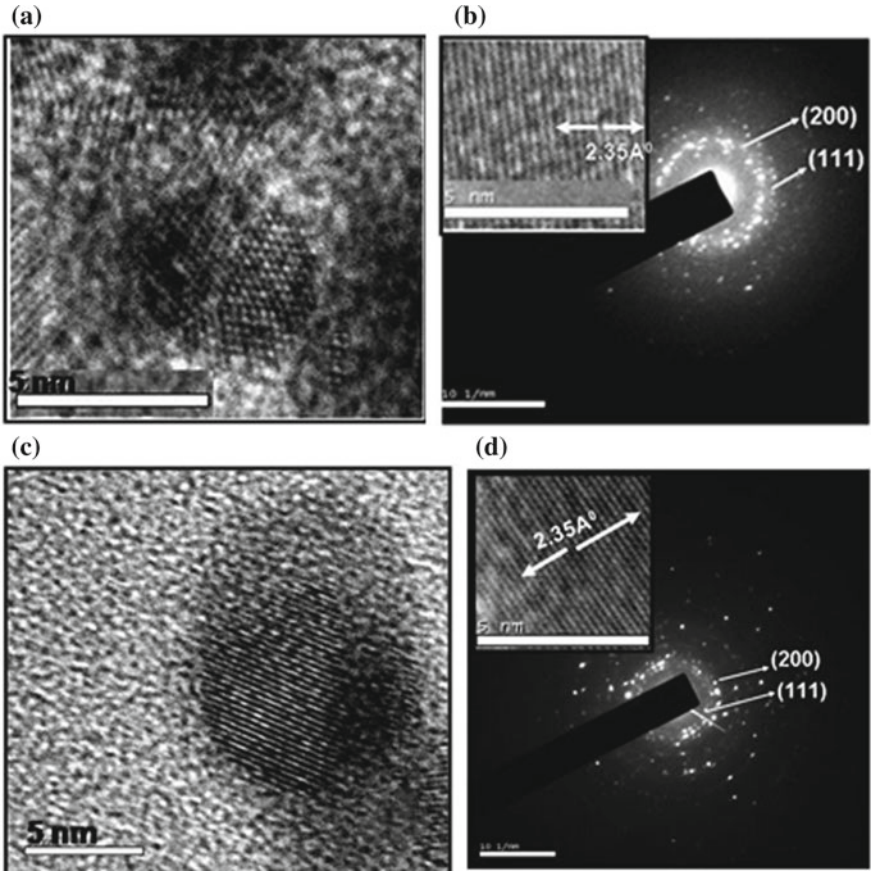

Fig. 6 HRTEM of Ag nanoparticles grown at a laser fluence of **a** 1.2 J/cm^2 and **c** 3.8 J/cm^2. **b** and **d** represent the SAED pattern of Ag nanoparticles (inset shows the parallel lines of atoms)

from the UV-Vis absorption spectra (Fig. 7), showing strong SPR peak at 520 nm. It was observed that with an increase in the duration of laser ablation, a gentle increase in the amplitude of the SPR peak is also visible. This corresponds to the increase in the concentration of the Au nanoparticles in the colloidal solution as noticed from the ICP-AES analysis. The plasmon peak remains at almost same wavelength owing to the fact that the particle size remains consistent with duration of laser ablation.

Figure 8 shows the UV-Vis absorption spectra of Ag nanoparticles grown at different duration of ablation by keeping particular laser fluence. Similar to gold nanoparticles, here also the amplitude of SPR peak is increasing with an increase in the duration of laser ablation and it is attributed to the increase in number of silver nanoparticles in water. It also shows that the SPR peak has a blue shift with an increase in the

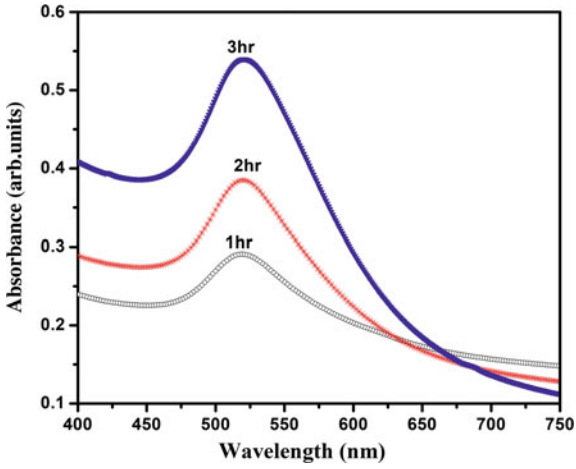

Fig. 7 UV-Vis absorption spectra of Au nanoparticles grown at various duration of ablation

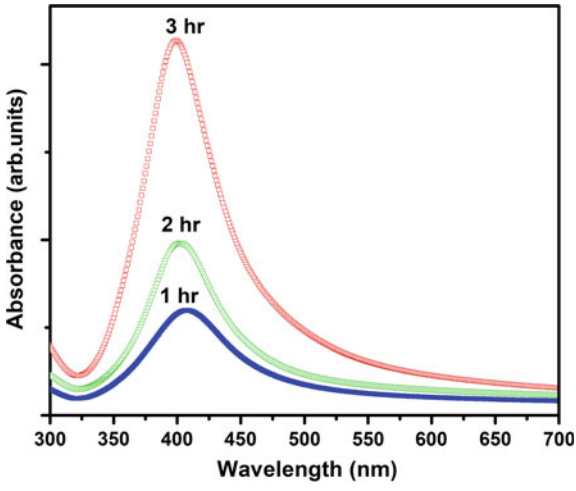

Fig. 8 UV-Vis absorption spectra of silver nanoparticles grown at a laser fluence of 1.2 J/cm^2 for different durations of ablation

duration of laser ablation, and it corresponds to the reduction in particle size due to the efficient radiation absorption by the previously ablated particles [80].

3 Semiconducting Nanoparticles by LP-PLA

ZnO nanoparticles were synthesized by employing a mosaic target of ZnO (99.99%) sintered at 1000 °C for 5 h. The target material was immersed in 15 mL of the liquid media with different pH and was irradiated by third harmonic of Nd:YAG laser (355 nm, repetition frequency of 10 Hz, pulse duration of 9 ns) at room temperature. A lens was used to focus the laser beam, and the ablation was done at a laser fluence of 15 mJ/ pulse. The spot size of the laser beam is about 1 mm. The duration of ablation was kept constant at 1 h. As a result, highly transparent dispersions of ZnO nanoparticles in liquid media were prepared by this simple LP-PLA technique at room temperature.

Transmission electron microscop e (JEOL, TEM) working at an accelerating voltage of 200 kV was used to confirm the formation of ZnO NPs. The sample for TEM was prepared by dropping ZnO nanoparticle colloidal solution onto standard carbon-coated copper grids and dried before recording the micrographs. TEM studies confirm the resulting product after laser ablation in different media contains particles in the nanoregime. The concentric rings in selective area electron diffraction (SAED) pattern correspond to formation of hexagonal ZnO. The result clearly proves the formation of crystalline ZnO NPs, and the formation of molecules like $Zn(OH)_2$ or ZnO/Zn core shell was not observed from these studies. The formation of ZnO constitutes the reaction of ejected molten material from the target with ambient medium at the outer surface [81]. Thereafter, the ejected plasma gradually cools down resulting in the formation of ZnO itself. The nanoparticles will be charged because there are many surface oxygen deficiencies. Since the isoelectronic points of ZnO (~9.3) are well above the pH (7.0) of pure water, it is observed that the as-grown ZnO nanoparticles by LP-PLA in pure water are normally charged [82]. As a result, this surface charge prevents the further aggregation, forming self-stabilized nanoparticles even in the absence of surfactant. Oxygen deficiency in the ZnO NPs synthesized by LP-PLA will also lead to positive charge which may prevent from agglomeration. It is found that there is a linear increase in the mean size of the particle with fluence of the laser pulses and is shown in Fig. 9.

However, higher laser fluence results in generation of bigger size particles with broad size distribution. Whereas, when the duration of ablation was increased maintaining lower fluence, the size of the NPs did not increase, but resulted in the increase in the particle density. But, even for ablation duration of more than 3 h at a laser energy of 45 mJ/pulse, the transparency of the ZnO nanoparticle colloid remained as such. While maintaining transparency, a maximum concentration of 17.5 μg/mL was obtained for ZnO nanoparticles [66].

Figure 10a details the TEM image of ZnO samples after laser irradiation with energy 25 mJ/pulse in the water (pH ~ 7). The observation indicates the formation

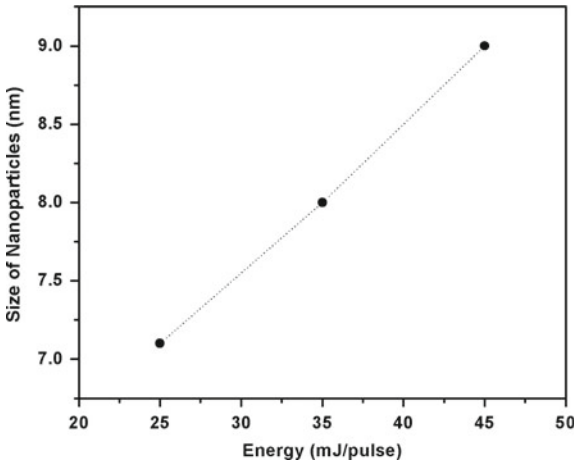

Fig. 9 Variation of size of the LP-PLA grown ZnO NPs with laser fluence [83]

of ZnO particles in the nanoregime. The particle size distribution of ZnO NPs was observed in a small range (Fig. 10b), and most of the particles are prone to have size of 7 nm. The HRTEM image (Fig. 10d) with inter-planar *d*-spacing value of 0.26 nm corresponds to the (002) plane of wurtzite ZnO. The particle size distribution was found to be nearly uniform. The selective area electron diffraction (SAED) pattern (Fig. 10c) displays sharp concentric rings corresponding to (100), (002), (102), (110) and (103) diffraction planes of hexagonal ZnO. Apparently, the results confirm the formation of crystalline ZnO NPs exhibiting random orientations. The high-resolution TEM image (inset Fig. 10d) clearly depicts the formation of ZnO NPs having hexagonal shape and the stacking of about 85 hexagonal unit cells makes 7-nm-sized NPs.

The TEM image shows that the particles are in spherical shape and it has an average size about 7 nm and the colloid is transparent in nature. The average particle size of Zn/ZnO composite nanoparticles grown by Zeng et al. [84] was 18 nm, and it was colored due to turbidity. Also, the ZnO NPs grown under oxygen bubbling into the water during laser ablation of ZnO targets are found to exhibit bigger size, while the size of the particles remains the same during nitrogen bubbling into water which is same as that grown in pure water. TEM images of the ZnO NPs grown in both oxygen and nitrogen atmosphere are shown in Fig. 11a. Figure 11b and c clearly shows that the NPs prepared in nitrogen atmosphere, keeping the other parameters of the experiment fixed have same size as those prepared in neutral water. But the oxygen bubbling during the ablation process results in increased amount of dissolved oxygen and promotes the growth of ZnO. This results in bigger ZnO NPs, whereas nitrogen bubbling in the solution during the LP-PLA process does not create any additional oxygen other than that produced by the laser interaction with the ZnO target. As a result, it is observed that the size of the particles remains the same as those obtained by LP-PLA in pure water.

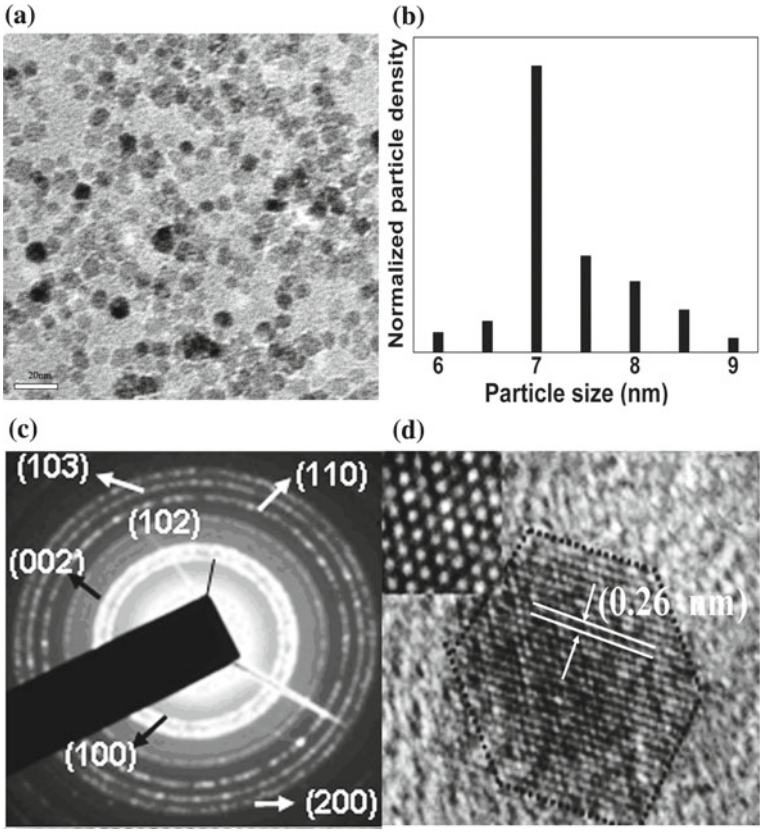

Fig. 10 **a** TEM image of ZnO NPs; **b** histogram representing size distribution; **c** SAED patterns matching hexagonal ZnO NPs prepared by LP-PLA technique with a fluence of 25 mJ/pulse in water. **d** HRTEM image for a single ZnO nanoparticle showing (002) crystalline plane and inset shows the stacking in hexagonal close-packed mode [66]

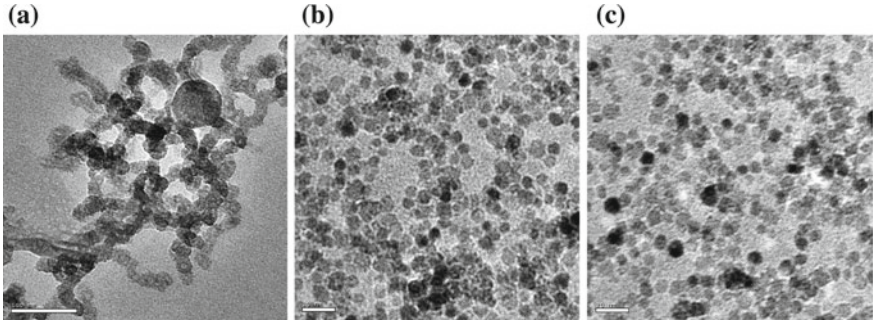

Fig. 11 TEM image of zinc oxide NPs grown by LP-PLA in water **a** oxygen atmosphere; **b** with nitrogen atmosphere and **c** without any gases [83]

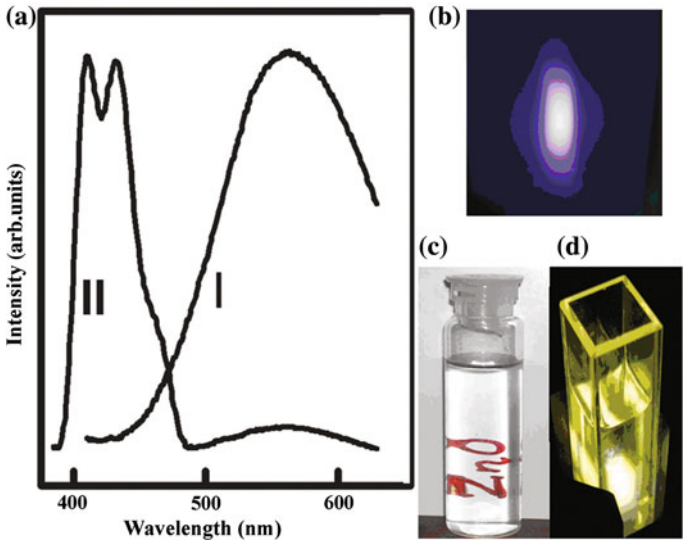

Fig. 12 **a** PL emission spectra of ZnO NPs grown without (curve I) and with (curve II) oxygen atmosphere at an excitation wavelength of 345 nm. **c** The photograph of synthesized transparent ZnO NPs and **d** its yellow PL emission under UV excitation. **b** The bluish-violet PL from the NPs grown in oxygen atmosphere [66]

Photoluminescence (PL) spectra were recorded using Jobin Yvon Fluoromax-3 spectrometer equipped with xenon lamp (150 W). PL measurement of NPs dispersed in neutral media was performed at an excitation wavelength of 345 nm. It was observed that the ZnO NPs dispersed in water show deep yellow luminescence as shown in Fig. 12. Figure 12c clearly pictures the photograph of ZnO NPs dispersed in water, which is highly transparent and its yellow emission under UV excitation (Fig. 12d). The origin of this yellow luminescence can be associated with the native oxygen defects [66] of the as-prepared ZnO NPs.

Oxygen bubbling experiment into the water during laser ablation of ZnO target was carried out to further confirm the origin of yellow luminescence due to oxygen vacancy. Bubbling of oxygen into water during laser ablation is found to suppress the yellow emission, resulting in PL emissions at 408 nm and 427 nm in the violet-blue region as shown in Fig. 12a (curve II). Photographic image displaying the deep bluish-violet emission is shown in Fig. 12b. The defect density was considerably reduced tending to more stoichiometric ZnO NPs due to the bubbling of oxygen into water during ablation, whereas the ZnO NPs grown under nitrogen atmosphere has similar size and PL emission characteristic as of those grown in neutral water without any gas bubbling. According to Lin et al. [85], the energy interval from valence band to zinc interstitials is found to be 2.9 eV. The PL emission at 427 nm for the ZnO NPs is very well consistent with these results. The weak Raman peak of the solvent corresponding to OH vibration was not detected in the PL spectra mainly because the PL emission intensity was very intense.

The ZnO NPs grown by LP-PLA method do not exhibit any green emission. However, the origin of green emission is still debatable. Nevertheless, there is strong evidence that it is presumably located at the surface [86]. And the absence of green PL emission proposes the desirable presence of $Zn(OH)_2$ on the surface of ZnO NPs grown through LP-PLA technique [87].

The growth mechanism of ZnO NPs by LP-PLA can be modeled as follows. The plasma on interaction of the laser beam with the ZnO target consisting of ionic and neutral species of Zn and oxygen [88] along with water vapor produced at the solid–liquid interface. High temperature (10^4–10^5 K) and pressure of few GPa [34] in the volume are produced due to the high intensity of the laser beam in the nanosecond scales. The adiabatic expansion of high-temperature plasma leads to the formation of ZnO which further interacts with the solvent water creating a thin layer of $Zn(OH)_2$ as ZnO is highly sensitive to H_2O environment [89]. As a result, a thin passivation layer of $Zn(OH)_2$ will be formed in ZnO NPs grown by LP-PLA in water. And the increase in the amount of dissolved oxygen due to oxygen bubbling into the water during the ablation process is found to promote the growth of ZnO NPs. This leads to the formation of bigger sized ZnO NPs. However, nitrogen bubbling into water does not make any extra oxygen other than that in the plasma produced by the laser interaction with the ZnO target. Hence, the particle size remains the same as those observed by LP-PLA in pure water.

Figure 13a shows the high-resolution transmission electron microscopic (HRTEM) image of the ZnO samples grown in acid media (pH ~ 5). The particles that have an elliptical shape with 15 nm size in the elongated region and 11 nm in the compressed region are observed from the HRTEM image. The SAED pattern (Fig. 13b) of the ZnO NPs prepared in acid media keeping all other experimental

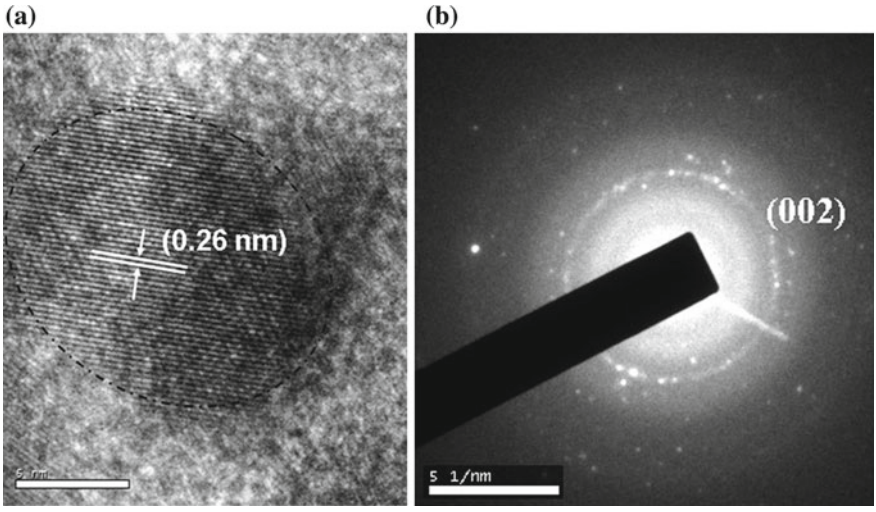

Fig. 13 **a** HRTEM image and **b** SAED pattern of ZnO NPs synthesized in acid media by LP-PLA method [83]

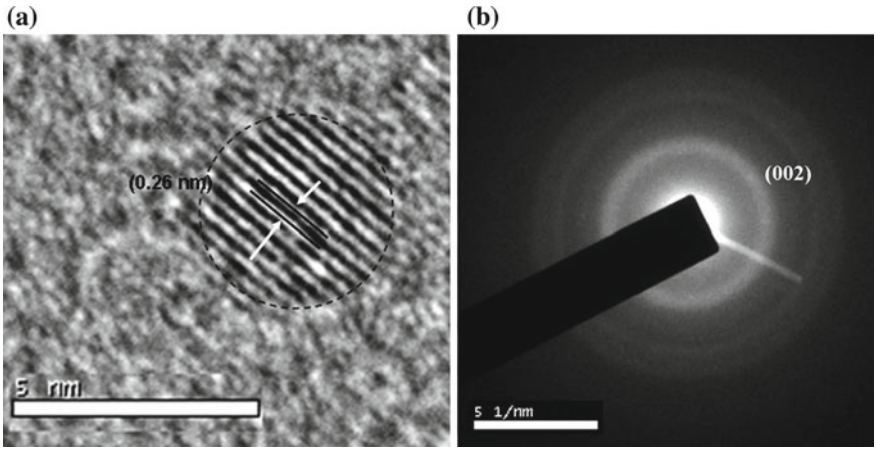

Fig. 14 **a** HRTEM image and **b** SAED pattern of ZnO NPs synthesized in basic media by LP-PLA method

parameters the same shows a ring pattern corresponding to the (002) plane of the wurtzite ZnO.

HRTEM and the SAED pattern of ZnO NPs prepared by pulsed laser ablation in basic media (pH ~ 9) are shown in Fig. 14a and b. Spherical particles having a size of about 4 nm were observed in the HRTEM image (Fig. 14a). SAED ring pattern indicates the (002) plane corresponding to the wurtzite ZnO. Altogether, these characterization results confirmed the formation of crystalline ZnO NPs by pulsed laser ablation in liquids.

The size of the ZnO NPs grown by LP-PLA in the acidic medium (pH = 5) shows relatively bigger than that synthesized in pure water under identical experimental conditions. Due to the higher dissolution rate of hydroxide in acidic medium, the formation of thin passivation layer of $Zn(OH)_2$ on the surface of the ZnO NPs during the cooling of laser plasma interacting with the liquid medium may be slower, thus favoring the formation of larger sized ZnO NPs. Whereas, the size of the ZnO NPs grown by ablation in alkali medium is smaller because the growth of $Zn(OH)_2$ is being favored by providing hydroxyl groups in the alkali medium. Thus, in conclusion, the thermodynamic conditions formed by the laser ablation plume in the liquid are localized to a nanometer regime which is not affected by the pH of the medium. Bigger sized NPs are formed with the increase in the energy of the laser beam due to ablation of large quantity of the material. The formation of hydroxide passivation layer is greatly determined by the pH of the solution which further alters the growth and size of the particles. As observed in the case of ablation of zinc metal targets in aqueous solution, no agglomeration of the particles was observed with the particles grown in neutral, acidic and alkaline media. Rather these particles were found to be well dispersed [90]. However, in the present study oxygen bubbling into water leads to the formation of bigger sized particles and agglomeration. As a result, the studies

suggest that the surface charge of ZnO NPs is mainly due to oxygen deficiency and less pronounced effect from pH of the medium.

4 Ceramic Nanoparticles by LP-PLA Technique

Optical imaging [91] is a powerful technique for imaging tissues or intracellular structures than magnetic resonance imaging [92] and radioactive molecular imaging (MRI) [93] because of its advantages such as low cost, high sensitivity and easy manipulation. The commonly used probes in optical imaging are fluorescent organic molecules and the other fluorescent nanoparticles. Traditional fluorescent dyes have limitations such as low fluorescence intensity and low photostability for using it as labeling agents [94].

There has been research interest in various luminescent semiconducting nanoparticles of CdSe, CdS, ZnS, InP, InAs, etc. as biological probes in diagnostic or targeted therapeutic applications. But many of these quantum dots are not suitable for medical application because of the presence of toxic materials such as cadmium or selenium, poor solubility and disposal issues. In this context, research has progressed to synthesize more suitable materials for medical and various biological applications. Researcher's main challenge is to develop a nanometer sized, highly biocompatible and biodegradable luminescent material for in-vivo imaging of human cells. Hydroxyapatite (HAp, $Ca_{10}(PO_4)_6(OH)_2$) is a typical green natural material because calcium phosphate is the inorganic mineral in bone and teeth. Lanthanide ions such as europium and terbium have interesting luminescence properties and which can be utilized for biological applications [95]. These rare-earth-doped materials exhibit narrow emission bands, and the emission color depends only on the dopant and doping concentration of lanthanide ions and not on the particle size. As pure hydroxyapatite is not able to exhibit substantial photoluminescence emissions, there is an ongoing research interest in the development of fluorescent lanthanide-doped hydroxyapatite which will demonstrate as promising materials for biomedical applications such as detection of tumor cells and as drug delivery vehicle to target tumor tissues or cells [96].

Nanoparticles of europium-doped HAp can be easily synthesized by the LP-PLA technique, and these nanoparticles emit light under UV and visible excitations. Fluorescent nanoparticles with visible excitation are ideal candidates for imaging of living cells. Pulsed laser ablation of a europium-doped HAp target immersed in 15 ml of water results in fluorescent HAp nanoparticles. Third harmonic of Nd-YAG laser (355 nm) with a repetition rate of 10 Hz is used for the LP-PLA experiment. Laser beam is focused on the target by using lens with a focal length of 20 cm. The target position was fixed at a position just before the focal point of the lens in order to avoid the pitting of target surface. The dependence of various processing parameters such as laser fluence, duration of ablation and the europium concentration on the properties of nanoparticles can be studied.

HRTEM image of the Eu-doped HAp sample shown in Fig. 15 confirms the formation of spherically shaped nanoparticles, and the average size of the nanoparticles is about 13 nm. The crystalline nature of the Eu-doped HAp nanoparticles is observed from the selected area electron diffraction (SAED) pattern, and the ring pattern corresponds to various planes of monoclinic structure of hydroxyapatite.

The dependence of laser fluence on the luminescence emission is studied by varying laser fluence from 1.9 to 5.7 J/cm^2. The variation of luminescence intensity with laser fluence is shown in Fig. 16. Eu-doped HAp nanoparticles exhibit PL emissions at 531, 572, 601 and 627 nm with an excitation wavelength of 325 nm. These emissions are originated from electronic transitions within the f-subshell and are assigned to ^5D_j–^7F_j transitions that are parity forbidden [97] by the Laporte selection rule. The emission line at 531, 572, 601 and 627 nm corresponds to $^5D_1$–$^7F_0$, $^5D_0$–$^7F_0$, $^5D_0$–$^7F_1$ and $^5D_0$–$^7F_2$ transition, respectively. This PL emission from the nanoparticles confirms the inclusion of europium in the HAp host lattice. These luminescence transition levels are due to the spin–orbit coupling of six electrons in the f-subshell, and the transitions are assigned to the mixing of odd terms due to the crystal field [98]. Unlike other Eu^{3+} phosphors, the PL peak corresponds to $^5D_0$–$^7F_0$ transition centered at 572 nm which is found to be stronger than that of $^5D_0$–$^7F_{1,2}$ transitions. It is also found that luminescence intensity increases with laser fluence (inset of Fig. 16) and is attributed to the increase in the production of nanoparticles.

The dependence of duration of ablation on the intensity of emission is also studied, and it is shown in Fig. 17. Here, the luminescent intensity decreases with duration of ablation, and it is shown in the inset of the figure. The nanoparticles formed during the LP-PLA process may absorb the incident photon energy leading to secondary processes such as heating/melting and welding/sintering and result in larger particles for longer duration of ablation [99]. The decrease in luminescence intensity with the increase in laser ablation time from 1 to 4 h is due to the increase in the particle size

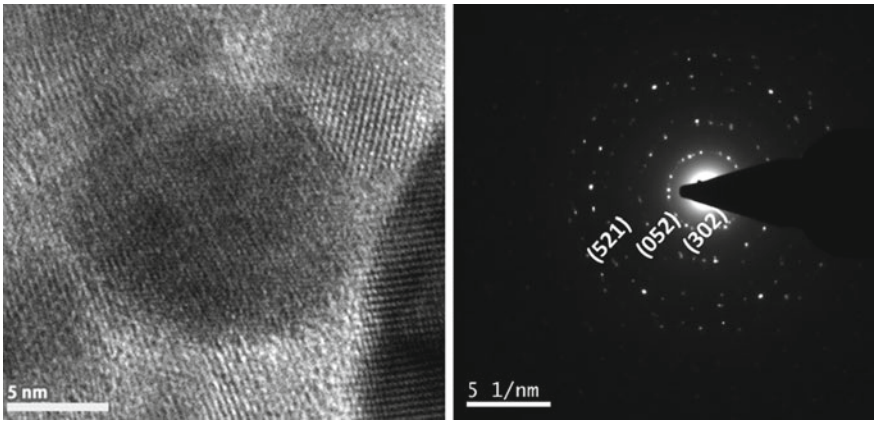

Fig. 15 HRTEM image (left) and SAED pattern (right) of Eu:HAp nanoparticles grown by LP-PLA technique

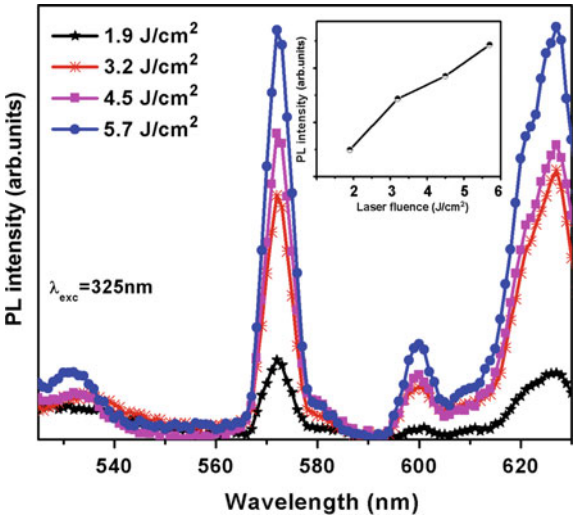

Fig. 16 PL emission spectra of Eu-doped HAp nanoparticles grown at different laser fluences. Inset shows the variation of PL intensity with laser fluence

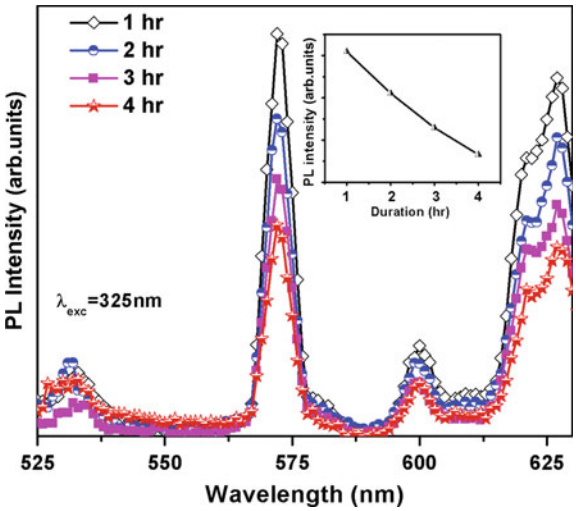

Fig. 17 PL spectra of Eu-doped HAp nanoparticles grown for different duration of ablation. Inset shows variation of PL intensity with duration of ablation

of the nanoparticles from 15 to 60 nm and which can be confirmed from the TEM images shown in Fig. 18.

Luminescent HAp nanoparticles with visible light excitation have applications in imaging of living cells for studying the change in situ at real time. Figure 19 (right)

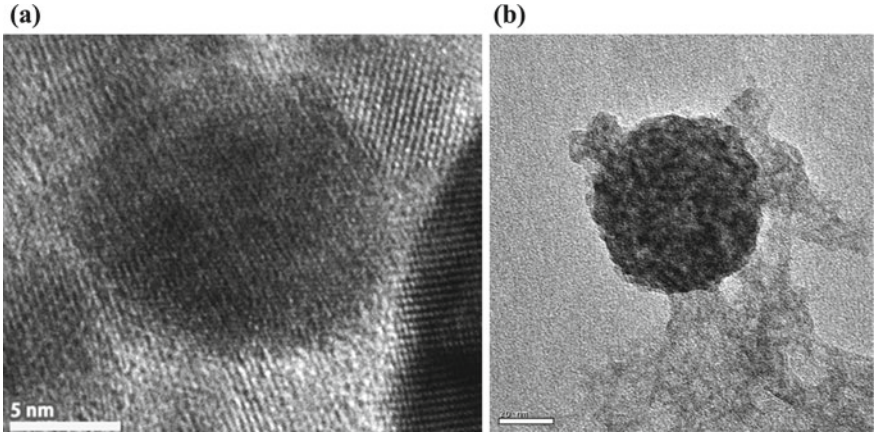

Fig. 18 TEM images of Eu-doped HAp nanoparticles grown at different duration of ablation. **a** 2 h and **b** 4 h

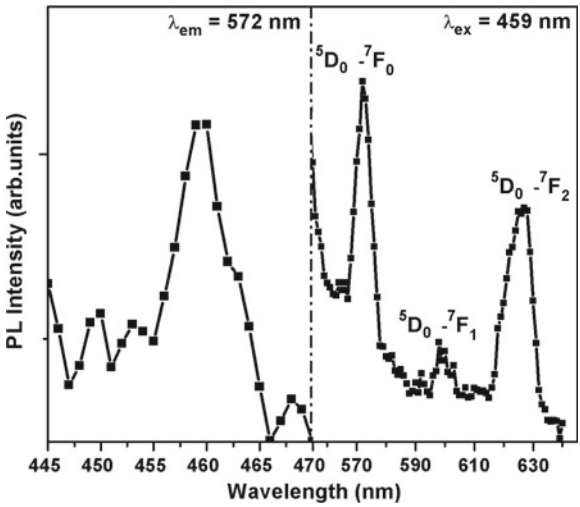

Fig. 19 Luminescence excitation (left) and emission (right) spectra under visible excitation of Eu-doped HAp nanoparticles

shows the PL spectra of Eu-doped HAp nanoparticles under visible excitation of 459 nm. It shows PL emissions at 572 nm, 601 nm and 627 nm and corresponds to the $^5D_0$–^7F_j (where $j = 0, 1, 2$) transitions of Eu^{3+} ion, respectively. A luminescence excitation spectrum monitored at emission wavelength 572 nm is shown in Fig. 19 (left). Excitation spectra showing a maximum at 459 nm correspond to the direct excitation of Eu^{3+} from the ground state to the higher level in the $4f^6$ configuration and can be assigned to $^7F_0$–$^5D_2$ transition.

5 Conclusions

Liquid phase-pulsed laser ablation (LP-PLA) is an excellent technique to synthesis nanoparticles of metals, semiconductors and ceramics without the addition of any surfactants. The properties of the particle can be modulated very easily by changing the parameters such as time of ablation, laser fluence, and pH of the medium. In summary, nanosized, chemically pure, gold (Au), silver (Ag), zinc oxide (ZnO) and europium (Eu^{3+})-doped Hydroxyapatite (HAp) nanoparticles were prepared through LP-PLA technique by varying the process parameters. The dependence of the work function on the ablation rate was explained using the example of LP-PLA of gold and silver nanoparticles. The ablation rate was found to increase with the decrease in work function. The size of the nanoparticles was found to increase with the increase of laser ablation fluence. The structural and luminescence properties of biocompatible ZnO and Eu^{3+}-doped HAp nanoparticles were studied in detail. These surfactant-free luminescent nanoparticles synthesized in water are ideal candidates for imaging of tumor cells and living cells and also for targeted drug delivery.

References

1. Yang PH, Sun X, Chiu J-F (2005) Transferrin-mediated gold nanoparticle cellular uptake. Bioconjugate Chem 16(3):494–496
2. Xueyi Z, Jianrong W, Gareth RW, Shiwei N, Qianqian Q, Li-Min Z (2019) Functionalized MoS_2-nanosheets for targeted drug delivery and chemo-photothermal therapy. Colloids Surf B 173(1):101–108
3. Gao X, Cui Y, Levenson M, Chung LWK, Nie S (2004) In vivo cancer targeting and imaging with semiconductor quantum dots. Nat Biotechnol 22(8):969–976
4. Chen J, Saeki F, Wiley BJ, Chang H, Cobb MJ, Li ZY, Au L, Zhang H, Kimmey MB, Li X, Xia Y (2005) Gold nanocages: bioconjugation and their potential use as optical imaging contrast agents. Nano Lett 5(3):473–477
5. Shengjie X, Dian L, Peiyi W (2015) One-pot, facile, and versatile synthesis of monolayer MoS_2/WS_2 quantum dots as bioimaging probes and efficient electrocatalysts for hydrogen evolution reaction. Adv Funct Mater 25(7):1127–1136
6. Kevin JM, Lihong J, Adam MB, Surangi J, Wen T, Mingyuan G, Robert L, Ana J (2018) Biocompatible semiconductor quantum dots as cancer imaging agents. Adv Mater 30(18):1706356 (1–18)
7. Brigger I, Dubernet C, Couvreur P (2002) Nanoparticles in cancer therapy and diagnosis. Adv Drug Deliv Rev 54(5):631–651
8. Chen J, Wiley B, Campbell D, Saeki F, Chang L, Au L, Lee J, Li X, Xia Y (2005) Gold nanocages: engineering their structure for biomedical applications. Adv Mater 17(18):2255–2261
9. Jeong-Eun P, Minho K, Jae-Ho H, Jwa-Min N (2017) Golden opportunities: plasmonic gold nanostructures for biomedical applications based on the second near-infrared window. Small Methods 1(3):1600032 (1–6)
10. Guanying C, Indrajit R, Chunhui Y, Paras NP (2016) Nanochemistry and nanomedicine for nanoparticle-based diagnostics and therapy. Chem Rev 116(5):2826–2885
11. Barcikowski S, Hustedt M, Chichkov BN (2008) Nanocomposite manufacturing using ultrashort-pulsed laser ablation in solvents and monomers. Polimery 53(9):657–662

12. Compagnini G, Scalisi AA, Puglisi O (2002) Ablation of Nobel metals on liquids: a method to obtain nanoparticles in a thin polymeric film. Phys Chem Chem Phys 4(12):2787–2791
13. Rybaltovskii AO, Buznik VM, Zavorotny YuS, Minaev NV, Timashev PS, Churbanov SN, Bagratashvili BN (2018) Synthesis of film nanocomposites under laser ablation and drift embedding of nanoparticles into polymer in supercritical carbon dioxide. Russ J Phys Chem B 12(7):1160–1165
14. Chacko L, Poyyakkara A, Kumar VBS, Aneesh PM (2018) MoS_2-ZnO nanocomposites as highly functional agents for anti-angiogenic and anti-cancer theranostics. J Mater Chem B. 6(19):3048–3057
15. Dijkkamp D, Venkatesan T, Wu XD, Shaheen SA, Jisrawi N, Minlee YH, Mclean WL, Croft M (1987) Preparation of Y-Ba-Cu oxide superconductor thin films using pulsed laser evaporation from high T_C bulk material. Appl Phys Lett 51(8):619–621
16. Silvia H, Kota H, Hikaru S, Hidenori H, Hideo H (2016) In-situ growth of superconducting $SmO_{1-x}F_xFeAs$ thin films by pulsed laser deposition. Sci Rep 6(35797):1–6
17. Pappas DL, Saenger KL, Bruley J, Krakow W, Cuomo JJ, Gu T, Collins RW (1992) Pulsed laser deposition of diamond-like carbon films. Appl Phys 71(11):5675
18. Cheng Y, Lu YM, Guo YL, Huang GJ, Wang SY, Tian FT (2017) Multilayers diamond-like carbon film with germanium buffer layers by pulsed laser deposition. Surf Rev Lett 24(02):1750014 (1–6)
19. Radhakrishnan G, Adams PM (1999) Pulsed-laser deposition of particulate-free TiC coatings for tribological applications. Appl Phys A 69(Suppl 1):S33–S38
20. Balakrishnan G, Elangovan T, Shin-Sung Y, Kim D-E, Kuppusami P, Venkatesh BR, Sastikumar D, Jungil S (2017) Microstructural and tribological studies of Al_2O_3/ZrO_2 nanomultilayer thin films prepared by pulsed laser deposition. Adv Mater Lett 8(4):410–417
21. Dureuil V, Ricolleau C, Gandais M, Grigis C, Lacharme JP, Naudon A (2001) Growth and morphology of cobalt nanoparticles on alumina. J Cryst Growth 233(4):737–748
22. Ayman MD, Wael HE, Ali AS, Mohamed HT (2015) Synthesis of nano-cadmium sulfide by pulsed laser ablation in liquid environment. Spectrosc Lett 48(9):638–645
23. Patil PP, Phase DM, Kulkarni SA, Ghaisas SV, Kulkarni SK, Kanetkar SM, Ogale SB, Bhide VG (1987) Pulsed-laser-induced reactive quenching at liquid–solid interface: aqueous oxidation of iron. Phys Rev Lett 58(3):238–241
24. Scherer GW (1985) Glasses and ceramics from colloids. J Non-Cryst Solids 73(1):661–667
25. Dahl JA, Maddux BL, Hutchison JE (2007) Towards greener nanosynthesis. Chem Rev 107(6):2228–2269
26. Hartmann S, Brandhuber D, Husing N (2007) Glycol-modified silanes: novel possibilities for the synthesis of hierarchically organized (hybrid) porous materials. Acc Chem Res 40(9):885–894
27. Mende S, Stenger F, Peukert W, Schwedes J (2004) Production of sub-micron particles by wet comminution in stirred media mills. J Mater Sci 39(16):5223–5226
28. Besner S, Kabashin AV, Winnik FM, Meunier M (2008) Ultrafast laser based "green" synthesis of non-toxic nanoparticles in aqueous solutions. Appl Phys A 93(4):955–959
29. Wang JB, Zhang CY, Zhong XL, Yang GW (2002) Cubic and hexagonal structures of diamond nanocrystals formed upon pulsed laser induced liquid–solid interfacial reaction. Chem Phys Lett 361(1–2):86–90
30. Suha IA, Adel KM, Zaineb FM (2015) Study the effect of different liquid media on the synthesis of alumina (Al_2O_3) nanoparticle by pulsed laser ablation technique. Manuf Sci Technol 3(4):77–81
31. Fabbro R, Fournier J, Ballard P, Devaux D, Virmont J (1990) Physical study of laser-produced plasma in confined geometry. J Appl Phys 68(2):775–784
32. Yang GW (2007) Laser ablation in liquids: applications in the synthesis of nanocrystals. Prog Mater Sci 52(4):648–698
33. Liu P, Cui H, Wang C, Yang GW (2010) From nanocrystal synthesis to functional nanostructure fabrication: laser ablation in liquid. Phys Chem Chem Phys 12(16):3942–3952

34. Berthe L, Fabbro R, Peyre P, Tollier L, Bartnicki E (1997) Shock waves from a water-confined laser-generated plasma. J Appl Phys 82(6):2826–2832
35. Zhu S, Lu YF, Hong MH (2001) Laser ablation of solid substrates in a water-confined environment. Appl Phys Lett 79(9):1396–1398
36. Zhu S, Lu YF, Hong MH, Chen XY (2001) Laser ablation of solid substrates in water and ambient air. J Appl Phys 89(4):2400–2403
37. Shaw SJ, Schiffers WP, Gentry TP, Emmony DC (1999) A study of the interaction of a laser-generated cavity with a nearby solid boundary. J Phys D 32(14):1612–1617
38. Takada N, Sasaki T, Sasaki K (2008) Synthesis of crystalline TiN and Si particles by laser ablation in liquid nitrogen. Appl Phys A 93(4):833–836
39. Rawat R, Tiwari A, Vendamani VS, Pathak AP, VenugopalRao S, Tripathi A (2018) Synthesis of Si/SiO_2 nanoparticles using nanosecond laser ablation of silicate-rich garnet in water. Opt Mater 75:350–356
40. Simakin AV, Voronov VV, Kirichenko NA, Shafeev GA (2004) Nanoparticles produced by laser ablation of solids in liquid environment. Appl Phys A 79(4):1127–1132
41. Anton AP, Gleb T, Noé D, Charlotte B, Khaled M, Nicola J, Al-Kattan A, Benoit L, Diane B, Serge M, Da Silva A, Marie-Anne E, Andrei VK (2019) Laser-synthesized TiN nanoparticles as promising plasmonic alternative for biomedical applications. Sci Rep 9(1):1194 (1–11)
42. Singh SC, Gopal R (2007) Zinc nanoparticles in solution by laser ablation technique. Bull Mater Sci 30(3):291–293
43. Neli M, Aljulaih AA, Wilfried W, Sergei AK, Satoru I (2018) Laser-ablated ZnO nanoparticles and their photocatalytic activity toward organic pollutants. Materials 11(7):1127 (1–11)
44. Tsuji T, Hamagami T, Kawamura T, Yamaki J, Tsuji M (2005) Laser ablation of cobalt and cobalt oxides in liquids: influence of solvent on composition of prepared nanoparticles. Appl Surf Sci 243(1–4):214–219
45. Borghei SM, Bakhtiyari F (2017) Study of the physical properties of cobalt/cobalt oxide particles synthesized by pulsed laser ablation in different liquid media. Acta Phys Pol A 131(3):332–335
46. Sreeja R, Reshmi R, Aneesh PM, Jayaraj MK (2012) Liquid phase pulsed laser ablation of metal nanoparticles for nonlinear optical applications. Sci Adv Mater 4(3–4):439–448
47. Dongshi Z, Wonsuk C, Jurij J, Mark-Robert K, Stephan B, Sung-Hak C, Koji S (2018) Spontaneous shape alteration and size separation of surfactant-free silver particles synthesized by laser ablation in acetone during long-period storage. Nanomaterials 8(7):529 (1–17)
48. Yeh MS, Yang YS, Lee YP, Lee HF, Yeh YH, Yeh CS (1999) Formation and characteristics of Cu colloids from CuO powder by laser irradiation in 2-propanol. J Phys Chem B 103(33):6851–6857
49. Marzun G, Bönnemann H, Lehmann C, Spliethoff B, Weidenthaler C, Barcikowski S (2017) Role of dissolved and molecular oxygen on Cu and PtCu alloy particle structure during laser ablation synthesis in liquids. Chemphyschem 18(9):1175–1184
50. Sylvestre JP, Poulin S, Kabashin AV, Sacher E, Meunier M, Luong JHT (2004) Surface chemistry of gold nanoparticles produced by laser ablation in aqueous media. J Phys Chem B 108(43):16864
51. Xiaoxia X, Lei G, Guotao D (2018) The fabrication of Au@C core/shell nanoparticles by laser ablation in solutions and their enhancements to a gas sensor. Micromachines 9(6):278 (1–13)
52. Dolgaev SI, Simakin AV, Voronov VV, Shafeev GA, Bozon-Verduraz F (2002) Nanoparticles produced by laser ablation of solids in liquid environment. Appl Surf Sci 186(1–4):546–551
53. De Bonis A, Santagata A, Galasso A, Laurita A, Teghil R (2017) Formation of titanium carbide (TiC) and TiC@C core–shell nanostructures by ultra-short laser ablation of titanium carbide and metallic titanium in liquid. J Colloid Interface Sci 489:76–84
54. Sugiyama M, Okazaki H, Koda S (2002) Size and shape transformation of TiO_2 nanoparticles by irradiation of 308-nm laser beam. Jpn J Appl Phys 41(7A):4666–4674
55. Wisam JA, Saja QA, Jassim NZ (2018) Production TiO_2 nanoparticles using laser ablation in ethanol. Silicon 10(5):2101–2107

56. Ankin KV, Melnik NN, Simakin AV, Shafeev GA, Voronov VV, Vitukhonovsky AG (2002) Formation of ZnSe and CdS quantum dots via laser ablation in liquids. Chem Phys Lett 366(3–4):357–360
57. Ismail RA, Hamoudi WK, Abbas HF (2018) New route for cadmium sulfide nanowires synthesis via pulsed laser ablation of cadmium in thiourea solution. Mater Res Express 5(2):025017 (1–26)
58. Xiao Y, Deng G, Feng G, Ning S, Wang S, Chen X, Yang H, Zhou S (2019) Femtosecond laser induced nano-meter size surface structures on ZnSe film. AIP Adv 9:015106 (1–6)
59. Compagnini G, Scalisi AA, Puglisi O (2003) Production of gold nanoparticles by laser ablation in liquid alkanes. J Appl Phys 94(12):7874–7877
60. Wang JB, Yang GW, Zhang CY, Zhong XL, Ren ZHA (2003) Cubic-BN nanocrystals synthesis by pulsed laser induced liquid–solid interfacial reaction. Chem Phys Lett 367(1–2):10–14
61. Yang L, May PW, Yin L, Smith JA, Rosser KN (2007) Growth of diamond nanocrystals by pulsed laser ablation of graphite in liquid. Diamond Relat Mater 16(4–7):725–729
62. Sasaki T, Liang C, Nichols WT, Shimizu Y, Koshizaki N (2004) Fabrication of oxide base nanostructures using pulsed laser ablation in aqueous solutions. Appl Phys A 79(4):1489–1492
63. Liang CH, Shimizu Y, Sasaki T, Koshizaki N (2003) Synthesis of ultrafine SnO_{2-x} nanocrystals by laser-induced reactive quenching in liquid medium. J Phys Chem B 107(35):9220–9225
64. Liang CH, Shimizu Y, Sasaki T, Koshizaki N (2005) Preparation of ultrafine TiO_2 nanocrystals via pulsed-laser ablation of titanium metal in surfactant solution. Appl Phys A 80(4):819–822
65. Zeng HB, Cai WP, Hu JL, Duan GT, Liu PS, Li Y (2006) Violet photoluminescence from shell layer of Zn/ZnO core–shell nanoparticles induced by laser ablation. Appl Phys Lett 88(17):171910 (1–3)
66. Ajimsha RS, Anoop G, Aravind A, Jayaraj MK (2008) Luminescence from surfactant-free Zno quantum dots prepared by laser ablation in liquid. Electrochem Solid-State Lett 11(2):K14–K17
67. Aneesh PM, Shijeesh MR, Aravind A, Jayaraj MK (2014) Highly luminescent undoped and Mn-doped Zns nanoparticles by liquid phase pulsed laser ablation. Appl Phys A: Mater Sci Process 116(3):1085–1089
68. Papavassiliou GC (1979) Optical properties of small inorganic and organic metal particle. Prog Solid State Chem 12(3–4):185–271
69. Festag G, Steinbruck A, Wolff A, Csaki A, Moller R, Fritzsche W (2005) Optimization of gold nanoparticle-based DNA detection for microarrays. J Fluoresc 15(2):161–170
70. Mishra YK, Mohapatra S, Avasthi DK, Kabiraj D, Lalla NP, Pivin JC, Sharma H, Kar R, Singh N (2007) Gold-silica nanocomposites for the detection of human ovarian cancer cells: a preliminary study. Nanotechnology 18(34):345606 (1–5)
71. Mulvaney P (1996) Surface plasmon spectroscopy of nanosized metal particles. Langmuir 12(3):788–800
72. Favier F, Walter EM, Zach MP, Benter T, Penner RM (2001) Hydrogen sensors and switches from electrodeposited palladium mesowire arrays. Science 293(5538):2227–2231
73. Hu J, Odom TW, Lieber CM (1999) Chemistry and physics in one dimension: synthesis and properties of nanowires and nanotubes. Acc Chem Res 32(5):435–445
74. Kabashin AV, Meunier M (2003) Synthesis of colloidal nanoparticles during femtosecond laser ablation of gold in water. J Appl Phys 94(12):7941–7943
75. Mafune F, Kohno JY, Takeda Y, Kondow T, Sawabe H (2000) Formation and size control of silver nanoparticles by laser ablation in aqueous solution. J Phys Chem B 104(39):9111–9117
76. Turkevich J, Stevenson PC, Hillier J (1951) A study of the nucleation and growth processes in the synthesis of colloidal gold. J Discuss Faraday Soc 11:55–75
77. Gamaly EG, Rode AV, Davies BL (2002) Ablation of solids by femtosecond lasers: ablation mechanism and ablation thresholds for metals and dielectrics. Phys Plasmas 9(9):949–957
78. Link S, El Sayed MA (2003) Optical properties and ultrafast dynamics of metallic nanocrystals. Annu Rev Phys Chem 54:331–366
79. Karthikeyan B, Thomas J, Philip R (2005) Optical nonlinearity in glass-embedded silver nanoclusters under ultrafast laser excitation. Chem Phys Lett 414(4):346–350

80. Tilaki RM, Irajizad A, Mahdavi SM (2006) Stability, size and optical properties of silver nanoparticles prepared by laser ablation in different carrier media. Appl Phys A 84(1):215–219
81. Nichols WT, Sasaki T, Koshizaki N (2006) Laser ablation of a platinum target in water: III. Laser induced reactions. J Appl Phys 100(11):114913 (1–7)
82. Kooli F, Chsem IC, Vucelic W, Jones W (1996) Synthesis and properties of terephthalate and benzoate in intercalates of Mg-Al layered double hydroxides possessing varying layer charge. Chem Mater 8(8):1969–1977
83. Aneesh PM, Aravind A, Reshmi R, Ajimsha RS, Jayaraj MK (2009) Dependence of size of liquid phase pulsed laser ablated ZnO nanoparticles on pH of the medium. Trans Mater Res Soc Jpn 34(4):759–763
84. Zeng HB, Cai WP, Li Y, Hu JL, Liu PS (2005) Composition/structural evolution and optical properties of ZnO/Zn nanoparticles by laser ablation in liquid media. J Phys Chem B 109(39):18260–18266
85. Lin BX, Fu ZX, Jia YB (2001) Green luminescent center in undoped zinc oxide films deposited on silicon substrates. Appl Phys Lett 79(7):943–945
86. Djurisic AB, Leung YH (2006) Optical properties of ZnO nanostructures. Small 2(8–9):944–961
87. Zhou H, Alves H, Hofmann DM, Kriegseis W, Meyer BK, Kaczmarczyk G, Hoffmann A (2002) Behind the weak excitonic emission of ZnO quantum dots: ZnO/$Zn(OH)_2$ core–shell structure. Appl Phys Lett 80(2):210–212
88. Joshy NV, Saji KJ, Jayaraj MK (2008) Spatial and temporal studies of laser ablated ZnO plasma. J Appl Phys 104(5):053307 (1–6)
89. Nakagawa M, Mitsudo H (1986) Anomalous temperature dependence of the electrical conductivity of zinc oxide thin films. Surf Sci 175(1):157–176
90. He C, Saski T, Usui H, Shimizu Y, Koshizaki N (2007) Fabrication of ZnO nanoparticles by pulsed laser ablation in aqueous media and pH-dependent particle size: an approach to study the mechanism of enhanced green photoluminescence. J Photochem Photobiol A: Chem 191(1):66–73
91. Weissleder R (2001) A clearer vision for in vivo imaging. Nat Biotechnol 19(4):316–317
92. Mahmoudi M, Hosseinkhani H, Hosseinkhani M, Boutry S, Simchi A, Journeay WS, Subramani K, Laurent S (2011) Magnetic resonance imaging tracking of stem cells in vivo using iron oxide nanoparticles as a tool for the advancement of clinical regenerative medicine. Chem Rev 111(2):253–280
93. Paulus MJ, Gleason SS, Easterly ME, Foltz CJ (2001) A review of high-resolution X-ray computed tomography and other imaging modalities for small animal research. Lab Anim 30(3):36–45
94. Zondervan R, Kulzer F, Kol'chenko MA, Orrit M (2004) Photobleaching of Rhodamine 6G in poly(vinyl alochol) at the ensemble and single-molecule levels. J Phys Chem A 108(10):1657–1665
95. Dosev D, Nichkova M, Kennedy IM (2008) Inorganic lanthanide nanophosphors in biotechnology. J Nanosci Nanotechnol 8(3):1052–1067
96. Yang C, Yang P, Wang W, Gai S, Wang J, Zhang M, Lin J (2009) Synthesis and characterization of Eu-doped hydroxyapatite through a microwave assisted microemulsion process. Solid State Sci 11(11):1923–1928
97. Chane-Ching JY, Lebugle A, Rousselot I, Pourpoint A, Pelle F (2007) Colloidal synthesis and characterization of monocrystalline apatite nanophosphors. J Mater Chem 17(28):2904–2913
98. Jagannathan R, Kottaisamy M (1995) Eu^{3+} luminescence: a spectral probe in $M_5(PO_4)_3X$ apatites (M = Ca or Sr; X = F^-, Cl^-, Br^- or OH^-). J Phys: Condens Mater 7(44):8453–8466
99. Yan Z, Chrisey DB (2012) Pulsed laser ablation in liquid for micro-/nanostructure generation. J Photochem Photobiol C 13(3):204–223

Chapter 4
Optical Properties of Quantum Well Structures

P. M. Aneesh, R. Reshmi and M. K. Jayaraj

1 Introduction

A *quantum well* is a layer of few nanometer thick which can confine electrons or holes (particles) in the dimension perpendicular to the surface of the layer, whereas in the other dimensions the movement is not restricted. Quantum wells can be realized by sandwiching a thin layer (confinement layer) of small bad gap semiconductor between the wider band gap semiconductors. It is a heterojunction between the smaller and the wider band gap semiconductors that creates a potential well confining the electrons and the holes in the smaller band gap material, and these structures are called type I quantum well. But in a type II quantum well, the electrons and the holes are confined in different layers. The band diagrams of type I and II quantum well structures formed with n-type semiconductors are shown in Figs. 1 and 2. Accordingly, the motions of the carriers, electrons and the holes are restricted in one dimension (along the thickness direction) and when the electrons are present in conduction band, it corresponds to a two-dimensional electron gas (2DEG) system.

The inherent band structure of semiconductors gives an insight into the optical properties of the bulk material. However, the carrier motion is restricted to quasi-two dimensions in quantum well structures. Also, the quantum confinement of carriers in the nanometer regime results in quantum size effects and hence reflected in the optical properties. The quantum well (QW) structures have very small volume. Therefore,

P. M. Aneesh (✉)
Department of Physics, Central University of Kerala, Tejaswini Hills, Periye, Kasaragod, Kerala 671320, India
e-mail: aneeshpm@cukerala.ac.in

R. Reshmi
Department of Physics, Union Christian College, Aluva, Kerala 683102, India

M. K. Jayaraj
Department of Physics, Cochin University of Science and Technology, Kochi 682022, India

M. K. Jayaraj (ed.), *Nanostructured Metal Oxides and Devices*,
Materials Horizons: From Nature to Nanomaterials,
https://doi.org/10.1007/978-981-15-3314-3_4

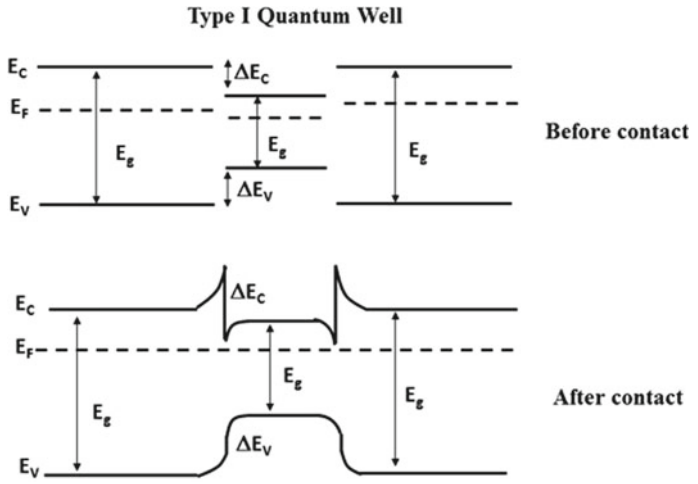

Fig. 1 Band diagram of type I quantum well structures formed by n-type semiconductors

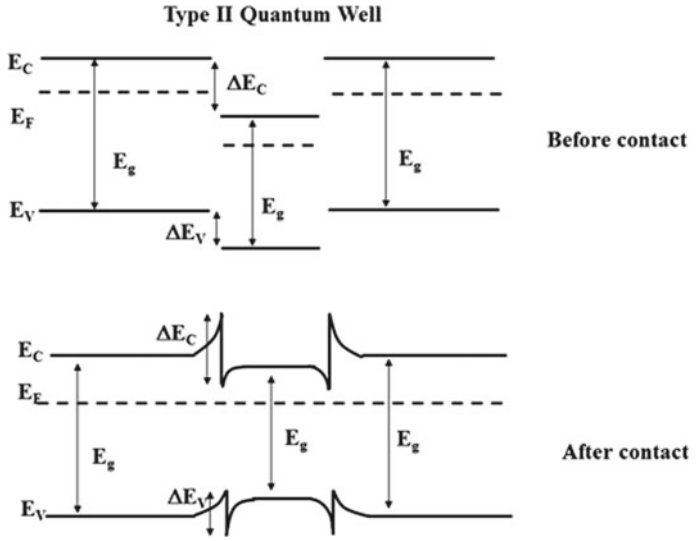

Fig. 2 Band diagram of n-type semiconductors forming type II quantum well

high concentration of free carriers will be observed when carriers are injected into a QW structure. As a result, high radiative efficiency is formed in QW structures at high free carrier concentrations as the non-radiative deep-level transitions are less likely to occur. Because of the small volume of active region in QW structures, small carrier density is required to achieve population inversion in QW lasers. Hence, the QW structures have low threshold current density. As compared to bulk material,

surface recombination is insignificant in QW structures because in QW structures, carriers cannot reach the surface as they are trapped by the QW. Multiple quantum well (MQW) consists of more than one well and offers better carrier confinement due to higher injection efficiency into the MQW. Band filling is one of the major problems associated with single QW structures. As a result, luminescence saturation will occur at high current densities if the QW is filled with carriers. MQW structure not only preserves the benefits of single QW structures but also can be operated even at high current densities due to its larger volume of active region.

Over the past decades, intriguing research studies have been tremendously made in single or multiple quantum wells based on wide band gap semiconductors used as the active region in lasers. Compared to the usual double heterostructure lasers, quantum well lasers offer enhanced performance with lower threshold current and lower spectral width. In quantum wells, one can independently vary compositions and widths of barrier and confinement layers that result in optical confinement and electron injection. It is to be noted that the confinement factor of the optical mode is significantly smaller for the single quantum well compared to the multiple quantum well lasers. Thus, the threshold current and carrier densities for single quantum well lasers are very high; however, by using a graded-index cladding structure the confinement factor of single quantum well lasers can be significantly increased [1]. The emission from the quantum well structures is defined by the quality of confinement and barrier layer and the interface between these layers. Thus, epitaxial layers are commonly used for the device applications.

The fabrication of single quantum well (SQW) and multiple quantum well (MQW) has given rise to novel optical and electrical devices together with new physical phenomena [2]. Dingle and co-workers explored the optical properties of quantum wells for the first time [3]. The potential application of quantum well structures in semiconductor laser diodes [4, 5] has attracted ample attention because of their superior properties, such as low threshold current density [6–8], low temperature dependence of threshold current [9, 10], excellent dynamic properties [11, 12] and tunability of lasing wavelength. The electron and hole wave functions can be modified by controlling the width of the quantum wells, which leads to the modification of material parameters. This leads to the improvements in the laser characteristics, as well as introduction of new concepts to semiconductor optical devices.

Total energy of the electron in quantum well can be considered as the sum of the kinetic energy due to its free motion along two directions (say x and y) and the allowed energies associated with the motion of these carriers along the confinement direction (say z-direction). Thus,

$$E_{\text{Total}} = \text{En}_z + \frac{\hbar^2}{2\text{ma}^2}(k_{x^2} + k_{y^2}) \tag{1}$$

where "a" is the thickness of the confinement layer corresponding to the width of the potential well, n_z is quantum number having values 1, 2, 3, etc., and k_x and k_y represent the wave vectors along x- and y-directions. Thus, in QW structure the

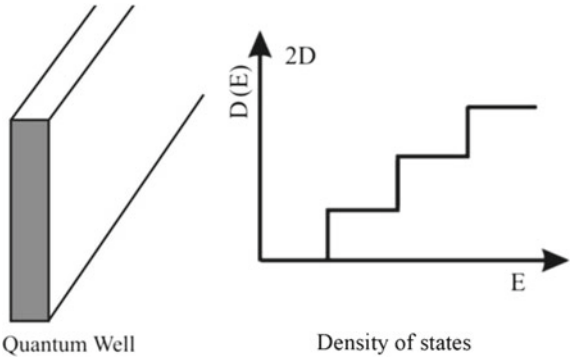

Fig. 3 Schematic illustration of quantum well structures and density of states

quasi-continuous energy band changes to discrete energy levels as a result of the confinement of the electron in one direction.

Density of states is the number of energy states present in a unit energy interval per unit volume. Density of states of a single QW is given by

$$\rho_c(E) = \sum_{n=1}^{\infty} \frac{m_c}{\pi \hbar^2} H[E - \mathrm{En}_z] \tag{2}$$

where $H[x]$, m_c and En_z are the Heaviside function, effective mass of the electrons and quantized energy levels of the electrons in the n^{th} sub-band of the QW, respectively. When the barriers are sufficiently high and barrier thickness is sufficiently large, then

$$\mathrm{En}_z = \frac{(n_z \pi \hbar)^2}{2 m_c L^2} \tag{3}$$

where L is the thickness of QW (Fig. 3).

The density of states of multiple quantum well structure is different from that of single QW. When the barrier layers between the confinement layers are thick enough, then each well is independent. In such cases, density of states of MQW with N number of QW is N times the density of states of electrons in a single QW [13].

$$\rho_c(E) = N \sum_{n=1}^{\infty} \frac{m_c}{\pi \hbar^2} H[E - \mathrm{En}_z] \tag{4}$$

If the barrier layer between the confinement layers is thin and the barrier height is small enough so that coupling between the adjacent wells is substantial, then the quantized energy levels are no longer degenerate and each single well level splits into N different energy levels. Density of states of electrons in this type of MQW is given by

$$\rho_c(E) = \sum_{n=1}^{\infty} \sum_{k=1}^{N} \frac{m_c}{\pi \hbar^2} H[E - \mathrm{En}_z k] \tag{5}$$

where $k = 1, 2, 3, \ldots, N$ corresponds to the splitting of energy level from the single well energy level. The density of states is constant within certain energy intervals for a quantum well with a rectangular profile.

Semiconductor lasers (or laser diodes, LDs), first demonstrated in 1962 and in those days, the entire laser industry is classified by many as industry of semiconductor lasers. The overall compactness and wall-plug efficiency make laser diodes a superior laser source. Major milestones in the development of semiconductor lasers include double heterostructure confining charge carriers in the active area and emitted light in the guiding layer. The extremely narrow active region of quantum well (QW) structures results in quantization of motion of carriers, electrons and holes and that results in a sharper density of state distribution in the energy domain and eventually to higher output efficiency. Wavelength selection and tunability with built-in diffraction gratings are the advantages of QW lasers. Distributed feedback (DFB), distributed Bragg reflector (DBR) lasers, quantum cascade (QC) lasers, etc., are some of the developments in this direction. Here, quantum tunneling resonances are responsible for the efficient population of the top energy level and depopulation of the bottom level. So, the wavelength range covered by semiconductor lasers can be increased through the introduction of new material systems.

QW laser is a promising light source for various applications, and thus considerable effort has been devoted to fabricate high-quality QW lasers. QW structures are used in optical modulators, optical bistable devices, p-i-n QW photodetectors, Q-switching laser light sources, etc. Multiple quantum wells (MQWs), with a spacing typically chosen large enough to avoid overlap of the corresponding wave functions, can be used if a large amount of optical gain or absorption is required.

2 Epitaxy

The word epitaxy comes from Greek in which *epi* means "above" and *taxis* means "in ordered manner." The word epitaxy was first used by a French scientist L. Royer in 1928. Epitaxy is defined as the growth of single-crystalline material on single-crystalline substrate. This phenomenon exists in the natural minerals itself where two crystals grow with a particular crystallographic orientation. Later in laboratory, some alkali halides were grown on alkali halides and mica, metals on metals and nonmetals, etc. The epitaxial growth of semiconductors opened new era in the field of thin-film technology in the 1950s. The epitaxial films of superconducting, ferroelectric, transparent conducting oxides are used in many day-to-day life devices such as Josephson junctions [14, 15], memory components [16, 17] and optoelectronic devices [18, 19]. Sophisticated techniques such as high-resolution X-ray diffraction and transmission electron microscopy are used for the analysis of these epitaxial films in terms of the

phase identification, composition determination, structure determination, defects in the crystals, orientation relationship, etc.

Epitaxy is in general classified into two categories, viz. homoepitaxy and heteroepitaxy. Homoepitaxy refers to a system with both substrate and the film of the same material. Epitaxial growth of ZnO films on ZnO substrate is considered as homoepitaxy. But if films of a particular material are epitaxially grown on another material, it is called heteroepitaxy. The epitaxial growth of ZnO on Al_2O_3 substrate is an example of heteroepitaxy. The crystal systems and the lattice parameters of the two phases determine the epitaxial growth of the material. In homoepitaxy, the lattice parameters of both substrate and film are the same. So, there will be no lattice strain at the interface. But in heteroepitaxy, there is generally a mismatch between the lattice parameters of film and substrate and the interface between them can be strained or relaxed depending on the difference between them. A film may grow on the substrate with a preferred orientation or may not have a preferred orientation in such a way that the interface energy must be a minimum. Lattice mismatch between the film and substrate is given by

$$f = \frac{a_\mathrm{f} - a_\mathrm{s}}{a_\mathrm{s}} \tag{6}$$

where a_f and a_s are the lattice parameters of the film and substrate, respectively.

The lattice mismatch in the heteroepitaxial growth can be minimized by rotating the planes of film with respect to substrate, or some plane of the film may align with the substrate plane. Another way to reduce the mismatch is by tilting the growth plane of the film with respect to that of the substrate by an angle.

3 Band Gap Tuning of ZnO

ZnO has been studied widely for the past years because of the intriguing optical properties and their applications in the optoelectronic devices. ZnO is a II–VI wide band gap (3.3 eV) semiconductor. It has a wurtzite structure with lattice constants of $a = b = 3.25$ Å and $c = 5.21$ Å. The high excitonic binding energy of ~60 meV is unique and represents excitonic contribution leading to fundamental absorption even at room temperature. Band structure modification by alloying is an important field of research for the fabrication of wide band gap heterostructures in ZnO. Like other semiconductors, ZnO also shows a possibility to tune its properties by substituting (alloying) bivalent metals like Cd, Mg, Be, etc., in place of Zn in the ZnO. The variation of band gap at room temperature of $A_xZn_{(1-x)}O$ alloy as a function of lattice constant is shown in Fig. 4. This plot indicates that theoretically the band gap of the $A_xZn_{(1-x)}O$ alloy can be tuned from 0.9 eV (CdO) to 10.3 eV (BeO) by varying the A concentration [20]. The band gap of ZnO is found to be decreasing with alloying of Cd, while it increases on alloying with Mg. This shows the possibility of band gap-engineered heterostructures for optoelectronic applications.

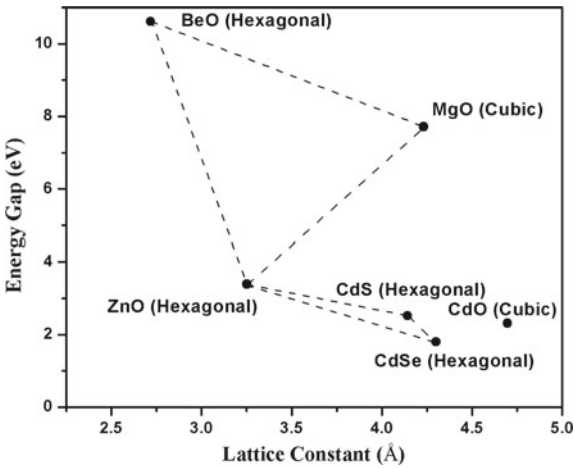

Fig. 4 Variation of band gap at room temperature of $A_xZn_{(1-x)}O$ alloy and its lattice parameters [21]

The band gap $E_g(x)$ of the ternary semiconductor $A_xZn_{1-x}O$ (where A = Mg or Cd) can be calculated by

$$E_g(x) = (1-x)E_{ZnO} + xE_{AO} - bx(1-x) \tag{7}$$

where b is the bowing parameter and E_{ZnO} and E_{AO} are the band gaps of binary compounds ZnO and AO, respectively. The bowing parameter depends on the difference in electronegativities of ZnO and AO.

Researchers are mainly focusing on the ternary ZnMgO and ZnCdO to fabricate devices based on ZnO heterostructures. The band gap can be tuned between 2.8 and 4 eV by alloying ZnO films with MgO or CdO (Fig. 5), which facilitates band gap

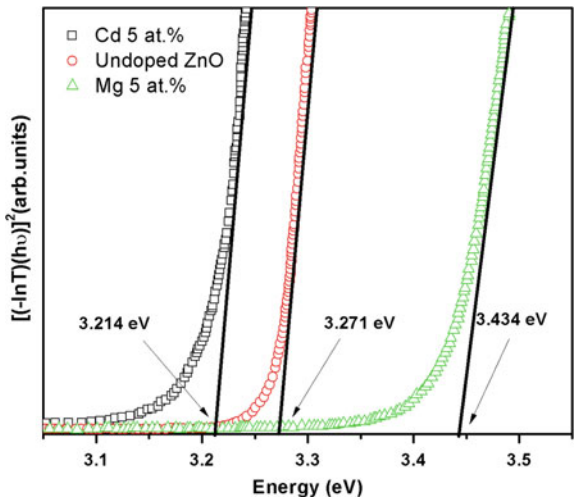

Fig. 5 Band gap energies of ZnO and 5 at.% Mg and Cd-doped ZnO thin films grown by PLD [22]

engineering in ZnO. Zinc oxide (ZnO) generally shows hexagonal wurtzite structure, whereas magnesium oxide (MgO) is cubic in nature. However, the ionic radii of Mg^{2+} (1.36 Å) and Zn^{2+} (1.25 Å) are almost equal, that allows some replacement in either structure. ZnO shows an excitonic binding energy of ~60 meV which results in the efficient excitonic emission, and based on these properties of ZnO, room-temperature lasing has been reported in thin films and micro-crystallites of ZnO [23]. $Zn_{1-x}Mg_xO$ films with wurtzite structure have been grown by pulsed laser ablation, and these films show a band gap tuning between 3.36 and 3.87 eV with increasing doping concentration of Mg atom resulting in ultraviolet photoluminescence at 4.2 K [24].

The understanding of ZnMgO alloy is much difficult because of the incompatible electronic configuration and crystal structure of ZnO (hexagonal structure with lattice constants $a = 3.24$ Å and $b = 5.20$ Å) and MgO (NaCl structure with lattice constant $a = 4.24$ Å). The solid solubility of MgO in ZnO is found to be less than 4 mol% which is evident from the phase diagram of the binary system ZnO–MgO [25]. However, these experimental outcomes are in contradiction with the standard semiconductor alloying like in AlGaAs and AlGaN, in which two or more components in the alloy have the same crystal structure so that the final alloy also has the same crystal structure.

The maximum achievable band gap without phase separation for hexagonal ZnMgO (Mg = 37 at.%) thin films is 4.28 eV. Further increase of Mg dopant concentration in $Zn_{(1-x)}Mg_xO$ alloy results in the mixing of hexagonal and cubic phases. Pure cubic phase $Zn_{(1-x)}Mg_xO$ (c-ZnMgO) appears when Mg composition in the thin film exceeds 62%, and depending upon the Zn/Mg content in the film, the band gap of the cubic MgZnO varies from ~5.4 to 7.8 eV [26]. Impurity in wide band gap semiconductors often causes dramatic changes in their electrical and optical properties [27–29].

The narrowing of the band gap results in the tuning of the emission wavelength into visible which is desirable for future optoelectronic devices. The incorporation of Cd into ZnO results in the narrowing of band gap efficiently because of the smaller band gap of cadmium oxide (CdO) (2.3 eV) than ZnO (3.3 eV), keeping the crystalline structure and lattice parameter close to ZnO. The incorporation of Mg or Cd into the ZnO lattice does not affect the overall transmission in the visible spectral range (Figs. 6 and 7). CdO generally shows cubic structure, whereas ZnO has hexagonal wurtzite structure. Li et al. studied the growth and optical properties of ZnCdO nanorods grown on copper substrate [30]. The effect of Cd incorporation on the microstructural and optical properties of ZnO thin films was investigated by Pillai et al. [31] and Mahmoud et al. have studied the dependence of temperature on the structure of Cd-doped ZnO nanopowders [32].

In order to design ZnO-based devices, it is imperative to have a clear understanding of band gap engineering to devise quantum wells and barrier layers in device heterostructures. The band gap of ZnO can be red shifted to blue or even to green spectral range with the doping of proper amount of Cd to ZnO, while keeping the crystalline structure and lattice parameter close to ZnO. ZnO-based light emitters and detectors based on the $ZnO/Zn_{(1-x)}Cd_xO$ heterojunction or superlattice can be

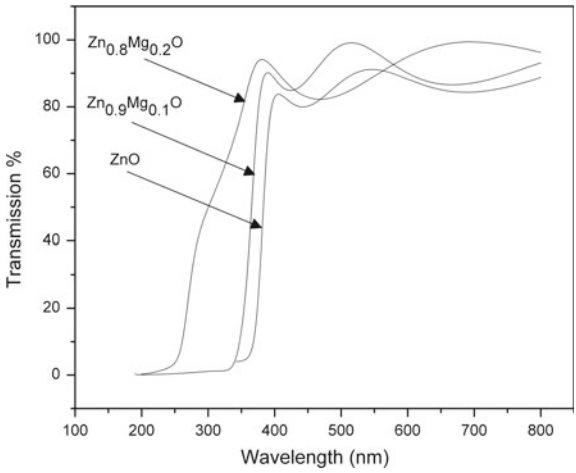

Fig. 6 Transmission spectra of $Zn_{0.8}Mg_{0.2}O$, $Zn_{0.9}Mg_{0.1}O$ and ZnO films grown on quartz substrate by PLD

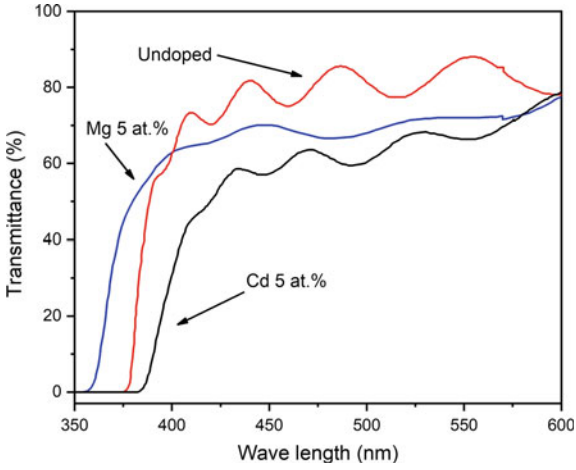

Fig. 7 Transmission spectra of ZnO and 5% Mg and Cd-doped ZnO films grown by PLD [22]

fabricated by the proper incorporation of Cd into ZnO. Because of the low thermodynamic solid solubility of Cd in ZnO bulk materials (2 at.%), the phase separation between wurtzite ZnO and rock salt CdO in a ZnCdO alloy is a major problem [33].

4 ZnO-Based Symmetric and Asymmetric Multiple Quantum Well Structures

Band gap engineering is an important research area for further ZnO-related applications. ZnO and its alloys have high luminous efficiency, high thermal conductivity, and mechanical and chemical robustness which makes it a good candidate

for optoelectronic device applications spanning from UV to red of the electromagnetic spectrum [34–36]. As compared to bulk semiconductors or III–V QWs, the excitons in ZnO-based quantum well (QW) heterostructures exhibit strong stability owing to the increase in the binding energy [37–39] and the reduction of the exciton–phonon coupling [40, 41] ascribed to quantum confinement. As a result, excitons are expected to play a substantial role in ZnO-based quantum wells. In order to design high-performance ZnO-based optoelectronic devices, it is necessary to have a deep understanding of the band gap engineering so as to forge barrier layers and quantum wells in heterostructure devices.

The ternary alloy semiconductor, $Zn_{(1-x)}Mg_xO$, is found to have larger band gap energy than ZnO with a lattice parameter exactly matching that of ZnO. Therefore, $Zn_{(1-x)}Mg_xO$ is predicted to be a promising candidate as barrier material for ZnO quantum wells. Recently, ZnO/ZnMgO multiple quantum wells (MQWs) are fabricated and studied for UV light-emitting applications [42–47]. Ohtomo et al. have used laser molecular beam epitaxy to grow ZnO/ZnMgO MQWs on lattice-mismatched sapphire substrates; however, no photoluminescence was observed above 150 K [48, 49]. Due to the poor quality of the grown MQW structures, quantum confinement effects could not be observed through optical absorption spectroscopy [49]. Krishnamoorthy et al. [50] fabricated single quantum wells of ZnO/ZnMgO on sapphire substrates using the pulsed laser deposition, and they reported size-dependent quantum confinement effects at 77 K employing pulsed PL measurements. A distinctive enhancement in the structural and optical characteristics of ZnO MQWs was accomplished by employing a lattice-matched substrate $ScAlMgO_4$ (SCAM) instead of lattice-mismatched sapphire substrates and was clear from their significant room-temperature photoluminescence [51] and apparent photoabsorption features [52]. However, compared to the sufficiently available sapphire substrates, the $ScAlMgO_4$ substrates are scarce and costly. It was therefore essential to refine and enhance the growth techniques of ZnO MQWs on sapphire substrates for efficient room-temperature PL studies.

Many semiconductor devices must take advantage of multiple quantum well structures for improved device performance. Many efforts must be devoted toward the understanding, design and fabrication of ZnO/ZnMgO MQWs for various optoelectronic applications. One of the major considerations regarding the design and fabrication of these MQW structures is to achieve maximum quantum efficiency, i.e., to maximize the optical emission from the confined states in the well regions and to minimize the optical losses outside the well regions. Recent studies on ZnO/ZnMgO MQWs have revealed that their structural and optical properties were greatly enhanced through the incorporation of lattice-matched substrates.

A ten-period $Zn_{0.9}Mg_{0.1}O/ZnO/Zn_{0.9}Mg_{0.1}O$ symmetric MQW was deposited by pulsed laser deposition (PLD) on Al_2O_3 substrates using the third (355 nm) and fourth (266 nm) harmonics of the Nd:YAG laser [53]. ZnO targets were prepared by hot-pressing high-purity ZnO powder and sintering at 1300 °C for 5 h in air. The hot-pressed $Zn_{0.9}Mg_{0.1}O$ target was prepared by sintering the mixture of ZnO and 10 at.% of MgO powder at 1300 °C.

Laser ablation experiments were carried out using Q-switched Nd:YAG laser of wavelengths 355 and 266 nm having repetition frequency 10 Hz with a pulse width of 6–7 ns. To avoid pitting of the surface, the target was rotated and the laser beam was concentrated on the target surface to a spot size of 2 mm. The growth chamber was evacuated by using turbo molecular pump backed with diaphragm pump to a base pressure of 10^{-6} mbar, and then O_2 (99.99% purity) was introduced as working gas, maintaining the pressure at 10^{-3} mbar. Oxygen pressure is required for the growth of crystalline films. The growth of crystalline films at high vacuum is very difficult due to the fact that the high energetic adatoms in the ablation plume will knock out the atoms which are already deposited on the substrate. The introduction of oxygen into the chamber increases the collisions of the ablated species. Thus, the energy of the ablated species reduces, thereby facilitating the oriented growth. However, the presence of large amount of oxygen pressure would largely reduce the energy of the species, thus restricting the movement of these species on the surface of the substrate to positions of least energy. So, a very high oxygen pressure also reduces the crystallinity. The target to substrate distance was 6 cm, and the substrate temperature of 600 °C was maintained. The laser ablation was performed at constant laser energy of 2 J/cm^2 for all the depositions. ZnO and ZnMgO targets were ablated independently, and stylus profiler was employed to measure the thickness of the deposited film. A growth temperature of 750 °C or higher is needed for the growth of crystalline and optical quality ZnO films on sapphire substrate [54, 55] through domain epitaxy [56], but the ZnO/ZnMgO hetero-interfaces and ZnMgO alloy are chemically stable only below 650 °C [57]. To accomplish these contradictory growth requirements, a buffer-assisted growth methodology has been used [54]. To eliminate the lattice mismatch, a 50-nm ZnO buffer layer was first grown on Al_2O_3 substrate at 700 °C by pulsed laser ablation. Ten periods of $Zn_{0.9}Mg_{0.1}O$/ZnO/$Zn_{0.9}Mg_{0.1}O$ layer were deposited on this ZnO buffer layer maintaining a substrate temperature of 600 °C, whereas all the other deposition parameters were kept constant. This assures the formation of high crystalline quality barrier and quantum well layers along with the physically and chemically sharp interfaces. The thickness of $Zn_{0.9}Mg_{0.1}O$ barrier layer was kept at 8 nm and that of ZnO confinement layer was varied from 2 to 6 nm. All the layers were deposited sequentially without breaking the vacuum.

Figure 8 represents the schematic of the ZnMgO/ZnO/ZnMgO symmetric system and corresponding band diagrams. The band diagram of the ZnMgO contains the band diagram of ZnO, and hence ZnMgO/ZnO heterojunction is considered as type I (straddling) heterojunction. The band diagram indicates that for a symmetric MQW, the confinement is in the ZnO layer for both the carriers.

The energy shift due to the quantum size effects can be easily determined from luminescence emission measurements. Since the last decades, the band-edge photoluminescence in bulk, thin films, quantum wells and other nanostructures of ZnO have been extensively investigated and these studies have proposed the emergence of the PL spectra in the near-band gap region [53, 58–61]. The PL spectra near the band-edge emission are contributed from the transitions of free and bound excitons at low temperatures, followed by the appearance of shoulder peak on the lower energy side which is identified as their longitudinal optical phonon replica [62, 63]. Due

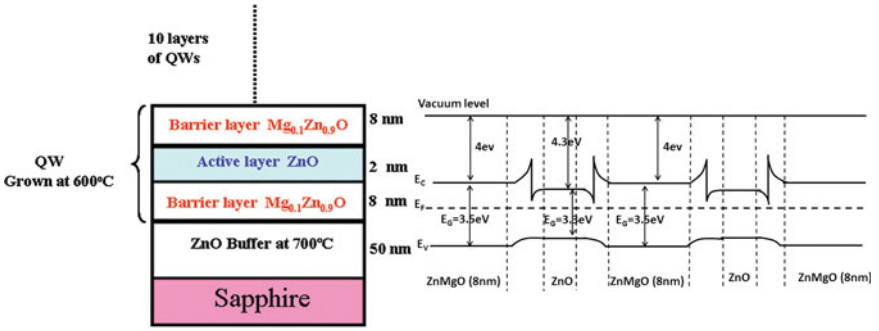

Fig. 8 Band diagram of the ZnMgO/ZnO/ZnMgO symmetric MQW systems grown by PLD [38]

to strong inhomogeneous broadening and thermal broadening, the near-band-edge PL spectra become broad at room temperature. Makino and colleagues investigated the band-edge PL emission of ZnO multiple quantum wells and reported that exciton recombination governs the photoluminescence emission at room temperature [43]. Furthermore, the weak PL spectrum due to thermal annihilation suggests that non-radiative recombination is dominant at room temperature compared to radiative recombination.

Room-temperature PL emission of ZnMgO/ZnO/ZnMgO symmetric MQW grown by third harmonic Nd:YAG laser ($\lambda_{ablation} = 355$ nm) shown in Fig. 9 has a broad peak with small spikes. The PL peak at 352 nm corresponds to the band edge

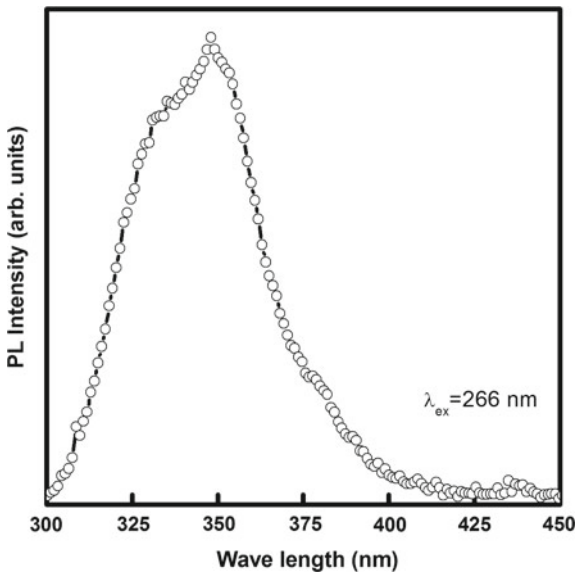

Fig. 9 Room-temperature PL emission ($\lambda_{ex} = 266$ nm) of ZnMgO/ZnO/ZnMgO symmetric MQW grown with third harmonic of Nd:YAG laser

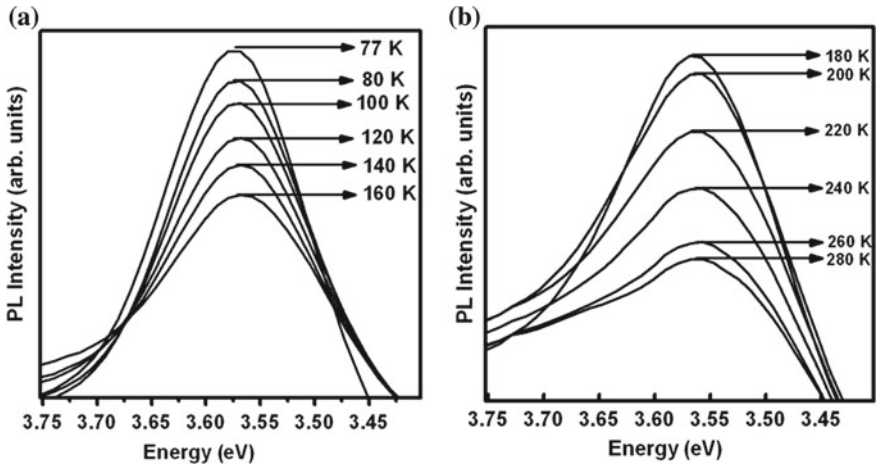

Fig. 10 Low-temperature PL (**a** 77–160 K and **b** 180–280 K) of symmetric ZnMgO/ZnO/ZnMgO MQW at an excitation of $\lambda_{ex} = 266$ nm

of ZnO. The large FWHM (~39 nm) and small spikes in the PL spectra are ascribed to the interface roughness and fluctuations in the well layer thickness.

Figure 10a and b represents the temperature-dependent PL spectra of ZnMgO/ZnO/ZnMgO symmetric MQW grown with third harmonic ($\lambda_{ablation} =$ 355 nm) of Nd:YAG laser. For symmetric MQW, the integral intensity of PL was found to decrease with increase in temperature. Thermal quenching of PL emission can be explained by [64]

$$I(T) = I(T = 0)/1 + C \exp(-E_a/\mathrm{KT}) \tag{8}$$

where $I(T)$ is the integrated PL emission intensity at temperature T, C is a constant describing the capture of carriers at center and E_a is the activation energy of the quenching process. The activation energy E_a can be obtained by fitting the PL intensity variation with temperature using Eq. (8). E_a was found to be comparable to the excitonic binding energy of ZnO, and its value was 46.57 meV. The decrease in E_a in the case of MQW may be due to quantum confinement effect.

The symmetric ZnMgO/ZnO/ZnMgO MQW grown by fourth harmonics of Nd:YAG laser with 2-nm confinement layer (ZnO layer) thickness shows a sharp PL emission peak centered at 362 nm at room temperature corresponding to the band edge of the ZnO (Fig. 11). The small peak at 350 nm can be attributed to the band-edge emission from the ZnMgO barrier layer [65]. The PL peak has smaller FWHM (~20 nm) compared to MQW grown by ablating with 355 nm (~39 nm), and spikes are absent in the spectrum which indicates the improvement in the layer quality. These investigations affirm the superiority of fourth harmonics of the Nd:YAG laser over third harmonics for the growth of MQW structures.

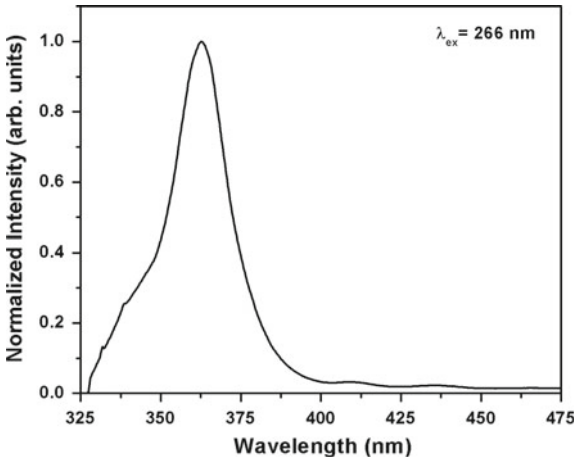

Fig. 11 Room-temperature PL emission of ZnMgO/ZnO/ZnMgO symmetric MQW grown with fourth harmonic of Nd:YAG laser (λ_{ex} = 266 nm)

The enhanced quality of barrier and confinement layers and the interface between these layers can be regarded to be the cause of improved PL emission from the MQW structure. Also, the improved properties of the layers can be associated with the laser ablation using fourth harmonic of Nd:YAG laser ($\lambda_{ablation} = 266$ nm). Higher absorption coefficients of the target material at shorter wavelength lead to the ablation of a thin surface layer of the material and are presumably noticed from the lower growth rate of materials during the ablation with fourth harmonic ($\lambda_{ablation} = 266$ nm) of Nd:YAG laser at a laser energy of 2 J/cm^2 than with third harmonic ($\lambda_{ablation}$ = 355 nm) of Nd:YAG laser. The lower laser wavelength, i.e., at higher incident photon energy, results in the highly energetic ablated particles, which improves the crystallinity of the layers.

Low-temperature PL measurements of the symmetric ZnMgO/ZnO/ZnMgO MQW structures having stronger electronic quantum confinement (i.e., ZnO thickness = 2 nm) are shown in Fig. 12. The peak intensity and the integral intensity of the PL emission were found to decrease with increase in temperature for symmetric MQWs. Thermal quenching of PL emission can be described by Eq. (1).

The integral intensity of the PL emission of symmetric MQWs with temperature is shown in Fig. 13. The activation energy of the carriers is calculated by fitting the experimental data with the theoretical equation given in (8). For the symmetric MQW structures, the activation energy was 24.6 meV. The constant C for symmetric MQW structures was 2.2×10^{10}.

Figure 14 shows the temperature dependence of PL peak position of the symmetric MQWs. A redshift in the PL peak position is observed with temperature which is ascribed to the temperature-induced band gap shrinkage. The full width at half maximum (FWHM) of PL peak also increases with temperature for symmetric MQWs (Fig. 14). The line width of PL peak of MQW gradually increases up to 200 K and then exponentially up to RT. The predominance of acoustic phonon scattering at lower temperatures is signified from the linear dependence of line width below

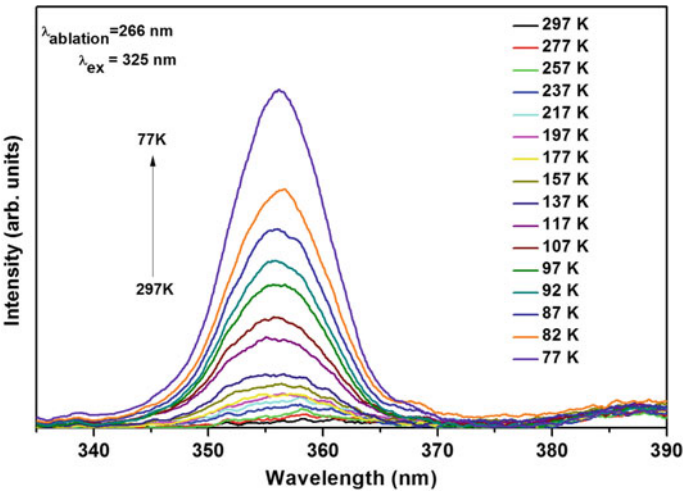

Fig. 12 Low-temperature PL emission of symmetric ZnMgO/ZnO/ZnMgO MQW grown by PLD [53]

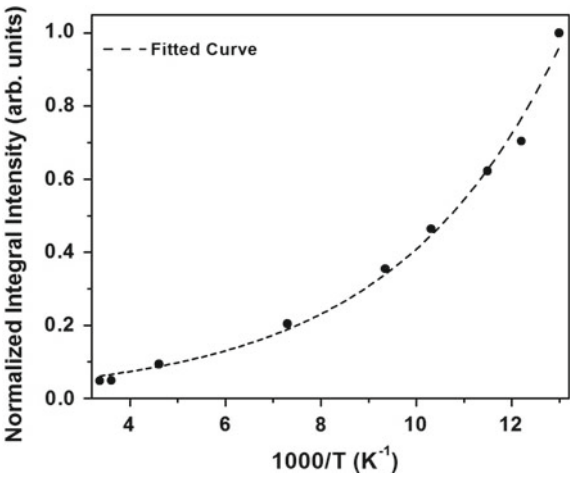

Fig. 13 Variation of PL integral intensity with temperature of the ZnMgO/ZnO/ZnMgO symmetric MQW grown by PLD [53]

200 K [66]. The exciton–longitudinal optic (LO) phonon interaction explains the exponential increase in PL line width at higher temperature range [67].

Figure 15 represents the room-temperature PL spectra of symmetric MQW structures for two different thicknesses of ZnO confinement layer (2 and 6 nm). As the thickness of ZnO well is reduced from 6 to 2 nm, a blueshift in the PL peak emission is observed as a result of the quantum confinement effect. As the confinement layer thickness is reduced, an increase in the FWHM of the PL bands is observed, which can be attributed to the fluctuations in well thickness or due to roughness at the interface for thinner wells.

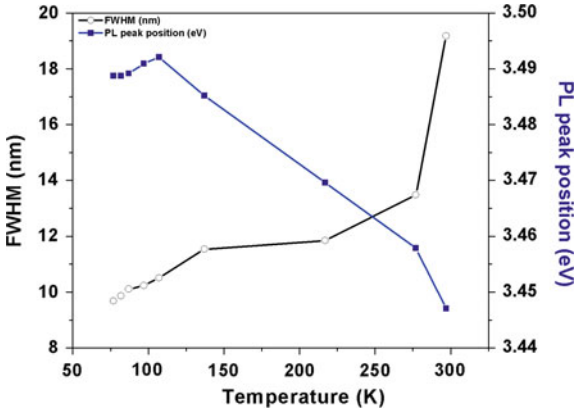

Fig. 14 Variation of FWHM and PL peak position of ZnMgO/ZnO/ZnMgO symmetric MQW with temperature [53]

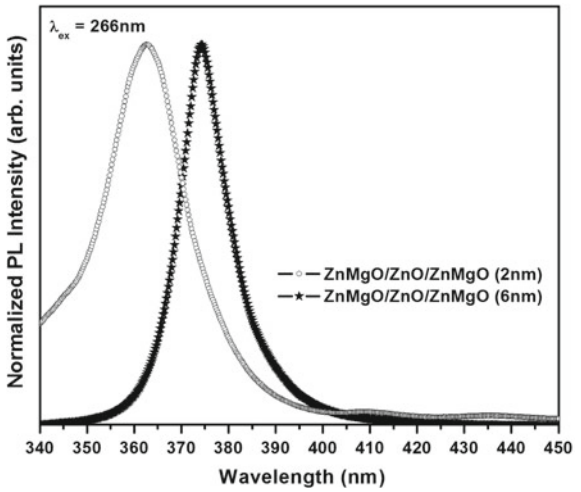

Fig. 15 Room-temperature PL emission spectra of ZnMgO/ZnO/ZnMgO symmetric MQWs for ZnO confinement layer thickness 2 and 6 nm [53]

Semiconducting optoelectronic devices making use of asymmetric quantum well heterostructures is a novel concept of band gap engineering. Initial results on lasers using asymmetric MQW heterostructure were described early in 1991 [68, 69]. In recent years, asymmetrical multiple quantum well systems have been the subject of extensive research interest because many new optical devices based on inter-sub-band transitions are being developed. This feature could facilitate the demand for adequate sources of coherent mid-infrared radiation having potential applications in several areas, such as communications, radar and optical electronics. Fabrication and application of quantum wells with varying widths and compositions give additional degrees of freedom to impose required laser regimes. Asymmetric MQW heterostructures are also used to investigate the dependence of the carrier relaxation and transport process on the quantum well parameters and laser structure design and to study the carrier distribution across the active region of the laser. Advantages of

asymmetric quantum wells [70] are that the electron–hole distance and hence the strength of the electron–hole interaction can be controlled by applying electric field perpendicular to the layer. Tsuchiya et al. reported the magnetic field dependence of the luminescence in GaAs/AlGaAs asymmetric quantum well as a function of applied electric field [71]. The luminescence emission studies of asymmetric quantum well structures based on ZnO are rare.

Normally, there are no electrons in the conduction band of semiconductors but upon excitation they can reach conduction band. When excited using optical radiation, the electron gets excited into the conduction band, leaving behind a hole in the valence band, thus forming exciton pairs. The excess energy present in the photon after the formation of exciton will be released as a phonon (heat). Usually, the energy corresponds to ground state in each well which is degenerate in nature. When an electric field is applied across the layers of the MQW, the degeneracy is lost and the potential appears as a slanted step function. When a photon have excess energy than that is needed for the formation of an exciton, it can cause an electron jump to a neighboring well having higher potential. Even if the energy of the photon is less than that required to excite an electron, an exciton can be formed by subsequently jumping the electron to a well with a lower ground-state potential. This type of carrier injection is prominent in p and n barriers in asymmetric MQW structures than in symmetric MQWs.

$CuMO_2$ (M = Ga, Al) is p-type transparent conducting oxide which finds applications in the field of transparent electronics [72–75]. $CuGaO_2$ is a direct band gap (3.4–3.6 eV) p-type semiconductor. In $CuGaO_2$ having delafossite structure, layers of A cations are linearly coordinated to two oxygen atoms and are alternatively stacked between layers of edge-shared $B^{3+}O_6$ octahedra oriented perpendicular to c-axis. Band structure calculations reveal a possibility of an indirect gap at 0.95 eV [76, 77]. The origin of p-type conductivity in delafossite structure arises from the +1 valence state of the Cu cation. The film will be a mixture of $CuGaO_2$, Cu_2O and $CuGa_2O_4$ at relatively low growth temperatures with a main phase of $CuGaO_2$ at higher temperatures. However, the challenge in the growth of $CuGaO_2$ thin films is in controlling and reducing the formation of impurity phases, mainly Cu_2O and $CuGa_2O_4$, induced by the variable valence states of Cu cations.

$CuGaO_2$/ZnO/$Zn_{0.9}Mg_{0.1}O$ asymmetric multiple quantum wells were successfully fabricated by laser ablation of ceramic targets in O_2 ambience. ZnO target was prepared by hot-pressing high-purity ZnO powder and sintering at 1300 °C for 5 h in air. On the other hand, $Zn_{0.9}Mg_{0.1}O$ target was synthesized from the mixture of ZnO and 10 at.% of high-purity MgO powder and then subjected to sintering at 1300 °C. Ultimately, through solid-state reaction of CuO and Ga_2O_3 powder, the $CuGaO_2$ target was developed which was followed by the sintering at 1100 °C in argon atmosphere.

Similar to the ZnMgO/ZnO/ZnMgO symmetric MQW, fourth harmonics of the Q-switched Nd:YAG laser (266 nm) were used for fabrication of $CuGaO_2$/ZnO/ZnMgO asymmetric MQW with repetition rate of 10 Hz and a pulse width of 6–7 ns. Laser beam was focused on to the surface of the target material to a spot size of 2 mm and

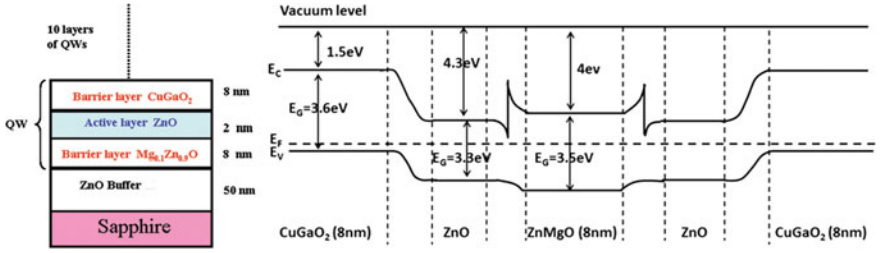

Fig. 16 Sample cross sections and band diagram of the asymmetric MQW $CuGaO_2$/ZnO/ZnMgO structure grown by PLD [53]

was rotated in order to avoid the non-uniform pitting of the target material. Employing turbo molecular pump backed with diaphragm pump, the growth chamber was evacuated to a base pressure of 10^{-6} mbar. Once the base pressure is attained, O_2 (99.99% purity) was introduced into the chamber, preserving the pressure at 10^{-3} mbar. The distance between the target and substrate was kept constant at 6 cm, and the substrate temperature was maintained at 600 °C. For all the depositions, the laser ablation was performed at constant laser energy of 2 J/cm^2. The targets, ZnO, ZnMgO and $CuGaO_2$, were laser ablated separately, and the deposited film thickness was calculated using stylus profiler. To eliminate the lattice mismatch-induced effects, 50-nm ZnO buffer layer was first grown on Al_2O_3 substrate at 700 °C by pulsed laser ablation. Then, at a substrate temperature of 600 °C, ten periods of $CuGaO_2$/ZnO/$Zn_{0.9}Mg_{0.1}O$ layer were grown on this ZnO template maintaining all the other deposition parameters the constant. The experiment confirmed the formation of high-quality crystalline barrier as well as ensured physically and chemically sharp interfaces between various layers. The thickness of $Zn_{0.9}Mg_{0.1}O$ and $CuGaO_2$ barrier layer was kept at 8 nm and that of ZnO confinement layer was varied from 2 to 6 nm. All the layers were deposited sequentially without breaking the vacuum.

Figure 16 shows the schematic representation of the $CuGaO_2$/ZnO/ZnMgO asymmetric MQW structure and corresponding band diagrams. As the valence band of the smaller band gap material (ZnO) lies below that of the larger band gap material ($CuGaO_2$), the $CuGaO_2$/ZnO heterojunction can be advised as type II (staggered) heterojunction. The band diagram indicates clearly that the holes will move to the $CuGaO_2$ side and electrons to the ZnO side in the asymmetric MQW.

The thickness of the individual layers of the MQW is affirmed by exploiting the cross-sectional images acquired using high-resolution transmission electron microscopy (HRTEM). Figure 17 represents the typical HRTEM image of the asymmetric MQW structure having confinement layer (ZnO layer) thickness 2 nm. The image shows the confinement layer has a thickness of 8 nm and the barrier layer has thickness of 16 nm. A divergence in the thickness was observed for asymmetric MQW measured from the rate of growth and the actual thickness.

Figure 18 signifies the low-temperature PL measurements of asymmetric MQW $CuGaO_2$/ZnO/ZnMgO structures from 77 K up to room temperature ($T = 293$ K) having confinement layers of thickness 6 nm. However, with increase of temperature

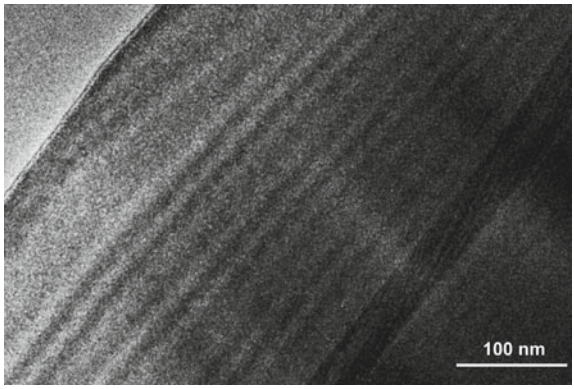

Fig. 17 Cross-sectional TEM image of the asymmetric MQW $CuGaO_2$/ZnO/ZnMgO structures grown by pulsed laser deposition [53]

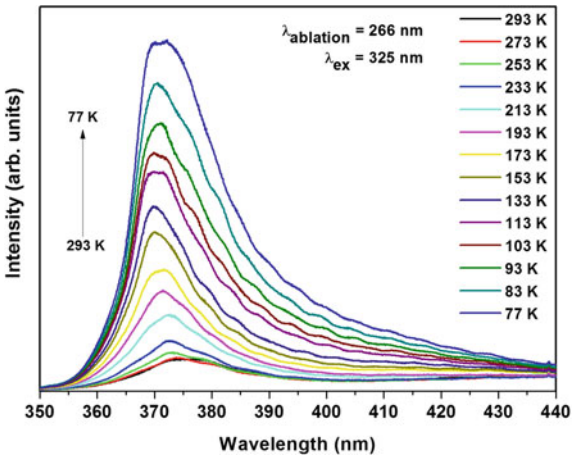

Fig. 18 Low-temperature PL of asymmetric $CuGaO_2$/ZnO/ZnMgO MQW grown by PLD [53]

in MQWs, it is noticed that the peak intensity and the integral intensity of the PL emission decrease. Thus, the thermal quenching of this emission line can be explained by Eq. (8).

Figure 19 shows the temperature dependence of integral intensity of the PL emission from the MQWs. The activation energy of the carriers is calculated by fitting the experimental data with the theoretical equation given in (2). The value of the activation energy for the asymmetric MQW structure was 32.71 meV. The constant C for asymmetric MQW structures was 22.03.

Figure 20 represents the temperature dependence of PL peak position of asymmetric MQWs. A redshift is observed in the PL peak position with increasing temperature ascribed to the temperature-induced band gap shrinkage. The variation of FWHM of PL peaks (Fig. 20) is found to increase with temperature. A progressive increase in the line width of PL peak of MQWs is noticed up to 200 K and further exponentially up to RT. The linear increase in line width below 200 K signifies the scattering of acoustic phonons at low temperatures [66]. The exciton–longitudinal

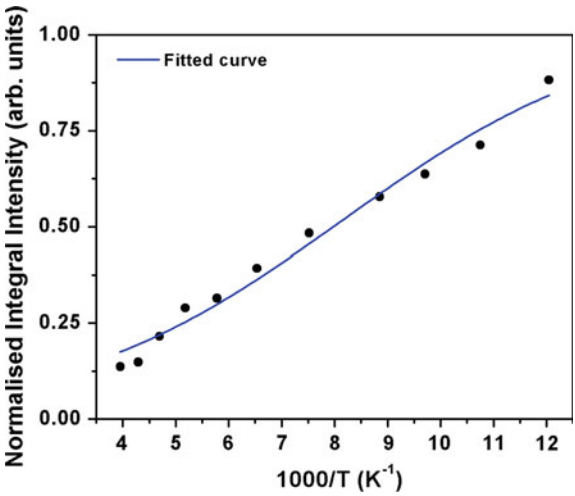

Fig. 19 Temperature-dependent PL integral intensity of $CuGaO_2$/ZnO/ZnMgO asymmetric MQW grown by PLD [53]

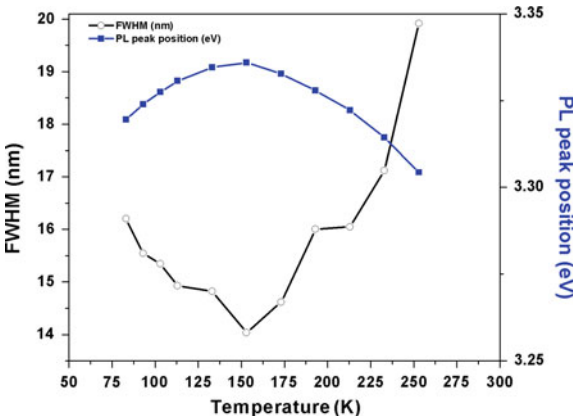

Fig. 20 Variation of FWHM and PL peak position of $CuGaO_2$/ZnO/ZnMgO asymmetric MQW with temperature [53]

optic (LO) phonon interaction results in the exponential increase in line width at higher temperature range [67].

Figure 21 shows PL spectra from the asymmetric MQW structures for two different thicknesses of ZnO confinement layer, 2 nm and 6 nm. As the thickness of ZnO well is reduced from 6 to 2 nm, a blueshift in the PL peak emission is noticed as a result of the quantum confinement effect. The FWHM of the PL bands increases as the confinement layer thickness is reduced which can be attributed to the fluctuations in well thickness or due to roughness at the interface for thinner wells.

Using infinite well approximation, the quantum energy state of carriers in the valence band well and the conduction band well is calculated. By taking into account the QW as an infinite well, it is feasible to analyze the energy shift of the PL emission with respect to the one in bulk ZnO as a function of the well thickness from the following expression

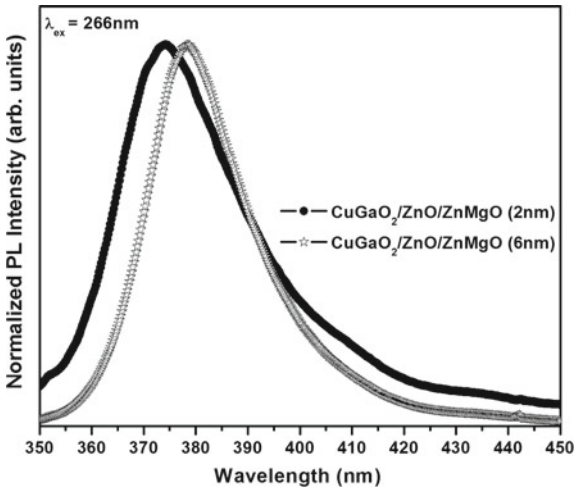

Fig. 21 Room-temperature PL emission from asymmetric MQW $CuGaO_2$/ZnO/ZnMgO with ZnO confinement layer thickness of 2 and 6 nm [53]

$$E_n = \frac{\hbar^2}{2m^*}\left[\frac{(n+1)\pi}{L_{QW}}\right]^2 \tag{9}$$

where m^* and L_{QW} are the effective mass of electron in bulk ZnO and the confinement layer thickness, respectively, while n is an integer that refers to the different excited states within the well (n equal to zero corresponds to the energy of the lowest energy state) [78].

On employing this simple model, it was observed that the confinement layer thickness of symmetric ZnMgO/ZnO/ZnMgO and asymmetric $CuGaO_2$/ZnO/ZnMgO MQW structures obtained from the PL peak position was found to be larger than that obtained using the growth rates. As calculated from the rate of growth, the 2-nm-thick confinement layer in the asymmetric MQW $CuGaO_2$/ZnO/ZnMgO is found to exhibit a thickness of 8 nm as noticed from the TEM images and is consistent with that calculated from the PL peak position. Accordingly, a comparably small blueshift in the PL peak positions was observed due to the larger thickness of the confinement layer.

Room-temperature PL emission of asymmetric $CuGaO_2$/ZnO/ZnMgO and symmetric ZnMgO/ZnO/ZnMgO MQWs having confinement layer thickness of 2 nm at an excitation wavelength of 266 nm is shown in Fig. 22. Also, for comparison, the typical spectra of ZnO thin film deposited on Al_2O_3 substrate by PLD with a thickness of 150 nm are bestowed. A sharp PL emission centered around 361 nm is observed for symmetric MQW corresponding to the band edge of ZnO. The observed blueshift in the PL peak position comparable to the bulk is assigned to quantum confinement effects [79]. The shoulder peaks in the PL spectrum at shorter wavelengths (≈350 nm) correspond to the emission from the ZnMgO barrier layer [65]. A similar

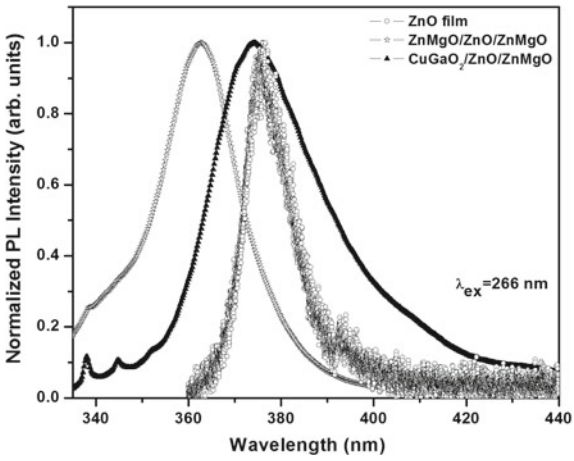

Fig. 22 Normalized room-temperature PL spectra of ZnO film, $CuGaO_2$/ZnO/ZnMgO asymmetric and ZnMgO/ZnO/ZnMgO symmetric MQW structures [53]

line shape is noticed for the PL spectrum of the asymmetric MQW sample with a red-shift corresponding to the higher thickness of the confinement layer than calculated from the rate of growth using Eq. (9).

5 Conclusions

Pulsed laser deposition has demonstrated an effective way to grow epitaxial metal oxide thin films. It allows the growth of the films in a high oxygen-rich environment. Efficient room-temperature photoluminescence emission and temperature dependence on the PL peak position, FWHM and integral intensity of PL emission were observed from the $CuGaO_2$/ZnO/ZnMgO asymmetric and ZnMgO/ZnO/ZnMgO symmetric multiple quantum well structures grown by buffer-assisted pulsed laser deposition using the fourth harmonic of a Nd:YAG laser. Ascribed to quantum confinement effects, a blueshift in the PL peak position was clearly noticed with the variation in the ZnO confinement layer thickness from 6 to 2 nm. Also, the FWHM of the PL bands increases with decreasing thickness of the confinement layer. Also, a blueshift in the PL peak position was observed for asymmetric and symmetric ZnO-based MQW than that of 150-nm-thick ZnO thin film.

References

1. Hersee SD, De Cremoux B, Duchemin JP (1984) Some characteristics of the GaAs/GaAlAs graded-index separate-confinement heterostructure quantum well laser structure. Appl Phys Lett 44(5):476–478

2. Esaki L, Tsu R (1970) Superlattice and negative differential conductivity in semiconductors. IBM J Res Dev 14(1):61–65
3. Dingle R, Gossard AC, Wiegmann W (1975) Direct observation of superlattice formation in a semiconductor heterostructure. Phys Rev Lett 34(21):1327–1330
4. van der Ziel JP, Dingle R, Miller RC, Wiegmann W, Nordland WA Jr (1975) Laser oxcillations from quantum states in very thin GaAs-$Al_{0.2}Ga_{0.8}As$ multilayer structures. Appl Phys Lett 26(8):463–465
5. Qiao Z, Tang X, Li X, Bo B, Gao X, Qu Y, Liu C, Wang H (2018) Monolithic fabrication of InGaAs/GaAs/AlGaAs multiple wavelength quantum well laser diodes via impurity-free vacancy disordering quantum well intermixing. IEEE J Electron Dev Soc 5(2):122–127
6. Tsang WT (1981) Extremely low threshold (AlGa)As modified multiquantum well heterostructure lasers grown by molecular beam epitaxy. Appl Phys Lett 39(10):786–788
7. Stange D, von den Driesch N, Zabel T, Armand-Pilon F, Rainko D, Marzban B, Zaumseil P, Hartmann J-M, Ikonic Z, Capellini G, Mantl S, Sigg H, Witzens J, Grützmacher D, Buca D (2018) GeSn/SiGeSn heterostructure and multi quantum well lasers. ACS Photonics 5(11):4628–4636
8. Qiao Z, Li X, Wang H, Li T, Gao X, Qu Y, Bo B, Liu C (2019) High-performance 1.06-μm InGaAs/GaAs double-quantum-well semiconductor lasers with asymmetric heterostructure layers. Semicond Sci Technol 34(5):055013 (1–6)
9. Arakawa Y, Sakaki H (1982) Multidimensional quantum well laser and temperature dependence of its threshold current. Appl Phys Lett 40(11):939–941
10. von den Driesch N, Stange D, Rainko D, Povstugar I, Zaumseil P, Capellini G, Schröder T, Denneulin T, Ikonic Z, Hartmann J-M, Sigg H, Mantl S, Grützmacher D, Buca D (2018) Advanced GeSn/SiGeSn group IV heterostructure lasers. Adv Sci 5(6):1700955 (1–7)
11. Arakawa Y, Vahala K, Yariv A (1985) Quantum noise and dynamics in quantum well and quantum wire lasers. Appl Phys Lett 45(9):950–952
12. Tabbakh TA, Likamwa PL (2019) Monolithically integrated InGaAsP multiple quantum well tunable laser diode for integrated optic surface plasmon resonance sensing. Opt Eng 57(12):120503
13. Harrison P (2005) Quantum wells, wires and dots: theoretical and computational physics of semiconductor nanostructures. Wiley, England, pp 1–482
14. Makise K, Sun R, Terai H, Wang Z (2015) Fabrication and characterization of epitaxial TiN-based Josephson junctions for superconducting circuit applications. IEEE Trans Appl Supercond 25(3):1–4
15. Cheng S-H, Zhang Y, Wang H-Z, Li Y-L, Yang C, Wang Y (2018) Fabrication and characterization of superconducting MgB_2 thin film on grapheme. AIP Adv 8(7):075015 (1–9)
16. Kim KL, Lee W, Hwang SK, Joo SH, Cho SM, Song G, Cho SH, Jeong B, Hwang I, Ahn J-H, Yu Y-J, Shin TJ, Kwak SK, Kang SJ, Park C (2016) Epitaxial growth of thin ferroelectric polymer films on graphene layer for fully transparent and flexible nonvolatile memory. Nano Lett 16(1):334–340
17. Liu J, Feng Y, Tang R, Zhao R, Gao J, Shi D, Yang H (2018) Mechanically tunable magnetic properties of flexible $SrRuO_3$ epitaxial thin films on mica substrates. Adv Electron Mater 4(4):1700522 (1–9)
18. Beaucarne G, Duerinckx F, Kuzma I, Van Nieuwenhuysen K, Kim HJ, Poortmans J (2006) Epitaxial thin-film Si solar cells. Thin Solid Films 511–512:533–542
19. Wu P, Chu Y (2018) Development of oxide heteroepitaxy for soft technology. J Mater Chem C 6(23):6102–6117
20. Ryu YR, Lee TS, Lubguban JA, Corman AB, White HW, Leem JH, Han MS, Park YS, Youn CJ, Kim WJ (2006) Wide-band gap oxide alloy: BeZnO. Appl Phys Lett 88(5):052103 (1–3)
21. Pyshkin S (2017) Optoelectronics: advanced materials and devices. IntechOpen Limited, United Kingdom, pp 25–58
22. Shan FK, Liu GX, Lee WJ, Shin BC (2006) Stokes shift, blue shift and red shift of ZnO-based thin films deposited by pulsed-laser deposition. J Cryst Growth 291(1):328–333
23. Tang ZK, Wong GKL, Yu P, Kawasaki M, Ohtomo A, Koinuma H, Segawa Y (1998) Room-temperature ultraviolet laser emission from self-assembled ZnO microcrystallite thin films. Appl Phys Lett 72(25):3270–3272

24. Ohtomo A, Kawasaki M, Koida T, Masubuchi K, Koinuma H, Sakurai Y, Yoshida Y, Yasuda T, Sewaga Y (1998) $Mg_xZn_{1-x}O$ as a II–VI widegap semiconductor alloy. Appl Phys Lett 72(19):2466–2468
25. Sarver JF, Katnack FL, Hummel FA (1959) Phase equilibria and manganese-activated fluorescence in the system $Zn_3(PO_4)_2$–$Mg_3(PO_4)_2$. J Electrochem Soc 106(11):960–963
26. Hullavarad SS, Hullavarad NV, Pugel DE, Dhar S, Takeuchi I, Venkatesan T, Vispute RD (2007) Homo- and hetero-epitaxial growth of hexagonal and cubic $Mg_xZn_{1-x}O$ alloy thin films by pulsed laser deposition technique. J Phys D Appl Phys 40(16):4887–4895
27. Sernelius BE, Berggren KF, Jin ZC, Granqvist CG (1988) Band-gap tailoring of ZnO by means of heavy Al doping. Phys Rev B 37(17):10244–10248
28. Teke A, Ozgur U, Dogan S, Gu X, Morkoc H, Nemeth B, Nause J, Everitt HO (2004) Excitonic fine structure and recombination dynamics in single-crystalline ZnO. Phys Rev B 70(19):195207 (1–10)
29. Wang FZ, He HP, Ye ZZ, Zhu LP (2005) Photoluminescence properties of quasialigned ZnCdO nanorods. J Appl Phys 98(8):084301 (1–4)
30. Li YJ, Wang CY, Lu MY, Li KM, Chen LJ (2008) Electrodeposited hexagonal ringlike superstructures composed of hexagonal Co-doped ZnO nanorods with optical tuning and high-temperature ferromagnetic properties. Cryst Growth Des 8(8):2598–2602
31. Kumar RV, Lethy KJ, Arunkumar PR, Krishnan RR, Pillai NV, Pillai VPM, Philip R (2010) Effect of cadmium oxide incorporation on the microstructural and optical properties of pulsed laser deposited nanostructured zinc oxide thin films. Mater Chem Phys 121(3):406–413
32. Mahmoud WE, Al-Ghamdi AA, Al-Heniti S, Al-Ameer S (2010) The influence of temperature on the structure of Cd-doped ZnO nanopowders. J Alloys Compd 491(1):742–746
33. Makino T, Segawa Y, Kawasaki M, Ohtomo A, Shiroki R, Tamura K (2001) Band gap engineering based on $Mg_xZn_{1-x}O$ and $Cd_yZn_{1-y}O$ ternary alloy films. Appl Phys Lett 78(9):1237–1239
34. Makino T, Segawa Y, Kawasaki M, Koinuma H (2005) Optical properties of excitons in ZnO-based quantum well heterostructures. Semicond Sci Technol 20:S78–S91
35. Pieniążek A, Teisseyre H, Jarosz D, Suffczyński J, Witkowski BS, Kret S, Boćkowski M, Reszka A, Godlewski M, Kozanecki A, Kowalski BJ (2019) Growth and optical properties of $ZnO/Zn_{1-x}Mg_xO$ quantum wells on ZnO microrods. Nanoscale 11(5):2275–2281
36. Rahman Faiz (2019) Zinc oxide light-emitting diodes: a review. Opt Eng 58(1):010901
37. Sun HD, Makino T, Tuan NT, Segawa Y, Tang ZK, Wong GKL, Kawasaki M, Ohtomo A, Tamura K, Koinuma H (2000) Stimulated emission induced by exciton-exciton scattering in ZnO/ZnMgO multiquantum well up to room temperature. Appl Phys Lett 77(26):4250–4252
38. Sun HD, Makino T, Segawa Y, Kawasaki M, Ohtomo A, Tamura K, Koinuma H (2002) Enhancement of exciton binding energies in ZnO/ZnMgO multiquantum wells. J Appl Phys 91(4):1993–1997
39. Bataev MN, Filosofov NG, Serov AYu, Agekyan VF, Morhain C, Kochereshko VP (2018) Excitons in ZnO quantum wells. Phys Solid State 60(12):2628–2633
40. Ozgur U, Alivov YI, Teke A, Liu C, Reshchikov MA, Dogan S, Avrutin V, Cho SJ, Morkoc H (2005) A comprehensive review of ZnO materials and devices. J Appl Phys 98(4):041301 (1–103)
41. Kang J-W, Song B, Liu W, Park S-J, Agarwal R, Cho C-H (2019) Room temperature polariton lasing in quantum heterostructure nanocavities. Sci Adv 5(4):eaau9338 (1–8)
42. Gruber T, Kirchner C, Kling R, Reuss F, Waag A (2004) ZnMgO epilayers and ZnO-ZnMgO quantum wells for optoelectronic applications in the blue and UV spectral region. Appl Phys Lett 84(26):5359–5361
43. Makino T, Chia CH, Tuan NT, Sun HD, Segawa Y, Kawasaki M, Ohtomo A, Tamura K, Koinuma H (2000) Room-temperature luminescence of excitons in ZnO/(Mg, Zn)O multiple quantum wells on lattice-matched substrates. Appl Phys Lett 77(7):975–977
44. Zhang BP, Binh NT, Wakatsuki K, Liu CY, Segawa Y, Usami N (2005) Growth of ZnO/MgZnO quantum wells on a sapphire substrates and observation of the two dimensional confinement effect. Appl Phys Lett 86(3):032105 (1–3)

45. Choi Y-S, Kang J-W, Kim B-H, Park S-J (2013) Enhanced ultraviolet emission of MgZnO/ZnO multiple quantum wells light-emitting diode by *p*-type MgZnO electron blocking layer. Opt Express 21(25):31560–31566
46. Kang J-W, Kim B-H, Song H, Jo Y-R, Hong S-H, Jung GY, Kim B-J, Park S-J, Cho C-H (2018) Radial multi-quantum well ZnO nanorod arrays for nanoscale ultraviolet light-emitting diodes. Nanoscale 10(31):14812–14818
47. Riane H, Mokaddem A, Temimi L, Doumi B, Bahlouli S, Hamdache F (2017) ZnO/ZnMgO: cubic quantum well laser in UV spectrum. Int J Adv Manuf Technol 89(1–4):629–633
48. Ohtomo A, Kawasaki M, Ohkubo I, Kojinuma H, Yasuda T, Segawa Y (1999) Structure and optical properties of ZnO/$Mg_{0.2}Zn_{0.8}O$ superlattices. Appl Phys Lett 75(7):980
49. Ohtomo A, Tsukazaki A (2005) Pulsed laser deposition of thin films and superlattices based on ZnO. Semicond Sci Technol 20(4):S1–S12
50. Krishnamoorthy S, Iliadis AA, Inumpudi A, Choopun S, Vispute RD, Venkatesan T (2002) Observation of resonant tunneling action in ZnO/$Zn_{0.8}Mg_{0.2}O$ devices. Solid-State Electron 46(10):1633–1637
51. Makino T, Tuan NT, Sun HD, Chia CH, Segawa Y, Kawasaki M, Ohtomo A, Tamura K, Suemoto T, Akiyama H, Baba M, Saito S, Tomita T, Koinuma H (2001) Temperature dependence of near ultraviolet photoluminescence in ZnO/(Mg, Zn)O multiple quantum wells. Appl Phys Lett 78(14):1979–1981
52. Sun HD, Makino T, Tuan NT, Segawa Y, Kawasaki M, Ohtomo A, Tamura K, Koinuma H (2001) Temperature dependence of exciton absorption spectra in ZnO/$Zn_{0.88}Mg_{0.12}O$ multiquantum wells grown on lattice-matched substrates. Appl Phys Lett 78(17):2464–2466
53. Aneesh PM, Jayaraj MK, Reshmi R, Ajimsha RS, Kukreja LM, Aldrin A, Rojas F, Bertomeu J, López-Vidrier J, Hernández S (2015) Observation of room temperature photoluminescence from asymmetric $CuGaO_2$/ZnO/ZnMgO multiple quantum well structures. J Nanosci Nanotechnol 15(5):3944–3950
54. Misra P, Kukreja LM (2005) Buffer-assissted low temperature growth of high crystalline quality ZnO films using pulsed laser deposition. Thin Solid Films 485(1):42–46
55. Ohkubo I, Matsumoto Y, Ohtomo A, Ohnishi T, Tsukazaki A, Lippmaa M, Koinuma H, Kawasaki M (2000) Investigation of ZnO/sapphire interface and formation of ZnO nanocrystalline by laser MBE. Appl Surf Sci 159–160:514–519
56. Narayan J, Larson BC (2003) Domain epitaxy: a unified paradigm for thin film growth. J Appl Phys 93(1):278–285
57. Ohtomo A, Shiroki R, Ohkubo I, Koinuma H, Kawasaki M (1999) Thermal stability of supersaturated $Mg_xZn_{1-x}O$ alloy films and $Mg_xZn_{1-x}O$/ZnO heterointerfaces. Appl Phys Lett 75(26):4088–4090
58. Monticone S, Tufeu R, Kanaev AV (1998) Complex nature of the UV and visible fluorescence of colloidal ZnO nanoparticles. J Phys Chem B 102(16):2854–2862
59. Shan W, Walukiewicz W, Ager JW III, Yu KM, Yuan HB, Xin HP, Cantwell G, Song JJ (2005) Nature of room-temperature photoluminescence in ZnO. Appl Phys Lett 86(19):191911 (1–3)
60. Yan D, Zhang W, Cen J, Stavitski E, Sadowski JT, Vescovo E, Walter A, Attenkofer K, Stacchiola DJ, Liu M (2017) Near band edge photoluminescence of ZnO nanowires: optimization via surface engineering. Appl Phys Lett 111(23):231901
61. Monreal RC, Apell SP, Antosiewicz TJ (2018) Quantum-size effects in visible defect photoluminescence of colloidal ZnO quantum dots: a theoretical analysis. Nanoscale 10(15):7016–7025
62. Sun CK, Sun SZ, Lin KH, Zhang KYJ, Liu HL, Liu SC, Wu JJ (2005) Ultrafast carrier dynamics in ZnO nanorods. Appl Phys Lett 87(2):023106 (1–3)
63. Sarkar K, Mukherjee S, Wiederrecht G, Schaller RD, Gosztola DJ, Stroscio MA, Dutta M (2018) Ultrafast carrier dynamics and optical pumping of lasing from Ar-plasma treated ZnO nanoribbons. Nanotechnology 29(9):095701
64. Dean JP (1967) Absorption and luminescence of excitons at neutral donors in gallium phosphide. Phys Rev 157(3):655–667

65. Zhu J, Kuznetsov AY, Han MS, Park YS, Ahn HK, Ju JW, Lee IH (2007) Structural and optical properties of ZnO/$Mg_{0.1}Zn_{0.9}O$ multiple quantum wells grown on ZnO substrates. Appl Phys Lett 90(21):211909 (1–3)
66. Hellmann R, Koch M, Feldmann J, Condiff ST, Gobel EO, Yakovlev DR, Waag A, Landwehr G (1993) Homogenous linewidth of excitons in semimagnetic CdTe/$Cd_{1-x}Mn_xTe$ mutiple quantum wells. Phys Rev B 48(4):2847–2850
67. O'Neill M, Oestreich M, Ruhle WW, Ashenford DE (1993) Exciton radiative decay and homogeneous broadening in CdTe/$Cd_{0.85}Mn_{0.15}Te$ multiple quantum wells. Phys Rev B 48(12):8980–8985
68. Kononenko VK, Lomashevich SA (1991) Semiconductor light amplifier. RU Patent 2062543
69. Kononenko VK (1992) Spectral characteristics of quantum-well heterolasers. Proc SPIE 1724:89–101
70. Juang C, Kuhn KJ, Darling RB (1991) Electric field effects in AlGaAs-GaAs symmetric and asymmetric coupled quantum wells. IEEE J Quantum Electron 27(9):2122–2128
71. Tsuchiya T, Katayama S, Ando T (1996) Phase of magnetic oscillation of luminescence energy in asymmetric quantum wells. Surf Sci 361–362:376–379
72. Ueda K, Hase T, Yanagi H, Kawazoe H, Hosono H, Ohta H, Orita M, Hirano M (2001) Epitaxial growth of transparent p-type conducting $CuGaO_2$ thin films on sapphire (001) substrates by pulsed laser deposition. J Appl Phys 89(3):1790–1793
73. Kawazoe H, Yasukawa M, Hyodo H, Kurita M, Yanagi H, Hosono H (1997) P-type electrical conduction in transparent thin films of $CuAlO_2$. Nature 389(6654):939–942
74. Bredar ARC, Blanchet MD, Comes RB, Farnum BH (2019) Evidence and influence of copper vacancies in p-type $CuGaO_2$ mesoporous films. ACS Appl Energy Mater 2(1):19–28
75. Wang C, Zhu H, Meng Y, Nie S, Zhao Y, Shin B, Fortunato E, Martins R, Shan F, Liu G (2019) Sol-gel processed p-type $CuAlO_2$ semiconductor thin films and the integration in transistors. IEEE Trans Electron Dev 66(3):1458–1463
76. Varadarajan V, Norton DP (2006) $CuGaO_2$ thin film synthesis using hydrogen-assisted pulsed laser deposition. Appl Phys A 85(2):117–120
77. Nie X, Wei SH, Zhang SB (2002) Bipolar doping and band-gap anomalies in delafossite transparent conductive oxides. Phys Rev Lett 88(6):066405 (1–4)
78. Davies JH (2006) The physics of low-dimensional semiconductors: an introduction, 6th reprint edn. Cambridge University Press, pp 1–438
79. Lin KF, Cheng HM, Hsu HC, Lin LJ, Hsieh WF (2005) Band gap variation of size-controlled ZnO quantum dots synthesized by sol-gel method. Chem Phys Lett 409(4):208–211

Chapter 5
Metal Oxides-Based SERS Substrates

Kudilatt Hasna and M. K. Jayaraj

1 Introduction to Surface Enhanced Raman Scattering

Surface-enhanced Raman scattering (SERS) is a process in which Raman signal of molecules is enhanced when the molecule is adsorbed to metal nanostructures. In 1974, the group Fleischmann, Hendra and McQuillan [1] observed that the intensity of Raman signals from pyridine molecule is anomalously enhanced when it is adsorbed to roughened silver electrode and later the effect was termed as surface-enhanced Raman scattering. It was Jean Maire and Van Duyne [2] and Albrecht and Creighton [3] who showed that the anomalous enhancement in intensity could not be attributed to increased surface area, but due to new phenomena that give rise to the idea of SERS cross section. It was discovered that enhancements in Raman intensity was due to strong electromagnetic field induced by excitation of localized surface plasmons present on nanoscale noble metals. The discovery of SERS has opened a capable way to overcome the traditional low sensitivity problem in normal Raman spectroscopy.

Surface-enhanced Raman scattering spectroscopy offers many advantages over other spectroscopic or spectrometric techniques including Fourier transform infrared (FT-IR) spectroscopy, fluorescence, UV-Vis-near infrared (NIR) absorption, nuclear magnetic resonance (NMR) spectroscopy, X-ray photoelectron spectroscopy (XPS) and mass spectrometry. SERS can extract a significant amount of information directly from complex environments such as biological fluids, living tissues and cells without any need for prior sample preparation. They also offer high sensitivity for small structural changes in macromolecules, non-invasive sampling capability, minimum

K. Hasna (✉)
Government Arts and Science College, Calicut, India
e-mail: hk462@cam.ac.uk

M. K. Jayaraj
Cochin University of Science and Technology, Kochi, India

M. K. Jayaraj (ed.), *Nanostructured Metal Oxides and Devices*,
Materials Horizons: From Nature to Nanomaterials,
https://doi.org/10.1007/978-981-15-3314-3_5

sample preparation and high spatial resolution. Simply, it can be said that SERS combines molecular fingerprint specificity with potential single-molecule sensitivity. Therefore, the SERS technique is identified as a potential tool for sensing trace amount of molecules within the field of chemical and biochemical analytics.

In order to enhance the Raman signal, the molecule must typically be adsorbed on the metal surface, or at least be very close to it (typically up to 10 nm). The energy produced due to enhanced electromagnetic field is transferred to the molecules located near the surface of the metal nanostructures. The magnitude of induced field is thus increased and results in the enhancement of Raman scattering efficiency drastically. It is accepted that the dominant effect in SERS is electromagnetic effect (EM) and EM enhancement is due to the electromagnetic property of metal nanostructures. The Raman signal enhancements in SERS span over several orders of magnitude compared to normal Raman scattering and the detection limit is down to the single-molecule level [4].

The field enhancement during LSPR is given by the equation [5]

$$E_{\text{out}} = E_0\hat{z} - \alpha E_0\left[\frac{\hat{z}}{r^3} - \frac{3z}{r^5}\left(x\hat{x} + y\hat{y} + z\hat{z}\right)\right]$$

where α is the metallic polarizability given by $\alpha = ga^3$, a being the radius of the sphere and g defined as

$$g = \frac{\epsilon_{\text{in}} - \epsilon_{\text{out}}}{\epsilon_{\text{in}} + 2\epsilon_{\text{out}}}$$

where ϵ_{in} and ϵ_{out} represent dielectric function of metal and external environment, respectively. When $\epsilon_{\text{in}} = -2\epsilon_{\text{out}}$, denominator of the equation approaches to zero and this is the condition for the occurrence of maximum electric filed enhancement. According to Mie theory, the condition $\epsilon_{\text{in}} = -2\epsilon_{\text{out}}$ occurs during localized surface plasmon resonance and occurs in visible region for coinage metals such as silver, gold and copper. The electric field enhancement in metal nanostructures with various shapes is given in Fig. 1.

In addition to the contribution of electromagnetic effect, molecular resonances and charge transfer transitions also contribute to Raman enhancement and are termed as chemical enhancement (CE) [6]. CE depends on the chemical interaction between adsorbed molecules and the SERS substrate and it amounts only about 2–3 orders of magnitude. Even though it is difficult to separate CE from EM enhancements, several studies have been focused on CE mechanism. Studies reveal that CE enhancement is a kind of resonance Raman scattering. The most acceptable mechanism is the charge transfer mechanism between adsorbate and metal due to the formation of metal-adsorbate complex. New electronic states arise as a result of direct covalent bonding of adsorbate to the SERS substrate. Then, the charge is transferred from Fermi level to lowest unoccupied molecular orbital (LUMO) or from highest occupied molecular orbital (HOMO) of adsorbate to Fermi level of the metal [7].

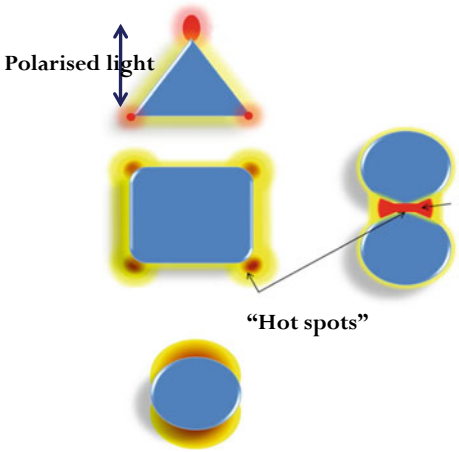

Fig. 1 Field enhancement in metal nanostructures (red colour represent region of enhanced electric field)

2 Metal Nanostructures as SERS Substrates

Metal nanocolloids with controlled size and shape, nanoparticles on solid substrates, or lithographically patterned metal nanostructures on solid substrates are the currently available SERS-active substrates [8]. Though the first SERS-active substrates were electrochemically roughened silver (Ag) electrode [1], later with the advancement of nanotechnology, colloidal suspensions of Ag nanoparticles were found to have similar properties that even single-molecule resonance measurements could be carried out for rhodamine 6G (R6G) using metal nanocolloids. The detection at single-molecule SERS is attributed to closely spaced nanoparticle dimers, or "hot spots". Therefore, the design of SERS-active substrates with "hot spots" has been in progress. Though colloidal nanoparticles are easy to synthesize, they suffer from poor reproducibility due to the inhomogeneous size distribution, dimer spacing and orientation with respect to the excitation polarization.

Different types of solid support SERS substrates such as templated colloidal crystal films, deposited metal island films and lithographically defined thin films have been reported with better performance than colloidal SERS substrates in reproducibility and sensitivity. The most promising manufacturing method for fabrication, reported over more than two decades is nanolithography. Various nanolithographic techniques include nanosphere lithography, electron beam lithography, nanoimprint lithography and focused ion beam milling. Some of them are lithographically patterned and etched microscale pyramidal pits in silicon coated with thin metal layers, gold nanopyramid arrays with nanoscale sharpness tips; however, they bear limited number of scattering hot spot sites. Even though a remarkable progress has been observed over the last three decades, still there is strong demand for SERS substrates that possess large number of "hot spots" accompanied by high reproducibility and stability in the SERS enhancement.

Further, fine-tuning of interparticle gap is possible by combining with electrochemical methods. Halas and co-workers [9] succeeded in generating nanobridges on the tip of array of bowtie structures by electromigration that allows creation of gaps of widths ranging from 1 nm to a few nm. This method of electromigration has benefits of relatively high yield and reproducible fabrication of SERS hot spots, with enhancement factor easily reaching the 10^8 range. Combining electron beam lithography (EBL) with bottom-up methods is a fascinating way to fabricate exact, parallel hot spots over surfaces. Gopinath et al. [10] decorated aperiodic patterns of EBL-fabricated Au posts with Au spheres which allow creation of SERS-active hot spots. Replacing the aperiodic substrate with a periodic surface again enhances the electromagnetic interactions and thus could be extended for the fabrication of controlled size gaps down to 1–2 nm size range.

Our group fabricated patterned SERS-active substrate using arrays of nanotriangular pillars by combining electron beam lithography with nanoimprinting technique [11]. Arrays of nanotriangular pits were fabricated in silicon by electron beam lithography (EBL). The disadvantages of EBL are that the fabrication technique is time consuming and expensive. Hence, nanoimprinting technique was employed for the replication of patterns from silicon into PMMA so that arrays of nanotriangular pillars are generated. Figure 2a shows field emission scanning electron microscopic (FESEM) image of silicon with nanotriangular pits of edge length 200 nm and depth 250 nm. The gap between the triangles is designed at 200 nm. The large area view and depth view are clearly shown in Fig. 2b, c. Figure 2d confirms the successful replication of patterns in silicon into PMMA. For the fabrication of SERS substrate, the PMMA substrate with arrays of triangular pillars is coated with silver film of thickness 60 nm. The SERS characterization of nanotriangles-based SERS substrate using benzene thiol (BT) molecules shows an enhancement factor of 2.9×10^{11}, which is the highest reported value for a patterned SERS substrate. The highest SERS activity is achieved for the SERS substrate with triangles of edge length 200 nm and is given in Fig. 3. The spectrum is reproducible from sample to sample and is also uniform over the substrate. Therefore, the SERS substrate using nanotriangular pillars performed as an efficient SERS substrate with uniform and reproducible Raman enhancement and highest enhancement factor. The multiple productions of replica from a single EBL silicon master offer a cost-effective technique for the fabrication of patterned SERS substrates.

3 Metal-Metal Oxide Hybrid Structures as SERS Substrates (SERS EM Enhancement Effect)

A very efficient way to increase the "hot spot" density is the development of 3D hybrid structures of metal oxides such as TiO_2 and ZnO. 3D hybrid structures are far superior to conventional substrate due to their potential to extend the arrangement of "hot spots" along the third dimension and thus enhance the "hot spot"

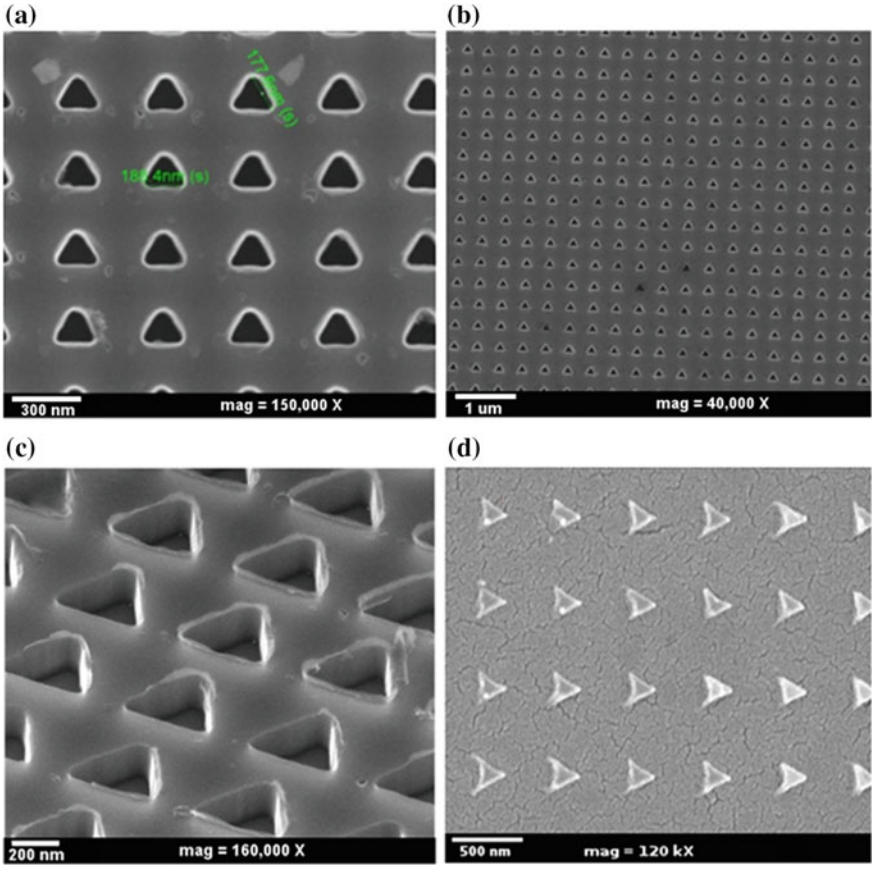

Fig. 2 FESEM images of silicon master with triangular pits with edge length 200 nm **a** top view, **b** large area view, **c** depth view and **d** its replica in PMMA

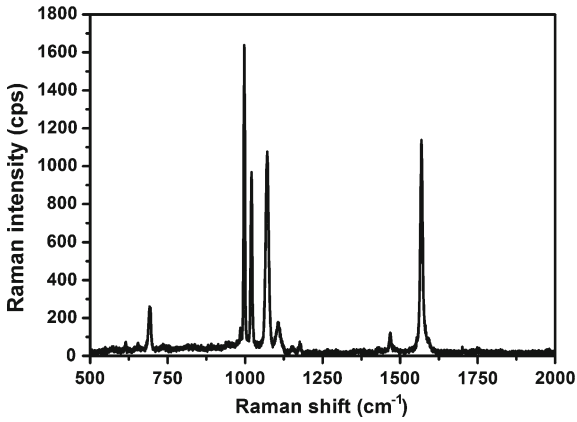

Fig. 3 SERS spectra of 10^3 M BT on nanotriangular pillar arrays of edge length 200 nm

density. They also supply increased surface area for adsorbing higher number of probe molecules. This cost-effective method for fabrication of renewable nanorod array is well known and noble metal nanoparticles can be decorated onto the arrays via simple electroless plating/seeding method. First report by Rijana and co-workers on SERS effect from semiconducting TiO_2 nanoparticles advances the growth of more and more semiconductor-noble metal nanocomposites-based SERS substrate such as Ga_2O_3-Ag, ZnO-Ag and TiO_2-Ag core-shell structures.

Marcin Pisareket al [12] introduced TiO_2 and Al_2O_3 nanoporous oxide layers decorated with silver nanoparticles as a SERS-active substrate. A very large enhancement factor comparable to that of roughened silver surface was achieved for Ag/Al_2O_3, but low value was achieved for Ag/Ti substrate. It was proposed that porous alumina interacts with Ag and effects the electronic structure of the Ag nanoparticles and hence enhances the Raman signal. These enhanced Raman signals are useful to detect the presence of small amounts of certain organic compounds and their interaction with composite substrates. With the manifestation of SERS intensity, the probe molecules can sense slight changes on distribution of the Ag deposit on the nanotubular structures.

3D self-assembly method is one strategy for producing 3D hierarchical SERS substrates. But poor control and reproducibility of this method make the essentiality of another template method. Various reduction methods are emerged for decorating noble metal nanoparticles on to 3D nanoscaffolds or nanorods structures. The examples are Au or Ag nanoparticles decorated onto the surface of metal oxide nanorods, anodic aluminium oxide (AAO) tubes and carbon nanotubes. Usually, arrays of vertically aligned nanowire or nanorods arrays are unsuitable for SERS-active applications because of limitation in massive amounts of loading of metal nanoparticles. Besides, the propagation of excitation light into the decorated nanoparticles is limited owing to significant scattering and adsorption which effectively decreases enhancement factor and the detection limit. To overcome these deficiencies, instead of vertical aligned structures, branch type substrates are designed that can expose the hot spots to excitation light. The emerged substrate includes branched scaffolds in ZnO nanorod arrays. The uniform spatial distribution of the branched scaffolds can efficiently supply the hot spots to SERS enhancement and thus improved sensitivity and reproducibility. ZnO/CuTCNQ nanotree arrays (TCNQ = 7,7,8,8-tetracyanoquinodimethane) are employed as SERS substrate in which trees are fabricated through chemical vapour deposition (CVD) route. ZnO nanorod arrays or graft of aligned ZnO nanorod arrays have been exploited as a universal backbone for the growth of branched structures. But with CVD, the density of CuTCNQ structures was low which do not provide favourable environment for the attachment of nanoparticles. Thus, silicon (Si) nanomaterial branches with dominant properties such as biocompatibility, stability and chemical properties are developed. Jian Huang et al. [13] developed a SERS substrate-based on silver nanoparticles decorated on the graft of Si nanoneedles which is supported onto surface of ZnO nanorod arrays. In the report, instead of CVD, a catalyst-assisted vapour–liquid–solid (VLS) growth mechanism was employed for the graft of silicon needles onto ZnO nanorods. The

decoration of Ag nanoparticles was carried out using galvanic displacement reaction. An enhancement factor of 8.7×10^7 and a detection limit of 10^{-16} M were achieved for the as-designed SERS substrate. The possibility of integrating such ordered Si/ZnO/Ag structures on a lab-on-chip device for label-free detection of chemical and biomolecules is also proposed.

3D SERS substrate was developed based on arrays of cone-shaped ZnO nanorods [14] for rapid detection of trace polychlorinated biphenyls. Cone-shaped ZnO arrays were fabricated by electrodeposition technique, and physical ion-sputtering was employed for the uniform deposition of silver nanoparticles. Due to the unique morphology of as-fabricated SERS substrate, three types of hot spots were formed by: (1) coupling between the small Ag nanoparticles (NP) that are grown on the same ZnO nanorod; (2) coupling between Ag nanoparticles growing on the two adjacent ZnO nanorods; (3) interaction between the large Ag spheres on the top ends of two neighbouring ZnO nanorods. Electroless plating method, photo-deposition method or galvanic reduction were also employed for decoration of metal nanoparticles onto ZnO nanorods. Alternatively, the surface was modified with amino or mercapto groups which promote the formation of Au-NP/ZnO-particle and Au- or Ag-NPs/ZnO-multipods hybrid structures. Li et al. [15] fabricated a multifunctional high sensitive recyclable SERS substrate of Au-coated TiO_2 nanotube arrays. The recyclable property of TiO_2 nanotubes eliminates single use of traditional SERS substrate. Additionally, as compared to ZnO, TiO_2 is more stable and the as-fabricated recyclable SERS substrate has been widely used for detection and degradation of organic pollutants.

Our group has fabricated metal-metal oxide nanocomposite via decorating silver nanoparticle onto TiO_2 nanorods. TiO_2 nanorods are grown by hydrothermal method which is a cost-effective non-vacuum technique. Silver nanoparticles are decorated onto the nanorods by chemical reduction method. In a typical growth of TiO_2 nanorods, initially, compact thin layers of TiO_2 nanoparticles were deposited onto the well-cleaned fused silica substrate by dip coating in an alcoholic titanium tetra-isopropoxide (TTIP) solution at room temperature followed by annealing at 800 °C for 1 h in air ambient. This TiO_2 layer acts as a seed layer for growth of TiO_2 nanorods by the solvothermal process. The steps involved in growth of TiO_2 nanorods are as follows: 0.6 ml of titanium tetra-isopropoxide (TTIP), $Ti\{OCH(CH_3)_2\}_4$ (97%; Alfa Aesar) was added to a mixture of 25 ml of de-ionized water and 25 ml of concentrated hydrochloric acid (HCl, 36.5% by weight). Then, mixture was transferred into a Teflon-lined autoclave and kept at 180 °C for 3 h.

The decoration procedure of silver nanoparticle on TiO_2 nanorods is schematically represented in Fig. 4. TiO_2 nanorods were dipped in $[Ag(NH_3)_2]^+$ solution for 5 min and subsequently dipped in de-ionized water for several seconds. Then, $[Ag(NH_3)_2]^+$ were reduced with 0.1 M glucose solution followed by dipping once again into the de-ionized water to remove any glucose molecule. This decorating procedure was repeated for several cycles to control the density and the size of silver nanoparticles on the surface of the TiO_2 nanorods. The Ag-TiO_2 samples prepared by one, two, three, four, five, six and seven cycles are named as C1, C2, C3, C4, C5, C6 and C7, respectively.

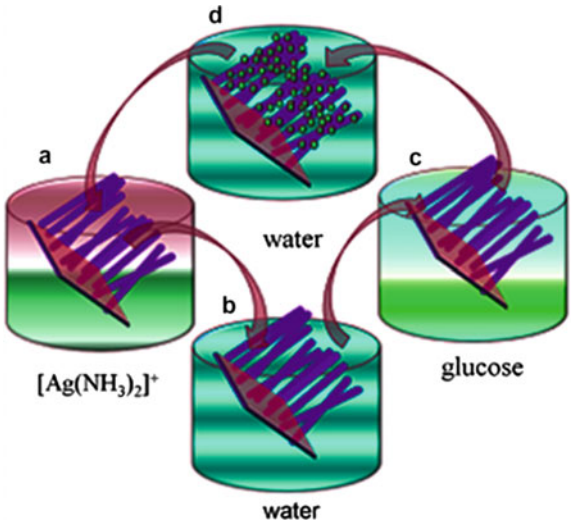

Fig. 4 Schematic of decoration of Ag on TiO_2 nanorods

The FESEM image of TiO_2 nanorod synthesized by hydrothermal method is shown in Fig. 5. From Fig. 5a, b, it can be seen that the nanorods are grown in an inclined direction with the substrate and are grown from the seed layer uniformly over the substrate. This inclined growth is favourable for increasing density of silver nanoparticles with "hot spots" in detection volume. The average diameter of nanorod is about 80 nm.

The decoration of silver nanoparticles on TiO_2 nanorods is confirmed with transmission electron microscopic (TEM) image given in Fig. 6. TEM image of sample C1, C6 and C7 is shown in Fig. 6. As the number of cycles increases from one to six, size and number of silver nanoparticles increases. It is also observed that nanoparticles are arranged with nanogaps so that "hot spots" are generated in the junction

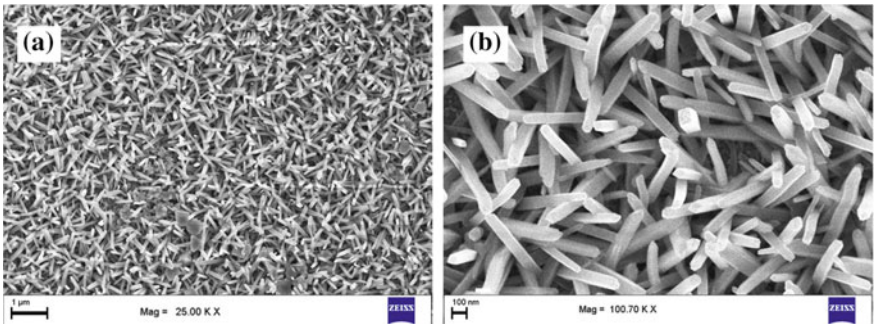

Fig. 5 FESEM image of TiO_2 nanorods synthesized via solvothermal method

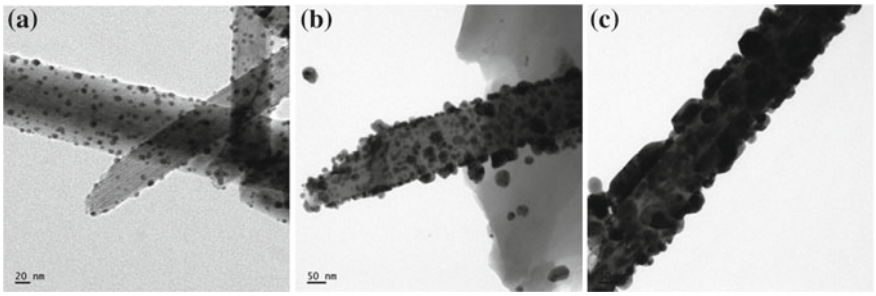

Fig. 6 TEM image of TiO_2 nanorods decorated with silver nanoparticles for a decoration cycle of **a** one, **b** six and **c** seven

between the nanoparticles. But for a decoration cycle of seven, tiny gaps combine to form bigger nanoparticles.

The SERS activity of Ag-TiO_2-based SERS substrate using 10^{-5} M rhodamine 6G molecules (R6G) is shown in Fig. 7. All characteristics peaks of R6G can be clearly identified in the spectra and the Raman peaks at 611, 771, and 1125 cm^{-1} are associated with C–C–C ring in-plane, out-of-plane bending, and C–H in-plane bending vibrations, respectively. The Raman bands at 1189, 1360, 1508 and 1649 cm^{-1} are assigned to symmetric modes of in-plane C–C stretching vibrations [16, 17]. As the number of Ag decoration cycles increase to six, the SERS activity also increased from 160 counts to 16,700 counts. It is because of high density of silver nanoparticles with "hot spots" and is consistent with TEM results. For a decoration cycle of seven, SERS activity is decreased showing the reduction in Raman peak intensity.

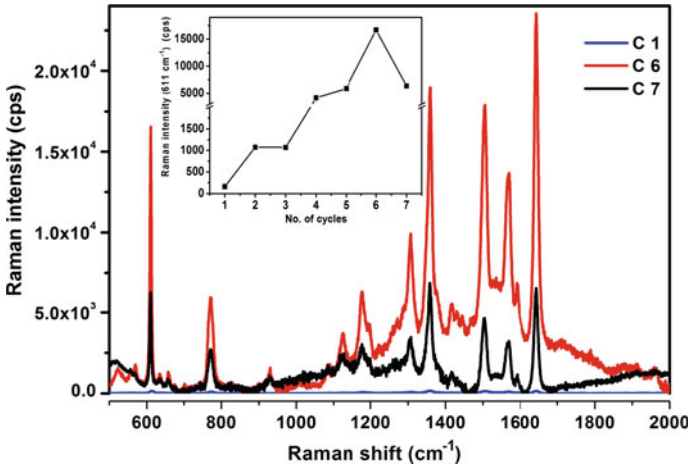

Fig. 7 SERS activity of Ag-TiO_2 using 10^{-5} M R6G molecules

The variation in SERS activity with Ag decoration cycles is given in the inset of Fig. 7.

The recycling capability of as-prepared Ag-TiO_2-based SERS substrate is schematically represented in Fig. 8. The SERS activity of as-prepared Ag-TiO_2 using 10^{-5} M R6G molecule is carried out and for the recycling of the SERS substrate, the samples were exposed to UV light (366 nm) for photodegradation. The corresponding SERS measurements are carried out and the spectrum does not show any signature of R6G which confirms complete degradation of the molecules and the corresponding spectrum is given in Fig. 9.

The SERS activity of Ag-TiO_2 substrate after photodegradation is checked for 10^{-5} M R6G and is compared with SERS activity of as-prepared Ag-TiO_2 (Fig. 10). The SERS substrates exhibit similar SERS activity before and after photodegradation which indicates the recyclable nature of Ag-TiO_2-based SERS substrate. The substrate possesses an average enhancement factor of about 2×10^8 with single-molecule detection capability.

The uniqueness of the present Ag-TiO_2-based SERS substrate over already reported TiO_2 nanorod array-based SERS substrate [15, 18] is the very large enhancement factor. The excellent performance of as-prepared Ag-TiO_2 is due to the formation of different types of "hot spots". In the as-prepared SERS substrate, nanorods are grown not vertically aligned which promotes the formation of "hot spots" in between adjacent nanorods. Also, the growth of nanorods is such that "hot spots" generated on the side wall of nanorods can efficiently contribute to total SERS intensity.

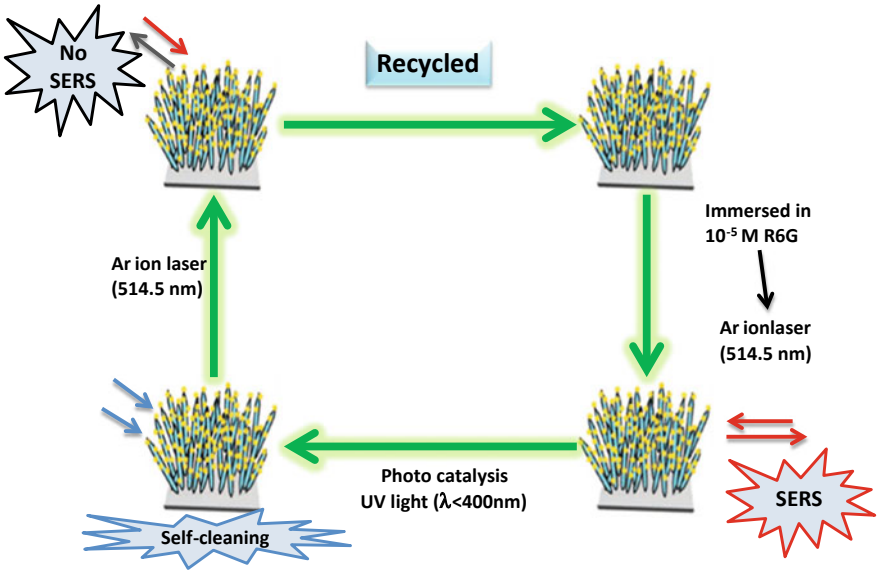

Fig. 8 Schematic of recycling nature of Ag-TiO_2-based SERS substrate

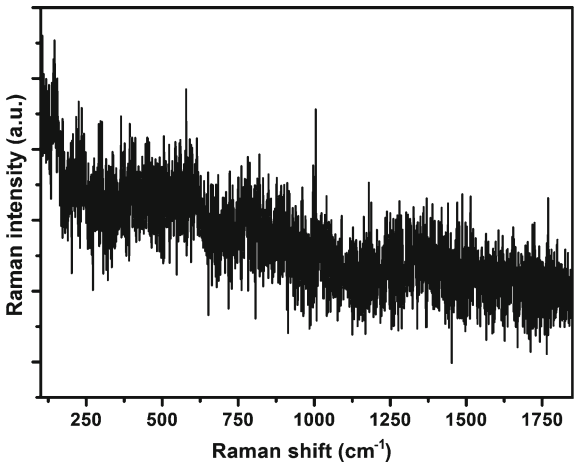

Fig. 9 Raman signal from Ag-TiO_2-based substrate after photodegradation

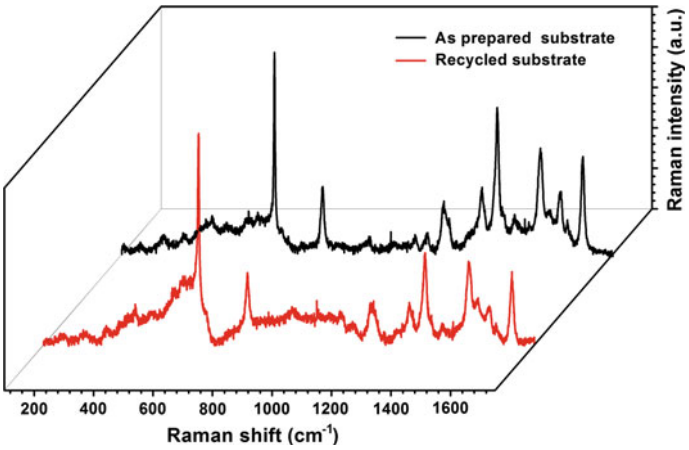

Fig. 10 SERS spectra of 10^{-5} M R6G molecule from as-prepared substrate and recycled substrate

4 Metal Oxide as SERS-Active Substrates (SERS Chemical Enhancement Effect)

One of the clearest experimental proofs for SERS chemical enhancement (CE) is photo-induced charge transfer (PICT) process between adsorbate and metal and is usually seen in semiconductor nanostructures such as ZnO, ZnS, CdS, CuO, CdTe and TiO_2. Initially, the growth of SERS-active substrate is focused on noble coinage metals and transition metals; nowadays, considerable research has been centred on semiconductor materials-based SERS-active substrates. Oxides such as NiO, ZnO, TiO_2, Fe_3O_4 and Cu_2O have been demonstrated as SERS-active substrates. The

SERS study on semiconductor-based substrate is significant from the semiconductor's point of view. Because SERS investigation of adsorbed species on surfaces and interfaces facilitates the analysis of semiconductor device. Semiconductor nanostructures are building blocks of novel nanodevices; hence, the performance of these devices depends critically on the properties of surface and interface features. SERS explore a spectroscopic means to investigate the integration of organic, inorganic and biological nanostructures to build novel functional systems. Therefore, SERS studies on semiconductor are an excellent spectroscopic analyzing tool in the field of nanoscience.

Quagliano et al. [19] were first in observing SERS effect from III-V semiconductor quantum dots nanostructures. The study explores the development of interesting SERS substrate based on metal oxides. Quagliano et al. [19] observed enhanced Raman signal for pyridine molecules on epitaxial InAs quantum dots. A new Raman band appeared corresponding to chemisorption of molecule to the semiconductor surface. It is also observed that magnitude of enhancement strongly depends on probe interfaces. This suggested that it is possible to study adsorption and reactions of molecules on the surfaces of III-V semiconductor quantum dots by means of SERS. A SERS-active substrate was fabricated using monolayers of haematite (α-Fe_2O_3), a n-type semiconductor, that finds application as catalysts, gas sensors, materials for optical and electromagnetic devices and also as medicine carriers. An enhancement factor of 10^4 is obtained and a correlation connecting morphology and SERS enhancement is observed. Thus, Fu et al. [20] proposed an enhancement mechanism relating structure and composition of surfaces and interfaces in non-metallic systems.

SERS studies were also conducted using CuO nanocrystals and 4-Mercaptopyridine (4-Mpy) complex system which again describe the possibility of SERS spectra for understanding chemisorption and reaction mechanism on the surface of semiconductor nanostructures. Wang et al. [21] conducted SERS studies on ZnO nanostructures using 4-Mercaptopyridine (4-Mpy) as adsorbed species and an enhancement factor of 10^3 was achieved. With the advancement in nanotechnology, investigation is extended to nanostructures of Titania. Rajh and co-workers [22] observed enhancement in Raman intensity of biomolecules such as neurotransmitters by adsorption on TiO_2 surface and a size-dependent Raman intensity is also observed. Later, Yang et al. [23] proposed TiO_2-to-molecule charge transfer mechanism for the Raman enhancement. Another important observation is that not only Raman signal of adsorbed species enhanced but also phonon modes of TiO_2 is enhanced due to adsorption of probe molecules. The studies on Raman enhancement of formic acid and dopamine on TiO_2 nanoparticles by Tarakeshwar and group [24] showed that vibronic coupling strengthen charge transfer from the HOMO of the molecule to the conduction band of the quantum dot and hence contribute to Raman enhancement. Xue et al. [25] explored enhanced phonon modes of semiconductor after molecular adsorption on semiconductor nanoparticles by observing Raman signal from 4-Mercaptobenzoic acid (4-MBA) TiO_2 nanoparticles complexes. With the support of highly monodispersed and controlled nanosized TiO_2 particles, a profile of Raman signal as a function of particle size is constructed. Using the profile it is observed that the phonon modes of TiO_2 and the molecule lines were enhanced simultaneously.

SERS studies on TiO_2 nanoparticle by Xue et al. [25] reveal that particle size is a critical parameter the effect SERS enhancement factor. In the study, Raman spectra of 4-MBA chemically bonded to TiO_2 nanostuctures of different particle size is investigated. A charge transfer resonance between the valence band of TiO_2 and the lowest unoccupied orbital of the molecule is observed in nanoparticle of size 10.9 nm. The correlation of particle size of semiconductor with Raman intensity enables to determine configuration of nanoparticle that contributes to advancements in the field of semiconductor-based sensors as well as solar cells. In order to design highly efficient solar cell, nanostructures that provide high rate of charge transfer is preferable, whereas to design a high sensitive sensor, nanostructure that provides excellent Raman enhancement property is desired. Yang et al. [26] observed SERS enhancement property of TiO_2 nanoparticle and a charge transfer mechanism is proposed for SERS effect of TiO_2 nanostructures. It is also proposed that surface defect states present in nanostructure promotes charge transfer between adsorbate and surface. Hence, the intrinsic nature of the adsorbed molecules and the surface property of semiconductor effect charge transfer process.

In order to improve the charge transfer effect, Yang et al. [23] incorporated silver onto TiO_2 through a photoreduction method. On a comparison between Ag-TiO_2 and pure TiO_2 surfaces, it is concluded that Ag-TiO_2 exhibits higher enhancement factor. The enhancement can be attributed to the fact that besides the intrinsic CT contribution of TiO_2-to-molecule, incorporation of Ag brings additional electrons into the molecules adsorbed on the TiO_2 surface through the conduction band of TiO_2 nanoparticles due to the localized surface plasmon resonance of silver. This work is significant both as development of a promising, nontoxic and biologically compatible SERS-active substrate and as a study of the CT mechanism between Ag and TiO_2 for the improvement of performance in photochemical and photo-electrochemical applications.

Various reports on enhancement mechanism in metal oxide show that the SERS enhancement is not attributed to electromagnetic enhancement mechanism. Because their SPR position lies in IR region of electromagnetic spectrum. Hence, it is impossible to obtain EM contribution from semiconductor under visible excitation. Therefore, the enhancement mechanism in semiconductor-based SERS substrate is described to chemical mechanism of SERS. When molecule is adsorbed to the surface of semiconductor, the molecules interact with the atoms of the substrate surface. As a result of such interaction, electron density distribution is varied that could affect the Raman scattering cross section of the molecular vibrational modes which enhances selectively various vibrational modes of molecules. The possible chemical enhancement is chemical bonding enhancement, photon-induced charge transfer enhancement (PICT) and surface complexes resonance enhancement. In these three mechanisms the enhancement in Raman scattering intensity would depend on the change of molecular polarizability of adsorbed species. In chemical bonding enhancement, increase in effective molecular volume and ground state polarizability due to partial charge transfer resulted in magnification of Raman scattering cross section. In the

second type of surface complexes resonance enhancement mechanism, new HOMO and LUMO levels are generated owing to new surface complexes. Thus, a resonant enhancement can be produced in these surface complexes under suitable excitation. The third type, PICT enhancement mechanism is the most appropriate mechanism for metal oxide-based SERS substrates.

In order to observe PICT enhancement mechanism, it is not essential to have molecules to be chemisorbed on to the SERS substrate. However, for the thermodynamically feasible CT, the HOMO and LUMO of the molecule should match the energy levels of valence band (VB) and conduction band (CB) of the substrate. The possible routes for PICT are between the molecule and the semiconductor substrate. Thus, during PICT, charge transfers either from semiconductor substrate to molecule or from molecule to semiconductor substrate. During the PICT process, an electron in VB of semiconductor is transferred to the CB by stimulation of incident light which creates a hole in valence band. The excited electron is quickly tunnelled to a matching energy level above the LUMO of the molecule through resonant transfer process (Fig. 11a). The transferred electron eventually is transferred back to VB of semiconductor and recombines with the hole. Similarly, an electron can be transferred from HOMO to LUMO level by incident light energy. Then, the excited electron transits quickly to CB of the semiconductor through resonant tunnelling (Fig. 11b). Finally, the electron is de-excited to a ground vibrational energy level of the molecule. Suppose the excitation wavelength is not sufficient to excite the electron from valence band to conduction band or from LUMO to HOMO level, surface defect states present in metal oxides mediate charge transfer between SERS substrate and adsorbed molecule (Fig. 11c). It happens in wide bandgap materials where excitation of electrons happens under UV excitation only.

Our group investigated SERS effect in TiO_2 nanoparticles synthesized via chemical route. Procedure for the synthesis of TiO_2 nanoparticles (TiO_2 NPs) is as follows. A mixed solution of 50 ml distilled water, 5 ml titanium isopropoxide and 15 ml isopropyl alcohol was kept at 100 °C until all the solvent gets evaporated. XRD shown in Fig. 12a confirms the anatase of TiO_2 nanoparticles and the average size of nanoparticles is estimated to be about 8 nm from FESEM image is given in Fig. 12b.

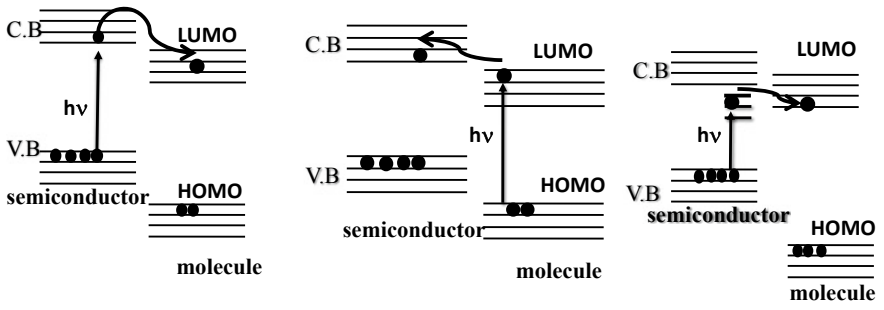

Fig. 11 Possible charge transfer during PICT

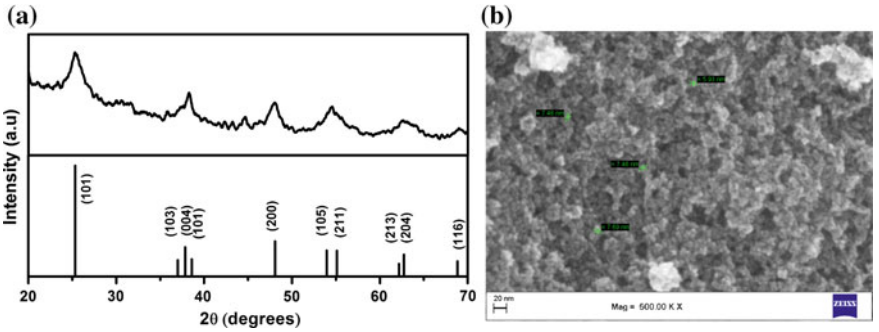

Fig. 12 **a** XRD spectra of TiO_2 nanoparticles and **b** FESEM image of TiO_2 nanoparticles

4-Mercaptobenzoic acid (4-MBA) is used as Raman probe and 10^{-3} M 4-MBA is chemically bonded to TiO_2 nanostructures using the procedure as follows. A mixture of 20 mg TiO_2 nanostructures and 20 ml 4-MBA, (1×10^{-3}M) ethanol solution was stirred for 2 h. Then, the precipitate was centrifuged at 10,000 rpm for 30 min and rinsed with de-ionized water. Finally, the solution is made into 3 ml by adding ethanol. A model for TiO_2 nanostructures modified by 4-MBA is given in Fig. 13.

Figure 14 compares the SERS spectra of 10^{-3} M 4-MBA using TiO_2 nanoparticles with the normal spectra of 4-MBA. The intensity and the position of Raman peaks in SERS spectrum of 4-MBA adsorbed on TiO_2 are different from the normal Raman spectra of 4-MBA solid powder. The SERS spectra are dominated by bands at about 1581 and 1073 cm^{-1}, which are assigned to ν_{8a} (a_1) and ν_{12} (a_1) aromatic ring characteristic vibrations, respectively [26]. The chemical bonding of 4-MBA with TiO_2 surface is confirmed by the presence of weak bands at about 1141 cm^{-1} (ν_{15}, b_2) and 1172 cm^{-1} (ν_9, a_1) corresponding to the C–H deformation modes. The number of molecules in detection volume during normal Raman spectrum measurement is 8.7 $\times 10^9$ and that corresponding to SERS measurement is 1.5×10^9. Hence, it is clear that the Raman signals of 4-MBA adsorbed on TiO_2 nanostructures are remarkably

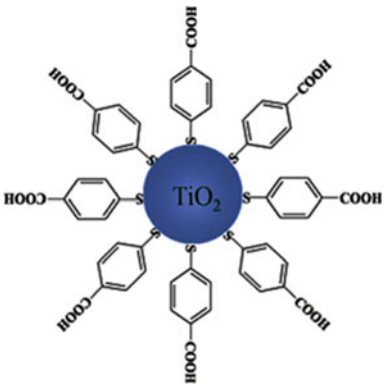

Fig. 13 Model for adsorption of 4-MBA molecules onto TiO_2 nanoparticles

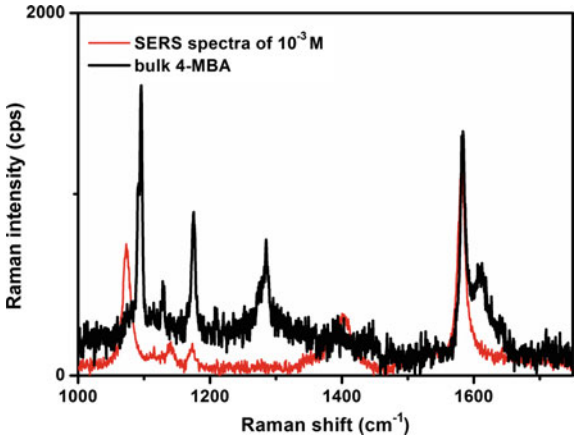

Fig. 14 Normal Raman spectra of bulk 4-MBA and SERS spectra of 10^{-3} M 4-MBA

enhanced relative to 4-MBA in bulk. Presence of extra peak at 1144 cm^{-1} confirms the charge transfer due to the chemical bond formation of 4-MBA with TiO_2.

514.5 nm of Ar ion laser is used as excitation wavelength for SERS measurement. The bandgap of synthesized TiO_2 nanoparticle is 3.16 eV. Therefore, the photo-induced charge transfer is not possible between valence band or conduction band of TiO_2 and HOMO or LUMO level of 4-MBA. The photoluminescence from TiO_2 nanorods with an excitation 517 nm exhibits an emission at 564 nm (Fig. 15) which confirm the presence of surface defect states in TiO2 nanoparticles which mediates the charge transfer between TiO_2 and 4-MBA. The role of surface defect states is confirmed by annealing the TiO_2 at 200, 400 and 600 °C in the presence of air. The SERS activity of TiO_2 decreases with increase in annealing temperature which is due to the decrease in number of surface defect states with annealing. The decrease in SERS activity with increase in annealing temperature is shown in Fig. 16. Hence, the photo-induced charge transfer depicted as in Fig. 17.

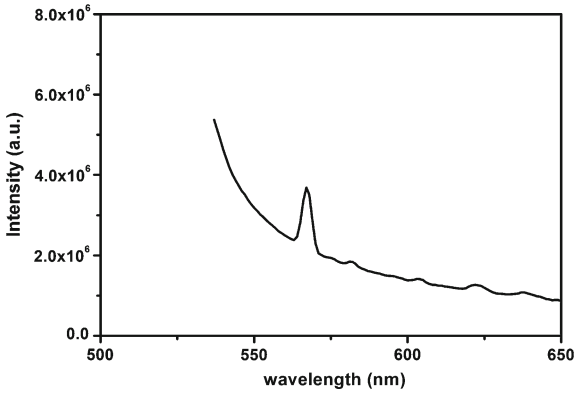

Fig. 15 Photoluminescence spectra from TiO_2 nanoparticles under 517 nm excitation

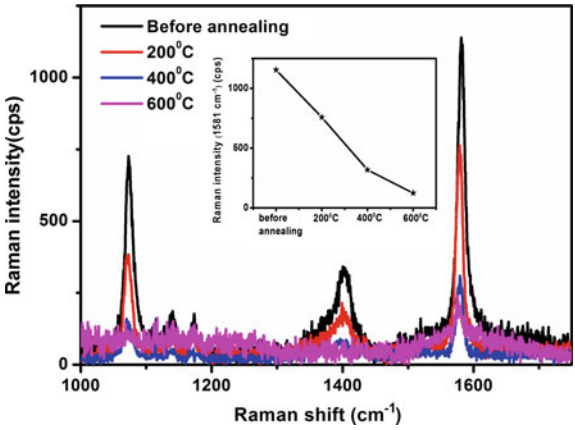

Fig. 16 SERS activity of TiO_2 nanoparticles for different annealing temperatures

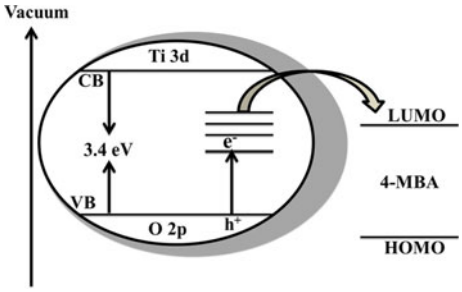

Fig. 17 Model for PICT mechanism in TiO_2-4-MBA complex

The bandgap of TiO_2 nanoparticles is 3.16 eV. Therefore, an electron in VB could not move to CB on excitation with 514.5 nm (2.4 eV). The presence of surface defect level state at 2.4 eV in TiO_2 nanoparticles mediates the charge transfer between TiO_2 and 4-MBA. Hence, an electron in VB is transferred to this surface defect states by stimulation of incident excitation laser which creates an electron in defect states and a hole in the valence band. The excited electron is quickly tunnelled to a matching energy level above the LUMO of 4-MBA through the resonant process. The excited electron eventually moves back to VB of TiO_2 and recombines with the hole. Hence, charge transfer between the metal oxide and adsorbate occurs and the SERS occurs due to CE effect in metal oxide nanostructures.

5 Applications of Metal Oxide-Based SERS Substrate

Compared to traditional SERS substrate, semiconductors possess high stability, biocompatibility and are highly sensitive to configuration and environment. Since the enhancement of certain Raman bands during SERS strongly depends on orientation

of the molecule with the metal surface and also on the distance between its functional groups from the surface on which it was adsorbed. The SERS spectra can be utilized for gathering specific information on chemical structure of adsorbed species and also its orientation with metal surface. Hence, semiconductor-based SERS substrate has been explored for potential applications both in fundamental studies and for biochemical detections.

5.1 Investigation of Semiconductor/Adsorbate Interface

SERS enhancement from semiconductor surface is attributed to charge transfer between the semiconductor and adsorbate complexes. Therefore, SERS signal allows study on semiconductor/adsorbate interface which provides important information about the surface science of the semiconductor and the chemisorption process of the adsorbate. Among the various techniques available, SERS is found to be very effective technique to investigate the semiconductor/adsorbate interface. Taking the performance of TiO_2-based dye-sensitized solar cell (DSSC), the nature of binding of dye on the surface of TiO_2 substrate determines its efficiency. Greijer et al. [27] investigated mechanism of thiocyanato to ligand exchange in DSSC via resonance Raman scattering and Leon et al. studied the interaction between ruthenium polypyridyl complexes and mesoporous TiO_2 via SERS and observed that ruthenium polypyridyl dyes could interact with metal ions via their carboxyl groups in several ways. These investigations allow deeper understanding on sensitization phenomena that can help to improve performance of solar cell. Therefore, recently researchers have been focusing on investigation on chemisorption and reaction mechanisms of molecules adsorbed on the semiconductor surface in practical systems via SERS. SERS is one of the well-developed techniques for probing these CT processes in microelectronic devices. Nature of contact, i.e., ohmic and schottky contact, play an important role in performance of (opto) electronic devices and which can be easily investigated via SERS. The studies on micro-nanoscale charge transfer (CT) in such junction are important to both the frontier of fundamental science and applications in molecular electronics.

5.2 Realization of Biochemical Detection

As SERS is high sensitive, selective and non-destructive detection method, the technique is widely applied in the field of biochemistry and biomedicine. Due to non-toxicity and biocompatibility, metal oxide SERS substrates are expected to be more suitable in such applications. The information on enhanced Raman signal of impurities via PICT transfer process provides an efficient method to eliminate impurities in practical system. The studies conducted by Musumeci et al. [28] on dopamine (DA) and TiO_2 system are utilized for eliminating the presence of DA in biologically

active enediol molecules. Zhang et al. [29] conducted SERS studies of cytochrome c (from bovine heart) and spores of the bacterium Bacillus subtilis using nanostructured aluminium/aluminium oxide-based SERS substrates. The aluminium oxide film formed under ambient conditions is biocompatible and is suitable for stabilizing lipid bilayers which is one of suitable method of the surface modification of biospecies. This experiment has demonstrated the practical utility of a nanostructured aluminium/aluminium oxide platform for biosensing.

Research has been focused on environmental problems such as detection of organic pollutants related to wastewater and polluted food as well as treatment of various pollutants. The organic dyes, organic pesticides, food adulterants, organic herbicides accumulate in living organism and causes carcinogenicity and acute toxicity. Among wide variety of detection method, SERS is one of the attractive spectroscopic tools for detection of organic pollutant. Tang et al. [14] demonstrated detection of polychlorinated biphenyls using Ag nanoparticles decorated on cone-shaped ZnO nanorods. It is possible to detect a kind of persistent organic pollutants PCB-77 with a detection limit as low as 10^{-11} M. Jian Huang et al. [13] fabricated nanoparticles decorated zinc oxide/silicon heterostructured nanomace arrays-based SERS substrate and is employed for detection of different concentrations of melamine aqueous solution (from 10^{-4} to 10^{-10} M). It was possible to establish relation between SERS intensity and the melamine concentration. Detection of melamine residual in pure milk is also successfully demonstrated. The result explores the potential of semiconductor-based SERS substrate in food inspection and in environmental protection. Li et al. [15] demonstrated multifunctional recyclable SERS substrate using Au-coated TiO_2 nanotubes. Since TiO_2 possesses photocatalytic activity, self-cleaning of adsorbed dye is possible under UV irradiation. Detection and photodegradation of herbicide 4-chlorophenol (4-CP), persistent organic pollutant (POP) dichlorophenoxyacetic acid (2, 4-D) and organophosphate pesticide methyl-parathion (MP) are successfully demonstrated which show promising application of multifunctional recycle SERS substrate for detecting other organic pollutants.

6 Conclusions

This chapter provides an overview of metal oxide-based SERS substrate by introducing traditional metal-based SERS substrate and their limitations, discussing fabrication of both metal and metal oxide-based SERS substrates, and some of its primary applications. It has been shown that an efficient recyclable metal oxide-based SERS substrate can be developed by decorating TiO_2 nanorods with silver nanoparticles. SERS chemical enhancement mechanism is also investigated using TiO_2 nanostructures in which it is seen that surface defects mediate a photon-induced charge transfer between the substrate and the analyte. The SERS technology based on metal oxide

nanostructures progress towards its applications in both fundamental science and biochemical detection. Hence, the study and development of metal oxide nanostructures-based SERS substrates would advance SERS technology as a facile and vital tool in future.

References

1. Fleischmann M, Hendra PJ, McQuillan AJ (1974) Raman spectra of pyridine adsorbed at a silver electrode. Chem Phys Lett 26:163–166. https://doi.org/10.1016/0009-2614(74)85388-1
2. Jeanmaire DL, Van Duyne RP (1977) Surface raman spectroelectrochemistry. J Electroanal Chem Interfacial Electrochem 84:1–20. https://doi.org/10.1016/S0022-0728(77)80224-6
3. Creighton JA, Blatchford CG, Albrecht MG (1979) Plasma resonance enhancement of Raman scattering by pyridine adsorbed on silver or gold sol particles of size comparable to the excitation wavelength. J Chem Soc Faraday Trans 75:790–798. https://doi.org/10.1039/F29797500790
4. Kneipp K, Wang Y, Kneipp H et al (1997) Single molecule detection using surface-enhanced Raman scattering (SERS). Phys Rev Lett 78:1667–1670. https://doi.org/10.1103/PhysRevLett.78.1667
5. Willets KA, Van Duyne RP (2007) Localized surface plasmon resonance spectroscopy and sensing. Annu Rev Phys Chem 58:267–297. https://doi.org/10.1146/annurev.physchem.58.032806.104607
6. Wu D-Y, Liu X-M, Duan S et al (2008) Chemical enhancement effects in sers spectra: a quantum chemical study of pyridine interacting with copper, silver, gold and platinum metals. J Phys Chem C 112:4195–4204. https://doi.org/10.1021/jp0760962
7. Park W, Kim ZH (2010) Charge transfer enhancement in the sers of a single molecule. Nano Lett 10(10):4040–4048. https://doi.org/10.1021/nl102026p
8. Dieringer JA, Mcfarland AD, Shah NC et al (2006) Surface enhanced Raman spectroscopy: new materials, concepts, characterization tools, and applications. Faraday Discuss 132:9–26. https://doi.org/10.1039/b513431p
9. West JL, Halas NJ (2003) Engineered nanomaterials for biophotonics applications: improving sensing, imaging, and therapeutics. Annu Rev Biomed Eng 5:285–292. https://doi.org/10.1146/annurev.bioeng.5.011303.120723
10. Gopinath A, Boriskina SV, Premasiri WR et al (2009) Plasmonic nanogalaxies: multiscale aperiodic arrays for surface-enhanced Raman sensing. Nano Lett 9:3922–3929. https://doi.org/10.1021/nl902134r
11. Hasna K, Antony A, Puigdollers J et al (2016) Fabrication of cost-effective, highly reproducible large area arrays of nanotriangular pillars for surface enhanced Raman scattering substrates. 9:3075–3083. https://doi.org/10.1007/s12274-016-1190-y
12. Pisarek M, Holdynski M, Roguska A (2014) TiO_2 and Al_2O_3 nanoporous oxide layers decorated with silver nanoparticles—active substrates for SERS measurements. J Solid State Electrochem 18:3099–3109. https://doi.org/10.1007/s10008-013-2375-x
13. Huang J, Chen F, Zhang Q et al (2015) 3D silver nanoparticles decorated zinc oxide/ silicon heterostructured nanomace arrays as high-performance surface- enhanced raman scattering substrates. ACS Appl Mater Interfaces 7:5725–5735. https://doi.org/10.1021/am507857x
14. Tang H, Meng G, Huang Q et al (2012) Arrays of cone-shaped ZnO nanorods decorated with Ag nanoparticles as 3D surface-enhanced Raman scattering substrates for rapid detection of trace polychlorinated biphenyls. Adv Funct Mater 22:218–224. https://doi.org/10.1002/adfm.201102274
15. Li BX, Chen G, Yang L et al (2010) Multifunctional Au-coated TiO_2 nanotube arrays as recyclable SERS substrates for multifold organic pollutants detection. Adv Funct Mater 20:2815–2824. https://doi.org/10.1002/adfm.201000792

16. Hildebrandt P, Stockburger M (1984) Surface-enhanced resonance Raman spectroscopy of Rhodamine 6G adsorbed on colloidal silver. J Phys Chem 88:5935–5944. https://doi.org/10.1021/j150668a038
17. Michaels AM, Nirmal M, Brus LE (1999) Surface-enhanced Raman spectroscopy of individual rhodamine 6G molecules on large Ag nanocrystals. J Am Chem Soc 121:9932–9939. https://doi.org/10.1021/ja992128q
18. Tan E, Yin P, You T et al (2012) Three dimensional design of large-scale TiO_2 nanorods scaffold decorated by silver nanoparticles as SERS sensor for ultrasensitive malachite green detection. ACS Appl Mater Interfaces 4:3432–3437. https://doi.org/10.1021/am3004126
19. Quagliano LG (2004) Observation of molecules adsorbed on III-V semiconductor quantum dots by surface-enhanced Raman scattering. J Am Chem Soc 126:7393–7398. https://doi.org/10.1021/ja031640f
20. Fu X, Bei F, Wang X et al (2009) Surface-enhanced Raman scattering of 4-mercaptopyridine on sub-monolayers of α-Fe_2O_3 nanocrystals (sphere, spindle, cube). J Raman Spectrosc 40:1290–1295. https://doi.org/10.1002/jrs.2281
21. Wang Y, Ruan W, Zhang J et al (2009) Direct observation of surface-enhanced Raman scattering in ZnO nanocrystals. J Raman Spectrosc 40:1072–1077. https://doi.org/10.1002/jrs.2241
22. Rajh T, Nedeljkovic JM, Chen LX et al (1999) Improving optical and charge separation properties of nanocrystalline TiO_2 by surface modification with vitamin C. J Phys Chem B 103:3515–3519. https://doi.org/10.1021/jp9901904
23. Yang L, Jiang X, Ruan W et al (2009) Charge-transfer-induced surface-enhanced Raman scattering on Ag-TiO_2 nanocomposites. J Phys Chem C 113:16226–16231. https://doi.org/10.1021/jp903600r
24. Tarakeshwar P, Finkelstein-Shapiro D, Hurst SJ et al (2011) Surface-enhanced Raman scattering on semiconducting oxide nanoparticles: oxide nature, size, solvent, and pH effects. J Phys Chem C 115:8994–9004. https://doi.org/10.1021/jp202590e
25. Xue X, Ji W, Mao Z et al (2012) Raman investigation of nanosized TiO_2: effect of crystallite size and quantum confinement. J Phys Chem C 116:8792. https://doi.org/10.1021/jp2122196
26. Yang L, Jiang X, Ruan W et al (2008) Observation of enhanced Raman scattering for molecules adsorbed on TiO_2 nanoparticles: charge-transfer contribution. J Phys Chem C 112:20095–20098. https://doi.org/10.1021/jp8074145
27. Greijer H, Lindgren J, Hagfeldt A (2001) Resonance Raman scattering of a dye-sensitized solar Cell: mechanism of thiocyanato ligand exchange. J Phys Chem B 105:6314–6320. https://doi.org/10.1021/jp011062u
28. Musumeci A, Gosztola D, Schiller T et al (2009) SERS of semiconducting nanoparticles (TiO_2 hybrid composites). J Am Chem Soc 131:6040–6041. https://doi.org/10.1021/ja808277u
29. Zhang X, Zhao J, Whitney AV et al (2006) Ultrastable substrates for surface-enhanced Raman spectroscopy: Al_2O_3 overlayers fabricated by atomic layer deposition yield improved anthrax biomarker detection. J Am Chem Soc 128:10304–10309. https://doi.org/10.1021/ja0638760

Chapter 6
One-Dimensional ZnO Nanostructure: Growth & Device Applications

L. S. Vikas, K. A. Vanaja and M. K. Jayaraj

1 Introduction

The ever-increasing demand for efficient, lightweight and compact electronic devices is a driving force for today's technology. The integrated circuit idea introduced by Kilby and Noyce [1–7] started the revolution in the electronic industry in 1959 itself. Their studies paved the way for the development of large-scale integrated circuits (LSI) and very large-scale integrated circuits (VLSI). The next milestone was the development of heterojunction devices, which was introduced by Z. I. Alferov in 1960s [8]. These developments reduced the size of computers which occupied an entire room to the size that can be fit into our pocket. Such complicated electronic devices require the use of materials with nanoscale dimensions and thinfilms. Intel has already succeeded in developing a number of processors with the size of transistors ranging up to 14 nm, and they are constantly trying to reduce the size even further to 10 nm, 7 nm or 5 nm with the help of new 3D transistor design [9–12]. Development of nanomaterials and nanotechnology has helped to achieve these goals faster. The invention of scanning tunnelling microscopy (STM) by Gerd Binning and Heinrich Rohrer in 1981 triggered the emergence of nanotechnology. STM technique was modified later to a more general area called scanning probe microscopy (SPM). Various new probing techniques created different flavours of SPM like atomic force microscopy (AFM), Kelvin probe force microscopy (KPFM), lateral force microscopy (LFM), etc. Along with SPM techniques, development

L. S. Vikas (✉)
Department of Physics, Govt. Arts College, Thiruvananthapuram, Kerala, India
e-mail: lsvikas.tvm@gmail.com

K. A. Vanaja
Maharaja's College, Ernakulam, India

M. K. Jayaraj
Cochin University of Science and Technology, Kochi 682022, India

M. K. Jayaraj (ed.), *Nanostructured Metal Oxides and Devices*,
Materials Horizons: From Nature to Nanomaterials,
https://doi.org/10.1007/978-981-15-3314-3_6

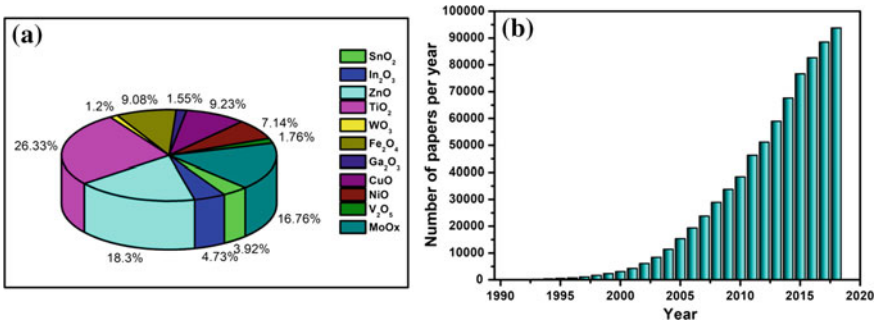

Fig. 1 **a** The total number of publications based on various oxide materials in the past 28 years. **b** The rising trend in a number of publications of ZnO

of various electron microscopic techniques like field emission scanning electron microscope (FESEM), high-resolution transmission electron microscope (HRTEM), focused ion beam microscope (FIB), etc. enabled scientists to visualize materials and devices even below nanometre scale. These recent developments have helped to create and characterize materials and devices in nanoscale.

Last few decades saw a tremendous increase in research on oxide materials mainly because of its stability and ruggedness. The contribution of research publications from various oxide materials in the last 28 years is shown in Fig. 1a. Among various oxides, ZnO has a major role. The number of publications (obtained from the web of knowledge via keyword search) showed a steep increase in the last few decades as shown in Fig. 1b. The sudden increase in research interest is aided by the development of nanotechnology.

The large increase in surface to volume ratio is observed for nanostructures, which also possess properties different from that of the bulk material. Among various forms of nanostructures, one-dimensional (1D) nanostructures offer a surface to volume ratio second to zero-dimensional (0D) nanostructures. One major problem associated with nanostructures, while using in electronic devices, is its grain boundaries. Grain boundaries offer barriers for the smooth flow of electrons. Since a number of grain boundaries are more for zero-dimensional nanostructures, their use in an electronic device can adversely affect its performance. One way to overcome this problem is by using 1D nanostructures, which has lesser number of grain boundaries compared to 0D nanostructures. Growth of vertically aligned 1D nanostructures directly over a substrate is hence advantageous for electronic devices for the smooth flow of carriers along the length of rods (Fig. 2).

2 1D Nanostructure Growth Techniques

A number of growth processes are developed for the growth of 1D nanostructures of ZnO. Depending on the process conditions and method, the quality of nanorods vary.

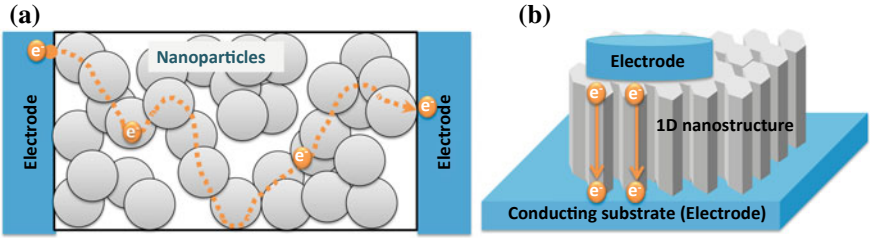

Fig. 2 Comparison of electron transport in **a** 0D nanostructures and **b** 1D nanostructures

The bottom-up approach in which the growth proceeds with atom by atom attachment is generally used for the fabrication of nanorods. Earlier studies were concentrated on metalorganic chemical vapour deposition (MOCVD), chemical vapour deposition (CVD) and vapour–liquid–solid (VLS) techniques, in which a suitable precursor was made to react to form ZnO molecules. Precise control of experimental conditions made the formation of ZnO nanorods possible. Recently, solution-based processes have started to dominate the ZnO nanorod growth techniques, as they are simple and easy to control.

2.1 Chemical Vapour Deposition

In chemical vapour deposition (CVD) method, vapour-phase precursors are allowed to react at the reaction zone to form ZnO, which is then transported to a substrate using a carrier gas. While growing ZnO nanorods by CVD technique, a Zn source is kept at a higher temperature. The Zn vapour starts to flow from this source to the substrate. Since chemical reaction takes place in the reaction zone, it will be kept at a suitable elevated temperature, whereas condensation happens near the substrate, so that it will be kept at a reduced temperature. Usually, the substrate is coated with a seed layer. ZnO nanorods thus formed will be longer near the source and shorter away from the source [13]. Usually, the CVD-grown nanorods are perpendicular to the substrate, and a seed is required to initiate the growth. In general, metallic islands are used as seeds for starting the nucleation process [14].

The diameter and length of *c*-axis oriented zinc oxide nanorods can be controlled by manipulating the O and Zn content in the reaction chamber [15]. Depending on the precursors used, the CVD technique is further classified into metalorganic chemical vapour deposition (MOCVD) [16–19] where organometallic precursors are used, vapour-phase epitaxy (VPE) [20], halide vapour-phase epitaxy (HVPE) [21], metalorganic vapour-phase epitaxy (MOVPE) [22], etc. Such techniques could grow the materials epitaxially. The diameter of the nanorods in MOVPE can be changed by changing the temperature during growth. Increasing the growth temperature decreases the diameter of the grown nanorods [22].

ZnO nanorods formed using these techniques are highly crystalline nanorods, and different types of devices can be fabricated using these nanorods.

2.2 Vapour–Liquid–Solid Growth

The vapour–liquid–solid (VLS) technique uses a metal catalyst (usually Au) to grow the nanorods. Zn vapour is produced by heating the sample in a boat. ZnO can also be reduced to Zn vapour in the presence of graphene and CO/CO_2 [23]. As the Zn vapour interacts with the metal catalyst, a Zn/Au alloy will be formed. As time increases, the Zn content in this alloy will saturate and then it reacts with oxygen to form ZnO. The ZnO formed moves below the Zn/Au alloy and nucleates. This process continues until a ZnO nanorod with Zn/Au alloy is formed on the tip. Changes in the diameter of ZnO nanorods can be achieved by changing the thickness of Au.

2.3 Solution Growth

ZnO is an amphoteric oxide which can react with both acids and bases. In a basic solution, a zinc salt hydrolyses to form an unstable zinc complex like zinc hydroxide. Under suitable pH conditions, these complexes recrystallize via dehydration to form ZnO. While forming crystalline ZnO in wurtzite structure, the termination in [0001] direction will be either Zn^{2+} or O^{2-}. Because of the high energy of the polar surfaces, new incoming elements easily get adsorbed on the polar surface. In one cycle, if the terminating element is Zn^{2+}, an O^{2-} will try to stick there in the next cycle, it is succeeded by an incoming Zn^{2+}. This cycle continues, and ZnO is crystalized [24]. Hence, the growth rate of ZnO in [0001] direction is faster than other crystal directions. The faster growth rate in one crystal plane easily results in the formation of crystalline ZnO nanorods.

In order to grow ZnO nanorods from solution, suitable salts like zinc nitrate ($Zn(NO_3)_2$) [25–27], zinc acetate ($Zn(COOH)_2$), zinc sulphate ($ZnSO_4$) [25], etc. are dissolved in suitable solvents, and it is then allowed to react with materials like sodium hydroxide (NaOH) [25], ammonium hydroxide (NH_4OH), dimethylsulphoxide (C_2H_6OS) (DMSO), hexamethylenetetramine ($C_6H_{12}N_4$) (HMTA) [26–28], etc. Initially, spontaneous nucleation occurs in the saturated solution under suitable pH, and then, nanorods are formed on these self-generated nucleation sites. Hence, the nanocrystals will be in powder form. If a suitably seeded substrate is kept in this precursor solution, the crystalizing ZnO tries to nucleate over the seeds, which may result in the growth of nanorods over the substrate.

2.4 Hydrothermal

Hydrothermal synthesis is a solution-based growth process, where the growth of ZnO nanorods takes place at an elevated temperature and pressure in a special container called autoclaves. The autoclave is Teflon-lined steel containers, which can withstand an enormous amount of indigenously developed pressure inside. The material of the container should be inert to the precursors used. Zinc containing material is used in the precursor solution along with some oxidizing agents to form intermediate unstable complexes like zinc hydroxide. The precursor solution is kept inside an airtight autoclave and on increasing the temperature, the pressure inside the autoclave increases to the range of megapascal. Under this elevated pressure and temperature, normally insoluble ZnO dissolves and a supersaturated zinc hydroxide is formed, which again recrystallizes to ZnO. There are many reports on the formation of ZnO nanorods via hydrothermal synthesis.

The hydrothermal synthesis of bulk ZnO crystal was reported in the 1950s by Laudise and Ballman [29]. The synthesis of ZnO rods was reported only in 1990 by Andre et al. by the hydrolysis of zinc chloride in the presence of HMTA [30, 31]. Later in 2000, Vayssieres et al. reported the formation of ZnO rods over a substrate using zinc nitrate and HMTA [32]. The water-soluble HMTA is thermally degraded to release hydroxyl ions. These ions will react with Zn^{2+} to form ZnO. Researchers used various combinations like $Zn(NO_3)_2$ and HMTA [13, 33–35], zinc acetate and ammonium hydroxide [36–38], zinc sulphate and ammonia [39], etc. as the precursors for the growth of ZnO by hydrothermal technique.

The pH of precursor solutions for hydrothermal synthesis ranges from 7 to 12. A pH of 9 is preferred for the growth of ZnO nanorods using zinc acetate and ammonium hydroxide. The initial chemical reactions involving Zn^{2+} and NH_3 results in the formation of $Zn(NH_3)_4^{2+}$ complex. This $Zn(NH_3)_4^{2+}$ complex will eventually decompose to form ZnO.

Aneesh et al. reported that during hydrothermal synthesis presence of NH_4OH with $Zn(COOH)_2$ will result in the formation of nanorods, whereas the use of NaOH instead of NH_4OH will result in the formation of ZnO nanoparticles [36, 40, 41].

The zinc salt, zinc acetylacetonate ($Zn(C_5H_7O_2)_2$), can act as a single-source precursor for the synthesis of ZnO nanorods [42]. Along with precursor solution, various surfactants such as polyvinyl alcohol (PVA), polyethylene glycol (PEG), sodium dodecyl sulphate ($CH_3(CH_2)_{11}OSO_3Na$), cetyltrimethylammonium bromide (CTAB) [43], carbamide, potassium iodide and hydrazine hydrate are used for controlling the morphology and size of the nanorods. Anodized alumina, amphiphilic block copolymers, etc. are used as templates for ZnO nanorod growth.

Major advantages of this technique are the better yield, simple technique, cheap process and control over nanostructure formation. Because of these advantages, there is a real boom in this topic for the last few years. This technique is perfect for the growth of aligned ZnO nanorods over suitable substrates. The wafer-scale production of ZnO nanorods was already reported, even with aligned growth of nanorods over a

substrate [44]. Using suitable hydrothermal condition, even nanorods can be grown epitaxially [35, 45].

2.5 Electrodeposition Growth

The electrodeposition is an electrochemical process in which ZnO is deposited at the cathode of an electrochemical cell using a suitable precursor solution. In this process, ZnO nanorods can be grown over any conducting substrate. The conducting substrate is to be kept as the cathode in the electrochemical cell. Usually, a three-terminal electrochemical cell is used. The cathode will be the working electrode, the counter electrodes may be a stable noble metal like Pt or Au and the saturated calomel electrode serves as the third reference electrode. The major advantage of electrodeposition is that irrespective of the substrate shape (flat, curved, flexible, etc.), nanorods can be grown over a conducting surface of the substrate. Because an electric potential is driving the growth process, uniform growth of nanorods over a large area can be achieved, and hence, it is a promising technique for wafer-scale production of nanorods over a substrate. The major disadvantage of electrodeposition is that it is impossible to grow or deposit a material over a non-conducting substrate.

Formation of ZnO by electrodeposition involves two steps. In the first step, hydroxylation of Zn occurs, and a zinc hydroxide complex is formed. In the second process, the zinc complex formed is decomposed to form crystalline or amorphous ZnO.

$$Zn^{2+} + 4OH^{-} \longrightarrow Zn(OH)_4^{2-} \tag{1}$$

$$Zn(OH)_4^{2-} \longrightarrow ZnO + 2H_2O \tag{2}$$

The growth rate of crystalline ZnO is different for each crystal directions. The maximum rate is, along the <0001> direction. Hence, usually electrodeposition yields nanorods with <0001> crystal direction along its longitudinal direction. By changing the deposition condition, growth rate along various crystal planes can be altered, which can lead to the formation of various nanostructures. Xu et al. reported the formation of hexagonal rods, woven nanoneedles, rhombohedral rods, etc. using zinc nitrate-based precursor solution using different salts such as KCl, NH_4F, ethylenediamine ($C_2H_4(NH_2)_2$) (EDA) and CH_3COONH_4 [46]. The concentration of the precursor solution also has a dependence on the shape of nanostructures formed. The use of two-step electrodeposition can also yield various hierarchical ZnO nanostructures [47]. Under suitable conditions, hexagonal ZnO nanorods can be fabricated using various precursor solutions such as $ZnSO_4$ and Na_2SO_4 along with H_2O_2 [48], $ZnCl_2$ with KCl solution [49, 50] and zinc acetate with DMSO [51].

According to Cui et al., the growth rate and nucleation density are more for samples grown from $ZnCl_2$-based electrolyte under an applied potential of −1.2 V [52]. The nucleation density can also be controlled by providing a ZnO seed layer. The

seed layers are usually deposited by spin coating, chemical bath deposition, sputtering, etc. The cyclic voltammetry studies also confirmed that a potential of −1.2 eV is essential for the formation of ZnO from the electrolyte. The temperature of the electrolyte during electrodeposition is also a critical condition which decides the morphology of the grown nanorods. Nanorods grown under suitable conditions showed good transparency, especially in the visible range. In a recent study, T. Frade et al. showed that better control on growth of well-defined ZnO nanorods with low coalescence and more homogenous distribution of nanorods can be achieved by using pulse electrodeposition [53]. The crystalline quality and other properties of these nanorods were comparable to that observed for nanorods obtained from conventional techniques. The major advantage when compared to other techniques is the uniform growth of nanorods with even distribution.

Though the use of any kind of template is not necessary for the formation of ZnO nanorods by electrodeposition, modified processes utilized template-assisted tools also. Lai et al. reported the growth of ZnO nanorods at the nuclear track found in the porous polycarbonate membrane [48]. ZnO nanorods were also electrodeposited from zinc sulphate and H_3BO_3 solution using anodized alumina template [54].

2.6 Pulsed Laser Deposition (PLD)

Pulsed laser deposition (PLD) is an effective tool for creating good quality thin films with a composition which exactly matches the target. Most other deposition tools lack this property. By controlling the chamber pressure during ZnO growth time, ZnO nanorods were successfully grown by PLD. The nanorods thus formed had a few hundred nm diameters and about 2 μm length [55, 56].

2.7 ZnO Nanotube Formation

ZnO nanotubes are generally grown by a two-step process. Initially, the ZnO nanorods are grown using any of the above-mentioned processes. Since the [0002] crystal direction of ZnO is polar in nature, the etch rate is faster in the direction compared to other crystal planes for an acidic or basic solution. If the etch rate can be suitably controlled, ZnO nanotubes can be formed easily. ZnO nanotubes also can be grown by a VLS process, directly from ZnO/Zn mixture [57].

2.8 Patterning Techniques

Patterning processes cannot be used to make ZnO nanorods directly, rather most reports use patterning as a tool for the selective and controlled growth of ZnO

nanorods over a particular substrate. Patterning processes utilize conventional lithographic processes like X-ray, UV, visible, ion beam lithography [58–60] and some of the latest techniques like monolayer assembly to decide where ZnO nanorods need to be grown. Patterning techniques or lithographic techniques which use the top-down approach for creating nanostructures from bulk are rarely used for ZnO nanorod fabrication.

The ZnO seed layer can be deposited using the above-mentioned techniques like spin coating, sputtering, PLD, etc. The produced thin film is then patterned and selectively etched using wet, dry or ion etching. This pattern acts like a patterned seed layer structure above which further ZnO nanorods can be grown using other growth techniques. Still, a major challenge associated with such techniques is the limitation of resolution of patterning. Recent techniques like interference lithography have greatly improved the resolution limit. Due to the technical limitations, e-beam lithography is usually preferred over photolithography.

Most recent advancements in lithographic tools allow skipping the masking process, by electronically controlling and directly writing the desired structure. FIB is an example of such a technique, where the ion beam is electronically controlled and exposed directly over the active material without any sacrificing layer. Hence, a good resolution can be achieved. Yet one major setback to this technique is its low yield. Depending on the depth of the nanostructure and the area over the substrate where the nanostructures are formed, the processing time may increase enormously.

Inkjet printing is another simple, economical method for the growth of the seed layer. The seed layer solution is kept as ink and can be printed in the predefined pattern. On drying, ZnO particles will remain on the printed substrate as a pattern. ZnO nanorods can be grown over this patterned seed layer to get patterned ZnO nanorods [61].

Monolayers of spherical-shaped particles can be self-assembled by themselves over a suitable substrate. Using this monolayer as a pattern, the seed layer can be deposited on the voids found in between the spheres. Growth of ZnO nanorods over these patterned surfaces helps to achieve growth of ZnO nanorods at the selected area [62–64].

Nanoimprint lithography (NIL) is the latest addition to this process, and here, pattern over a master is created and is transferred to a substrate. Later, ZnO nanorods are grown over this patterned substrate [65, 66]. Resolution can be improved dramatically, and the yield is also high in this process. Recently, self-assembly is also used to fabricate ZnO nanorod-based solar cell [67].

3 ZnO 1D Nanostructure-Based Devices

ZnO is a wide bandgap semiconductor with large exciton binding energy. ZnO intrinsically shows n-type conductivity, because of the oxygen vacancies and zinc interstitial donor levels. At the same time, inducing p-type conductivity in wide bandgap oxides is very difficult. Though p-type conduction has been reported in

ZnO, its reproducibility is still a problem. This led to the development of ZnO-based heterostructures with n-ZnO and various p-type materials like GaN, Cu_2O, etc.

3.1 Heterojunction

One of the most studied applications of ZnO nanostructures is the formation of heterojunctions. Since n-type conductivity is easily observed and is stable, the majority of such heterojunction devices have ZnO as the n-type layer. The p-layer may be CuO, GaN, $MgAl_2O_4$, $ScAlMgO_4$, p-Si [31, 68, 69], NiO [70, 71], etc.

A heterojunction is realized by combining a p-type material with another n-type material. For an n-type semiconductor, the Fermi level is near the conduction band, and for a p-type semiconductor, the Fermi level is near the valance band.

As the two semiconductors are made to intimate contact on the atomic scale, the Fermi level of both the semiconductors try to align, forcing the valance band and conduction band edges of both the semiconductors to bend near the junction as shown in Fig. 3a. Due to the bending of energy bands, the charge carriers see the barriers which stop the flow of majority carriers, which is why heterojunctions show rectifying behaviour. The charge conduction through the device is completed by diffusion and drift of charge carriers through the semiconductor.

The dependence of junction current (I) on biasing voltage (V_D) is given by the ideal diode equation

$$I = I_0\left(e^{\frac{V_D}{nV_T}} - 1\right) \tag{3}$$

where I_0 is the saturation current, $V_T = \frac{kT}{q}$ denotes the thermal voltage, k is Boltzmann constant, q the electric charge and T is the temperature in absolute scale and

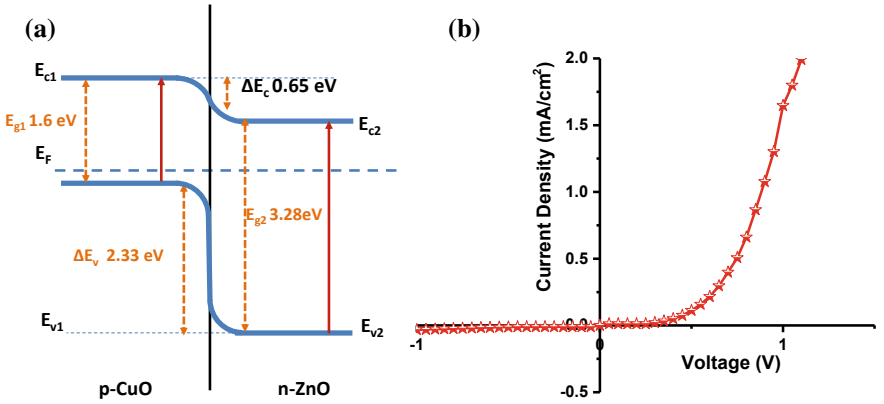

Fig. 3 **a** Band diagram and **b** V–I characteristics of p-CuO/n-ZnO heterojunction

n is the ideality factor or quality factor, its value is 1 or 2 for ideal diodes. The value of V_T at room temperature (300 K) is 25.85 mV. The constant current observed in reverse bias is the reverse saturation current I_0. Extrapolation of the linear region of the curve to the x-axis in the forward bias region will give the turn-on voltage or knee voltage (V_k) which is also a built-in potential (V_{bi}).

Any p-type materials like CuO can be deposited over n-ZnO nanorods to form a p-CuO/n-ZnO nanorod-based heterojunction. Band diagram of such a heterojunction is shown in Fig. 3a, and the plot of J versus V_{D} of the heterojunction is shown in Fig. 3b. The theoretically predicted band diagram matches with experimentally observed I–V characteristics. The knee voltage observed was 0.65 V.

Though proper ohmic contacts were provided at the two ends of the heterojunction device, there still will be some residual contact resistance. Also, the semiconductor region itself will offer some resistance. Altogether the different resistance (R_{s}) values can be added together and can be considered as the series resistance of the diode. When a current passes through the heterojunction device, there will be a potential drop of IR_{s} across this resistance. Moreover, at the junction, there will be a potential drop of V_k. The applied voltage V will be distributed to IR_{s} and V_k.

So, the applied voltage

$$V = V_k + \text{IR}_{\text{s}} \tag{4}$$

The potential drop due to the series resistance of the heterojunction is $\text{IR}_{\text{s}} = V - V_k$. Hence, plotting $\Delta V = V - V_k$ versus the current I in the forward bias region will give a straight line with slope R_{s}. Determining the slope of the straight line region of this curve will give the series resistance (R_{s}) of the heterojunction device. For the heterojunction shown in Fig. 3b, the series resistance was 17 kΩ.

For V_{D} > knee voltage, the junction current is given by the equation

$$I = I_0 \text{e}^{\frac{V_{\text{D}}}{nV_{\text{T}}}} \tag{5}$$

or

$$\log(I) = \frac{qV_{\text{D}}}{nkT} + \log(I_0) \tag{6}$$

From the plot of the $\log(I)$ versus V_{D} of the forward region of V–I characteristics of the biased heterojunction, the slope of the linear region of this curve can be calculated, which is mathematically equal to slope $= \frac{q}{nkT} = \frac{1}{nV_{\text{T}}}$. From this relation, the ideality factor of the heterojunction can be found out as $n = \frac{1}{\text{slope} \times V_{\text{T}}}$. Oxide heterojunctions especially n-ZnO nanorod-based heterojunctions are generally reported to have an ideality factor much greater than 2, due to poor heterojunction interfaces. Yet an ideality factor of around 2 can be obtained for carefully crafted p-CuO/n-ZnO-based heterojunctions [50].

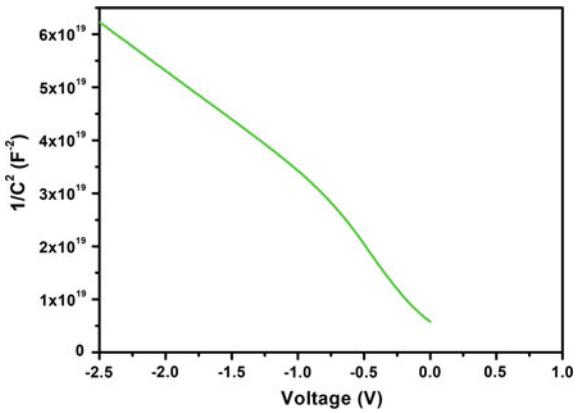

Fig. 4 Capacitance–voltage characteristics of the p-CuO/n-ZnO nanorod heterojunction

A heterojunction diode under reverse bias works as a dielectric sandwiched between two electrodes, which is simply a capacitor. Hence, it is possible to evaluate the heterojunction capacitance for various reverse biasing voltages (Fig. 4).

For an abrupt step junction, the junction capacitance can be connected with the expression [72],

$$C_j = \frac{K_s \varepsilon_0 A}{\left[\frac{2K_s\varepsilon_0}{qN_D}(V_{bi} - V)\right]^{1/2}} \tag{7}$$

Or we can write

$$\frac{1}{C_j^2} = \frac{2}{qN_D K_s \varepsilon_0 A^2}(V_{bi} - V) \tag{8}$$

Hence, plotting the $\frac{1}{C_j^2}$ versus the applied voltage V will give a straight line having a slope which is inversely proportional to the carrier concentration N_D at the junction. Thus, the carrier concentration N_D can be calculated from the slope of the heterojunction. On extrapolation, the above curve will intercept at V_b. When calculating the carrier concentration and other electrical properties of an asymmetric abrupt heterojunction, the heavily doped side of the heterojunction can be ignored, as the depletion region will be extending towards the lightly doped semiconductor region of the heterojunction. Hence, the carrier concentration of lightly doped semiconductor for this heterojunction can be determined from the above relation. As an example, for an-ZnO/p-CuO heterojunction, the carrier concentration of lightly doped semiconductor (ZnO nanorod) is determined from the capacitance characteristics as 8.75 $\times 10^{14}$ cm^{-3}. This is an indirect method to measure the carrier concentration of ZnO nanorods.

Apart from the use of a heterojunction as a rectifier, carefully crafted heterojunctions can perform as light-emitting diodes (LEDs), light sensors (detectors), etc.

3.2 Light-Emitting Diode (LED)

Light-emitting diodes (LED) are one of the widely used illumination sources mainly due to its high efficiency and low power consumption. The use of LEDs from small-scale signal sources to large-area illumination sources even in the industry was possible only after the development of high-power white-light LEDs. LEDs are nothing but a semiconductor heterojunction, where the energetic electrons in conduction band combine with holes in valence band by releasing the energy in the form of photons. Depending on the specific band structure of the device, emission wavelengths ranging from IR to UV can be generated. While the forward bias voltage increases beyond turn-on voltage, a large amount of current starts to flow through the heterojunction, carrier recombination rate increases and in turn, the number of photons generated also increases which increases the intensity of emission. For an LED, the region where recombination of holes and electrons takes place is critical, since it decides the quality of the light emission. If the interface crystalline quality is poor, non-radiative recombination will dominate, resulting in a drastic reduction in emission. Hence, it is extremely important to choose the right method and condition for the fabrication of an LED device.

ZnO and GaN are wide bandgap materials, and most of the emissions that arise from ZnO/GaN heterojunction is due to the band-to-band transition, which is in the UV region [73]. Band structure modification or additional use of phosphors [74] is another technique employed to obtain visible emissions. ZnO is intrinsically rich with various defect levels. GaN also has its due share when it is doped with materials like Mg, which is used to induce p-type conductivity. Selectively participating in the right energy levels for the emission process results in longer wavelength emissions.

The emission threshold in p-GaN/n-ZnO of LEDs demonstrated by Wu et al. is greater than 10 V, and they also studied as from where the p-GaN/n-ZnO heterojunction the light emission originate [38]. They demonstrated the growth of ZnO with the defect-free interface over GaN by hydrothermal method. They investigated the influence of seed layer on the quality of ZnO grown and its impact on the performance of the devices and observed that the emission originates from the p-GaN side for ZnO/p-GaN heterojunction devices where the ZnO nanorods were grown without any seed layer. At the same time, for devices, where ZnO nanorods are grown over the sol–gel deposited ZnO seed layer, the emission is originating from ZnO [38]. Since emission originates from different materials, the emission properties of these devices will also be different. Similarly, Ng et al. studied the dependence on the interface and its quality by using different seed layer and different growth techniques for the growth of ZnO nanorods over GaN substrate [75]. It has been observed that on GaN/ZnO heterojunction devices, even slight variations induced at the interface can

result in dramatic variations in its electroluminescence (EL) emission. Here, though the photoluminescence was same for all the devices, its electroluminescence properties vary as the GaN/ZnO interface changes. Seed layers are employed to change the interface states, which triggered the fluctuations in interfacial band alignment which again reflects in the emission spectra.

The quality of the interface between the n-type semiconductor and p-type semiconductor is crucial for achieving light emission. Schuster et al. studied the emission dependence on the polarity of terminating ion in ZnO nanorod while forming GaN/ZnO heterojunction [76]. They theoretically proposed that by choosing suitable polarity, even UV lasing is possible with such structures. Hence, it is essential to study the growth dynamics as well as the terminating atom on the surface while a nanostructure is grown.

Visible emissions like violet [39, 77], blue [17, 78, 79], yellow [78, 80], red [74], etc. have been achieved from ZnO nanorod-based LEDs. Recent research attention is on white-light LEDs due to its wide applications as an illumination source. ZnO nanorods has also shown its potential in white-light LEDs [17, 78] using GaN as a p-type substrate. Some devices have shown UV and broad visible emission similar to characteristic luminescence from ZnO semiconductor [70]. Apart from GaN-based LEDs, p-Si/n-ZnO have also shown a broad visible emission [68, 81]. GaN/ZnO heterojunction LED recorded an external quantum efficiency of ~2.5%, and they also showed stable operation for about 90 h [82].

The wavelength of EL emission also depends on ZnO nanorod length. Due to the light interference inside the nanorod interfaces, emission wavelength does change in a periodic manner with the length of the nanorod [83]. This property adds another parameter to tune the emission wavelength of ZnO/GaN heterojunction LED. At the same time, the intensity of light emission increases with the diameter of the nanorod, but it shows a saturation trend [84].

Chen et al. fabricated a heterojunction using n-ZnO and p-GaN which showed white emission on doping ZnO with Ga, whereas devices without Ga doping emitted bluish light [17]. ZnO layer formed via thermal CVD process reduced the turn-on voltage to as low as 1 V compared to the devices fabricated by other techniques. Lupan et al. showed that the emission will shift from the UV region to the violet region on a similar device structure. Here, the ZnO nanorods are grown by solution processes like hydrothermal synthesis and electrodeposition, and the turn-on voltage was around 4 V [39].

Light emission has also been observed in ZnO/p-GaN heterojunction even under reverse bias [34, 80, 85]. Wang et al. believe the emission under reverse bias is due to tunnelling breakdown due to hot carrier injection and associated recombination which occur predominantly in the GaN region of the heterojunction. Zhang et al. also reported white emission under forward bias, while emission colour shifts from yellow to blue and then to UV emissions as the reverse bias increased from 3 to 7 V [78].

Contrary to the majority of the researchers, Du et al. studied the electroluminescence emission perpendicular to the polar axis [86]. With a simple preparation step,

they showed UV/blue emission perpendicular to *c*-axis. Here, it can be seen that the junction is also formed perpendicular to the *c*-axis.

If the LED is fabricated on a transparent device with fully transparent structure, the light emission on both sides is possible. Wang et al. demonstrated this on a structure with p-NiO/n-ZnO heterojunction [70]. According to Abbasi et al., adding a NiO layer in between ZnO and GaN interface results in an enhancement in emission properties for both nanorods and nanotubes [87].

An important characteristic of 1D ZnO nanorod-based LED is the light coupling efficiency due to the waveguide nature of the nanorod. Since the generated light inside the nanorod possesses multiple total internal reflections inside the nanorod, the light emission can be expected from the end faces of the nanorods. ZnO nanorod-based LEDs also offer enhancement in light emission due to its waveguide nature [88, 89]. The possibility to couple optical fibre to the end face of the nanorod improves the light extraction efficiency. Further enhancement of light emission is possible using ZnO microcylinder [90]. The microcylinders in effect collect the light from side walls of nanorods and reduce scattering. This enables the emitting light to get confined in it to a solid angle giving an improvement in light emission efficiency. There are also the reports suggesting the replacement of nanorod with cone-shaped semiconductors, which reduces the total internal reflections, which results in enhancement of output light [91].

Most of the earlier studies showed that the heterojunction interface affects the overall performance of the heterojunction. Hence to study the effect of crystallinity on the performance of the heterojunction, we have fabricated a n-ZnO nanorod/p-GaN heterojunction. ZnO nanorods were grown hydrothermally over a c-cut p-type GaN:Mg substrate, to form the heterojunction. ZnO nanorods over the single-crystalline GaN:Mg substrate and followed the crystal structure of the substrate. The nanorods showed no twinning or twisting while growing over the substrate. Thus, nanorods with less interfacial defects between n-ZnO and p-GaN:Mg substrate were obtained. After providing sufficient metallic contacts, the electrical studies were performed. The device emitted light, and the emission threshold was as low as 5 V. Two types of devices were fabricated, one with as-grown ZnO nanorods (GZn) and one with annealed ZnO nanorods (GZnA). On annealing, apart from the slight increase in crystallinity, there was a tremendous change in defect states of ZnO nanorods, which is visible from the photoluminescence studies as shown in Fig. 5a. As-prepared ZnO nanorods showed a broad deep-level defect emission apart from the band edge emission. On annealing, the defect emission almost suppressed completely leaving only the band-to-band transition. Corresponding devices showed a significant change in emission properties also. The GZn device showed white-light emission, whereas on annealing, the device (GZnA) showed UV-blue emission. Almost all white-light emissions were suppressed as it is seen in photoluminescence emissions. In this case, the wavelength of emission was able to be tuned by selectively changing the defect states in ZnO because the defect states in ZnO actively participate in the emission of light from the device [92]. While considering the application as an LED the most

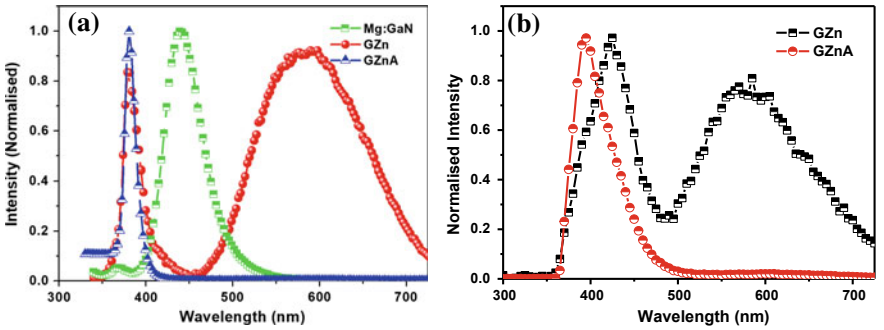

Fig. 5 **a** Photoluminescence emission from GaN:Mg substrate, ZnO/GaN heterojunction, before (Zn) and after(GZnA) annealing. **b** Electroluminescence from as-prepared (GZn) and annealed (GZnA) devices

important parameter is the spectral purity. The colour quality of the device is represented by finding its CIE coordinates, which is calculated on the perception of human colour vision.

Due to the piezophotonic effect of ZnO nanorods, emission intensity increases with the piezopower, while the peak positions remain the same. Yang et al. demonstrated 17 times enhancement in emission on applying compressive stress [93].

The light emission is also observed from SnO_2/ZnO/PEDOT structure, in which the PEDOT acts as the organic p-layer [94]. The hybrid LED had a threshold emission at 6 V. The device had a strong emission around 390 nm and a broad emission in the visible-NIR region.

Wei et al. demonstrated white-light LED from ZnO nanorod/polymer blend heterojunction device [95]. They have shown that such devices can have superior chromaticity values compared to GaN–ZnO-based LEDs.

Schottky LEDs based on ZnO nanorods and nanotubes which emit white light have also been reported [96]. For higher voltages like 20 V, 350 mA junction current is observed, which is very close to the silicon technology. Hence, achieving higher efficiency is possible.

3.3 Photodetector

In the case of a detector, the quality parameters include responsivity and fastness. For a photodetector to work, it should record the presence of even a feeble light signal as fast as possible. Here, the responsivity can be defined as the ratio of change in response to the original dark response value. Higher the order of response, the better is the device.

The fastness of the detector can be found out in a number of ways. One simple way is to illuminate the detector with suitable light, and the change in junction current is recorded over time. This technique has a serious drawback as the current measuring device (usually source measure unit (SMU)) has a low temporal resolution. Typical data acquisition rate is few milliseconds. To record the response of detectors which are faster than such devices, a chopper mechanism can be used as shown in Fig. 6. Here, an optical chopper is used to chop a continuous laser beam. By controlling the speed and width of the chopper blades used, the temporal width of the laser light pulse can be adjusted. The digital multimeter connected in this circuit can record the voltage variation across the resistor *R* which is a function of heterojunction current as shown in Fig. 6. Yet another powerful approach is to use a nanosecond/femtosecond pulsed laser light. Again, the junction response to the short laser light pulse is recorded (Fig. 7).

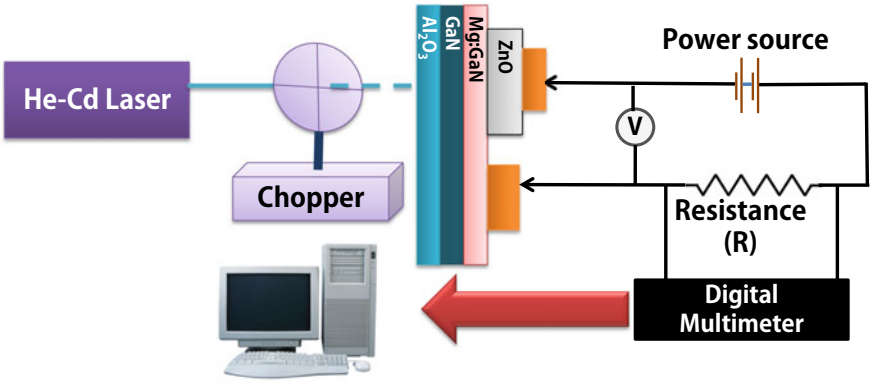

Fig. 6 Schematic diagram of the arrangement for measuring the response of the detector

Fig. 7 Photoresponse of a typical detector

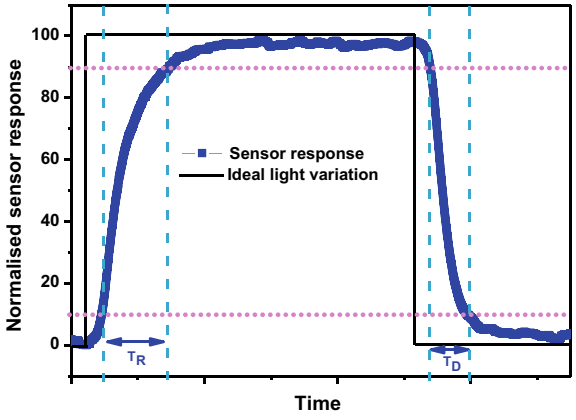

After acquiring the junction response data, mathematical fitting is done on the response curve and decay constants can be found out using the equation,

$$Y = Y_0 + A_1 \exp\left(-\frac{t}{t_1}\right) + A_2 \exp\left(-\frac{t}{t_2}\right) \tag{9}$$

Depending on the mechanism of working of a device, single, double, triple or more decay time constants can be present. In this equation, two decay constants t_1 and t_2 are considered. Each time constants can be attributed to different charge transfer/transport mechanisms. This method of calculating time constants is used especially when the device takes a longer time to respond for an incident light signal or if stable response level is not achieved at all. Mathematically, we can see that the rise/decay time is the time required by the device to respond between the $1/e^{\text{th}}$ level of response and 100% level. The industry standard is to measure the time taken for the device to respond between its 90 and 10% response value. Thus, the rise time is the time taken by the device to respond from its 10% level to 90% response level, and the time for transition from 90 to 10% is the decay time. At present microsecond or even nanosecond responding devices are on production.

Another parameter is the spectral selectivity of the detector. Here, light with multiple wavelengths are illuminated over the device with one wavelength at a time, and the corresponding photoresponse can be recorded. This measurement tells us which wavelength region will give better performance for the device. It also suggests whether the device can be used for its intended use. The response of the device for different intensity of incident light is yet another measure. The fluctuations in the response parameter are usually plotted as a function of incident power. This measurement gives the efficiency of the device to convert an incident photon to an electron. This measurement will give information on the threshold (the least light energy required to produce a minimum response from the device) and saturation levels (the maximum incident light energy or intensity that can be converted to a corresponding response) of the device.

Initial attempts to develop ZnO-based photodetector were carried out with ZnO in thin film form [97–100]. Such structure generally utilizes the resistivity variation of ZnO on the absorption of light, especially UV light. There was even attempt using ZnO microrods as UV detectors in the resistive mode [101].

MOCVD-grown ZnO:As-based detectors respond within 2 ms for 368 nm, 10 mW light source. The p-type ZnO:As and n-type GaN constitute a heterojunction. The device shows a response to both visible and UV light, but the response to UV is superior to visible light [102].

In yet another approach, Pt wire is wound over the ZnO nanowire in n-ZnO nanowire/NiO heterojunction to form a 3D photodetector. This setup will respond to UV light and tensile stress. It couples piezoelectric and heterojunction properties together. The piezoelectric properties seem to enhance light sensing properties [19].

Another novel idea includes the fabrication of Si/ZnO surface acoustic waves (SAW) oscillator, in which the light detection is triggered by a shift in SAW oscillator

frequency [103]. A frequency shift of 1017 kHz is recorded for UV light having an intensity of 551 $\mu W/cm^2$.

Single-nanorod-based UV photodetector has been fabricated by Das et al. [104]. The Schottky junction fabricated showed a reasonable response to UV light even at a low light intensity. For lower power detection, such structure is a promising technology.

Among the various reports mentioned above, heterojunction devices offer better performance compared to resistor devices. GaN/ZnO is a promising heterojunction, which offered good UV detection capabilities. Zhang et al. reported GaN/ZnO nanorod-based UV photodetectors with pin structure recorded response time less than one second [105]. CVD-grown ZnO nanorods over GaN can produce much faster UV response. Zhang et al. recorded a 64 ms rise time and a 270 ms decay time for UV response on ZnO/GaN heterojunction [14], and the ZnO/GaN heterojunction barriers are suggested as the reason for such large rise/decay time. Thus, an improvement on the interface can increase the performance of the heterojunction.

As already discussed, performance of a heterojunction depends on the quality of the p-n junction interface. The sophisticated growth techniques like MOCVD, CVD, VLS, etc. are generally used for fabricating good quality ZnO heterojunctions. Though several efforts based on solution process and hydrothermal synthesis methods were employed for the growth of ZnO, the UV detection capabilities of such devices were inferior compared to heterojunction fabricated by a process like CVD. Inferior crystalline quality is one of the reasons for the poor performance of such heterojunctions fabricated using solution techniques. We have demonstrated a simple technique for fabricating n-ZnO nanorods over p-GaN:Mg single-crystalline substrate. Hydrothermal synthesis using zinc nitrate and ammonium hydroxide aqueous solution is used to grow nanorods over GaN:Mg. Field emission scanning electron microscope(FESEM) studies revealed hexagonally shaped vertically aligned ZnO nanorods, as shown in Fig. 8a. The crystalline quality of such nanorods was analysed using high-resolution X-ray diffraction studies. Independent (0002) peaks corresponding to GaN and ZnO are visible under the rocking curve analysis. Similarly, the reciprocal space map shows two ring structures. The most compact concentric ring corresponds to GaN, and the second concentric ring structure is from ZnO. The reciprocal space map proves the excellent crystalline quality of ZnO (Fig. 8b). The ZnO rings are also as compact as the GaN substrate suggesting its high-quality crystal structure similar to GaN substrate. The FESEM studies also reveal no twinning between nanorods. Pole figure analysis of the nanorods also suggested no twinning observation. Thus, the above studies suggest that nanorods follow the crystal structure of the GaN:Mg substrate. Hence, the interface between ZnO and GaN have minimum crystalline defects.

The performance of the heterojunction is analysed to check the effect of crystallinity on device performance. The device showed rectifying nature and showed a change in junction current on light illumination. Further study on the response time of the device is performed using UV light pulses from a He-Cd laser source (325 nm), as shown in the experimental setup in Fig. 6. The response of the device for UV light pulses gave change in response as shown in Fig. 9a. The rise time and fall time were

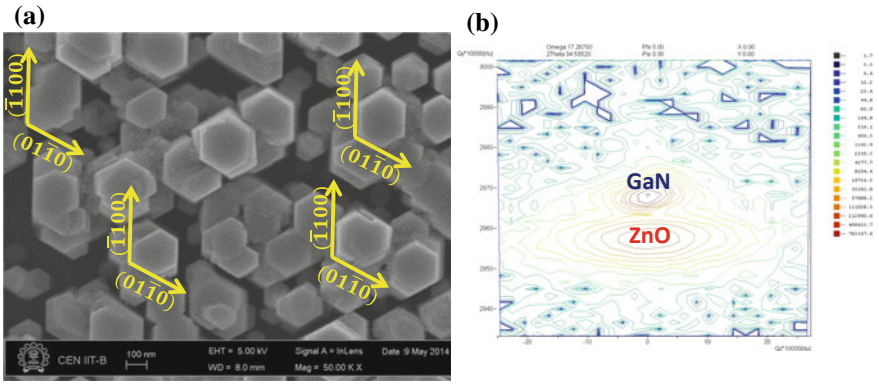

Fig. 8 Well-ordered hexagonal facets of ZnO nanorods grown by hydrothermal synthesis over Mg:GaN substrate (**a**). The high-resolution reciprocal space map of (0002) peak of ZnO nanorods over GaN substrate (**b**)

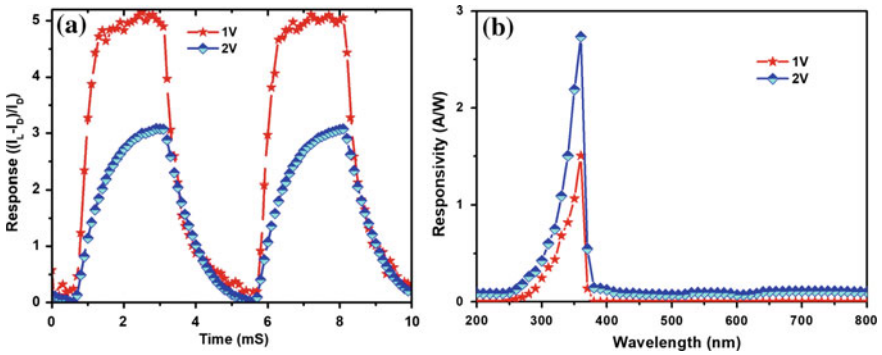

Fig. 9 **a** UV response of ZnO/GaN heterojunction for UV light pulses of 325 nm He-Cd laser light and **b** the photoresponse of the device for various wavelengths

calculated as 288 μs and 323 μs, respectively. The faster UV response of the device is due to the improvements made on the crystalline quality.

The photoresponse of the device for each incident wavelength of light is also performed as shown in Fig. 9b). The device showed a maximum response at UV wavelength suggesting its selectivity property. The selective response of the device may be due to the high bandgap of ZnO and GaN. Table 1 indicates that the present device shows the fastest response from a solution-grown ZnO nanorod-based UV light detectors.

Vertically aligned ZnO nanocones showed promising anti-reflection capabilities. Such structure was successfully applied over an MIS photodetector, which showed a 15 times increase in the photodetection capabilities [106].

Table 1 Recent reports on ZnO nanorod-based photodetectors and their response parameters

	Type	Growth techniques	Nanostructure	Peak detection wavelength (nm)	Maximum photosensitivity	Responsivity (A/W)	Bias (V)	Rise time	Fall time	Year of publication	References
1	Resistor	Vapour-phase transport	Single nanowire	365	10×10^4 to 10×10^6	–	1	<1 s	<1 s	2002	[107]
2	Resistor	Direct vapour phase	Nanowire + sphere	~370 nm	10^6	–	1	2.3 s	0.5 s	2007	[108]
3	Resistor	Chemical vapour deposition	Nanowire	397	10^2	–	–	–	58.5 s	2009	[109]
4	Resistor	Aqueous chemical growth method	Nanowire	<400		–	–	–	149 s	2009	[110]
5	Resistor	Sputtering	Thin film		10^4	–	5	86 ms	355 ms	2010	[111]
6	Heterojunction	Dip coating	Nanowire	370	–	–	–	10 s	62 s	2010	[112]
7	Resistor	Solution growth	Nanowire	UV	27	–	8	–	60 s	2010	[113]
8	Schottky junction	Vapour–liquid–solid technique	Nanowire	25	9	–	–	–	–	2010	[114]
9	Schottky junction	Metalorganic chemical vapour deposition	Nanowire	–	–	–	–	–	–	2010	[104]
10	Heterojunction	Solution growth	Nanorod	370	–	–	5	–	–	2011	[115]
11	Heterojunction	Metalorganic chemical vapour deposition	Nanowire	365	1344.5	30	−5	<160 ms	<350 ms	2011	[116]
12	Resistor	Vapour–liquid–solid technique	Nanowire	369	24,200	–	2.5	>10 s	>10 s	2011	[117]

(continued)

Table 1 (continued)

	Type	Growth techniques	Nanostructure	Peak detection wavelength (nm)	Maximum photosensitivity	Responsivity (A/W)	Bias (V)	Rise time	Fall time	Year of publication	References
13	Heterojunction	Chemical vapour deposition	Nanowire	367	10^6	–	3	20 μs	219 μs	2011	[118]
14	Heterojunction	Chemical vapour deposition	Nanowire	365	–	–	5	64 ms	30 ms	2012	[14]
15	Heterojunction	Molecular beam epitaxy	Thin film	374	–	6.2 m	−2	–	<2 ms	2013	[102]
16	Heterojunction	Chemical vapour deposition	Nanowire	365	8	–	1	7.5 s	8.6 s	2014	[19]
17	Resistor	Floating zone method	Microwire	390	–	5.6 m	5	–	–	2014	[101]
18	Resistor	Hydrothermal	Nanorod	370	10^3	1.7	5	72 s	110 s	2014	[119]
19	Heterojunction	Electrodeposition	Nanorod	<400	–	22	0.65	>10 s	>10 s	2014	[50]
20	Heterojunction	Hydrothermal	Nanorod	365	–	–	1	1.69 s	13.56 s	2014	[120]
21	Heterojunction	Hydrothermal	Nanorod	362	–	1.81	-10	<1 s	<1 s	2015	[105]
22	Resistor	Hydrothermal	Nanorod	365	–	–	3	80 s	20 s	2015	[121]
23	Transistor	Hydrothermal	Nanorod	<350	–	$3x10^5$	1	1.2 s	1.9 s	2015	[122]
24	Heterojunction	Solution process	Nanorod	360	–	–	5	1.345 s	0.132 s	2015	[123]
25	Resistor	Hydrothermal	Nanorod	365	37.4	–	10	–	26.1 s	2015	[124]
26	Resistor	Solution process	Nanorod	–	–	–	5	3 s	30 s	2015	[125]
27	Heterojunction	Hydrothermal	Nanorod	360	5	11	4	288 μs	323 μs	2016	[126]

μs microseconds, *ms* milliseconds

Thus, the above results also suggest that the heterojunction devices offer much faster responses compared to resistor devices. Current research trend shows the successful implementation of ZnO nanorod-based photodetectors with response time in microsecond time scale. With the improvements made on the heterojunction interface quality, the heterojunction devices showed improvements in response time. The device recorded a rise time and fall time well below 1 ms as shown in Table 1. The device showed a responsivity of a few A/W, which is also comparable to similar solution-grown devices. The overall performance of this device is on par with similar devices formed using expensive and sophisticated growth techniques.

3.4 Solar Cells

Organic solar cells fabricated using ZnO nanorods grown by VLS technique, combined with Poly(3,4-ethylenedioxythiophene) (PEDOT), shows an open-circuit voltage of 0.9 V [23]. Dependence of piezotronic effect on the open-circuit voltage of ZnO nanorod/Poly(3-hexylthiophene-2,5-diyl) (P3HT) solar cells showed an increase in hundreds of millivolts even for stress lesser than 0.35% tensile or compressive stress [127]. Rao et al. reported solution growth-based method to fabricate self-assembled *c*-axis oriented ZnO nanorods, which gave an efficiency of 3.2% and a fill factor of 50% [67]. They observed that on UV ozone treatment, the device shows an improvement in device performance.

Even before the development of dye-sensitized solar cell, Gerischer and Tributsch proposed that ZnO can be used as an effective photoanode [128]. ZnO has a similar bandgap and higher electron mobility compared to TiO_2. Due to the higher electron mobility, the number of recombinations can be reduced if ZnO is used as a photoanode [129–132]. A lot of effort is being made to improve the efficiency of ZnO-based DSSC. ZnO-based nanostructures were investigated to understand its light collection ability and to be used as an effective photoanode.

Recently, solution-grown ZnO nanorod-based perovskite solar cell showed a remarkable photon to the current conversion efficiency of 11% [133]. The effect of the seed layer on the growth of ZnO-based nanorods and eventually on the efficiency of the solar cell is fabricated using those nanorods [134]. By controlling the nanorod growth condition, they were able to observe photoconversion efficiency (PCE) of 14%, which is a promising result in this field. Hussain et al. showed that the length of ZnO nanorod has an impact on the efficiency of CuO/ZnO nanorod-based solar cells [135]. The optimum length observed for them was 2 μm. Similarly, Sharma et al. showed 6.25% efficiency on Al-doped ZnO nanorod-based solar cell [136]. They claim that on careful adjustments to other parameters of the solar cell, the efficiency can be improved up to 15%.

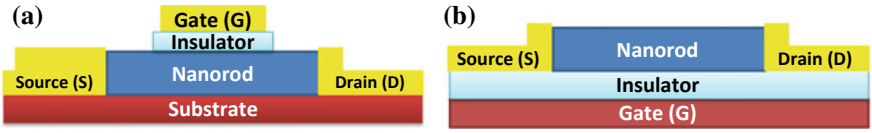

Fig. 10 Schematic diagram of top gate staggered structure (**a**) and bottom gate (inverted) staggered structure (**b**) of nanorod-based transistors

3.5 Transistors

Analysis of the semiconductor nature of nanorods is a difficult task. Especially to evaluate the resistance, carrier concentration and mobility of a single nanorod, providing electrical contacts at the ends of the nanorod is a difficult task. Most of these semiconductor properties can be easily extracted from the *V*–*I* characteristics of ZnO nanorod-based transistors. In general, two types of devices can be fabricated using nanorods as shown in Fig. 10.

In both methods, the channel is taken along the length of the nanorod. Source and drain are connected to the two endpoints of the nanorod. The only difference between these two structures is the position of the gate electrode. In the top gate contact structure, a suitable gate electrode is deposited on top of an insulator which is deposited over the nanorod. In the second configuration, the substrate itself acts as the gate electrode (Fig. 10b). Here, the substrate should be a conducting substrate and on top of that, a suitable insulator is deposited. The nanorod is placed over this insulator, and source and drain are connected to the two endpoints of the nanorod (Fig. 11).

Early work in this field is performed by Heo et al., where they studied the electrical properties of a single ZnO nanorod, by making it as a resistor [141]. ZnO nanorods are initially grown by techniques such as MOCVD and hydrothermal synthesis. As-grown nanorods are distributed over a substrate using techniques like self-assembly, spin coating, etc. E-beam lithography is also coupled along with the fabrication process to produce metallic contacts with the nanorods. Both bottom gate and top gate configuration devices were demonstrated successfully [137–140]. Field-effect transistor based on ZnO nanorods and different nanorod-based field-effect devices were fabricated, and their comparison is given in Table 2.

3.6 pH Sensor

Chemical sensors work by participating in a chemical reaction. pH sensor is one such system, in which the pH change in the chemical environment is being sensed. Only a few groups have looked into the chemical sensing property of ZnO. The amphoteric nature of ZnO is utilized to fabricate a pH sensor. Because of the amphoteric nature of ZnO, it will react with various pH environments giving rise to changes in surface

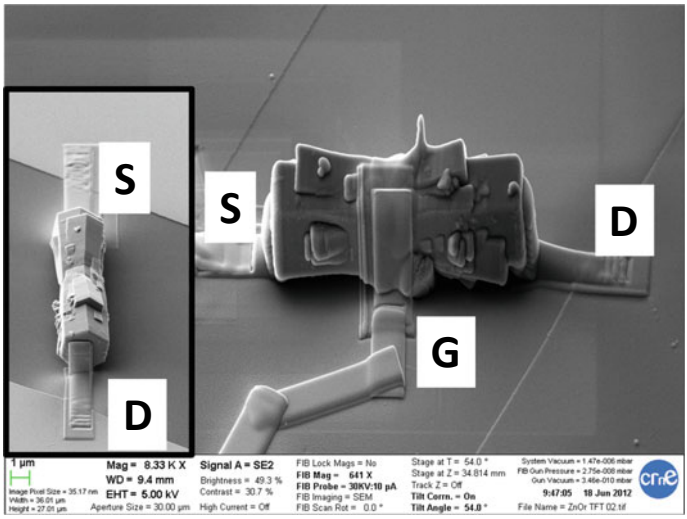

Fig. 11 The FESEM image shows the implementation of a single ZnO nanorod-based top gate transistor. Inset shows the top view of the same nanorod after connecting *S* and *D*

Table 2 Parameters of transistors from a recent report

S. No.	Electron mobility (cm^2/Vs)	On/off ratio current	Electron concentration (cm^{-3})	Transconductance	References
1	–	10^7	–	240 nS	[137]
2	38.7	10^5	1.06×10^{15}	0.39 μS	[138]
3	1200	–	–	1.8 μS	[139]
4	1.4	–	–	–	[140]

potentials. The pH of a solution is determined by the ability of the solution to protonate or deprotonate effectively. The surface of ZnO nanostructures are sensitive to H^+ as the surface bonding sites will hydrogenate when the ZnO surface makes contact with a solution. Because of the electrolyte-dependent protonation or deprotonation occurring at the surface of ZnO, the surface potential will change. Hence, monitoring the change in the surface potential of ZnO gives a direct measure of the pH of its surroundings. Several groups reported the ability of these nanostructures to detect pH from 1 to 16 [142, 143]. Fulati et al. reported the reproducible nature of such devices even after several days of operation [142]. Using ZnO nanorods, intracellular pH variations can also be found out [144, 145].

An important advantage of nanorod-based sensor is that the active sensing area is so small of the order of nanometres. The tip of the nanorod alone can sense the fluctuations in the surrounding pH. Because the active sensing area is so small, even intracellular pH fluctuations can be detected. This opens a new window to detect

biological malfunctions inside a cell efficiently. Another advantage of such devices is their sensitivity. As the active area is so small, a tiny fraction of the detecting medium is enough to induce an electrical response. Hence, such pH sensors can increase the sensitivity beyond ppm levels.

Compared to nanorods, nanotubes offer an increased surface area. Since the heart of a pH sensor is the nanostructure/electrolyte interface, an increase in surface area means an increase in detection capabilities, which is demonstrated by Fulati et al. [142]. They observed a doubling of detector performance using nanotubes compared to nanorods.

3.7 Nanogenerators

Nanogenerator applications of ZnO utilize its piezoelectric properties and semiconducting properties together. Because of the piezoelectric nature of ZnO, on applying pressure there will be fluctuations in potential across the nanostructures, which can be effectively converted to a source of electricity. In general, mechanical force is applied over ZnO nanorods and the pressure-induced current is converted using a semiconductor–metal (Schottky) junction. Voltages of the order of few hundreds of millivolt and currents of the order of few nanoamperes were successfully demonstrated by several groups [146–149]. The generated current will be alternating current. A. Yu et al. demonstrated that the layer-by-layer stacking procedure can be used to combine multiple nanogenerators together. Moreover, they also demonstrated that the voltage and current produced in the stacking procedure follow similar behaviour as to stacking of batteries [148]. In this way, one can generate enough voltage and current levels using an array of nanogenerators. This application is in its infancy and requires a lot of improvements for practical applications.

3.8 Switching Memory Device

The use of ZnO nanorods for novel resistive switches was first demonstrated by Wu et al. [150]. The polarization charges created due to strain varies with external force [150]. They demonstrated the electromechanical memory applications of such devices with effective read–write operations of binary stress levels. Recent achievements on the large-area synthesis of ZnO nanorod suggest that they can be utilized to fabricate ZnO-based memory devices using ZnO nanorods.

4 Conclusions

Research on one-dimensional ZnO nanostructures is recent. Various applications demonstrated so far shows the potential of one-dimensional metal oxide nanostructures especially ZnO. Rigorous efforts are being carried out on ZnO-based homo- and heterojunction devices. Efficient LEDs and other heterojunction devices developed recently strengthened this research area. Gas sensors have also shown its potential, with the large and selective response to gases and high stability. Many devices are near the verge of industrial deployment. Various applications mentioned here especially photodetectors shown evidence of outperforming existing Si-based devices. In the near future, oxide semiconductors will replace Si technology, which currently dominates the electronic industry.

References

1. Noyce RN (1964) Semiconductor circuit complex having isolation means. US Patent 3150299
2. Kilby JS (1964) Miniaturized self contained circuit modules and method of fabrication. US Patent 3138744
3. Kilby JS (1964) Miniaturized electronic circuits. US Patent 3138743
4. Noyce RN (1961) Semicomductor Device And Lead Structure. US Patent 2981877
5. Kilby JS, Dilger LRE (1960) Milwaukee: component mounting for printed circuits. US Patent 2945163
6. Noyce RN (1959) Field effect transistor. US Patent 2869055
7. Kilby JS (1976) Invention of the integrated circuit. IEEE Trans Electron Devices 23:648–654. https://doi.org/10.1109/T-ED.1976.18467
8. Alferov ZI, Andreev VM, Garbuzov DZ, Zhilyaev YV, Morozov EP, Portnoi EL, Trofim VG (1971) Investigation of the influence of the AlAs-GaAs heterostructure parameters on the laser threshold current and the realization of continuous emission at room temperature. Sov Phys-Semicond 4:1573–1575
9. Clark RD, Tapily KN, Consiglio SP, Hakamata T, O'Meara D, Newman D, Collings M, Szymanski D, Wajda CS, Leusink GJ (2016) Process and integration of dielectrics required for 10 nm and beyond scaling R. D. Clark. ECS Trans 72:319–327
10. Karl E, Guo Z, Conary JW, Miller JL, Ng YG, Nalam S, Kim D, Keane J, Bhattacharya U, Zhang K (2015) A 0.6 V 1.5 GHz 84 Mb SRAM Design in 14 nm FinFET CMOS Technology. In: IEEE international solid-state circuits conference, pp 308–309
11. Rahman A, Bai P, Curello G, Hicks J, Jan CH, Jamil M, Park J, Phoa K, Rahman MS, Tsai C, Woolery B, Yeh JY (2013) Reliability studies of a 22 nm SoC platform technology featuring 3-D tri-gate, optimized for ultra low power, high performance and high density application. In: IEEE international reliability physics symposium proceedings, pp 1–6
12. Jan CH, Al-Amoody F, Chang HY, Chang T, Chen YW, Dias N, Hafez W, Ingerly D, Jang M, Karl E, Shi SKY, Komeyli K, Kilambi H, Kumar A, Byon K, Lee CG, Lee J, Leo T, Liu PC, Nidhi N, Olac-Vaw R, Petersburg C, Phoa K, Prasad C, Quincy C, Ramaswamy R, Rana T, Rockford L, Subramaniam A, Tsai C, Vandervoorn P, Yang L, Zainuddin A, Bai P (2015) A 14 nm SoC platform technology featuring 2nd generation Tri-Gate transistors, 70 nm gate pitch, 52 nm metal pitch, and 0.0499 um2 SRAM cells, optimized for low power, high performance and high density SoC products. In: IEEE symposium on VLSI circuits, digest of technical papers, pp T12–T13

13. Podrezova LV, Porro S, Cauda V, Fontana M, Cicero G (2013) Comparison between ZnO nanowires grown by chemical vapor deposition and hydrothermal synthesis. Appl Phys A 113:623–632. https://doi.org/10.1007/s00339-013-7838-5
14. Zhang X, Han X, Su J, Zhang Q, Gao Y (2012) Well vertically aligned ZnO nanowire arrays with an ultra-fast recovery time for UV photodetector. Appl Phys A 107:255–260. https://doi.org/10.1007/s00339-012-6886-6
15. Willander M, Nur O, Zhao QX, Yang LL, Lorenz M, Cao BQ, Zúñiga Pérez J, Czekalla C, Zimmermann G, Grundmann M, Bakin A, Behrends A, Al Suleiman M, El Shaer A, Che Mofor A, Postels B, Waag A, Boukos N, Travlos A, Kwack HS, Guinard J, Le Si Dang D (2009) Zinc oxide nanorod based photonic devices: recent progress in growth, light emitting diodes and lasers. Nanotechnology 20:332001. https://doi.org/10.1088/0957-4484/20/33/332001
16. Zhang Y, Gu S, Tang K, Ye J, Ge H, Yao Z, Zhu S, Zheng Y (2015) Fabrication and characterization of highly oriented N-doped ZnO nanorods by selective area epitaxy. J Nanomater 854074:1–9. https://doi.org/10.1155/2015/854074
17. Chen CH, Chang SJ, Chang SP, Li MJ, Chen IC, Hsueh TJ, Hsu AD, Hsu CL (2010) Fabrication of a white-light-emitting diode by doping gallium into zno nanowire on a p-gan substrate. J Phys Chem C 114:12422–12426. https://doi.org/10.1021/jp101392g
18. Wang D, Zhou F, Liu Y, Liu W (2008) Synthesis and characterization of anatase TiO_2 nanotubes with uniform diameter from titanium powder. Mater Lett 62:1819–1822. https://doi.org/10.1016/j.matlet.2007.10.011
19. Chen J, Ding L, Zhang X, Chu L, Liu N (2014) Photodetecting of ZnO nanowires on a Ni wire by coupling of piezotronics effect and pn junction. Opt Express 22:7090–7097. https://doi.org/10.1364/OE.22.003661
20. Bakin A, Che Mofor A, El-Shaer A, Waag A (2007) Vapour phase transport growth of ZnO layers and nanostructures. Superlattices Microstruct 42:33–39. https://doi.org/10.1016/j.spmi.2007.04.067
21. Fujii T, Yoshii N, Kumagai Y, Koukitu A (2011) Halide vapor phase epitaxy of ZnO studied by thermodynamic analysis and growth experiments. J Cryst Growth 314:108–112. https://doi.org/10.1016/j.jcrysgro.2010.11.097
22. Kitamura K, Yatsui T, Ohtsu M, Yi GC (2008) Fabrication of vertically aligned ultrafine ZnO nanorods using metal-organic vapor phase epitaxy with a two-temperature growth method. Nanotechnology 19:175305. https://doi.org/10.1088/0957-4484/19/17/175305
23. Podzemský J, Schade W (2006) Organic solar cells based on ZnO nanowires layer. In: EEIC, pp 1–4
24. Xu S, Wang ZL (2011) One-dimensional ZnO nanostructures: solution growth and functional properties. Nano Res 4:1013–1098. https://doi.org/10.1007/s12274-011-0160-7
25. Peterson RB, Fields CL, Gregg BA (2004) Epitaxial chemical deposition of ZnO nanocolumns from NaOH solutions. Langmuir 20:5114–5118. https://doi.org/10.1021/la049683c
26. Vayssieres L (2003) Growth of arrayed nanorods and nanowires of ZnO from aqueous solutions. Adv Mater 15:464–466. https://doi.org/10.1002/adma.200390108
27. Volk J, Nagata T, Erdélyi R, Bársony I, Tóth AL, Lukács IE, Czigány Z, Tomimoto H, Shingaya Y, Chikyow T (2009) Highly uniform epitaxial ZnO nanorod arrays for nanopiezotronics. Nanoscale Res Lett 4:699–704. https://doi.org/10.1007/s11671-009-9302-1
28. Consonni V, Sarigiannidou E, Appert E, Bocheux A, Guillemin S, Donatini F, Robin IC, Kioseoglou J, Robaut F (2014) Selective area growth of well-ordered ZnO nanowire arrays with controllable polarity. ACS Nano 8:4761–4770. https://doi.org/10.1021/nn500620t
29. Laudise RA, Ballman AA (1960) Hydrothermal synthesis of zinc oxide and zinc sulfide. J Phys Chem 64:688–691. https://doi.org/10.1021/j100834a511
30. Verges MA, Mifsud A, Serna CJ (1990) Formation of rod-like zinc oxide microcrystals in homogeneous solutions. J Chem Soc Faraday Trans 86:959. https://doi.org/10.1039/ft9908600959
31. Choi JW, Lee CM, Park CH, Lim JH, Park GC, Joo J (2018) Effect of annealing temperature on morphology and electrical property of hydrothermally-grown ZnO nanorods/p-Si heterojunction diodes. J Nanosci Nanotechnol 19:1640–1644. https://doi.org/10.1166/jnn.2019.16186

32. Vayssieres L, Keis K, Lindquist S-E, Hagfeldt A (2001) Purpose-built anisotropic metal oxide material: 3D highly oriented microrod array of ZnO. J Phys Chem B 105:3350–3352. https://doi.org/10.1021/jp010026s
33. Solís-Pomar F, Martínez E, Meléndrez MF, Pérez-Tijerina E (2011) Growth of vertically aligned ZnO nanorods using textured ZnO films. Nanoscale Res Lett 6:524. https://doi.org/10.1186/1556-276X-6-524
34. Ng AMC, Xi YY, Hsu YF, Djurisić AB, Chan WK, Gwo S, Tam HL, Cheah KW, Fong PWK, Lui HF, Surya C (2009) GaN/ZnO nanorod light emitting diodes with different emission spectra. Nanotechnology 20:445201. https://doi.org/10.1088/0957-4484/20/44/445201
35. Wu W, Hu G, Cui S, Zhou Y, Wu H (2008) Epitaxy of vertical ZnO nanorod arrays on highly (001)-oriented ZnO seed monolayer by a hydrothermal route. Cryst Growth Des 8:4014–4020. https://doi.org/10.1021/cg800210m
36. Aneesh PM, Subha PP, Vikas LS, Mohan S, Jayaraj MK (2010) Growth of vertically aligned ZnO nanorods on various substrates by hydrothermal method. In: Proceedings of SPIE, vol 7766, pp 776606–776606–7. https://doi.org/10.1117/12.860292
37. Process CH, Zhang H, Yang D, Li D, Ma X, Li S (2005) Controllable growth of ZnO microcrystals by a 2005. Growth (Lakeland) 3–6
38. Wu JH, Liu SY, Li S, Jiang YL, Ru GP, Qu XP (2012) The influence of ZnO seed layers on n-ZnO nanostructure/p-GaN LEDs. Appl Phys A 109:489–495. https://doi.org/10.1007/s00339-012-7060-x
39. Lupan O, Pauporté T, Chow L, Chai G, Viana B, Ursaki VV, Monaico E, Tiginyanu IM (2012) Comparative study of the ZnO and $Zn_{1-x}Cd_xO$ nanorod emitters hydrothermally synthesized and electrodeposited on p-GaN. Appl Surf Sci 259:399–405. https://doi.org/10.1016/j.apsusc.2012.07.058
40. Aneesh PM, Vanaja KA, Jayaraj MK (2007) Synthesis of ZnO nanoparticles by hydrothermal method. Semiconductors 6639(66390J):1–9. https://doi.org/10.1117/12.730364
41. Aneesh PM, Cherian CT, Jayaraj MK, Endo T (2010) Co^{2+} doped ZnO nano fl owers grown by hydrothermal method. J Ceram Soc Jpn 118:333–336
42. Tang L, Bao X-B, Zhou H, Yuan A-H (2008) Synthesis and characterization of ZnO nanorods by a simple single-source hydrothermal method. Phys E Low-dimens Syst Nanostruct 40:924–928. https://doi.org/10.1016/j.physe.2007.11.024
43. Li F, Hu L, Li Z, Huang X (2008) Influence of temperature on the morphology and luminescence of ZnO micro and nanostructures prepared by CTAB-assisted hydrothermal method. J Alloys Compd 465:L14–L19. https://doi.org/10.1016/j.jallcom.2007.11.009
44. Greene LE, Law M, Goldberger J, Kim F, Johnson JC, Zhang Y, Saykally RJ, Yang P (2003) Low-temperature wafer-scale production of ZnO nanowire arrays. Angew Chem Int Ed Engl 42:3031–3034. https://doi.org/10.1002/anie.200351461
45. Liew LL, Le HQ, Goh GKL (2011) Chemical solution epitaxy of ZnO nanorods. Mater Res Innov 15:357–360. https://doi.org/10.1179/1433075X11Y.0000000002
46. Xu L, Guo Y, Liao Q, Zhang J, Xu D (2005) Morphological control of ZnO nanostructures by electrodeposition. J Phys Chem B 109:13519–13522. https://doi.org/10.1021/jp051007b
47. Xu L, Chen Q, Xu D (2007) Hierarchical ZnO nanostructures obtained by electrodeposition. J Phys Chem C 111:11560–11565. https://doi.org/10.1021/jp071536a
48. Lai M, Riley DJ (2006) Templated electrosynthesis of zinc oxide nanorods. Chem Mater 18:2233–2237. https://doi.org/10.1021/cm051613j
49. Belghiti H El, Pauporté T, Lincot D (2008) Mechanistic study of ZnO nanorod array electrodeposition. Phys Status Solidi 205:2360–2364. https://doi.org/10.1002/pssa.200879443
50. Vikas LS, Sanal KC, Jayaraj MK, Antony A, Puigdollers J (2014) Vertically aligned ZnO nanorod array/CuO heterojunction for UV detector application. Phys Status Solidi A 211:2493–2498. https://doi.org/10.1002/pssa.201431221
51. Lu X, Wang D, Li G, Su C, Kuang D, Tong Y (2009) Controllable electrochemical synthesis of hierarchical ZnO nanostructures on FTO glass. J Phys Chem C 2:13574–13582
52. Cui J, Gibson UJ (2005) Enhanced nucleation, growth rate, and dopant incorporation in ZnO nanowires. J Phys Chem B 109:22074–22077. https://doi.org/10.1021/jp054160e

53. Frade T, Siopa D, Martins AF, Carreira JFC, Rodrigues J, Sedrine NB, Correia MR, Monteiro T, Tena-Zaera R, Gomes A (2018) Optoelectronic characterization of ZnO nanorod arrays obtained by pulse electrodeposition. J Electrochem Soc 165:D595–D603. https://doi.org/10.1149/2.0131813jes
54. Li Y, Meng GW, Zhang LD, Phillipp F (2000) Ordered semiconductor ZnO nanowire arrays and their photoluminescence properties. Appl Phys Lett 76:2011. https://doi.org/10.1063/1.126238
55. Liu ZW, Ong CK, Yu T, Shen ZX (2006) Catalyst-free pulsed-laser-deposited ZnO nanorods and their room-temperature photoluminescence properties. Appl Phys Lett 88:1–3. https://doi.org/10.1063/1.2168675
56. Ajimsha RS, Manoj R, Aneesh PM, Jayaraj MK (2010) Violet luminescence from ZnO nanorods grown by room temperature pulsed laser deposition. Curr Appl Phys 10:693–697. https://doi.org/10.1016/j.cap.2009.09.002
57. Xing YJ, Xi ZH, Xue ZQ, Zhang XD, Song JH (2003) Optical properties of the ZnO nanotubes synthesized via vapor phase growth. Appl Phys Lett 83:1689–1691. https://doi.org/10.1063/1.1605808
58. Kumar PS, Maniam SM, Sundaramurthy J, Arokiaraj J, Mangalaraj D, Rajarathnam D, Srinivasan MP, Jian LK (2012) Growth specificity of vertical ZnO nanorods on patterned seeded substrates through integrated chemical process. Mater Chem Phys 133:126–134. https://doi.org/10.1016/j.matchemphys.2011.12.076
59. Oliveira JWL, Cauduro ALF, Baptista DL (2013) Growth of ZnO nanowires and microbeam lithography for field emission applications. In: Chip Curitiba 2013—SBMicro 2013 28th symposium on microelectronics technology and devices. https://doi.org/10.1109/sbmicro.2013.6676176
60. Nicaise SM, Cheng JJ, Kiani A, Gradečak S, Berggren KK (2015) Control of zinc oxide nanowire array properties with electron-beam lithography templating for photovoltaic applications. Nanotechnology 26:075303. https://doi.org/10.1088/0957-4484/26/7/075303
61. Kitsomboonloha R, Baruah S, Myint MTZ, Subramanian V, Dutta J (2009) Selective growth of zinc oxide nanorods on inkjet printed seed patterns. J Cryst Growth 311:2352–2358. https://doi.org/10.1016/j.jcrysgro.2009.02.028
62. Liu DF, Xiang YJ, Wu XC, Zhang ZX, Liu LF, Song L, Zhao XW, Luo SD, Ma WJ, Shen J, Zhou WY, Wang G, Wang CY, Xie SS (2006) Periodic ZnO nanorod arrays defined by polystyrene microsphere self-assembled monolayers. Nano Lett 6:2375–2378. https://doi.org/10.1021/nl061399d
63. Ramírez D, Gómez H, Lincot D (2010) Polystyrene sphere monolayer assisted electrochemical deposition of ZnO nanorods with controlable surface density. Electrochim Acta 55:2191–2195. https://doi.org/10.1016/j.electacta.2009.11.055
64. Bulliard X, Yun S, Ihn S-G, Choi YS, Kim Y, Choi D, Choi JY, Choi W (2010) Density control of ZnO nanorod arrays on mixed self-assembled monolayers. Cryst Growth Des 10:4697–4700. https://doi.org/10.1021/cg100956w
65. Jung M-H, Lee H (2011) Selective patterning of ZnO nanorods on silicon substrates using nanoimprint lithography. Nanoscale Res Lett 6:159. https://doi.org/10.1186/1556-276X-6-159
66. Deng S, Chen T, Liu S (2010) Highly ordered growth of ZnO nanostructures by combination of nanoimprint lithography and hydrothermal method. In: 2010 3rd international nanoelectronics conference, pp 941–942. https://doi.org/10.1109/inec.2010.5425115
67. Rao AD, Karalatti S, Thomas T, Ramamurthy PC (2014) Self-assembled, aligned ZnO nanorod buffer layers for high-current-density, inverted organic photovoltaics. ACS Appl Mater Interfaces 6:16792–16799. https://doi.org/10.1021/am503955k
68. Bao J, Zimmler MA, Capasso F, Wang X, Ren ZF (2006) Broadband ZnO single-nanowire light-emitting diode. Nano Lett 6:1719–1722. https://doi.org/10.1021/nl061080t
69. He Y, Wang J, Zhang W, Chen X, Huang Z, Gu Q (2009) Colour electroluminescence with end light-emitting from ZnO nanowire/polymer film. J Phys: Conf Ser 152:012054. https://doi.org/10.1088/1742-6596/152/1/012054

70. Wang JY, Lee CY, Chen YT, Chen CT, Chen YL, Lin CF, Chen YF (2009) Double side electroluminescence from p-NiO/n-ZnO nanowire heterojunctions. Appl Phys Lett 95:131117. https://doi.org/10.1063/1.3232244
71. Xi YY, Hsu YF, Djurišić AB, Ng AMC, Chan WK, Tam HL, Cheah KW (2008) NiO/ZnO light emitting diodes by solution-based growth. Appl Phys Lett 92:113505. https://doi.org/10.1063/1.2898505
72. Robert PF (1996) Semiconductor device fundamentals. Addison-Wesley, Boston
73. Jha S, Wang CD, Luan CY, Liu CP, Bin H, Kutsay O, Bello I, Zapien JA, Zhang WJ, Lee ST (2012) Near-ultraviolet light-emitting devices using vertical ZnO nanorod arrays. J Electron Mater 41:853–856. https://doi.org/10.1007/s11664-012-1919-7
74. Viana B, Pauporte T, Lupan O, Devis L, Gacoin T (2014) Blue-red electroluminescence from hybrid Eu:phosphors/ZnO-nanowires/p-GaN LED. Proc SPIE 8987:89871T. https://doi.org/10.1117/12.2041772
75. Ng AMC, Chen XY, Fang F, Hsu YF, Djurišić AB, Ling CC, Tam HL, Cheah KW, Fong PWK, Lui HF, Surya C, Chan WK (2010) Solution-based growth of ZnO nanorods for light-emitting devices: hydrothermal vs. electrodeposition. Appl Phys B 100:851–858. https://doi.org/10.1007/s00340-010-4173-9
76. Schuster F, Laumer B, Zamani RR, Magén C, Morante JR, Arbiol J, Stutzmann M (2014) p-GaN/n-ZnO heterojunction nanowires: optoelectronic properties and the role of interface polarity. ACS Nano 8:4376–4384. https://doi.org/10.1021/nn406134e
77. Jiao SJ, Zhang ZZ, Lu YM, Shen DZ, Yao B, Zhang JY, Li BH, Zhao DX, Fan XW, Tang ZK (2006) ZnO p-n junction light-emitting diodes fabricated on sapphire substrates. Appl Phys Lett 88:031911. https://doi.org/10.1063/1.2166686
78. Zhang L, Li Q, Qu C, Zhang Z, Huang R, Zhao F (2013) White electroluminescence from ZnO nanorods/p-GaN heterojunction light-emitting diodes under reverse bias. J Opt 15:025003. https://doi.org/10.1088/2040-8978/15/2/025003
79. Jeong MC, Oh BY, Ham MH, Lee SW, Myoung JM (2007) ZnO-nanowire-inserted GaN/ZnO heterojunction light-emitting diodes. Small 3:568–572. https://doi.org/10.1002/smll.200600479
80. Chen X, Man Ching Ng A, Fang F, Hang Ng Y, Djurišić AB, Lam Tam H, Wai Cheah K, Gwo S, Kin Chan W, Wai Keung Fong P, Fei Lui H, Surya C (2011) ZnO nanorod/GaN light-emitting diodes: the origin of yellow and violet emission bands under reverse and forward bias. J Appl Phys 110:094513. https://doi.org/10.1063/1.3653835
81. Lee SW, Cho HD, Panin G, Won Kang T (2011) Vertical ZnO nanorod/Si contact light-emitting diode. Appl Phys Lett 98:093110. https://doi.org/10.1063/1.3562608
82. Xu S, Xu C, Liu Y, Hu Y, Yang R, Yang Q, Ryou J-H, Kim HJ, Lochner Z, Choi S, Dupuis R, Wang ZL (2010) Ordered nanowire array blue/near-UV light emitting diodes. Adv Mater 22:4749–4753. https://doi.org/10.1002/adma.201002134
83. Chao CH, Lin WH, Chen CH, Changjean CH, Lin CF (2009) Tunable light extraction efficiency of GaN light emitting diodes by ZnO nanorod arrays. Semicond Sci Technol 24:105017. https://doi.org/10.1088/0268-1242/24/10/105017
84. Dai KH, Wang LS, Huang DX, Soh CB, Chua SJ (2011) Influence of size of ZnO nanorods on light extraction enhancement of GaN-based light-emitting diodes. Chin Phys Lett 28:098501. https://doi.org/10.1088/0256-307X/28/9/098501
85. Wang X, Cole J, Dabiran AM, Jacobs HO (2007) Electroluminescence of ZnO nanowire/p-GaN heterojunction light emitting diodes. Department of Electrical and Computer Engineering, University of Minnesota, Minneapolis, MN 55455. NSTI-Nanotech 2007, vol 4, pp 526–529
86. Du CF, Lee CH, Cheng CT, Lin KH, Sheu JK, Hsu HC (2014) Ultraviolet/blue light-emitting diodes based on single horizontal ZnO microrod/GaN heterojunction. Nanoscale Res Lett 9:446. https://doi.org/10.1186/1556-276X-9-446
87. Abbasi MA, Ibupoto ZH, Hussain M, Nur O, Willander M (2013) The fabrication of white light-emitting diodes using the n-ZnO/NiO/p-GaN heterojunction with enhanced luminescence. Nanoscale Res Lett 8:320. https://doi.org/10.1186/1556-276X-8-320

88. Kim KS, Kim SM, Jeong H, Jeong MS, Jung GY (2010) Enhancement of light extraction through the wave-guiding effect of ZnO sub-microrods in InGaN blue light-emitting diodes. Adv Funct Mater 20:1076–1082. https://doi.org/10.1002/adfm.200901935
89. Kim KK, Lee SD, Kim H, Park JC, Lee SN, Park Y, Park SJ, Kim SW (2009) Enhanced light extraction efficiency of GaN-based light-emitting diodes with ZnO nanorod arrays grown using aqueous solution. Appl Phys Lett 94:071118. https://doi.org/10.1063/1.3077606
90. Yin Z, Liu X, Yao H, Wu Y, Hao X, Han M, Xu X (2013) Light extraction enhancement of GaN LEDs by hybrid ZnO micro-cylinders and nanorods array. IEEE Photonic Technol Lett 25:1989–1992
91. Yin Z, Liu X, Wu Y, Hao X, Xu X (2012) Enhancement of light extraction in GaN-based light-emitting diodes using rough beveled ZnO nanocone arrays. Opt Express 20:1013–1021
92. Vikas LS, Sruthi CK, Jayaraj MK (2015) Defect assisted tuning of electroluminescence from p-GaN/n-ZnO nanorod heterojunction. Bull Mater Sci 38:901–907. https://doi.org/10.1007/s12034-015-0920-1
93. Yang Q, Wang W, Xu S, Wang ZL (2011) Enhancing light emission of ZnO microwire-based diodes by piezo-phototronic effect. Nano Lett 11:4012–4017. https://doi.org/10.1021/nl202619d
94. Könenkamp R, Word RC, Godinez M (2005) Ultraviolet electroluminescence from ZnO/polymer heterojunction light-emitting diodes. Nano Lett 5:2005–2008. https://doi.org/10.1021/nl051501r
95. Wei X, Yao R, Jiang Z, Guo T, He F, Wang W, Xie Z, Duan L (2019) Cirtopic white LED with a 490 nm emission peak based on He-Zn annealed ZnO nanorods/polymer blend p-n heterojunction. J Alloys Compd 306–311 (accepted). https://doi.org/10.1016/j.jallcom.2018.11.285
96. Guo H, Lin Z, Feng Z, Lin L, Zhou J (2009) White-light-emitting diode based on ZnO nanotubes. https://doi.org/10.1021/jp902607c
97. Bi Z, Zhang J, Bian X, Wang D, Zhang X, Zhang W, Hou X (2007) A high-performance ultraviolet photoconductive detector based on a ZnO film grown by RF sputtering. J Electron Mater 37:760–763. https://doi.org/10.1007/s11664-007-0329-8
98. Xu Z, Deng H, Xie J, Li Y, Li Y, Zu X, Xue S (2005) Photoconductive UV detectors based on ZnO films prepared by sol-gel method. J Sol-Gel Sci Technol 36:223–226. https://doi.org/10.1007/s10971-005-3612-2
99. Krivchenko VA, Lopaev DV, Pashchenko PV, Pirogov VG, Rakhimov AT, Suetin NV, Trifonov AS (2008) UV detectors based on nanocrystalline ZnO films. Tech Phys 53:1065–1069. https://doi.org/10.1134/S1063784208080148
100. Choi YS, Lee JY, Im S, Lee SJ (2011) Photoresponse characteristics of n-ZnO/p-Si heterojunction photodiodes. J Vac Sci Technol B 2384:10–14. https://doi.org/10.1116/1.1524152
101. Ding M, Zhao D, Yao B, Qiao Q, Xu X (2014) High-performance UV photodetectors and temperature-dependent photoluminescence of individual ZnO hexagonal-prism microwire. Appl Phys A 118:1267–1271. https://doi.org/10.1007/s00339-014-8828-y
102. Przeździecka E, Gościński K, Stachowicz M, Dobosz D, Zielony E, Sajkowski JM, Pietrzyk MA, Płaczek-Popko E, Kozanecki A (2013) Spectrum selective UV detectors from an p-ZnO:As/n-GaN diodes grown by Molecular Beam Epitaxy. Sens Actuators A Phys 195:27–31. https://doi.org/10.1016/j.sna.2013.02.021
103. Wei CL, Chen YC, Cheng CC, Kao KS, Cheng DL, Cheng PS (2010) Highly sensitive ultraviolet detector using a ZnO/Si layered SAW oscillator. Thin Solid Films 518:3059–3062. https://doi.org/10.1016/j.tsf.2009.07.207
104. Das SN, Moon KJ, Kar JP, Choi JH, Xiong J, Lee TI, Myoung JM (2010) ZnO single nanowire-based UV detectors. Appl Phys Lett 97:022103. https://doi.org/10.1063/1.3464287
105. Zhang L, Zhao F, Wang C, Wang F, Huang R, Li Q (2015) Optoelectronic characteristics of UV photodetector based on GaN/ZnO nanorods p-i-n heterostructures. Electron Mater Lett 11:682–686. https://doi.org/10.1007/s13391-015-5128-4

106. Kim H, Bae J (2013) Metal-insulator-silicon semiconductor photodetectors using ZnO nanocones as an efficient anti-reflective coating. Phys Status Solidi 210:2510–2514. https://doi.org/10.1002/pssa.201329323
107. Kind H, Yan H, Messer B, Law M, Yang P (2002) Nanowire ultraviolet photodetectors and optical switches. Adv Mater 14:158–160. https://doi.org/10.1002/1521-4095(20020116)14:2%3c158:AID-ADMA158%3e3.0.CO;2-W
108. Hullavarad SS, Hullavarad NV, Karulkar PC, Luykx A, Valdivia P (2007) Ultra violet sensors based on nanostructured ZnO spheres in network of nanowires: a novel approach. Nanoscale Res Lett 2:161–167. https://doi.org/10.1007/s11671-007-9048-6
109. Hullavarad S, Hullavarad N, Look D, Claflin B (2009) Persistent photoconductivity studies in nanostructured ZnO UV sensors. Nanoscale Res Lett 4:1421–1427. https://doi.org/10.1007/s11671-009-9414-7
110. Bera A, Basak D (2009) Role of defects in the anomalous photoconductivity in ZnO nanowires. Appl Phys Lett 94:2009–2011. https://doi.org/10.1063/1.3123167
111. Yadav HK, Sreenivas K, Gupta V (2010) Study of metal/ZnO based thin film ultraviolet photodetectors: the effect of induced charges on the dynamics of photoconductivity relaxation. J Appl Phys 107:1–9. https://doi.org/10.1063/1.3291133
112. Bera A, Basak D (2010) Photoluminescence and photoconductivity of ZnS-coated ZnO nanowires. ACS Appl Mater Interfaces 2:408–412. https://doi.org/10.1021/am900686c
113. Liu J, Park J, Park KH, Ahn Y, Park JY, Koh KH, Lee S (2010) Enhanced photoconduction of free-standing ZnO nanowire films by L-lysine treatment. Nanotechnology 21:485504. https://doi.org/10.1088/0957-4484/21/48/485504
114. Chen MW, Chen CY, Lien DH, Ding Y, He JH (2010) Photoconductive enhancement of single ZnO nanowire through localized Schottky effects. Opt Express 18:14836–14841. https://doi.org/10.1364/OE.18.014836
115. Chang H, Sun Z, Ho KYF, Tao X, Yan F, Kwok WM, Zheng Z (2011) A highly sensitive ultraviolet sensor based on a facile in situ solution-grown ZnO nanorod/graphene heterostructure. Nanoscale 3:258–264. https://doi.org/10.1039/C0NR00588F
116. Kim DC, Jung BO, Lee JH, Cho HK, Lee JY, Lee JH (2011) Dramatically enhanced ultraviolet photosensing mechanism in a n-ZnO nanowires/i-MgO/n-Si structure with highly dense nanowires and ultrathin MgO layers. Nanotechnology 22:265506. https://doi.org/10.1088/0957-4484/22/26/265506
117. Dhara S, Giri P (2011) Enhanced UV photosensitivity from rapid thermal annealed vertically aligned ZnO nanowires. Nanoscale Res Lett 6:504. https://doi.org/10.1186/1556-276X-6-504
118. Bie YQ, Liao ZM, Zhang HZ, Li GR, Ye Y, Zhou YB, Xu J, Qin ZX, Dai L, Yu DP (2011) Self-powered, ultrafast, visible-blind UV detection and optical logical operation based on ZnO/GaN nanoscale p-n junctions. Adv Mater 23:649–653. https://doi.org/10.1002/adma.201003156
119. Humayun Q, Kashif M, Hashim U, Qurashi A (2014) Selective growth of ZnO nanorods on microgap electrodes and their applications in UV sensors. Nanoscale Res Lett 9:29. https://doi.org/10.1186/1556-276X-9-29
120. Yi F, Liao Q, Yan X, Bai Z, Wang Z, Chen X, Zhang Q, Huang Y, Zhang Y (2014) Simple fabrication of a ZnO nanorod array UV detector with a high performance. Phys E Low-Dimens Syst Nanostruct 61:180–184. https://doi.org/10.1016/j.physe.2014.03.025
121. Albiss BA, AL-Akhras MA, Obaidat I (2015) Ultraviolet photodetector based on ZnO nanorods grown on a flexible PDMS substrate. Int J Environ Anal Chem 95:339–348. https://doi.org/10.1080/03067319.2015.1016010
122. Dang VQ, Trung TQ, Kim DI, Duy LT, Hwang BU, Lee DW, Kim BY, Toan LD, Lee NE (2015) Ultrahigh responsivity in graphene-ZnO nanorod hybrid UV photodetector. Small 3054–3065. https://doi.org/10.1002/smll.201403625
123. Humayun Q, Hashim U, Ruzaidi CM, Foo KL (2015) The strategy to control the morphology of ZnO nanostructure UV sensor. IOP Conf Ser Mater Sci Eng 99:012017. https://doi.org/10.1088/1757-899X/99/1/012017

124. Ko YH, Nagaraju G, Yu JS (2015) Fabrication and optimization of vertically aligned ZnO nanorod array-based UV photodetectors via selective hydrothermal synthesis. Nanoscale Res Lett 10:1032. https://doi.org/10.1186/s11671-015-1032-y
125. Al Hardan N, Abdul Hamid M, Ahmed N, Jalar A, Shamsudin R, Othman N, Keng L, Mohammad S (2015) A study on the ultraviolet (UV) photo-response of hydrothermally-grown zinc oxide (ZnO) nanorods with different aspect ratios. IEEE Sens J 15:8611–8618. https://doi.org/10.1109/JSEN.2015.2464311
126. Vikas LS, Vanaja KA, Subha PP, Jayaraj MK (2016) Fast UV sensing properties of n-ZnO nanorods/p-GaN heterojunction. Sens Actuators A Phys 242:116–122. https://doi.org/10.1016/j.sna.2016.02.038
127. Yang Y, Guo W, Zhang Y, Ding Y, Wang X, Wang ZL (2011) Piezotronic effect on the output voltage of P3HT/ZnO micro/nanowire heterojunction solar cells. Nano Lett 11:4812–4817. https://doi.org/10.1021/nl202648p
128. Kashyout AB, Soliman M, El Gamal M, Fathy M (2005) Preparation and characterization of nano particles ZnO films for dye-sensitized solar cells. Mater Chem Phys 90:230–233. https://doi.org/10.1016/j.matchemphys.2004.11.031
129. Chiu WH, Lee CH, Cheng HM, Lin HF, Liao SC, Wu JM, Hsieh WF (2009) Efficient electron transport in tetrapod-like ZnO metal-free dye-sensitized solar cells. Energy Environ Sci 2:694. https://doi.org/10.1039/b902595m
130. Karst N, Rey G, Doisneau B, Roussel H, Deshayes R, Consonni V, Ternon C, Bellet D (2011) Fabrication and characterization of a composite ZnO semiconductor as electron transporting layer in dye-sensitized solar cells. Mater Sci Eng B 176:653–659. https://doi.org/10.1016/j.mseb.2011.02.009
131. Omar A, Abdullah H, Yarmo MA, Shaari S, Taha MR (2013) Morphological and electron transport studies in ZnO dye-sensitized solar cells incorporating multi- and single-walled carbon nanotubes. J Phys D-Appl Phys 46:8. https://doi.org/10.1088/0022-3727/46/16/165503
132. Lu L, Li R, Peng T, Fan K, Dai K (2011) Effects of rare earth ion modifications on the photoelectrochemical properties of ZnO-based dye-sensitized solar cells. Renew Energy 36:3386–3393. https://doi.org/10.1016/j.renene.2011.05.010
133. Son DY, Im JH, Kim HS, Park NG (2014) 11% efficient perovskite solar cell based on ZnO nanorods: an effective charge collection system. J Phys Chem C 118:16567–16573. https://doi.org/10.1021/Jp412407j
134. Son DY, Bae KH, Kim HS, Park NG (2015) Effects of seed layer on growth of ZnO nanorod and performance of perovskite solar cell. J Phys Chem C 119:10321–10328. https://doi.org/10.1021/acs.jpcc.5b03276
135. Hussain S, Jacob J, Usman Z, Mahmood K, Ali A, Arshad MI, Khan WS, Farooq Z, Farooq MU, Ashfaaq A, Rehman U (2019) Length dependent performance of Cu_2O/ZnO nanorods solar cells. Superlattices Microstruct 126:181–185. https://doi.org/10.1016/j.spmi.2019.01.004
136. Sharma JR, Das G, Roy AB, Bose S, Mukhopadhyay S (2019) Design analysis of heterojunction solar cells with aligned AZO nanorods embedded in p-type Si wafer. Silicon 1–12
137. Kim HJ, Lee CH, Kim DW, Yi GC (2006) Fabrication and electrical characteristics of dual-gate ZnO nanorod metal–oxide semiconductor field-effect transistors. Nanotechnology 17:S327–S331. https://doi.org/10.1088/0957-4484/17/11/S16
138. Tsai JK, Wu TC, Shih JH, Meen TH, Liu YS, Jheng YC (2011) Manufacture and characterization of the single ZnO nanorod field-effect transistor. In: The 4th IEEE international nanoelectronics conference, pp 1–2. IEEE
139. Park WI, Kim JS, Yi GC, Bae MH, Lee HJ (2004) Fabrication and electrical characteristics of high-performance ZnO nanorod field-effect transistors. Appl Phys Lett 85:5052. https://doi.org/10.1063/1.1821648
140. Sun B, Sirringhaus H (2006) Surface tension and fluid flow driven self assembly of ordered ZnO nanorod films for high-performance field effect transistor. J Am Chem Soc 128:16231–16237

141. Heo YW, Tien LC, Norton DP, Kang BS, Ren F, Gila BP, Pearton SJ (2004) Electrical transport properties of single ZnO nanorods. Appl Phys Lett 85:2002. https://doi.org/10.1063/1.1792373
142. Fulati A, Ali SMU, Riaz M, Amin G, Nur O, Willander M (2009) Miniaturized pH sensors based on zinc oxide nanotubes/nanorods. Sensors 9:8911–8923. https://doi.org/10.3390/s91108911
143. Al-Hilli SM, Al-Mofarji RT, Willander M (2006) Zinc oxide nanorod for intracellular pH sensing. Appl Phys Lett 89(173119):1–3. https://doi.org/10.1063/1.2367662
144. Al-Hilli SM, Al-Mofarji RT, Willander M (2006) Zinc oxide nanorod for intracellular pH sensing. Appl Phys Lett 89:173119. https://doi.org/10.1063/1.2367662
145. Al-Hilli S, Al-Mofrarji R, Klason P, Gutman N, Saar A, Ost A, Stralfors P, Williander M (2007) Zinc oxide nanorods as an intracellular pH sensor
146. Wang X, Song J, Liu J, Wang ZL (2007) Direct-current nanogenerator driven by ultrasonic waves. Science 316:102–105. https://doi.org/10.1126/science.1139366
147. Yang R, Qin Y, Li C, Dai L, Wang ZL (2009) Characteristics of output voltage and current of integrated nanogenerators. Appl Phys Lett 94:022905. https://doi.org/10.1063/1.3072362
148. Yu A, Li H, Tang H, Liu T, Jiang P, Wang ZL (2011) Vertically integrated nanogenerator based on ZnO nanowire arrays. Phys status solidi—Rapid Res Lett 5:162–164. https://doi.org/10.1002/pssr.201105120
149. Chen CY, Huang JH, Song J, Zhou Y, Lin L, Huang PC, Zhang Y, Liu CP, He JH, Wang ZL (2011) Anisotropic outputs of a nanogenerator from oblique-aligned ZnO nanowire arrays. ACS Nano 5:6707–6713. https://doi.org/10.1021/nn202251m
150. Wu W, Wang ZL (2011) Piezotronic nanowire-based resistive switches as programmable electromechanical memories. Nano Lett 11:2779–2785. https://doi.org/10.1021/nl201074a

Chapter 7
Metal Oxide Semiconductor Gas Sensors

Subha P. P, Pillai Aswathy Mohan and M. K. Jayaraj

1 Introduction

Various toxic gases such as carbon monoxide (CO), hydrogen sulphide (H_2S), nitrogen oxides (NO_x) and volatile organic compounds (VOCs) emitted from industries and automobiles cause short-term as well as long-term impacts on human health and the environment even at very low concentrations. The development of high-precision gas sensors with high response, faster response and recovery, better selectivity, lower detection limit, low-temperature operation, long-term stability, etc., have significant importance in the current scenario. Various types of gas sensors including resistive [1], optical [2], thermoelectric [3], electrochemical [4], etc., have been developed for detecting the presence of traces of gases. Among these, resistive type sensors based on metal oxide semiconductors (MOS) are the most popular because of their high response, response to a wide range of chemicals, easy fabrication, stability, etc. The tunable electronic properties, charge transport mechanisms, defect states and chemical properties of metal oxide semiconductors received great attention in the development history of gas sensors [5–7].

In recent years, the size-dependent properties of nanomaterials have contributed significant improvements in the gas sensor industry [8–10]. When the size of the particles is of the order of the wavelength of electrons, quantum size effects play an important role in modifying their properties which help in the fabrication of efficient gas sensors [10, 11]. Gas response down to parts per billion has been achieved with

S. P. P (✉)
Department of Physics, Cochin University of Science and Technology, Kochi, India

P. A. Mohan
St. Stephen's College, Pathanapuram, India

M. K. Jayaraj
Department of Physics, Cochin University of Science and Technology, Kochi 682022, India

M. K. Jayaraj (ed.), *Nanostructured Metal Oxides and Devices*,
Materials Horizons: From Nature to Nanomaterials,
https://doi.org/10.1007/978-981-15-3314-3_7

oxide nanostructures such as rods, particles and wires because of their large surface-to-volume ratio and enhanced electron transfer kinetics [11, 12]. The nanometre size helps scientists and researchers to develop portable low power consuming sensors [13, 14]. The blue shift in the optical spectra and increased luminescence efficiency of quantum-confined particles make them suitable for developing various optoelectronic devices [15, 16].

2 Metal Oxide Semiconductor Gas Sensors (MOS)

Real-time monitoring of hazardous toxic gases has become a major issue due to more stringent environmental or safety regulations worldwide. Exposure to the various hazardous gases released into the atmosphere causes shortness of breath, nausea, swelling of tissues in the throat, impair immunity system and in the worst case, they may even cause death [17]. The major disadvantages of using conventional gas detection techniques like gas chromatography spectrophotometry, high-performance liquid chromatography, etc., are lack of portability, expensive, trained personalities are needed to do the job and all these techniques require time-consuming pre-treatment steps [18]. The use of MOS-based sensors can overcome all these issues to a great extent. The gas molecules interact with the sensing material inducing some changes in the resistance, conductance or capacitance of the material which is transduced as a measurable output signal.

A gas sensor is a type of chemical sensor which detects the presence of gases in an area, usually as a part of the safety system. In ancient times, people used canary birds to find out the presence of toxic gases like methane, carbon monoxide, etc., in coal mines because the anatomy of canaries are in such a way that they need more oxygen and they are not able to withstand if the concentration of oxygen is below a particular level. In 1953, W. H. Brattain and J. Bardeen observed that the resistance of germanium (Ge) changes with the changes in the surrounding ambient [19]. In 1954, G. Heiland found that MOS like zinc oxide (ZnO) also can modify their electrical properties with the variations in the surrounding atmosphere [20]. Later, in 1962, T. Seiyama and A. Kato showed that semiconductors like ZnO, when heated up to 300 °C, exhibited much better variation in resistance to the presence of traces of gases in the air than at room temperature [21]. In 1967, Shaver [22] explained the effects of noble metal (Au, Ag, Pd, etc.) addition on the gas sensing properties of metal oxide semiconductors. At the beginning of 1970s, N. Taguchi developed a gas sensor using tin dioxide (SnO_2) thick film as the sensing material, and he brought the same into an industrial product also [23]. World's first chemiresistive gas sensor was developed and patented by Taguchi using SnO_2. Even today, Taguchi-type sensors are the leading gas sensor manufacturers in the world, and it is the present-day Figaro Engineering Inc. in Japan. By the end of 1980s, semiconducting oxide-based gas sensors became the thrust area of research in the sensor community, and the dramatic development in the understanding of material science and material chemistry helped people in this area to fabricate high-performance gas sensors.

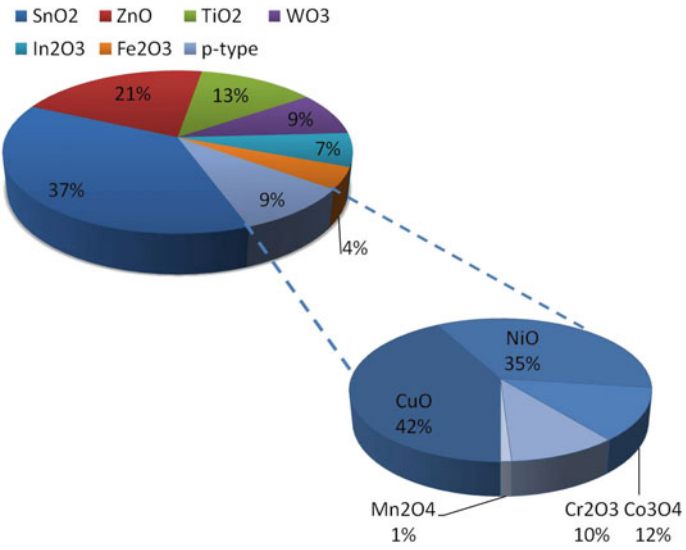

Fig. 1 Studies on n- and p-type oxide semiconductor gas sensors [15]

Generally, MOS based gas sensors show several unpleasant characteristics such as slow response, high cross-sensitivity, poor selectivity and long-term signal drift [24, 25]. Also, poor understanding of the sensing mechanism forced people to do trial and error strategy in search of suitable sensing material. Binary semiconducting metal oxides such as SnO_2 [26], ZnO [27] and TiO_2 [28] are the commonly used sensing materials. The most successful investigations were connected with SnO_2. Figure 1 represents the current status of studies on n- and p-type oxide semiconductor gas sensors.

2.1 Gas Sensing Mechanisms of Metal Oxide Semiconductors

Over the years, scientists and researchers have conducted several promising studies to understand the sensing mechanism of metal oxide semiconductor gas sensors. In the early days, Wolkenstein's electron theory of chemisorption and catalysis on semiconductors has been used for explaining the sensing mechanism [29]. At the beginning of 1980s, charge transport properties of MOS in air and other gases have been investigated in detail [30, 31]. Based on these theories, the fundamental sensing mechanism of semiconducting oxide sensors relies on the change in resistance upon gas adsorption. The resistance change occurs due to the interaction between adsorbed oxygen ions and target gas molecules [11, 32–34]. When an n-type semiconductor is in contact with ambient air, oxygen molecules get adsorbed on its surface by withdrawing electrons from the conduction band. Based on the operating temperature

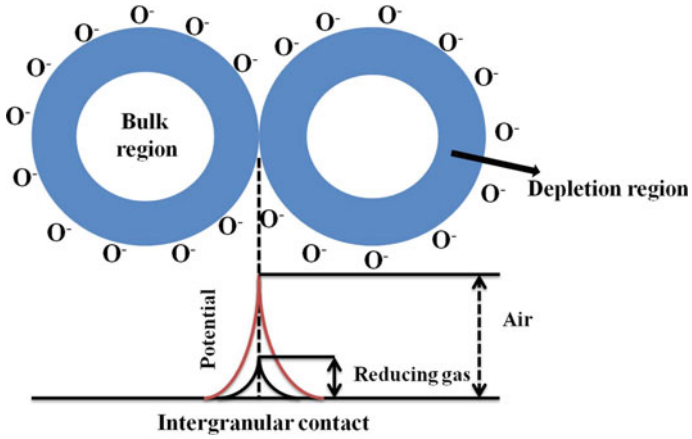

Fig. 2 Schematic depicting the potential barrier developed at the intergranular contact of two oxide particles

of the sensor, the oxygen can be adsorbed as either $O_2^-(T < 50°C)$ or $O^-(T > 150°C)$ [32, 35–38]. As a result, a depletion region and a corresponding potential barrier are developed at the surface of the sensor which increases the resistance of the material. The electrons must acquire enough energy to overcome this double Schottky barrier to flow through the material. The reverse phenomenon will happen if the sensing material is p-type. The process of oxygen adsorption is schematically represented in Fig. 2.

When a reducing gas like ethanol is introduced into the sensing material, the gas molecules interact with the adsorbed oxygen ions releasing the trapped electrons back to the material, and hence, the width of the depletion region and the height of the potential barrier decrease. All these processes together generate a measurable change in the resistance of the sensing material.

The mechanism of gas adsorption and the subsequent changes in the resistance of MOS sensors involve three major functions: receptor function, transducer function and utility factor [6, 39, 40] as shown in Fig. 3. Receptor function is the ability of the sensing material to respond to the atmosphere containing oxygen and other target gas molecules. It depends on the adsorption-desorption parameters of the sensing material. There are mainly two different types of adsorption phenomena: physisorption and chemisorption.

Weak van der Waals forces are involved in physisorption and the adsorbate requires no activation energy for getting adsorbed on the material, whereas covalent or ionic bonds are involved in chemisorption and the adsorbate needs activation energy. The activation energy is defined as the minimum energy required for undergoing a chemical reaction. The receptor function can be modified by loading the oxide surface with additives like noble metals, other oxide materials, etc., for improving the sensing properties [31].

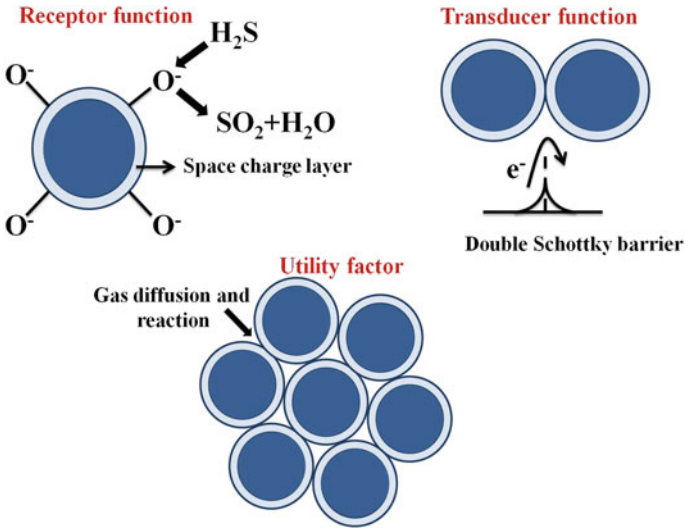

Fig. 3 Factors determining the response of metal oxide semiconductor gas sensor

The transducer function can be defined as the capability of the sensing material to convert the induced surface changes into a measurable electrical signal. This function depends on the grain size, grain boundaries, contacts between the sensing material and the electrode and electrochemical interaction between the sensing material and the oxide surface [41, 42]. The grain size has a significant role in controlling the transducer function which is schematically shown in Fig. 4 [9, 39]. When the grain size D of the sensing material is very much larger than the Debye length $L_D (D \gg 2L_D)$, the interactions between gases will take place only at the surface of the material and the bulk of the oxide semiconductor remain unaffected. In this case, the sensing mechanism is independent of the grain size, i.e., the effects are almost similar to the case of a bulk semiconductor. If $D \geq 2L_D$, the conducting channel within the sensing material is influenced as shown in Fig. 4. Compared to the previous case, the response will be better because of the increase in surface-to-volume ratio of the

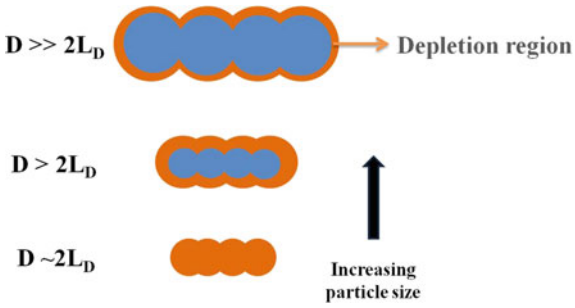

Fig. 4 Schematic representation of grain size effects

semiconductor. If the grain size $D \sim 2L_D$, the sensing material will be fully depleted of free charge carriers as shown in Fig. 4 and the sensor will exhibit excellent response to the target gases.

The utility factor is related to the microstructure of the sensing material, and it is associated with the accessibility of the inner oxide grains to the adsorbed gas molecules. If the sensing material is sufficiently porous, the penetration depth of the gas molecules will be high, resulting in very good sensor characteristics. The utility factor depends on the thickness of the sensing film, grain size, operating temperature of the gas sensor, etc.

2.2 *Importance of Sensing Layer Morphology on the Sensing Properties of Metal Oxide Semiconductor Gas Sensors*

The sensing layer morphology has a substantial effect on the gas sensing characteristics. Generally, sensing material can be classified into dense and porous and are schematically shown in Figs. 5 and 6, respectively [38, 43]. In dense or compact material, the gas interactions will take place only at the surface of the material and the inner regions are not accessible. In the schematic diagram, Z_g, Z_0 and qV_s are sensing layer thickness, the thickness of the depletion region and band bending, respectively. In this case, both the geometric surface and the active surface are the same where interaction takes place.

In porous sensing materials, the gas molecules are able to penetrate into the material, so that gas interactions take place at the surface of each grain, grain–grain boundaries and also at the interface of sensing material and the electrode; hence, the active surface will be much larger than the geometric surface. As a result, the material

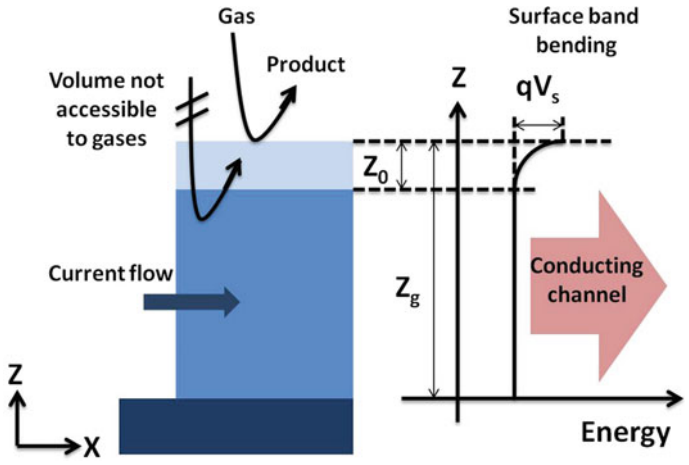

Fig. 5 Schematic representation of a compact sensing layer

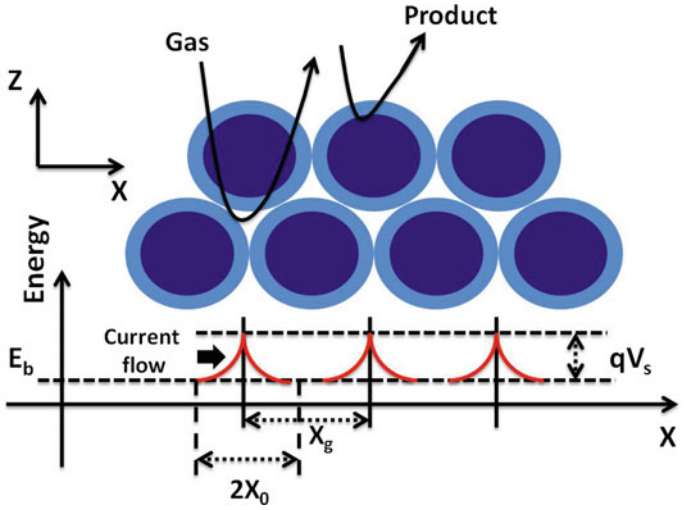

Fig. 6 Schematic representation of a porous sensing layer

will exhibit much better sensing properties than a compact one. In Fig. 6, X_g, X_0, X_b and qV_s are grain size, depletion layer thickness and minimum of the conduction band in the bulk and band bending, respectively. For a better gas sensor, a significant amount of porosity is necessary. Porous materials can be defined as continuous solid materials filled with voids. International Union of Pure and Applied Chemistry (IUPAC) classified porous materials into macroporous, mesoporous and microporous based on the pore size. Microporous materials have pore size less than 2 nm, pore size is in between 2 and 50 nm for mesoporous, and if it is greater than 50 nm, the material is called macroporous [44]. Among the different classes of porous materials, mesoporous materials have the highest potential for gas sensing applications.

2.3 The Performance Parameters of MOS-Based Gas Sensors

The performance of a gas sensor can be evaluated by considering several parameters [5]. Typical response curve of a chemiresistive gas sensor is schematically shown in Fig. 7.

The response curve of a gas sensor is characterized by the following parameters.

1. Response: The response 'S' is defined as the ratio of the change in resistance of the sensor R_g to the resistance in ambient air R_a. The sensitivity of a gas sensor is defined as the slope of the calibration curve, i.e., sensor response vs concentration.

$$S = \frac{R_g - R_a}{R_a} \tag{1}$$

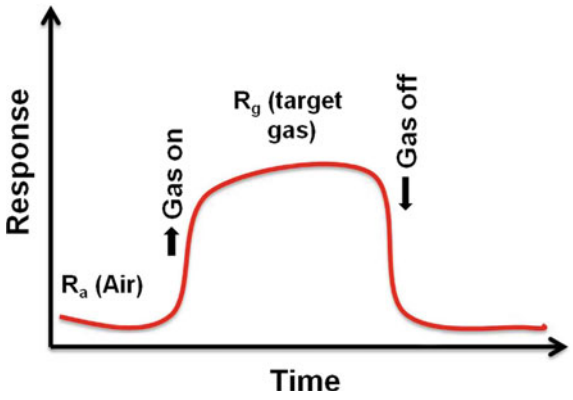

Fig. 7 The typical response curve of a chemiresistive gas sensor

Usually, the gas adsorption on a surface can be empirically represented as

$$S = 1 + aC^b \tag{2}$$

where 'C' is the gas concentration, and 'a' and 'b' are constants.

$$\log(S - 1) = \log(a) + b\log(C) \tag{3}$$

It can be seen from the above equation that $\log(S - 1)$ has a linear relation with $\log(C)$ with slope 'b'. The 'b' value which represents the charge state of adsorbed oxygen ion species on the surface of the metal oxide can be obtained from the slope of a plot between $\log(S - 1)$ and $\log(C)$.

2. Selectivity: The ability of the sensor to respond to a specific gas in a mixture of gases can be called selectivity. It can be expressed in terms of the selectivity coefficient. The selectivity coefficient of a gas, namely 'X' to another gas 'Y', can be written as

$$Q_X = \frac{S_X}{S_Y} \tag{4}$$

where S_X and S_Y are sensitivities of the sensor to gases 'X' and 'Y', respectively.

3. Stability: It is the capability of a sensor to generate reproducible results for a period of time which means retaining the parameters sensitivity, selectivity, response time and recovery time after repeated use.
4. Response time: It can be defined as the time taken for the sensor to reach 90% of the maximum response.
5. Recovery time: It is defined as the time taken for the sensor to reach 10% of the maximum response. A good sensor should have a small value of response and recovery times to be used for practical applications.

6. Detection limit: It is the lowest value of the gas concentration, which can be detected by the sensor.
7. Dynamic range: It is the capability of the sensor to respond to a wide range of target gas concentrations.

2.4 Sensor Response Formula for Chemiresistive Gas Sensors

Every gas sensor has an optimum operating temperature, and the adsorption of oxygen depends on the working temperature [45]. At lower temperatures (<150 °C), oxygen molecules are adsorbed on the metal oxide surface by withdrawing electrons and forming oxygen ion molecules.

$$O_{2(gas)} + e^- \leftrightarrow O^-_{2(ads)} \tag{5}$$

At high temperatures (>150 °C), oxygen ion molecules are dissociated into oxygen ion atoms with singly or doubly negative electric charge following the equations

$$\frac{1}{2}O_2 + e^- \overset{k_{oxy}}{\Leftrightarrow} O^-_{(ads)} \tag{6}$$

$$\frac{1}{2}O_2 + 2e^- \overset{k_{oxy}}{\Leftrightarrow} O^{2-}_{(ads)} \tag{7}$$

k_{oxy} is the reaction rate constant.

The chemical reaction between a gas molecule and oxygen can be generally written as

$$X + O^{b-}_{(ads)} \rightarrow X' + be^- \tag{8}$$

X and X' are target gas and out gas, b is the number of electrons, and k_{gas} is the reaction rate constant.

The rate equation for electron density 'n' can be written as

$$\frac{dn}{dt} = k_{gas}[O_{ads}]^b[X]^b \tag{9}$$

where

$$k_{gas} = A\exp(-E_a/k_BT) \tag{10}$$

'E_a' is the activation energy of a reaction, 'k_B' is the Boltzmann constant, and 'T' is the absolute temperature.

Integrating Eq. (9), we will get

$$n = \Gamma_t k_{\text{gas}} [\text{O}_{\text{ads}}]^b [X]^b + n_0 \tag{11}$$

'Γ_t' is a time constant, and 'n_0' is the carrier concentration in air ambient. The carrier concentration 'n' is defined as

$$n = \frac{\alpha}{R} \tag{12}$$

'α' is the proportionality constant and 'R' is the resistance. Substituting Eq. (12) in (11)

$$\frac{1}{R_g} = \frac{\Gamma_t k_{\text{gas}} [\text{O}_{\text{ads}}]^b [X]^b}{\alpha} + \frac{1}{R_a} \tag{13}$$

Using Eqs. (1) and (13), the response S can be written as

$$S = \frac{\Gamma_t k_{\text{gas}} [\text{O}_{\text{ads}}]^b [X]^b}{n_0} + 1 \tag{14}$$

From the Eq. (14), the response is directly proportional to rate constant k_{gas} and inversely proportional to electron density n_0. These two factors compete with each other, and maximum response is obtained at the optimum temperature. The Eq. (14) works well for thin film and bulk. In order to use the equation in case of nanostructures, the effect of surface-to-volume ratio and depletion layer width has to be taken into account.

(a) **Surface-to-volume ratio**

The surface-to-volume ratio in terms of adsorbed oxygen ions can be written as

$$[\text{O}_{\text{ads}}] = \frac{\sigma_0 \emptyset V_m}{V_s} \tag{15}$$

where 'σ_0' is the number of oxygen ion per unit area, '$\emptyset$' is a ratio of surface area per volume of material 'V_m' and 'V_s' is the system volume. Substituting in Eq. (14)

$$S = \frac{\Gamma_t k_{\text{gas}} (\sigma_0 \emptyset (V_m / V_s) X)^b}{n_0} + 1 \tag{16}$$

Now, the sensitivity depends directly on the surface-to-volume ratio which is well suited for sensors based on metal oxide nanomaterials.

(b) **Depletion layer width**

According to the depletion layer or space charge model [46], the Debye length L_D which is a characteristic length for semiconductors can be written as

$$L_D = \left(\frac{\varepsilon k_B T}{q^2 N_d}\right)^{1/2} \tag{17}$$

where 'ε' is the static dielectric constant, 'q' is the electrical charge of the carrier and 'n' is the carrier concentration. Debye length is a measure of the distance over which a charge imbalance is neutralized by majority charge carriers under steady-state or equilibrium conditions [47]. From Eq. (17), it is seen that if the temperature is kept constant, L_D depends only on the carrier concentration. Let us assume that the sensing material is in the shape of a cylinder whose conducting channel is along the axis of the cylinder. In air ambient, the depletion layer is formed on the surface due to oxygen adsorption. The width of the depletion layer decreases upon adsorbing a reducing gas. The carrier concentration of the depletion region in terms of Debye length can be written as

$$n' = n_0 \frac{\pi (D - 2L_D)^2}{\pi D^2} \tag{18}$$

Now, the response can be written as

$$S = \left[\frac{\Gamma_t k_{\text{gas}} (\sigma_0 \emptyset (V_m / V_s))^b}{n_0}\right] \frac{D^2 X^b}{(D - 2L_D)^2} + 1 \tag{19}$$

1. **Case I**: **if** $\boldsymbol{D \gg 2L_D}$
   In this case, the depletion layers have no effect, and Eq. (19) can be approximated to (14).
2. **Case II**: **If** $\boldsymbol{D > 2L_D}$
   Here also, the depletion layer has no significant effect on the response. But, the sensor response will be higher compared to the previous case because of the increased oxygen ion density due to the large surface-to-volume ratio.
3. **Case III**: **If** $\boldsymbol{D \sim 2L_D}$
   In this case, the depletion layer strongly affects the sensor response. Thus, Eq. (19) can be used for evaluating the sensitivity of metal oxides having any size variations.

3 Metal Oxide Semiconductor-Based Heterostructures for Gas Sensing

The integration of semiconducting oxide sensing materials with other metal oxides or noble metal nanoparticles is an efficient method for improving the gas sensing characteristics of chemiresistive sensors [26, 48–52]. The physical interface between two different materials is called a heterojunction, and the combination of multiple

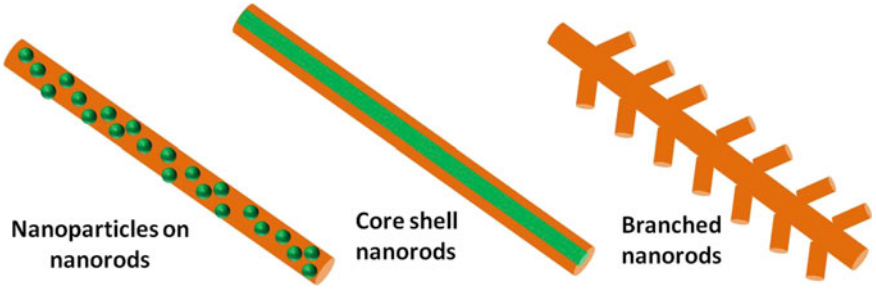

Fig. 8 Schematic for heterostructures

heterojunctions together in a device is called a heterostructure. Noble metal nanoparticles such as Pd, Pt, Au and Ag and metal oxide nanoparticles like CuO, ZnO, TiO_2, etc., on the surface of the sensing material can enhance the sensing characteristics [53–56]. The presence of these additive particles increases the surface area of the sensing material, thereby increasing the number of active sites for gas adsorption. Also, most of these additive particles are very good catalysts which can reduce the activation energy for gas adsorption-desorption reactions and make it faster. Another effect is that the gas molecules react with the adsorbed oxygen ions in one material constituting the junction, the by-product may readily react with the oxygen ions in the second material to complete the reaction, and this is called the synergistic effect. One-dimensional oxide semiconductor nanostructures can be considered as a suitable host material for forming heterostructures. Few examples for one-dimensional nanorod heterostructures are shown in Fig. 8.

When there is a difference in work function between the materials forming a junction, electrons flow from the material having lower work function to that having higher work function until thermal equilibrium is reached [47, 51, 57–60]. Because of this migration of electrons, there forms a depletion region at the former side and also at the interface of the two materials. Hence, the resistance of the heterostructure in ambient air (R_a) will be high compared to that of individual materials constituting the junction. Due to the increased number of gas adsorption sites of the heterostructure and the reduced activation energy for the adsorption-desorption reaction, the resistance in the presence of target gases R_g will be low, and hence, the response will be high for the heterostructure sensors. Here, we discuss the influence of metal/semiconductor and semiconductor/semiconductor heterojunctions on the gas sensing properties.

3.1 Schottky Junction

The noble metal nanoparticles on the surface of metal oxide semiconductors obviously increase the conductivity as well as the active surface area of the whole

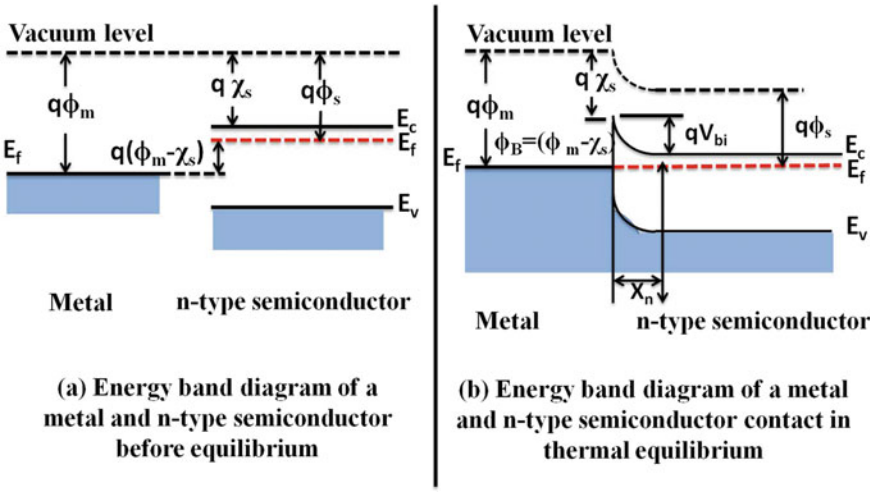

Fig. 9 Schematic diagram showing the possible band structures at Schottky junction **a** before and **b** after thermal equilibrium

structure. The barrier height, Φ_B, after contact is given by

$$\Phi_B = \Phi_m - \chi_s \tag{20}$$

where 'Φ_m' is the work function of the metal and 'χ_s' is the electron affinity of the semiconductor. Usually, metal-semiconductor junction in Schottky contact facilitates the gas sensing characteristics. Consider the case of metal and n-type semiconductor, forming a junction where the metal work function is larger than the semiconductor work function (Fig. 9). Here, electrons flow from the semiconductor to the metal until equilibrium is reached.

As a result, there develops a space charge layer at the metal-semiconductor interface whose width is given by 'X_n',

$$X_n = \left[\frac{2\varepsilon V_{\text{bi}}}{qN_n}\right]^{1/2} \tag{21}$$

where 'V_{bi}' is the built-in potential at the interface and 'N_n' is the donor concentration in the n-type semiconductor. The increased electron concentration due to migration of carriers and the catalytic properties of metal nanoparticles together facilitate additional oxygen adsorption–desorption reactions, resulting in the dramatically improved gas sensing characteristics.

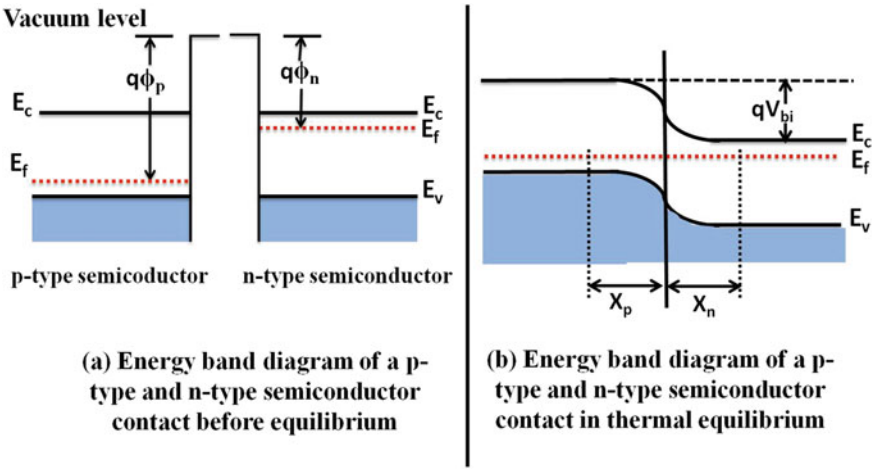

Fig. 10 Schematic diagram showing the possible band structures at p–n junction **a** before and **b** after thermal equilibrium

3.2 p-n Junction

Generally, n-type semiconductors are widely used for gas sensing applications than p-type, because of their stability in low-oxygen environments. The n-type and p-type materials can be combined to explore the effects of p-n junction on the sensing properties. p-n junction is the most common heterojunction interface used for modulating the gas sensing properties of oxide-based sensors. Based on the difference in the work function of the materials, charge carrier migration takes place leading to the formation of depletion layer on n-side, accumulation layer on p-side and junction at the interface due to electron-hole recombination (Fig. 10).

The width of the depletion layer in n-type and p-type [61] can be written as

$$X_n = \left\{ \frac{2\epsilon_n V_{\text{bi}}}{q} \left[\frac{N_p}{N_n} \right] \left[\frac{1}{N_n + N_p} \right] \right\}^{1/2} \tag{22}$$

$$X_p = \left\{ \frac{2\epsilon_p V_{\text{bi}}}{q} \left[\frac{N_n}{N_p} \right] \left[\frac{1}{N_n + N_p} \right] \right\}^{1/2} \tag{23}$$

where 'ϵ_n' and 'ϵ_p', 'N_n' and 'N_p' are the static dielectric constants and carrier concentration of n- and p-type semiconductor metal oxide semiconductors, respectively.

4 p-CuO/n-ZnO Heterojunction Sensor for Room-Temperature Gas Sensing Applications

Both zinc oxide (ZnO) and copper oxide (CuO) are well-known inorganic semiconducting materials, where ZnO is generally n-type and CuO is p-type. Generally, MOS-based sensors operate at high temperatures which limit their applications in several fields. Also, high-temperature operation increases the power consumption of the device. In this context, the development of room-temperature sensors has significant importance in the gas sensor industry.

p-CuO/n-ZnO heterojunction sensors were fabricated by whole solution process, and its room-temperature ethanol sensing properties were studied in detail [62, 63]. Heterojunction sensors were fabricated by decorating ZnO nanorods with CuO nanoparticles. Vertically aligned ZnO nanorods were grown by seed-mediated hydrothermal method, and CuO nanoparticles were synthesized by wet chemical method. Circular gold electrodes were deposited by thermal evaporation technique, and room-temperature gas sensing properties were investigated. The schematic of the device structure is shown in Fig. 11.

The room-temperature response curves of ZnO/CuO heterojunction sensors to various concentrations of ethanol are shown in Fig. 12. For an ethanol concentration of 50 ppm, the response value has been enhanced to 5.8 for ZnO/CuO heterojunction sensor, whereas the value was 2.4 for ZnO. The response value increases with increase in the concentration of ethanol for both ZnO and ZnO/CuO, and improved response characteristics were obtained for the heterojunction sensors. In Fig. 13, the variation of response time and recovery time of the sensors with the concentration of ethanol is shown where we can see that the response time decreases with increase in concentration and recovery time increases with increase in concentration. The calculated values of the response time of ZnO and ZnO/CuO sensors to 50 ppm ethanol were 98 and 30 s, respectively. The recovery time calculated was 508 and 420 s, respectively, for ZnO and ZnO/CuO to 50 ppm ethanol. This is because, at higher concentration of ethanol, the number of molecules having minimum required energy for the reaction is high, so that more and more molecules will react with the adsorbed oxygen leading to a faster change in response. The high value of recovery

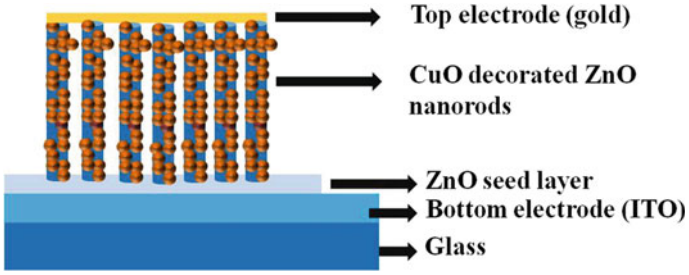

Fig. 11 Schematic of the p-CuO/n-ZnO heterojunction sensor device

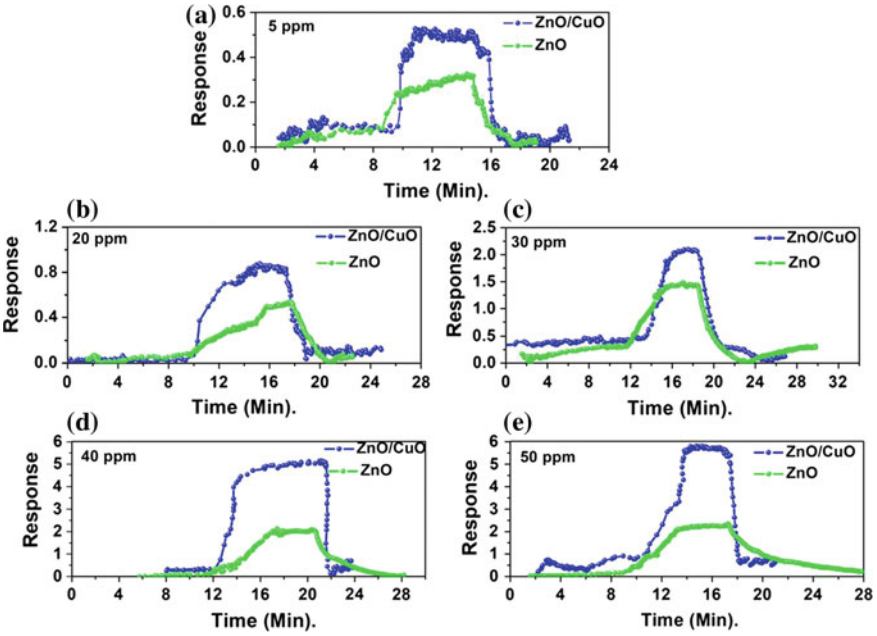

Fig. 12 Room-temperature response characteristics of ZnO and ZnO/CuO heterojunction sensors to different concentrations of ethanol

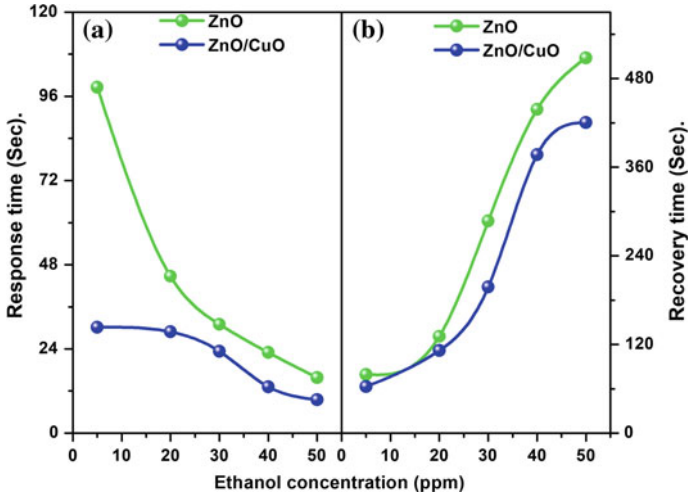

Fig. 13 Variation of **a** response time and **b** recovery time of ZnO and ZnO/CuO sensors with the concentration of ethanol

time is due to the slow desorption rate of ethanol at room temperature [64]. Using the fabricated experimental set-up for sensing measurements, the lowest concentration of ethanol detected was 5 ppm. The increased active surface area for gas adsorption reactions due to the vertical alignment of the ZnO nanorods and the presence of CuO nanoparticles together with the formation of p-n heterojunctions at the interface of ZnO and CuO contributed to the better sensing properties of ZnO/CuO sensor [50, 51, 65].

The detailed sensing mechanism of ZnO/CuO heterojunction sensor can be explained by considering the energy band diagram of the heterojunction before and after thermal equilibrium. The values of band gaps and electron affinities of ZnO and CuO are shown in Fig. 14 [65–68]. The ethanol molecules react with the adsorbed oxygen ions, the generated free electrons on adsorption of ethanol gas in ZnO can easily transport through the p-n junction due to the low value of $\Delta E_C(0.28\,\mathrm{e}V)(\Delta E_C = \chi_2 - \chi_1)$, and at the same time, the holes in CuO will accumulate at the valence band of p-CuO due to the large value of $\Delta E_V(1.74\,\mathrm{e}V)\left[\Delta E_V = \left(E_{g2} - E_{g1}\right) - \Delta E_C\right]$. At low temperatures, ethanol molecules dissociate into aldehyde (CH_3CHO) and water [69–72]. The dehydrogenation of ethanol molecules generates OH^- ions (breaking of C–O bond) and $[CH_3CH_2O]^-$ ions (breaking of O–H bond) due to their lower bond-breaking energies. The dehydrogenated ionic fragment $[CH_3CH_2O]^-$ of ethanol molecules can be easily attached to metal oxide surfaces through the interaction of adsorbed oxygen on their surfaces represented by Eq. (24). In addition, at the interface of ZnO/CuO junction, ethanol molecules react with holes in CuO followed by Eq. (25) [73–76].

$$CH_3CH_2OH_{(g)} + O^-_{2(ads)} \rightarrow \begin{cases} [CH_3CH_2O]^-_{(ads)} + OH^-_{(ads)} \\ CH_3CHO + H_2O + e^- \end{cases} \tag{24}$$

$$CH_3CH_2OH_{(g)} + 2h^+ + e^- + O^-_{2(ads)} \rightarrow CH_3CHO + H_2O + e^- \tag{25}$$

These reactions release excess free electrons leading to enhanced room-temperature gas sensing performance of p-CuO/n-ZnO heterojunction device.

5 Summary

In this chapter, the basic working principles, the performance parameters and factors affecting the gas sensing characteristics of chemiresistive gas sensors have been discussed. The gas sensing mechanism of MOS gas sensors has been explained for a better understanding of the working principles. The operating principles of heterojunction-based sensors and how they improve the response characteristics are also discussed. As an example for heterojunction sensors, p-CuO/n-ZnO sensors were fabricated and discussed in detail.

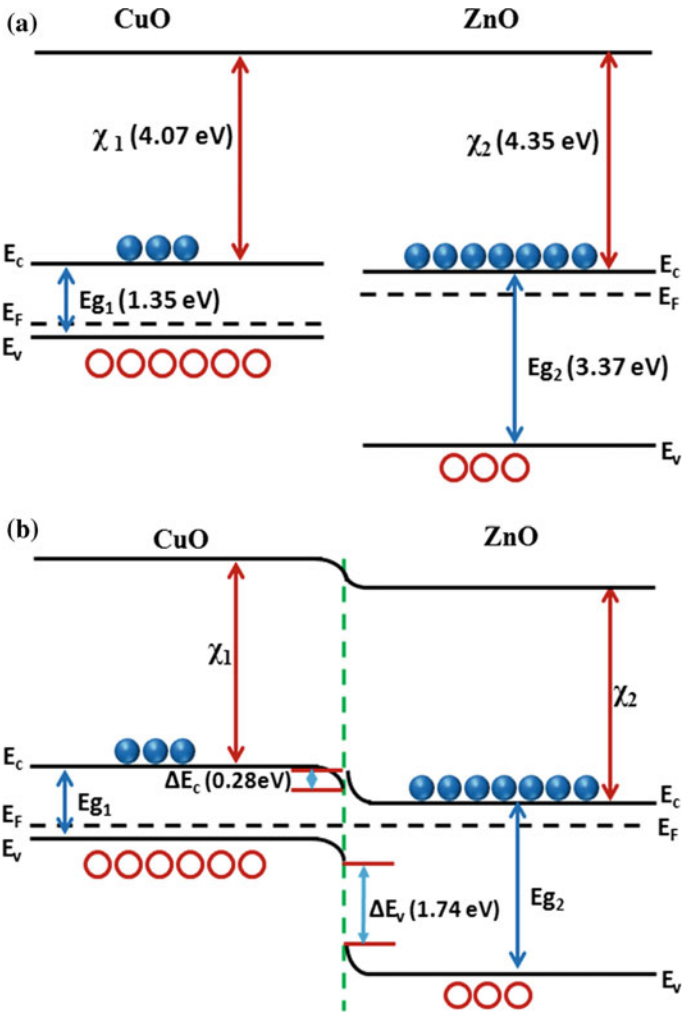

Fig. 14 Energy band diagram of **a** ZnO and CuO and **b** ZnO/CuO heterojunction device at thermal equilibrium

References

1. Di Francia G, Alfano B, La Ferrara V (2009) Conductometric gas nanosensors. J Sens 1–18. https://doi.org/10.1155/2009/659275
2. Hodgkinson J, Tatam RP (2012) Optical gas sensing: a review. Meas Sci Technol 24:12004–12062. https://doi.org/10.1088/0957-0233/24/1/012004
3. Durig U (2017) Fundamentals of micromechanical thermoelectric sensors. J Appl Phys 98:044906–044919. https://doi.org/10.1063/1.2006968
4. Bakker E, Telting-diaz M (2002) Electrochemical sensors. Anal Chem 74:2781–2800. https://doi.org/10.1021/ac0202278

5. Liu X, Cheng S, Liu H, Hu S, Zhang D, Ning H (2012) A survey on gas sensing technology. Sensors 12:9635–9665. https://doi.org/10.3390/s120709635
6. Yamazoe N, Sakai G, Shimanoe K, Sakai G, Shimanoe K (2003) Oxide semiconductor gas sensors. Catal Surv Asia. 7, 63–75. https://doi.org/10.1023/a:1023436725457
7. Fine GF, Cavanagh LM, Afonja A, Binions R (2010) Metal oxide semi-conductor gas sensors in environmental monitoring. Sensors 10:5469–5502. https://doi.org/10.3390/s100605469
8. Yamazoe N (2005) Toward innovations of gas sensor technology. Sens Actuators B Chem 108:2–14. https://doi.org/10.1016/j.snb.2004.12.075
9. Huang X-J, Choi Y-K (2007) Chemical sensors based on nanostructured materials. Sens Actuators B Chem 122:659–671. https://doi.org/10.1016/j.snb.2006.06.022
10. Jiménez Cadena G, Riu J, Rius FX (2007) Gas sensors based on nanostructured materials. Analyst 132:1083–1099. https://doi.org/10.1039/b704562j
11. Sharma S, Madou M (2012) A new approach to gas sensing with nanotechnology. Philos Trans A Math Phys Eng Sci 370:2448–2473. https://doi.org/10.1098/rsta.2011.0506
12. Tao J, Batzill M (2013) Surface science studies of metal oxide gas sensing materials. In: Metal Oxide Nanowires for chemical sensors. Springer Science & Business Media, Germany, pp 35–68
13. Kolmakov A, Moskovits M (2004) Chemical sensing and catalysis by one-dimensional metal-oxide nanostructures. Annu Rev Mater Res 34:151–180. https://doi.org/10.1146/annurev.matsci.34.040203.112141
14. Comini E, Baratto C, Concina I, Faglia G, Falasconi M, Ferroni M, Galstyan V, Gobbi E, Ponzoni A, Vomiero A, Zappa D, Sberveglieri V, Sberveglieri G (2013) Metal oxide nanoscience and nanotechnology for chemical sensors. Sens Actuators B Chem 179:3–20. https://doi.org/10.1016/j.snb.2012.10.027
15. Zeng H, Duan G, Li Y, Yang S, Xu X, Cai W (2010) Blue luminescence of ZnO nanoparticles based on non-equilibrium processes: defect origins and emission controls. Adv Funct Mater 20:561–572. https://doi.org/10.1002/adfm.200901884
16. Meyer BK, Alves H, Hofmann DM, Kriegseis W, Forster D, Bertram F, Christen J, Hoffmann A, Straßburg M, Dworzak M, Haboeck U, Rodina AV (2004) Bound exciton and donor-acceptor pair recombinations in ZnO. Phys Status Solidi Basic Res 241:231–260. https://doi.org/10.1002/pssb.200301962
17. Azad AM, Akbar SA, Mhaisalkar SG, Birkefeld LD, Goto KS (1992) Solid-state gas sensors: a review. J Electrochem Soc 139:3690–3704. https://doi.org/10.1149/1.2069145
18. Čajka T, Hajšlová J (2004) Gas chromatography—high-resolution time-of-flight mass spectrometry in pesticide residue analysis : advantages and limitations. J Chromatogr A 1058:251–261. https://doi.org/10.1016/j.chroma.2004.07.097
19. Brattain WH, Bardeen J (1953) Surface properties of germanium. Bell Labs Tech J 32:1–41. https://doi.org/10.1002/j.1538-7305.1953.tb01420.x
20. Heiland G (1954) On the influence of adsorbed oxygen on the electrical conductivity of zinc oxide crystals. Zeitschrift ftir Phys 138:459–464. https://doi.org/10.1007/BF01340692
21. Seiyama T, Kato A (1962) A new detector for gaseous components using semiconductive thin films. Anal Chem 34:1502–1503. https://doi.org/10.1021/ac60191a001
22. Shaver PJ (1967) Activated tungsten oxide gas detectors. Appl Phys Lett 11:255–257. https://doi.org/10.1063/1.1755123
23. Taguchi N (1972) Gas-detecting device
24. Meixner H, Lampe U (1996) Metal oxide sensors. Sens Actuators B Chem 33:198–202. https://doi.org/10.1016/0925-4005(96)80098-0
25. Sun YF, Liu SB, Meng FL, Liu JY, Jin Z, Kong LT, Liu JH (2012) Metal oxide nanostructures and their gas sensing properties: a review. Sensors 12:2610–2631. https://doi.org/10.3390/s120302610
26. Korotcenkov G (2005) Gas response control through structural and chemical modification of metal oxide films: state of the art and approaches. Sens Actuators B 107:209–232. https://doi.org/10.1016/j.snb.2004.10.006

27. Afaah AN, Khusaimi Z, Rusop M (2013) A review on zinc oxide nanostructures: doping and gas sensing. Adv Mater Res 667:329–332. https://doi.org/10.4028/www.scientific.net/AMR.667.329
28. Tricoli A, Righettoni M, Pratsinis SE (2009) Minimal cross-sensitivity to humidity during ethanol detection by SnO_2-TiO_2 solid solutions. Nanotechnology 20:315502. https://doi.org/10.1088/0957-4484/20/31/315502
29. Wolkenstein T (1961) Effect of ionizing radiation on the adsorptive and catalytic properties of semiconductors. Discuss Faraday Soc 31:209. https://doi.org/10.1039/df9613100209
30. Morrison SR (1981) Semiconductor gas sensors. Sens Actuators 2:329–341. https://doi.org/10.1016/0250-6874(81)80054-6
31. Yamazoe N, Kurokawa Y, Seiyama T (1983) Effects of additives on semiconductor gas sensors. Sens Actuators 4:283–289. https://doi.org/10.1016/0250-6874(83)85034-3
32. Shankar P, Bosco J, Rayappan B (2015) Gas sensing mechanism of metal oxides: the role of ambient atmosphere, type of semiconductor and gases—a review. Sci Lett J 4(126):1–18
33. Kohl D (1992) Oxidic semiconductor gas sensors. In: Sberveglieri G (ed) Gas sensors. Springer, Berlin, pp 43–88
34. Neri G (2015) First fifty years of chemoresistive gas sensors. Chemosensors 3:1–20. https://doi.org/10.3390/chemosensors3010001
35. Retamal JRD, Chen CY, Lien DH, Huang MRS, Lin CA, Liu CP, He JH (2014) Concurrent improvement in photogain and speed of a metal oxide nanowire photodetector through enhancing surface band bending via incorporating a nanoscale heterojunction. ACS Photonics 1:354–359. https://doi.org/10.1021/ph4001108
36. Wongrat E, Hongsith N, Wongratanaphisan D, Gardchareon A, Choopun S (2012) Control of depletion layer width via amount of AuNPs for sensor response enhancement in ZnO nanostructure sensor. Sens Actuators B Chem 171–172:230–237. https://doi.org/10.1016/j.snb.2012.03.050
37. Shimizu Y, Egashira M (1999) Basic aspects and challenges of semiconductor gas sensors. MRS Bull 24:18–24. https://doi.org/10.1557/S0883769400052465
38. Barsan N, Weimar UDO (2001) Conduction model of metal oxide gas sensors. J Electroceramics 7:143–167. https://doi.org/10.1023/A:1014405811371
39. Gardon M, Guilemany JM (2013) A review on fabrication, sensing mechanisms and performance of metal oxide gas sensors. J Mater Sci Mater Electron 24:1410–1421. https://doi.org/10.1007/s10854-012-0974-4
40. Vander Wal RL, Hunter GW, Xu JC, Kulis MJ, Berger GM, Ticich TM (2009) Metal-oxide nanostructure and gas-sensing performance. Sens Actuators B Chem 138:113–119. https://doi.org/10.1016/j.snb.2009.02.020
41. Yamazoe N (1991) New approaches for improving semiconductor gas sensors. Sens Actuators B Chem 5:7–19. https://doi.org/10.1016/0925-4005(91)80213-4
42. Xu C, Tamaki J, Miura N, Yamazoe N (1991) Grain size effects on gas sensitivity of porous SnO_2-based elements. Sens Actuators B Chem 3:147–155. https://doi.org/10.1016/0925-4005(91)80207-Z
43. Barsan N, Weimar U (2003) Understanding the fundamental principles of metal oxide based gas sensors; the example of CO sensing with SnO_2 sensors in the presence of humidity. J Phys Condens Matter 15:R813–R839. https://doi.org/10.1088/0953-8984/15/20/201
44. Tiemann M (2007) Porous metal oxides as gas sensors. Chem A Eur J 13:8376–8388. https://doi.org/10.1002/chem.200700927
45. Comini E (2006) Metal oxide nano-crystals for gas sensing. Anal Chim Acta 568:28–40. https://doi.org/10.1016/j.aca.2005.10.069
46. Ogawa H, Nishikawa M, Abe A (1982) Hall measurement studies and an electrical conduction model of tin oxide ultrafine particle films. J Appl Phys 53:4448–4455. https://doi.org/10.1063/1.331230
47. Schroder DK (1998) Semiconductor material and device characterization. Wiley, Arizona
48. Zhang J, Qin Z, Zeng D, Xie C (2017) Metal-oxide-semiconductor based gas sensors: screening, preparation, and integration. Phys Chem Chem Phys 19:6313–6329. https://doi.org/10.1039/c6cp07799d

49. Li Z, Li H, Wu Z, Wang M, Luo J (2019) Advances in designs and mechanisms of semiconducting metal oxide nanostructures for high-precision gas sensors operated at room temperature. Mater Horizons 6:18–21. https://doi.org/10.1039/c8mh01365a
50. Miller DR, Akbar SA, Morris PA (2014) Nanoscale metal oxide-based heterojunctions for gas sensing: a review. Sens Actuators B Chem 204:250–272. https://doi.org/10.1016/j.snb.2014.07.074
51. Li T, Zeng W, Wang Z (2015) Quasi-one-dimensional metal-oxide-based heterostructural gas-sensing materials: a review. Sens Actuators B Chem 221:1570–1585. https://doi.org/10.1016/j.snb.2015.08.003
52. Roduner E (2014) Understanding catalysis. Chem Soc Rev 43:8226–8239. https://doi.org/10.1039/C4CS00210E
53. Zainelabdin A, Amin G, Zaman S, Nur O, Lu J, Hultman L, Willander M (2012) CuO/ZnO Nanocorals synthesis via hydrothermal technique: growth mechanism and their application as humidity sensor. J Mater Chem 22:11583–11590. https://doi.org/10.1039/c2jm16597j
54. Guo Z, Chen X, Li J, Liu JH, Huang XJ (2011) ZnO/CuO hetero-hierarchical nanotrees array: hydrothermal preparation and self-cleaning properties. Langmuir 27:6193–6200. https://doi.org/10.1021/la104979x
55. Wang L, Wang S, Xu M, Hu X, Zhang H, Wang Y, Huang W (2013) A Au-functionalized ZnO nanowire gas sensor for detection of benzene and toluene. Phys Chem Chem Phys 15:17179–17186. https://doi.org/10.1039/c3cp52392f
56. Ding J, Zhu J, Yao P, Li J, Bi H, Wang X (2015) Synthesis of ZnO-Ag hybrids and their gas-sensing performance toward ethanol. Ind Eng Chem Res 54:8947–8953. https://doi.org/10.1021/acs.iecr.5b01711
57. Neamen DA (2003) Semiconductor physics and devices basic principles. McGraw-HIII Education, New York
58. Kwiatkowski M, Bezverkhyy I, Skompska M (2015) ZnO nanorods covered with a TiO_2 layer: simple sol–gel preparation, and optical, photocatalytic and photoelectrochemical properties. J Mater Chem A 3:12748–12760. https://doi.org/10.1039/C5TA01087J
59. Liu B, Sun Y, Wang D, Wang L, Zhang L, Zhang X, Lin Y, Xie T (2014) RSC Advances Construction of a branched ZnO–TiO_2 nanorod array heterostructure for enhancing the photovoltaic properties in quantum dot-sensitized. RSC Adv 4:32773–32780. https://doi.org/10.1039/C4RA05736H
60. Sze SM, Ng KK (2006) Physics of semiconductor devices. Wiley, New Jersey
61. Pierret RF (1996) Semiconductor device fundamentals. Addison-wesley Publishing Company, United States of America
62. Subha PP, Jayaraj MK (2019) Enhanced room temperature gas sensing properties of low temperature solution processed ZnO/CuO heterojunction. BMC Chem 1–11. https://doi.org/10.1186/s13065-019-0519-5
63. Subha PP, Jayaraj MK (2018) Fabrication of room temperature gas sensors based on metal oxide semiconductor nanostructures
64. Batzill M (2006) Surface science studies of gas sensing materials: SnO_2. Sensors 6:1345–1366. https://doi.org/10.3390/s6101345
65. Zhang YB, Yin J, Li L, Zhang LX, Bie LJ (2014) Enhanced ethanol gas-sensing properties of flower-like p-CuO/n-ZnO heterojunction nanorods. Sens Actuators B Chem 202:500–507. https://doi.org/10.1016/j.snb.2014.05.111
66. Zainelabdin A, Zaman S, Amin G, Nur O, Willander M (2012) Optical and current transport properties of CuO/ZnO nanocoral p-n heterostructure hydrothermally synthesized at low temperature. Appl Phys A 108:921–928. https://doi.org/10.1007/s00339-012-6995-2
67. Park S, Ko H, Kim S, Lee C (2014) Role of the Interfaces in multiple networked one-dimensional core-shell nanostructured gas sensors. ACS Appl Mater Interfaces 6:9595–9600. https://doi.org/10.1021/am501975v
68. Wang C, Fu XQ, Xue XY, Wang YG, Wang TH (2007) Surface accumulation conduction controlled sensing characteristic of p-type CuO nanorods induced by oxygen adsorption. Nanotechnology 18:145506. https://doi.org/10.1088/0957-4484/18/14/145506

69. Yu MR, Suyambrakasam G, Wu RJ, Chavali M (2012) Performance evaluation of ZnO-CuO hetero junction solid state room temperature ethanol sensor. Mater Res Bull 47:1713–1718. https://doi.org/10.1016/j.materresbull.2012.03.046
70. Hazra A, Dutta K, Bhowmik B, Bhattacharyya P (2015) Highly repeatable low-ppm ethanol sensing characteristics of p-TiO_2-based resistive devices. IEEE Sens J 15:408–416. https://doi.org/10.1109/JSEN.2014.2345575
71. Song W, Liu P, Hensen EJM (2014) A mechanism of gas- phase alcohol oxidation at the interface of Au nanoparticles and a MgCuCr2O4 spinel support. Catal Sci techology 4:2997–3003. https://doi.org/10.1039/c4cy00462k
72. Hyodo T, Hashimoto T, Ueda T, Nakagoe O, Kamada K, Sasahara T, Tanabe S, Shimizu Y (2015) Adsorption/ combustion-type VOC sensors employing mesoporous γ-alumina co-loaded with noble-metal and oxide. Sens Actuators B Chem 220:1091–1104. https://doi.org/10.1016/j.snb.2015.06.065
73. Mendoza F, Hernández DM, Makarov V, Febus E, Weiner BR, Morell G (2014) Room temperature gas sensor based on tin dioxide-carbon nanotubes composite films. Sens Actuators B Chem 190:227–233. https://doi.org/10.1016/j.snb.2013.08.050
74. Chen Y, Yu L, Feng D, Zhuo M, Zhang M, Zhang E, Xu Z, Li Q, Wang T (2012) Superior ethanol-sensing properties based on Ni-doped SnO_2 p-n heterojunction hollow spheres. Sens Actuators B Chem 166–167:61–67. https://doi.org/10.1016/j.snb.2011.12.018
75. Chen YJ, Zhu CL, Xiao G (2008) Ethanol sensing characteristics of ambient temperature sonochemically synthesized ZnO nanotubes. Sens Actuators B 129:639–642. https://doi.org/10.1016/j.snb.2007.09.010
76. Acharyya D, Bhattacharyya P (2016) Alcohol sensing performance of ZnO hexagonal nanotubes at low temperatures: a qualitative understanding. Sens Actuators B Chem 228:373–386. https://doi.org/10.1016/j.snb.2016.01.035

Chapter 8
Zno-Based Dilute Magnetic Semiconductors

Arun Aravind and M. K. Jayaraj

1 Introduction

II–VI-based novel thin films and heterostructures are technologically attractive for future devices due to their exciting electrical and magneto-optical properties [1–3]. The direct band gap ZnO is emerging as a potential candidate due to its ability to tailor electronic, magnetic, and optical properties through doping and alloying [2–6]. ZnO is also an efficient UV emitter. The free-exciton binding energy of ZnO (60 meV) is more than twice that of GaN (25 meV). The radiative recombination in ZnO is mediated by excitons which lead to narrow emission line width. So ZnO-based system has major role in wide range of devices, such as blue and UV light-emitting diodes, spintronic devices based on diluted magnetic semiconductors, transparent conducting transistors, and resonant tunneling devices [2–7].

In II–VI semiconductors, each anion is coordinated by four cations at the corners of a tetrahedron. This tetrahedral coordination is nature of the covalent bond having sp3 hybridization. So the coordinations of Zn^{2+} and O^{2-} are both fourfold. Semiconductors that normally crystallize in wurtzite include nitrides, II–VI semiconductors (ZnS, CdS, ZnSe, CdSe, ZnTe, CdTe, SiC, InAs, etc.). The various forms of crystal structure of ZnO are rock salt or Rochelle salt (B1), zinc blende (B3), and wurtzite (B4); B1, B3, and B4 are designations for the three phases. Wurtzite structure is the most thermodynamically stable phase of ZnO thin films. When it grows on cubic substrates, it shows zinc blende structure, but the rock salt structure is obtained only at high pressures. The wurtzite structure has a hexagonal unit cell with the lattice parameters '*a*' and '*c*' in the ratio of $c/a = 1.633$ [8]. Under the ordinary preparation

A. Aravind (✉)
Centre for Advanced Functional Materials, Department of Physics, Bishop Moore College, Mavelikara, India
e-mail: bmcarun@gmail.com

M. K. Jayaraj
Cochin University of Science and Technology, Kochi 682022, India

M. K. Jayaraj (ed.), *Nanostructured Metal Oxides and Devices*,
Materials Horizons: From Nature to Nanomaterials,
https://doi.org/10.1007/978-981-15-3314-3_8

conditions, excess zinc is always found in ZnO. Due to this zinc excess, ZnO is a non-stoichiometric compound and a n-type semiconductor. ZnO is a direct band gap semiconductor (3.37 eV) having an exciton binding energy of 60 meV at room temperature. So ZnO shows near-ultraviolet and the visible defect emissions. The band-edge emission is centered at approximately 380 nm, and the visible deep-level emission is in the range of 450–730 nm. UV emission is the near-band-edge emission which depends on the crystal quality of the film or nanostructures while the visible emissions are related to various intrinsic defects in ZnO crystal [4, 7]. But theses emissions are influenced by growth techniques and conditions.

Diluted magnetic semiconductors (DMS) are semiconductor alloys which contain a small fraction of magnetic impurities. DMSs are mainly based on II–VI materials such as CdTe and ZnSe with transition-metal ions (e.g., Mn, Fe, or Co) substituting the cations. Magnetic ions with +2 valency are easily incorporated into the host II–VI crystals by replacing group II cations of the host lattice. There are also DMS materials based on IV–VI (e.g., PbTe, SnTe) and recently III–V (e.g., GaAs, InSb) crystals, and the rare earth elements (e.g., Eu, Gd, Er) are also used as dopants. In II–VI-based DMS, such as (CdMn)Se, magneto-optic properties were extensively studied and optical isolators were recently fabricated using their large Faraday effect [10]. Recently, ZnO has renewed interest since it was found that high-quality epitaxial thin film shows ultraviolet laser action at room temperature [11, 12]. The band gap of this compound can be extended up to 4 eV by synthesizing alloys of $Zn_{1-x}TM_xO$ (TM = Mn, Co, Ni, etc.). Heavy electron doping was readily achieved in ZnO in contrast to the other II–VI compound semiconductors. According to Ruderman–Kittel–Kasuya–Yosida (RKKY) interaction, the above-mentioned factors favor strong correlation between the magnetic ions and spins of the band carriers of host materials [9, 13–15].

Spintronics is an emerging technology exploiting the intrinsic spin of the electron and its magnetic moment, other than the fundamental electronic charge. Recent past witnessed many advances, particularly in the wide band gap, III–V- and II–VI-based spintronic materials. But practical applications using such materials were limited to low temperature owing to the low Curie temperature (T_C) of the magnetic dopants. Dietl et al. [15] theoretically predicted the possibility of room-temperature ferromagnetism in III–V- and II–VI-based DMS materials. A few transition-metal elements (Mn, Co, Ni, Cu, etc.) that doped ZnO [5, 9, 13–15] exhibits T_C much above 300 K (Fig. 1). TM-doped ZnO is interesting due its room-temperature ferromagnetism and unique transport properties.

Spintronics is becoming an area of active research because it can exploit the spin degree of freedom of the electrons along with its charge. So spintronics can combine standard microelectronics with spin-dependent effects that arise from the interaction between electrons and a magnetic field. So we can expect new generation devices with various functionalities. The magnetic devices should be non-volatile, less electric power consumption, and increased integration densities compared to microelectronics. The discovery of giant magnetoresistance (GMR) [16] in magnetic multilayers has triggered intense experimental as well as theoretical studies to exploit the potential technological applications and to understand the underlying physical phenomena that cause this effect. GMR is realized in metallic multilayers

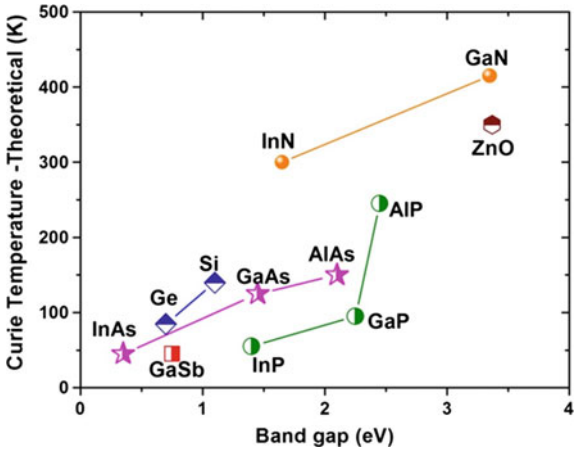

Fig. 1 Predicted Curie temperature for semiconductors [5, 9]

which have alternating layers of ferromagnetic and non-magnetic metallic layers. So in GMR, resistance of the multilayer stack depends on relative orientation of ferromagnetic layers due to spin-dependent scattering at the interfaces. Transition-metal oxide (TMO) is very rich in physics because of unusual magnetic, optical, and electrical properties and has tremendous device applications. Some of the recently discovered applications of TMO are based on superconductors, transparent conducting electronics, optoelectronics, and spintronics [5, 6, 9, 13, 14]. These oxides thin film form have attracted much attention from last decade due to their wide variety of applications such as gas sensors, optical switches, windows for solar cell, thin-film batteries, and photo-catalysis. ZnO is emerging as a potential candidate due to its direct band gap, and also we can tailor the optical and magnetic and properties through doping and alloying [13].

The radiative recombination in ZnO is mediated by excitons which lead to narrow emission line width. So ZnO system has a role for a wide range of devices such as blue and UV light-emitting heterojunction diodes, transparent thin-film transistor for display, and spintronic devices based on diluted magnetic semiconductors. ZnO thin films and nanostructures can be prepared at low temperatures by RF sputtering, pulsed laser deposition, chemical vapor deposition, hydrothermal method, and chemical method [17–21]. Due to ionic nature of ZnO, it lends itself to ease in the microfabrication process using both wet and dry etching techniques. Despite recent experimental success, a fundamental description of ferromagnetism in semiconductors remains incomplete. Recent theoretical treatments have yielded useful insight the possible mechanisms in DMS.

2 Magnetic Interactions in DMS

DMS can be considered as two interacting subsystems, one comprising the host semiconductor with delocalized conduction and valence electrons and the other diluted system of localized magnetic moments associated with the magnetic atoms. The host semiconductors have extended states made by delocalized band electrons. So the optical and electronic properties of DMS are described by the effective mass of the carriers. Magnetic nature of DMS mainly depends on the magnetic moments of the magnetic ions and their interaction with the host semiconductor lattice. Most of them show *sp-d* and *sp-f* interactions for transition-metal ions and rare earth magnetic ions. The spin–spin interaction between magnetic ions can be classified into four major types. RKKY mechanism (Ruderman–Kittel–Kasuya–Yoshida) leads to spin polarization of the conduction electrons of the semiconductors. The band polarization is occurred by Bloembergen–Rowland (BR) interaction [13, 22]. Virtual transition between the magnetic ions and neighboring anions leads to superexchange and double-exchange interactions.

2.1 Carrier-Single Magnetic Interaction

The interaction between the magnetic impurity ion and the conduction and valence band electrons of the host is described by direct Coulomb exchange, i.e., first-order perturbation effect. The direct Coulomb exchange is represented by the ferromagnetic Kondo Hamiltonian [9, 13–15, 22].

$$H_{\text{ex}} = -xN_0\alpha\langle S_{//}\rangle S_{//}$$

'xN_0' is the concentration of magnetic ions with mole fraction 'x', 'α' is the exchange constant for s electrons, and $\langle S_{//}\rangle$ is the average magnetic moment along the field direction. $N_0\alpha$ is the spin exchange integral for conduction band. The value of α is of the about ~0.2 eV for II–VI-based DMS.

2.2 Superexchange Interaction

Superexchange mechanism arises due to the spin-dependent kinetic exchange interaction between each of the two magnetic ions and the valence bands [13, 22]. The four virtual transitions from p-like valence band state to the ions and back to the valence band are schematically represented in Fig. 2. When a band electron is transferred to one of these ions, it leads to a hole in the valence band. So the intermediate state is having one magnetic ion with N and second with $N + 1$ electrons. Second

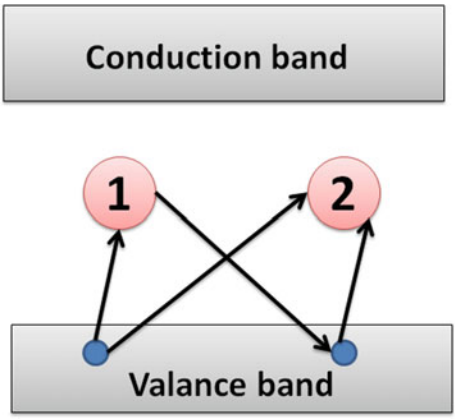

Fig. 2 Schematic representation of four virtual transitions of the superexchange ion–ion interactions [20]

transition arises another possibility with $N + 1$ electron on both ions and two holes in the valence band or one with $N + 1$ and $N - 1$ electrons and no holes in the valence band.

2.3 Double-Exchange Interaction

According to Zener, the double-exchange mechanism is the coupling between the magnetic ions in the different charge states by virtual hopping of the extra electron from one ion to another [13–15, 22]. In Mn^{2+}–Mn^{3+} system, the *d*-electron will hop between these ions through the *p*-orbitals.

2.4 RKKY (Ruderman–Kittel–Kasuya–Yoshida) Interaction

RKKY mechanism describes the exchange coupling between the magnetic impurity ion and the band electrons of the host semiconductor lattice. In a degenerated DMS, the interaction is described by *s-d* Kondo Hamiltonian—first-order perturbation effect [13, 14, 22]. The conduction electron gas gets magnetized by the magnetic ion, and the degree of polarization decreases in an oscillatory fashion with distance from the magnetic ion. This kind of indirect exchange coupling between the magnetic ions may lead to ferromagnetic or antiferromagnetic interaction depending upon the distance of separation of the interacting atoms. The coupling at a distance 'r' having Fermi surface (k_F) is

$$J_{RKKY}(r) \propto \frac{\mathrm{Cos}(2k_F r)}{r^3}$$

2.5 Impurity-Band Exchange and Bound Magnetic Polarons

The ferromagnetic exchange interactions between magnetic moments in n-type DMS are discussed based on its tendency to form shallow donors. Generally, DMS can be represented as $(A_{1-x}M_x)[O■]_n$; A non-magnetic cation, M = Magnetic ion, ■ = Donor defects and $n = 1$ or 2. An electron associated with a particular defect will be treated as a hydrogen atom, and the dimension of electron traps is therefore of the order of a few tenths of Å. Consider now the interaction of the magnetic cations M with the hydrogenic electrons in the impurity band. As a result, donors tend to form bound magnetic polarons by coupling the $3d$ moments. The cations present an extra random potential, which extends the localized region of the ions within their orbits [13, 23–26]. Overlap between a hydrogenic electron and the cations within its orbit leads to ferromagnetic exchange coupling between them [25, 26]. This interaction may be written in terms of the s–d exchange parameter J_{s-d} as [13].

$$J_{s-d} S.s |\psi(r)|^2 \Omega$$

where S is the spin of the $3d$ cations that have volume Ω, and s is the donor electron spin. Ferromagnetism in DMS arises due to percolation of bound magnetic polarons (Fig. 3). The coupled interaction between localized holes of the polarons and the transition metal producing an effective magnetic field hence aligns the spins. Below the Curie temperature, the neighboring polarons overlap forming clusters of polarons [13, 23–26]. Ferromagnetic transition is possible when the size of the cluster nearly matches the sample size. Despite the low carrier density bound magnetic polarons, the model is applicable to both n-type and p-type host materials.

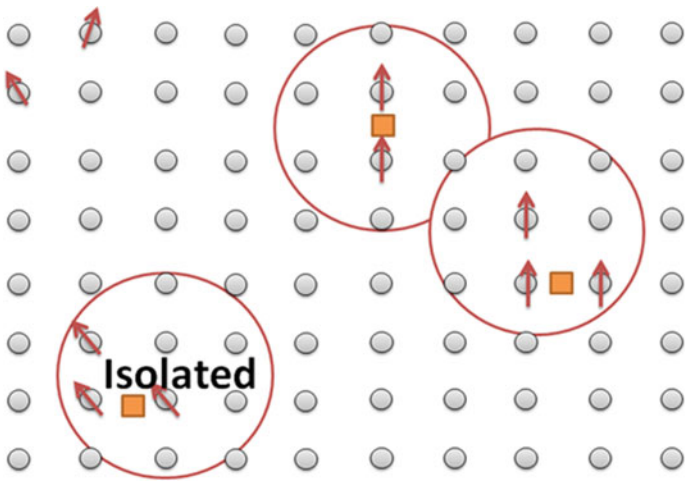

Fig. 3 Schematic representation of magnetic polarons with magnetic cation concentration $x = 0$. Cation sites are represented by small circles [23]

3 Brief Report on TM-Doped Semiconductors

Compared to non-oxide semiconductors, the oxide semiconductors have many advantages. So the wide band gap makes them transparent and also suitable for short-wavelength applications. II–VI group oxides can easily grow at low temperature. So the oxides grow on a plastic substrate and are ecologically safe and durable besides being low in cost. In addition, strong electronegativity of oxygen is expected to produce strong *p-d* exchange coupling between band carriers and localized spins, a prerequisite for DMS [13]. Some of the reports on oxide semiconductor-based DMS are summarized here.

3.1 TiO_2-Based DMS

TiO_2 has been extensively studied due to its unique properties, like high refractive index, excellent optical transmittance in the visible and near-infrared region, and high dielectric constant. TiO_2 crystallizes in three forms—rutile, anatase, and brookite. It has been shown by Matsumoto et al. [27] that the anatase form of TiO_2 doped with several percent of Co is ferromagnetic at room temperature. Films of $Ti_{1-x}Co_x$ O_2 with different x values were made on $LaAlO_3$ (001) and $SrTiO_3$ (001) single crystal substrates. Ferromagnetic long-range ordering was seen in anatase TiO_2 doped with 'Co' in the images taken by scanning superconducting quantum interference device (SQUID) microscope. An increase in spontaneous magnetization with the increase in Co content is observed. TiO_2 doped with Co shows room-temperature ferromagnetism, with magnetic moment of 0.32 μ_B/Co atom. Matsumoto et al. [27] agree that a possibility of Co clusters cannot be ruled out though XRD and TEM showed no sign of metal granules within the detection limit. In a later article, Matsumoto et al. state that room-temperature ferromagnetism exists in rutile phase of $Ti_{1-x}Co_xO_2$ with a moment of 1 μ_B/Co atom for 3% Co substitution. Chambers et al. [28] have grown $Ti_{1-x}Co_xO_2$ films by molecular-beam epitaxy on $SrTiO_3$ substrates having magnetic moment of 1.26 μ_B/Co atom for $x = 0.03$. Chambers et al. [28] also report that the cobalt distribution in their films depends strongly on growth conditions leading to some of their films being non-magnetic. From X-ray absorption spectroscopy measurements, they determine that in the magnetic films the cobalt ions are in the +2 oxidation state and substitute on the Ti site of TiO_2. TiO_2:Co transparent films grown on both $LaAlO_3$ (001) and $SrTiO_3$ (001) substrates by pulsed laser deposition (PLD) are reported by Stampe et al. [29] which show room temperature ferromagnetism (moment ~ 1.7 μ_B). Cobalt segregation was seen in TEM images. But Kim et al. [30] reported the origin of magnetism by 'Co' nanoclusters in epitaxial $TiCoO_2$ films. Magnetic Circular Dichroism (MCD) studies done on Co-doped anatase TiO_2 films also revealed MCD spectral line shape identical to Co metal [30]. Despite all this work, the key question remains to be answered is that if Co is indeed substitution or forms clusters to form ferromagnetic regions within the films?

3.2 SnO_2 Materials

SnO_2 is semiconductor with rutile structure having octahedral coordination similar to anatase TiO_2 [31]. The magnetic measurements revealed almost paramagnetic behavior without any ferromagnetic ordering. A few works were reported on Mn:SnO_2. PLD-grown Co-doped $SnO_{2-\delta}$ thin films showed room temperature ferromagnetism [32]. Co content in PLD-grown $Sn_{1-x}Co_xO_{2-\delta}$ films was higher due to high evaporation rate of Sn. The neighboring magnetic moments of cobalt matrix are unquenched so it shows giant magnetic moments. The origin of giant magnetic moment is still debatable, but the result seems to be promising to explore SnO_2-based DMS.

3.3 Importance of TM-Doped ZnO

The strong correlation of '3*d*' orbitals of transition metals with '*s*' and '*p*' orbitals of the anions can modify electronic structure of ZnO host lattice. ZnO-based DMS gained much attention owing to room-temperature ferromagnetic predictions by Diet et al. [15]. ZnO normally exhibits wurtzite structure, and TM elements have valence electrons in the partially filled *d* orbitals and in 4*s* orbitals. TM ions can incorporate into ZnO host lattice contributing its 4*s* electron to the s-p^3 bonding to give a TM^{2+} state.

Theoretical calculations on ZnO by Sato et al. [33] and Yoshida et al. [34] predicted ferromagnetism at 5% Mn doping without any additional dopants. In order to control electron carrier concentration in Mn-doped ZnO thin films, low-temperature process is preferred [35]. In contradictory [36, 37] to earlier reports, researchers achieved room-temperature ferromagnetism in Mn-doped ZnO [38, 39]. But its reproducibility is still controversial because magnetic properties are very sensitive to thin-film preparation conditions. Pulsed laser deposition has the following advantages such as deposition at relatively high oxygen pressure, high deposition rate, and growth of highly oriented crystalline films at relatively low substrate temperature. ZnO nanostructures were easily grown by hydrothermal and chemical methods. Due to catalyst-free, environmental friendliness, and less hazardous nature, hydrothermal techniques are widely used for large production of nanostructures. The incorporation of Mn^{2+} into hexagonal ZnO lattice even at relatively low temperatures is shown by phase diagram analysis with 13% solubility. Lattice constants of ZnO host lattice changes with increase of Mn content. Similarly, Zn^{2+} shows 10% solubility in MnO at 800 °C [40, 41]. Epitaxial ZnMnO thin films were grown on sapphire substrates at substrate temperatures in the range from 600 to 750 °C. The maximum solubility of Mn in ZnO films is 35%, which is higher than its bulk counterpart. But cobalt-doped ZnO thin films show two magnetic behaviors: a paramagnetic component and a low-field ferromagnetic component. Co-doped ZnO samples grown at high vacuum exhibit ferromagnetism because more oxygen vacancies are inducing free electrons which mediate the ferromagnetic exchange interaction. The formation of cobalt clusters

inhomogeneous film during the growth process favors in ferromagnetism [42]. Optical studies of Co-doped ZnO films show characteristic absorption peaks at 660, 615, and 568 nm. Depending on the growth conditions and preparation techniques, the band gap of Co:ZnO samples shows blue shift or red shift. ZnO films are color less, but $Zn_{1-x}Co_xO$ exhibits light green to dark green color with increase of Co concentration.

Early studies on Cu-doped ZnO system by various groups showed contradiction with each other showing non-magnetic and magnetic nature. Theoretical studies of 25% Cu-doped ZnO system showed non-magnetic behavior but at lower doping levels, 3.125 and 6.25% Cu on ZnO show ferromagnetic nature. Spin-polarized density functional calculations predict that certain ZnO:Cu structures should be ferromagnetic [15]. Under appropriate growth conditions, PLD-grown ZnO:Cu films show ferromagnetism [43]. Jin et al. [44] reported that ferromagnetism was not observed in Cu-doped ZnO thin films prepared by combinatorial laser molecular-beam epitaxy method. Recently, Buchholz et al. [45] reported non-ferromagnetic behavior in n-type Cu-doped ZnO and RTFM in p-type Cu-doped ZnO thin films. Ye et al. [46] theoretically showed that the energy of ferromagnetic state is lower than that of the antiferromagnetic state for Cu-doped ZnO (p-type and n-type) so we can achieve RTFM in this system. According to theoretical modeling, the relative position of copper atoms can strongly affect the magnetic properties of ZnO:Cu system. Some reports show that the stability of ferromagnetism in ZnCuO system depends on the copper atom separation. If copper atoms were separated by 5.20 Å along the c-axis, the ferromagnetic state was favored, but copper atoms were separated by 3.25 Å within the basal plane the antiferromagnetic state was favored. Sato's work looked consistent with other theoretical calculations and together establishing the importance of copper atom placement in the doping process [39]. The metallic copper is not magnetic, and neither Cu_2O nor CuO is ferromagnetic, so ZnO:Cu system is free of ferromagnetic precipitates. Ueda et al. [41] also investigated $Zn_{1-x}TM_xO$ films [n-type ($x = 0.05$–0.25): TM = Co, Mn, Cr, Ni] grown by PLD. The Co-doped ZnO films showed the maximum solubility limit of 30%. In $Zn_{1-x}Co_xO$, only a few films showed ferromagnetic features, while the others showed spin-glass-like behaviors. A few of them exhibited ferromagnetic behaviors with a Curie temperature higher than room temperature with lesser reproducibility. Here also ferromagnetism is directly related to the presence of oxygen vacancies. Detection limits of microstructural characterization will not overrule the possibilities of magnetic impurities like nanosized clusters, substitutional and interstitial impurities over the intrinsic magnetic nature of the thin films [42, 47–49]. In order to determine whether the magnetic atoms substituting into the ZnO host lattice are forming alloys or interstitial defects or impurities, researchers employ X-ray diffraction analysis, transmission electron microscopy, and X-ray absorption studies. It is very difficult to categorize the origin of the ferromagnetism which depends on the level of magnetic dopants. In addition, there are still extreme variations in the reported magnetic behavior with some films exhibiting only paramagnetism and even those with ferromagnetism showing a wide range of apparent Curie temperatures. So the origin of ferromagnetism is till debatable.

Compared to large number of publications on RTFM of Co/Mn-doped ZnO systems, only a few have reported in Ni-doped ZnO systems. But some of them were able to report intrinsic RTFM in Ni-doped ZnO DMS [50–53] or due to Ni clusters [47, 54]. In contradictory to above some reported paramagnetism in Ni-doped ZnO systems [48, 49], ferromagnetism is found only in inhomogeneous films supporting the formation of nickel clusters within the experimental detection limit. Ni:ZnO shows larger magnetism; it cannot be attributed by weak magnetization of nickel oxide. Wakano et al. reported ferromagnetism at 2 K, which becomes superparamagnetism at 30 K and maintain it up to 300 K for Ni:ZnO system [51]. The reported magnetic properties are discrepant, and the origin of ferromagnetism is still controversial.

4 Proposed Spintronic Devices

Spintronic devices came into action after the discovery of the 'giant magnetoresistance (GMR)' in 1988 by French and German physicists [55]. It is due to electron-spin effects in ultrathin 'multilayers' of magnetic materials, their electrical resistance changes with applied magnetic field. In GMR, a non-magnetic metal is sandwiched magnetic metals. The electrical resistance changes from small (parallel magnetizations) to large (antiparallel magnetizations) depending upon the relative magnetic orientations of the magnetic layers. The magnitude of this change is two orders of magnitude larger than is possible with conventional materials, hence the name 'giant magnetoresistance' [16]. IBM found that incorporating GMR materials in read heads would be able to sense much smaller magnetic fields, so hard disk storage capacity can increase from 1 to 20 Gb [56]. IBM launched GMR-based read heads, into the market in 1997. The advantage of magnetic random access memory (MRAM) is that it is 'non-volatile'—information is not lost when the system is switched off but it can be smaller and faster. MRAM devices use less power and would be much more robust in extreme conditions such as high temperature or high-level radiation or interference.

4.1 Overview of Spin-Based Devices and Its Applications

The realization of spintronic devices depends how we can create and control spin-polarized charge carriers in our existing semiconductors. This can be accomplished by optical pumping using appropriately polarized laser light. The working of spintronic devices outlined as: (1) information is stored into the particular spin orientations of spins (up or down), (2) it is attached to mobile electrons for carrying the information along a wire (3), and the information is read at the output terminal [21]. Spintronic devices are attractive for memory storage and magnetic sensor applications. Due to larger coherence length, it is a potential candidate for quantum computing where electron spin would represent information as qubit [17].

Semiconductor-based spintronic devices like to add the unique features of magnetic devices to our conventional electronic devices like field-effect transistors and light-emitting diodes [16, 57]. So the memory and microprocessor functions can be integrated into the same chip. The successful realization of most spintronic application depends critically on the ability to create spin-polarized charge carriers in a conventional semiconductor device. So the spin-polarized carriers can be injected from a spin-polarized source or effective spin-filtering at the interfaces. The spin injection from a conventional ferromagnetic metal into a semiconductor is highly inefficient than other methods. Using spin-polarized dilute magnetic semiconductor as our injector or by paramagnetic semiconductors at high magnetic field as a spin filter, we can successfully demonstrate spin injection in semiconductor tunnel diodes.

The most effective measurement of the quality of the oxide-based ferromagnetic materials will be in the operation of device structures, such as spin-field-effect transistors (FET) (Fig. 4), or photo-induced ferromagnets. Using ferromagnetic semiconductors as the injection source, one should directly measure the efficiency and spin transport length. ZnO-based test structure will exploit or demonstrate the novel aspects of ferromagnetism in the devices. (Zn, Mn)O is showing antiferromagnetic spin-glass-like insulating behavior, and Mn-Co-doped ZnO is having half-metallic ferromagnetic nature. The negative gate bias brings holes into (Zn, Mn)O, and it can be converted to half-metallic ferromagnetic state. Using ferromagnetic (Zn, Co)O as the source and drain contact material, it should be possible to have a 100% spin-polarized electron flow in the (Zn, Mn)O channel. Spin FET can be fabricated by growing source and drain on top of (Zn, Mn)O layer and etching away the selective region for the growth of gate oxide and deposition of the gate metal.

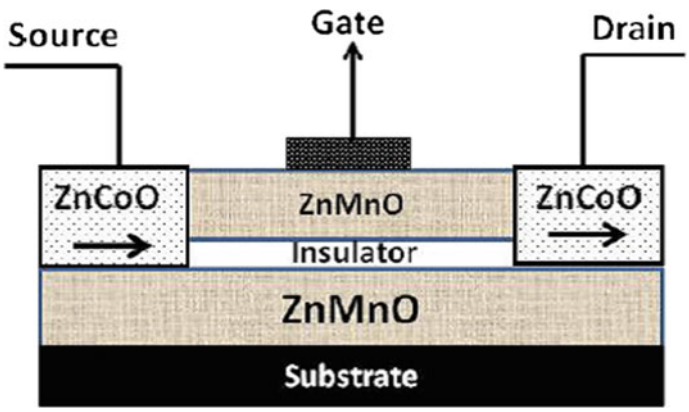

Fig. 4 Spin FET—single transistor non-volatile memory [6, 16, 57]

4.2 Co-Doped ZnO-Based Magnetic Tunnel Junctions

In order to study the effect of spin injection and spin polarized transports in spintronic devices TM doped ZnO based heterostructures have been developed [6, 16]. (Zn, Co)O used for fabrication of two FM electrodes and insulating ZnO layer as the barrier, because it allows the epitaxial growth of (Zn, Co)O layer [16, 57]. (Zn, Co)O/ZnO/(Zn, Co)O epitaxial structures (Fig. 5) satisfy two primary requirements for spin injection: a minimum conductance mismatch and high spin-polarized contacts [58]. Tunnel magnetoresistance (TMR) is expected to persist up to RT (room temperature) and exhibit high $V_{1/2}$ to overcome one of the main shortcomings of magnetic tunnel junctions (MTJs). In order to study the effect of spin injection and spin polarized transports in spintronic devices TM doped ZnO based heterostructure have been developed [6, 16] (Fig. 6).

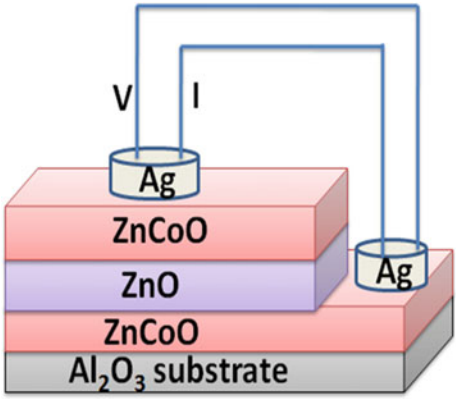

Fig. 5 Schematic representation of a (Zn,Co)O/ZnO/(Zn,Co)O junction [6, 16]

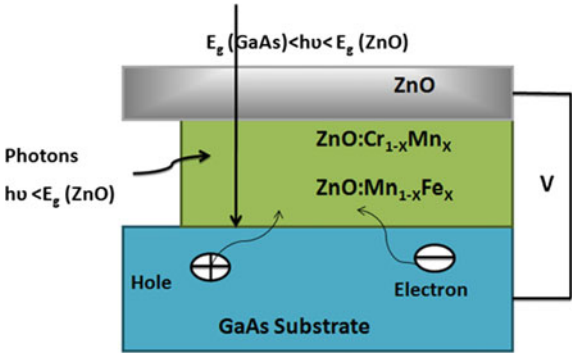

Fig. 6 Schematic of ZnO-based transparent photomagnet [57]

5 Theoretical and Experimental Hurdles in the Realization of RTFM in TMOs

A lack of stability and reproducibility prevents definitive conclusions from being drawn from much of the data on high-temperature ferromagnetism. It is often difficult to recover the same magnetic behavior in different laboratories or even within the same laboratory at different times. Furthermore, the ferromagnetic signals frequently prove to be transient, decaying in time over periods of days or months. Recent work on spintronic focuses on achieving higher transition temperature magnetic materials for technological applications. While the progress in synthesizing and controlling magnetic properties of group III-arsenide compound semiconductors has been astounding, the reported Curie temperatures are too low (~172 K) [15, 59] to have a significant practical impact. A key development that focused on wide band gap semiconductors as being the most promising for achieving high Curie temperatures was the work of Dietl et al. [24]. According to Zener model of ferromagnetism, they predict T_C values for several materials. The schematic diagram (Fig. 7) showing the predicted T_C values is given below [5, 15].

Carrier-mediated ferromagnetism on DMS depends on the nature of magnetic dopants carrier type, concentration and carrier density. When these systems approaching metal–insulator transition, carrier density is increased as result ferromagnetism is observed. They observed a gradual progression from localized states to itinerant electronic states as the carrier density increases. During metallic transition, the population density of some of the electrons can be extended while others can occupy the impurity states. The extended states become localized while crossing the metal–insulator boundary, and as a result, the localization radius decreases gradually. For interactions on a lengthy scale smaller than the localization length, the electron wave function remains extended. The long-range interactions between localized spins are

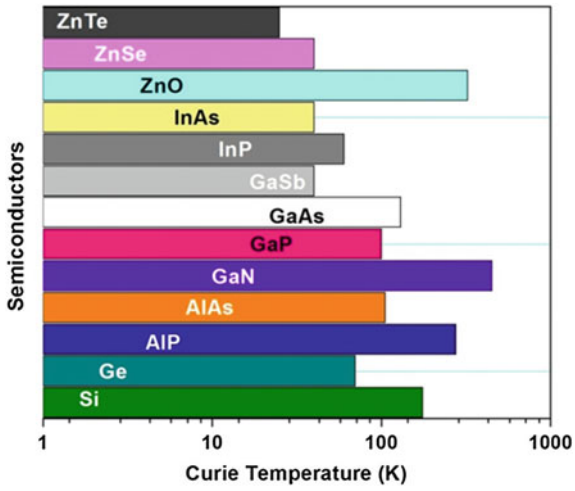

Fig. 7 Experimental prediction of ferromagnetism in various semiconductors [5]

possible due to holes in extended or weakly localized states. So the carrier-mediated ferromagnetic interactions may be possible for heavily doped semiconducting oxides. A lot of studies were on the electronic structure of the ZnO-based TMOs, and their interactions are done based on ab initio calculations or first principle studies [59–67].

(a) **Electronic structures of (Zn,TM)O (TM: V, Cr, Mn, Fe, Co, and Ni) in the self-interaction-corrected calculations**

Origin of magnetism in DMS is always a debatable one, so the electronic studies are a field of interest for the theoretical physicists' in DMS. Fukumura et al. [40] successfully grown Zn(Mn)O, after that a large number of experiments on ZnO-based DMS have been conducted by various groups across the world. But there is a markable discrepancy in the magnetic ground state and magnetic moments. Sometimes secondary phases or even nanoclusters were responsible for the experimental observable magnetic behavior in DMS. So one must be well aware of the growth parameters and the artifacts rose during structural and optical characterizations. Sometimes the observed ferromagnetism is mediated by holes in the valence band or by conduction electrons so the electric natures, oxidation states of the DMS are studied thoroughly. So the theoretical works like first principle studies have come into play. Toyoda et al. [65] calculated the electronic structures of ZnO-based dilute magnetic semiconductors within the self-interaction-corrected local density approximation (LDA). Their results are good agreement with earlier data calculated using standard local density approximation theory. We found that there are differences in the band gap energy, the energetic position of the Zn 3*d* bands, and the description of the transition-metal *d* bands [64–66].

The presence of self-interaction is the main short comings of LDA studies. So Toyoda et al. [65] carried out the calculations on ZnO-based DMS by using a self-interaction-corrected LDA approach. They also presented the systematic comparison of the electronic structures of ZnO-based DMS calculated within the self-interaction-corrected LDA and the standard LDA. The transition-metal 3*d* bands change more drastically, and a chemical trend is seen in the shapes of partial density of states (DOS) of those. In (Zn, V)O and (Zn, Cr)O, the 3*d* bands shift downward in energy by 1 eV, but still appear within the band gap as they are in LDA. According to standard LDA studies, the transition-metal d-density of states at the Fermi level plays an essential role for getting the ferromagnetic ordering in the ZnO-based DMS. The ferromagnetic ground state is stabilized through the double-exchange interaction and hopping of d-electrons. Extensive studies were done on (Zn, Co)O after the observation of room temperature ferromagnetism [68–71]. In LDA, the Fermi level lies in the gap of the tetrahedral-like crystal field splitting of the d-states, but due to the band broadening, d-density of states exists at the Fermi level. Compared to those calculated within the standard LDA (1), the larger band gap energy, (2) the Zn 3*d* bands are correctly separated from the valence band (3), and the qualitatively different descriptions of the transition-metal 3*d* states are obtained. These features, especially the description of the transition-metal 3*d* states, could affect the predicted magnetic properties [60, 64–66]. The researchers believed that in order to get useful

devices, we need to have single-phase dilute magnetic oxides, because the spin-polarized charger carriers transform the spin information. But multi-phase materials also found applications in magneto-optical devices.

The wide band gap semiconductor-based spintronic applications need the coupling between the ferromagnetism and the semiconducting properties. As initial results, at room temperature, ferromagnetic oxides were obtained in anatase and rutile-type TiO_2:Co [27–30]. Ferromagnetism in magnetically doped ZnO has been both predicted [5, 15] and observed [6–8, 23, 40, 41, 59–61, 68–71]. In addition to Mn doping and additional charge carriers, the ferromagnetic ordering occurs when the magnetic indirect exchange interaction is mediated by hole though the host valence band. This is also suggested to occur for Cr, Fe, Co, and Ni dopants [61]. The key aspect of Pearton et al. [60] work is to achieve soluble concentrations of the transition-metal ions well above their equilibrium solubility limit. In order to achieve this, we have to use non-equilibrium methods such as low-temperature epitaxy or ion implantation. In the remainder of this review, the detailed results for specific combinations of hosts and transition-metal ions will be discussed. Ferromagnetism appears in degenerated or non-degenerated semiconductors and in insulators, if the concentrations of $3d$ dopants are less than the threshold value required for nearest-neighbor cation coupling. The average moment per dopants cation approaches (or even exceeds) the spin-only moment at low dopants concentrations (x), and it falls progressively with increase of dopant concentration (x_p). Superexchange interaction, which is predominantly antiferromagnetic and short-ranged [13, 23], cannot be invoked because the magnetic order appears at concentrations of magnetic cations $x < x_p$. The ferromagnetic double-exchange mechanism, as described by Zener with reference to mixed-valence manganites, can produce large moments, but it is also a nearest-neighbor interaction that requires mixed cation valence, so that $3d_n \leftrightarrow 3d_{n+1}$ configuration fluctuations can occur. There is no evidence that mixed valence is a common feature of these dilute oxides. Longer-range ferromagnetic exchange can be mediated by carriers in a spin-polarized band.

A large number of reports on TM-doped ZnO DMS have been published during the last decade. Literately, a few research works were on V-, Cr-, Ti-doped ZnO-based DMSs compared to Co and Mn dopants [6, 38–44, 68, 72–75]. According to literature reviews, ZnO films doped with 5 at.% Co commonly exhibit much stronger RTFM than ZnO doped with other TM elements, because Co is more soluble in ZnO host lattice [6, 41–44, 68]. Room-temperature magnetic moments reported for 5 at.% TM-doped ZnO films are summarized in Fig. 8. In terms of concentration-dependent magnetization, the largest moments have been observed for ZnO doped with different TM concentrations, i.e., 2–5 at.% for Co [6, 41–44, 68, 76], 2 at.% for Mn [6, 38–41, 72–75], and 1 at.% for Ni and Cu [6, 40–44, 77]. According to these studies, ZnO films with higher dopants contents tend to show much lower magnetic moments. Therefore, besides ideal moment discrepancies for these TM ions in ZnO films, different solubility and different maximum dopants' concentration would also account for different magnetic moments in 5 at.% TM-doped ZnO films (Fig. 8).

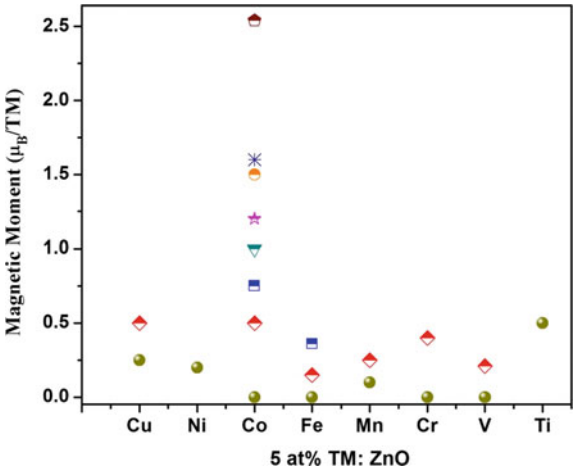

Fig. 8 Plots of magnetic moment per transition-metal cation (5 at.%) doped in ZnO thin films [6]

5.1 Experimental Limitations in Magnetic Measurements

Modern solid-state physics make use of sensitive magnetometry an essential tool to study the magnetic properties in ultrathin films and nanostructures. Recent developments and intensive magnetic measurements in the field of colossal magnetoresistance (CMR), tunneling magnetoresistance (TMR), anisotropic ferromagnetism, etc., pave way to studies which discuss the influence of artifacts in improper sample handling and residual magnetic signals in SQUID magnetometer. The magnetic measurements of thin films and powder samples are performed using Quantum Design SQUID magnetometer MPMS (XL). The wide acceptance of MPMS-SQUID is mainly due to its high degree of user-friendly automation and reliability, as well as the lack of commercial alternatives. SQUID magnetometer is one of the most sensitive experimental techniques used for high-sensitivity magnetic characterizations. But in practice, especially for thin-film samples, the magnetic signal recorded with a commercial MPMS-SQUID magnetometer is dominated by artifacts below 0.5×10^{-6} emu.

(a) **Artifices due to improper sample handling**

Normally, the precise magnetic measurements have been taken with an MPMS XL (5T) MPMS (XL) by Quantum Design [78, 79]. For all measurements, the reciprocating sample option (RSO) of the MPMS was used which offers a higher sensitivity than the standard DC transport. In Quantum Design SQUID magnetometer, we use drinking straw as the sample holder. Most of the researchers exclusively use the unit emu in their magnetic measurements. During low signal measurements, the absolute size of the overall signal determines how close magnetic signals are to artifact-level of the instruments.

In order to point out the magnetic anomalies due to improper sample, Ney et al. [79] have studied the hysteresis measurements of sapphire after cleaving. The raw

data show a clear discontinuity of the signal after passing the zero value. The step-like behavior with saturation magnetization is obtained after the subtraction of the diamagnetic background. The corresponding x-position of the measured magnetic moment is plotted. A big step is correlated with the kinks in the hysteresis curves [79]. Finally, the same sample was measured after intensive cleaning which demonstrates that the previous signal may from ferromagnetic contaminations due to improper sample handling. The signature of x-position is typical for edge contamination. During a measurement, the sample is moved along the pickup coils while the respective voltage is recorded. SQUID magnetometer uses fitting routine to correlate the amplitude and position of the signal from the sample to overview the possible shifts due to temperature or positional changes during the measurements.

Other kinds of artifacts occur when magnetic measurements on the non-homogeneous ferromagnetic sample on diamagnetic substrates are performed, viz. nanoparticles grown on substrate, magnetic ions implanted on thin films, or uneven distribution in samples prepared by lithography. Due to cleaving of the samples into suitable dimensions, the tendency of magnetic contamination at the edge also increases. Normally, we use a diamond stencil for cleaving in which a tiny piece of diamond attached to a stainless-steel rod. If this rod touches the edge of a very hard substrate material like sapphire or carbides, the chances of small particles of the metal which get abraded are very high. So we need a thorough cleaning of the substrates especially if sapphire or single crystals are used for thin-film deposition. In case of softer substrates, the situation is less critical because the cleaving does not produce any detectable ferromagnetic contaminations. It is better practice to use plastic or non-contaminative tweezers for sample handling to avoid unintentional magnetic contamination during film preparation and transferring it to SQUID system.

(b) **Artifices from the SQUID system**

SQUID itself will give artifacts which may lead to pick up wrong magnetic signals from samples other due its improper handling. In MPMS-SQUID, the actual magnetic field is merely determined by the voltage drop over a shunt resistor. The magnetic field of the magnetometer is measured by the voltage drop over two shunt resistors which account for different field ranges. So this magnetic field control has to be well calibrated on a regular basis using the manual from Quantum Design. In order to operate in wide field range of the MPMS, the instruments have two shunt resistors with respective amplifiers, both of which have to be calibrated to avoid discrepancies in the applied magnetic field. But a very careful calibration of both detection channels usually results more or less 1% of discrepancy between the actual magnetic fields in the two modes. The second calibration concerns the zero-current offset of the regulated power supply arrangement in the MPMS. Sometimes the FC/ZFC (field cooled/zero field cooled) measurements exhibit a negative magnetization after the diamagnetic background for the nominal field value of 10 mT has been subtracted [78, 79]. The magnetic field control of the SQUID can cause offset fields which lead to inverted hysteresis curves or FC/ZFC curves with negative magnetization values (even though a positive measuring field is applied). A residual misfit of about 1% remains typically and can cause artifacts at about 350 mT.

During the small signal measurements of DMS, the diamagnetic signal of the substrate dominates the weak ferromagnetic or superparamagnetic magnetic response at high magnetic fields. Typical substrate sizes lead to a diamagnetic response of the order of 10^4 emu at higher magnetic fields. Sometimes the real signal from the thin film is very small, but the total signal becomes larger with increasing magnetic field due to diamagnetic contributions from the substrate. Such a dynamic range can be accessed 'autoranging' option where the sensitivity range is selected automatically. In this mode, MPMS will adjust two different factors, which are termed 'gain' and 'range'. 'Gain' simply changes the gain of the voltmeter card by a multiplication factor. The 'range' refers the time constant of rf-amplifier integrator in the rf-SQUID. When there is a clear change in slope of the measured data, then the shunt resistors have to be re-calibrated for realistic data. So these kinds of artifacts are removed by subtracting a different diamagnetic background which is account for the different magnetic field scale.

(c) **Residual magnetic signals**

Normally, the magnetic measurement of crystals or thin films at different temperatures shows hysteresis loop, but it reveals a paramagnetic signal at low temperatures and high magnetic fields. The reduction of coercivity at low temperature is due to superimposition of paramagnetic contribution from the sample. The absence of a true ferromagnetic signal is inferred by the FC/ZFC curves which are not separated at any temperature. The residual magnetic signals also create artifacts during magnetic measurement sequences. The residual hysteresis can be attributed to residual magnetic flux trapped in the superconducting magnet. The residual magnetic flux is independent of the charging state, and it adds to the magnetic field but aligns with the direction of the overall field. So if one should use the magnet reset option during a sequence, we can detect very small residual signals.

The artifacts and limitations of a commercial MPMS-SQUID magnetometer demonstrate that the hysteresis measurements are only a necessary but not a sufficient criterion to prove the existence of ferromagnetism if the size of the signal is small. But the artifacts from contaminated cleave edges of the sample or misaligned magnetic field controls are easily ruled out. Although MPMS is a very versatile and convenient magnetometer but when a thin film on a substrate is inserted, imperfections of the sample mounting, size effects, possible contaminations, and especially the overall diamagnetic background of any used substrate make reliable detection of signals up to 0.5×10^{-6} emu.

5.2 Effect of Growth Parameters

Most of the reports and recent reviews are mainly focused on the enhancement of magnetic behavior of II–VI oxides and its dependence on preparation conditions such as the doping concentration, substrate temperature, and oxygen partial pressure [6, 9, 23–25, 42, 59–61, 68, 80, 81]. A few of them have directly investigated the

substrate-dependent magnetic behavior, substrate orientation and substrate temperature, deposition rate, etc. [6, 80–82]. In reality, most groups have focused on doping concentrations below the solubility limit to obtain true DMS. The different groups show distinct magnetic behaviors owing to the effects of the preparation method and growth parameters. So it is worth to evaluate the effect of dopants' concentrations on magnetization from a series of experiments.

(a) **Effect of substrates**

The most commonly used substrates for ZnO:TM thin films depositions are quartz [6, 72–74, 82, 83], Si [6, 84–88], Al_2O_3 [6, 42, 89–92], and ZnO [93–95]. The local structure and magnetization of ZnO:TM have direct dependence on experimental conditions, the preparation method, oxygen partial pressure, substrate temperature, etc. However, ZnO:TM films deposited on different substrates with the same deposition parameters show distinct magnetization. Sudakar et al. [96] showed that Cu (6 at.%)-doped ZnO films on quartz and sapphire substrates exhibit 1.6 and 1.2 μ_B/Cu magnetization at 300 K. Similarly, RTFM with a magnetic moment of 1.5 μ_B/Co atom was observed for $Zn_{0.95}Co_{0.05}O$ films deposited on ZnO substrate, but only weak FM signals were detected for films grown on Al_2O_3 [97]. This difference can be explained by different structural properties, and defect densities in the films arise due to difference in the crystalline nature of the substrates [6, 42, 68, 80, 81, 95–97]. Thus, it seems that the substrate most likely impacts the local 'TM' structure and magnetization of TM-doped ZnO due to defects in the film or at the boundaries. The magnetic moment of ZnO:Co thin film varies as 0.62, 0.66, and 0.24 μ_B/Co for films deposited on Al_2O_3, Si, and NaCl single crystal, respectively. So it is clear that crystalline nature of substrate has a direct influence on the magnetic behavior of Co-doped ZnO films. ZnO:Co thin films deposited on glass substrate does not exhibit any RTFM [82]. Normally, the diamagnetic background of the substrate has been subtracted from all of the magnetization data, indicating that the difference in moments in ZnO:Co films does not arise from the substrate. It is worth pointing out that reorganization of the defects could partly occur due to the comparatively weak polarization of the SiO_2 piezoelectric substrate, leading to a lower moment per Co atom in Co-doped ZnO film, e.g., 1.1 μ_B/Co. Although the Co dopant exists in a '+2' state when substituting for Zn^{2+}, randomly distributed defects would lead to very weak moments or no RTFM in Co-doped ZnO films on other single substrates (e.g., Al_2O_3, Si, and NaCl) and glass substrate, respectively [82]. $Zn_{0.962}Co_{0.038}O$ films deposited on $LiTaO_3$(1 1 0), (0 1 2) and (0 1 8) substrates by DC reactive magnetron co-sputtering exhibited different magnetization of 1.21, 2.42, 0.65 μ_B/Co, respectively. It is likely that the magnetization differences for Co-doped ZnO films on three oriented $LiTaO_3$ substrates can be attributed to the film microstructure and the Co–O bond length, which primarily depends on mismatch between the film and the different oriented substrates [6, 95–98]. Some of the works on Co-doped ZnO thin films show that the boundary between film and substrate is the defect formation region which in turn affects the magnetization [6, 60, 68, 82, 95–98]. According to a large volume of reviews and repots, we can easily conclude that the substrate, its

crystalline nature, and orientation strongly affect the magnetization of TM-doped ZnO films to certain extents.

(b) **Influence of post-annealing and formation of secondary phases**

Annealing has a direct impact on the microstructure of the thin films with reduction or enhancement of defects with respect to the annealing atmosphere. Some of the experimental results of ZnO:TM systems on annealing demonstrate that magnetism have direct dependence on intrinsic defects like vacancy of oxygen V_O and zinc interstitial Zn_i. Normally, the magnetization of ZnO:TM thin films or nanocrystals annealed in vacuum or a reducing atmosphere should be enhanced [6, 60, 68, 74, 77, 83, 86, 89, 92, 99–108]. It is mainly due to the introduction of V_O [6, 68, 74, 83, 89, 92, 100, 103, 105] or Zn_i, which are critical for RTFM in TM-doped ZnO [6, 68, 86, 92, 101, 105, 107, 109]. The free electrons of the host are locally trapped by these defects which occupy an orbital overlapping with the 'd' shells of TM neighbors to form a bound magnetic polaron(BMP), which in turn accounts for the intrinsic RTFM in DMS. Annealing of Co-doped ZnO films in air and Zn vapor atmosphere, Kittilstved et al. [107] demonstrated reversible cycling of saturated magnetic moments in ZnO:Co thin films. The microstructure and magnetic properties of $Zn_{0.92}Co_{0.08}O$ films annealed at different temperatures (200, 400, and 600 °C) in vacuum and air were systematically investigated by Liu et al. [105]. At same annealing temperature, the magnetic moment increased at vacuum and decreased at ambient air conditions. The vacuum-annealed film shows saturation magnetization (M_S) of approximately 0.45 μ_B/Co, which is slightly greater than for the as-grown film (0.34 μ_B/Co), whereas the value for the air-annealed film (0.21 μ_B/Co) is much lower than Ms of the as-grown film. But annealing at higher temperature normally improves the crystal quality and a corresponding decrease in structural defects in the film as a result the defect mediated magnetism also reduces. On the other hand, annealing in air at high temperature (≥600 °C) TM^{2+} ions may segregate from the crystal and form secondary impurity phases or metal precipitates, which will reduce the RTFM. So we can conclude that low temperature and reducing atmosphere favor the defects formation and enhance FM ordering.

(c) **Comparison of experimental works on ZnO doped with TMs**

A large number of reports on TM-doped ZnO have been published in the last decade. Most of the research groups mainly focus on Co- [6, 41, 68, 82, 83, 92, 98, 105, 107, 110] and Mn-doped ZnO films [6, 38–41, 72–75]. The dopants used to attain room-temperature ferromagnetism in ZnO are shown in Fig. 9. Transition-metal ions show different thermal solubility in ZnO host lattice. Co and Mn show much higher thermal solubility limits than those of Ti, V, Cr, Fe, Ni, and Cu [6, 41–44, 68]. ZnO films doped with 5 at.% TM commonly exhibit much stronger RTFM than ZnO doped with other TM elements. This is consistent with results obtained by Ueda et al. [41] and Venkatesan et al. [110] for ZnO doped with a series of TM elements; such studies can exclude the influence of the preparation parameters on magnetic ordering. It is evident that ZnO films doped with different TMs exhibit RTFM with different M_S values, as well as very small magnetic moments indicating negligible

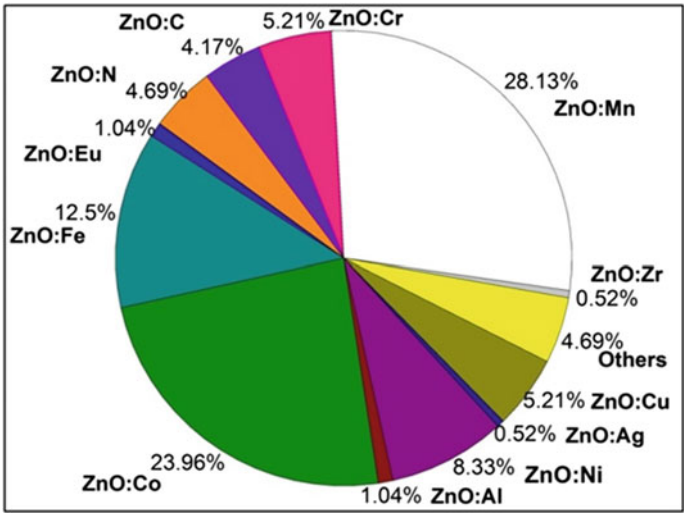

Fig. 9 Pie chart of ZnO-based DMS with different TM dopants [6, 41–44]

FM. Normally, the TM-doped ZnO films are either conducting or semiconducting, as characterized by strong coupling between localized d-electrons of the TM ions and the extended s and p carriers of ZnO. So we can spin-polarize the carriers as a result FM ordering of magnetic moments of TM ions can maintained in the oxide lattice. Some groups showed RTFM with an inverse correlation between magnetization and electron density. So the intrinsic RTFM of TM-doped ZnO systems always remains an open question for the research community.

(d) **Effect of co-doping in magnetic properties**

As per above discussions, earlier works show that the RTFM in ZnO:TM can be enhanced by the increase of the carrier concentration by controlling the experimental parameters like decrease of deposition pressure, low-temperature deposition, post-annealing, etc. In contradiction to this, some researchers have reported that the creation of free carriers is not a sufficient condition for RTFM [73, 76]. Some groups also reported the RTFM in the absence of free carriers [6, 23, 80, 90, 111–115]. If the carrier concentration can enhance RTFM or there is a relation between them, researches use co-doping to generate additional electrons/holes. ZnO is intrinsically n-type semiconductor [89, 93, 116–120], whereas N, Li, and Cu are used for hole doping [119, 121–124]. So these studies show that the increase of carrier concentrations by additional dopants can enhance the RTEM. Ivill et al. [117] designed a series of experiments on (Mn, Sn)-Co-doped ZnO with varying Sn concentration (0–0.1 at.%). But they found an inverse correlation between magnetization and electron density, as a function of the Sn doping. This phenomenon is most consistent with the bound magnetic polaron (BMP) model in which bound acceptors mediate FM doping. RTFM arises with increase of donor defects or electron carrier concentrations,

but these two factors coexist in most doped ZnO systems and are hard to distinguish. Similarly, Al doping in the $Zn_{0.95}Co_{0.05}O$ thin film, implying a decrease in crystalline quality and an increase in structural defects on inclusion of a trace amount of Al [119], in turn enhances the magnetic moment per Co ion of ZnO:Co films. Normally, the co-dopants could trigger other defects, which in turn enhance the FM but the concentration of the co-dopants plays crucial role. Ueda et al. [41] showed that ZnO:Co system exhibits ferromagnetic nature above 280 K for 5–25% Co and 1% Al, without any secondary phases or clusters. After the theoretical predictions [1–3, 5–7, 14, 15], most of experimental works have proved the existence of room temperature ferromagnetism in Mn, Co, Ni, and Cu-doped ZnO, but the nature and origin of room temperature ferromagnetism (RTFM) is still debatable.

5.3 Growth and Characterization of PLD-Grown ZnO:TM Thin Films

$Zn_{1-x}TM_xO$ thin films (TM: Mn/Co/Ni/Cu) were grown on fused silica substrates by pulsed laser deposition (PLD) technique. The fourth harmonic of Nd:YAG laser (266 nm) with repetition rate of 10 Hz and pulse width 6–7 ns was used for ablation. The ablation was carried out at laser energy density of 1.1 J cm^{-2}. $Zn_{1-x}TM_xO$ thin films with various TM concentrations were grown at different substrate temperature (350–650 °C) and oxygen pressure 0.05–5 × 10^{-4} mbar. The deposition duration was 1 h resulting a film thickness ~200 nm. XRD pattern of TM-doped ZnO and pure ZnO thin films deposited at 450 °C on fused silica substrate show the characteristic peak of ZnO corresponding to the wurtzite structure of the ZnO. No trace of secondary phases or binary zinc transition-metal phase is observed within the detection limit of XRD.

The colors of $Zn_{0.95}Mn_{0.05}O$, $Zn_{0.95}Co_{0.05}O$, $Zn_{0.95}Ni_{0.05}O$, and $Zn_{0.95}Cu_{0.05}O$ film becomes, respectively, yellowish, greenish blue, light green, and light blue with the incorporation of TMs. Ni- and Co-doped ZnO shows predominant visible d-d transitions in the tetrahedral geometry (Fig. 10). The Co have absorption around 1.89, 2.03 and 2.19 eV corresponding to $^4A_2(F) \rightarrow {}^2A_1(G)$, $^4A_2(F) \rightarrow {}^4T_1(P)$ and $^4A_2(F) \rightarrow {}^2E_1(G)$ d-d transitions respectively which are in agreement with the one observed in Co^{2+}. The Ni-doped ZnO thin films show absorptions around 2.10, 2.26, and 2.39 eV, the corresponding d-d transitions $^3A_2(G) \rightarrow {}^3T_2(G)$, $^3A_2(G) \rightarrow {}^3T_1(G)$, and $^3A_2(G) \rightarrow {}^3T_1(P)$. The band gap of $Zn_{1-x}Mn_xO$ and $Zn_{1-x}Co_xO$ thin films shows blue shift, while $Zn_{1-x}Cu_xO$ and $Zn_{1-x}Ni_xO$ shows red shift compared to pristine ZnO. The Burstein–Moss effect and sp-d exchange interaction are responsible for the observed blue and red shift in the TM-doped ZnO thin films. The s-d and p-d exchange interactions will give negative and positive corrections to conduction band and valence band of the host semiconductors, and it leads to band shrinking [33]. In heavily doped semiconductors, the donor electrons occupy the bottom of the conduction band, and it will in turn block the low energy transitions, which provide

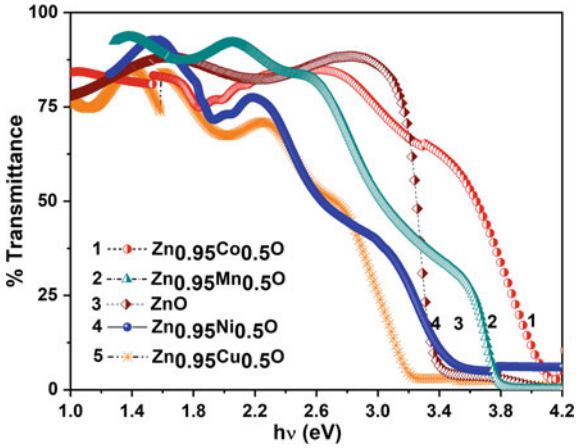

Fig. 10 Transmission spectra of $Zn_{1-x}TM_xO$ films for $x = 0.05$

the band gap widening and is known as Burstein–Moss shift [125]. The character of the band gap becomes more indirect with the addition of Co/Mn. The increase of carrier concatenation in Mn- and Co-doped ZnO thin films was confirmed by Hall measurements.

Raman scattering is one of the effective techniques to investigate the crystallization, structure, and defects in the thin films. The non-polar E_2 modes of ZnO have two frequencies, namely E_2^{high} and E_2^{low}, associated with the motion of oxygen atoms along with zinc. The Raman spectra of the $Zn_{0.95}TM_{0.05}O$ thin films (Fig. 11) show three predominant modes at (99 cm^{-1}), E_2^{low}, (435 cm^{-1}) E_2^{high}, and E_1^{LO}(585 cm^{-1}). All the $Zn_{1-x}TM_xO$ films have spectra similar to ZnO, indicating that the wurtzite structure is not changed with the TM doping [126–130]. The boarding of the E_2^{high} modes and its red shift indicates the substitution of TM into the ZnO sublattice [129–134].

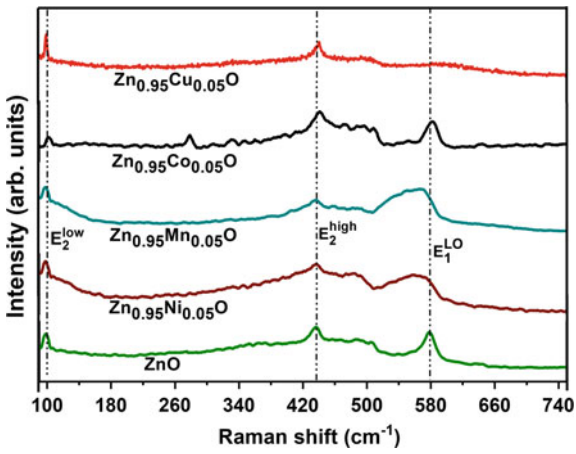

Fig. 11 Room-temperature Raman spectra of $Zn_{0.95}TM_{0.05}O$ films (TM = Mn/Co/Ni/Cu)

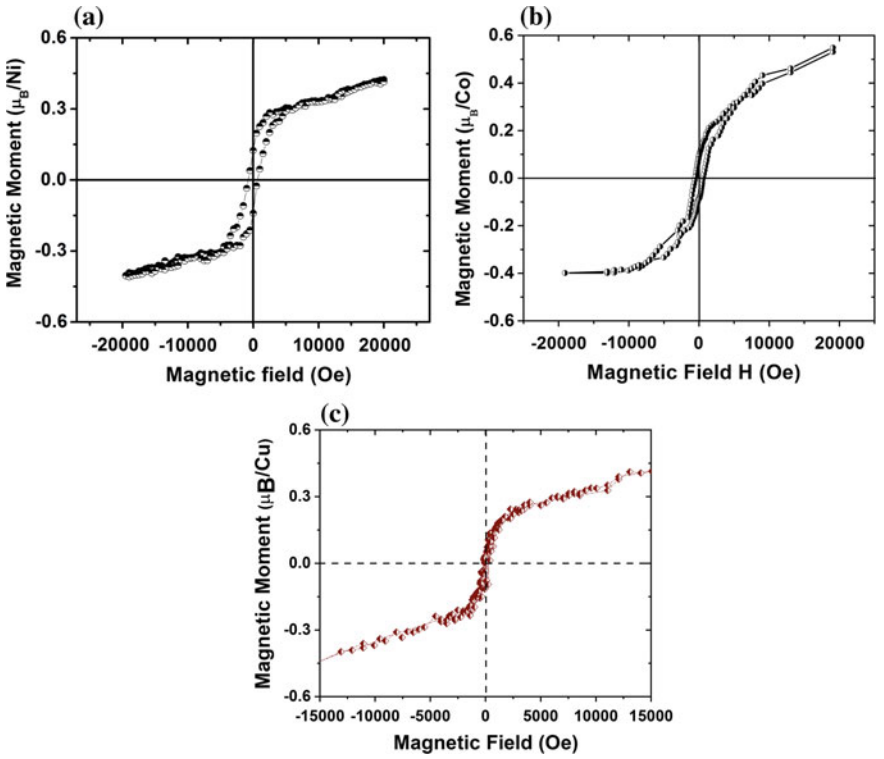

Fig. 12 Room-temperature M-H curve of **a** $Zn_{0.97}Ni_{0.03}O$, **b** $Zn_{0.95}Co_{0.05}O$ and **c** $Zn_{0.97}Cu_{0.03}O$ films

M-H curve of the $Zn_{0.97}Ni_{0.03}O$ (a), $Zn_{0.95}Co_{0.05}O$ (b), and $Zn_{0.97}Cu_{0.03}O$ (c) thin films at 300 K (Fig. 12). The curve shows the room-temperature ferromagnetism for the entire TM-doped ZnO thin films [18–20]. The saturation magnetic moment of $Zn_{0.95}Co_{0.05}O$ thin film is 0.42 μ_B/Co atom. Similarly, $Zn_{0.97}Ni_{0.03}O$ and $Zn_{0.97}Cu_{0.03}O$ thin films show saturation magnetization of 0.28 μ_B/Ni atom and 0.24 μ_B/Cu atoms, respectively. But the pristine ZnO thin films grown by PLD show diamagnetic nature. The shape of the curve reveals that there is some trace of paramagnetism in $Zn_{0.95}Co_{0.05}O$ thin film also. According to Ruderman–Kittel–Kasuya–Yoshida (RKKY) theory, the magnetism is due to the exchange interaction between local spin-polarized electrons and conduction electrons. The spin polarization of the conduction electrons in ZnO films performs an exchange interaction with spin-polarized electrons of other TM ions. The magnetization increases in the films, when the oxygen partial pressure during the deposition of the films decreases, due to the formation of defects or increased carrier concentrations [6, 9, 35, 41, 68, 73–75, 83, 115, 117, 120, 135, 136]. $Zn_{0.97}TM_{0.03}O$ thin films prepared at 450 °C and 0.05 mbar oxygen pressure show lower saturation magnetization than one prepared at 5×10^{-4} mbar pressure. Higher oxygen pressure results in less oxygen vacancies

and reduces the carrier concentration. This supports the assumption that magnetism is due to the exchange interaction between local spin-polarized electrons and conduction electrons. At higher concentrations, the TM clusters and transition-metal oxides suppress the room-temperature ferromagnetism in $Zn_{1-x}TM_xO$ thin films and paramagnetism is observed [6, 35, 73, 74, 83, 92, 115]. X-ray diffraction pattern, Raman spectra, and XPS measurements overruled the formation of secondary phases in $Zn_{1-x}TM_xO$ films within the experimental detection limit.

5.4 Growth of ZnO:TM Nanostructures by Hydrothermal Technique

ZnO nanoparticles can be prepared on a large scale by low-cost simple solution-based methods, such as chemical precipitation [137, 138], sol-gel synthesis [139], and solvothermal/hydrothermal reaction [140–142]. The advantages of low-cost hydrothermal process are catalyst-free growth, large area production, and eco-friendly. The existence of RTFM in Cu-/Ni-/Mn-doped ZnO is visualized by various groups [6, 35, 73–75, 83, 120, 143–146]. But the origin of ferromagnetism is still debatable whether it is due to the formation of impurity phases or clusters during the growth process [6, 41, 68, 115, 147]. The hydrothermal synthesis of ZnO and ZnO:TM nanostructures and the effect of TM concentration on the structural, optical, morphological, and magnetic properties have been reported from our laboratory [148, 149].

(a) **Growth parameters**

Pristine ZnO and ZnO:TM nanostructures were grown by hydrothermal method. An appropriate amount of ammonium hydroxide was added to the mixture of zinc acetate (0.3–1 M) and copper acetate or nickel acetate or manganese acetate (0.001–0.1 M) solution to maintain the pH value around 11. ZnO:TM nanostructures were synthesized hydrothermally at 150 °C for 3 h by keeping the concentration of $Zn(CH_3COO)_2$ as 1 M in all reactions, while the concentration of $TM(CH_3COO)_2$ was varied from 0.001 M to 0.1 M. The molarity of TM in nanostructures is varied by adjusting the concentrations of zinc acetate and TM acetate precursors. After the reaction was complete, the resulting solid products were washed with methanol, filtered, and then dried in air in a laboratory oven at 60 °C.

(b) **Characterizations**

Phase purity of hydrothermally grown pristine and TM-doped ZnO shows wurtzite phase without any impurity phases within the experimental detection limit. All samples show diffraction pattern match with the reported ICSD data [150]. SEM images of pristine ZnO- and TM-doped ZnO nanostructures prepared using 0.05 M $TM(CH_3COO)_2$ in the precursor solution at 150 °C for 6 h are shown in Fig. 13. SEM images confirm the formation of ZnO nanostructures and are assembled like

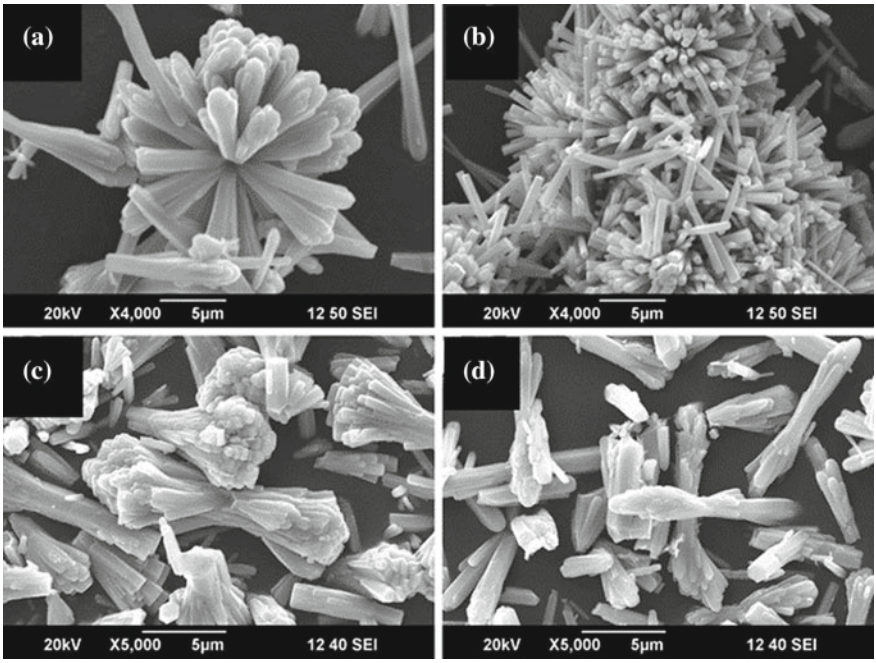

Fig. 13 SEM images of pristine ZnO and ZnO:TM nanostructures synthesized at 150 °C for 6 h **a** pristine ZnO and ZnO doped with 0.05 M, **b** $Cu(CH_3COO)_2$, **c** $Mn(CH_3COO)_2$, **d** $Ni(CH_3COO)_2$ in the precursor solution

branched structures. The 'TM' doping changes the morphology, and we get uniformly elongated nanorods in the form of bunches.

The band gap of ZnO:TM nanostructures shows red shift with increase of TM doping. The red shift shown by transition-metal-doped II–VI semiconductors is due to '*s-d*' and '*p-d*' exchange interactions between the band electrons of the host lattice and localized d-electrons of substituted magnetic impurities. Diouri et al. [151] and Bylsma et al. [152] had theoretically explained the mechanism behind '*s-d*' and '*p-d*' exchange interactions using second-order perturbation theory attributed to band gap narrowing. The red shift of the band gap confirms the substitution of TM into the ZnO lattice, and the band gap narrowing is due to the exchange interactions [152–154]. Figure 14 shows the photoluminescence spectra of ZnO:TM nanostructures ($\lambda_{exc} = 325$ nm). ZnO:Cu nanostructures have two emission bands, an ultraviolet (UV) emission band at 370 nm and a broad orange-red emission centered at 630 nm [155]. Other TM (Mn/Ni)-doped ZnO nanostructures have PL spectra similar to pristine ZnO nanostructures. But the UV emission is attributed to the near-band-edge free-exciton transition [156]. Green and yellow emissions are the most commonly observed defect emissions in ZnO nanostructures [157, 158]. The green emission is attributed to oxygen vacancies or zinc interstitials [159]. Yellow defect emission is

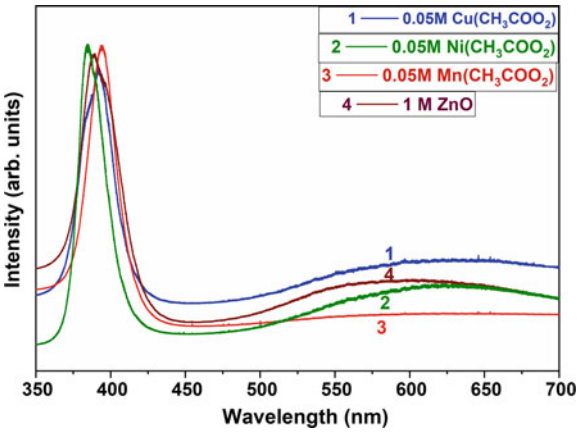

Fig. 14 Room-temperature PL spectra (λ_{exc}= 325 nm) of ZnO:TM nanostructures synthesized at 150 °C for 3 h with 0.05 M TM concentration

typically attributed to oxygen interstitials [160]. The intensity of the green–yellow-related emission due to defect was found to be dependent also on the nanowire diameter [157]. Cu impurities have been proposed as origin of the green emission in Cu-doped ZnO materials [161]. According to Fan et al. [162], ZnO dendritic wires and nanosheets show visible emission components centered at ~540 and ~610 nm.

Characteristics of Raman modes E^2_{low}(100 cm^{-1}), second phonon line-2 E^M_2(332 cm^{-1}), A^{TO}_1(380 cm^{-1}), E^2_{high} (437 cm^{-1}), and A^{LO}_1(580 cm^{-1}) of TM-doped ZnO nanostructures are shown in Fig. 15. The slight broadening of the E^2_{high} modes and its red shift from the bulk value indicates the substitution of TM ions into the ZnO sublattice [126–134]. Structural disorders, crystal defects, and enhanced residual stress are responsible for the observed peak broadening and mode shifts in TM-doped ZnO nanostructures.

The field-dependent magnetization curve of ZnO:TM (TM = Cu, Mn, Ni) nanostructures at 300 K is shown in Fig. 16. The noticeable coercivity of M-H loops

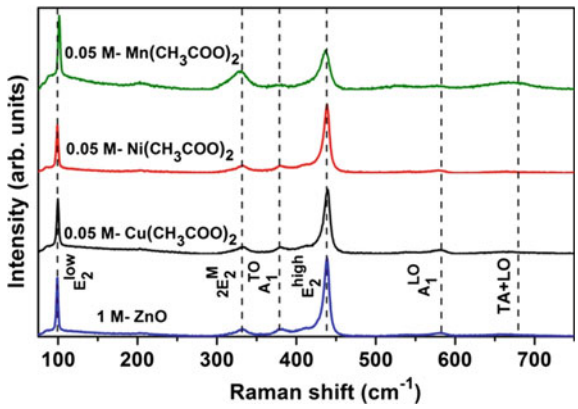

Fig. 15 Raman spectra of ZnO:TM nanostructures synthesized at 150 °C for 3 h with 0.05 M TM concentration

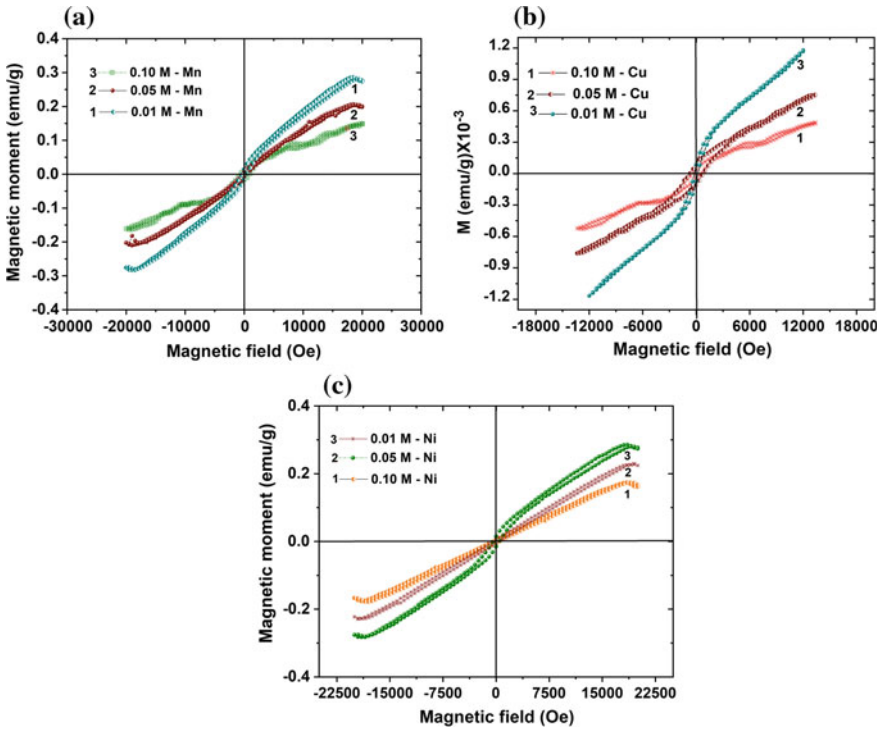

Fig. 16 Room-temperature M-H loop of ZnO:TM nanostructures with various concentrations of TM doping

could be attributed to strong ferromagnetism at room temperature. The ferromagnetic behavior of nanostructures imputed to the presence of small magnetic dipoles located at the surface of nanostructures. So the nearest-neighbor interactions can make the magnetic dipoles of neighboring dipoles oriented along the direction of the applied magnetic field. Surface-to-volume ratio is large for nanostructures; as a result, the population of oriented magnetic dipoles will increase at the surface. At higher TM doping concentrations enhanced antiferromagnetic interaction between neighboring TM-TM ions suppress the ferromagnetism. The hysteresis loop of ZnO:TM nanostructures was not saturated, so we one can expect some traces of paramagnetism. Origin of magnetism in DMSs is still controversial; the most common mechanism for observed ferromagnetism in ZnO:TM nanostructures is the carrier-induced ferromagnetism (RKKY mechanism), often reported for DMSs [6, 35, 68, 74, 83, 92, 149]. Secondary phases or clusters are even responsible for the observed magnetic nature. The broadening and the shift of (97) peaks in the XRD pattern confirm the incorporation of TM ions into the ZnO lattice X-ray diffraction, and Raman spectra analysis could not find any cluster or secondary phase formation in ZnO:TM nanostructures.

5.5 *Origin of Ferromagnetism in ZnO-Based DMSs*

Before elucidating the mechanisms of intrinsic RTFM, it must first be confirmed whether the magnetic hysteresis loops measured are intrinsic or extrinsic. Magnetic contamination [68], measurement errors [78, 79], and secondary phases [6, 68, 92] are all possibilities for FM signals. Both metals and their oxides have been identified as being responsible for FM behavior in TM-doped ZnO films, such as Co [6, 41, 68], Mn [6, 163], CoFe [6], CoO [6, 68], Co_3O_4 [6, 68, 92, 115], Fe_3O_4 [6], and CuO [6]. These types of TM-doped ZnO films are not genuine DMS. However, these non-magnetic semiconductors with embedded secondary FM phases may exhibit an anomalous Hall effect (AHE) [6], which was previously considered an indicator of whether a doped sample was a DMO or not. AHE was observed in FM ZnO and in non-FM Cu-doped ZnO films, indicating that AHE does not uniquely demonstrate FM behavior [6, 164]. Therefore, checking for basic experimental reproducibility, in addition to carrying out careful characterizations, is highly warranted.

(a) **Co-doped ZnO**

It has been examined that ferromagnetic interactions may originate from Co_3O_4 like secondary phases in ZnCoO system [165]. Sharma et al. [166] reported the carriers mediated mechanism in Co-doped ZnO-based DMS material. 'Double exchange' [167] and 'mean field Zener model' [168] have also been reported as the possible mechanisms for ferromagnetism in this composition. In addition, it was also detected that ferromagnetism in this system might arise because of simple substitution of 'Co' at Zn sites [169] or oxygen vacancies [170]. More recently, Zhang [169] expected that Al substitution played a crucial role to achieve the ferromagnetic behavior through first principle calculations. Hence, the origin of RT ferromagnetic interactions in ZnO-based DMSs has remained controversial among research community and still required further studies for its clarification. The controversies among researchers suggest that ferromagnetic behavior and its origin in DMSs depend on composition, synthesis conditions, annealing parameters, and additional dopants for varying the concentration of carriers as well. Moreover, origin of room temperature ferromagnetism can only be clarified when prepared materials will be free from any impurity or secondary phases. So we need to synthesize phase pure DMSs to explore its magnetic properties and mechanisms.

(b) **Mn-doped ZnO**

It has been observed that ferromagnetic behavior in ZnO:Mn materials may originate from the Mn_3O_4 like secondary phases [163]. But recently, Yang and co-workers [171] observed that origin of room temperature ferromagnetic interactions could not be derived from any secondary or impurity phase. Mn substitution at Zn sites in ZnO structure might be the main reason for existence of this ferromagnetism. According to the RKKY theory [172], this ferromagnetism arises from the magnetic exchange interactions between conduction electrons and local spin-polarized electrons (for instance, the electrons of Mn^{2+}). Free charge carriers, i.e., electrons, play crucial role

in establishment of magnetic phase and consequently the ferromagnetic behavior in magnetic element-doped ZnO [173–175].

(c) **Ni-doped ZnO**

According to RKKY theory [176], the presence of exchange interactions among conduction electrons and local spin-polarized carriers (as electrons of Ni^{2+} ions) is the main reason of ferromagnetism in DMS materials. Secondary phases or interactions among two magnetic atoms like Ni-Ni [177] might also be responsible for ferromagnetism. Moreover, vacancy [178] and carrier's induced magnetism [179–181] have also been reported for Ni-doped ZnO. On the other hand, it was also observed that ferromagnetism in these materials was independent of carrier concentration.

(d) **Magnetic behavior of pure ZnO**

Transition-metal-doped ZnO is one of the most studied systems due to its predicted ferromagnetic transition temperature above room temperature [5, 15]. However, the experimental findings from different groups are sometimes vastly contradictory. While many groups report room temperature ferromagnetism of Co-doped ZnO [6, 41, 68, 83, 92], there are many other groups reporting the absence of ferromagnetism or suppression of RTFM with Co-doping [6, 10–12, 115]. This suggests that the properties of these materials are highly process-dependent and the origins of ferromagnetism in these materials are still under debate. It has been shown very recently that intrinsic ferromagnetism is observed in pure TiO_2 and ZnO thin films and nanostructures. There is a lot of discussion going on about the extrinsic and the intrinsic origins of ferromagnetism in TM-doped oxide semiconductors. Using magnetic measurements and magnetotransport studies, Sayak et al. [115] showed that the doping with transition metal is not a prerequisite for observing magnetic moments in ZnO thin films. Also they emphasize the fact that the doping of the transition metal in the ZnO matrix in fact lowers the magnetic moment of the pure ZnO film [92]. They tuned the intrinsic magnetic moment in pure ZnO film by appropriate oxygenation. In the magnetoresistance data for the undoped film, a clear change of sign is observed, which clearly indicates that there is change in the intrinsic property of the sample between before and after the oxygen treatment. Again magnetotransport results support the magnetization data which suggest that pristine ZnO is a better candidate for room-temperature semiconductor spintronic devices than Co-doped ZnO.

6 Summary

Dilute magnetic semiconductors are useful materials for future spintronic applications due to semiconducting host lattice and half-metallicity. But most of DMS shows low Curie temperatures. In this article, we have discussed the origin of ferromagnetism and correlated it with ab initio calculations for the electronic and magnetic properties of transition-metal-doped ZnO semiconductors. Most of the results point

of the existence of DMS with different magnetic interactions. In systems with localized majority d-states deep in the valence band, the ferromagnetism is induced by Zener's p-d exchange interaction, leading to holes in the majority p-valence band. At higher TM concentrations, the Curie temperature is reduced due to enhanced antiferromagnetic interactions via superexchange interactions. In systems with impurity bands in the band gap (heavily doped systems), the ferromagnetism is driven by Zener's double-exchange, magnetic polarons, or RKKY interactions. Here the magnetic coupling is strong, but it is short-ranged. A way to achieve higher Curie temperatures might be to try to increase the impurity concentration without forming secondary or binary compounds. Recently, A. Tiwari's groups have realized a prototype spintronic device [182]. A lot of groups have produced contradictory results, and all these lead to the conclusion that the realization of the spintronic device needed a careful preparation and device formation technique. The future of spintronic device is really big, so the technological revolution will be unfolded to mankind in a few decades (Table 1).

Table 1 Summary of method of synthesis and properties of selected DMS

Obtained morphology	Fabrication method	Magnetic state	Magnetization	Proposed theories	References
Nanoparticles	Forced hydrolysis	Weak RTFM	0.2 to ~1.5 memu/g	Zn interstitials and O vacancies induced by annealing enhanced magnetization	[183]
Nanopowder	Mechanical milling and annealing	RTFM	3 memu/g	Zn vacancies at grain surface	[184]
Nanoparticles	Mechanical milling	RTFM		Zinc vacancies	[185]
Nanorods	Chemical vapor deposition (high temperature)	RTFM	0.031 emu/g	Single-ionized oxygen vacancies for BMPs (EPR and PL analysis)	[186]
	Chemical bath deposition (low temperature)		0.06 emu/g		
Nanoparticle pellet	Annealing in oxygen	Diamagnetism	–	Zn vacancy + OH bonding complex results in a net magnetization	[187]
	Annealing in hydrogen	Weak RTFM	0.7 emu/g		

(continued)

Table 1 (continued)

Obtained morphology	Fabrication method	Magnetic state	Magnetization	Proposed theories	References
Nanoparticle	Solution route and annealing in N_2, Ar, and O_2	RTFM	1.5 memu/g	Singly ionized oxygen vacancies	[188]
Nanowire	Vapor transport	RTFM	0.0076 μ_B / V_o	Oxygen vacancies	[185]
Nanowire	Hydrothermal and annealing in air and O_2	RTFM	1 memu/g	Singly ionized oxygen vacancies	[189]
Nanorod	Wet chemical	RTFM	1.5 memu/g	Size effect; singly ionized oxygen vacancies	[190]
Nanoparticles	Wet chemical method	RTFM	1.5 memu/g	Singly ionized oxygen vacancies	[182]
Nanorod array	Hydrothermal and annealing in H_2 and O_2	RTFM	0.15 emu/g	Oxygen vacancies	[191]
Nanowire	Chemical vapor deposition	Weak RTFM	0.2 memu/g	Surface defects and dynamic exchange between O_2 and O_2	[192]
	Pulsed laser vaporization	Diamagnetism	–		
Nanoparticles and nanorods	Chemical method	RETM with super paramagnetism	1.75 emu/g	Inhomogeneities created due to NPs	[193]

References

1. Service RF (1997) Science 276:895
2. Bangall DM, Chen YF (1997) Appl Phys Lett 70:2230
3. Chen YF, Bangall DM (1997) J Appl Phys 84:3912
4. Djurisic AB, Leung YH (2006) Small 2:944
5. Ohno H (1998) Science 281:951
6. Pan F, Song C, Liu XJ, Yang YC, Zeng F (2008) Mater Sci Eng Res 62:1–35
7. Singh S, Thiyagarajan P, Kant KM, Anita D, Thirupathiah S, Rama N, Tiwari B, Kottaisamy M, Rao MSR (2007) J Phys D Appl Phys 40:6312–6327
8. Ozgur U, Alivov YI, Liu C, Teke A, Reshchikov MA, Dogan S, Avrutin V, Cho SJ, Morko H (2005) J Appl Phys 98:041301
9. Pearton SJ, Heo WH, Ivill M, Norton DP, Steiner T (2004) Semicond Sci Technol 19:R59–R74
10. Tanaka M (1998) J Vac Sci Technol, B 16:2267
11. Ohtomo A, Kawasaki M, Koida T, Masubuchi K, Koinuma H, Sakurai Y, Yoshida Y, Segawa Y (1998) Appl Phys Lett 72:2466
12. Matsukura F, Ohno H, Schen A, Sugawara Y (1998) Phys Rev B 57:R2037

13. Morkoc H, Ozgur U (2009) Zinc oxide fundamentals, materials and device technology. Wiley-VCH Verlag GmbH & Co. KGaA, Weinheim
14. Wolf SA, Awschalom DD, Buhrman RA, Daughton JM, von Molnar S, Roukes ML, Chtchelkanova AY, Treger DM (2001) Science 294:1488
15. Dietl T, Ohno H, Matsukura F (2000) Science 287:1019
16. Sarma SD (2001) Am Sci 89:516
17. King SL, Gardeniers JGE, Boyd IW (1996) Appl Surf Sci 96:811
18. Gao PX, Lao CS, Hughes WL, Wang ZL (2005) Chem Phys Lett 408:174
19. Yang HY, Lau SP, Yu SF, Abiyasa AP, Tanemura M, Okita T, Hatano H (2006) Appl Phys Lett 89:011103–11111
20. Li C, Fang G, Su F, Li G, Wu X, Zhao X (2006) Nanotechnology 17:3740
21. Arun Aravind A, Jayaraj MK, Kumar M, Chandra R (2013) Appl Surf Sci 286:54–60
22. Blundell S (2001) Magnetism in condensed matter. Oxford University Press, New York
23. Coey JMD, Venkatesan M, Fitzgerald CB (2005) Nat Mater 4:173
24. Dietl T, Spalek JJ (1983) Phys Rev B 28:1548–1563
25. Angelescu DE, Bhatt RN (2002) Phys Rev B 65:075211
26. Durst AC, Bhatt RN, Wolff PA (2002) Phys Rev B 65:235205
27. Matsumoto Y, Murakami M, Shono T, Hasegawa T, Fukumura T, Kawasaki M, Ahmet P, Chikyow T, Koshihara SY, Koinuma H (2001) Science 291:854
28. Chambers SA, Thevuthasan S, Farrow RFC, Marks RF, Thiele JU, Folks L, Samant MG, Kellock AJ, Ruzycki N, Ederer DL, Diebold U (2001) Appl Phys Lett 79:3467
29. Stampe PA, Kennedy RJ, Yan X, Parker JS (2002) J Appl Phys 92:7114
30. Kim JY, Park JH, Park B-G, Noh HJ, Oh SJ, Yang JS, Kim DH, Bu SD, Noh TW, Lin HJ, Hsieh HH, Chen CT (2003) Phys Rev Lett 90:017401-
31. Kimura H, Fukumura T, Kawasaki M, Inaba K, Hasegawa T, Koinuma H (2002) Appl Phys Lett 80:94
32. Ogale SB, Choudhary RJ, Buban JP, Lofland SE, Shinde SR, Kale SN, Kulkarni VN, Higgins J, Lanci C, Simpson JR, Browning ND, Das Sarma S, Drew HD, Greene RL, Venkatesan T (2003) Phys Rev Lett 91:077205
33. Sato K, Yoshida HK (2001) Jpn J Appl Phys 40:L334
34. Yoshida HK, Sato K (2003) Phys B 327:337
35. Sharma P, Gupta A, Rao KV, Owens FJ, Sharma R, Ahuja R, Guillen JMO, Johansson B, Gehring GA (2003) Nature Mater 2:673
36. Fukumura T, Kawasak M (2001) Appl Phys Lett 78:958
37. Kim SS, Moon JH, Lee BT, Song OS, Je JH (2004) J Appl Phys 95:454
38. Pradha K, Zhang K, Mohanty S (2005) Appl Phys Lett 86:152511
39. Chang YQ, Wang DB, Luo XH (2002) Appl Phys Lett 83:4020
40. Fukumura T, Jin C, Ohtomo A, Koinuma H, Kawasaki M (1999) Appl Phys Lett 75:3366
41. Ueda K, Tabata H, Kawai T (2001) Appl Phys J Appl Phys 39:988
42. Kim JH, Kim H, Kim D, Ihm YE, Choo WK (2002) J Appl Phys 92:6066
43. Chakraborti D, Narayan J, Prater JT (2007) Appl Phys Lett 90:062504
44. Jin Z, Fukumura T, Kawasaki M, Ando K, Saito H, Yoo YZ, Murakami M, Matsumoto Y, Hasegawa T, Koinuma H (2001) Appl Phys Lett 78:3824
45. Buchholz DB, Chang RPH, Song JH, Ketterson JB (2005) Appl Phys Lett 87:082504
46. Ye JD, Gu SL, Qin F, Zhu SM, Liu SM, Zhou X, Liu W, Hu LQ, Zhang R, Shi Y, Zheng YD, Ye YD (2005) Appl Phys A 81:809
47. Mao X, Zhong W, Du Y (2008) J Magn Magn Mater 320:1102
48. Bodker F, Hansen MF (2000) J Magn Magn Mater 221:32
49. Yin Z, Chen N (2005) J Magn Magn Mater 135:430
50. Lu JJ, Lin TC, Tsai SY, Mo TS, Gan KJ (2011) J Magn Magn Mater 323:829
51. Ma L, Ma S, Chen H, Ai X, Huang X (2011) Appl Surf Sci 257:10036
52. Samanta K, Arora AK, Katiyar RS (2011) J Appl Phys 110:043523
53. Hu YM, Wang CY, Lee SS, Han TC, Chou WY, Chen GJ (2011) J Ramanspec 42:434
54. Li T, Qiu H, Wu P (2007) Thin Solid Films 515:3905

55. Baibich MN, Broto JM, Fert A, Nguyen Van Dau F, Petroff F, Etienne P, Creuzet G, Friederich A, Chazelas J (1988) Phys Rev Lett 61:2472
56. Parkin SS (1995) Gaint magnetoresistance in magnetic nanostructures. In: Wessels BW (ed) Annual review of materials science, vol 25. Annual Reviews Inc., Palo Alto, CA, p 357
57. Sato K, Yoshida HK (2001) Materials research society symposium proceedings, vol 666, F4.6.1
58. Ramachandran S, Prater JT, Sudhakar N, Kumaer D, Narayan J (2008) Solid State Commun 145:18
59. Dietl T, Ohno H, Matsukura F (2001) Phys Rev B 63:195205
60. Gacic M, Jakob G, Herbort C, Adrian H (2007) Phys Rev B 75:205206
61. Sato K, Yoshida HK (2000) Jpn J Appl Phys 39:L555
62. Akai H, Dederichs PH (1993) Phys Rev B 47:8739
63. Filippetti A, Spaldin NA (2003) Phys Rev B 67:125109
64. Yun SY, Cha GB, Kwon Y, Cho S, Hong SC (2004) J Magn Magn Mater 272–276:e1563–e1564
65. Toyoda M, Akai H, Sato K, Yoshida HK (2006) Phys B 376–377:647
66. Chien CH, Chiou SH, Guo GY, Yao YD (2004) J Magn Magn Mater 282:275–278
67. Pemmaraju CD, Archer T, Hanafin R, Sanvito S (2007) J Magn Magn Mater 316:e185
68. Ivill M, Pearton SJ, Rawal S, Leu L, Sadik P, Das R, Hebard AF, Chisholm M, Budai JD, Norton DP (2008) New J Phys 10:065002
69. Lee HJ, Jeong S-Y, Cho CR, Park CH (2002) Appl Phys Lett 81:18
70. Samanta K, Bhattacharya P, Katiyar RS (2006) Phys Rev B 73:245213
71. Prellier W, Fouchet A, Mercey B (2003) J Phys Condens Matter 15:R1583–R1601
72. Yang SG, Pakhomov AB, Hung ST, Wong CY (2002) IEEE Trans Magn 38:2877
73. Sharma P, Gupta A, Owens FJ, Inoue A, Rao KV (2004) J Magn Magn Mater 282:115
74. Aravind A, Jayaraj MK, Kumar M, Chandra R (2012) Mater Sci Eng B 177:1017
75. Ma JG, Liu YC, Mu R, Zhang JY, Lu YM, Shen DZ, Fan XW (2004) J Vac Sci Technol B 22:94
76. Alaria J, Bieber H, Colis S, Schmerber G, Dinia A (2006) Appl Phys Lett 88:112503
77. Chambers SA, Droubay TC, Wang CM, Rosso KM, Heald SM, Schwartz DA, Kittilstved KR, Gamelin DR (2006) Mater Today 9:28
78. Abraham DW, Frank MM, Guha S (2005) Appl Phys Lett 87:252502
79. Ney A, Kammermeier T, Ney V, Ollefs K, Ye S (2008) J Magn Magn Mater 320:3341–3346
80. Song C, Geng KW, Zeng F, Wang XB, Shen YX, Pan F, Xie YN, Liu T, Zhou HT, Fan Z (2006) Phys Rev B 73:024405
81. Janisch R, Gopal P, Spaldin NA (2005) J Phys Condens Matter 17:R657
82. Song C, Zeng F, Geng KW, Liu XJ, Pan F, He B, Yan WS (2007) Phys Rev B 76:045215
83. Aravind A, Hasna K, Jayaraj MK, Kumar M, Chandra R (2014) Appl Phys A 115:843
84. Herng TS, Lau SP, Yu SF, Chen JS, Teng KS (2004) J Magn Magn Mater 315:107
85. Lin YH, Ying M, Li M, Wang X, Nan CW (2007) Appl Phys Lett 90:222110
86. Khare N, Kappers MJ, Wei M, Blamire MG, Macmanus-Driscoll JL (2006) Adv Mater 18:1449
87. Zhang YB, Liu Q, Sritharan T, Gan CL, Li S (2006) Appl Phys Lett 89:042510
88. Herng TS, Lau SP, Yu SF, Yang HY, Ji XH, Chen JS, Yasui N, Inaba H (2006) J Appl Phys 99:086101
89. Tuan AC, Bryan JD, Pakhomov AB, Shutthanandan V, Thevuthasan S, McCready DE, Gaspar D, Engelhard MH, Rogers JW Jr, Krishnan K, Gamelin DR, Chambers SA (2004) Phys Rev B 70:054424
90. Dinia A, Schmerber G, Pierron-Bohnes V, Mény C, Panissod P, Beaurepaire E (2005) J Magn Magn Mater 286:37
91. Li XL, Wang ZL, Qin XF, Wu HS, Xu XH, Gehring GA (2008) J Appl Phys 103:023911
92. Ghoshal S, Anil Kumar PS (2008) J Magn Magn Mater 320:L93
93. Zheng Y, Boulliard JC, Demaille D, Bernard Y, Pétroff JF (2005) J Cryst Growth 274:156
94. Mandal SK, Das AK, Nath TK, Karmakar D (2006) Appl Phys Lett 89:144105

95. Nielsen K, Bauer S, Lubbe M, Goennenwein STB, Opel M, Simon J, Mader W, Gross R (2006) Phys Stat Sol A 203:3581
96. Sudakar C, Thakur JS, Lawes G, Naik R, Naik VM (2007) Phys Rev B 75:054423
97. Kioseoglou G, Hanbicki AT, Sullivan JM, van'TErve OMJ, Li CH, Erwin SC, Mallory B, Yasar M, Petrou A, Jonker BT (2004) Nat Mater 3:799
98. Liu XJ, Song C, Yang PY, Zeng F, Pan F (2008) Appl Surf Sci 254:3167
99. Park SY, Kim PJ, Lee YP, Shin SW, Kim TH, Kang JH (2007) Adv Mater 19:3496
100. Hsu HS, Huang JCA, Huang YH, Liao YF, Lin MZ, Lee CH, Lee JF, Chen SF, Lai LY, Liu CP (2006) Appl Phys Lett 88:242507
101. MacManus-Driscoll JL, Khare N, Liu Y, Vickers ME (2007) Adv Mat 19:2925
102. Lee S, Shon Y, Lee SW, Hwang SJ, Lee HS, Kang TW, Kim DY (2006) Appl Phys Lett 88:212513
103. Ramachandran S, Narayan J, Prater JT (2006) Appl Phys Lett 88:242503
104. Song C, Pan SN, Liu XJ, Li XW, Zeng F, Yan WS, He B, Pan F (2007) J Phys Condens Matter 19:176229
105. Liu XJ, Song C, Zeng F, Wang XB, Pan F (2007) J Phys D Appl Phys 40:1608
106. Schwartz DA, Gamelin DR (2004) Adv Mater 16:2115
107. Kittilstved KR, Schwartz DA, Tuan AC, Heald SM, Chambers SA, Gamelin DR (2006) Phys Rev Lett 97:037203
108. Chambers SA (2006) Surf Sci Rep 61:345
109. Kundaliya DC, Ogale SB, Lofland SE, Dhar S, Metting CJ, Shinde SR, Ma Z, Varughese B, Ramanujachary KV, Salamanca-riba L, Venkatesan T (2004) Nat Mater 3:709
110. Venkatesan M, Fitzgerald CB, Lunney JG, Coey JMD (2004) Phys Rev Lett 93:177206
111. Coey JMD, Douvalis AP, Fitzgerald CB, Venkatesan M (2004) Appl Phys Lett 84:1332
112. Liu H, Zhang X, Li L, Wang YX, Gao KH, Li ZQ, Zheng RK, Ringer SP, Zhang B, Zhang XX (2007) Appl Phys Lett 91:072511
113. Song C, Zeng F, Geng KW, Wang XB, Shen YX, Pan F (2007) J Magn Magn Mater 309:25
114. Behan AJ, Mokhtari A, Blythe HJ, Score D, Xu X-H, Neal JR, Fox AM, Gehring GA (2008) Phys Rev Lett 100:047206
115. Ghoshal S, Anil Kumar PS (2008) J Phys Condens Matter 20:192201
116. Norton DP, Pearton SJ, Hebard AF, Theodoropoulou N, Boatner LA, Wilson RG (2003) Appl Phys Lett 82:239
117. Ivill M, Pearton SJ, Norton DP, Kelly J, Hebard AF (2005) J Appl Phys 97:053904
118. Xu XH, Blythe HJ, Ziese M, Behan AJ, Neal JR, Mokhtari A, Ibrahim RM, Fox AM, Gehring GA (2006) New J. Phys. 8:135
119. Liu XJ, Song C, Zeng F, Pan F (2007) J Phys Condens Matter 19:296208
120. Tiwari A, Snure M, Kumar D, Abiade JT (2008) Appl Phys Lett 92:062509
121. Han SJ, Song JW, Yang CH, Park SH, Park JH, Jeong YH, Rhie KW (2002) Appl Phys Lett 81:4212
122. Hong NH, Brize V, Sakai J (2005) Appl Phys Lett 86:082505
123. Jayakumar OD, Gopalakrishnan IK, Kulshreshtha SK (2006) Adv Mater 18:1857
124. Yan W, Sun Z, Liu Q, Li Z, Shi T, Wang F, Qi Z, Zhang G, Wei S, Zhang H, Chen Z (2007) Appl Phys Lett 90:242509
125. Kim KJ, Park YR (2001) Appl Phys Lett 81:1420
126. Scott JF (1970) Phys Rev B 2:1209
127. Porto SPS, Krishnan RS (1967) J Chem Phys 47:1009
128. Ricchter H, Wang ZP, Ley L (1981) Solid State Commun 39:625
129. Ko HJ, Chen YF, Zhu Z, Hanada T, Yao T (2000) J Cryst Growth 208:389
130. Arnold MS, Avouris P, Pan ZW, Wang ZL (2003) J Phys Chem B 107:6599
131. Manjon FJ, Mari B, Serrano J, Romero AH (2005) J Appl Phys 97:053516
132. Wang XB, Song C, Geng KW, Zeng F, Pan F (2007) Appl Surf Sci 253:6905
133. Hu YM, Wang CY, Lee SS, Han TC, Chou WY (2010) Thin Solid Films 519:1272
134. Hu YM, Wang CY, Lee SS, Han TC, Choub WY, Chen GJ, Raman J (2011) Spectroscopy 42:434

135. Kodama RH, Makhlouf SA, Berkowitz AE (1997) Phys Rev Lett 79:1393
136. Calderon MJ, Sarma SD (2007) Annals Phys 322:2618
137. Zhong QP, Matijevic E (1996) J Mater Chem 3:443
138. Lingna W, Mamoun M (1999) J Mater Chem 9:2871
139. Bahnemann DW, Kormann C, Hoffmann MR (1987) J Phys Chem 91:3789
140. Hui Z, Deren Y, Xiangyang M, Yujie J, Jin X, Duanlin Q (2004) Nanotechnology 15:622
141. Zhang J, Sun LD, Yin JL, Su HL, Liao CS, Yan CH (2002) J Mater Sci Lett 14:4172
142. Li WJ, Shi EW, Zheng YQ, Yin ZW (2001) J Mater Sci Lett 20:1381
143. Lee CY, Tseng TY, Li SY, Lin P (2006) J Appl Phys 99:024303
144. Guo S, Du Z, Dai S (2009) Phys Stat Sol B 246:2329
145. Cheng ZX, Wang XL, Dou SX, Ozawa K, Kimura H, Munroe P (2007) J Phys D Appl Phys 40:6518
146. Ankiewicz AO, Gehlhoff W, Martins JS, Pereira S, Pereira S, Hoffmann A, Kaidashev EM, Rahm A, Lorenz M, Grundmann M, Carmo MC, Trindade T, Sobolev NA (2009) Phys Stat Sol B 246:766
147. Andriotis AN, Menon M (2011) Phys Stat Sol B 248:2032
148. Aneesh PM, Cherian CT, Jayaraj MK, Endo T (2010) J Ceramic Soc Jpn 118:333
149. Aravind A, Jayaraj MK, Kumar M, Chandra R (2012) J Mater Sci Mater Electron 24:106–112
150. ICSD. Number 086254
151. Diouri J, Lascaray JP, El Amrani M (1985) Phys Rev B 31:7995
152. Bylsma RB, Becker WM, Kossut J, Debska U (1986) Phys Rev B 33:8207
153. Gamelin DR (2002) J Am Chem Soc 124:15192
154. Radovanovic PV, Gamelin DR (2003) Phys Rev Lett 91:157202
155. Dai L, Chen XL, Wang WJ, Zhou T, Hu BQ (2003) J Phys Condens Matter 15:2221
156. Wang H, Wang HB, Yang FJ, Chen Y, Zhang C, Yang CP, Li Q, Wong SP (2006) Nanotechnology 17:4312
157. Huang MH, Mao S, Feick H, Yan H, Wu Y, Kind H, Weber E, Russo R, Yang P (2001) Science 292:1897
158. Meng XQ, Shen DZ, Zhang JY, Zhao DX, Lu YM, Dong L, Zhang ZZ, Liu YC, Fan XW (2005) Solid State Commun 135:179
159. Liu X, Wu X, Cao H, Chang RPH (2004) J Appl Phys 95:3141
160. Greene LE, Law M, Goldberger J, Kim F, Johnson JC, Zhang Y, Saykally RJ, Yang P (2003) Angew Chem 115:3030
161. Garces NY, Wang L, Bai L, Giles NC, Halliburton LE, Cantwell G (2002) Appl Phys Lett 81:622
162. Fan HJ, Scholz R, Kolb FM, Zacharias M (2004) Appl Phys Lett 85:4142
163. Wang HB, Wang H, Zhang C, Yang FJ, Yang CP, Gu HS, Zhou MJ, Li Q, Jiang Y (2009) Mater Chem Phys 113:884
164. Prestgard MC, Tiwari A (2014) Appl Phys Lett 104:122402
165. Zhou X, Ge S, Yao D, Zuo Y, Xia Y (2008) Phys B 403:3336
166. Sharma VK, Xalxo R, Varma GD (2007) Crys. Res. Tech. 42:34
167. Li BB, Shen HL, Zhang R, Xiu XQ, Xie Z (2007) Chin Phys Lett 24:3473
168. Yang JH, Zhao LY, Ding X, Yang LL, Zhang YJ, Wang YX, Liu HL (2009) Mater Sci Eng B 162:143
169. Zhang XM, Mai W, Zhang Y, Ding Y, Wang ZL (2009) Solid State Commun 149:293
170. Singhal RK, Arvind S, Xing YT, Sudhish K, Dolia SN, Deshpande UP, Shripathiand T, Saitovitch EB (2010) J All Comp 496:324
171. Yang T, Li Y, Zhu MY, Li YB, Huang J, Jin HM, Hu YM (2010) Mater Sci Eng B 170:129
172. Sharma VK, Xalxo R, Varma GD (2007) Cryst Res Tech 42:34
173. Singh S, Rama N, Rao R (2006) Appl Phys Lett 88:222111
174. Kittilstved KR, Norberg NS, Gamelin DR (2005) Phys Rev Lett 94:147209
175. Kittlstved KR, Liu WK, Gamelin DR (2006) Nat Mater 5:291
176. Tong LN, He XM, Han HB, Hu JL, Xia AL, Tong Y (2010) Sol Stat Comm 150:1112
177. Huang GJ, Wang JB, Zhong XL, Zhou GC, Yan HL (2007) J Mater Sci 42:6464

178. Yu Z, Ge S, Zuo Y, Wang G, Zhang F (2010) Appl Surf Sci 256:5813
179. Pei G, Xia C, Cao S, Zhang J, Wu F, Xu J (2006) J Magn Magn Mater 302:340
180. Cheng C, Xu G, Zhang H, Luo Y (2008) Mater Lett 62:1617
181. Xu Q, Schmidt H, Zhou S, Potzger K, Helm M, Hochmuth H, Lorenz M, Setzer A, Esquinazi P, Meinecke C, Grundmann M (2008) Appl Phys Lett 92:082508
182. Xu X, Xu C, Dai J, Hu J, Li F, Zhang S (2013) J Phys Chem C 116:8813
183. Rainey K, Chess J, Eixenberger J, Tenne DA, Hanna CB, Punnoose A (2014) J Appl Phys 115:17D727
184. Ghose S, Sarkar A, Chattopadhyay S, Chakrabarti M, Das D, Rakshit T, Ray SK, Jana D (2013) J Appl Phys 114:073516
185. Phan TL, Zhang YD, Yang DS, Nghia NX, Thanh TD, Yu SC (2013) Appl Phys Lett 102:072408
186. Xu X, Xu C, Lin Y, Li J, Hu J (2013) J Phys Chem C 117:24549
187. Xue X, Liu L, Wang Z, Wu Y (2014) J Appl Phys 115:033902
188. Liu W, Li W, Hu Z, Tang Z, Tang X (2011) J Appl Phys 110:013901
189. Xing GZ, Wang DD, Yi JB, Yang LL, Gao M, He M, Yang JH, Ding J, Sum TC, Wu T (2010) Appl Phys Lett 96:112511
190. Podila R, Queen W, Nath A, Arantes JT, Schoenhalz AL, Fazzio A, Dalpian GM, He J, Hwu SJ, Skove MJ (2010) Nano Lett 10:1383
191. Kushwaha A, Tyagi H, Aslam M (2013) AIP Adv 3:042110
192. Xu X, Xu C, Lin Y, Ding T, Fang S, Shi Z, Xia W (2012) J Appl Phys Lett 100:172401
193. Chanda A, Gupta S, Vasundhara M, Joshi SR, Muttae GR, Singh J (2017) RSC Adv 7:50527

Chapter 9
Domain Matched Epitaxial Growth of Dielectric Thin Films

P. S. Krishnaprasad and M. K. Jayaraj

1 Introduction

Since the discovery of ferroelectricity by Joseph Valsek in 1920 in a single-crystal Rochelle salt ($KNaC_4H_4O_6{\cdot}4H_2O$) [1] and the development in the realm of polycrystalline and epitaxial thin films during the mid-1990s, there has been a continuous evolution of new materials and technologies based on these phenomena. Among these dielectric materials, transition metal oxides belong to a fascinating [2] class of materials which exhibit a wide range of properties and phenomena ranging from insulating, semiconducting, superconducting, magnetic, ferroelectric, piezoelectric, nonlinear optical and many more.

After the discovery of ferroelectricity in Rochelle salt, the area of ferroelectricity was more widened by the reports on potassium dihydrogen phosphate (KDP) in 1935 [3]. One of the major turning points in the evolution of ferroelectric materials was the discovery of the unusual dielectric properties in a number of oxide materials with perovskite structure, which came in the early 1940s. $BaTiO_3$ was the first perovskite structure exhibiting ferroelectricity [4]. Subsequently, more materials with different structures exhibiting ferroelectric phenomena were discovered. The perovskite oxide class of materials is one of the most important and fundamental ferroelectric candidates. They also paved way to the industrial applications of ferroelectrics.

Dielectric materials store electric energy under the influence of electric field by the field-induced separation of electric charges. This phenomenon of dielectric materials is called polarization. Larger the separation of these charges and larger the number of

Part of the work published in journal applied physics, reprinted from Krishnaprasad et al. [16], with the permission of AIP Publishing.

P. S. Krishnaprasad (✉)
Government Polytechnic College, Kothamangalam, India

M. K. Jayaraj
Cochin University of Science and Technology, Kochi, India

M. K. Jayaraj (ed.), *Nanostructured Metal Oxides and Devices*,
Materials Horizons: From Nature to Nanomaterials,
https://doi.org/10.1007/978-981-15-3314-3_9

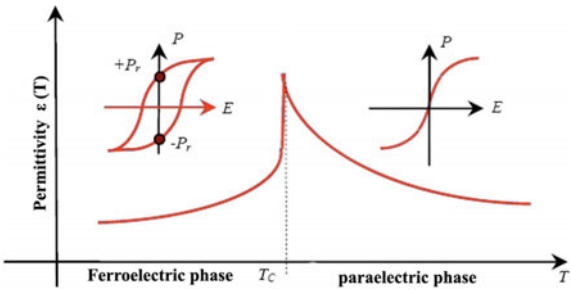

Fig. 1 Hysteresis loop in ferroelectric and paraelectric phases

dipoles result in larger polarization and dielectric permittivity [5]. There are several possible contributions to this polarizability, and three general mechanisms important in dielectric materials are electronic, atomic and ionic polarization [6]. A ferroelectric material can be defined as an insulating system with two or more discrete stable or metastable states each having a nonzero value of polarization even in the absence of applied electric field. Once the ions are pulled into a particular configuration by the application of electric field, they cannot get back to its previous state due to the lattice hindrance, even after the removal of the electric field. Thus, ferroelectrics possess a residual polarization even after the field is removed. These polarization states are switchable among themselves by the application of electric field. Thus, ferroelectric material is characterized by its spontaneous polarization and also shows a hysteric dependence on the applied electric field whereas non-polar or a paraelectric material does not show a hysteresis behaviour (Fig. 1). The paraelectric materials which possess large tunable dielectric constant as a function of the electric field are usually used in tunable microwave devices. The temperature dependence of dielectric constant for these materials finds application in infrared detectors. The magnetic, electric, dielectric, mechanical, temperature and optical properties of these multifunctional materials find a wide range of applications.

A capacitor with a ferroelectric material as a dielectric medium is the basic building block for all ferroelectric-based devices. Electronic devices like memory cells, tunable phase shifters, delay lines, etc., based on ferroelectric materials possess several benefits over competing technologies due to reduced power consumption, size and cost. The dielectric tunability may be defined by the formula

$$T\% = \frac{\varepsilon_{\max} - \varepsilon_{\min}}{\varepsilon_{\max}} \times 100 \tag{1}$$

Potential applications for ferroelectric thin films are high k varactors, memory devices, smart sensors, micro-electro-mechanical systems (MEMS), tunable microwave devices, optoelectronic components and many more. These wide range of applications has motivated many scientist and engineers to systematically study the synthesis, structural, microstructural and dielectric properties of this class of dielectric materials. The ever-increased need for miniaturization of devices and the potential integration of ferroelectric materials with semiconductor microelectronic

circuits have also been a constant driving force for the discovery of new materials and improving the performance by doping and growth of epitaxial dielectric thin films.

Among the various applications of ferroelectric materials, the tunable microwave phase shifters and filters are the typical devices where the significance of ferroelectricity has demonstrated the most. They can be used for rejecting undesirable frequencies in microwave receivers and transmitters, and combining different frequency signals in multiplexers and de-multiplexers and form an essential component in modern radars [7]. Various technologies have been implemented for frequency tuning in microwave devices like mechanical tuning, varactor diodes, MEMS and ferroelectric thin film technologies [7]. Unlike PIN diodes and RF-MEMS switches, ferroelectric capacitors present an interesting way to design reconfigurable filters since their permittivity can be tuned in an analog way and the switching time is in the nanosecond range. The variation of dielectric constant with applied bias voltage is the basic principle behind the usage of ferroelectric materials for tunable microwave devices [8]. Ferroelectric thin film varactors in both interdigital and parallel plate configurations have been used to demonstrate tunable filter, phase shifters [9, 10], tunable matching networks [11] and delay lines [12]. Ferroelectric thin film varactors can be compact because of their large dielectric constant, and also, they offer a good tunability, fast tuning speed (~ns) and have low power consumption [7, 13]. Interdigital ferroelectric varactors are easy to fabricate, and they exhibit high capacitance density and tunability. Ferroelectric thin films can also be deposited on a wide variety of substrates using standard deposition technique, and also, they are consistent with existing silicon technology.

In spite of the quite promising properties, the tunable ferroelectric materials are not widely accepted for practical microwave systems, mostly due to the high dielectric losses, lack of stoichiometry and poor crystallinity. It has been found that the deposition techniques that are used to deposit dielectric thin films play a major role in determining the film's material properties and consequently its dielectric and electrical properties. Several techniques are available to deposit dielectric thin films, such as RF sputtering, pulsed laser ablation deposition (PLD) and molecular beam epitaxy (MBE). Of these, PLD has been found to be very successful for the growth of high-quality single-crystalline dielectric thin films.

2 Paraelectric Materials for Tunable Microwave Applications

Dielectric materials with low dielectric loss and moderate dielectric tunability can be used for making tunable microwave devices, regardless of whether they are in polar and non-polar phases. But in most applications materials in their paraelectric phase (i.e. non-polar phase) are preferred, since they do not possess hysteresis associated

with the domains. Also, they possess lower dielectric loss and higher tunability compared to the ferroelectric phase. Quantum paraelectric materials like $SrTiO_3$, $CaTiO_3$, etc., are the most suitable materials in this respect, for tunable applications, since they are incipient ferroelectrics, they do not possess any transition to ferroelectric phase at any temperatures. But the problem with these incipient ferroelectrics is that they have to be cooled down to low temperatures to have a reasonable dielectric constant and tunability, whereas commercial applications of these devices prefer room temperature operations.

There are some materials like $Ba_{0.5}Sr_{0.5}TiO_3$ (BST), $Bi_{1.5}Zn_1Nb_{1.5}O_7$ (BZN), $Ca_xSr_{1-x}TiO_3$, $(Pb,La)(Nb,Ti)O_3$, $Ba_{1-x}(La_{0.5}Na_{0.5})_xTiO_3$ [14–18], etc., which are in the paraelectric phase near room temperature and also possess reasonable dielectric constant and large tunability. Among these materials, BST, BZN and doped $SrTiO_3$ are the most commonly used microwave tunable materials, since their Curie temperature, dielectric constant and tunability can be tuned by changing the composition. The main advantages of ferroelectric films for microwave applications include frequency-independent tunability, high tuning speed (<1.0 ns), extremely small leakage currents, high breakdown field and lower power consumption.

3 Major Degradation Factors of Ferroelectric Materials

Major degradation factors that limit the use of ferroelectric materials for applications in random access memories and tunable microwave devices are dielectric loss, fatigue, imprint and logic state retention loss. Even though bulk and thin film phases of materials are chemically the same, the ferroelectric properties are substantially, sometimes even drastically different from each other. The presence of dead layer at the film–electrode interface also causes changes in the ferroelectric properties of thin films, and this effect becomes more pronounced when the thickness of the film itself becomes comparable to that of the dead layer. The lattice misfit between the film and substrate also plays an important role in the deviation of dielectric properties of thin films from that of the bulk. Other than these parameters like lack of stoichiometry, surface defects and oxygen deficiency in the films, different impurities in the films also contribute to the change in the dielectric properties of the thin films from that of the bulk. The ferroelectrics must possess a high crystallinity in order to have a high dielectric constant. For example in the case of $BaTiO_3$, the dielectric constant of the amorphous state is low compared to its crystalline phase, because the polarization contribution of the Ti moving in the crystal cage is lost when there is no crystal structure to support it.

4 Advantage of Combining Semiconductor with Ferroelectric Material

For the past few years, progress has been achieved in the area of tunable dielectrics, making it possible to develop dielectric capacitors with performance better than semiconductor analogues in the microwave frequency range. Additionally, due to the large dielectric constant of ferroelectric materials, considerable size reduction can be achieved for ferroelectric material-based devices compared with semiconductor-based devices. The extra flexibility in terms of tuning, enhanced functionalities and performances of tunable devices may be achieved by a combination of ferroelectrics with ferrites or ferroelectrics with semiconductors [19]. Interfacing dielectric oxides with semiconductors will allow us to take advantage of such material properties for multifunctional devices. During the growth of dielectric thin films or post-deposition treatment of the thin films, the oxidation at the film–substrate interface can degrade the electrical properties of the heterostructure, which demand the use of buffer layers [20] a necessity. For example, ferroelectric oxides are often thermodynamically unstable in contact with silicon and indeed act as catalysts to silicate formation [21]. This amorphous dead layer formed in between the ferroelectric/semiconductor interface acts as a source for interfacial trap centres and provides a tunnelling path for carriers. This leads to large leakage current through the device. Also, the changes in the properties of the interfacial amorphous layer and trap densities due to ageing cause instabilities in the device performance. The use of an oxide semiconductor as the buffer layer eliminates this problem and thus offers a chemically stable heterostructure. Reports show that when a thin buffer layer of Ti is used for the growth of $BaTiO_3$ thin films on GaAs substrate, it resulted in an abrupt interface without any interfacial dead layers [22].

But most of the ferroelectric materials that have been studied for the device applications are chemically unstable when they make contact with traditional semiconductors like silicon, because of the complex structure of ferroelectric materials. Some semiconducting materials like zinc oxide [23, 24], indium oxide [25] and tin oxide [26] have been investigated and found to be promising. Among these, ZnO is a wide band gap semiconductor and it has been widely used as buffer layer for the growth of dielectric films for different applications [27–30]. The wide acceptance of ZnO is mainly due to its large band gap (3.3 eV at room temperature). Due to its wide band gap, ZnO is transparent to visible light and excess zinc is always found in ZnO under normal growth conditions. Due to this zinc excess, ZnO is a non-stoichiometric compound and an n-type semiconductor, and hence, one of the most studied transparent conducting oxides. Studies show that ZnO is stable and chemically compatible with other oxide materials and dielectrics. So, high-quality dielectric thin films with low defect density at the interface can be produced over the ZnO buffer layer. One of the important applications of these ferroelectric-ZnO interfaces is the use of these structures in ferroelectric solar cells and field-effect devices, where the ferroelectric polarization charge can modulate the conductivity of the semiconductor layer. These

heterostructures also find applications in sensor [31], transistors [32], ferroelectric solar cells [33] and highly integrated memory cells [34–36].

The current problems with ferroelectric/semiconductor heterostructure-based devices, like fatigue, imprint and limited endurance, are directly related to the poor quality of the ferroelectric/semiconductor interface. Imprint is the gradual deterioration to prefer one polarization direction over the other. The large leakage current through the device due to the presence of high interfacial trap densities also worsen the problems like imprint [37]. The endurance problem with the Ferroelectric RAM (FeRAM) devices can be improved with a non-destructive read-out mechanism. Destructive read-out techniques affect the reliability of memory cells. A non-destructive read-out mechanism can be realized by incorporating both memory and addressing functionalities into a single device. This can be done with ferroelectric thin films transistors (FeTFT), where ferroelectric thin films act as the gate oxide and semiconducting thin films are used as a channel layer of the TFT. So with this non-destructive read-out mechanism, the ferroelectric thin films are less affected in terms of degradation and fatigue. Thus, the current problems with ferroelectric thin film-based devices can be improved by growing high-quality epitaxial thin films on semiconductor materials.

Since ZnO does not suffer from interfacial oxidation and chemically stable material, it can form a good buffer layer for the growth of ferroelectric thin films. Also, ZnO forms a favourable band line-up with many ferroelectric materials such as PZT and BST [38–40]. The devices based on multifunctional materials also offer several advantages; for example in the case of delay lines and phase shifters, it is possible to tune the delay time while maintaining the input/output impedances on the desired level.

5 Methods for Improving Tunability and Dissipation Factor

There are several points that have to be improved in these materials for a large-scale use. The main parameters that have been identified to affect the properties of dielectric thin film are processing methods, film composition, oxygen deficiency, microstructure, post-deposition annealing conditions, interface structure, film stress, electrode materials and their correlation. For the past few years, many improvements have been made in the processing methods to make stoichiometric thin films. Many oxide-based electrodes have also been developed to be used along with dielectric thin films that improve dielectric properties [41–44]. Oxygen vacancy formation at the film–electrode interface is identified as one of the major reason for the performance degradation of dielectric thin films that produce high dielectric loss and leakage current. Despite the efforts made by many groups, there is still a lot more to improve on these aspects.

Oxygen deficiency is commonly present in oxide materials, and they behave like charged defects. In thin films, the density of oxygen vacancies is closely related to the deposition parameters. Oxygen vacancies within the dielectric thin films, usually

created due to insufficient oxygenation of the film during the growth process, has a key role in the electrical as well as dielectric properties of the films. Oxygen vacancies near the film–electrode interface also act as the major source for large polarization fatigue, since they act as domain wall pinning sources in the deposited thin films [45–47]. Fatigue can be improved by using oxide materials as electrode instead of metals since the oxide electrodes can control the concentration of oxygen vacancies within the sample. This again indicates that the oxygen vacancies play an important role in the dielectric properties of the thin films. The present research interests in the development of dielectric oxide thin films are focused on achieving improved performance by optimizing the growth parameters, reducing the dielectric loss and leakage current density by suitable dopants, fabricating composite or multilayer thin films and epitaxial growth of thin films [48, 49]. The dielectric properties of thin films may be improved by several methods. The problems due to oxygen deficiencies can be overcome by metal doping, rare earth doping, non-metal doping and stoichiometric epitaxial growth, etc.

5.1 Acceptor Doping

A small concentration of dopants can effectively modify the properties of dielectric materials. For example in the case of perovskite materials, when the A- or B-sites are replaced with two or more different atoms, the dielectric properties make drastic changes. In perovskites, B-site doping can induce ferroelectric-to-relaxor transitions in Pb-based systems [50] or order-of-magnitude changes in the dielectric loss properties of alkaline earth-based microwave dielectrics [51]. Several dopants like Fe^{2+}, Fe^{3+}, Co^{2+}, Co^{3+}, Mn^{2+}, Mn^{3+}, Ni^{2+}, Mg^{2+}, Al^{2+}, Ga^{3+}, In^{3+}, Cr^{3+}, and $Sc^{3+}$when doped into perovskite structures, show improved dielectric properties [52–55]. These dopants occupy the B-sites of the ABO_3 perovskite structure. Doping with these materials found to decrease the leakage current and dielectric loss, since the ionic state is less than 4+, which can substitute for Ti^{4+} in BST. Thus, these dopants behave like electron acceptor centres. When doped with these acceptors, they neutralize the donor action of the oxygen vacancies and thereby the reduction of Ti^{4+} to Ti^{3+} is decreased. The hopping of oxygen vacancies between Ti ions is the basic mechanism behind the dielectric loss. Thus, the addition of acceptor dopants results in the reduction of dielectric loss. The leakage current in BST thin films can be decreased with acceptor (Mn, Ni) doping [56]. The decrease in leakage current is due to the expansion of the depletion region width, which in turn decreases the tunneling current across the film–electrode interface. The ageing effect in BST can be reduced by the Mn doping in B-site atoms of BST [57]. Rare earth doping also can improve the dielectric properties of BST thin films. For example, a small percentage of La has a strong influence on the material properties of BST thin films [52].

Perovskite materials usually have divalent species on the A-site, although some newer compositions incorporate trivalent rare earth cations on the A-site with charge compensation conferred by the simultaneous incorporation of a trivalent species like

Al^{3+} on the B-site, e.g. $(Ca_{1-x}Nd_x)(Ti_{1-x}Al_x)O_3$. A significant reduction of the loss tangent, enhanced film resistivity and good dielectric tunability can be obtained for BST thin films when A-site is doped with Mg [52]. When Ba^{2+} is replaced by the smaller La^{3+} cation on the A-site, the presence of B-site vacancies resulted in a rapid decrease in T_C [58]. Rare earth element Ce doping can increase the dielectric constant and effectively suppress the leakage current in BST thin films [59, 60]. XPS results on Ce-doped BST (CeBST) thin films show that it has a strong influence on the valence band and core levels and that the Fermi level is lowered by Ce doping. These Ce-doping effects can induce an increase in the barrier height for the thermionic emission and eventually reduce leakage current in CeBST thin films [60]. The reduction of the leakage current is attributed to the effect of acceptor Ce^{3+} doping. Such types of doped dielectric systems are useful in DRAM as well as microwave tunable applications.

More recently, Kamba et al. investigated the crystal symmetry and dielectric properties of Pb substituted $Sr_9Ce_2Ti_{12}O_{36}$ ceramics [61]. The samples with low content of Pb exhibit paraelectric behaviour, while higher content of Pb induces displacive ferroelectric phase transition and Curie–Weiss temperature T_C increases linearly with Pb concentration. Among these materials, $Sr_3Pb_6Ce_2Ti_{12}O_{36}$ (SPCTO) ceramics possess the highest dielectric constant and a reasonably low dielectric loss at microwave frequencies. The structural and dielectric properties of SPCTO thin films directly depend on the crystallinity as well as the Pb content in the thin film [62].

5.2 Metal Doping or Metal Compositing

Dielectric properties of metal-ferroelectric composites near their percolation limit have been an intense area of research for the past few years because of their extraordinary enhancement in dielectric properties. In order to implement these ferroelectric-metal composites for device applications, it is important to understand the dielectric enhancement mechanism in these composites, i.e. what happens when metal particles are introduced into an insulating matrix. Studies suggest two major mechanisms for large dielectric enhancement: one is the micro-capacitor model and the second one is the space charge polarization [63, 64]. The metallic component should neither react nor dissolve in the ferroelectric phase. Hence, noble metals are most commonly utilized. A large improvement in the dielectric properties of PZT thin films can be achieved by the addition of Pt particles [65]. The dielectric constant of the composites was up to about 4 times higher than that of pure PZT ceramics, while the dielectric loss remained almost the same. The dielectric tunability also much improved in the Pt-PZT composite. Near the percolation limit, the composite exhibited a very low coercive field as low as half the value of pure PZT ceramic with remnant polarization comparable to that of the pure PZT bulk value.

Metals like Pt, Au, Cu, Ag, Ni, Mg, etc., are usually used for making metal-dielectric composites. Of these, Ag possess advantages like low sintering temperature, low cost and no oxidation problems [66]. Sebastian et al. studied the percolation

phenomenon in barium samarium titanate-silver composite prepared by the solid-state ceramic route and found that silver addition reduces the sintering temperature of the composite and also improves other dielectric properties of barium samarium titanate [67].

Ag addition in BST thin films by simple blending procedure improved the dielectric properties with a large increase in dielectric constant, which is nearly frequency and temperature independent [68]. Dielectric relaxation studies on PZT-Ag composites revealed that the addition of Ag particles causes relaxation of transformation-induced internal stresses [69]. The dielectric properties of PZT-Ag composites were also studied by Xiang et al. They found a significant increase in the dielectric constant with Ag addition, with a small increase in the dissipation factor. The dielectric constant was almost frequency independent [70]. Ag addition to $Bi_{1.5}Zn_1Nb_{1.5}O_7$ (BZN) by solid-state ceramic synthesis reduced the sintering temperature of BZN. The dielectric constant of these metal composites increased with an increase in Ag concentration with respect to the power law. However, above the percolation limit, the dielectric loss, as well as conductivity, was also increased with increase in Ag content [67].

Even though there are several studies on ferroelectric-metal composites in bulk form, only a few studies have been conducted on metal-ferroelectric composite thin films. Jayadevan et al. studied the surface and leakage current density characteristics of nanocrystalline Ag-BST thin films. Silver addition enhances the binding energy of surface oxygen and reduces the leakage current density of Ag-BST thin films [46, 71]. Studies on Ag-BST composite thin film were also conducted by Srivastava et al. and found that the dielectric properties of BST thin films were highly improved by Ag doping [47]. Studies on Mg-BST composite thin films show an improvement in dielectric and insulating properties of BST thin films [72]. The improvement in the properties has been generally explained on the basis of probable enhancement in oxygenation and absence of pinning of domain wall in the presence of silver.

5.3 Epitaxial Growth of Thin Films

Yet another method to improve the dielectric properties of ferroelectric thin films is to grow epitaxial ferroelectric thin films. Over the past few years, a tremendous advancement has been achieved in the epitaxial growth of thin films of various complex oxides. Depending on the growth parameters and growth techniques adopted, the resultant thin films may be amorphous, polycrystalline or monocrystalline. The superior properties of epitaxial thin films over polycrystalline thin films have attracted the attention of research community.

Epitaxial growth of single-crystalline complex oxide thin films, such as perovskite ferroelectric thin films, requires knowledge on the processing conditions and crystal structure of film and substrate. Since many ferroelectric oxides possess complex structures, the available nucleation sites on the substrate and initial monolayer formation decide different orientations of the epitaxial thin films. The dielectric properties

of ferroelectric thin films depend on the orientation of the films, so these initial growth conditions play a crucial role in the device properties. Other important concerns in the growth of ferroelectric epitaxial thin films are the lattice misfit and strain across the film–substrate interface which can even affect the film roughness and dielectric properties. Deposition parameters like temperature, oxygen partial pressure, pre- and post-deposition treatments also can significantly affect the microstructure, defect density, epitaxial quality and other physical properties of the thin films. Yet another factor which affects the strain and relaxation behaviour of the film is the termination layer of the substrate. Substrate termination layer can be controlled by chemical etching, thermal annealing of the substrate or by the deposition of ultrathin atomic layers of suitable materials on the surface of the substrate. Thus to optimize the quality of epitaxial thin films and device performances, it is mandatory to give predominant concern to the parameters like growth temperature and pressure, the selection of substrates, surface quality and initial nucleation sites and the nucleation process and growth dynamics.

The heteroepitaxial growth of thin films results in changes in electronic, optical, magnetic and mechanical properties of thin films. The mismatch between film and substrate also gives rise to a nonzero interfacial energy, which increases with increase in mismatch. The interfacial energy is mainly contributed from two factors, viz. due to the formation of the new interface and elastic strain energy due to lattice mismatch. A preferred orientation of the thin films can be obtained by the minimization of this interfacial energy. The lattice mismatch f, which is a measure of interfacial stress and hence interfacial energy between the film and substrate, can be calculated as

$$f = (a_f - a_s)/a_s \tag{2}$$

where a_f and a_s are the lattice parameters of the film and the substrate. For growing epitaxial thin films, the lattice strain and defect concentrations should be as small as possible. As the device features get smaller and smaller, even a single defect can deteriorate the device performance. Therefore, making high-quality thin films and control of defects in thin films are a very important concern in thin film growth. It is a common belief that epitaxial thin films can only be grown if the film–substrate misfit is less than about 8%. Smaller the misfit, smaller will be the interfacial energy and coherent epitaxy is formed. Otherwise, films will grow polycrystalline in nature. But in fact in principle epitaxial thin films can be grown on substrates with any misfit. In terms of the lattice mismatch between the film and substrate, the epitaxial thin film growth modes can be classified as (1) lattice matching epitaxy and (2) domain matching epitaxy.

(a) **Lattice Matching Epitaxy (LME)**

LME is a common method usually used for growing epitaxial thin films on substrates with lattice mismatch less than 8%. If there is a small lattice mismatch between film and substrate, the systems will have low interfacial energy and we can expect a two-dimensional growth of thin film [73]. During the LME growth, the heteroepitaxial film first grows pseudo-morphically, which means the epilayer is elastically strained

to have the same interatomic spacing as the substrate. According to the theory of Frank and Merwe, the initial stage of growth of epitaxial thin films is the formation of the immobile monolayer, homogeneously deformed to fit the substrate surface, so as to have same lattice constant as that of the substrate [74, 75]. This is called a pseudomorphic monolayer. Once this monolayer is formed, a thick epitaxial film can then be grown by repetition. But soon after the growth of a few atomic layers, the strain energy in the films increases with thickness. Thus only when the film thickness is small, this kind of pseudomorphical growth is energy favourable. As the film thickness increases total elastic strain energy and in turn, the total energy of the system increases and the film becomes unstable so that dislocation is originated at the free surface [75]. This technique is usually used for the growth of oxide epitaxial thin film with film and substrate having the same structure and similar lattice parameters as in the case of ZnO–ZnMgO, ZnO–GaN, $BaSrTiO_3$–$SrTiO_3$, etc. [76–80]. The lattice matching epitaxy is particularly useful for homoepitaxy systems and low misfit systems. They also suffer certain drawbacks like there is a probability for threading dislocations, which can adversely affect device performances.

(b) **Domain Matching Epitaxy (DME)**

In domain matching epitaxy, the misfit across the film–buffer interface is accommodated by matching of integral multiples of lattice planes of the film with those of buffer layer [29, 73]. This is schematically illustrated in Fig. 2. The film–buffer lattice misfit can vary from being very small to very large, and in the case of small lattice misfit, DME reduces to LME. The size of the domain varies depending on the lattice misfit between film and buffer in order to accommodate the additional misfit. In domain matching epitaxy, most of the strain across the film–buffer (or film–substrate) interface is relieved within a couple of monolayers near the interface itself and the rest of the film can be grown free of defects and lattice strain. So domain matching epitaxial growth concept can be used to grow high-quality epitaxial thin films on substrates that have large lattice misfit with the thin film material. Thus through DME, epitaxial growth can also be observed in large lattice mismatch systems, which can be described in terms of domains [73, 81]. The domain matching length gets itself repeated along with the interface.

Since the concept of DME was first proposed, DME growth has been playing more and more important role for growing heterostructures on which thin films have been grown epitaxially on the foreign substrates with large lattice misfit. First, principle study on the domain matching epitaxy growth of semiconductor hetero-interface was done by Tuoc [82]. He studied the structural and electronic properties of the GaN

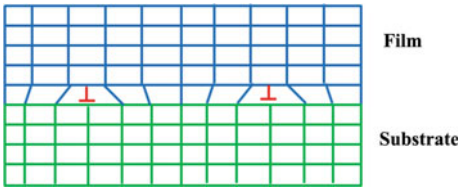

Fig. 2 Schematic illustration of domain matched epitaxial growth

(0001)/S (111) interface grown by domain matching epitaxy [82]. A unified model for domain matching epitaxy was proposed by Narayan and Larsen [73]. They have shown that it is possible to grow epitaxial thin films on substrates with small as well as large lattice misfit, by matching an integral multiple of lattice planes across the film–substrate interface. They have demonstrated DME using a number of systems like TiN–Si (100) [83], III-nitride epitaxy on Si (111) [84], and ZnO [85] and III-nitrides on sapphire (0001) [86], $SrTiO_3$/TiN on Si (100) [87], etc.

Sánchez deposited ferrimagnetic spinel $CoFe_2O_4$ (CFO) films on Si (111) with Sc_2O_3 buffer layers by domain matching epitaxy [88]. The huge lattice mismatch between CFO and Sc_2O_3 is accommodated by a 7/6 domain matching, resulting in a semicoherent sharp interface and epitaxial growth of very flat films. Liu made use of this technique to deposit high-quality ZnO thin film using a Y_2O_3 buffer layer on Si (111) [89]. Y_2O_3 layer well serves as a template for integrating ZnO-based optoelectronic devices with Si substrate.

Despite the very different lattice parameters, In_2O_3 thin films were epitaxially deposited by matching different integral multiples of lattice planes of In_2O_3 with those of Al_2O_3 [90]. The residual strain is released by periodic misfit dislocation localized at the interface. Zhuang was able to deposit wide band gap $Mg_xZn_{1-x}O$ alloy films on $LaAlO_3$ (100) substrates by pulsed laser deposition. They observed a domain matching epitaxy by TEM with the sequence 5/4 and 4/3 for $Mg_xZn_{1-x}O$–$LaAlO_3$ system [91]. Song demonstrated domain matching epitaxy between Ag film and GaN with nine lattices of (111) Ag film and eight lattices of GaN (0001) substrate [92]. The (111) oriented Ag contact has the smallest surface energy, which resulted in the reduction of surface diffusion to a smaller surface plane. Thus, DME provides a convenient and effective way to deposit high-quality epitaxial thin films for different optoelectronic applications. Compared to LME where dislocations are generated on the surface of the film beyond the critical thickness, most of the strain in DME is relieved within a couple of monolayers [73].

The domain matched epitaxial growth of dielectric thin films by pulsed laser ablation has been realized in our laboratory. The effect of a thin ZnO buffer layer on the growth mechanism BST was also studied. Epitaxial growth of single-crystalline complex oxide thin films, such as perovskite ferroelectric thin films, requires detailed knowledge on the deposition and processing conditions. The nucleation and initial structures formed on the substrates can be very complicated, and the initial monolayer formation can even result in the formation of different oxide or phase structures. Also, the interface structures and surface roughness can even be varied by the strain accumulation and relief from the lattice misfit across the film–buffer interface. Growth procedures such as temperature, pressure, pre- and post-treatment can significantly affect the microstructure, defect density, epitaxial quality and physical properties of the as-grown films. Therefore, knowledge of the oxide thin film growth mechanisms, nucleation sites present over the substrate and atomic-scale growth kinetics and dynamics will enable the control of the microstructures, physical properties, epitaxial quality and interface structures [2].

6 Domain Matched Epitaxial Growth of Barium Strontium Titanate ($Ba_{1-x}Sr_xTiO_3$)

Barium strontium titanate (BST) is the solid solution of barium titanate (BTO) and strontium titanate (STO). $Ba_{1-x}Sr_xTiO_3$ has the perovskite structure ABO_3. Since the Curie temperature of the solid solution depends on the composition, the dielectric properties can be tuned by varying the composition of the $Ba_{1-x}Sr_xTiO_3$ solid solution [93]. The BST thin films have attracted a great deal of attention because of their potential applications in electrically tunable microwave devices, dynamic random access memory (DRAM), and phase shifters [94–96]. To successfully use these films for technological applications, the material and electrical properties of these films need to be better understood. Among the various ferroelectric materials, $Ba_{1-x}Sr_xTiO_3$ is considered to be a promising material for the realization of various applications because its T_c can be controlled by varying the mole fraction of Sr. Thus, BST is an environment-friendly lead-free material, which finds applications in different microelectronic devices.

The high dielectric constant and tunability result from the displacement of Ti ion from the centre of the oxygen octahedron. $Ba_{1-x}Sr_xTiO_3$ (BST) exhibits complete solid solubility over all compositions [97], with a cubic structure at room temperature for $0.3 \leq x \leq 1$, changing to tetragonal for $0 \leq x \leq 0.3$. With the addition of $BaTiO_3$ into $SrTiO_3$, the lattice parameter changes from $a = 3.90$ Å corresponding to $SrTiO_3$, to $a = 3.99$ Å and $c = 4.03$ Å for $BaTiO_3$. At room temperature, $Ba_{1-x}Sr_xTiO_3$ with $x = 0.3$ exhibits a tetragonal distortion which corresponds to ferroelectric phase [93]. The Curie temperature of $Ba_{1-x}Sr_xTiO_3$ decreases with increase in Sr content in the composition. For BST in its ferroelectric phase, the dielectric loss is high due to the presence of hysteresis loss. So for microwave applications, BST in its paraelectric phase is preferred [98]. BST possess large dielectric tunability and low loss tangent for the composition $Ba_{0.5}Sr_{0.5}TiO_3$. So this composition is usually preferred for microwave applications. But for memory applications, $Ba_{0.7}Sr_{0.3}TiO_3$ is preferred due to its large dielectric constant at room temperature.

Ferroelectric thin films have been successfully deposited by RF sputtering [49, 99], metal organic chemical vapour deposition [100], sol gel [101] and pulsed laser deposition [100, 102–104]. Among these processes, the laser ablation process is the most superior since it possesses the advantages, viz. lower synthesis temperature, easier in controlling the stoichiometry of thin films, possibility in depositing oxide films of high melting point and materials of metastable phase [100]. Oxygen pressure during the film deposition also plays an important role in tailoring structural and electrical properties of oxide thin films [105, 106]. It is reported that films deposited at higher oxygen pressure show $a > c$ while films deposited at lower pressure show $a < c$ [107]. The unit cell volume of the films increases monotonically with decreasing oxygen pressure revealing a higher concentration of oxygen vacancies for the BST thin films deposited at lower oxygen pressure. Oxygen vacancies result in an increased lattice parameter. The dielectric constant can be affected by strain, and the degree of strain differs with the choice of supporting substrate. Several

reasons have been suggested for the degradation of the dielectric properties of thin films like stress/strain at the film–substrate interface due to the lattice mismatch [13, 108, 109], charged defects and structural imperfections which cause local strains and polar regions [110], a 'dead layer' near the interface between the substrate and the electrodes [111] and the lack of stoichiometry. Thus, the crystallinity, as well as defect concentration in the thin film, has an important role in the BST thin film-based devices. These characteristics can be improved by the epitaxial growth of BST thin films. The electrical properties of BST epitaxial thin films reported in the literature are summarized in the table. *(It should be noted that the measurements have been made at various electric fields in each case)* (Table 1).

From the table, it is clear that till now, the highest tunability reported for BST is 84% in the MHz frequency range [116], in which BST thin film was deposited on *a*-plane sapphire by RF magnetron sputtering using a double bridge layer consisting of ZnO and MgO prepared by plasma-assisted molecular beam epitaxy. Here, we discuss the domain matched epitaxial growth of BST, as well as BZN thin films on Al_2O_3 substrate with ZnO buffer layer, by which we have obtained a large enhancement in crystallinity and dielectric tunability [16, 29].

BST thin films were deposited directly on Al_2O_3 as well as with ZnO buffer layer. ZnO buffer layer was deposited on Al_2O_3 at a substrate temperature of 600°C and at various oxygen partial pressures. Structural properties of the as-deposited thin films were studied using high-resolution *X*-ray diffraction (HRXRD). Figure 3 shows the ω-2θ scan of BST thin films grown on Al_2O_3 with and without ZnO buffer layer. Figure 3b shows the XRD spectrum for the BST thin film deposited directly on to Al_2O_3 substrate at 700°C and oxygen partial pressure of 0.01 mbar, indicating a polycrystalline nature. From Fig. 3c–f, the crystallinity of the ZnO buffer layer increases with an increase in oxygen partial pressure up to 7×10^{-4} mbar; thereafter, it decreases. BST thin films were deposited at 700 °C and oxygen partial pressure of 0.01 mbar, on to these ZnO buffer layers deposited at various oxygen partial pressures. Compared to the polycrystalline nature of BST thin films directly deposited on (0001) Al_2O_3, highly crystalline BST thin films were obtained with ZnO buffer layer. Highly oriented epitaxial BST thin films were obtained when the films were deposited above the ZnO buffer layer deposited at 7×10^{-4} mbar. The observed high-intense reflection from BST (111) plane and absence of any other reflections indicate well-aligned BST thin film over ZnO buffer layer. The d-spacing calculated from XRD pattern (2.29 Å) well agrees with that of bulk value (2.28 Å). It has been reported that in the presence of intermediate layers like TiO_x, TiN and GaN as a buffer layer, BST thin film grow along the [110] direction [117, 123, 133].

The ZnO buffer layer deposited over Al_2O_3 changes the available lattice sites for the growth of BST thin film. The orientation of the Zn atoms in ZnO over Al_2O_3 substrate is schematically represented in Fig. 4a. ZnO has a hexagonal structure with $a = 3.252$ Å and $c = 5.21$ Å, and Al_2O_3 has lattice constants $a = 4.76$ Å and $c = 12.991$ Å. In the growth process of the ZnO buffer layer on Al_2O_3 substrate, the c-planes of ZnO rotates by 30° in the basal c-plane of Al_2O_3 [73]. The hexagonally placed oxygen sites in Al_2O_3 (001) plane (Fig. 4a) have a lattice spacing of 2.75 Å (i.e. $aAl_2O_3/\sqrt{3}$), and the bulk lattice constant of ZnO is 3.24 Å [29].

Table 1 Comparison of electrical properties of epitaxial BST thin films deposited on various substrates (IDC-interdigital capacitor structure, PPC-parallel plate capacitor structure)

S. No.	Material	Buffer/substrate	Tunability (%)	Loss tangent	Frequency	Electrode structure	References
1	$Ba_{0.6}Sr_{0.4}TiO_3$	MgO–SiO_2/Si	46.8	0.35	1 MHz	IDC	Kang et al. [112]
2	$Ba_{0.6}Sr_{0.4}TiO_3$	MgO	61	10^{-2}	1 MHz	PPC	Park et al. [113]
3	$Ba_{0.5}Sr_{0.5}TiO_3$	$DyScO_3$	48	0.021	1 MHz	PPC	Liu et al. [114]
4	$Ba_{0.75}Sr_{0.25}TiO_3$	MgO	25	0.007	100 kHz	IDC	Zhu et al. [115]
5	$Ba_{0.5}Sr_{0.5}TiO_3$	MgO/ZnO–Al_2O_3	84	0.02	1 MHz	IDC	Xiao et al. [116]
6	$Ba_{0.3}Sr_{0.7}TiO_3$	TiN–Al_2O_3	38	10^{-2}	8 GHz	IDC	Yamada et al. [117]
7	$Ba_{0.6}Sr_{0.4}TiO_3$	MgO	65	0.015	1 MHz	IDC	Park et al. [118]
8	$Ba_{0.7}Sr_{0.3}TiO_3$	GaAs	30	0.045	1 MHz	IDC	Yang and Hao [119]
9	$Ba_{0.4}Sr_{0.6}TiO_3$	MgO	65	0.06	1 GHz	IDC	Carlson et al. [120]
10	$Ba_{0.5}Sr_{0.5}TiO_3$	STO	59	0.02	10 GHz	IDC	Leach et al. [121]
11	$Ba_{0.7}Sr_{0.3}TiO_3$	$MgAl_2O_4$	30			IDC	Zhou et al. [122]
12	$Ba_{0.6}Sr_{0.4}TiO_3$	Al_2O_3	41	0.056	40 GHz	IDC	Yang et al. [123]
13	$Ba_{0.7}Sr_{0.3}TiO_3$	$LaAlO_3$	69		1 MHz	PPC	Lin et al. [124]
14	$Ba_{0.6}Sr_{0.4}TiO_3$	$LaNiO_3$	82	0.032	10 kHz	PPC	Qin et al. [125]

(continued)

Table 1 (continued)

S. No.	Material	Buffer/substrate	Tunability (%)	Loss tangent	Frequency	Electrode structure	References
15	$Ba_{0.5}Sr_{0.5}TiO_3$	MgO	33	0.0057	1 MHz	IDC	Kim et al. [126]
16	$Ba_{0.5}Sr_{0.5}TiO_3$	$SrRuO_3$	45	0.0092	1 MHz	PPC	Zhu et al. [127]
17	$Ba_{0.5}Sr_{0.5}TiO_3$	Amorphous SiO_2–Al_2O_3	66	0.016	100 kHz		Li et al. [128]
18	$Ba_{0.5}Sr_{0.5}TiO_3$	Al_2O_3	56		10 GHz		Fardin et al. [129]
19	Graded BST	$LaAlO_3$	78	10^{-1}	1 MHz		Lu et al. [130]
20	$Ba_{0.6}Sr_{0.4}TiO_3$	MgO–Al2O3	83		100 kHz	IDC	Choi et al. [131]
21	$Ba_{0.6}Sr_{0.4}TiO_3$	MgO	55		9 GHz	IDC	Moon et al. [132]
22	$Ba_{0.5}Sr_{0.5}TiO_3$	Al_2O_3	95	10^{-2}	1 MHz	IDC	Krishnaprasad et al. [16]

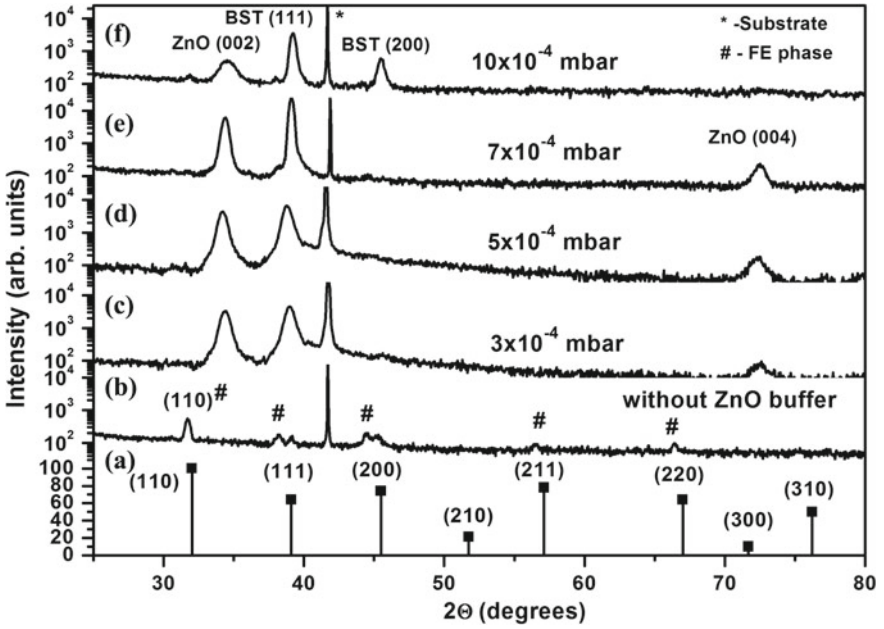

Fig. 3 **a** JCPDS data of $Ba_{0.5}Sr_{0.5}TiO_3$, **b** the XRD ω-2θ scan of the BST film deposited directly on to Al_2O_3 substrate and (**c**–**f**) the XRD ω-2θ scan of the BST films with a ZnO buffer layer deposited at various oxygen partial pressures, **c** 3×10^{-4} mbar, **d** 5×10^{-4} mbar, **e** 7×10^{-4} mbar and **f** 10×10^{-4} mbar. In all the cases, BST was deposited at an optimized oxygen partial pressure of 0.01 mbar and substrate temperature of 700 °C. Reprinted from Krishnaprasad et al. [16], with the permission of AIP Publishing

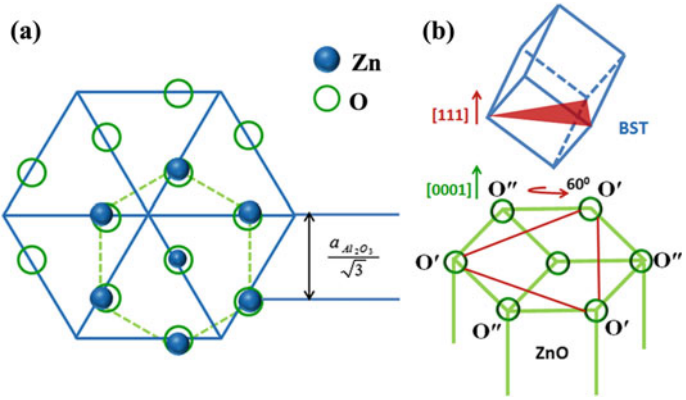

Fig. 4 **a** Schematic representation of atoms in the base plane of ZnO and Al_2O_3 [29] and **b** schematic diagram of the observed epitaxial relationship between BST and ZnO. Reprinted from Krishnaprasad et al. [16], with the permission of AIP Publishing

Here, we propose a model for the growth of (111)-oriented BST thin film on ZnO(001) buffer layer. The incorporation of ZnO buffer layer provides a matrix of hexagonal O-sites along the ZnO (001) plane for the growth of stacked structure of AO_3^{4-} and B^{4+} layers along the (111) direction of the ABO_3 structured BST lattice. Thus, ZnO buffer layer promotes the epitaxial growth of (111)-oriented BST thin films by the arrangement of A-site atoms in BST (111) plane of ABO_3 perovskite structure on to the hexagonally placed oxygen sites of (001) planes of ZnO as shown in Fig. 4a and b. The set of three O′ and O″ oxygen sites of ZnO (001) are separated by a distance of 5.53 Å (Fig. 4b) which well agrees with the separation of A-site atoms (5.58 Å) in the ABO_3 structure along the (111) plane. From Fig. 4b, it is clear that two equally probable orientations are possible for the BST (111) plane: one is along with the O′ sites and other is along the 60º rotated O″ sites. The in-plane orientations of BST, ZnO and Al_2O_3 layers in the BST/ZnO/Al_2O_3 heterostructure were established by XRD phi-scans. Figure 5a–c shows Φ-scan measurements for BST (111)/ZnO ($11\bar{2}0$)/Al_2O_3 ($11\bar{2}3$) heterostructure, and Fig. 5d shows the pole figure plot fixed at 2θ angle corresponding to BST (111). The Φ-scan for ZnO ($11\bar{2}0$) is consistent with the expected six-fold symmetry, with 60º equally spaced peaks, for a hexagonal layer. The phi-scan of BST (111) was performed at $2\theta = 39.02°$. The pole figure plot corresponding to BST (111) plane (Fig. 5d) shows one strong spot at the centre ($\psi = 0°$ and $\varphi = 0°$) and a sixfold reflection at $\psi = 70.5°$ at every 60° along the phi axis. Normally cubic structures with orientation along (111) direction will produce one pole at $\psi = 0°$ and $\varphi = 0°$ and three poles at $\psi = 70.5°$ with an angular distance of 120° in φ [($11\bar{1}$), ($1\bar{1}1$), ($\bar{1}11$) diffractions] in the pole figure plot [134, 135]. These reflections are represented by A circles in Fig. 5b. However, there is an additional set of three strong symmetrical poles with an azimuthal interval of 120° represented by the B circles. The three additional diffraction poles at $\psi = 70.5°$

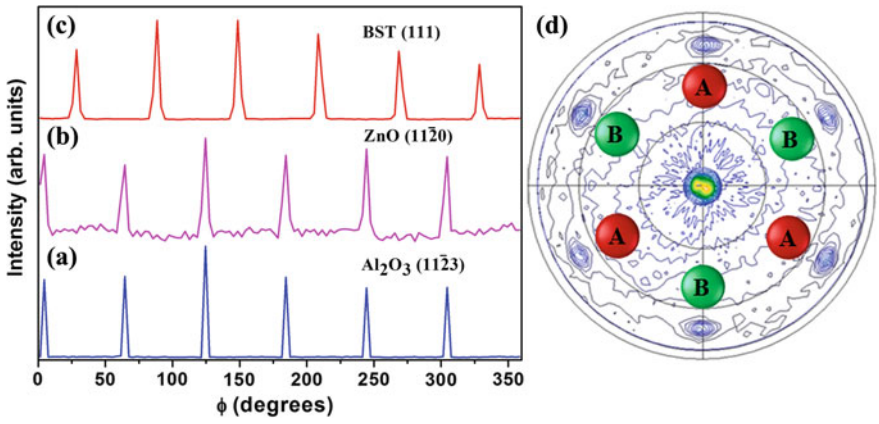

Fig. 5 *X*-ray diffraction Φ-scan for **a** Al_2O_3 ($11\bar{2}3$), **b** ZnO ($11\bar{2}0$) buffer layer, **c** BST(111) thin film and **d** (111) pole figure of BST thin films deposited on ZnO buffer. Reprinted from Krishnaprasad et al. [16], with the permission of AIP Publishing

can be obtained by rotating the (111)-oriented crystals by 60° about normal to the film surface. They can be represented as $(\bar{1}\bar{1}1)$, $(\bar{1}1\bar{1})$, $(1\bar{1}\bar{1})$. This result indicates that there are two kinds of (111) domains which are 60° rotated between each other, thus giving a sixfold symmetry in the diffraction pattern. The similar intensities of all the six spots (2×3 reflections) indicate that both the orientations of BST (111) planes (both in-plane and 60° twinned) are equally probable [29].

Another well-known dielectric material BZN thin film has also been grown epitaxially by domain matching epitaxy method. BZN in its cubic pyrochlore phase with $A_2B_2O_7$ stoichiometry has been demonstrated as a potential candidate for microwave application due to its low dielectric loss and medium permittivity (ε) in the microwave region and compositionally tunable temperature coefficients of capacitance (t_c) [136]. BZN thin films were deposited on the double ZnO buffer layer [29]. The preferential arrangement of BZN (222) on the ZnO buffer layer occurs by the hexagonal arrangement of A-site atoms in BZN for the (111) plane of pyrochlore structure corresponding to the hexagonally placed oxygen sites of ZnO (0001) plane. Thus, there is a domain matching of BZN $(2\bar{2}0)$ plane with ZnO $(\bar{1}00)$ plane across the film–buffer interface. In the growth process, (222) planes of BZN were also rotated by 60° about the normal to the film surface, which resulted in an additional pair of three diffraction poles at $\psi = 70.5°$ in the BZN (222) pole figure [29]. Thus, in the growth process of BST as well as BZN, twinning has been found to play an important role in accommodating the lattice misfit between the film and buffer layer and still maintaining an epitaxial relationship. The reciprocal space mapping of BST (111) along with reflections from Al_2O_3 (001) and ZnO (002), respectively, is shown in Fig. 6. The elongation of the reciprocal lattice point corresponding to BST (111) is comparatively large along the omega direction and small in ω-2θ direction indicating a uniform d-spacing distribution over the sample, compared to angular distribution.

Domain matching epitaxy, where integral multiples of lattice planes are matched across the interface, can be used to explain the interfacial ordering of BST-ZnO and BZN-ZnO heterostructures. Cross-sectional HRTEM measurements were performed over the BST-ZnO and BZN-ZnO interfaces to confirm this interfacial ordering. The

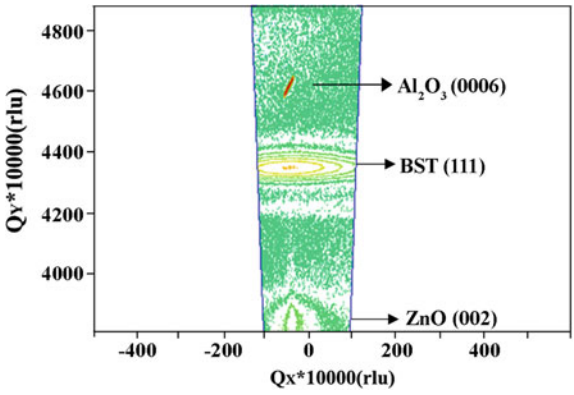

Fig. 6 Reciprocal space mapping of (111) planes of BST thin film with a ZnO buffer layer on Al_2O_3 substrate. Reprinted from Krishnaprasad et al. [16], with the permission of AIP Publishing

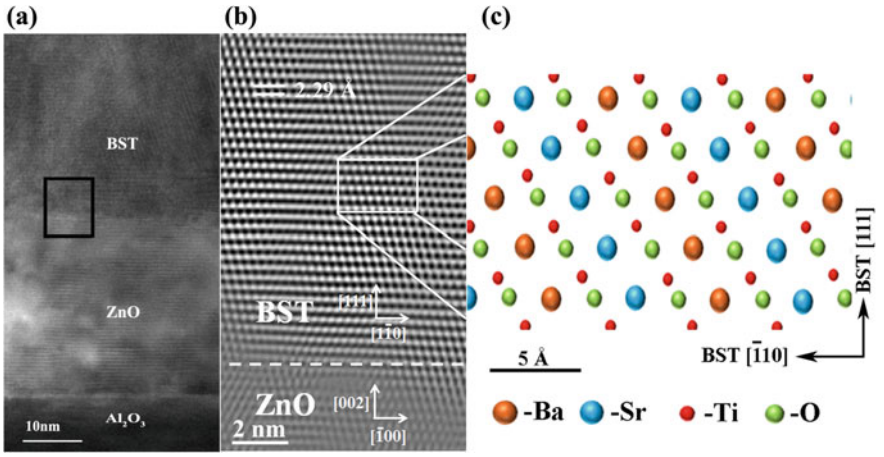

Fig. 7 **a** HRTEM image of BST-ZnO-Al_2O_3 film cross section. **b** Fourier-filtered HRTEM image of the black box area marked in figure (**a**) showing alignment of BST (111) orientation with d-spacing of 2.29Å. **c** Schematic representation of BST along (111) direction of the selected area in figure (**b**). Reprinted from Krishnaprasad et al. [16], with the permission of AIP Publishing

cross-sectional HRTEM image (Fig. 7a) shows a clear abrupt interface between BST and ZnO thin film. Fourier transform of the selected black box area in Fig. 7a shows a well-aligned BST(111) orientation with d-spacing 2.29 Å (Fig. 7b). The corresponding lattice constant was found to be 3.97 Å which agrees well with the bulk value 3.95 Å. The schematic representation of the arrangement of atoms along BST (111) direction in the selected area of Fig. 7b is shown in Fig. 7c.

Domain epitaxial growth of BST (1$\bar{1}$0) with a cubic perovskite structure on ZnO ($\bar{1}$00) substrate occurs via matching of 8 or 9 ZnO ($\bar{1}$00) planes with 9 or 10 BST (1$\bar{1}$0) planes. The spacing of BST (1$\bar{1}$0) planes (2.8107 Å) has close to −11.9% residual mismatch with ($\bar{1}$00) planes of ZnO (3.19 Å). Taking the 9 × d{BST (1$\bar{1}$0)} and 8 × d{ZnO ($\bar{1}$00)} domain matching structure, we have a residual mismatch defined by [90, 92]

$$m = \left(9 \times a_e/\sqrt{2} - 8 \times a_b\right)/(8 \times a_b) = -0.008$$

and for 9 × d{BST (1$\bar{1}$0)} and 10 × d{ZnO ($\bar{1}$00)}, the residual strain is

$$m = \left(10 \times a_e/\sqrt{2} - 9 \times a_b\right)/(9 \times a_b) = -0.021$$

where a_e and a_b are the lattice constants of the epilayer BST and buffer layer ZnO, respectively [29, 90, 92]. Thus, by introducing periodic dislocations localized at the interface, the 9/8 domain matching structure effectively accommodates −11.9% mismatch of BST-ZnO interface, leaving a residual −0.8% tensile strain in the BST films. This quasi-periodic dislocation can be clearly seen in the Fourier-filtered image

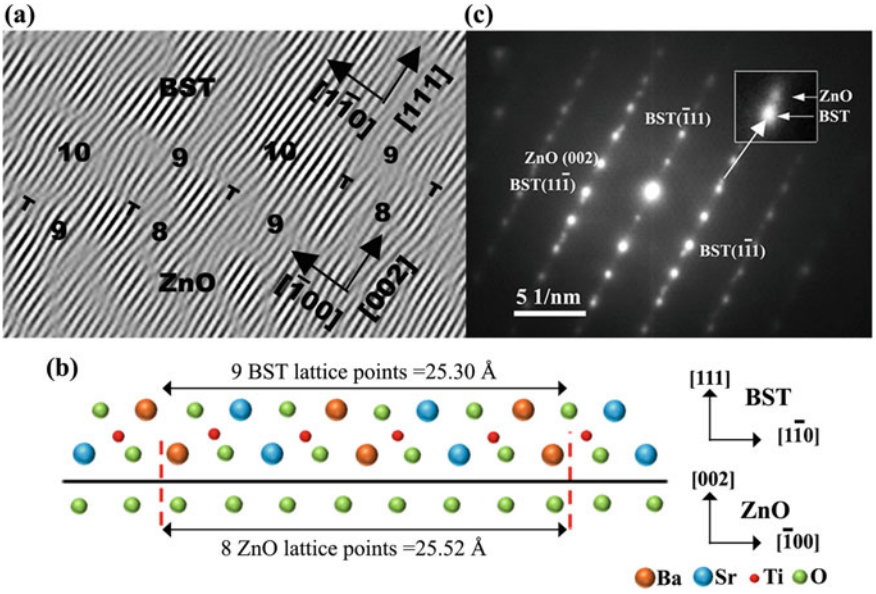

Fig. 8 **a** Domain matching epitaxy in the BST/ZnO system, Fourier-filtered image of matching of BST (1$\bar{1}$0) and ZnO ($\bar{1}$00) planes for 9/8 and 10/9 domains across the BST-ZnO interface, **b** schematic representation of 9/8 domain matching in the BST-ZnO interface and **c** corresponding electron diffraction pattern showing the alignment of planes in BST and ZnO. Reprinted from Krishnaprasad et al. [16], with the permission of AIP Publishing

of the BST-ZnO interface, with every 9 or 10 planes of BST (1$\bar{1}$0) matches with 8 or 9 planes of ZnO ($\bar{1}$00) as shown in Fig. 8a. This gives clear confirmation of the DME of BST thin films on the ZnO buffer layer. Schematic arrangement of atoms in the 9/8 domain matching across the BST-ZnO interface is shown in Fig. 8b. Figure 8c shows the SAED pattern of the BST-ZnO interface, where the alignment of BST (111) planes with ZnO (002) planes is clearly shown. The sharp intense spots in the SAED pattern indicate the highly crystalline nature of BST thin films.

In the domain matched epitaxial growth of BZN (2$\bar{2}$0) on ZnO ($\bar{1}$00) substrate, seven planes of ZnO ($\bar{1}$00) match with six planes of BZN (2$\bar{2}$0) planes (Fig. 9). The spacing of BZN (2$\bar{2}$0) planes (3.77 Å) is close to 17.8% residual mismatch with ($\bar{1}$00) planes of ZnO (3.20 Å). The domain matching of 6 × d{BZN (2$\bar{2}$0)} and 7 × d{ZnO ($\bar{1}$00)} results in less than 1% residual strain [29].

$$m = \left(6 \times a_e/2\sqrt{2} - 7 \times a_b\right)/(7 \times a_b) = 0.0098$$

The capacitance measurements of epitaxial BST thin films were performed on interdigital capacitors (IDC) patterned over the BST thin films by a standard photolithographic process. Capacitance-voltage measurements (Fig. 10) were performed at 1 MHz, and the voltage applied was swept from −5 to +5 V. The epitaxial BST

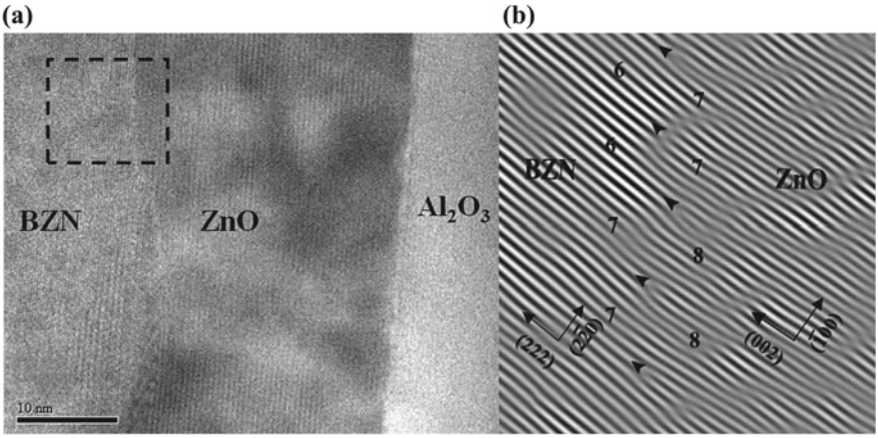

Fig. 9 Domain matching epitaxy in the BZN/ZnO system, **a** HRTEM image of BZN-ZnO–Al_2O_3 film cross section. **b** Fourier-filtered image of the selected area in (**a**) showing domain matching of BZN (2$\bar{2}$0) and ZnO ($\bar{1}$00) planes for 7/8 and 6/7 domains across the BZN-ZnO interface

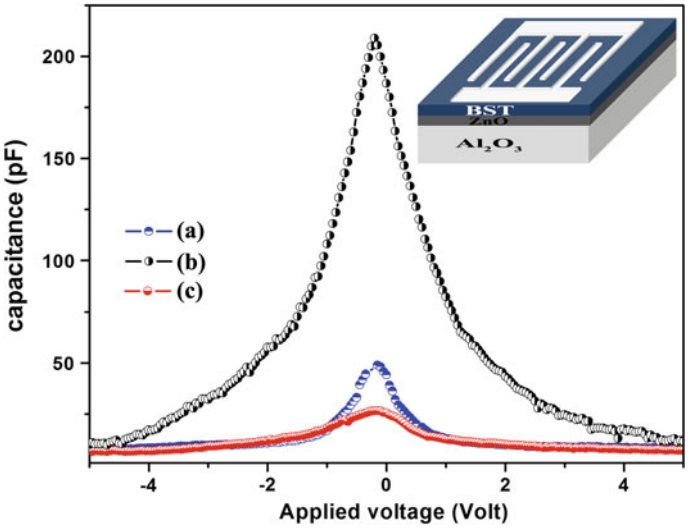

Fig. 10 Capacitance-voltage measurements for the fabricated IDC over BST films with ZnO buffer layer. The ZnO buffer layers were deposited at various oxygen partial pressures, **a** 5×10^{-4} mbar, **b** 7×10^{-4} mbar, and **c** 10×10^{-4} mbar and BST thin films were deposited at optimized conditions. Schematic representation of the IDC structure patterned over the BST thin film is shown in the inset. Reprinted from Krishnaprasad et al. [16], with the permission of AIP Publishing

thin films on Al_2O_3 with ZnO buffer layer deposited at oxygen partial pressures (a) 5×10^{-4} mbar, (b) 7×10^{-4} mbar exhibit a high dielectric tunability ($T = [C_{max} - C_{min}/C_{max}]\%$) of 95% and 85%, respectively, even at an applied voltage of 5 V, whereas for the polycrystalline BST thin film with ZnO buffer layer deposited at 10×10^{-4} mbar exhibits a tunability of 71%. Dissipation factor (tanδ) was also measured as a function of bias voltage. The measured dissipation factor was of the order of 10^{-2} in the MHz range. These results indicate that the epitaxial growth of BST thin film on ZnO buffer layer has contributed to the enhancement in dielectric tunability keeping the dielectric loss low. The large observed tunability can be attributed to the (111)-oriented domain structure, epitaxial nature of the film and lower residual strain. This high tunability with low loss tangent makes these films well-suited for microwave phase shifter applications. DME growth of BZN also resulted in a large enhancement in dielectric tunability keeping low dielectric loss [137–139].

Variation of capacitance and dissipation factor as a function of frequency measured at 1 V is shown in Fig. 11. The measurement has been carried out on the epitaxial BST thin film with its ZnO buffer layer deposited at 7×10^{-4} mbar. The low value of dielectric loss ($\approx 10^{-2}$) can be ascribed to the high crystalline quality of the thin film and the absence of interfacial defects. It can be seen that the dielectric constant, as well as dissipation factor, shows no noticeable dispersion with frequency in the high-frequency range, indicating the high crystalline quality of the thin films. The

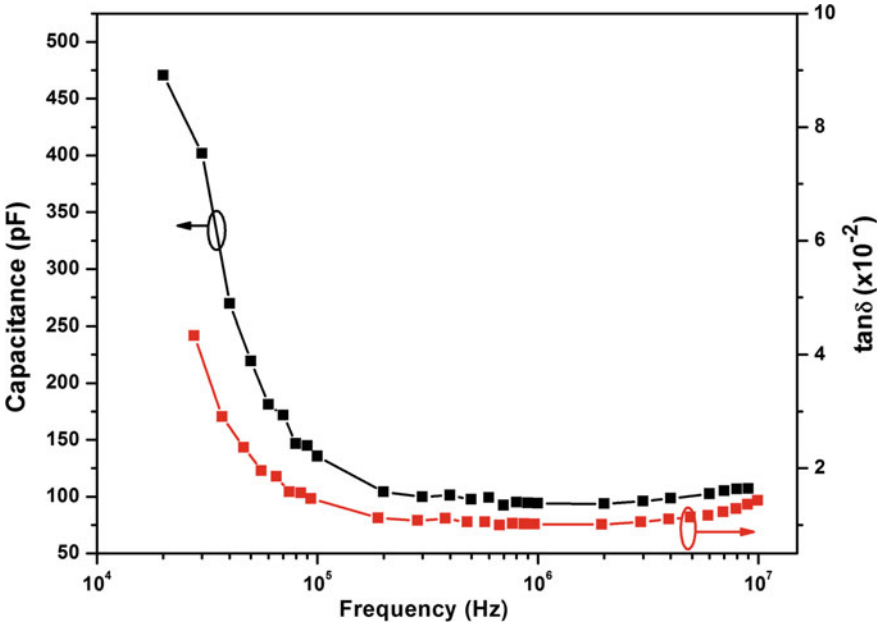

Fig. 11 Variation of capacitance and dielectric loss of the epitaxial BST thin film as a function of the frequency. Reprinted from Krishnaprasad et al. [16], with the permission of AIP Publishing

decreasing tendency in dielectric constant, as well as dissipation factor up to 100 kHz, may be due to the higher contribution from DC conduction process in the low-frequency region [140].

7 Conclusion

The ever-increasing need for miniaturization of devices and the potential integration of ferroelectric materials with semiconductor microelectronic circuits have been a constant driving force for the development of highly sophisticated new dielectric materials and improving their performance by doping and growing them epitaxially. Potential applications for ferroelectric thin films include high k varactors, memory devices, smart sensors, micro-electro-mechanical systems, tunable microwave devices, optoelectronic components and many more. This wide range of applications and increased demand for dielectric material with improved properties suitable for modern integrated circuits have motivated many scientists and engineers to systematically study their synthesis, structural, microstructural and dielectric properties. Perovskite and pyrochlore materials with high and tunable dielectric constant such as $SrTiO_3$, (Ba, Sr)TiO_3, $Sr_3Pb_6Ce_2Ti_{12}O_{36}$ and $Bi_{1.5}Zn_1Nb_{1.5}O_7$ have been investigated as materials for future memory and tunable applications [94, 136, 141–143]. Among these materials, BST and BZN are the most studied materials for memory and tunable microwave applications. BST and BZN thin films were deposited directly on single-crystalline Al_2O_3 substrates as well as with ZnO buffer layer. The use of ZnO buffer layer has promoted epitaxial (111)-oriented $Ba_{0.5}Sr_{0.5}TiO_3$ thin films on Al_2O_3 (0001) substrate. In the case of BZN, thin films which are deposited directly onto Al_2O_3 were polycrystalline in nature. A double ZnO buffer layer has effectively reduced the lattice mismatch and favoured the domain matching epitaxial growth of BZN thin film on ZnO buffer layer. Different *X*-ray techniques like ω-2θ, Φ-scan and reciprocal space mapping confirmed the epitaxial growth. The domain matched the growth of BST thin films over the ZnO buffer layer was confirmed using Fourier-filtered HRTEM images of the film–buffer interface. Thus, the incorporation of ZnO buffer layer effectively suppressed the lattice mismatch and promoted domain matched epitaxial growth of BST and BZN thin films. Significant improvement in dielectric tunability has been observed in epitaxial films over polycrystalline thin films. Thus, the growth approach based on domain matching epitaxy for dielectric thin films gives a convenient way to fabricate high-quality epitaxial ferroelectric films that can be used for fabrication of microwave phase shifters as well as memory devices.

References

1. Valasek J (1921) Piezo-electric and allied phenomena in rochelle salt. Phys Rev 17:475–481. https://doi.org/10.1103/PhysRev.17.475
2. Eason R (2007) Pulsed laser deposition of thin films. Wiley, New Jersey
3. Busch G, Scherrer P (1987) A new seignette-electric substance. Ferroelectrics 71:15–16. https://doi.org/10.1080/00150198708224825
4. Wainer E, Salomon N (1943) Electrical reports titanium alloys manufacturing division. Natl Lead Co. Reports. No. 8, 9, 1
5. Haertling GH (1999) Ferroelectric ceramics: history and technology. J Am Ceram Soc 82:797–818. https://doi.org/10.1111/j.1151-2916.1999.tb01840.x
6. Kittel C (1996) Introduction to solid state physics. Wiely Eastern Limtd
7. Wang XU (2009) Tunable microwave filters using ferroelectric thin films. https://etheses.bham.ac.uk//id/eprint/1227/1/Wang09PhD.pdf
8. Tagantsev AK, Sherman VO, Astafiev KF, Venkatesh J, Setter N (2003) Ferroelectric materials for microwave tunable applications. J Electroceramics 11:5–66. https://doi.org/10.1023/B:JECR.0000015661.81386.e6
9. Kuylenstierna D, Ash E, Vorobiev A, Itoh T, Gevorgian S (2006) X-band left handed phase shifter using thin film $Ba_{0.25}Sr_{0.75}Tio_3$ ferroelectric varactors. In: 2006 European microwave conference, IEEE, pp 847–850
10. Kim KB, Yun TS, Lee JC, Chaker M, Park CS, Wu K (2007) Integration of microwave phase shifter with BST varactor onto TiO_2/Si wafer. Electron Lett 43:757. https://doi.org/10.1049/el:20070448
11. Vicki Chen L-Y, Forse R, Chase D, York RA (2004) Analog tunable matching network using integrated thin-film BST capacitors. In: 2004 IEEE MTT-S international microwave symposium digest (IEEE Cat. No. 04CH37535), IEEE, pp 261–264
12. Kuylenstierna D, Vorobiev A, Linner P, Gevorgian S (2005) Ultrawide-band tunable true-time delay lines using ferroelectric varactors. IEEE Trans Microw Theory Tech 53:2164–2170. https://doi.org/10.1109/TMTT.2005.848805
13. Bao P, Jackson TJ, Wang X, Lancaster MJ (2008) Barium strontium titanate thin film varactors for room-temperature microwave device applications. J Phys D Appl Phys 41:063001. https://doi.org/10.1088/0022-3727/41/6/063001
14. Yan X, Ren W, Shi P, Wu X, Yao X (2011) Enhanced tunable dielectric properties of $Ba_{0.5}Sr_{0.5}TiO_3/Bi_{1.5}Zn_{1.0}Nb_{1.5}O_7$ multilayer thin films by a sol–gel process. Thin Solid Films 520:789–792. https://doi.org/10.1016/j.tsf.2011.04.118
15. Chen CL, Feng HH, Zhang Z, Brazdeikis A, Huang ZJ, Chu WK, Chu CW, Miranda FA, Van Keuls FW, Romanofsky RR, Liou Y (1999) Epitaxial ferroelectric $Ba_{0.5}Sr_{0.5}TiO_3$ thin films for room-temperature tunable element applications. Appl Phys Lett 75:412. https://doi.org/10.1063/1.124392
16. Krishnaprasad PS, Antony A, Rojas F, Jayaraj MK (2015) (Domain matched epitaxial growth of (111) $Ba_{0.5}Sr_{0.5}TiO_3$ thin films on (0001) Al_2O_3 with ZnO buffer layer. J Appl Phys 117:124102. https://doi.org/10.1063/1.4915949
17. Ranjan R, Pandey D, Schuddinck W, Richard O, De Meulenaere P, Van Landuyt J, Van Tendeloo G (2001) Evolution of crystallographic phases in $(Sr_{1-x}Ca_x)TiO_3$ with composition (x). J Solid State Chem 162:20–28. https://doi.org/10.1006/jssc.2001.9336
18. Kitamura N, Mizoguchi T, Itoh T, Idemoto Y (2014) Ferroelectric performances and crystal structures of (Pb, La) (Zr, Ti, Nb)O_3. J Solid State Chem 210:275–279. https://doi.org/10.1016/j.jssc.2013.11.038
19. Gevorgian S (2009) Ferroelectrics in microwave devices, circuits and systems. Springer Science & Business Media, New York
20. Fujisaki Y, Iseki K, Ishiwara H (2003) Characterization of metal-ferroelectric-metal-insulator-semiconductor (MFMIS) fets using $(Sr,Sm)_{0.8}Bi_{2.2}Ta_2O_9$ (SSBT). Thin Films Mater Res Soc Symp Proc 786:297. https://doi.org/10.1557/proc-786-e9.8/c9.8

21. Schlom DG, Guha S, Datta S (2008) Gate oxides beyond SiO_2. MRS Bull 33:1017–1025. https://doi.org/10.1557/mrs2008.221
22. Liang Y, Kulik J, Wei Y, Eschrich T, Curless J, Craigo B, Smith S (2003) Hetero-epitaxy of crystalline perovskite oxides on GaAs(001). MRS Proc. 786:E8.4.1–E8.4.6. https://doi.org/10.1557/proc-786-e8.4
23. Chen DY, Murphy TE, Phillips JD (2005) Properties of ferroelectric Pb(Zr, Ti)O_3 thin films on ZnO/Al_2O_3(0001) epilayers. Thin Solid Films 491:301–304. https://doi.org/10.1016/j.tsf.2005.06.007
24. Ashkenov N, Schubert M, Twerdowski E, Wenckstern HV, Mbenkum BN, Hochmuth H, Lorenz M, Grill W, Grundmann M (2005) Rectifying semiconductor-ferroelectric polarization loops and offsets in Pt-$BaTiO_3$-ZnO-Pt thin film capacitor structures. Thin Solid Films 486:153–157. https://doi.org/10.1016/j.tsf.2004.11.226
25. Evans JT, Suizu RI, Boyer LL (1997) Functionality of the ferroelectric/oxide semiconductor interface. Appl Surf Sci 117–118:413–417. https://doi.org/10.1016/S0169-4332(97)80116-X
26. Afanas'ev VP, Bulat DY, Kaptelov EY, Pronin IP (2004) The effect of optical radiation on the semiconductor conductivity in a thin-film ferroelectric-semiconductor structure. Tech Phys Lett 30:518–521. https://doi.org/10.1134/1.1773355
27. Cho K-H, Kang M-G, Oh S-M, Kang C-Y, Lee Y, Yoon S-J (2010) Low voltage ZnO thin-film transistors with Ti-substituted BZN gate insulator for flexible electronics. Thin Solid Films 518:6277–6279. https://doi.org/10.1016/j.tsf.2010.03.061
28. Wu J, Wang J (2010) ZnO as a buffer layer for growth of $BiFeO_3$ thin films. J Appl Phys 108:034102. https://doi.org/10.1063/1.3460108
29. Krishnaprasad PS, Antony A, Rojas F, Bertomeu J, Jayaraj MK (2014) Domain matched epitaxial growth of $Bi_{1.5}Zn_1Nb_{1.5}O_7$ thin films by pulsed laser deposition. J Alloys Compd 586:524–528. https://doi.org/10.1016/j.jallcom.2013.10.025
30. Wu J, Wang J (2010) Diodelike and resistive hysteresis behavior of heterolayered $BiFeO_3$/ZnO ferroelectric thin films. J Appl Phys 108:094107. https://doi.org/10.1063/1.3500498
31. Muralt P (2000) Ferroelectric thin films for micro-sensors and actuators: a review. J Micromech Microeng 10:136. https://doi.org/10.1088/0960-1317/10/2/307
32. Sakai S, Takahashi M (2010) Recent progress of ferroelectric-gate field-effect transistors and applications to nonvolatile logic and FeNAND flash memory. Mater (Basel) 3:4950–4964. https://doi.org/10.3390/ma3114950
33. Butler KT, Frost JM, Walsh A (2015) Ferroelectric materials for solar energy conversion: photoferroics revisited. Energy Environ Sci 8:838–848. https://doi.org/10.1039/C4EE03523B
34. Wu SY (1974) A new ferroelectric memory device, metal-ferroelectric-semiconductor transistor. IEEE Trans Electron Devices 21:499–504. https://doi.org/10.1109/T-ED.1974.17955
35. Evans JT, Womack R (1988) An experimental 512-bit nonvolatile memory with ferroelectric storage cell. IEEE J Solid-State Circ 23:1171–1175. https://doi.org/10.1109/4.5940
36. Ma TP, Han JP (2002) Why is nonvolatile ferroelectric memory field-effect transistor still elusive? IEEE Electron Device Lett 23:386–388. https://doi.org/10.1109/LED.2002.1015207
37. Grossman M, Lohse O, Bolten D, Boettger U, Waser R (2002) Hetero-epitaxy of crystalline perovskite oxides on GaAs(001). In: MRS symposium proceedings, vol. 688, pp C3.4.1–C3.4.9
38. Cagin E, Chen DY, Siddiqui JJ, Phillips JD (2007) Hysteretic metal–ferroelectric–semiconductor capacitors based on PZT/ZnO heterostructures. J Phys D Appl Phys 40:2430–2434. https://doi.org/10.1088/0022-3727/40/8/003
39. Siddiqui J, Cagin E, Chen D, Phillips JD (2006) ZnO thin-film transistors with polycrystalline (Ba, Sr) TiO_3 gate insulators. Appl Phys Lett 88:1–4. https://doi.org/10.1063/1.2204574
40. Reshmi R, Asha AS, Krishnaprasad PS, Jayaraj MK, Sebastian MT (2011) High tunability of pulsed laser deposited $Ba_{0.7}Sr_{0.3}TiO_3$ thin films on perovskite oxide electrode. J Alloys Compd 509:6561–6566. https://doi.org/10.1016/j.jallcom.2011.02.074
41. James KK, Krishnaprasad PS, Hasna K, Jayaraj MK (2015) Structural and optical properties of La-doped $BaSnO_3$ thin films grown by PLD. J Phys Chem Solids 76:64–69. https://doi.org/10.1016/j.jpcs.2014.07.024

42. Hartmann AJ, Neilson M, Lamb RN, Watanabe K, Scott JF (2000) Ruthenium oxide and strontium ruthenate electrodes for ferroelectric thin-films capacitors. Appl Phys A Mater Sci Process 70:239–242. https://doi.org/10.1007/s003390050041
43. Yang Q, Cao J, Zhou Y, Sun L, Lou X (2016) Dead layer effect and its elimination in ferroelectric thin film with oxide electrodes. Acta Mater 112:216–223. https://doi.org/10.1016/j.actamat.2016.04.036
44. Vijay DP (1993) Electrodes for $PbZr_xTi_{1-x}O_3$ ferroelectric thin films. J Electrochem Soc 140:2640. https://doi.org/10.1149/1.2220877
45. He L, Vanderbilt D (2003) First-principles study of oxygen-vacancy pinning of domain walls in $PbTiO_3$. Phys Rev B. 68:134103. https://doi.org/10.1103/PhysRevB.68.134103
46. Jayadevan KP, Liu CY, Tseng TY (2005) Surface chemical and leakage current density characteristics of nanocrystalline Ag-$Ba_{0.5}Sr_{0.5}TiO_3$ thin films. J Am Ceram Soc 88:2456–2460. https://doi.org/10.1111/j.1551-2916.2005.00441.x
47. Srivastava A, Kumar D, Singh RK, Venkataraman H, Eisenstadt WR (2000) Improvement in electrical and dielectric behavior of (Ba, Sr)TiO_3 thin films by Ag doping. Phys Rev B 61:7305–7307. https://doi.org/10.1103/PhysRevB.61.7305
48. Lee SY, Tseng TY (2002) Electrical and dielectric behavior of MgO doped $Ba_{0.7}Sr_{0.3}TiO_3$ thin films on Al_2O_3 substrate. Appl Phys Lett 80 1797. https://doi.org/10.1063/1.1458067
49. Jayadevan KP, Tseng TY (2002) Composite and multilayer ferroelectric thin films: processing, properties and applications. J Mater Sci: Mater Electron 13:439–459. https://doi.org/10.1023/A:101612931
50. Cross LE, Newnham RE (1987) History of ferroelectrics. Ceram Civiliz III:289–305
51. Kawashima S, Nishida M, Ueda I, Ouchi H (1983) Ba($Zn_{1/3}Ta_{2/3}$)O_3 ceramics with low dielectric loss at microwave frequencies. J Am Ceram Soc 66:421–423. https://doi.org/10.1111/j.1151-2916.1983.tb10074.x
52. Cole MW, Joshi PC, Ervin MH (2001) La doped $Ba_{1-x}Sr_xTiO_3$ thin films for tunable device applications. J Appl Phys 89:6336. https://doi.org/10.1063/1.1366656
53. Cole MW, Joshi PC, Ervin MH, Wood MC, Pfeffer RL (2000) The influence of Mg doping on the materials properties of $Ba_{1-x}Sr_xTiO_3$ thin films for tunable device applications. Thin Solid Films 374:34–41. https://doi.org/10.1016/S0040-6090(00)01059-2
54. Xu Y (2013) Ferroelectric materials and their applications. Elsevier Science, Amsterdam
55. Weston TB, Webster AH, Mcnamara VM (1969) Lead zirconate-lead titanate piezoelectric ceramics with iron oxide additions. J Am Ceram Soc 52:253–257. https://doi.org/10.1111/j.1151-2916.1969.tb09178.x
56. Ahn KH, Baik S, Kim SS (2002) Significant suppression of leakage current in (Ba, Sr)TiO_3 thin films by Ni or Mn doping. J Appl Phys 92:2651. https://doi.org/10.1063/1.1495526
57. Zhou Y, Xue D, Ding X, Zhang L, Sun J, Ren X (2013) Modeling the paraelectric aging effect in the acceptor doped perovskite ferroelectrics: role of oxygen vacancy. J Phys: Condens Matter 25:435901. https://doi.org/10.1088/0953-8984/25/43/435901
58. Morrison FD, Sinclair DC, West AR (1999) Electrical and structural characteristics of lanthanum-doped barium titanate ceramics. J Appl Phys 86:6355. https://doi.org/10.1063/1.371698
59. Sedlar M, Sayer M, Weaver L (1995) Sol-gel processing and properties of cerium doped barium strontium titanate thin films. J Sol-Gel Sci Technol 5:201–210. https://doi.org/10.1007/BF00487017
60. Wang SY, Cheng BL, Wang C, Redfern SAT, Dai SY, Jin KJ, Lu HB, Zhou YL, Chen ZH, Yang GZ (2005) Influence of Ce doping on leakage current in $Ba_{0.5}Sr_{0.5}TiO_3$ films. J Phys D Appl Phys 38:2253. https://doi.org/10.1088/0022-3727/38/13/025
61. Kamba S, Savinov M, Laufek F, Tkáč O, Kadlec C, Veljko S, John EJ, Subodh G, Sebastian MT, Klementová M, Bovtun V, Pokorný J, Goian V, Petzelt J (2009) Ferroelectric and incipient ferroelectric properties of a novel $Sr_{9-x}Pb_xCe_2Ti_2O_{36}$ ($x = 0$–9) ceramic system. Chem Mater 21:811–819. https://doi.org/10.1021/cm803058q
62. Krishnaprasad PS, Mohanan P, Subodh G, Sebastian MT, Jayaraj MK (2014) A novel $Sr_3Pb_6Ce_2Ti1_2O_36$ ferroelectric thin film grown by pulsed laser ablation. Appl Phys A 116:199–206. https://doi.org/10.1007/s00339-013-8085-5

63. Kaiser WJ, Logothetis EM, Wenger LE (1985) Dielectric response of small metal particle composites. J Phys C: Solid State Phys 18:L837–L842. https://doi.org/10.1088/0022-3719/18/26/013
64. Chýlek P, Srivastava V (1984) Effective dielectric constant of a metal-dielectric composite. Phys Rev B 30:1008–1009. https://doi.org/10.1103/PhysRevB.30.1008
65. Duan N, ten Elshof JE, Verweij H, Greuel G, Dannapple O (2000) Enhancement of dielectric and ferroelectric properties by addition of Pt particles to a lead zirconate titanate matrix. Appl Phys Lett 77:3263. https://doi.org/10.1063/1.1325405
66. Li Y, Shu L, Zhou Y, Guo J, Xiang F, He L, Wang H (2013) Enhanced flexoelectric effect in a non-ferroelectric composite. Appl Phys Lett 103:142909. https://doi.org/10.1063/1.4824168
67. George S, James J, Sebastian MT (2007) Giant permittivity of a bismuth zinc niobate-silver composite. J Am Ceram Soc 90:3522–3528. https://doi.org/10.1111/j.1551-2916.2007.01935.x
68. Huang J, Cao Y, Hong M, Du P (2008) Ag–$Ba_{0.75}Sr_{0.25}TiO_3$ composites with excellent dielectric properties. Appl Phys Lett 92:90–93. https://doi.org/10.1063/1.2836764
69. Hwang HJ, Nagai T, Ohji T, Sando M, Toriyama M, Niihara K (2005) Curie temperature anomaly in lead zirconate titanate/silver composites. J Am Ceram Soc 81:709–712. https://doi.org/10.1111/j.1151-2916.1998.tb02394.x
70. Xiang PH, Dong XL, Feng C De, Liang RH, Wang YL (2006) Dielectric behavior of lead zirconate titanate/silver composites. Mater Chem Phys 97:410–414. https://doi.org/10.1016/j.matchemphys.2005.08.034
71. Jayadevan KP, Liu CY, Tseng TY (2004) Dielectric characteristics of nanocrystalline Ag–$Ba_{0.5}Sr_{0.5}TiO_3$ composite thin films. Appl Phys Lett 85:1211. https://doi.org/10.1063/1.1780596
72. Joshi PC, Cole MW (2000) Mg-doped $Ba_{0.6}Sr_{0.4}TiO_3$ thin films for tunable microwave applications. Appl Phys Lett 77:289. https://doi.org/10.1063/1.126953
73. Narayan J, Larson B (2003) Domain epitaxy: a unified paradigm for thin film growth. J Appl Phys 93:278–285. https://doi.org/10.1063/1.1528301
74. Maissel LI, Glang R (1970) Handbook of thin film technology. McGraw-Hill, New York
75. Frank FC, van der Merwe JH (1949) One-dimensional dislocations. I. Static theory. Proc R Soc Lond A Math Phys Sci 198:205–216. https://doi.org/10.2307/98165
76. Stevens BL, Cohen DJ, Barnett SA (2008) Structure and interdiffusion of epitaxial ZnO/ZnMgO nanolayered thin films. J Vac Sci Technol A: Vacuum, Surfaces, Film 26:1538. https://doi.org/10.1116/1.2993257
77. Yano M, Ogata K, Yan F, Koike K, Sasa S, Inoue M (2002) ZnO and ZnMgO growth by molecular beam epitaxy. MRS Proc 744, M3.1. https://doi.org/10.1557/proc-744-m3.1
78. Vispute RD, Talyansky V, Choopun S, Sharma RP, Venkatesan T, He M, Tang X, Halpern JB, Spencer MG, Li YX, Salamanca-Riba LG, Iliadis AA, Jones KA (1998) Heteroepitaxy of ZnO on GaN and its implications for fabrication of hybrid optoelectronic devices. Appl Phys Lett 73:348. https://doi.org/10.1063/1.121830
79. Visinoiu A, Scholz R, Chattopadhyay S, Alexe M, Hesse D (2002) Formation of epitaxial $BaTiO_3/SrTiO_3$ multilayers grown on Nb-doped $SrTiO_3$(001) substrates. Jpn J Appl Phys 41:6633
80. Shimoyama K, Kiyohara M, Kubo K, Uedono A, Yamabe K (2002) Epitaxial growth of $BaTiO_3/SrTiO_3$ structures on $SrTiO_3$ substrate with automatic feeding of oxygen from the substrate. J Appl Phys 92:4625. https://doi.org/10.1063/1.1506196
81. Jin C (2003) Growth and characterization of ZnO and ZnO based alloys MgxZn_{1-x}O and MnxZn_{1-x}O
82. Tuoc VN (2008) First principle study on the domain matching epitaxy growth of semiconductor hetero-interface. Mater Trans 49:2491–2496. https://doi.org/10.2320/matertrans.MB200818
83. Vispute RD, Chowdhury R, Tiwari P, Narayan J (1994) Pulsed laser deposition and characterization of epitaxial Cu/TiN/Si(100) heterostructures. Appl Phys Lett 65:2565–2567. https://doi.org/10.1063/1.112994

84. Zheleva T, Jagannadham K, Narayan J (1994) Epitaxial growth in large-lattice-mismatch systems. J Appl Phys 75:860–871. https://doi.org/10.1063/1.356440
85. Narayan J, Dovidenko K, Sharma AK, Oktyabrsky S (1998) Defects and interfaces in epitaxial ZnO/α-Al_2O_3 and AlN/ZnO/α-Al_2O_3 heterostructures. J Appl Phys 84:2597. https://doi.org/10.1063/1.368440
86. Vispute RD, Wu H, Narayan J (1995) High quality epitaxial aluminum nitride layers on sapphire by pulsed laser deposition. Appl Phys Lett 67:1549. https://doi.org/10.1063/1.114489
87. Vispute RD, Narayan J, Dovidenko K, Jagannadham K, Parikh N, Suvkhanov A, Budai JD (1996) Heteroepitaxial structures of $SrTiO_3$/TiN on Si(100) by in situ pulsed laser deposition. J Appl Phys 80:6720. https://doi.org/10.1063/1.363798
88. Sánchez F, Bachelet R, de Coux P, Warot-Fonrose B, Skumryev V, Tarnawska L, Zaumseil P, Schroeder T, Fontcuberta J (2011) Domain matching epitaxy of ferrimagnetic $CoFe_2O_4$ thin films on Sc_2O_3/Si(111). Appl Phys Lett 99:211910. https://doi.org/10.1063/1.3663216
89. Liu W-R, Li Y-H, Hsieh WF, Hsu C-H, Lee WC, Lee YJ, Hong M, Kwo J (2009) Domain matching epitaxial growth of high-quality ZnO film using a YO buffer layer on Si(111). Cryst Growth Des 9:239–242. https://doi.org/10.1021/cg8003849
90. Zhang KHL, Lazarov VK, Galindo PL, Oropeza FE, Payne DJ, Egdell RG (2012) Domain matching epitaxial growth of In_2O_3 thin films on α-Al_2O_3(0001). Cryst Growth Des 12:1000–1007. https://doi.org/10.1021/cg201474h
91. Zhuang L, Wong KH, Pang GKH (2007) Domain matching epitaxy of cubic $Mg_xZn_{1-x}O$ films on $LaAlO_3$ by pulsed laser deposition. Appl Phys A Mater Sci Process 89:543–546. https://doi.org/10.1007/s00339-007-4121-7
92. Song YH, Son JH, Yu HK, Lee JH, Jung GH, Lee JY, Lee JL (2011) Domain matching epitaxy of Mg-containing Ag contact on p-type GaN. Cryst Growth Des 11:2559–2563. https://doi.org/10.1021/cg200323h
93. Ezhilvalavan S, Tseng TY (2000) Progress in the developments of (Ba, Sr)TiO_3 (BST) thin films for Gigabit era DRAMs. Mater Chem Phys 65:227–248. https://doi.org/10.1016/S0254-0584(00)00253-4
94. Setter N, Damjanovic D, Eng L, Fox G, Gevorgian S, Hong S, Kingon A, Kohlstedt H, Park NY, Stephenson GB, Stolitchnov I, Taganstev AK, Taylor DV, Yamada T, Streiffer S (2006) Ferroelectric thin films: review of materials, properties, and applications. J Appl Phys 100:051606. https://doi.org/10.1063/1.2336999
95. Vélu G, Blary K, Burgnies L, Marteau A, Houzet G, Lippens D, Carru J (2007) A 360 BST phase shifter with moderate bias voltage at 30 GHz. IEEE Trans Microw Theory Techn 55:438–444. https://doi.org/10.1109/TMTT.2006.889319
96. Van Keuls FW, Romanofsky RR, Bohman DY, Winters MD, Miranda FA, Mueller CH, Treece RE, Rivkin TV, Galt D (1997) ($YBa_2Cu_3O_{7-\delta}$,Au)/$SrTiO_3$/$LaAlO_3$ thin film conductor/ferroelectric coupled microstrip line phase shifters for phased array applications. Appl Phys Lett 71:3075. https://doi.org/10.1063/1.120251
97. Basmajian JA, Devries RC (1957) Phase equilibria in the system $BaTiO_3$–$SrTiO_3$. J Am Ceram Soc 40:373–376. https://doi.org/10.1111/j.1151-2916.1957.tb12556.x
98. Tagantsev AK, Sherman VO, Astafiev KF, Venkatesh J, Setter N (2005) Permittivity, tunability and loss in ferroelectrics for reconfigurable high frequency electronics. Springer Science, Heidelberg
99. Panda B, Dhar A, Nigam GD, Bhattacharya D, Ray SK (1998) Optical properties of RF sputtered strontium substituted barium titanate thin films. Thin Solid Films 332:46–49. https://doi.org/10.1016/S0040-6090(98)01012-8
100. Cheng HF (1996) Structural and optical properties of laser deposited ferroelectric ($Sr_{0.2}Ba_{0.8}$)TiO_3 thin films. J Appl Phys 79:7965. https://doi.org/10.1063/1.362346
101. Adikary SU, Chan HLW (2003) Ferroelectric and dielectric properties of sol–gel derived $Ba_xSr_{1-x}TiO_3$ thin films. Thin Solid Films 424:70–74. https://doi.org/10.1016/S0040-6090(02)00918-5
102. Roy D, Krupanidhi SB (1993) Excimer laser ablated barium strontium titanate thin films for dynamic random access memory applications. Appl Phys Lett 62:1056–1058. https://doi.org/10.1063/1.108793

103. Knauss LA, Pond JM, Horwitz JS, Chrisey DB, Mueller CH, Treece R (1996) The effect of annealing on the structure and dielectric properties of $Ba_xSr_{1-x}TiO_3$ ferroelectric thin films. Appl Phys Lett 69:25. https://doi.org/10.1063/1.118106
104. Tarsa EJ, Hachfeld EA, Quinlan FT, Speck JS, Eddy M (1996) Growth-related stress and surface morphology in homoepitaxial SrTiO3 films. Appl Phys Lett 68:490. https://doi.org/10.1063/1.116376
105. Chen CL, Shen J, Chen SY, Luo GP, Chu CW, Miranda FA, Van Keuls FW, Jiang JC, Meletis EI, Chang HY (2001) Epitaxial growth of dielectric $Ba_{0.6}Sr_{0.4}TiO_3$ thin film on MgO for room temperature microwave phase shifters. Appl Phys Lett 78:652–654. https://doi.org/10.1063/1.1343499
106. Zhu X, Zhu J, Zhou S, Liu Z, Ming N, Lu S, Chan HL-W, Choy C-L (2003) Recent progress of (Ba,Sr)TiO_3 thin films for tunable microwave devices. J Electron Mater 32:1125–1134. https://doi.org/10.1007/s11664-003-0098-y
107. Kim WJ, Wu HD, Chang W, Qadri SB, Pond JM, Kirchoefer SW, Chrisey DB, Horwitz JS (2000) Microwave dielectric properties of strained $(Ba_{0.4}Sr_{0.6})TiO_3$ thin films. J Appl Phys 88:5448. https://doi.org/10.1063/1.1314619
108. Sirenko AA, Bernhard C, Golnik A, Clark AM, Hao J, Si W, Xi XX (2000) Soft-mode hardening in $SrTiO_3$ thin films. Nature 404:373–376. https://doi.org/10.1038/35006023
109. Chang W, Horwitz JS, Carter AC, Pond JM, Kirchoefer SW, Gilmore CM, Chrisey DB (1999) The effect of annealing on the microwave properties of $Ba_{0.5}Sr_{0.5}TiO_3$ thin films. Appl Phys Lett 74:1033. https://doi.org/10.1063/1.123446
110. Sirenko AA, Akimov IA, Fox JR, Clark AM, Li H-C, Si W, Xi XX (1999) Observation of the first-order Raman scattering in $SrTiO_3$ thin films. Phys Rev Lett 82:4500–4503. https://doi.org/10.1103/PhysRevLett.82.4500
111. Natori K, Otani D, Sano N (1998) Thickness dependence of the effective dielectric constant in a thin film capacitor. Appl Phys Lett 73:632. https://doi.org/10.1063/1.121930
112. Kang BS, Lee J-S, Stan L, Lee J-K, DePaula RF, Arendt PN, Nastasi M, Jia QX (2004) Dielectric properties of epitaxial $Ba_{0.6}Sr_{0.4}TiO_3$ films on SiO_2/Si using biaxially oriented ion-beam-assisted-deposited MgO as templates. Appl Phys Lett 85:4702. https://doi.org/10.1063/1.1812573
113. Park BH, Peterson EJ, Jia QX, Lee J, Zeng X, Si W, Xi XX (2001) Effects of very thin strain layers on dielectric properties of epitaxial $Ba_{0.6}Sr_{0.4}TiO_3$ films. Appl Phys Lett 78:533. https://doi.org/10.1063/1.1340863
114. Liu H, Avrutin V, Zhu C, Özgür U, Yang J, Lu C, Morkoç H (2013) Enhanced microwave dielectric tunability of $Ba_{0.5}Sr_{0.5}TiO_3$ thin films grown with reduced strain on $DyScO_3$ substrates by three-step technique. J Appl Phys 113:044108. https://doi.org/10.1063/1.4789008
115. Zhu X, Chong N, Chan HL-W, Choy C-L, Wong K-H, Liu Z, Ming N (2002) Epitaxial growth and planar dielectric properties of compositionally graded $(Ba_{1-x}Sr_x)TiO_3$ thin films prepared by pulsed-laser deposition. Appl Phys Lett 80:3376. https://doi.org/10.1063/1.1475367
116. Xiao B, Liu H, Avrutin V, Leach JH, Rowe E, Liu H, Özgür Ü, Morkoç H, Chang W, Alldredge LMB, Kirchoefer SW, Pond JM (2009) Epitaxial growth of (001)-oriented $Ba_{0.5}Sr_{0.5}TiO_3$ thin films on a-plane sapphire with an MgO/ZnO bridge layer. Appl Phys Lett 95:210–212. https://doi.org/10.1063/1.3266862
117. Yamada T, Muralt P, Sherman VO, Sandu CS, Setter N (2007) Epitaxial growth of $Ba_{0.3}Sr_{0.7}TiO_3$ thin films on Al_2O_3(0001) using ultrathin TiN layer as a sacrificial template. Appl Phys Lett 90:142911. https://doi.org/10.1063/1.2719673
118. Park BH, Gim Y, Fan Y, Jia QX, Lu P (2000) High nonlinearity of $Ba_{0.6}Sr_{0.4}TiO_3$ films heteroepitaxially grown on MgO substrates. Appl Phys Lett 77:2587. https://doi.org/10.1063/1.1318233
119. Yang Z, Hao J (2012) In-plane dielectric properties of epitaxial $Ba_{0.7}Sr_{0.3}TiO_3$ thin films grown on GaAs for tunable device application. J Appl Phys 112:054110. https://doi.org/10.1063/1.4749270

120. Carlson CM, Rivkin TV, Parilla PA, Perkins JD, Ginley DS, Kozyrev AB, Oshadchy VN, Pavlov AS (2000) Large dielectric constant ($\varepsilon/\varepsilon_0 > 6000$) $Ba_{0.4}Sr_{0.6}TiO_3$ thin films for high-performance microwave phase shifters. Appl Phys Lett 76:1920. https://doi.org/10.1063/1.126212
121. Leach JH, Liu H, Avrutin V, Xiao B, Özgür Ü, Morkoç H, Das J, Song YY, Patton CE (2010) Large dielectric tuning and microwave phase shift at low electric field in epitaxial $Ba_{0.5}Sr_{0.5}TiO_3$ on $SrTiO_3$. J Appl Phys 107:10–15. https://doi.org/10.1063/1.3359707
122. Zhou XY, Heindl T, Pang GKH, Miao J, Zheng RK, Chan HLW, Choy CL, Wang Y (2006) Microstructure and enhanced in-plane ferroelectricity of $Ba_{0.7}Sr_{0.3}TiO_3$ thin films grown on $MgAl_2O_4$(001) single-crystal substrate. Appl Phys Lett 89:232906. https://doi.org/10.1063/1.2402900
123. Yang L, Ponchel F, Wang G, Rémiens D, Légier J-F, Chateigner D, Dong X (2010) Microwave properties of epitaxial (111)-oriented $Ba_{0.6}Sr_{0.4}TiO_3$ thin films on Al_2O_3(0001) up to 40 GHz. Appl Phys Lett 97:162909. https://doi.org/10.1063/1.3478015
124. Lin Y, Lee J-S, Wang H, Li Y, Foltyn SR, Jia QX, Collis GE, Burrell AK, McCleskey TM (2004) Structural and dielectric properties of epitaxial $Ba_{1-x}Sr_xTiO_3$ films grown on $LaAlO_3$ substrates by polymer-assisted deposition. Appl Phys Lett 85:5007. https://doi.org/10.1063/1.1827927
125. Qin WF, Xiong J, Zhu J, Tang JL, Jie WJ, Wei XH, Zhang Y, Li YR (2007) Fabrication and characterization of epitaxial $Ba_{0.6}Sr_{0.4}TiO_3/LaNiO_3$ heterostructures. J Mater Sci Mater Electron 18:973–976. https://doi.org/10.1007/s10854-007-9150-7
126. Kim J, Choi JS, Park BH (2005) Low-temperature growth of epitaxial $Ba_{0.5}Sr_{0.5}TiO_3$ films applicable to microwave tunable devices. J Korean Phys Soc 46:183–185
127. Zhu X, Zheng D, Peng W, Miao J, Li J (2004) Structural and electrical properties of epitaxial $Ba_{0.5}Sr_{0.5}TiO_3/SrRuO_3$ heterostructures grown by pulsed laser deposition. J Cryst Growth 268:192–197. https://doi.org/10.1016/j.jcrysgro.2004.04.112
128. Li H, Finder J, Liang Y, Gregory R, Qin W (2005) Dielectric properties of epitaxial $Ba_{0.5}Sr_{0.5}TiO_3$ films on amorphous SiO_2 on sapphire. Appl Phys Lett 87:072905. https://doi.org/10.1063/1.2011774
129. Fardin EA, Holland AS, Ghorbani K, Reichart P (2006) Enhanced tunability of magnetron sputtered $Ba_{0.5}Sr_{0.5}TiO_3$ thin films on c-plane sapphire substrates. Appl Phys Lett 89:022901. https://doi.org/10.1063/1.2220530
130. Lu SG, Zhu XH, Mak CL, Wong KH, Chan HLW, Choy CL (2003) High tunability in compositionally graded epitaxial barium strontium titanate thin films by pulsed-laser deposition. Appl Phys Lett 82:2877–2879. https://doi.org/10.1063/1.1569427
131. Choi W, Kang BS, Jia QX, Matias V, Findikoglu AT (2006) Dielectric properties of ⟨001⟩-oriented $Ba_{0.6}Sr_{0.4}TiO_3$ thin films on polycrystalline metal tapes using biaxially oriented $MgO/\gamma\text{-}Al_2O_3$ buffer layers. Appl Phys Lett 88:062907. https://doi.org/10.1063/1.2173232
132. Moon SE, Kim EK, Kwak MH, Ryu HC, Kim YT, Kang KY, Lee SJ, Kim WJ (2003) Orientation dependent microwave dielectric properties of ferroelectric $Ba_{1-x}Sr_xTiO_3$ thin films. Appl Phys Lett 83:2166–2168. https://doi.org/10.1063/1.1609658
133. Cho CR, Hwang JY, Kim JP, Jeong SY, Yoon SG, Lee WJ (2004) Growth and characterization of $(Ba_{0.5}Sr_{0.5})TiO_3$ films epitaxially grown on (002) GaN/(0006) Al_2O_3 electrode. Jpn J Appl Phys 43:L1425–L1428. https://doi.org/10.1143/jjap.43.l1425
134. Fewster PF (2003) X ray scattering from semiconductors. Imperial College Press, Covent Garden, London
135. Tachibana T, Yokota Y, Kobashi K, Shintani Y (1997) X-ray diffraction pole figure measurements of diamond films grown on platinum(111). J Appl Phys 82:4327. https://doi.org/10.1063/1.366240
136. Alldredge LMB, Chang W, Qadri SB, Kirchoefer SW, Pond JM (2007) Ferroelectric and paraelectric $Ba_{0.5}Sr_{0.5}TiO_3$ film structure distortions at room temperature and their effects on tunable microwave properties. Appl Phys Lett 90:212901. https://doi.org/10.1063/1.2741610
137. Cao LZ, Fu WY, Wang SF, Wang Q, Sun ZH, Yang H, Cheng BL, Wang H, Zhou YL (2007) Effects of film thickness and preferred orientation on the dielectric properties of

$(Bi_{1.5}Zn_{0.5})(Zn_{0.5}Nb_{1.5})O_7$ films. J Phys D Appl Phys 40:2906–2910. https://doi.org/10.1088/0022-3727/40/9/036
138. Lu J, Stemmer S (2003) Low-loss, tunable bismuth zinc niobate films deposited by rf magnetron sputtering. Appl Phys Lett 83:2411–2413. https://doi.org/10.1063/1.1613036
139. Ren W, Trolier-McKinstry S, Randall CA, Shrout TR (2001) Bismuth zinc niobate pyrochlore dielectric thin films for capacitive applications. J Appl Phys 89:767. https://doi.org/10.1063/1.1328408
140. Zhu X, Zhu J, Zhou S, Liu Z, Ming N, Chan HL-W, Choy C-L, Wong K (2008) Epitaxial growth, dielectric response, and microstructure of compositionally graded (Ba,Sr)TiO_3 thin films grown on (100) MgO substrates by pulsed laser deposition. J Mater Res 23:737–744. https://doi.org/10.1557/JMR.2008.0086
141. Ramesh R (2013) Thin film ferroelectric materials and devices. Springer, New York
142. Pertsev NA, Koukhar VG (2000) Polarization instability in polydomain ferroelectric epitaxial thin films and the formation of heterophase structures. Phys Rev Lett 84:3722–3725. https://doi.org/10.1103/PhysRevLett.84.3722
143. Li YL, Choudhury S, Liu ZK, Chen LQ (2003) Effect of external mechanical constraints on the phase diagram of epitaxial $PbZr_{1-x}Ti_xO_3$ thin films—thermodynamic calculations and phase-field simulations. Appl Phys Lett 83:1608. https://doi.org/10.1063/1.1600824

Chapter 10
Metal-Oxide Transistors and Calculation of the Trap Density of States in the Band Gap of Semiconductors

M. R. Shijeesh, M. Jasna and M. K. Jayaraj

1 Introduction

Transparent electronics has gained much attention during the past decades, and its excellent electronic performance leads to one of the most promising technologies for the next generation of flat-panel displays. Thin-film transistors (TFTs) are an active component that is integrated into flat-panel displays. The need for optical transparency with larger band gaps (>3.3 eV) causes an incompatibility with high electronic conduction. The materials exhibiting high optical transparency and high electrical conductivity are rare. Wide band gap semiconductors, especially transparent conducting oxides (TCO) and transparent semiconducting oxides (TSO), are exceptional materials which show transparency and electrical conductivity. These are the promising class of thin-film transistor materials which lead to the remarkable progress in the display applications in a short span of time [1]. Indium tin oxide (ITO) is the first TCO, reported by Rupprecht [2] in 1954. Metal-oxide-based devices like transistors, inverters, etc., have been reported and provide a platform for fully transparent devices, with all components of transistors like substrate, channel, gate dielectric, gate and source/drain contacts fabricated using transparent materials having transparency greater than 70% in the visible spectrum. Intensive research progresses in display industries have demonstrated advanced flat-panel display (FPD) technology using metal oxides which include organic light-emitting diode displays (OLEDs), electronic paper (e-paper) and liquid crystal displays (LCDs) [3, 4]. Hence, the FPD market has been undergoing a quick shift from liquid crystal (LC) to OLED displays.

M. R. Shijeesh (✉)
Graphene & 2D Systems Laboratory, Department of Physics, Indian Institute of Technology Madras, Chennai 300036, India
e-mail: shijeesh.mr@gmail.com

M. Jasna · M. K. Jayaraj
Cochin University of Science and Technology, Kochi, India

M. K. Jayaraj (ed.), *Nanostructured Metal Oxides and Devices*,
Materials Horizons: From Nature to Nanomaterials,
https://doi.org/10.1007/978-981-15-3314-3_10

The foremost driving force for this rapid transformation was the introduction of novel oxide semiconductor materials as the channel layer in TFTs.

2 Development of Oxide TFTs

Among the electronic devices, the history of TFTs is more than 80 years old. The TFT was invented in 1925 and was patented in 1930 by Lilienfeld [5–7] and Heil [8]. Nevertheless, at that time, not much was known about semiconductor materials and vacuum techniques for thin-film production. Therefore, these reports are concept patents which do not give any evidence about the production of devices, but it gave the idea of controlling the current flow in a material due to the transversal electrical field. Lilienfeld's patent published in 1930 describes the principle of metal- semiconductor field-effect transistors and concepts of the introduction of an insulating layer of thickness 100 nm between semiconductors which are very similar to the structure used nowadays in TFTs, also published in Lilienfeld's other patent [9].

Since materials and fabrication technologies were inadequate, it took one more decade for the production of the first TFT by Weimer at the RCA Laboratories in 1962 [10, 11]. He used a thin film of polycrystalline cadmium sulphide (CdS) n-type semiconductor as a channel layer, silicon monoxide as an insulator and gold as source/drain electrodes using vacuum evaporation method with the aid of shadow masks to pattern these layers. Weimer used coplanar structure for the fabrication of TFT. His published paper, "The TFT—A New Thin-Film Transistor", in the proceedings of the IEEE, in 1962 got worldwide attention [10]. Oxide semiconductor TFT with evaporated SnO_2 as a channel layer was reported in 1964 [12]. But the electrical performance of the device was very poor. The first ZnO-based TFT was reported in 1968, however, with poor performance. Metal-oxide TFTs have now achieved the desired characteristics [13]. In LCD and OLED flat-panel displays, amorphous silicon (a-Si) and poly-silicon thin-film transistors are widely used. Nevertheless, conventional silicon-based TFTs have limitations with size and resolution of the displays, while the display industry demands high-end products, the realization of which using these TFTs seems challenging. Also, a-Si-based TFTs have relatively low mobility (<1 cm^2/Vs), bias instability and high fabrication cost.

Hoffmann et al. reported a fully transparent TFTs based on ZnO using ion beam sputtering in 2003 [14]. Carcia et al. also reported transparent ZnO TFT using RF magnetron sputtering [15]. After, Hosono's group reported TFT from amorphous indium gallium zinc oxide (a-IGZO) semiconductor in 2004 [16], and then oxide semiconductors were adopted as channel layers in flexible and transparent displays due to high electrical mobility, amorphicity and high optical transparency. Furthermore, amorphous oxide semiconductors (AOSs) have a lower density of states (DOS), containing tail and deep-level states, compared to that of a-Si [17]. These features indicate that oxide semiconductors will be an alternative candidate for the present and future of TFTs, which circumvents the drawbacks of existing technologies and offers

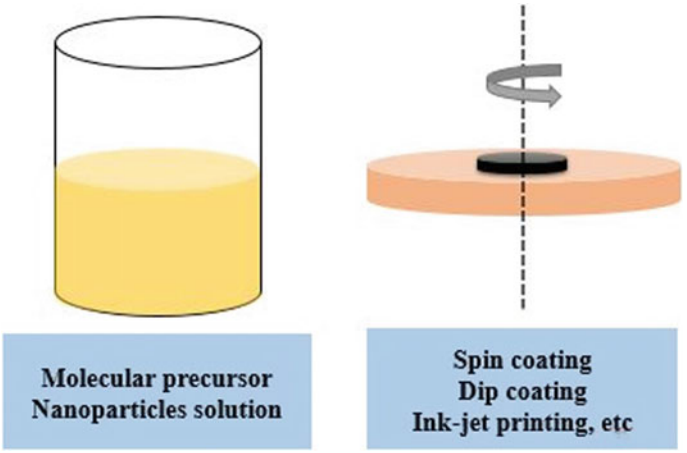

Fig. 1 Schematic diagram of the different types of solution process and types of materials

transparent, low-cost, low-temperature and high-performance devices for emerging technologies.

As discussed above, all of the oxide semiconductor-based TFTs were fabricated using high-vacuum technology leads to high fabrication cost. The rapidly emerging printable electronics demand low-cost fabrication process for the device production. Solution process is the attractive method for the fabrication of printable displays that suitable for low-cost large-area production. Figure 1 shows the schematic diagram of commonly used solution process such as spin coating, dip coating and inkjet printing and type of materials for the fabrication of oxide semiconductor TFTs. A thin film of oxide semiconductor can be obtained by spin coating or printing of precursor solution followed by annealing in air. Solution methods can offer an innovative cost-reduced method and large-area production with less number of masking stages [18]. ZnO-based solution-processed oxide TFTs were fabricated with the desired performance by employing the spin coating method in 2003 [19]. Ong et al. also fabricated spin-coated ZnO TFT by controlling the growth of ZnO in a (*002*) preferred orientation to enhance the mobility of the device [20]. Cheng et al. fabricated low-temperature ZnO-based TFT using chemical bath deposition (CBD) [21]. Therefore, the solution process provides a way for the fabrication of TFTs at low cost and high yield.

3 Device Structure

TFTs are three-terminal field-effect transistors whose working principle is similar to that of metal-oxide field-effect transistor (MOSFET). It consists of a substrate, gate electrode and semiconductor called channel layer, source/drain electrodes and an insulator. The device working principle relies on the modulation of the current flowing

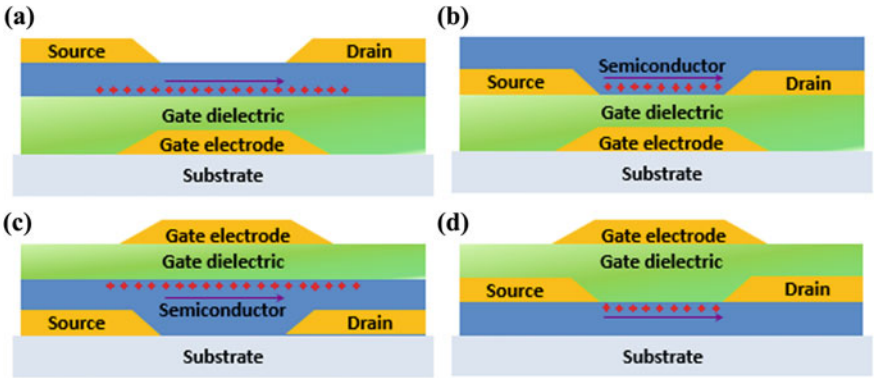

Fig. 2 Schematic diagram of the different device structure of TFT: **a** bottom-gate staggered TFT, **b** bottom-gate coplanar TFT, **c** top-gate staggered TFT, **d** top-gate coplanar TFT

in a semiconductor between two source/drain electrodes by the capacitive injection of carriers close to the dielectric/semiconductor interface known as field effect [9]. Figure 2a–d) shows schematic diagram of the most common structures of TFT. Based on the position of source/drain electrodes with respect to semiconductor layer, TFT structures can be classified according to Weimer's definition [22]. Depending on the position gate electrode, TFT structures can be also categorized as top- and bottom-gate structures. Each structure has advantages and disadvantages that depend on the type of TFT materials used for its fabrication. For instance, the staggered bottom-gate structure is normally preferred for the fabrication of a-Si-H TFTs due to its easy of processing and application in LCD. Coplanar top-gate configuration is favoured for the fabrication of poly-Si TFTs. Moreover, the semiconductor is exposed to air in both bottom-gate staggered and coplanar structure leading to instability of the device. But, the exposure to air can easily modify the properties of the semiconductor if annealed or plasma treated in appropriate atmosphere.

4 Calculation of the Trap Density of States in the Band Gap of Semiconductors

4.1 Crystalline Semiconductors

In a crystal, all the atoms are arranged in a pattern that repeats periodically in three dimensions to an infinite extend. The periodic nature of crystalline solid may lead to perfect electronic structure of the material. The density of electronic states takes the form of alternating energy region called bands separated by band gap. The band represents the large densities of electronic states, and no states are possible in the band gap. The well-defined structures in the valance and conduction bands are the main

features of the crystalline semiconductors. The energy distributions of the density of electronic states have the sudden ends at the valence band maximum and the conduction band minimum. Both long-range and short-range orders empower the perfect band structure of the crystalline solids. Even though crystalline solids are characterized by long-range periodic order, they contain defects such as vacancies, interstitials and dislocations.

4.2 Amorphous Semiconductors

The structure of amorphous semiconductors is defined by three principle features—the short-range order, the long-range disorder and the coordination defects. Amorphous and crystalline phases of the same material have comparable band gaps because of the similarity of the covalent bonds in crystalline and amorphous solids. The overall electronic structure of amorphous material compared to equivalent crystal arises from the preservation of the short-range order. Though the amorphous solid has short-range order, its long-range order is destroyed, and hence, they have long-range structural disorder [23].

The deviation from the perfect structure of bands in amorphous solid arises from the change in the bond length and bond angles of solid. Such disorder may cause electron and hole localization and scattering of carriers. The shape of abrupt band edges of crystal is changed to a broadened tail states and extends to forbidden band gap which arises from the long-range structural disorder (Fig. 3). The broadened tail states have significant effect on the electronic transport because electronic transport takes place at the band edge [24].

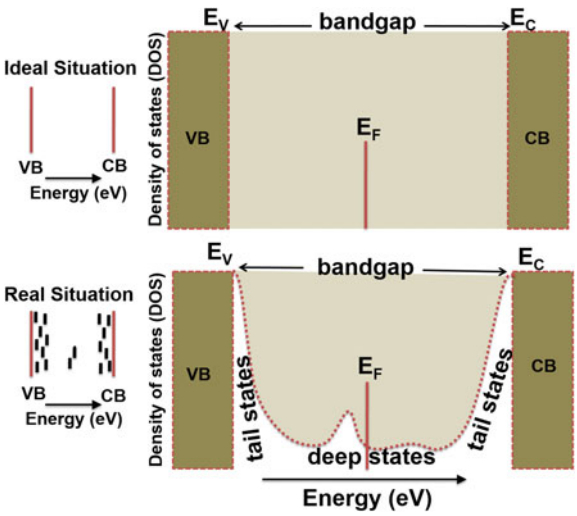

Fig. 3 Schematic representation of density of localized states in the band gap

Electronic states called deep states which lie in the band gap arises from the defects in the solids called coordination defects. Deep states are the consequences of broken bonds in the amorphous solid which determine many properties by controlling trapping and recombination. The densities of these localized tail and deep states in amorphous solids have profound effect on the electronic transport mechanism [25].

Charge transport in silicon transistors has been studied from the temperature-dependent transistor characteristics. In amorphous semiconductors, localized states induced by defects or impurities are distributed in the band gap. A variety of methods for the determination of the distribution of the trap DOS have been reported, and an exponential distribution of the DOS has been established. The knowledge about subgap DOS inside the channel material is essential for improving the device performance because DOS strongly affects the electrical properties of the thin-film transistors with disordered materials.

The localized gap states in amorphous silicon that limit electronic transport can be divided into two types, tail states and deep states [26]. The tail states exist just below the conduction band mobility edge, and they are formed by the broadening of conduction band of amorphous silicon. The Fermi level can be easily shifted through the exponential distribution of the localized states by applying gate voltage, so that thin-film transistors are useful tool for the study of DOS. These tail states determine the above threshold conduction (*ON* state of TFT) and hence the field-effect mobility. The deep states actually arise from the defect in amorphous silicon which decides the threshold voltage and subthreshold swing of TFT [27]. Density and nature of those localized states determine the transition from below-to-above threshold conduction (transition from *OFF* to *ON* state of TFT), and rate of transition can relate to the activation energy. More clearly, by applying the gate voltage, the Fermi level in the accumulation region moves from the deep to tail states in the energy band gap. The movement of Fermi level, and hence the rate of change of activation energy, with gate voltage gives a clear idea about the localized trap density in the band gap of semiconductor [28].

4.3 Analytical Description of an Ideal Thin-Film Transistor

The density of localized states in the band gap of amorphous solid was determined by fabricating a thin-film transistor and measuring its temperature-dependent field-effect conductivity for various gate voltages. The basic principles of device physics were used for the computation of trap DOS [26, 28]. Figure 4 shows the schematic structure of thin-film transistor.

To estimate the DOS in the band gap, electrical characterization of n-type TFT such as output characteristics and transfer characteristics is done by varying the temperature. Different parameters like threshold voltage, field-effect mobility, saturation mobility, and subthreshold voltage swing are then derived from these characteristics. The output characteristics of TFT are similar to those of the MOSFET. Hence, the drain current can be expressed by the relations [29]:

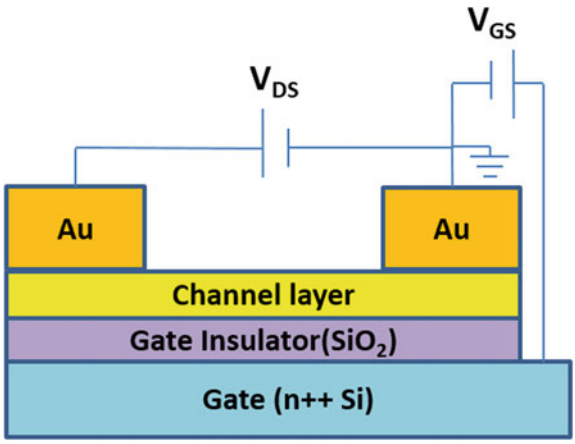

Fig. 4 Schematic structure of n-type thin-film transistor

$$I_{\mathrm{D}} = \mu C_i \frac{W}{L}\left[(V_{\mathrm{GS}} - V_{\mathrm{T}})V_{\mathrm{DS}} - \frac{V_{\mathrm{DS}}^2}{2}\right], \quad \text{for } V_{\mathrm{DS}} \leq V_{\mathrm{GS}} - V_{\mathrm{T}} \tag{1}$$

and

$$I_{\mathrm{D}} = \frac{1}{2}\mu C_i \frac{W}{L}(V_{\mathrm{GS}} - V_{\mathrm{T}})^2, \quad \text{for } V_{\mathrm{DS}} \geq V_{\mathrm{GS}} - V_{\mathrm{T}} \tag{2}$$

where μ is the average mobility of the carriers in the channel, C_i is the capacitance of the insulator per unit area, W is the channel width, L is the channel length, V_{GS} is the gate–source voltage, V_{DS} is the drain–source voltage, and V_{T} is the threshold voltage.

The band mobility and threshold voltage can be estimated from the linear dependence of the drain current on the effective gate voltage (Fig. 5). They are the most important device performance parameters, and its numerical values give overall idea about the defect levels in the semiconductor channel layer. The threshold voltage is defined as the gate voltage above which all the added gate-induced charge is free; it depends on the trap density in the semiconductor channel layer. For TFTs, operating in the linear region ($V_{\mathrm{DS}} \leq V_{\mathrm{GS}} - V_{\mathrm{T}}$) Eq. (1) can be written as:

$$I_{\mathrm{D}} \approx \mu C_i \frac{W}{L}(V_{\mathrm{GS}} - V_{\mathrm{T}})V_{\mathrm{DS}} \tag{3}$$

The high field-effect mobility and the near-zero threshold voltage show the existence of low trap density at insulator–semiconductor interface. The threshold voltage also depends on the flat band voltage, which describes the applied gate voltage in order to enforce flat bands at the insulator–semiconductor interface. The charge that is permanently trapped at the insulator–semiconductor interface or within the gate dielectric influences the flat band voltage. As a result, there exists a Fermi level

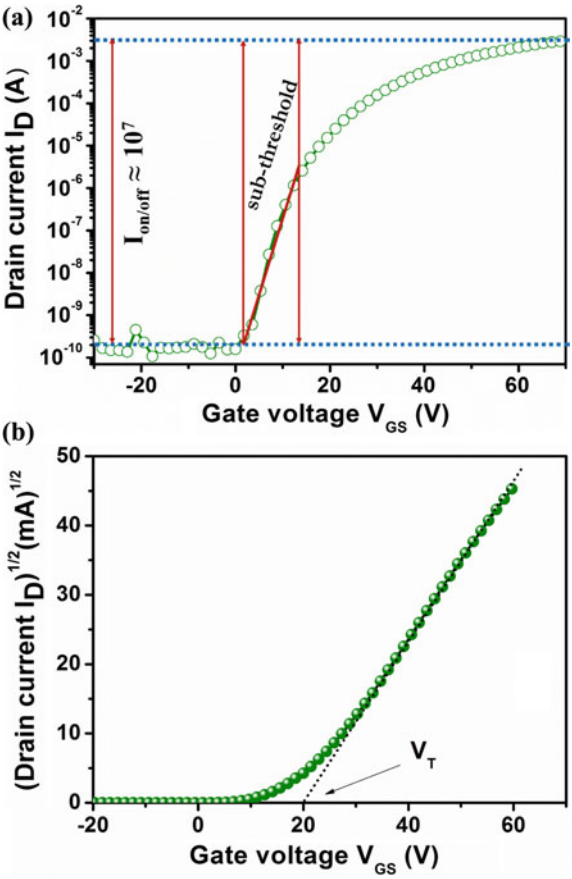

Fig. 5 Extraction of n-type TFT parameters from the transfer characteristics

dissimilarity between the semiconductor and the gate electrode and may cause the nonzero flat band voltage [30].

The high trap density results in the drain current to increase more rapidly, and hence, the trans-conductance increases monotonically with gate voltages. The deviations from the ideal actions are due to the increasing fraction of the gate-induced charges that are free with gate voltage. Such deviations of drain current may result in the indistinct determination of threshold voltage and mobility. In this type of devices, that have high trap density, the threshold voltage is not reached even at very high gate voltage. Both the amorphous silicon and organic field-effect transistors show such behaviour since they have high density of localized states in the band gap of semiconductor.

Figure 6 illustrates the basic operation behind the n-type TFT by plotting density of states of the electronic sates. The amount of band bending and the occupancy of electronic states can be controlled by applied gate voltage. At zero gate voltage, the bands have no bending, i.e. in flat band condition. When nonzero gate voltage applied

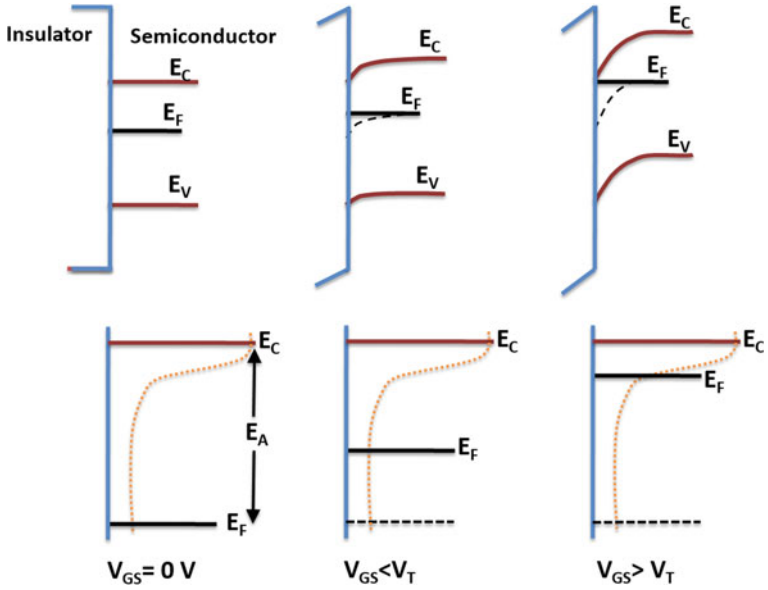

Fig. 6 Schematic representation of the basic operation behind the n-type TFT by plotting density of states of the electronic sates

(say positive voltage), below threshold voltage leads to downward band bending. Small gate voltage enables Fermi level movement through the deep states and the occupancy of deep states. As increasing voltage slightly, the band bending increases and the space charge in the deep states increases which results in exponential current increase in the pre-threshold region. Further increase in gate voltage, above threshold voltage, the space charge in the tail states increases linearly with the gate voltage and has well-defined thermally activated field-effect mobility [30].

The above-mentioned equations are valid for devices with a low trap density and insignificant contact resistances. The trapping and release time of carries in traps are expected to be much shorter than the time needed to measure a transistor characteristic [31]. But in reality, the high density of traps has made deviations in the characteristics, and in order to use such equations, following assumptions are made [32].

(1) The semiconductor is homogenous perpendicular to the insulator–semiconductor interface, and hence, the charge density is homogenous along the transistor channel
(2) Insulator surface states only contribute to a nonzero flat band voltage
(3) Fermi function for the trapped carries is approximated by a step function.

The calculated trap DOS from the measured data can have a significant effect on the assumptions. The incorrect simplification may lead to ambiguous output which results in underestimation of density of trap sates.

The drain current in the linear regime may be written as

$$I_{\mathrm{D}} = \frac{W}{L}\sigma V_{\mathrm{DS}} \tag{4}$$

and the field-effect conductivity is

$$\sigma = \mu C_i (V_{\mathrm{GS}} - V_{\mathrm{FB}}) \tag{5}$$

V_{FB} is the flat band voltage and μ is the gate-voltage-dependent field-effect mobility. The field-effect conductivity can be calculated from:

$$\sigma(V_{\mathrm{GS}}) = \frac{L}{W}\frac{I_{\mathrm{D}}}{V_{\mathrm{DS}}}. \tag{6}$$

5 Density of States Calculation of n-Type Amorphous Zinc Tin Oxide TFT

In order to study the distribution of the trap states in the ZTO channel layer, we have examined the temperature-dependent transfer characteristics of transistors in the temperature range between 310 and 360 K (Fig. 7) [33].

For this method, the activation energy $E_{\mathrm{A}}(V_{\mathrm{GS}})$ is defined by

$$\sigma(V_{\mathrm{GS}}) = A \exp\left(-\frac{E_{\mathrm{A}}}{kT}\right) \tag{7}$$

and A is assumed to be a constant.

The activation energy is determined from the measured data with a linear regression of Arrhenius plot drawn between $\ln I_{\mathrm{D}}$ versus $1000/T$ for each gate voltage. We have an equation connecting E_{A} and I_{D} as,

$$\ln I_{\mathrm{D}} = \ln A - E_{\mathrm{A}}/kT \tag{8}$$

The slope of these curves for each gate voltages gives the activation energy. The E_{A} is the difference in energy between the Fermi level and the transport band edge. The Fermi level positions in the semiconductor for each gate voltages can be easily found out from the E_{A} values.

The large E_{A} is attributed to a comparatively large number of charge traps existing in the band gap; the traps prevent the Fermi level from approaching to the conduction band edge, because of the charge induced by V_{GS} is trapped. As gate voltages increases, the Fermi level moves to band edge and the rate of change of variation with respect to the gate voltage is determined by the trap levels inside the semiconductor. The direct connection between Fermi level and E_{A} enables the identification of trap states by plotting the variation of E_{A} with respect to gate voltage. The E_{A}

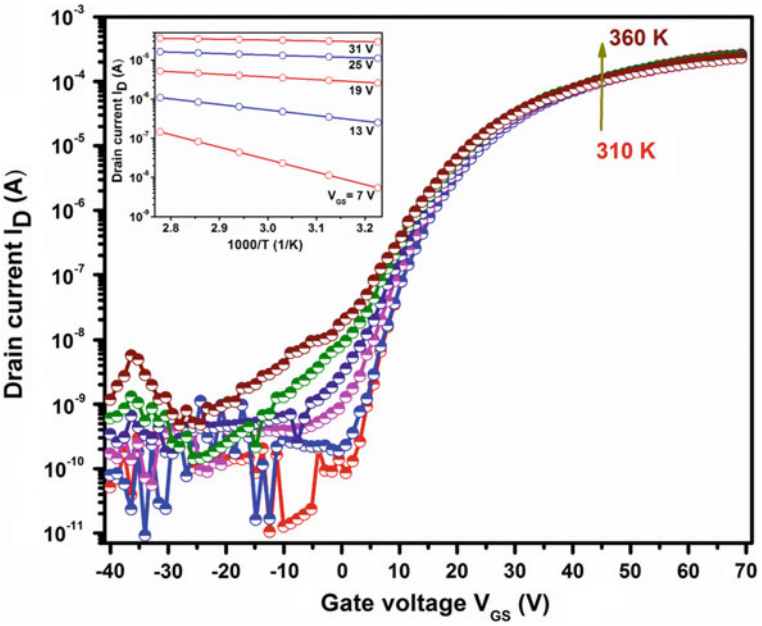

Fig. 7 Transfer characteristics measured at different temperatures during heating of ZTO TFT. Inset figure shows the Arrhenius plot of the drain current versus 1000/T for different gate voltages

decreases exponentially with increasing gate voltage, and the rate of change of E_A with respect to gate voltage gives the direct quantification of the localized traps states in the semiconductor (Fig. 8).

The activation energy E_A in the multiple trapping and thermal release model (MTR) is interpreted as the energy barrier for thermal release of trapped carriers. In particular, the activation energy reduces with increasing the gate voltage as the Fermi level moves towards the band edge. The existence of low trap density of states indicated by the fast variation of E_A with V_{GS} and a high DOS in the gap would result in slower variations of E_A with V_{GS}. Then, assuming that charge density within the channel is dominated by trapped carriers, concentration of free carriers is much less as compared with the concentration of trapped carriers, the DOS can be related to the derivative of the activation energy with respect to gate bias [28].

$$N(E) = \frac{C_i}{q} \frac{1}{t \frac{dE_A}{dV_{GS}}} \tag{9}$$

where E is the energy measured from the valence band edge, C_i is the capacity of the insulator per unit area and q is the elementary charge. A channel thickness (t) of 5 nm has been considered for the calculation DOS. Figure 9 shows the density of states in the band gap of ZTO channel calculated from the derivative of the activation energy of ZTO TFT [33].

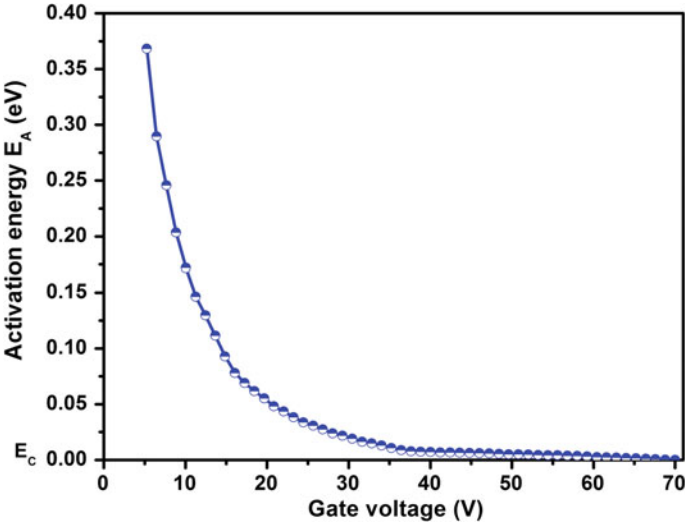

Fig. 8 Dependence of E_A with the gate voltage of ZTO TFT

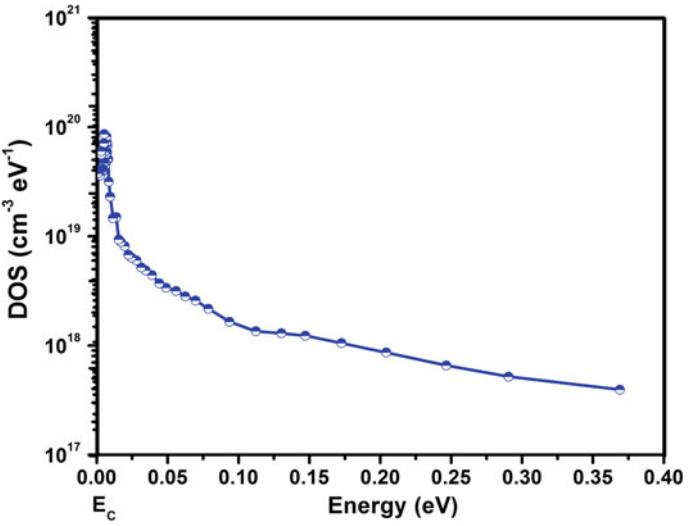

Fig. 9 Density of states in the band gap of ZTO channel calculated from the derivative of the activation energy of ZTO TFT

The estimated defect-induced subgap density of states was around 10^{20} cm^{-3} eV^{-1}, and those large amounts of electronic trap states in ZTO semiconductors severely affect the performance of ZTO TFTs.

6 Density of States Calculation of Organic Thin-Film Transistor

The multiple trapping and thermal release models can be used in the case of organic semiconductors also because such materials have large number of localized traps that exist in the band gap. In inorganic amorphous semiconductors, the n-type materials are more stable and give better device performance. In contrary, organic n-type semiconductor materials are not stable because of interactions with the ambient atmosphere, but the p-type materials like pentacene are giving better stability with surrounding environment. Nowadays, the field of organic electronics emerges with great interest because of the realization of the application of low-cost flexible devices. The major problem of the organic devices is their poor performance and environmental stability. The performances of organic n-type and p-type-based devices such as organic thin-film transistor (OTFT) mainly depend on the density of localized trap states in the band gap of materials. So it is very important to explore the amount of traps states in those materials because it will help the enhancement of device performance by optimizing the fabrication conditions.

6.1 Density of States Calculation of n-Type PTCDI-C8 Thin-Film Transistor

The n-type *N*,*N*′-Dioctyl-3,4,9,10-perylenedicarboximide (PTCDI-C8) was used as the channel layer for the fabrication of OTFT. During the electrical characterization, the device temperature was varied from 300 to 360 K (Fig. 10a). Figure 10b shows the variation of E_A with respect to the gate voltages, and the exponential decrease in the activation energy with gate voltage indicated that Fermi level moved towards the band edge very quickly. In the organic semiconductor theory, E_A indicates the energy difference between Fermi level position and the transport band edge (here, Lowest Unoccupied Molecular Orbit/LUMO level). Then, assuming that the charge density within the organic channel layer is dominated by trapped carriers, the DOS can be determined from the derivative of the activation energy with respect to gate bias.

The exponential region of the DOS can be assumed as band tail of localized states induced by structural disorder (Fig. 10c). The large amount of subgap DOS ($>10^{18}$ cm^{-3} eV^{-1}) is the reason for the small value of field-effect mobility extracted in fabricated OTFTs. The instability of n-OTFTs was due to the trapping of electrons in the localized trap states created by absorbed oxygen in the PTCDI-C8 layer. These electron traps were found to be situated at around 0.15 eV above the LUMO level. The study of DOS in OTFTs will give complete understanding of trap-limited transport in organic thin-film semiconductors [34].

In brief, the valuable information about the DOS in the active layer can be collected from the gate voltage-dependent activation energy of the channel conductance.

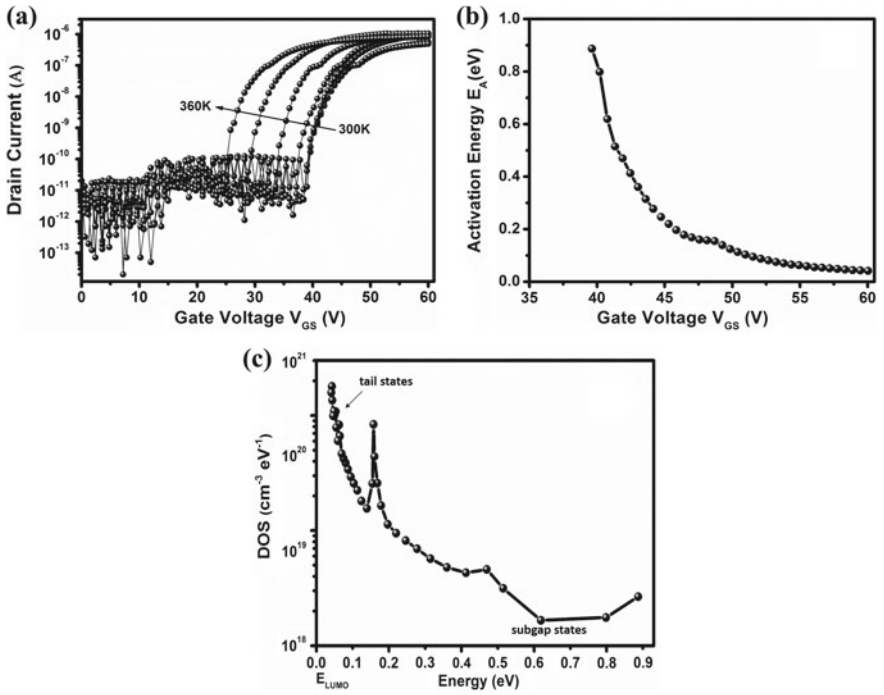

Fig. 10 **a** Transfer characteristics of OTFTs measured at different temperatures during heating. **b** E_A variation with the gate voltage. **c** Calculated density of states in the gap of PTCDI-C8 [34]

The electronic trap states in amorphous oxide and organic semiconductors rigorously affect the performance of such devices; therefore, the understanding of such defect states is important to enhance the device parameters. For instance, in TFT the key device parameters such as the field-effect mobility, the threshold voltage, the sub-threshold swing as well as the electrical and environmental stability are significantly influenced by trap states inside the semiconductor. Also, by studying the nature of the trap states inside the novel materials, the prediction of their optical and electrical properties can be properly accounted for future prospects.

References

1. Wager JF, Hoffman R (2011) Thin, fast, and flexible. IEEE Spectr 48. https://doi.org/10.1109/mspec.2011.5753244
2. Rupprecht G (1954) Investigations of the electrical and photoelectric conductivity of thin indium oxide layers. Z Phys 139:504–517. https://doi.org/10.1007/BF01374559

3. Park JS, Kim TW, Stryakhilev D, Lee JS, An SG, Pyo YS, Lee DB, Mo YG, Jin DU, Chung HK (2009) Flexible full color organic light-emitting diode display on polyimide plastic substrate driven by amorphous indium gallium zinc oxide thin-film transistors. Appl Phys Lett 95:93–96. https://doi.org/10.1063/1.3159832
4. Riedl T, Gorrn P, Kowalsky W (2009) Transparent electronics for see-through AMOLED displays. IEEE/OSA J Disp Technol 5:501–508. https://doi.org/10.1109/JDT.2009.2023093
5. Lilienfeld JE (1930) US patents# 1,745,175, 18 Jan 1930
6. Lilienfeld JE (1932) US patents 1,877,140, 13 Sept 1932
7. Lilienfeld JE (1933) US Patent 1900018
8. Heil O (1935) British Patent 439 457, Appl. filed, vol 4
9. Tickle AC (1969) Thin-film transistors: a new approach to microelectronics
10. Weimer PK (1962) The TFT—a new thin-film transistor. Proc IRE 50(50):1462–1469. https://doi.org/10.1109/JRPROC.1962.288190
11. Olsen LC, Bohara RC, Urie MW (1979) Explanation for low-efficiency Cu_2O Schottky-barrier solar cells. Appl Phys Lett 34:47–49. https://doi.org/10.1063/1.90593
12. Klasens HA, Koelmans H (1964) A tin oxide field-effect transistor. Solid State Electron 7:701–702. https://doi.org/10.1016/0038-1101(64)90057-7
13. Boesen GF, Jacobs JE (1968) ZnO field-effect transistor. Proc IEEE 56:2094–2095. https://doi.org/10.1109/PROC.1968.6813
14. Norris BJ, Wager JF, Hoffman RL (2003) ZnO-based transparent thin-film transistors. Appl Phys Lett 82:733. https://doi.org/10.1063/1.1542677
15. Carcia PF, McLean RS, Reilly MH, Nunes G (2003) Transparent ZnO thin-film transistor fabricated by rf magnetron sputtering. Appl Phys Lett 82:1117–1119. https://doi.org/10.1063/1.1553997
16. Nomura K, Ohta H, Takagi A, Kamiya T, Hirano M, Hosono H (2004) Nature 432:488. https://doi.org/10.1038/nature03090
17. Kamiya T, Nomura K, Hosono H (2010) Present status of amorphous In-Ga-Zn-O thin-film transistors. Sci Technol Adv Mater 11:044305. https://doi.org/10.1088/1468-6996/11/4/044305
18. Han S, Lee D, Herman GS, Chang C (2009) Inkjet-printed high mobility transparent–oxide semiconductors. J Disp Technol 5:520–524. https://doi.org/10.1109/JDT.2009.2024330
19. Norris BJ, Anderson J, Wager JF, Keszler DA (2003) Spin-coated zinc oxide transparent transistors. J Phys D Appl Phys 36:L105–L107. https://doi.org/10.1088/0022-3727/36/20/L02
20. Ong BS, Li C, Li Y, Wu Y, Loutfy R (2007) Stable, solution-processed, high-mobility ZnO thin-film transistors. J Am Chem Soc 129:2750–2751. https://doi.org/10.1021/ja068876e
21. Cheng HC, Chen CF, Lee CC (2006) Thin-film transistors with active layers of zinc oxide (ZnO) fabricated by low-temperature chemical bath method. Thin Solid Films 498:142–145. https://doi.org/10.1016/j.tsf.2005.07.101
22. Wallmark JT, Johnson H (1966) Field-effect transistors: physics, technology and aplications. Prentice Hall, Upper Saddle River
23. Weaire D, Thorpe MF (1971) Electronic properties of an amorphous solid. I. A simple tight-binding theory. Phys Rev B 4:2508–2520. https://doi.org/10.1103/physrevb.4.2508
24. Unger K (1981) Amorphous semiconductors. Krist Tech 16:12
25. Marshall JM, Owen AE (1971) Drift mobility studies in vitreous arsenic triselenide. Philos Mag 24:1281–1305. https://doi.org/10.1080/14786437108217413
26. Powell MJ (1989) The physics of amorphous-silicon thin-film transistors. IEEE Trans Electron Devices 36:2753–2763. https://doi.org/10.1109/16.40933
27. Slade HC, Shur MS, Deane SC, Hack M (1996) Below threshold conduction in a-Si: H thin film transistors with and without a silicon nitride passivating layer. Appl Phys Lett 69:2560–2562. https://doi.org/10.1063/1.117739
28. Globus T, Slade HC, Shur M, Hack M (1994) Density of deep bandgap states in amorphous silicon from the temperature dependence of thin film transistor current. MRS Proc 336:823. https://doi.org/10.1557/PROC-336-823
29. Kagan CR, Andry P (2003) Thin-film transistors. CRC Press, New York

30. Shur M, Hack M (1984) Physics of amorphous silicon based alloy field-effect transistors. J Appl Phys 55:3831–3842. https://doi.org/10.1063/1.332893
31. Jackson WB (1988) Connection between the Meyer-Neldel relation and multiple-trapping transport. Phys Rev B 38:3595–3598. https://doi.org/10.1103/physrevb.38.3595
32. Kalb WL, Batlogg B (2010) Calculating the trap density of states in organic field-effect transistors from experiment: a comparison of different methods. Phys Rev B-Condens Matter Mater Phys 81:1–13. https://doi.org/10.1103/physrevb.81.035327
33. Shijeesh MR, Saritha AC, Jayaraj MK (2018) Investigations on the reasons for degradation of zinc tin oxide thin film transistor on exposure to air. Mater Sci Semicond Process 74:116–121. https://doi.org/10.1016/j.mssp.2017.10.015
34. Shijeesh MR, Vikas LS, Jayaraj MK, Puigdollers J (2014) Degradation study and calculation of density-of-states in PTCDI-C8 channel layer from the electrical characteristics of thin-film transistors. J Appl Phys 116:024507. https://doi.org/10.1063/1.4890023